



AFRL-OSR-VA-TR-2015-0196

Reduced Basis and Stochastic Modeling of Liquid Propellant Rocket Engine as a Complex System

william sirignano
UNIVERSITY OF CALIFORNIA IRVINE

07/02/2015
Final Report

DISTRIBUTION A: Distribution approved for public release.

Air Force Research Laboratory
AF Office Of Scientific Research (AFOSR)/ RTE
Arlington, Virginia 22203
Air Force Materiel Command

REPORT DOCUMENTATION PAGE			Form Approved OMB No. 0704-0188	
<p>The public reporting burden for this collection of information is estimated to average 1 hour per response, including the time for reviewing instructions, searching existing data sources, gathering and maintaining the data needed, and completing and reviewing the collection of information. Send comments regarding this burden estimate or any other aspect of this collection of information, including suggestions for reducing the burden, to Department of Defense, Executive Services, Directorate (0704-0188). Respondents should be aware that notwithstanding any other provision of law, no person shall be subject to any penalty for failing to comply with a collection of information if it does not display a currently valid OMB control number.</p> <p>PLEASE DO NOT RETURN YOUR FORM TO THE ABOVE ORGANIZATION.</p>				
1. REPORT DATE (DD-MM-YYYY) 21-07-2015	2. REPORT TYPE Final Performance	3. DATES COVERED (From - To) 01-06-2012 to 30-05-2015		
4. TITLE AND SUBTITLE Reduced Basis and Stochastic Modeling of Liquid Propellant Rocket Engine as a Complex System		5a. CONTRACT NUMBER		
		5b. GRANT NUMBER FA9550-12-1-0156		
		5c. PROGRAM ELEMENT NUMBER		
6. AUTHOR(S) william sirignano		5d. PROJECT NUMBER		
		5e. TASK NUMBER		
		5f. WORK UNIT NUMBER		
7. PERFORMING ORGANIZATION NAME(S) AND ADDRESS(ES) UNIVERSITY OF CALIFORNIA IRVINE 5171 CALIFORNIA AVE STE 150 IRVINE, CA 92617 US			8. PERFORMING ORGANIZATION REPORT NUMBER	
9. SPONSORING/MONITORING AGENCY NAME(S) AND ADDRESS(ES) AF Office of Scientific Research 875 N. Randolph St. Room 3112 Arlington, VA 22203			10. SPONSOR/MONITOR'S ACRONYM(S) AFOSR	
			11. SPONSOR/MONITOR'S REPORT NUMBER(S)	
12. DISTRIBUTION/AVAILABILITY STATEMENT A DISTRIBUTION UNLIMITED: PB Public Release				
13. SUPPLEMENTARY NOTES				
14. ABSTRACT The four-institution research team has developed a framework for stochastic analysis of nonlinear combustion instability with triggering and in the use of reduced-basis models (RBM), large-eddy simulations, and multi-scale asymptotic models for the analysis. Results published during these three years and ongoing researches are briefly discussed and addenda with more detail are provided.				
15. SUBJECT TERMS Rocket Engine, Stochastic				
16. SECURITY CLASSIFICATION OF: a. REPORT b. ABSTRACT c. THIS PAGE		17. LIMITATION OF ABSTRACT UU	18. NUMBER OF PAGES	19a. NAME OF RESPONSIBLE PERSON william sirignano
				19b. TELEPHONE NUMBER (Include area code) 948-824-3700

**Reduced Basis and Stochastic Modeling of a
Liquid Propellant Rocket Engine as a Complex System**
Final Performance Report: June 1, 2012 - May 31, 2015
AFOSR Grant FA 9550-12-1-0156, Mitat Birkan: Program Manager

Prepared by

W. A. Sirignano (PI), A. Sideris, P.P. Popov, University of California, Irvine;
S. Menon, S. Srinivasan, R. Ranjan, T. Dawson, P. Tudisco, Georgia Institute of Technology;
R. Munipalli, Z. Liu, D. Ota, HyPerComp Inc.; and
D. R. Kassoy, Kassoy Innovative Science Solutions.

Submitted June 15, 2015.

Summary

The four-institution research team has developed a framework for stochastic analysis of nonlinear combustion instability with triggering and in the use of reduced-basis models (RBM), large-eddy simulations, and multi-scale asymptotic models for the analysis. Results published during these three years and ongoing researches are briefly discussed and addenda with more detail are provided.

Table of Contents

Summary	1
I. Introduction	2
II. Stochastic Model Development	3
III. Large Eddy Simulations	7
IV. Thermomechanical Processes	12
V. Reduced Basis Modeling for Combustion Dynamics	16
VI. Concluding Remarks	20

Addenda

1. Driving Mechanisms for Combustion Instability, W. A. Sirignano.
2. Transverse Combustion Instability in a Rectangular Rocket Motor, P. P. Popov, A. Sideris and W. A. Sirignano.
3. Triggering of Combustion Instability by Acceleration of the Rocket Motor, P. P. Popov, A. Sideris and W. A. Sirignano.
4. Nonlinear Two-time-scale Perturbation Theory for Liquid-Rocket Transverse Combustion Instability, W. A. Sirignano and J. Krieg.
5. Experimental and Numerical Investigation for a GOX-GCH₄ Shear-Coaxial Injector Element, M. P. Celano, S. Silvestri, G. Schlieben, C. Kirchberger, O. J. Haidn, T. Dawson, R. Ranjan, and S. Menon.
6. LES of GCH₄/GOX, Shear-Coaxial, Single Element, High Pressure Rocket Combustor: Effects of Thermal Condition and Chemical Kinetics, R. Ranjan, and S. Menon.
7. On the Application of the Time-Domain Admittance Boundary Conditions in the LES of a High-Pressure, Shear-Coaxial Injector Combustor, P. Tudisco, R. Ranjan, S. Menon, S. Jaensch, and W. Polifke.
8. Flame Dynamics During Combustion Instability in a High-Pressure, Shear-Coaxial Injector Combustor, S. Srinivasan, R. Ranjan, and S. Menon.

9. Numerical Investigation of Transverse Combustion Instability in a Multi-Element, Shear-Coaxial, High Pressure Combustor, P. Tudisco, R. Ranjan, and S. Menon,
10. The Zel'dovich Spontaneous Reaction Wave Propagation Concept in the Fast/ Modest Heating Limits, D. R. Kassoy

I. Introduction:

The research follows the plan outlined in the proposal and sketched here in Figure 1. Work has proceeded on the development of various foundational material: basic injection and combustion, wave-dynamic, and asymptotic models; framework for stochastic analysis; large-eddy simulation capability; and reduced-basis modelling capability.

The model studies, stochastic analysis framework, large-eddy simulations, and reduced-basis modelling have advanced well.. The physical understanding of triggering mechanisms and driving mechanisms has been advanced. Some early progress on mitigation and control has been seen. Discussion in the next four sections will provide some detail. Additional detail is provided through the addenda.

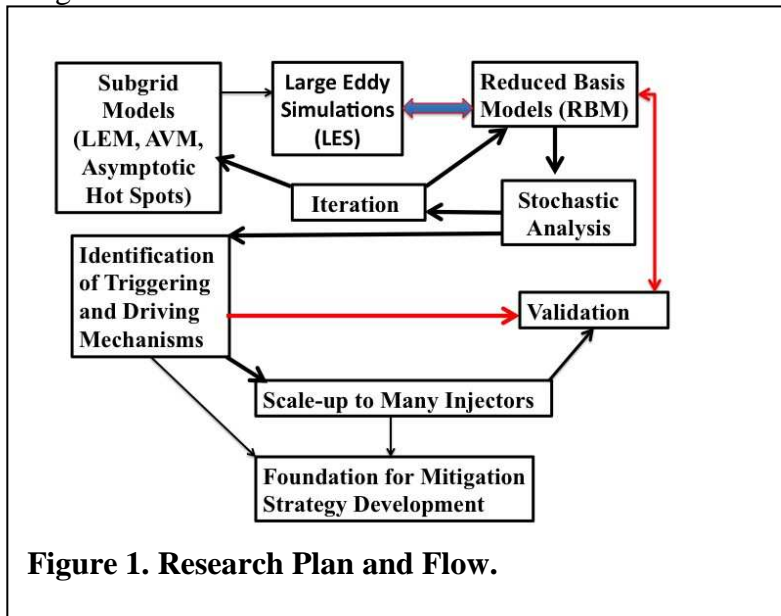


Figure 1. Research Plan and Flow.

The research team members have been directly interactive with each other, the Air Force Research Lab personnel, and the Purdue University experimental rocket group. Communications have been maintained with the general combustion / propulsion community and the combustion instability community through journal publications, conference participation, and through various informal mechanisms.

The development of stochastic models at UCI is discussed in the next section and Addenda 1, 2, 3, and 4. The LES advancements at Georgia Tech are presented in Section III and Addenda 5, 6, and 7. In Section IV and the Addenda 8, we present the research on thermomechanical processes at KISS. The HyPerComp research on RBM is discussed in Section V. Concluding remarks are briefly made in Section VI.

II. Stochastic Model Development - UCI

The major accomplishments of the three-year effort at UCI include several forefront developments in terms of both analysis and findings. (1) A computational model has been developed for nonlinear LPRE instability in a cylindrical combustion chamber with multi-port co-axial injection of bi-propellants which is able to predict based on injector configuration, mixture ratio, mean chamber pressure, and mean flow Mach number the three types of stability zones: unconditionally unstable, unconditionally stable and bi-stable (aka conditionally stable or conditionally unstable). Triggering is possible in the bi-stable domain. (2) The model has been extended to include coupling between the flow upstream through the injectors and the chamber oscillations. (3) To make a comparison with experiments conducted at Purdue University, a parallel model has been developed for a rectangular chamber with seven linearly aligned co-axial injectors. Very good agreement with experiment was found. (4) The descriptive parameters of the stochastic triggering disturbance have been represented as random variables and the probability and marginal probabilities of a limit-cycle oscillation developing have been determined. (5) A stochastic analytical approach based on polynomial chaos expansions (PCE) has been shown to be much more efficient than Monte Carlo methods for this type of calculation. (6) Three types of triggering pulses have been examined: rogue events in the combustion or flow within the chamber; partial blockage in the injector flow; and transverse acceleration or vibration of the combustion chamber as a rigid body. All three types can produce triggering if their amplitudes are sufficient. The identification of motor acceleration as a plausible trigger is novel. (7) It has been shown that any of these types of disturbances can potentially be used deliberately in a control mechanism which arrests the growth of the instability and maintains a stable operation of the engine. (8) The PCE method was extended to use polynomials in both the random variables describing the disturbance and design parameters describing key features of the injector configuration. (9) A perturbation analysis based on the two-time-variable approach has been developed to give useful insights and guides to the computationally intensive problem.

Basic Model: The combustion oscillations were modelled with a multi-scale approach. The equations of wave dynamics were inviscid on the larger scale; energy from the combustion process was provided via coupling from the flame dynamics which were evaluated on a finer scale for each co-axial injector exit jet; a multi-orifice short nozzle was considered; the emphasis was placed on transverse waves and the equations were averaged over the main-flow direction, reducing the system to a two-dimensional unsteady formulation. The combustion dynamics were analyzed for each co-axial methane-oxygen jet emerging from the injectors. On the finer-scale analysis, axisymmetric transport, reaction, and advection were examined for the unsteady flow. The combustion process was coupled to the wave dynamics through the local pressure, temperature, and velocity values of the wave which were described as ambient values for the jet. Disturbances were provided as either small-amplitude resonant waves or focused pulses in the chamber, with the latter representing rogue behavior in the combustion or turbulent processes.

The results showed that, depending on mixture ratio and mass flow, three types of stability behavior were identified: unconditional stability where any disturbance decays to steady-state operation; unconditional instability where any disturbance, no matter how small, grows to a limit-cycle oscillation; and conditional instability where disturbances below a threshold decay while those above the threshold grow to large amplitude. These results are contained in

W. A. Sirignano and P. Popov, "Two-dimensional Model for Liquid-Rocket Transverse Combustion Instability", *AIAA Journal* 51, Issue 12, pp.2919-34, 2013. doi: 10.2514/1.J052512.

which was appended in a previous Annual Report. A more recent overview of our work and some related background information is given in

W. A. Sirignano, "Driving Mechanisms for Combustion Instability," invited paper, Forman Williams Commemorative Issue, *Combustion Science and Technology* 187, pp. 1-44, 2014

which is appended here. Since adequate experimental data for unstable circular combustion chambers did not exist, a parallel model was developed for a particular chamber with rectangular cross-section.

Experimental Verification: The parallel model was developed for the analytical of the Purdue University combustor with a rectangular-chamber, seven linearly aligned co-axial injectors, and long, divergent, choked nozzle. Agreement with experiment was excellent with predictions of the observed unconditional instability and a very good match for frequencies and limit-cycle amplitudes for all of several experimental injector configurations. The model predicted bi-stable behavior in regions that were not studied experimentally. The work is reported in

P. P. Popov and W. A. Sirignano, "Transverse Combustion Instability in a Rectangular Rocket Motor," submitted to *Journal of Propulsion and Power*, 2015

which is appended here. The verification supported the validity of the major assumptions in the model.basic

Stochastic Formulation and Polynomial Chaos Expansion: The characteristics of the stochastic disturbance were described as random variables. The equations were re-cast into a larger system governing the coefficients in the Legendre-polynomial expansion of the dependent variables. Several forms of disturbances were applied at random locations in chamber with random magnitude, duration, orientation, and frequency. The probability and marginal probabilities of triggering growth to the deterministic limit cycle were calculated. The types of disturbances included oscillating dipoles, directed pulses, and initial small-amplitude waves. To establish travelling or spinning waves, an orientation of the pulse was required. Standing waves were established in cases where the disturbance had no initial orientation. The results were reported in P. P. Popov, A. Sideris, and W. A. Sirignano, "Stochastic Modeling of Transverse Wave Instability in a Liquid Propellant Rocket Engine," *Journal of Fluid Mechanics* 745, pp. 62-91, 2014. doi:10.1017/jfm.2014.96 which was appended in a previous Annual Report.

The Polynomial Chaos Expansion (PCE) was shown to converge and for this problem to be much more efficient than the Monte Carlo method. The calculations indicated how probabilities changed with each parameter that represented a characteristic of the triggering disturbance. This PCE approach formed a basis for our following studies.

Injector Coupling: The coupling with injector flows modifies both the stability and natural frequency. In the extended study to include injector coupling, partial blockage on an injector was allowed for a specific duration. Again, the same three types of stability zones described above were identified in this analysis. The work is described in

P. P. Popov, A. Sideris, and W. A. Sirignano, "Propellant Injector Influence on Liquid Propellant Rocket Engine Instability," *Journal of Propulsion and Power* 31 (1), pp. 320-31, 2015a

which was appended in a previous Annual Report.

The probability of triggering growth to a limit-cycle oscillation in the combustion chamber was determined. In addition to using the random variables describing the disturbance in the PCE, additional variables related to injector design were used. Thus, the marginal probability of triggering based on design variables could also be determined.

A New Triggering Mechanism – Motor Acceleration: Following a suggestion from Dr. D. Talley of the Air Force Research Labs, the potential for rigid body transverse acceleration of vibration was examined as a possible cause of triggered combustion instability. Both the circular chamber and rectangular were studied with linear transverse acceleration. The circular chamber was also studied for situations where the transverse acceleration vector direction was rotating. It was revealed for the first time that accelerations at plausible magnitudes could trigger instability. PCE was used to predict probability and marginal probabilities a function of magnitude, duration, and frequency of the acceleration pulse. The results are reported in P. P. Popov, A. Sideris, and W. A. Sirignano, “Triggering of Combustion Instability by Acceleration of the Rocket Motor,” submitted to *AIAA Journal*, 2015b which is appended here.

Potential Control Mechanism: In the above-mentioned recent papers, Pavel et al. 2015a, 2015b, The use of “anti-pulses” of the oscillating dipole, blocked-injector flow, and motor-acceleration types were shown, with proper design and timing, to be capable of arresting the growth of a triggered instability. Thus, it forms a plausible basis for control of combustion instabilities and should open new promising research directions.

Nonlinear Perturbation Theory: Although, the UCI program has advanced our knowledge based on computational analysis, much insight, information, and guidance becomes available through nonlinear perturbation theory. A third-order, two-time variable method was used where oscillations were described on the fast scale while change of amplitude and phase were described using the slower scale. Unstable limit cycles and transient behavior were predicted. The method provided a direct method to describe the amplifying or damping role of each term in the analysis. A survey over parameter space could be accomplished much more swiftly. The study is described in

W. A. Sirignano and J. Krieg, “Nonlinear Two-time-scale Perturbation Theory for Liquid-Rocket Transverse Combustion Instability,” near ready for journal submission, 2015c which is appended here. This approach is expected to provide useful guidance in the future.

Interactions with Team Members: We have shared drafts of our publications with other team members as early as feasible. Results from the various team member have been discussed. Copies of our computer code have been shared with HyPerComp for use in guiding the Reduced-basis Modeling calculations. Meetings and phone conversations with Dr. Munipalli have occurred often during the course of this program.

Conference Papers: Several conference papers were also presented as pre-cursors to the journal papers.

W. A. Sirignano and P. Popov, “Two-dimensional Model for Liquid-Rocket Transverse Combustion Instability,” *AIAA Aerospace Sciences Meeting*, Grapevine, Texas, January 2013.

P. P. Popov, A. Sideris, and W. A. Sirignano, “Stochastic Modeling of Transverse Wave Instability in a Liquid Propellant Rocket Engine,” *Joint Propulsion Conference*, San Jose, CA, July 2013.

P. P. Popov, A. Sideris, and W. A. Sirignano, “Propellant Injector System Influence on Rocket Engine Combustion

Instability," *AIAA Aerospace Sciences Meeting*, National Harbor, MD, January 2014.

P. P. Popov, A. Sideris, and W. A. Sirignano, "Uncertainty Quantification of Non-linear Oscillation Triggering in a Multi-injector Liquid-propellant Rocket Combustion Chamber," *American Physical Society Fluid Dynamics Meeting*, November 2014, San Francisco, CA.

W. A. Sirignano, "Combustion Instability: Triggering, Transients, and Limit Cycles," US National Combustion Meeting, Cincinnati OH, May 2015.

P. P. Popov, A. Sideris, and W. A. Sirignano, "Triggering and Re-stabilizing Potential of Acceleration Pulses in Liquid-Propellant Rocket Motors," *Joint Propulsion Conference*, July 2015.

P. P. Popov and W. A. Sirignano, "Wave Dynamics for Transverse Acoustic Instabilities in a Rectangular Rocket Motor," *Joint Propulsion Conference*, July 2015.

W. A. Sirignano, "Nonlinear Two-time-scale Perturbation Theory for Transverse Combustion Dynamics," *ICDERS*, Leeds, UK, 2015.

III. Large Eddy Simulations - Georgia Institute of Technology

The research under this project has focused on large-eddy simulations (LES) of thermo-acoustic combustion instabilities, which are typically observed in high-pressure, shear-coaxial rocket combustors. The focus of the present study is to characterize the role of geometry, inflow conditions, thermal boundary conditions and chemical kinetics on stable/unstable behavior of model rocket combustors through large-eddy simulation and then use the results further to develop novel reduced-order modeling approaches, which in turn can be used to conduct efficient predictive analysis of stable/unstable behavior of such combustors. In this study, we have considered a range of model rocket combustors for which experimental data is available to build a database with increasing degree of complexity to validate and improve the reduce-order modeling approach. The considered test cases include a shear coaxial rig (TUM) at Technical University (Munich), the Continuous Variable Rocket Combustor (CVRC) at Purdue University and Transverse Instability Combustion (TIC) also at Purdue University. TUM is a stable high-pressure test bench, whereas CVRC exhibits longitudinal model combustion instability and TIC (which is a 7-injector system) demonstrated transverse instability. Simulations show good agreement with available data and in particular, for the CVRC shows the ability of LES to capture the changes in frequency and amplitude of the instability when the injector length is changed (which causes a change in the characteristic impedance of the system).

Introduction and Background: The design of rocket engines is dictated by several requirements such as a stable combustion, low operating cost, low emission characteristics and high performance throughput under a range of operating conditions. The elements of these engines such as type of propellant, injector design, thermal conditions of the combustion chamber wall etc., play an important role on the overall performance. In particular, the injector design plays a crucial role as it affects the performance by altering the flame and flow dynamics and may lead to thermo-acoustic instability within the combustor. Since the overall performance of the engine depends upon interplay of the geometry, inflow conditions, mixing, and heat-transfer characteristics of the combustor wall, therefore, understanding their role under different operating conditions is very important for design evaluation and performance improvement of rocket engines. Large-eddy simulation (LES) based numerical investigation provides a promising approach to study such reactive flow systems and has been used successfully as a design tool for predictive analysis. However, numerical modeling of such systems becomes challenging due to an increase in the geometrical complexity of the injector design and involvement of large number of parameters that affect the overall performance of such systems. Therefore, reduced-order modeling (ROM) and reduced basis modeling (RBM) provides alternate efficient means to study such systems. However, such ROM and RBM methods require careful validation and for this an extensive database is needed. This project focused on this goal.

In this study, we use LES to study stable and unstable combustion within three model combustors and perform a comprehensive validation of the LES results by comparing them with the measured experimental data. In the second part of this study, we develop a ROM based on the admittance boundary conditions and use it to predict longitudinal thermo-acoustic instability within one of the model combustors.

The LES studies have focused on experimental configurations for which some data (primarily pressure signal) is available. It is noted that to experimentally sustain combustion instability in a test facility can be nearly impossible due to the possibility of damage and explosion. Also, because of high pressure and hot operating conditions, detailed measurements are nearly impossible. Therefore, only pressure fluctuation data is available from wall sensors and combustion instability is inferred from such a signature. In some cases wall temperature is also available and can provide additional information.

We consider three operating high pressure rigs for the LES studies and these are briefly noted below:

1. Shear Coaxial Test Bench at Technical University (Munich)

This single element, shear-coaxial, high pressure combustor, referred here onwards as TUM is currently being investigate for stable high pressure combustion and it employs a methane-oxygen combustion system. Pressure and wall temperature data for different operating conditions is available for comparison with LES.

2. Continuously Varying Resonance Combustion (CVRC) at Purdue University

This facility is also nominally methane-oxygen single injector high shear facility developed at Purdue University (Yu et al., 2008, 2009, 2012), which has shown spontaneous longitudinal mode combustion instability for a range of operating conditions. Again only pressure data is available so details of the combustion process have to be predicted and then matched with data. An added advantage of this rig is that its injector length can be changed during or in-between the tests and it has been shown that the acoustic wave-modes in the injector can either constructively or destructively interact with the acoustic modes of the combustor resulting in stable or unstable combustion behavior. Thus, this facility offers a unique opportunity to investigate different operating conditions that bracket the conditions for combustion instability.

3. Transverse Instability Chamber (TIC) at Purdue University

A more complex high-pressure rig is the TIC at Purdue University, which focuses on transverse high frequency instability that can be responsible for the highest wall heat-release effect, as well as, the fastest behavior which can lead to detrimental effects on the combustor. This system is a rectangular chamber with seven injector elements, which can supply both fuel and oxidizer under different configurations. According to reports (Morgan1, Shipley1), the main reason of instability sustainment is the vortex shedding phenomenon, caused by the impact of vortical fluid structures on the chamber walls. These structures originally contain both fuel and oxidizer so that their impact at the wall produces a concentrated combustion region with a consequent unsteady heat-release. The coupling with such an unsteady source of heat and the acoustic transverse waves generates an increase of pressure amplitude according to the Rayleigh criterion. Before proceeding with the full seven injectors case, a three injectors device in which the three central injector elements are maintained in their whole geometry, while the last two couple of injectors, considered to be responsible of the vortex shedding, are instead modeled as a simple constant mass inflow section. In this manner, the physics of the injection process is altered, especially near the chamber walls. Therefore, it is expected that instability does not occur unless the chamber walls are intentionally forced as discussed by (Shipley1).

Key Achievements: In the following we discuss some of the key highlights of these studies. More details of the setup and other numerical issues, as well as detailed discussion are in the attached papers.

1. Study of stable combustion in TUM Rig

We study the role of heat transfer, mixing processes and flame holding dynamics of thermo-acoustically stable combustion occurring within a high pressure, single element shear-coaxial injector combustor. Gaseous methane-oxygen chemistry is used in a subgrid linear-eddy-mixing (LEM) model for closure in the LES. The operating conditions match the experimental investigation conducted at TUM. The results obtained from simulations are compared with experimental data for pressure and heat flux on the surface of the combustion chamber demonstrating good agreement. The flame holding dynamics reveal a stable flame structure showing a good agreement with the experimental observations. Currently, we are still investigating the role of thermal boundary conditions and more detailed chemical kinetics on the wall pressure and heat flux statistics.

Publications

Dawson, T., Menon, S. and Haidn, O., “Large Eddy Simulation of a Subscale Combustion Chamber,” Proceedings of the *Sonderforschungsbereich/Transregio 40, Summer Program Report*, Technical University (Munich), August 2013,

which was appended in a previous Annual Report and the following three publications which are appended here.

Celano, M. P., Silvestri, S., Schlieben, G., Kirchberger, C., Haidn, O. J., Dawson, T., Ranjan, R., and Menon, S., “Experimental and Numerical Investigation for a GOX-GCH₄ Shear-Coaxial Injector Element,” SP-2014-2969417, 2014 Space Propulsion Conference, Cologne, Germany, May 2014.

R. Ranjan, and S. Menon, “LES of GCH₄/GOX, Shear-Coaxial, Single Element, High Pressure Rocket Combustor: Effects of Thermal Condition and Chemical Kinetics,” *Sonderforschungsbereich/Transregio 40, Summer Program*, Technical University (Munich), August 2015.

Tudisco, P., Ranjan, R., Menon, S., Jaensch, S. and Polifke, W., “On the Application of the Time-Domain Admittance Boundary Conditions in the LES of a High-Pressure, Shear-Coaxial Injector Combustor,” draft paper, to be submitted to *Flow, Turbulence and Combustion*, July 2015.

2. Study of Longitudinal Combustion Instability in CVRC

LES based investigation of the longitudinal combustion instability is conducted in the CVRC, which is also a high-pressure, shear-coaxial injector combustor. An important characteristic of the CVRC setup is the role that the oxidizer injector length plays on the stable/unstable combustion dynamics occurring within the combustor. We perform three simulations corresponding to different stability regions; one is a semi-stable case whereas the other two cases are unstable. The acoustic pressure fluctuation exhibits a limit cycle behavior in all cases. An abrupt change in the predicted amplitude between stable and unstable cases is also observed, consistent with the experimental trends. Further investigations are carried out to characterize the mechanism driving such abrupt change in the stability pattern when the oxidizer injector length is varied. Results show that the acoustic interactions with the flow field lead to subtle changes in the vorticity (and mixing) dynamics, which significantly alters the distribution of species and heat release. These changes affect the heat release and hence the measured pressure oscillations in the chamber. In addition, aspects related to flame stabilization such as the mean flame anchoring location and the mode of burning, premixed or non-premixed, are also affected. The analysis of flame structures shows the presence of multi-mode burning regions where premixed and non-premixed flames appear to coexist. However, the dominant burning mode switches from

premixed to non-premixed within an acoustic cycle, potentially playing an important role in flame stabilization.

Publications

Guezennec, N., Dawson, T., Sierra, P. and Menon, S., "Flame Holding Dynamics During Combustion Instability in a Shear-Coaxial Injector Combustor," *8th Turbulent Shear Flow Phenomenon*, Poitier, France, August 2013.
Munipalli, R., Liu, Z., Zhu, X., Menon, S., Hesthaven, J.S., "Model reduction opportunities in detailed simulations of combustion dynamics," AIAA paper 2014-0820, 52nd AIAA Aerospace Sciences Meeting, January 2014.
Srinivasan, S., Ranjan, R. and Menon, S., "Flame Dynamics During Combustion Instability in a High-Pressure, Shear-Coaxial Injector Combustor," *Flow, Turbulence and Combustion*, Vol. 94, pp. 237-262, 2015.

The first two papers above were appended in a previous Annual Report while the third paper is appended here.

Invited Presentations (not appended)

"Modeling and Computational Challenges to Simulate Combustion Instability in High Pressure Combustion Systems," Technische Universität München, Munich, Germany, Aug 7th 2013.
"Modeling and Computational Challenges for Large-Eddy Simulation of Turbulent Combustion Systems," California Institute of Technology, CA, October 23, 2014.
"Turbulent Combustion Modeling and Simulations," University of Rouen, CORIA, France, December 18, 2014.

3. Study of combustion processes in the TIC

We analyze transverse combustion instability in a model, high-pressure, shear-coaxial, multi-element rocket engine noted as TIC. This is an experimental rig at Purdue University that comprises of a rectangular combustion chamber and **seven** injectors, which can supply both fuel and oxidizer with different possible combinations. Experimental data show that a self-sustained instability is observed in this particular system resulting from the vortex shedding phenomenon and impingement of the vortical structures on the chamber wall. First, we analyze a three-element configuration to demonstrate ability of LES to predict characteristic reactive flow features. Only the three central injector elements are retained, while the other injector elements, which are considered to be responsible of the vortex shedding, are instead modeled as a simple constant mass inflow section. As expected and reported in other studies, the flame dynamics change particularly near the chamber walls leading to a stable combustion. LES was able to predict all the relevant reactive flow features and flame dynamics. Currently, we are extending the study to model the entire seven-element configuration to demonstrate the ability of LES to predict self-sustained transverse combustion instability in this rig.

Publication

Tudisco, P., Ranjan, R. and S. Menon, "Numerical Investigation of Transverse Combustion Instability in a Multi-Element, Shear-Coaxial, High Pressure Combustor," draft report, submitted to AIAA Sci Tech 2016, which is appended here.

Conclusions: We are developing LES tools and reduced order/basis modeling tools to investigate both longitudinal and transverse instability in high-pressure systems. In this project three different rigs are considered since they are representative of a rocket combustor and for which some experimental data is available for validation. These rigs include the single-element shear-coaxial system at Technical University Munich (TUM), the single-element Continuously Variable Resonance Combustor (CVRC) at Purdue University and the seven-element Transverse Instability Combustor (TIC) also at Purdue University. TUM, CVRC and TIC exhibit stable,

longitudinally unstable and transverse unstable combustion under specific conditions, respectively, and therefore, cover a wide range of operating conditions. We show here that in general the LES we have employed is able to predict the combustion behavior in all of these test cases. The numerical results are further examined to analyze the effects of inflow boundary conditions, injector design modifications, thermal boundary conditions, finite-rate chemical kinetics and turbulence-chemistry interaction on the predicted stable/unstable combustion behavior and reactive flow and flame dynamics. These test cases are considered as a database for development of novel ROM technique for study of combustion instabilities under operating conditions of a typical rocket engine.

As a final progression towards the goal of this research, a time-domain impedance boundary condition (TDIBC) formulation based on the linearized Euler equation is extended to the LES formulation as a ROM so that injector elements can be implicitly modeled rather than having an explicit geometrical representation. Results show that this approach is able to capture all the key physics of longitudinal combustion instability in the CVRC without affecting the reactive flow dynamics in the combustor and without explicit modeling of the injector. Such an approach can not only substantially reduce the computational cost but also provide a new capability to model injector elements, especially in multi-injector systems.

In the future, both the LES and the ROM technique can focus on transverse combustion instability, not only in the TIC rig but also simulations may begin for supercritical systems such as LOX-GCH₄ and LOX-GRP1 systems using multi-injector assembly. Further extensions and refinements of the ROM will be carried out. For example, currently, the method does not employ viscous losses and non-linear effects. Therefore, a natural extension of the ROM approach is to include such terms so that it is robust and accurate. In addition, the approach will be extended to a real-gas system so that it can be used to investigate model multi-element liquid rocket combustors in a computationally efficient manner. Finally, we can include the RBM methods being developed under another project within the LES studies.

IV. Thermomechanical Processes -- Kassoy Innovative Science Solutions

Liquid propellant rocket engine (LPRE) combustion and fluid dynamics provide an excellent opportunity to quantify the thermomechanical response of the gas to transient, spatially distributed, chemical energy deposition. Objectives include identifying the specific physical processes that are the source of operationally observed pressure oscillations, (1), as well as to explain how thermal energy is converted to kinetic energy, leading to a thermally-induced gas motion. The fundamental physical concepts, mathematical methods and models needed to quantify combustion-driven mechanical disturbances and accompanying thermodynamic variations are described in a sequence of journal publications ,(2-4). The full conservation equations are non-dimensionalized with the objective of identifying parameters used to characterize the basic physics occurring in gaseous environments. Vanishingly small Knudsen numbers, modulate all transport terms in each thermomechanical system considered. This provides a rational justification for the neglect of viscous and mass diffusion, conduction and dissipation, relative to the reactive gasdynamic terms in the Euler equations, but with a quantifiable understanding of what has been ignored. It also precludes the consideration of classical flame propagation.

The nondimensionalized Euler equations contain two additional parameters, absolutely *crucial* to understanding the diversity of thermomechanical responses to localized, transient, spatially resolved energy addition from any source including that associated with exothermic chemical reactions;

1. $\varepsilon = t_R' / t_A'$, the ratio of the characteristic chemical reaction time scale for energy addition, t_R' , to the characteristic acoustic time scale, $t_A' = L' / a_0'$, where L' is the characteristic length scale of the volume heated and a_0' is the characteristic speed of sound therein.

2. $\alpha = Q_R' t_R' / e_0'$, the ratio of the characteristic chemical *energy* deposition, $Q_R' t_R'$, to the characteristic internal energy in the volume, e_0' , where Q_R' is the characteristic chemical *power* addition

Ref. 2 as well as Refs. 3 &4 (see Addenda 7&8 in the most recent Annual Report June 1, 2013-May 31, 2014) describe physical phenomena resulting from wide ranging combinations of ε and α . Two of the important non-intuitive conclusions include:

1. Rapid, relatively large energy addition within a *microvolume*, defined by $\varepsilon \ll O(1)$ and $\alpha \gg O(1)$, is the source of nearly constant volume heating to a large temperature value, with pressure proportional to temperature, creating a high pressure and temperature hot spot with a subsonic induced volumetric Mach number, $M_i \ll O(1)$, compatible with nearly constant volume heat addition. Gas expelled through the initial volume surface acts as a piston to drive weak acoustic disturbances into the external cold environment. *In contrast*, when α exceeds a defined threshold, defined by $\alpha = 1/\varepsilon^2$, the rapid heating process is fully compressible, including an $O(1)$ induced Mach number. The internal gas expansion is the source of significant mechanical disturbances (compression waves), including shocks propagating into the cold environment. Detailed results for $\varepsilon = O(1)$ and a wide range of α -magnitudes can be found in Refs. 2-4.
2. When $\varepsilon = O(1)$ and $\alpha \ll O(1)$ in a confined *macrovolume* the time scale for heating is similar to the acoustic time and the energy addition is relatively weak. Variations in thermodynamic variables are $O(\alpha)$, as is the magnitude of M_i . The weak pressure variation is described by a nonhomogeneous acoustic wave equation, driven by the rate of change of power deposition,

subject to boundary conditions relevant to the volume shape. In contrast, when $\alpha=O(1)$, the energy addition is more robust. Changes in the thermodynamic variables are $O(1)$ and $M_i = O(1)$. The physics of the thermomechanics are described by fully compressible equations related to the dimensional forms used by Popov and Sirignano, (5). More details can be found in Refs. 2-4. The thermomechanical response of a gas to localized, spatially resolved, transient heat addition is the immediate source of pressure disturbances with magnitudes dependent on the interaction between ε and α .

Spontaneous Reaction Wave Propagation: More recent work in Ref. 6, describes a quantitative mathematical model for the propagation of a “*spontaneous reaction wave*”, conceptualized by Zeldovich, (7). The research provides a quantitative model for the spread of a non-diffusive reaction wave through a local hot spot microvolume containing a region of negative temperature gradient. The application might be to a localized temperature inhomogeneity in a turbulent reacting flow. These concepts are applied to the conservation equations for a reactive gas undergoing an exothermic, high activation energy one-step Arrhenius chemical reaction. The reaction is initiated at the temperature maximum of an initially imposed negative temperature gradient within a finite hot spot volume. A high activation energy thermal explosion (t.e) asymptotic analysis is developed to describe the traditional induction-period combustion initiation, characterized by a t.e. singularity occurring at the induction-time appropriate to the local temperature on the imposed gradient. In the fast heating limit that time-scale is asymptotically small compared to the characteristic acoustic time scale of the spot. Formal asymptotic analysis quantifies the supersonic propagation Mach number of the thermal explosion singularity as a “*spontaneous reaction wave*”. The induction-period thermal explosion is characterized by small changes in the temperature, pressure and fuel concentration prior to the singularity, as well as much smaller changes in density, compatible with a limited induced gas speed. Nearly inertially-confined physics prevail when the fast heating limit is employed. The propagating t.e. singularity represents the leading edge of an intense narrow reaction zone characterized by total reactant consumption, concomitant full heat of reaction release, $O(1)$ spatially homogeneous proportional increases in the local temperature and pressure and significantly smaller variation in the density. The relevant reaction zone time-scale, sometimes known as the excitation time, is exponentially short compared to the induction period time-scale, (8), while the reaction zone dimension just behind the front is similarly small relative to the volume dimension. As the reaction zone propagates it leaves behind a localized high temperature and pressure spot, which cannot expand during the relatively short excitation time-scale. In analogy with a shock tube, the subsequent expansion of the spot, driven by a significant overpressure relative to that in the cold environmental gas, is the immediate source of a relatively strong shock. Its subsequent propagation into the neighboring, colder unreacted mixture beyond the original hot spot can be the source of a propagating coupled shock-reaction zone: a localized detonation/explosion; hypothetically, a potential trigger for instability in a LPRE combustion chamber.

The high activation energy induction period physics are altered considerably when the thermal energy addition time-scale is similar in magnitude to the volumetric acoustic time-scale, $\varepsilon = O(1)$. The mathematical model for the small thermodynamic variable perturbations, fuel concentration consumption (proportional to the small inverse activation energy parameter), and the equally small induced speed describe a weakly compressible heating process characterized by

the presence of wave-like disturbances. The temperature perturbation equation has a linear acoustic wave operator and a nonhomogeneous, nonlinear driver. The pressure and induced fluid speed are also described by nonhomogeneous, linear acoustic wave equations with drivers that depend on the properties of the temperature perturbation. The equations for the temperature and pressure perturbations as well as for the induced speed can be interpreted physically to explain the appearance of propagating mechanical disturbances within the volume of interest. The ensemble of equations is equivalent to Clarke's equation, (9), but more appealing from a physical interpretation perspective. This compressible response is in contrast to that for the fast heating limit where the heat addition process is constant volume to a first approximation. Details can be found in Addenda 13.

Current Research Activity: A current thermomechanics-based study is motivated by the liquid propellant rocket engine (LPRE) instability studies of Sirignano and Popov (5) and Popov, Sideris and Sirignano, (10). A dimensional, 3-D “nonlinear wave equation”, (x, r, φ), driven by energy deposition is formulated. Averaging in the axial direction, (x), of a cylindrical volume is used to reduce the equation to two dimensions, (r, φ). The latter is used to describe the transverse wave propagation pressure response to an imposed initial transverse wave disturbance and energy deposition within the volume. Computational solutions of the initial-boundary value problem demonstrate that instability (sustained limit cycle pressure oscillations) occurs if the imposed disturbance is larger than an identifiable threshold value, in the context of the energy deposition source actually responsible for the pressure transient. This result verifies the possibility for triggering a LPRE instability. The mathematical models include the impact of energy deposition from both a model energy source and from methane-oxygen combustion associated with numerous coaxial injectors at the head end of the combustion chamber. The use of dimensional equations precludes discovering the nondimensional parameters that characterize the combustion-driven (energy deposition) instability. The objective of current research is to use methodologies and concepts in Refs. 2-4 and 6 to identify parameters of interest in idealized LPRE combustion chambers. A formulation similar to that in (2) is used, to quantify the thermomechanical response of gas in a *macrovolume* to a very general source of transient, spatially resolved thermal energy for diverse sets of the parameter values, ε, α and M_i . Detailed results will be presented in a technical paper in progress and at the Aerospace Sciences meeting in January 2016, (see Ref. (11 for an extended Abstract). These methods have been applied to the 3-D conservation equations in (5) [Eqs. 1-3 and 9.] in order to identify parameter values relevant to the data sets generated by computational means. If $\varepsilon=O(1)$, $\alpha=O(1)$ and $M_i=O(1)$, all terms in the equations are similar in magnitude and the thermomechanical response to heating is fully compressible. It is noted that the threshold pressure disturbance magnitude in Fig. 3 of (5), 54 atms. is relatively small compared to the assumed initial high pressure of 200 atms. The imposed initial disturbance initiates a physical process that evolves to a pressure limit cycle instability driven entirely by the energy deposition.

References

1. Harrje. D. & Reardon, F. 1972 Liquid propellant rocket combustion instability. *NASA Technical Report SP-194*. National Aeronautics and Space Administration
2. Kassoy, D.R. 2010 The response of a compressible gas to extremely rapid transient, spatially resolved energy addition: an asymptotic formulation. *J. Eng. Math.* **68**, 249-262.

3. Kassoy, D.R. 2014a Non-diffusive ignition of a gaseous reactive mixture following time resolved, spatially distributed energy addition. *CTM* **18** 101-116.
4. Kassoy, D.R. 2014b Mechanical disturbances arising from thermal power deposition in a gas *AIAA J.* **52** 2328-2335.
5. Sirignano, W.A. & Popov, P.P. 2013 Two-dimensional model for liquid-rocket transverse combustion instability. *AIAAJ.* **51** 2919-2924.
6. Kassoy, D.R. 2015 The Zeldovich spontaneous reaction wave propagation concept in the fast/modest heating limits, **submitted** to the *Journal of Fluid Mechanics*.
7. Zeldovich, Ya. B. 1980 Regime classification of an exothermic reaction with nonuniform initial conditions *Combust. Flame.* **39** 211-214.
8. Kassoy, D.R. 1977 The supercritical spatially homogeneous thermal explosion: initiation to completion. *Q. Jl. Mech. Appl. Math.* **30** 71-89.
9. Clarke, J.F. 1978 A progress report on the theoretical analysis of the interaction between a shockwave and an explosive gas mixture. *College of Aeronautics Report 7801*, Cranfield Institute of Technology, Cranfield, U.K.
10. Popov, P.P., Sideris, A. & Sirignano, W.A. 2014 Stochastic modeling of transverse wave instability in a liquid-propellant rocket engine. *J. Fluid Mech.* **745**, 62-91.
11. Kassoy, D.R. 2015 Formulation of Wave Equations to Describe the Thermomechanical Response of a Gas to Transient, Spatially Resolved Thermal Energy Addition, Abstract for the 2016 ASM/AIAA meeting

V. Reduced Basis Modeling for Combustion Dynamics – HyPerComp

In this project, we have sought to build a mathematical framework for reduced basis modeling (RBM) of large scale unsteady nonlinear differential equation systems encountered in the large eddy simulations of turbulent combustion. In a sequence of steps, we developed and tuned a nonlinear RBM method with supporting mathematical toolkit. Two scenarios are considered for RBM in liquid rocket engines. The first is a ``full RBM'' approach where an entire combustor is modeled by a low-cost surrogate model. The second is a domain decomposition variant ``RBM-interface'', where we replace subdomains such as injectors with equivalent RBMs and model interaction between them. During the course of this reporting period, HyPerComp commenced a phase-II STTR project to transition these developments to a commercial grade software suite. The STTR project includes Prof. Dongbin Xiu (from the applied mathematics department at the University of Utah) and Prof. Jan Hesthaven (EPFL). The STTR focuses on efficient multi-parameter RBM models using a ``multi-fidelity'' approach. This effort attempts to chart new pathways in blending current advancements in applied mathematics of RBM with analytical methods and state of the art solvers in turbulent combustion. Figure 1 depicts the manner in which this research is coordinated across the various collaborating research groups.

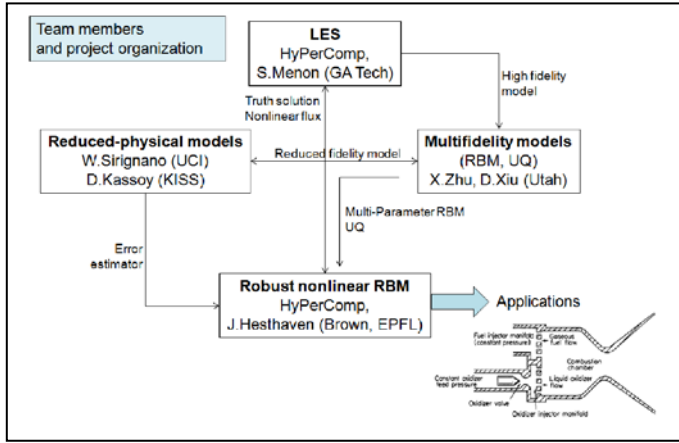


Figure 1. Team member interactions in AFOSR/AFRL RBM development.

Highlights of progress made in the last year of this project are:

An initial implementation and demonstration of RBM-interface was made in LESLIE-3D;

Full RBM implementation was initiated in LESLIE-3D;

A new research team member, Dr. Kaushik Balakrishnan (lately of NASA-JPL) has joined the HyPerComp team and will lead the development of interface RBM in injector analysis; and Multi-fidelity modeling for unsteady CFD problems has commenced at the University of Utah.

This report summarizes progress on these various fronts. Tools and techniques from this project are being transitioned to commercial grade software under a current phase-II STTR project. A progress report on that project has been submitted separately.

RBM-method Development and Software Interfaces in LESLIE-3D: We continue to add the Carlberg et al. (2013) method and Audoze et al. (2009, 2013) space-time RBM method to our core HDrbm framework. The overall RBM approach has been considerably refined following

several discussions within the team and is presented in this report. A preliminary porting of the interface RBM method to LESLIE-3D has been made and sample CVRC results were obtained.

Work has commenced on a rigorous and complete implementation within LESLIE-3D. We note that an ad hoc implementation was made in prior months to identify potential problem areas. That implementation was successful and functional, though not optimal. We are continuing the pursuit of an optimal RBM implementation in LESLIE. Simultaneously, we are prototyping RBM method variants using the HYCE code at HyPerComp. Progress on both of these fronts will be discussed in the next report.

Applications and demonstrations: Both RBM-full and RBM-interface have been successfully demonstrated in CFD codes with laminar flow and nonlinear equations. Last year we presented mathematical RBM procedures for nonlinear dynamics in elementary problems and an initial demonstration of test cases for RBM-full. During the past year we investigated applications of RBM-interface and an initial application in a turbulent reacting gas LES simulation of the CVRC experiment.

To demonstrate the apparatus needed and verify the consistency of the procedure, we selected a demonstration problem. We considered laminar flow in a cylindrical channel with a sudden expansion, matching CVRC dimensions in the channel diameters and "injector" length. Flow enters from the smaller pipe section at an inflow Mach number of 0.1 and Reynolds number of 500. The inflow velocity was perturbed after the computed flow reached a steady state, as:

$$u(t) = u_0 + 0.1 u_0 (\sin \omega_1 t + \sin \omega_2 t)$$

where ω_1 and ω_2 are the fundamental longitudinal acoustic frequencies of the pipe.

The full unsteady CFD problem was simulated first. Snapshots were generated for the ``injector'' portion of the flow. A reduced basis model based on POD was developed for the interface flow quantities and fluxes. While several thousand snapshots were used to generate the POD basis functions, we found that by using about 20 modes we were able to completely recover the dynamics of the full CFD solution using RBM-interface. A comparison of the computed velocity at two lateral locations is shown in Figure 2. The symbols in this figure represent the solution with 20 modes, virtually identical with the full CFD solution.

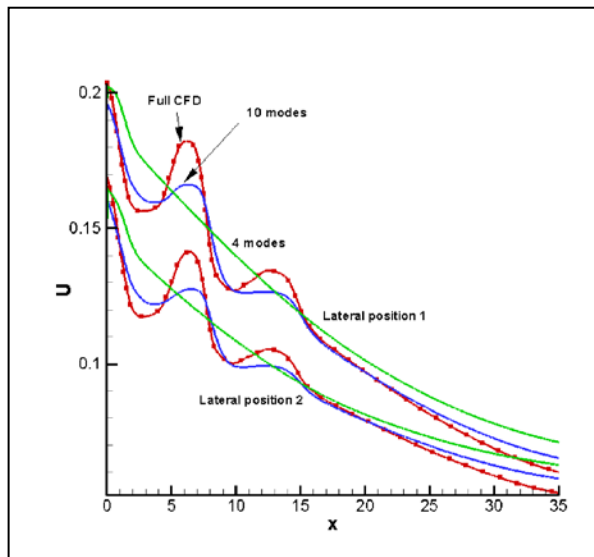
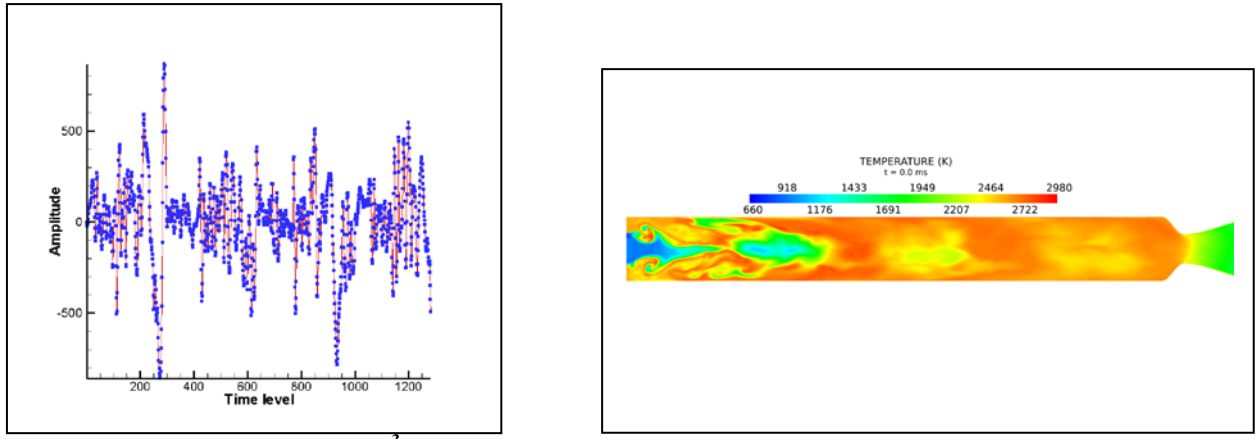


Figure 2. Comparison of computed velocity from full CFD and RBM. The velocity is normalized by the inflow speed of sound.

The above process essentially verified the usability of the RBM apparatus in an injector-type flow situation with nonlinear partial differential equations using significant problem size reduction. We then began integrating these developments in the LESLIE-3D solver. The first example used to demonstrate this procedure, was the CVRC simulation that was discussed in earlier reports. An index-mapping procedure was carried out in order to manually map the full LES grid to the truncated grid. In future, this part of the procedure is to be automated. Then, an offline POD based solution was generated using snapshots of the flow at the injector interface. This solution was used as a boundary condition to run the LES simulation. Figure 3(a) shows the amplitude of the mode shapes reconstructed using Kriging, which permits sampling the data at frequencies that are significantly lower than the high frequencies resolved in LES time-stepping. A preliminary RBM solution interface to LESLIE was made, and an initial exploratory result is shown in Figure 3(b).



(a) Mode-1 CVRC amplitude (J/m^3) using Kriging. (b) Truncated CVRC solution.

Figure 3. Kriging procedure and RBM-interface solution.

Semi-analytical models: We have proposed using semi-analytical models such as that of Sirignano and Popov (2013) in our work for two purposes: (a) As fast error estimators in developing a multi-parameter solution, and, (b) As a low-fidelity component in a multi-fidelity RBM analysis as discussed in the next section. We present briefly the semi-analytical approach in this section. The formulation, as implemented by Sirignano and Popov, models transverse waves in a combustor that is fed by coaxial injectors. In this section we present a summary of this formulation for the sake of reference as we formulate the multi-fidelity approach in the course of the next reporting period. The immediate goal of this study is to investigate the multi-fidelity analysis for the transverse instability chamber (TIC) experiments conducted at Purdue University. We note that the analytical model in this section, as well as high-fidelity LES-based models are currently being used to model combustion instability in TIC, thus presenting an attractive opportunity to demonstrate the multi-fidelity approach. UC-Irvine had provided the software to solve the equations of this section to HyPerComp. At the same time, HyPerComp has commenced high performance computer simulations of the TIC chamber under the ALREST and VISP programs supported by the Air Force. Results from the above will be used as input to the multi-fidelity analysis.

Multi-Fidelity Modeling in CFD: Details of the multi-fidelity approach were provided in the STTR progress report submitted recently. The goal of this approach is to use low-fidelity or semi-analytical models in developing error estimates as well as minimizing the number of high

fidelity solutions needed in developing a multi-parameter RBM. We wish to transition this development towards the TIC problem by first solving a problem in pure hydrodynamic instability. This will serve as a benchmark and a guide to future efficiency improvements in the method. In this section, we first consider the 2D incompressible NS equations, and use an example problem from Munipalli et al. (2014) which was appended to last year's Annual Report.

The following problem is defined on the computational domain $\Omega \in [-0.2, 2] \times [-0.2, 0.2]$ in meter units. The inflow boundary conditions are uniform flow as follows:

$$u(0, y, t) = (0.41)^{-2} 6(y+0.2)(0.21-y) ; v(0, y, t) = 0 ; \rho(0, y, t) = 1.0$$

for pressure, natural conditions are imposed at the inlet. No-slip boundary conditions are imposed on walls and the surface of the square. At the outflow, a constant pressure is prescribed and natural boundary condition is considered for velocity and density ρ . We shall consider the viscosity coefficient μ as the parameter, where $\mu \in [2 \times 10^{-3}, 2 \times 10^{-4}]$ in units of kg/(m s).

We took the sophisticated DG solver in Munipalli et al. (2014) to run the simulation with P_2 order element on a mesh with 236 elements until $T = 8$ as the low fidelity model and use P_4 order element on the same mesh as the high fidelity model. Following the completion of this demonstration we will transition this method to more advanced applications.

Summary: In this section, we have described the present status of RBM implementation and two important ingredients in our proposed strategy for RBM methods in liquid propellant rocket engine analysis: (a) A low-fidelity model that can be used as an error estimator for the high-fidelity LES simulations, and (b) The multi-fidelity approach which is needed for a large parameter space exploration when high-fidelity solutions are prohibitively expensive. As we proceed with this effort, we will continue developments to the basic RBM technique, and provide a demonstration of the multi-fidelity method in a series of increasingly complex flow situations leading to the transverse instability chamber experiments conducted at Purdue University.

References

Audoze, C., Vuyst, F.D. and Nair, P.B., "Reduced-order modeling of parameterized PDEs using time-space – parameter principal component analysis", *International Journal for Numerical Methods in Engineering* 80, pp. 1025 – 1057, 2009.

Audoze, C., Vuyst, F.D., and Nair, P.B., "Nonintrusive reduced-order modeling of parametrized time-dependent partial differential equations", *Numerical Methods for Partial Differential Equations* 29, pp. 1587 – 1628, 2013.

Sirignano, W.A. and Popov, P.P., "Two-dimensional model for liquid-rocket transverse combustion instability," *AIAA Journal* 51, pp. 2919 – 2934, 2013.

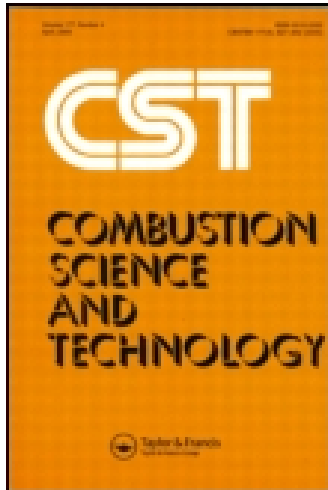
Carlberg, K., Farhat, C., Cortial, J., and Amsallem, D., "The GNAT method for nonlinear model reduction: Effective implementation and application to computational fluid dynamics and turbulent flows", *Journal of Computational Physics* 242, pp. 623 – 647, 2013.

Munipalli, R. , Zhu, X., Menon, S., and Heesthaven, J. S. "Model reduction Opportunities in Detailed Simulations of Combustion Dynamics," AIAA Paper 2014-0829, Aerospace Sciences Meeting, National harbor, MD, January 2014.

VI. Concluding Remarks

The team has made progress in following the research plan. New insights have been acquired; new methods have been refined and advanced. The program has been productive in terms of publications and conference presentations. Interactions have been maintained with Air Force Lab researchers and with the general LPRE combustion instability community through publications, conferences, and informal communications.

The attempt at experimental validation was successful. New ways of evaluating and predicting combustion instability have been established. These provide a strong foundation for future research and engineering analysis. Suggestions for plausible methodologies for control of combustion instability have emerged. New young researchers and engineers have been introduced to this major area of engineering. The team for this project remains fully engaged with the problem area and interactive with each other.



Combustion Science and Technology

Publication details, including instructions for authors and subscription information:

<http://www.tandfonline.com/loi/gcst20>

Driving Mechanisms for Combustion Instability

William A. Sirignano^a

^a Department of Mechanical and Aerospace Engineering, University of California, Irvine, California, USA

Published online: 10 Dec 2014.



CrossMark

[Click for updates](#)

To cite this article: William A. Sirignano (2015) Driving Mechanisms for Combustion Instability, Combustion Science and Technology, 187:1-2, 162-205, DOI: [10.1080/00102202.2014.973801](https://doi.org/10.1080/00102202.2014.973801)

To link to this article: <http://dx.doi.org/10.1080/00102202.2014.973801>

PLEASE SCROLL DOWN FOR ARTICLE

Taylor & Francis makes every effort to ensure the accuracy of all the information (the "Content") contained in the publications on our platform. However, Taylor & Francis, our agents, and our licensors make no representations or warranties whatsoever as to the accuracy, completeness, or suitability for any purpose of the Content. Any opinions and views expressed in this publication are the opinions and views of the authors, and are not the views of or endorsed by Taylor & Francis. The accuracy of the Content should not be relied upon and should be independently verified with primary sources of information. Taylor and Francis shall not be liable for any losses, actions, claims, proceedings, demands, costs, expenses, damages, and other liabilities whatsoever or howsoever caused arising directly or indirectly in connection with, in relation to or arising out of the use of the Content.

This article may be used for research, teaching, and private study purposes. Any substantial or systematic reproduction, redistribution, reselling, loan, sub-licensing, systematic supply, or distribution in any form to anyone is expressly forbidden. Terms &

Conditions of access and use can be found at <http://www.tandfonline.com/page/terms-and-conditions>

DRIVING MECHANISMS FOR COMBUSTION INSTABILITY

William A. Sirignano

Department of Mechanical and Aerospace Engineering, University of California, Irvine, California, USA

The processes affecting the nonlinear acoustic stability of a combustor are examined in an overview fashion. Emphasis is placed on liquid-propellant rocket motors but other systems are briefly mentioned and some broadly applied principles and observations are discussed. A nonlinear wave equation is developed for a two-phase mixture and the roles of various terms in the equations are discussed. A review is made of various combustion processes, their associated characteristic times, and the impacts on stability in certain cases. Many relevant scales for length and time are identified. Special issues for supercritical and transcritical combustion are discussed. Bistable operational domains are shown to be present in some systems, making nonlinear triggering of an instability a possibility. Relations between the natural frequency of oscillation for the combustion chamber and the characteristic combustion times are identified with regard to impact on the combustor stability. The amplitude of the limit cycle and the transient time for limit-cycle development are related to the mean-flow Mach number. The role of shock-wave dissipation in amplitude determination is described.

Keywords: Combustion instability; Continuous combustion; Unsteady combustion

1. INTRODUCTION

Combustion instability in rocket engines and other continuous-combustion engines has provided a major design challenge for the engineer and a substantial intellectual challenge to the researcher. It demands an understanding of unsteady combustion processes and nonlinear acoustical resonance. The researcher must address the intertwined, multidisciplinary issues of combustion, transport, fluid dynamics, acoustics, and nonlinear dynamics. While many examples in this discussion will be related to liquid-propellant rocket engines, not all are. More importantly, two points must be understood: (i) all acoustic oscillations in partially confined gaseous chambers relate to each other regardless of shape or application; and (ii) combustion processes, such as phase change, mixing, and oxidation, regardless of the particular combustion chamber in which they occur are related. Therefore, many principles and observations will have value for a range of combustor applications.

Received 15 August 2014; revised 20 September 2014; accepted 30 September 2014.

Published as part of the Special Issue in Honor of Professor Forman A. Williams on the Occasion of His 80th Birthday with Guest Editors Chung K. Law and Vigor Yang.

Address correspondence to William A. Sirignano, Dept. of Mechanical & Aerospace Engineering, University of California, Irvine, CA 92697-3975, USA. E-mail: sirignan@uci.edu

Color versions of one or more of the figures in the article can be found online at www.tandfonline.com/gcst.

There are two general types of acoustical combustion instability: “driven” instability and “self-excited” instability as noted by Culick (2006). He describes evidence in some solid-propellant rockets of the former (driven) type where vortex shedding (a more organized noise) causes kinematic waves (i.e., waves carried with the moving gas) of vorticity or entropy to travel to some point where an acoustical reflection occurs. The reflected wave causes more vortex shedding after traveling back and a cyclic character results. These driven types do not rely on acoustical chamber resonance and acoustical waves traveling upstream are the only type of consequence with kinematic waves only traveling downstream by the kinematic definition. They are much smaller in amplitude since the energy level is limited by the driving energy. This type of instability has also been observed in ramjet combustors but never in liquid rockets. They will not be addressed here. Self-excited instabilities are the primary type relevant to liquid-propellant rockets but also appear elsewhere. These instabilities involve an acoustical resonance, which relies on a coupling between the acoustical waves and the combustion process where energy is added in a cyclic fashion to the acoustically resonant gas in the combustion chamber.

It has been well established based on experiment and development-test experience (Harrje and Reardon, 1972) that three types of stability zones can be found: unconditionally stable operation where the amplitude of any disturbance (large or small) decays in time to the steady-state operation; unconditionally unstable operation where the amplitude of any disturbance (large or small) grows in time to a limit-cycle oscillation; and bistable operation where growth to a limit-cycle occurs for disturbance amplitudes above a specific threshold but decay to the steady state results for disturbances of a magnitude below the threshold.

The particular resonant mode is a characteristic of the particular combustion chamber and convergent portion of the nozzle. Any partially confined gas volume has an infinity of different theoretically possible resonant acoustic modes. These resonant mode oscillations and their frequencies are predictable by linear theory. They depend on chamber shape, boundary conditions for the chamber flow, and the field values for speed-of-sound and velocity vector through the chamber gas. The lowest frequency mode is identified as the fundamental mode while the other modes are overtones. Only in special situations are the overtones also harmonics of the fundamental mode; that is, their frequencies are integer multiples of the fundamental frequency. Generally, the harmonics are not predicted by linear theory to occur in isolated fashion. It is well known from the theory of nonlinear oscillations that, for many mechanical systems, nonlinear resonance can involve any of several developments: the generation of harmonics superimposed on the basic resonant mode; the simultaneous excitement of other resonant modes by transfer of energy among modes; and the transfer of energy to a subharmonic mode whose frequency is lower than the basic mode and related arithmetically to two or more resonant modes (e.g., the difference between two resonant frequencies).

These self-excited instabilities are not limited in amplitude by the energy of the initiation action; they find the energy within their own “macro” (i.e., chamber or acoustic wavelength scale) behavior as the oscillations grows and develops. So, the initiation can be micro-level (at least one order of magnitude smaller than chamber scale) but the instability becomes macro-level. These instabilities include those linear unstable (i.e., unconditionally unstable) situations where normal low-level engine noise is sufficient to initiate the instability oscillation and those triggered (i.e., conditionally stable or equivalently conditionally unstable) instabilities, which require a larger initial disturbance to initiate the nonlinear

oscillation. Physically, the rogue disturbance is some deviant behavior in the operation that has uncertainty with regard to location in the physical coordinates, duration, and magnitude. The deviant behavior “jolts” the steady-state behavior. Sometimes, there is a recovery and a return to the steady-state but, at other times, the development of the oscillation occurs with a growing of the oscillation amplitude until the limit cycle is reached. The needed jolt to initiate instability can sometimes come during a rapid start of the engine so that steady state never appears.

With the self-excited instability, a gradual and continuous change in some direction of operating conditions (e.g., mixture ratio or mass flow) or design (e.g., nozzle throat area or injector detail) could cause a variation through the several instability domains: unconditionally stable, conditionally stable, unconditionally unstable, and perhaps back to conditionally stable and unconditionally stable. Moderate (normal “steady-state” rumbling) noise might initiate the linear instability in certain operational domains and large disruptive noise (e.g., an experimental bomb, a large operational change, a large but temporary rogue injector blockage or injector exit vortex) might trigger the nonlinear instability in some other operational domain. In those cases, noise or disruptions are typically only initiators with modest energy levels compared to the energy of the ultimate oscillation. The initiators can be turned off or disappear naturally once the instability starts and the oscillation will remain and grow. That is, it is driven by a coupling between combustion and acoustics. The stochastic nature pertains only to the initiation mechanism, which moves the dynamics from the steady-state (or nonoscillatory starting transient) to a stable limit cycle (the periodic or chaotic nonlinear oscillation). The limit cycles and the equilibrium points are neither stochastic in nature nor stochastic with regard to the ultimate driving mechanism.

In order to drive a combustion instability, certain relations between the resonant frequency and the characteristic times associated with the combustion process are required. The limit-cycle amplitude of the oscillation will also be related to certain parameters describing the combustion process. In situations where triggering of an oscillation occurs, the threshold amplitude (or unstable-limit-cycle amplitude) will be related to certain combustion parameters. Certain damping mechanisms will also affect the behavior. An overview of these issues will be presented here. Examples will be chosen that are most familiar to the author. It is not claimed that a thorough review of the literature is being offered; rather, the focus will be on the underlying concepts. Obviously, the work of the author will find preference among the examples. For more detailed reviews of combustion instability, see Crocco and Cheng (1956), Harrje and Reardon (1972), Yang and Anderson (1995), and Culick (2006).

In the next section, we formulate the governing differential equations and boundary conditions in a general form for a two-phase flow undergoing chemical reaction and exchanges of mass, momentum, and energy between the phases. The third section develops those equations into a useful form for studying wave oscillations in a combustion chamber/convergent-nozzle configuration. The characteristic times associated with the injection and combustion processes and their connection with unstable oscillations are discussed in the fourth section. This subject relates to sub-grid models in large-eddy simulations (LES) for combustion chambers. In the fifth section, the factors determining the threshold for triggering and the limit-cycle amplitude are discussed. Then, a summary of key conclusions is given in the last section.

2. TWO-CONTINUA, TWO-PHASE FORMULATION

In this section, we will present the two-continua system of equations in the forms that are commonly used. It is noteworthy (Sirignano, 2005b, 2005a, 2010) that this general approach was first developed for specific application to longitudinal-mode liquid-propellant rocket engine combustion instability in the PhD dissertation of S.-I. Cheng working with L. Crocco (Crocco and Cheng, 1953, 1956). The basic concept developed there in the 1950s of two superimposed continuous fields has since been extended to dusty gases, bubbly flows, and flows through porous material. Properties are averaged over a sufficiently large neighborhood of any point that both carrier-fluid (continuous-phase) and discrete-phase properties exist at any point. Here, we use a three-dimensional (3D) version of the theory. This formulation is designed to address a common situation in a combustor where the gas is laden with droplets or particles, e.g., a spray combustion situation. In particular, averaging of properties is done over a neighborhood scale larger than droplet size or distance to nearest droplets. Exchanges of mass, momentum, and energy occur between the phases and must be tracked. The higher order quantities, which relate to differences between products (and a ratio) of averages and averages of products (and a ratio), are neglected in the following formulation. The bar symbol is used over the density in order to distinguish between bulk density and the mass per unit volume of the mixture. Details are provided by Sirignano (2010).

In the following discussion, we examine the various conservation principles for the gas and liquid phases. The hyperbolic nature of the liquid-phase equations and the consequences are examined. The interactions between the two phases will introduce many new length scales and time scales that can be consequential. These scales will be surveyed in section 4.

2.1. Mass Conservation

We consider the various forms of mass continuity or conservation equations for the gas and liquid phases. Mass conservation of individual chemical species or of individual classes of liquid droplets will also be considered. The conservation of droplet numbers will be explored. The gas-phase mass-conservation equation is:

$$\frac{\partial \bar{\rho}}{\partial t} + \frac{\partial}{\partial x_j} (\bar{\rho} u_j) = \dot{M} \quad (1)$$

The term on the right side does not appear if no mass is exchanged between the phases.

The liquid-phase mass-conservation equation is:

$$\frac{\partial \bar{\rho}_l}{\partial t} + \frac{\partial}{\partial x_j} (\bar{\rho}_l u_{l,j}) = -\dot{M} \quad (2)$$

where \dot{M} is the mass vaporization rate per unit volume. Models for evaluating the vaporization rate \dot{M} are required. As a result of vaporization, mass is not conserved for each phase but the mass of the mixture is conserved.

For a constant bulk liquid density ρ_l , $\bar{\rho}_l = (1 - \theta) \rho_l$, where θ is the local volume fraction occupied by gas.

Consider now the gas-phase species-mass conservation. The integer index m represents the particular species. The mass fraction Y_m is described by:

$$\frac{\partial}{\partial t} (\bar{\rho} Y_m) + \frac{\partial}{\partial x_j} (\bar{\rho} u_j Y_m) - \frac{\partial}{\partial x_j} \left(\bar{\rho} D \frac{\partial Y_m}{\partial x_j} \right) = \dot{M}_m + \bar{\rho} \dot{w}_m \quad (3)$$

where

$$\dot{M} = \sum_m \dot{M}_m = \sum_m \varepsilon_m \dot{M} \quad \sum_m \dot{w}_m = 0$$

The mass diffusivity is assumed above to be the same for all species. Other options can be considered (Sirignano, 2010). ε_m is the fractional vaporization rate for species m and, for a quasi-steady gas phase, becomes a species mass-flux fraction. Obviously, $\sum_m \varepsilon_m = 1$. Summation over all components in Eq. (3) yields the continuity equation (1). Therefore, if we have N different species, only $N - 1$ species-conservation equations need be solved together with Eq. (1).

2.2. Momentum Conservation

Now, let us consider the gas-phase momentum equation constructed in a simple form with neglect of body forces:

$$\frac{\partial}{\partial t} (\bar{\rho} u_i) + \frac{\partial}{\partial x_j} (\bar{\rho} u_j u_i) + \theta \frac{\partial \rho}{\partial x_i} - \theta \frac{\partial \tau_{ij}}{\partial x_j} = \dot{M} u_{l,i} - F_{Di} \quad (4)$$

where

$$\tau_{ij} = \mu \left(\frac{\partial u_i}{\partial x_j} + \frac{\partial u_j}{\partial x_i} - \frac{2}{3} \delta_{ij} \frac{\partial u_i}{\partial x_j} \right)$$

Equation (4) includes momentum sources and sinks due to droplet-vapor mass sources, reaction to droplet drag, and body forces on the gas. The drag and lift forces F_{Di} in Eq. (4) can be related to the relative droplet-gas velocity and the droplet radius through the use of drag and lift coefficients. The equations are written for a laminar flow but turbulence modeling can be included in various ways. The simplest way would be to use an eddy viscosity μ_t in place of μ above.

The gas-phase momentum equation may be rewritten in a form where all effects of viscosity and mass and momentum exchanges appear as terms on the right side of the equation included together as a term \dot{I}_i giving impulse per unit volume:

$$\frac{\partial}{\partial t} (\bar{\rho} u_i) + \frac{\partial}{\partial x_j} (\bar{\rho} u_j u_i) + \frac{\partial p}{\partial x_i} = \dot{I}_i \quad (5)$$

$$\dot{I}_i \equiv (1 - \theta) \frac{\partial p}{\partial x_i} + \theta \frac{\partial \tau_{ij}}{\partial x_j} + \dot{M} u_{l,i} - F_{Di} \quad (6)$$

The liquid-phase momentum equation can be written as:

$$\frac{\partial}{\partial t} (\bar{\rho} u_{l,i}) + \frac{\partial}{\partial x_j} (\bar{\rho} u_{l,j} u_{l,i}) = -\dot{M} u_{l,i} + F_{Di} + \rho (1 - \theta) \left[\frac{\partial u_i}{\partial t} + u_j \frac{\partial u_i}{\partial x_j} \right] \quad (7)$$

The last term in Eq. (7) implies that the acceleration that would have been given to the gas (if it were to exist in the fractional volume occupied by liquid), because of the pressure and the viscous stresses transferred from the neighboring gas, is transmitted as a force on the droplets. The neglected additions due to droplet interactions to the last term in Eq. (7) can be shown to be of the order of $(1 - \theta)^2$. Note that the reaction to this force is already implied in the gas momentum equation (5) and need not be explicitly represented.

2.3. Energy Conservation

The perfect gas law is given as:

$$\theta p = \bar{\rho} RT \quad \bar{\rho} e = \bar{\rho} h - \theta p \quad (8)$$

The analysis could utilize a cubic form of the gas law that would apply better at high pressures. However, it will not change our major conclusions.

Then, the energy equation can be written as:

$$\begin{aligned} & \frac{\partial}{\partial t} (\bar{\rho} h) + \frac{\partial}{\partial x_j} (\bar{\rho} u_j h) - \frac{\partial}{\partial x_j} \left(\lambda \frac{\partial T}{\partial x_j} \right) - \frac{\partial}{\partial x_j} \left(\bar{\rho} D \sum_m h_m \frac{\partial Y_m}{\partial x_j} \right) \\ &= \theta \frac{dp}{dt} + \Phi + \bar{\rho} \sum_m \dot{w}_m Q_m - \dot{M} L_{eff} + \dot{M} h_s \end{aligned} \quad (9)$$

L_{eff} is defined as the ratio of the conductive heat flux from gas to liquid surface to the vaporization mass flux. For the case where no heat passes to liquid interior (constant-liquid-temperature case), $L_{eff} = L$, the latent heat of vaporization. Note that,

$$h = \int_{T_{ref}}^T c_p dT' = \int_{T_{ref}}^T \left[\sum_m Y_m c_{pm}(T') \right] dT'$$

and

$$\frac{dp}{dt} \equiv \frac{\partial p}{\partial t} + u_j \frac{\partial p}{\partial x_j} \quad (10)$$

For low Mach number, the viscous dissipation Φ can be neglected.

We reorganize the energy equation (9) to place the viscous term, terms related to conductive and mass transport of energy, and terms related to energy exchange between the phases into one source-sink term identified as $\dot{\varepsilon}$. Also, we define the energy conversion rate term to be:

$$E \equiv \bar{\rho} \sum_m \dot{w}_m Q_m \quad (11)$$

$$\begin{aligned} \frac{\partial}{\partial t} (\bar{\rho} h) + \frac{\partial}{\partial x_j} (\bar{\rho} u_j h) - \frac{\partial p}{\partial t} - u_j \frac{\partial p}{\partial x_j} - E &= \dot{\varepsilon} \\ \dot{\varepsilon} \equiv (\theta - 1) \frac{dp}{dt} + \Phi + \frac{\partial}{\partial x_j} \left(\lambda \frac{\partial T}{\partial x_j} \right) + \frac{\partial}{\partial x_j} \left(\bar{\rho} D \sum_m h_m \frac{\partial Y_m}{\partial x_j} \right) - \dot{M} L_{eff} + \dot{M} h_s \end{aligned} \quad (12)$$

The liquid-phase temperature will generally vary spatially and temporally within the liquid droplet. A Navier–Stokes solver or some approximate algorithms can be used to determine the temperature field in the droplet, including the surface temperature. In the special case of a uniform but time-varying liquid temperature in the droplet, an equation for the thermal energy contained in the droplet can be useful. If e_l is the liquid internal energy per unit mass, then $\bar{\rho} e_l$ is the liquid internal energy per unit volume of mixture. In the case in which a spacial variation of temperature occurs in the droplet, e_l could be considered as the average over the droplet. However, an equation for e_l would not be so useful here since the difference between the average value and the surface value is not specified but yet the results are most sensitive to the surface temperature. Viscous dissipation can be neglected in the liquid-phase energy equations. The liquid energy equation can be written as:

$$\frac{\partial}{\partial t} [\bar{\rho}_l e_l] + \frac{\partial}{\partial x_j} [\bar{\rho}_l u_{lj} e_l] = \dot{M} [L_{eff} - L - e_{ls}] \quad (13)$$

3. WAVE DYNAMICS

Equations (1), (5), and (12) can be re-stated together with Eq. (8) to form the basis for the development of a wave equation. The superscript bar is omitted here for convenience in further analysis.

$$\begin{aligned} \frac{\partial \rho}{\partial t} + \frac{\partial}{\partial x_j} (\rho u_j) &= \dot{M} & \frac{\partial}{\partial t} (\rho u_i) + \frac{\partial}{\partial x_j} (\rho u_j u_i) + \frac{\partial p}{\partial x_i} &= \dot{I}_i \\ p = \rho R T & \quad \frac{\partial}{\partial t} (\rho h) + \frac{\partial}{\partial x_j} (\rho u_j h) - \frac{\partial p}{\partial x_j} - E &= \dot{\varepsilon} \end{aligned} \quad (14)$$

The development of a wave equation begins by subtracting the divergence of the momentum equation from the time derivative of the continuity equation above. This yields

$$\frac{\partial^2 \rho}{\partial t^2} - \frac{\partial^2 p}{\partial x_j \partial x_j} = \frac{\partial^2 (\rho u_i u_j)}{\partial x_i \partial x_j} + \frac{\partial \dot{M}}{\partial t} - \frac{\partial \dot{I}_j}{\partial x_j} \quad (15)$$

Neglect of the variation of the gas constant R due to the multicomponent nature of the fluid, assumption of constant specific heats c_p and c_v with $h = c_p T$ and $\gamma = c_p/c_v$, and differentiation of the perfect gas equation gives

$$\frac{\partial \rho}{\partial t} = \frac{\gamma}{a^2} \frac{\partial p}{\partial t} - \frac{(\gamma - 1) \rho}{a^2} \frac{\partial h}{\partial t} \quad (16)$$

Use of the combined First and Second Laws of Thermodynamics to write:

$$\rho \frac{\partial h}{\partial x_i} = \frac{\partial p}{\partial x_i} + \rho T \frac{\partial s}{\partial x_i}$$

and substitution for $\partial h / \partial x_i$ in the energy equation (12) using the continuity equation (1) leads to

$$\rho \frac{\partial h}{\partial t} = \frac{\partial p}{\partial t} - \rho u_j T \frac{\partial s}{\partial x_j} + E + \dot{\varepsilon} - h \dot{M} \quad (17)$$

Combine Eqs. (16) and (17) to eliminate enthalpy and differentiate again with respect to time to obtain a second derivative of density with respect to time. Eliminate by substitution that second derivative from Eq. (15). Note that, for a perfect gas, $(\gamma - 1) h = a^2$.

$$\frac{\partial^2 p}{\partial t^2} - a^2 \frac{\partial^2 p}{\partial x_j \partial x_j} = \frac{\partial \rho}{\partial t} \frac{\partial a^2}{\partial t} + a^2 \frac{\partial^2 (\rho u_j u_i)}{\partial x_i \partial x_j} + (\gamma - 1) \frac{\partial E}{\partial t} + S_3 \quad (18)$$

where the 3D source term S_3 is given by

$$S_3 \equiv (\gamma - 1) \left[\frac{\partial \dot{\varepsilon}}{\partial t} - \dot{M} \frac{\partial h}{\partial t} - \frac{\partial (\rho T u_j \partial s / \partial x_j)}{\partial t} \right] - a^2 \frac{\partial \dot{l}_j}{\partial x_j} \quad (19)$$

This equation may be solved simultaneously with Eq. (5) to solve for pressure p and velocity components u_i . Other inputs are needed for coupling with liquid phase behavior and energy release from combustion processes.

The left-hand side of Eq. (18) represents the wave operator in three dimensions. A mild nonlinearity appears through the coefficient a^2 . The first and second terms on the right-hand side are strongly nonlinear terms that are conservative and do not drive or damp the oscillation. However, they will affect the wave shape. The third and fourth terms on the right represent the influence of the chemical energy conversion rate E , viscous and transport effects embedded in the rates \dot{l}_i and $\dot{\varepsilon}$, impact of volume fraction θ , and exchanges of mass, momentum, and energy between the phases embedded in the rates \dot{M} , \dot{l}_i , and $\dot{\varepsilon}$, respectively. These terms can be strong drivers or strong dampers of the nonlinear oscillation; consequently, they will be discussed further below.

Entropy gradients in the flow can be neglected for the purpose of developing a model equation. Thus, one term in the definition given by Eq. (19) can be neglected. One can assume that fine-scale mixing eliminates these entropy gradients. The length scales for transverse gradients of entropy, other scalar properties and vorticity are of the order of the injector diameter, the order of spacing between adjacent injectors, or smaller. These dimensions are smaller than the common wavelengths of oscillations in the combustion chamber. Also, these properties advect and diffuse but are not propagated by acoustic waves. Turbulent mixing will uniformize these quantities rapidly while acoustical pressure and velocity oscillations will not be vitiated by turbulence. These comments would not pertain to entropy generation if the acoustic waves form shock waves or detonations, which are possibilities for longitudinal oscillations and, in an annular chamber, for transverse oscillations. In that case, the entropy generation (i.e., shock dissipation) can be significant in determining the limit-cycle oscillation amplitude.

In evaluating driving and damping mechanisms for the wave equation (18), realize that a hypothetical first-time-derivative-of-pressure term appearing on the right side with a positive coefficient would be a driving term through which energy is added to the oscillation. With a negative coefficient on the right side, the term would provide damping for the oscillations. Consequently, the question is whether E , \dot{M} , and $\dot{\varepsilon}$ are in-phase or out-of-phase with the oscillating pressure. Thus, if the rate at which energy is added locally via oxidation or transport is in-phase (out-of-phase) with pressure, driving (damping) of the oscillation is occurring at that location. If the divergence of the impulse I_i is in-phase (out-of-phase) with the pressure first time derivative, damping (driving) of the oscillation appears. “In-phase” or “out-of-phase” each implies a band so that phase angle can vary by $\pm 90^\circ$.

Equation (18) is coupled with the velocity; thus, it should be solved simultaneously with Eq. (5). The system has higher derivatives appearing through the viscous and transport terms, which are included in source terms as presented. These higher derivatives create an elliptical system of equations if they are important terms. Typically, however, transport and viscosity manifest their impacts on a much smaller length scale than the acoustic wavelength. Therefore, the phenomenon remains hyperbolic rather than elliptical for practical purposes. One could set the viscous and transport terms to zero, yielding the following definitions of the inviscid sources $\dot{\varepsilon}_I$ and $\dot{I}_{i,I}$:

$$\begin{aligned}\dot{\varepsilon}_I &\equiv (\theta - 1) \frac{dp}{dt} - \sum_k n^{(k)} \dot{m}^{(k)} L_{\text{eff}}^{(k)} + \sum_k n^{(k)} \dot{m}^{(k)} h_s^{(k)} \\ \dot{I}_{i,I} &\equiv (1 - \theta) \frac{\partial p}{\partial x_i} + \sum_k n^{(k)} \dot{m}^{(k)} u_{l,i}^{(k)} - F_{Di}\end{aligned}\quad (20)$$

Equation (18) will still be coupled with Eq. (5) to solve for velocity and pressure; however, for consistency, the viscous terms in the momentum equation should be neglected to solve for the wave behavior on the scale of the acoustic wavelength (or equivalently on the scale of the combustion chamber size). The aerodynamic force per volume for the condensed phase F_{Di} includes both lift and drag; exceptions are made to retain this term in the inviscid limit because it affects droplet motion and position. Equation (18) now is strictly in hyperbolic form. The input for E can involve an analysis on a finer length scale, accounting for transport and viscous terms. For a single-phase flow, the system is much simpler with the source terms \dot{M} , $\dot{I}_{i,I}$, and $\dot{\varepsilon}_I$ becoming identically zero. Nevertheless, the terms giving the highest derivatives remain the same for both the single-phase equation and the two-phase equation, reflecting the similarity of the wave propagation in both cases.

In the above formulation of the equations for the wave dynamics, selected consideration of turbulence has been advocated. Under the assumption that turbulent length scales are small compared to acoustical wavelengths, the affect on the dynamics is neglected. For the shorter kinematic (i.e., entropy, temperature, and vorticity) waves, turbulence is assumed to help uniformize those quantities and reduce the importance of those waves. For the many flames that have shorter characteristic lengths, the impact of turbulence can be important and must be evaluated. For example, consider a combustion chamber with many injectors, each of a size scale that is much smaller than the chamber size. If mixing is fast and chemical kinetics is controlling, the effect of the small-scale turbulence is not too important. However, if mixing is rate controlling, the small scales of turbulence can be very important.

3.1. Models for Source Terms

There is a need to close the conservation equations by describing the various source terms that appear: $\dot{\omega}_m$, \dot{M} , \dot{I}_i , and $\dot{\varepsilon}$. The chemical kinetic rates in a high-temperature, high-pressure rocket environment are commonly much faster than mixing and vaporization rates. Thus, great accuracy in their determination is generally not required because they are not rate controlling and do not significantly affect time lags. For that reason, a one-step chemical reaction model often suffices. Westbrook and Dryer (1984) provides useful one-step models for $\dot{\omega}_m$ in the case of hydrocarbon oxidation. A typical rate law for burning a hydrocarbon C_xH_y would be of the form $\dot{\omega}_{C_xH_y} = A\rho^{a+b-1}Y_{C_xH_y}^a Y_{O_2}^b \exp[-E_A/(R_u T)]$.

For the modeling of \dot{M} for spray flows, knowledge of the droplet size distribution or average droplet size produced in the atomization process is needed; the vaporization rate and lifetime of the individual droplet will depend on its initial size and \dot{M} at \vec{x} , t will depend on the vaporization rates of the droplets in that neighborhood at that instant. Then, a vaporization model is needed for the slower vaporizing propellant, which is the hydrocarbon fuel in liquid-hydrocarbon/oxygen engines but becomes the liquid oxygen with hydrogen/oxygen engines. Pioneering works on the vaporization and burning fuel droplets are described by Godsave (1953), Spalding (1953), and Williams (1958, 1959, 1960, 1985). Generally, the early theory focused on the burning of isolated droplets with spherically symmetric, quasi-steady gas phase and steady liquid temperature. More recent models add the effects of transient liquid-phase heat transfer, which is typically the slowest process in droplet heating, and vaporization in high temperature environments (Sirignano, 2010), internal liquid circulation and convective liquid heating, and gas-film convective heat transfer. The most-often-used model having those attributes was developed by Abramzon and Sirignano (1989). An extension of that model to address multi-component fuels was developed by Continillo and Sirignano (1988). It is desirable to have extensions that would account for interactions of the droplets with neighboring droplets and with the smaller turbulent eddies. We know that these interactions modify Nusselt number, Sherwood number, and drag coefficient from the values for isolated droplets. Consequently, vaporization rates and drag forces are modified. Sirignano (2014) reviews recent progress in those directions. Related issues will be discussed in the next section.

3.2. Boundary Conditions

Wall conditions. Equation (4) shows that the total normal stress is zero at a wall where the normal velocity of each phase must go to zero. For the inviscid case, this means both normal velocity and normal pressure gradient are zero at the wall; tangential velocity may be non-zero. For the viscous case, normal velocity and normal pressure gradient can be set to zero also because normal viscous stress should be negligible; tangential velocity is also zero. If a wall has an acoustic liner, the admittance for that liner may be used as a boundary condition (Sirignano, 1972; Tang and Sirignano, 1973; Tang et al., 1973).

Injector or burning surface. For a liquid-propellant rocket engine, portions of an injector face will essentially be a wall with wall-type boundary conditions on the normal vectors. Other portions will be orifice exits where jet flows occur. Here, traditional inflow conditions can be placed on mass flow (or velocity), temperature, and composition. If mass inflow is controlled, the boundary conditions can be placed on mass flux with density and velocity allowed to adjust with pressure oscillation. If the injector experiences internal oscillations, a coupled analysis of injector and chamber flow might be needed with

boundary conditions set upstream at a plenum (Popov et al., 2014; Sirignano and Popov, 2013). At the gasifying surface of a solid propellant in a solid-propellant or hybrid rocket engine, the mass flux per unit area of the propellant (equal to the product of the regression rate and solid density) must be analyzed by coupling the gas-phase mixing and reaction layer with the solid-phase thermal layer (Krier et al., 1968; Sirignano, 1968).

Choked nozzle flow. The nozzle provides an important damping mechanism and modifier of natural frequencies. The nozzle has an acoustical impact between those of the open-end chamber and the closed-end chamber. Like the open-end, acoustical energy continually flows out. On the other hand, the convergent walls provide some reflection of waves. The modifications of effective chamber size by the addition of the convergent nozzle affects the natural resonant frequencies as well, generally reducing the magnitude as the nozzle volume increases.

Early work on the boundary condition at the entrance to the convergent choked nozzle for linear longitudinal-mode combustion-chamber oscillations was done by Tsien (1952) and Crocco and Cheng (1953, 1956). Extensions to 3D oscillations and nonlinear theory was performed by Crocco and co-workers (Crocco and Sirignano, 1967, 1966; Zinn and Crocco, 1968). The linear theory used admittance coefficients, which related pressure oscillations in the nozzle entrance plane to oscillations of velocity components and entropy (or temperature) at the same location. These coefficients were obtained by integration by Crocco and Sirignano (1967) of the equations governing the oscillations in the convergent portion of the nozzle. For a choked nozzle, acoustic signals will not propagate upstream from the throat; hence, the behavior of the flow in the divergent portion of the nozzle has no consequence on the chamber instability. In the limit of a short nozzle, the wavelength of the oscillation becomes much longer than the convergent length; thus, a quasi-steady nozzle flow can be assumed. For longitudinal oscillations, that means the chamber length is much greater than the convergent nozzle length and the Mach number at the nozzle entrance remains constant under oscillation although pressure and velocity fluctuate.

The short-nozzle boundary assumption applies for transverse-mode and 3D oscillations if the length of the convergent portion of the nozzle is of negligible length compared to both the chamber length and circumference and if the exit plane has many small closely-spaced equally sized and shaped nozzle holes so that the angle of convergence is not too large. Then, the relationship developed by Crocco and Sirignano (1966) applies. For isentropic nozzle flow of a perfect gas with constant specific heats,

$$\frac{1}{M_x} \left[1 + \frac{\gamma - 1}{2} (M_x^2 + M_y^2) \right]^{(\gamma+1)2(\gamma-1)} = \left(\frac{\gamma + 1}{2} \right)^{(\gamma+1)/2(\gamma-1)} \left(\frac{A_c}{A_t} \right) \quad (21)$$

where a is the speed of sound at the entrance to the nozzle capture zone and the two components of Mach number at that entrance are $M_x = u/a$ and $M_y = v/a$. A_c and A_t are the nozzle flow capture area and throat area. The capture area is determined by following streamlines upstream for a short distance from the nozzle hole. The nozzle holes are considered to be sufficiently densely packed so that the nozzle entrance area and capture area differ only slightly. Furthermore, distances are sufficiently smaller than wavelengths so that quasi-steady flow is assumed and streamlines may be defined. For zero-valued transverse-velocity component (i.e., longitudinal-mode oscillation or steady state), $M_y = 0$ and therefore $M_x = u/a$ is constant, which provides a simple boundary condition. With a transverse component to the oscillation, both M_x and M_y can oscillate. Therefore, Eq. (21)

relates the two velocity components $u(t, L, Y)$ and $v(t, L, y)$ with the thermodynamic variable $a(t, L, y)$ at the chamber exit. Another form of the same relation is informative and is provided below:

$$\gamma^{1/2} \left[\frac{1 + [(\gamma - 1)/2] (M_x^2 + M_y^2)}{(\gamma + 1)/2} \right]^{(\gamma+1)/[2(\gamma-1)]} = \frac{A_c}{A_t} u (RT_c)^{-1/2} = \frac{\dot{m} (RT_c)^{1/2}}{A_t p_c} \quad (22)$$

where \dot{m} , P_c , and T_c are the individual nozzle mass flux, capture-flow static pressure, and capture-flow static temperature. Note that the quantity on the far right side of Eq. (22) is constant for steady-state or longitudinal oscillations but p_c , T_c , and \dot{m} may still oscillate there. Obviously, they can oscillate also for transverse modes where M_x and M_y also oscillate.

Using perturbation theory, Zinn and Crocco (1968) extended the use of 3D nozzle admittance coefficients to third order in a perturbation series of pressure amplitude.

4. MECHANISMS AND CHARACTERISTIC COMBUSTION TIMES

The combustion process generally responds to fluctuations and oscillations in density and temperature (which relate to pressure) and velocity. Gasification rates, mixing rates, and chemical rates can vary as these quantities fluctuate. Thereby, the rate E in Eq. (18) depends upon the histories of the pressure p and other variables. Consequently, an oscillation in E might lag the oscillation in p . The classical Rayleigh criterion for optimal driving of the oscillation by the energy addition E is met when E and p are exactly in phase (or equivalently when E lags p by a time equal to the period of oscillation multiplied by any positive integer). Some reduced amount of driving occurs when E differs from one of the optimal lag values by less than one-quarter of the time period. The oscillation is damped when it lags by an amount that differs from every optimal value by more than one-quarter of the time period. Substantial analysis is required to determine the time lag associated with combustion under these oscillatory conditions.

Combustion can be viewed and well approximated as a sequence of processes for the reactants with each process coming to completion for a given infinitesimal element of mass before the next process: e.g., injection and atomization, vaporization, mixing, and exothermic chemical reaction. The overall time duration τ for N sequential processes is the sum of the time durations of all processes. The rate r of a process can be taken as the reciprocal of its duration. Thereby, the reciprocal of the overall rate r_o becomes the sum of the reciprocal rates of the individual processes:

$$\tau = \sum_{i=1}^N \tau_i = \sum_{i=1}^N \frac{1}{r_i} = \frac{1}{r_o} \quad (23)$$

If one process $i = *$ becomes an order of magnitude larger in its duration than any other, we may approximate $r_o = r_*$; i.e., the slowest rate becomes controlling. Of course, if the overall duration τ of the combustion process becomes significant in magnitude compared to the period of oscillation, the combustion process is not quasi-steady and a history (i.e., time-lag) effect exists. The rate E in Eq. (18) has units of energy per unit time per unit volume and differs from the r_i values; however, the rate $E(t, \vec{x})$ will depend on the values

of r_i over the duration of the combustion process prior to time t for the element of mass that completes combustion at time t and point \vec{x} .

Combustion processes introduce many length and time scales. Those length scales generally are smaller than the acoustic wavelength and some of the flow structures. Some of the combustion time scales can be of the order of a wave travel time or period of oscillation. In the following subsections, the various descriptions of combustion processes are discussed. The Sensitive-Time-Lag approach was the early attempt to bypass a detailed description of combustion and is discussed first. The other subsections discuss specific combustion processes and their possible impacts on combustion instability.

4.1. Sensitive Time-Lag Theory

During the 1950s, when our knowledge of unsteady combustion processes was rather poor, Crocco and Cheng (1953) proposed the heuristic approach named the Sensitive Time-Lag Theory. Previously, a constant time lag had been used to explain the delayed response of injected liquid-propellant mass flux into a combustion chamber, which experienced a varying chamber pressure. The new theory differed because the time lag itself varied under oscillation of thermodynamic properties in the combustion chamber. In its first version, the combustion process rate was related only to pressure p .

The theory assumed that the energy release rate E at time t required a certain history prior to the instant of energy release at t ; specifically, the pressure history had to satisfy the condition that the integral $\int_{t-\tau(t)}^t p(t')^n dt' = C$ where n , τ , and C are, respectively, the constant (positive) interaction index, the instantaneous value of the time lag, and a constant independent of pressure. By a shortening (lengthening) of the time lag due to a positive (negative) pressure fluctuation, the mass burning rate became instantaneously faster (slower) than the injection rate of mass. The values of the interaction index and steady-state time lag f were intended to be determined empirically from choice of propellants and injector design.

Using perturbation theory, $p = \bar{p} + p'$, $\tau = \bar{\tau} + \tau'$ and $E = \bar{E} + E'$ linear theory shows that the time derivative of the time lag $d\tau/dt = d\tau'/dt = -n[p'(t) - p'(t - \bar{\tau})]$. Furthermore, it follows that:

$$\frac{\partial E}{\partial t} = \frac{\partial E'}{\partial t} = -\frac{\partial \tau}{\partial t} = -\frac{\partial \tau'}{\partial t} = n[p'(t) - p'(t - \bar{\tau})] \quad (24)$$

This presentation is somewhat simplified by the assumption that the mass undergoing the combustion process during the time lag does not change its position significantly during that duration. For a more general analysis, see Crocco and Cheng (1956). It can be seen that if the time lag $\bar{\tau}$ is the product of one-half the period of oscillation and an odd positive integer, the energy rate E will be perfectly in phase with the pressure. If $\bar{\tau}$ differs by less than a quarter of an oscillation period from one of those optimal magnitudes, an in-phase component of E will still be present supporting the oscillation in accordance with the Rayleigh criterion.

The theory met with some success in characterizing and predicting instability. For the transverse (i.e., 3D oscillation modes), the rate of combustion and subsequent time lag needed to be coupled with both pressure and gas velocity (Reardon et al., 1964). In the transverse oscillation, velocity had a stronger effect on atomization, vaporization, and mixing. The time-lag theory was extended to nonlinear analyses using a perturbation series

in amplitude (Crocco and Mitchell, 1969; Mitchell et al., 1969; Sirignano, 1964; Zinn, 1968). Zinn and Powell (1971) later used the time-lag theory with the Galerkin method for nonlinear oscillations.

The theory is strictly violated if, in order to match experimental data, $\bar{\tau}$ and/or n must be considered as functions of the frequency of oscillation. This need to assume a frequency dependence has happened in some situations. A more general way to view the Sensitive Time-Lag Theory is as a two-parameter system where each of the parameters n , $\bar{\tau}$ can be functions of propellant selection, injector design, and oscillation frequency. Then, it becomes analogous to a gain-phase representation for the admittance E'/p' as a complex number. In fact, n and $\bar{\tau}$ can easily be related to gain, phase, and frequency. Others later legitimately used gain and phase for liquid-rocket instability analysis (Culick, 2006). As this author knows from personal communications, Professor Crocco viewed the Sensitive Time-Lag Theory (also known as the n , τ theory) as a heuristic attempt to analyze combustion instability until superior knowledge of unsteady combustion processes was developed.

4.2. Premixed Combustible Gaseous Propellants or Rapidly Mixed Propellants

In cases where the propellants are prevaporized and premixed before injection or rapidly mixed upon injection, the duration for the combustion processes can be very much shorter than the typical period of oscillation in a chamber. For example, the characteristic residence time for flow through a premixed flame can be $O(10^{-4} \text{ sec})$ while oscillation periods in combustors with dimensions of several tens of centimeters or greater will have periods of $O(10^{-3} \text{ sec})$ or larger. Thus, a reasonable approximation is that the rate E responds to the instantaneous pressure or temperature without a lag. For the premixed flame, two rates enter Eq. (23): heating or mixing rate r_M and chemical rate r_R . Since, in the quasi-steady flame, chemical rate determines heating rate in proportion, the overall rate (and the flame speed) becomes proportional to the square root of the product $r_M r_R$. This also determines the overall rate E . If the combustion zone is viewed as a well-stirred reactor where the mixing time is negligible and chemical kinetic rates are controlling, the chemical rate r_R determines approximately the overall energy release rate per unit volume E .

These assumptions fit a certain experimental gas-rocket motor (Bowman, 1967; Bowman et al., 1965), which was analyzed using a nonlinear perturbation approach based on a 1D unsteady characteristic-coordinate method (Sirignano and Crocco, 1964). The results from experiment and theory agreed very well. That is, for combustible mixtures with high flame temperatures, the region with near-stoichiometric mixture ratio was stable while the lean and rich regions were unstable (see Figures 1 and 2). As the combustible mixture is diluted, the flame temperature lowers and the stability limits approach closer to the stoichiometric conditions for hydrogen fuel in Figure 1. For methane and air in Figure 2, the flame temperature is sufficiently low that the stoichiometric and near-stoichiometric region is unstable. However, enrichment of the air with oxygen yields higher flame temperatures and thus leads to separation into two zones of instability. In particular, one instability zone is for fuel-rich mixtures and the other is for fuel-lean mixtures with a stable zone near stoichiometric conditions. Periodic longitudinal-mode oscillations were observed with a shock wave traveling back and forth with reflections at the injector face and entrance to a short nozzle; near-sawtooth pressure profile oscillations were measured and predicted. The

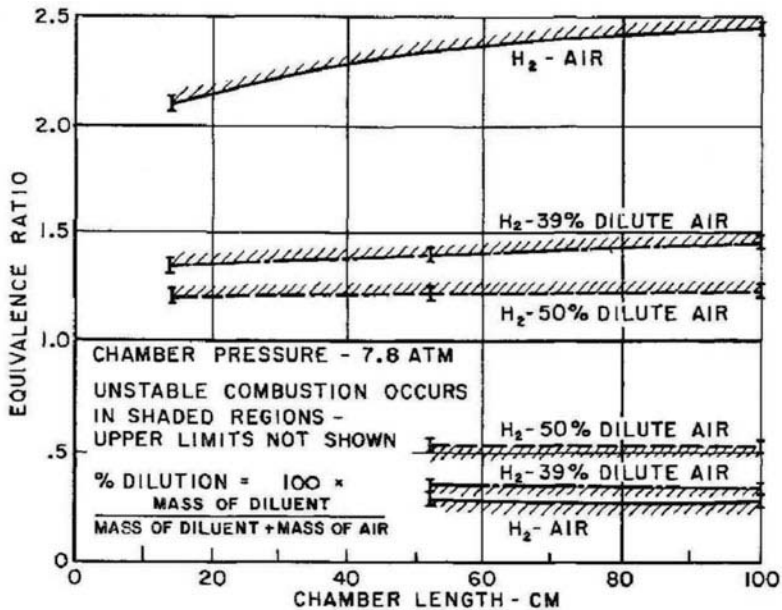


Figure 1 Gas rocket instability domain as a function of chamber length and mixture ratio. (Reprinted from Bowman et al., 1965, with permission from AIAA)

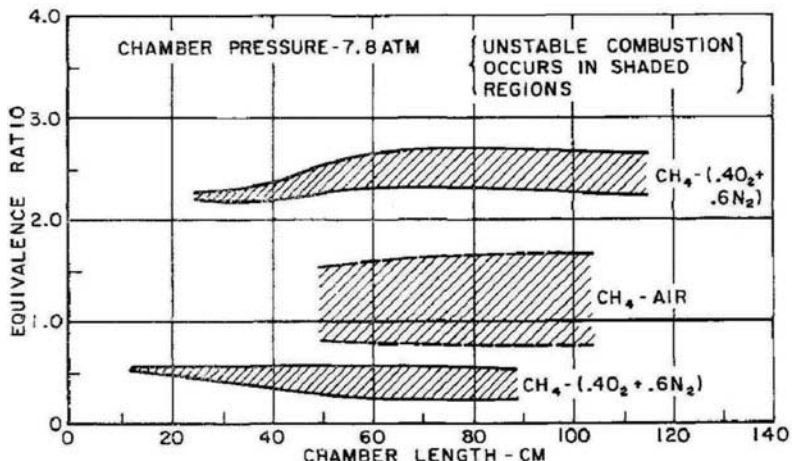


Figure 2 Gas rocket instability domain as a function of chamber length and mixture ratio. (Reprinted from Bowman et al., 1965, with permission from AIAA)

amplitude of the oscillation was proportional to the mean-flow Mach number in the chamber at a fixed mixture ratio and grew as the mixture became more lean (for a lean mixture) or more rich (for a rich mixture). The flame temperatures at the rich and lean stability limits were identical at a value less than the stoichiometric adiabatic flame temperature.

The appearance of the identical value of temperature at both rich and lean was explained using a one-step chemical kinetic model by Sirignano and Crocco (1964). Their

theory used the inviscid equations in 1D form and considered only the single phase, i.e., gas. Therefore, $\theta = 1$, $\dot{\varepsilon} = 0$; $\dot{I}_i = 0$; $\dot{M} = 0$ in Eqs. (4) and (18). Using the characteristic coordinate form of the equations, it was possible to capture the discontinuous shock wave. Entropy waves were neglected and, since entropy jump across the shock is third order in pressure amplitude, that higher-order effect was neglected. If kinetics were rate controlling, $E \sim e^{-E_A R_u T}$, where E_A , R_u , and T are the activation energy, universal gas constant, and flame temperature, respectively. From perturbation theory and the assumption of a polytropic relation between temperature and pressure (accurate to second order in amplitude), it follows that, for a well-stirred reactor model of the gas-rocket combustor,

$$E' \sim \frac{E_A T'}{R_u \bar{T} \bar{T}} e^{-E_A R_u \bar{T}} \sim \frac{E_A}{R_u \bar{T}} \bar{E} \frac{p'}{\bar{p}} \quad (25)$$

Therefore, for a given pressure perturbation, the fractional increase in burning rate E'/\bar{E} becomes larger as the steady-state flame temperature \bar{T} becomes smaller, i.e., as the mixture ratio moves further from the stoichiometric value in either direction. The mean burning rate $\bar{E} \sim M$ is the mean flow Mach number. Also, the nozzle admittance coefficient is proportional to M . Consequently, the nonlinear wave amplitude becomes proportional to M .

In this situation where the characteristic combustion time is negligibly small compared to the period of oscillation, the energy release rate E is essentially instantaneously responsive to and in phase with the time-varying pressure p . Note that a very similar result appears with a quasi-steady premixed-flame model of the gas-rocket combustor. The only difference is that the square-root dependence makes $E_A/(2R_u T)$ replace the nondimensional factor $E_A/(R_u T)$, which appears in the well-stirred reactor model.

4.3. Mixing-Controlled Combustion

In some liquid-propellant rocket applications, the propellants are gaseous as they enter the combustion chamber. They might have been heated by prior use as a wall coolant as they flow towards the injectors. Or they might have flowed through a separate burner and been used to drive a turbo-pump before injection into the main combustor in a vitiated and heated form. Consequently, the two relevant rates are for mixing and exothermic chemical reaction, r_M and r_R . A model for transverse combustion instability in this type of combustor has recently been created and used by Sirignano and Popov (2013) and Popov et al. (2014). The problem can be approached as a multi-scale problem.

On the scale of the wavelength, the wave dynamics can be considered as non-heat conducting, non-diffusive, and inviscid. Also, we have a single gaseous phase. Thus, $\theta = 1$, $\dot{\varepsilon} = 0$; $\dot{I}_i = 0$; $\dot{M} = 0$; in Eqs. (4) and (18). On the contrary, for the scale of the injector ports, which relate to the combustion scales, terms associated with viscosity, heat conduction, and mass diffusion were retained in the analysis of the flames. In particular, a separate analysis on a finer scale coupled Eqs. (1), (3), (5), and (12). That is, a turbulent, axisymmetric, transient jet-flame model was created for each injector to indicate spatial and temporal variations in temperature, species mass fractions, and chemical reaction rates in response to the local pressure oscillations. The value for E in Eq. (18) was obtained from the N jet-flame models for the N co-axial injectors.

Figure 3 shows the magnitude of the in-phase response of E' for one isolated co-axial methane-oxygen injector with imposition of a given amplitude magnitude of the sinusoidal

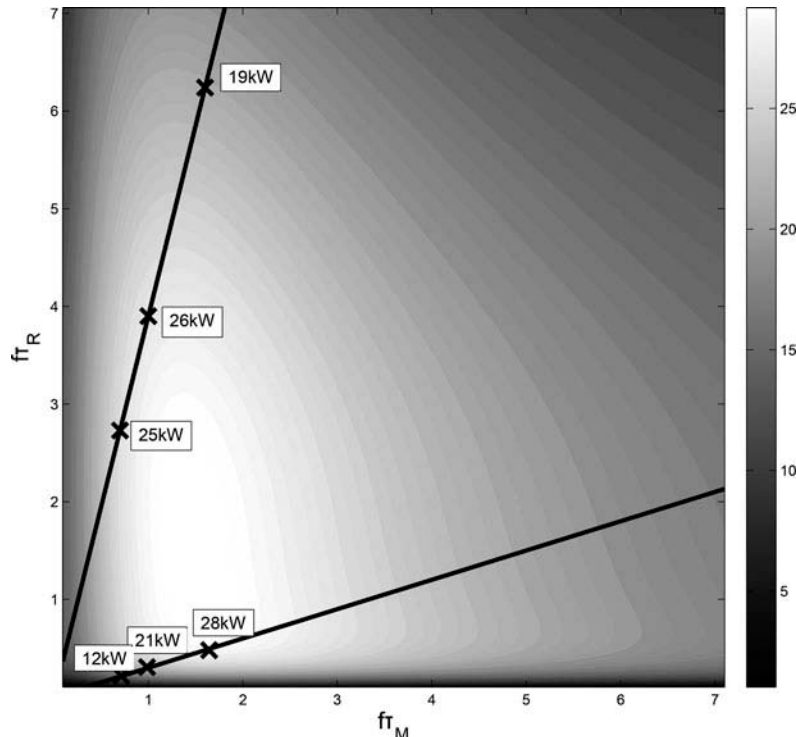


Figure 3 Oscillation amplitude of in-phase component of E for a given sinusoidal oscillation of p . The volume-integrated value of E for an injector is presented in kilowatt units. [© William A. Sirignano. From Sirignano and Popov (2013). Reproduced by permission of William A. Sirignano. Permission to reuse must be obtained from the rightsholder.]

oscillation of p' . The contour plot shows the amplitude of the volume integral of E contributed by that single coaxial methane-oxygen coaxial injector as a function of the two characteristic times normalized by the period of oscillation: $f\tau_M$ and $f\tau_R$ where f is the oscillation frequency. Each straight line in the figure considers a fixed ratio of the characteristic combustion times, τ_M/τ_R with varying f . The cross markings indicate locations of resonant transverse-mode oscillations for a given 28-cm-diameter, ten-injector combustion chamber. They correlate with regions of high response for E . One-step chemical kinetics and turbulent jet mixing models were used in the calculations by Sirignano and Popov (2013); the line slopes indicate that one path with the smaller slope has a longer mixing time while the other path with the steeper slope has a longer chemical time. Consequently, the first line corresponds to mixing-rate control while the other applies to kinetic-rate control. The oscillation of E lags the pressure p indicating that at least one of the characteristic combustion times is sufficiently long to produce the time-lag effect. The line with the lower value of the slope corresponds to actual experimental observations for methane oxidation. The case with the larger slope was artificially chosen to demonstrate the dependence.

At the high temperatures and pressures in the combustion chamber, the kinetics will be fast and mixing will become rate controlling. Turbulent diffusivities for heat and mass and a turbulent viscosity are chosen, which depend on the jet velocity at the exit of the injector and the injector radius. The jet velocity and, therefore, the diffusivities and

viscosity will oscillate with pressure in the two cases studied: (1) injector mass flux remains constant with pressure oscillation or (2) the flow through the injector is acoustically coupled to combustion chamber oscillation.

4.4. Vaporization-Controlled Combustion

In the case where liquid fuel (and/or liquid oxygen) is injected into the combustion chamber, two other characteristic combustion times are added. In addition to a gas mixing time and a chemical reaction time, a time for liquid stream breakup into droplets and a time for droplet vaporization are present. The atomization time is commonly of $O(10^{-5} - 10^{-4}$ sec), which means that it usually is fast enough compared to the oscillation period so that it can be taken as instantaneous. It usually is modified most from the nonoscillatory behavior by transverse velocity oscillations and changes would be in phase with that velocity. Thus, for a transverse spinning or traveling wave, the atomization process oscillation will be in phase with pressure while it is 90° out of phase for a tangential or radial standing mode. The fluctuation in the atomization process is very important because it affects the droplet-size distribution and, therefore, indirectly has substantial impact on combustion time lag.

For hydrocarbon fuels burning with oxygen or air, the vaporization time is commonly longer than the chemical time and mixing time. Therefore, it is rate controlling and determines the time lag in oscillatory combustion. Early works by Priem and Heidmann (1960) and Heidmann and Wieber (1965) considered implicitly a time lag in the heating of the liquid droplet interior, using a quasi-steady gas-phase assumption. However, they assumed that the temperature remained uniform through the liquid interior although time varying. This would increase the impact of the thermal inertia and underestimate fluctuations in surface temperature and vaporization rate during oscillation. In analyses by Strahle (1965a, 1965b, 1965c, 1967) and Williams (1965), the emphasis was placed on gas-phase unsteadiness while liquid-phase temperature did not oscillate. Flat-plate, stagnation-point, and wake-flame models were used. The examination of a time lag due to liquid heating with both spatial and temporal variations in the liquid-phase was first done by T'ien and Sirignano (1971) with the emphasis on the rocket combustion instability problem; a flat-plate model was used. The heating time of the liquid is the slowest process and, therefore, rate-controlling for the vaporization time. Consequently, the liquid-phase unsteadiness determines frequency range where vaporization rate is most responsive to fluctuations in the ambient gas. The most advanced droplet modeling is built on this premise (Sirignano, 2010).

For combustion instability cases where vaporization is rate controlling, the frequency domain where instability is most probable will align with the characteristic time for heating of the droplet liquid interior. (Exceptions can occur at high pressures in the near-critical domain, which is discussed in the next subsection.) One study of longitudinal-mode instability in a liquid-fueled ramjet combustor by Bhatia and Sirignano (1991) shows some interesting and relevant results for rockets as well as ramjets. They consider a 1D analysis of a combustion chamber at elevated pressure with inflowing decane droplets and air and a short, choked exit nozzle. Configurations with various chamber lengths, average initial droplet size, and mixture ratios were examined. Thereby, both the characteristic combustion time and the natural longitudinal frequency were varied widely. They used a vaporization model that accounted for transient heating of the droplet liquid interior and convective heating through a gas-film boundary layer and a liquid internal circulation due to relative

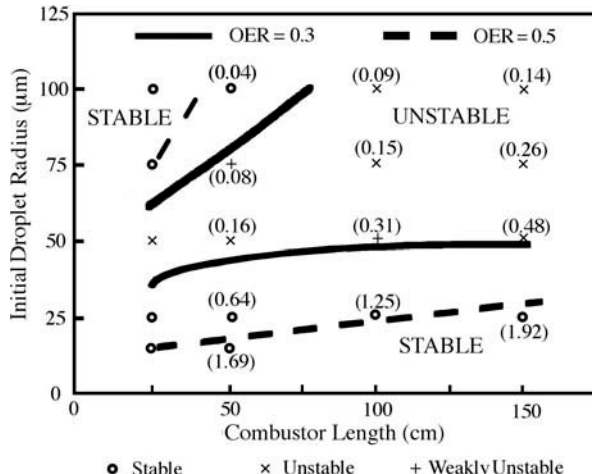


Figure 4 Oscillation in spray combustor with choked nozzle. Stability limits for two overall equivalence ratios. Numbers in parentheses are ratios of oscillation period to droplet heating time. [© William A. Sirignano. From Bhatia and Sirignano (1991). Reproduced by permission of William A. Sirignano. Permission to reuse must be obtained from the rightholder.]

gas-droplet motion (Abramzon and Sirignano, 1989). One-step chemical kinetics were used following Westbrook and Dryer (1984). The droplet vaporization time is controlled by the time to heat the liquid interior and in this way depends on initial droplet size. For vaporization control, we expect vaporization time and combustion time to vary with initial droplet radius to a power between one and two (Sirignano, 2010).

Figure 4 shows the correlation between oscillation frequency (or period) and characteristic combustion time lag. The unstable region centers around a certain range of time ratios. For the leaner mixture, the zone of instability becomes more narrow, which is expected because the energy per unit mass added to the gas through combustion decreases with equivalence ratio. Note that these results differ from the findings in subsection 4.2 since chemical-kinetic-rate control and mixing/vaporization-rate control produce different dependencies for the rate. For very small droplet size, the two results are expected to come closer, which is seen to some extent. As the droplet size becomes smaller, the combustion time lag becomes shorter and the instability limit depends less on the frequency (or equivalently the chamber length). Note that finding about frequency dependence is consistent with the experimental and theoretical results for the kinetics-controlled unstable combustor (Bowman et al., 1965; Sirignano and Crocco, 1964) where the limit became virtually independent of frequency. The time-ratio for maximum instability of about 0.15 is consistent with the calculations of Tong and Sirignano (1989) when adjustments are made for different normalization schemes.

There are various other physical phenomena with new time and length scales that can affect vaporization rates. Turbulence can interact with droplets. Smaller scales of turbulence can modify transport rates substantially through modification of Nusselt and Sherwood numbers. Larger scales of turbulence can modify ambient conditions and move droplets through drag forces. In a dense spray, transport properties can be significantly reduced from the values for an isolated droplet. These effects are reviewed by Sirignano (2014) and Sirignano (2010) and will not be discussed in detail here.

4.5. Transcritical and Supercritical Combustion

Development of aerospace propulsion engines is generally in the direction of increasing combustion chamber pressure. Thereby, injection and combustion of propellants at near-critical and supercritical thermodynamic conditions are relevant. There are key challenges associated with combustion at near-critical and supercritical conditions. The distinction between liquids and gases disappears at high pressures above the thermodynamic critical point, which has a strong nonlinear dependence on the composition. This introduces some crucial phenomena that are neglected when the compositional distinction between the original liquid and its surrounding gases in the combustor were neglected. Also, the reduced surface tension can cause a new mechanism to be the rate-controlling factor for energy conversion. Introductions of the major scientific issues for transport and thermodynamics in this new combustor environment are given by Yang (2000), Zong and Yang (2006), Schmitt et al. (2011), Sirignano and Delplanque (1999), and Sirignano (2010).

Transitions in the propellant flow between subcritical conditions and supercritical conditions can occur in several ways. Two or more initially supercritical propellant flows might be mixed to yield a mixture that is subcritical at the same pressure. A flow initially at supercritical pressure but at subcritical temperature can be heated by combustion to achieve supercritical temperature. Propellant flows, which are initially at supercritical pressure, might be expanded to subcritical pressure. These situations can create transcritical behavior in a spatial sense and/or a temporal sense.

As a subcritical flow enters the near-critical domain, some interesting phenomena may occur. Decreasing and ultimately disappearing values of the coefficient of surface tension and the energy of vaporization must be considered. There is a need for accurate equations of state. Consequently, a more sophisticated analysis of the thermodynamics is required than is normally used for combustion and liquid injection at lower pressures. The rate-controlling mechanisms for combustion can change as the critical point is approached or exceeded. For example, at low surface tension values, the secondary atomization of “parent” droplets and vaporization of resulting smaller droplets might be faster than the vaporization rate of the parent droplet. Or the breakup of the injected stream could result in a very different distribution of droplet size. Another possibility is that, with reduced energy of vaporization, mixing of vapors with surrounding gas might be slower than the vaporization rate. Depending on the propellant combination, the role as the liquid propellant with the slower vaporization rate could change between fuel and oxidizer as the critical point for one of the propellants is approached. Thereby, it is necessary to consider a range of possible transitions, giving several interpretations to the description of transcritical behavior.

High-pressure and supercritical ambient conditions have a considerable influence on the mechanisms controlling engine behavior and performance. Most of these effects are related to droplet behavior. When liquid is injected into a combustion chamber that is filled with a gas at supercritical thermodynamic conditions, all aspects of the combustion process from atomization to chemical reaction can be expected to depart significantly from the better-known subcritical patterns. Many practical applications involve the introduction of the spray into an environment where the ambient pressure is supercritical for the liquid but the liquid starts with a subcritical temperature below the ambient gas temperature. In this case, there is a distinction between the phases in spite of the supercritical pressure; discontinuities in density and composition occur across the interface between the droplets in the spray and the surrounding gas. Typically, the ambient gas is a different species from the liquid. The case where the liquid is introduced into an environment that consists solely

of its own vapor is of very limited interest. Generally, heat is supplied from the higher temperature gas to vaporize the liquid. Heat transfer takes a finite, albeit very short, time. While the liquid is heating, some vaporization occurs. The liquid temperature at the interface can eventually rise to the critical temperature for the given pressure. Once that surface temperature reaches the critical value, there is a continuous variation of density and other properties across the “interface.” Quotation marks are used because the lack of any discontinuity there removes its right to be called a true interface. Anyway, this “interface” becomes a surface along which the critical temperature exists with liquid on one side (for subcritical temperature) and the supercritical fluid on the other side. With time and continued heating, this surface propagates into the liquid until all of the liquid reaches a critical temperature.

Proper algorithms are needed to formulate computational models, including subgrid models, to address these transcritical situations where propellants or fuel pass through phase transitions related to the thermodynamic critical point. Models for vaporization of hydrocarbon fuels in an oxidizing gaseous environment have been developed by Hsiao et al. (2011), Zong and Yang (2006), and Hsieh et al. (1991). For oxygen droplets vaporizing in a hydrogen gas environment, see Delplanque and Sirignano (1993) and Yang and Lin (1994). Delplanque and Sirignano (1995) considered vaporization at transcritical conditions with droplets moving in a convective environment; Delplanque and Sirignano (1994) considered the effects of liquid stripping from the droplet surface at reduced surface tension. Delplanque and Sirignano (1996) analyzed these effects in an unstable combustor.

Consider a spherically symmetric, constant-pressure situation in which Fick’s law governs mass diffusion. The gas solubility in the liquid becomes important near the critical point so that even if the liquid phase is initially monocomponent, it is necessary to consider multicomponent behavior in the liquid phase. The liquid density must also be considered as variable rather than constant. Therefore, the same unsteady forms of the continuity, species, and energy equations are used in both the liquid and the gas phases. Note, however, that the energy of vaporization will decrease as the critical point is approached; now, it must be considered to be strongly dependent on the thermodynamic state. The thermal, mechanical, and chemical equilibria at the interface are expressed by the continuity across the interface of the temperature, pressure, and chemical potential, respectively.

Typical models (Delplanque and Sirignano, 1993) include a detailed computation of the high-pressure phase equilibria based on a cubic equation of state. A prevalent cubic equation of state used in this range of pressures and temperatures by the spray combustion community has been the Redlich-Kwong equation of state:

$$p = \frac{RT}{(v - b)} - \frac{a}{T^{0.5}v(v + b)} \quad (26)$$

where v is the specific volume. This empirical cubic equation has only two parameters, a and b .

The enthalpy of vaporization to be used in the energy-balance condition at the interface is the energy per unit mass (or per mole if preferred) required for vaporizing at the given temperature and pressure and into the particular surrounding gaseous mixture. On the other hand, the latent heat used at conditions well below initial values is the energy per unit mass required for vaporizing the liquid into an environment composed of its own vapor. The enthalpy of vaporization for each species can be determined as a function of interface temperature, mole fractions on both sides of the interface, and the molecular weight.

Another challenging issue inherent in the simulation of transcritical-phase processes is the evaluation of transport properties. Some transport properties (e.g., thermal conductivity) are expected to diverge at the critical transition. To quantify this singular behavior, a given transport property is considered to be the sum of a low-density value, an excess value due to high-pressure effects, and a critical enhancement, including the singular effects at the critical transition. While these transport-property singularities are important to our understanding of critical phenomena, their macroscopic effects on droplet behavior in conditions relevant to actual processes (e.g., convective droplet heating and vaporization) might not be so pertinent.

The predictions of current models are qualitatively consistent. After the introduction of a droplet into a hot, supercritical, quiescent environment, it is heated by conduction, and its diameter increases because the liquid density decreases as the temperature rises. Density inside the droplet is nonuniform and internal circulatory liquid convection can occur under shear forces produced by relative gas-droplet motion. The droplet surface temperature rises until it reaches the computed critical mixture value. During this phase, the mixture composition on either side of the liquid-gas interface is imposed by the chemical equilibrium and mass diffusion that occurs in the droplet.

See [Figure 5](#) from the analysis by Delplanque and Sirignano (1993), which relates to the vaporization in LOX/H₂ liquid-propellant rocket motors. It shows regimes with distinct phases for the oxygen liquid and hydrogen gas. Pr is the pressure divided by the critical pressure for pure oxygen. At pressures above the critical pressure (e.g., $Pr = 2$ through 7 in the figure) but temperatures below the critical temperature (about 154 K), it is still possible to obtain a phase equilibrium with, of course, distinction between the phases. When the liquid exists with the ambient gas differing from the pure vapor of the liquid, some mass exchange occurs; the vapor of the liquid enters the gas phase and some of the gas molecules enter the liquid. This exchange becomes more important as the critical point is approached. The figure shows that as Pr increases, the equilibrium has a decreasing fraction of oxygen and an increasing fraction of hydrogen in the liquid at the interface. That is, more hydrogen has dissolved. The temperature value above which the phases are no longer distinct will decrease with increasing pressure. The energy of vaporization is non-zero in this domain but decreases with increasing temperature until it reaches zero at the temperature value where phase distinction disappears. The figure shows that for $Pr = 1$ or less, the liquid is nearly pure oxygen while the gas at the liquid interface might have a significant fraction of the vapor from the liquid. The vapor fraction goes to unity as the liquid temperature goes to the saturation value. This saturation temperature increases with pressure, reaching the critical temperature as the critical pressure is reached. Above that critical temperature value, the distinction between phases is lost. In an unpublished work, Yang and co-workers have made similar calculations for liquid dodecane C₁₂H₂₆ surrounded by oxygen gas.

Consider a droplet of liquid component *A* in gaseous component *B* at pressure p_a . The liquid initial temperature is T_l and the initial ambient temperature is $T_a > T_l$. For conditions well below the critical conditions, temperature varies continuously throughout the surrounding gas and liquid interior and is continuous across the liquid-gas interface. A negligible amount of the ambient gas dissolves in the liquid; composition and densities are discontinuous across the interface but piecewise continuous in the gas and in the liquid. As the critical conditions are approached, ambient gas dissolves in the liquid and the magnitudes of the interface discontinuities in density and in composition decrease. Still, the critical temperature and the critical composition do not occur at the same point in space

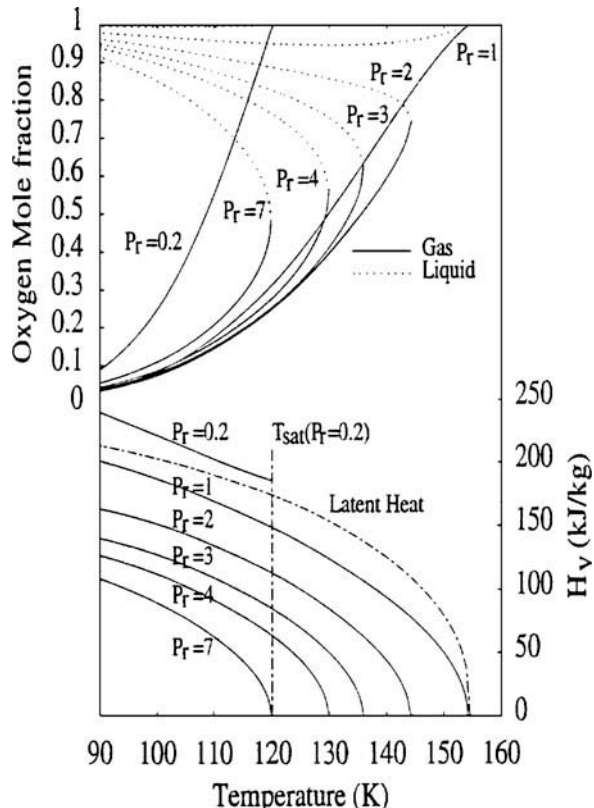


Figure 5 Computed phase equilibrium of the oxygen/hydrogen system. [Reprinted from *International Journal of Heat and Mass Transfer*, vol. 36(2), J.-P. Delplanque and W.A. Sirignano, “Numerical study of the transient vaporization of an oxygen droplet at sub- and super-critical conditions,” pp. 303–314, 1993, with permission from Elsevier.]

and time. At the point when and where the discontinuity first disappears, the temperature, composition, and density assume their critical values simultaneously. After that time, the critical isotherm and the critical mass fraction isopleth must coincide. This critical surface that has replaced the interface will regress as further heating and mixture occur, until it reaches the droplet center. Therefore, the phenomena of mixing and vaporization can involve situations in which both a subcritical spacial domain and a supercritical spacial domain can exist simultaneously. This situation is described as transcritical.

Practical environments, such as those found in engines, are characterized by significant relative velocity between the gas and the droplet with subsequent strong convection. The first effect is that heat and mass transfer are enhanced by the convection. With near-critical and supercritical environments, the surface-tension coefficient of a droplet decreases to zero as the interface temperature approaches the critical conditions. Hence, the second effect is that droplet deformation and secondary atomization can be initiated by smaller values of the droplet-gas relative velocity. The aerodynamic consequence of droplet motion is that the fore and the aft pressures on the surface become greater than the pressures on the side. At reduced surface tension, there is a tendency therefore for the droplet to deform in an axisymmetric manner to the shape of a lens. The surface-tension force

will resist this deformation since it increases the surface area. For small values of Weber number $We = \rho_l U_s^2 L_s / \sigma_s$, and Bond number $Bo = a_s \rho_l L_s^2 / \sigma_s$, there is some vibration but no significant deformation or breakup. ρ_l , U_s , a_s , L_s , and σ_s are the liquid stream density, velocity, acceleration, characteristic length dimension, and surface tension, respectively. Above $We = 5$, aerodynamic forces have some effect on the droplet shape. A critical value of We occurs in the range 10–20, above which continuous deformation of the droplet occurs; the droplet has a convex side and a concave side and takes the shape of a bag or an umbrella. Viscosity does not play a significant role in this deformation. When We is above the critical value, the shear on the droplet surface will cause stripping of liquid from the surface. The critical value for the Bond number is 11.22 according to Harper et al. (1972); above that value, surface waves grow exponentially. The first unstable mode appears at and above $Bo = 11.22$. Other unstable modes will appear in sequence as Bo is continually increased. However, they remain small enough in magnitude until $Bo = O(10^4)$ so that the aerodynamic forces dominate. Experimental data for shock-wave interaction with a water droplet from Ranger and Nicholls (1972) indicates that stripping occurs above $Bo = 10^2$, filling the near wake with a mist.

Delplanque and Sirignano (1993) showed for droplet vaporization in a supercritical convective environment (with neglect of secondary atomization), based on the Abramzon and Sirignano (1989) film model, that a LOX droplet injected into a rocket engine is likely to reach the critical state before it disappears, much sooner than in a quiescent atmosphere. However, they showed that, because of the behavior of the surface-tension coefficient at near-critical conditions, a LOX droplet in a rocket engine is likely during its lifetime to undergo secondary atomization in the stripping regime (mass removal from its surface by aerodynamic shearing) before the droplet interface reaches the critical mixing conditions. Results obtained with this model confirmed that the stripping rate is much larger than the gasification rate. The predicted droplet lifetime was found to be reduced by at least one order of magnitude when stripping occurred. An important consequence is that, in most cases, the droplet disappears before the interface can reach the critical mixing conditions.

Now, it can be seen how this result can affect the predicted overall performance of propulsion systems and, in particular, the likelihood of combustion instability. The open-loop response of LOX droplets to prescribed oscillatory ambient conditions consistent with liquid rocket engines was investigated by Delplanque and Sirignano (1996) who used the supercritical droplet-combustion models described above both for isolated droplets and droplet arrays. This study evaluated the longitudinal-mode stability of the combustion chamber assuming concentrated combustion at the injector end, short nozzle, and isentropic flow downstream of the combustion zone, following the work of Crocco and Cheng (1956). A response factor G was computed to quantify the Rayleigh criterion, which states that an initially small-pressure perturbation will grow if the considered process adds energy in phase (or with a small enough phase lag) with pressure:

$$G = \iint (E' p') dt dz / \iint (p')^2 dt dz \quad (27)$$

The primes denote fluctuations with respect to the nonoscillatory values. Delplanque and Sirignano (1996) note that an underlying assumption to this definition of G is that the gasification rate provides a good approximation of the energy release rate E .

Figure 6 indicates that, at some frequency, the response factor, determined under the modeling assumptions by the droplet-gasification process, becomes large enough to drive

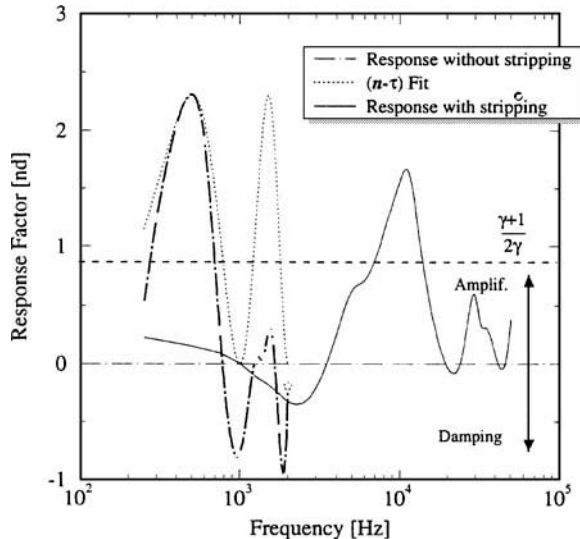


Figure 6 Response factor for an isolated LOX droplet with and without stripping. $T_\infty = 1000$ K, $p_\infty = 100$ atm, $\Delta U = 20$ m/s. [© William A. Sirignano. From Delplanque and Sirignano (1996). Reproduced by permission of William A. Sirignano. Permission to reuse must be obtained from the rightsholder.]

longitudinal-mode combustion instability in a hydrogen-oxygen rocket engine. This conclusion applies whether the model includes droplet stripping or not. However, the unstable frequency domain for the stripping model is substantially higher. Obviously, the frequency at which the peak response factor occurs is mainly correlated to the droplet lifetime through the assumptions. Therefore, since secondary atomization in the stripping mode results in a reduction in droplet size and a one-order-of-magnitude reduction in droplet lifetime, it causes a substantial corresponding shift in the peak frequency, as shown in the figure. Consequently, when stripping occurs, the peak frequency is significantly larger than the acoustic frequencies of the common modes for standard cryogenic rocket engine chambers.

Delplanque and Sirignano (1996) argued that, since in these engines droplets with low surface tension are likely to undergo secondary atomization in the stripping regime for most of their lifetime, this phenomenon could explain the observed better stability of hydrogen/oxygen rocket engines compared with that of storable propellant engines (see Harrje and Reardon, 1972). Although their analysis applied strictly to the longitudinal mode, the qualitative implication for the transverse mode is even greater because both primary and secondary atomization processes with transverse modes could be more significant on droplet-size reductions.

Estimates by Delplanque and Sirignano (1996) of the influence of neighboring droplets on the droplet response to an oscillatory field obtained with the droplet-stream model described above indicate that the isolated droplet configuration underestimates the driving potential of the gasification process. In a dense spray, steady-state vaporization rate is reduced compared to vaporization rates in a dilute spray. Here, then, we have a situation similar qualitatively to the findings of the gas-rocket researches by Sirignano and Crocco (1964) and Bowman et al. (1965); instability is more likely as mean energy conversion rate is decreased. That is, the fractional increase in energy release rate for a given pressure perturbation increases as mean energy release rate decreases.

4.6. Solid-Propellant Burning

Although the emphasis in this article is on liquid fuels and propellants, brief mention can be made of time lags existing in solid propellant burning. The intent is to show the potential for fundamental similarities between solid burning, liquid burning, and the burning of gaseous propellants. While the condensed phase now is solid, it still possesses a characteristic time for heating. Commonly, gas-phase processes are more rapid and can be considered as unsteady. Models using an unsteady solid-phase heating coupled with a quasi-steady gas phase have been presented by Krier et al. (1968), Denison and Baum (1961), and Culick (1967). There have also been many approaches where a two-parameter model, e.g., gain and phase of response, has been used to represent combustion processes (Culick, 1976). These earlier models used a quasi-steady gas-phase model. Some more recent efforts treat more general conditions; for example, see Roh et al. (1995) and Jackson (2012) for models of homogeneous and heterogeneous propellant modeling, respectively.

The model of Krier et al. (1968) (KTSS) used an empirical correlation to relate the quasi-steady gas-flame behavior to the oscillating pressure. However, it allowed the solid surface temperature to fluctuate. Essentially, the pressure value primarily affected the heat flux from the flame back towards the solid-gas interface. The equation for unsteady heat diffusion in the solid was solved. With the frame of reference fixed to the regressing interface, a 1D convective-diffusive equation resulted. The regression rate was caused by temperature-dependent pyrolysis to give a closed system of equations. Sirignano (1968) used the KTSS model to describe longitudinal combustion instability in an end-burning solid rocket motor with a short (i.e., quasi-steady) nozzle. The fluctuating gaseous velocity at the solid surface was related via a history integral to the pressure fluctuation at the surface. Essentially, a time lag appeared implicitly in the formulation through a kernel in the history integral; the characteristic time for heat transfer in the solid was given by $\alpha(\bar{r})^2$ where α and \bar{r} are the solid-phase thermal diffusivity and average surface regression rate, respectively.

5. DETERMINATION OF LIMIT-CYCLE AMPLITUDE AND TRIGGERING THRESHOLD

It is interesting to examine what factors control the amplitude of the limit cycle and the magnitude of the triggering threshold. Here, “limit cycle” means the stable limit cycle, which is approached as time goes to positive infinity, while “triggering threshold” means the unstable limit cycle that is theoretically approached as time goes to negative infinity. Some older results from perturbation theory and some more modern results from computational fluid dynamics will be discussed. Longitudinal-mode and transverse-mode oscillations will be examined, with and without shock wave formation. We can examine both old results from perturbation theory and new results from computational fluid dynamics (CFD) methods. Fewer assumptions are required for CFD but those results are less powerful in identification of the key mechanisms and the parameter dependencies.

Our perturbation approaches follow the coordinate perturbation approach initiated by Henri Poincaré (Minorsky, 1962) and expanded by Lighthill and Kuo to the method now known as the PLK method or method of strained coordinates (Crocco, 1972; Kevorkian and Cole, 1996).

5.1. Nonlinear Shock Wave Oscillations

Consider the first cases with shock formation that were studied in the 1960s using perturbation theory. Sirignano and Crocco (1964) and Sirignano (1964) analyzed nonlinear longitudinal-mode rocket motor oscillations with combustion concentrated at the injector; no time lag or history effect in the combustion response; and a short, quasi-steady choked exit nozzle. Sirignano (1968) considered a longitudinal-mode oscillation for an end-burning solid-rocket motor with combustion concentrated at the solid-propellant surface; a history effect on the combustion response through a history integral reflecting the solid-phase heating process; and a short, quasi-steady choked exit nozzle. Longitudinal-mode rocket motor oscillations with combustion concentrated at the injector; a time lag in the combustion response; and a short, quasi-steady choked exit nozzle were examined by Mitchell et al. (1969). Two cases were studied by Crocco and Mitchell (1969): (i) longitudinal-mode rocket motor oscillations with combustion distributed arbitrarily through the combustor; a time lag in the combustion response through the use of the Sensitive Time-Lag Theory; and a short, quasi-steady choked exit nozzle and (ii) tangential-mode rocket motor oscillations in an annular combustor with combustion distributed arbitrarily through the combustor; a time lag in the combustion response through the use of the Sensitive Time-Lag Theory; and a multi-orifice exit with many short, quasi-steady choked nozzles.

These perturbation theories sought the limit-cycle behavior using first- and second-order perturbation. In accordance with typical analyses in nonlinear mechanics, the complete description of the first-order terms could only be obtained through examination of second-order terms. That is, the first-order result is very different from the result of linear perturbation theory. The nonlinear theory predicts a sawtooth wave profile for pressure with shock discontinuities while linear theory would predict continuous, sinusoidal waveforms. Linear theory cannot predict limit-cycle amplitude. A good estimate of amplitude and a more exact determination of frequency comes from the second-order theory. To first order, these above-cited longitudinal-mode nonlinear theories obtain first-order solutions for velocity perturbation u_1 , speed-of-sound perturbation a_1 , and pressure perturbation p_1 in the forms:

$$\begin{aligned} u_1 &= f(\theta - x) - f(\theta + x) \\ a_1 &= \frac{\gamma - 1}{2} [f(\theta - x) + f(\theta + x)] \\ p_1 &= \frac{\gamma \bar{p}}{\bar{a}} [f(\theta - x) + f(\theta + x)] \end{aligned} \quad (28)$$

where the function f has velocity units, \bar{p} and \bar{a} are steady-state values for pressure and sound speed, θ is time normalized by one-half of the oscillation period, and x is chamber axial position measured from the injector and normalized by chamber length L . The frequency and period of oscillation are not known a priori. Thus, the transformation to θ involves the introductions of a new strained coordinate and a perturbation series in an amplitude parameter for the period of oscillation. Thus, $0 \leq \theta \leq 2$ and $0 \leq x \leq 1$. For the transverse mode in the annular chamber, x should be replaced by a nondimensional circumferential position y and the axial velocity perturbation u_1 should be replaced by the tangential velocity perturbation v_1 . Also, in that configuration, a traveling (spinning) wave represented by either $f(\theta - y)$ or $f(\theta + y)$ or the standing wave given by a sum of the

two functions can appear. The first-order analysis determines the forms given in Eq. (28); however, the determination of the specific function f requires a second-order analysis.

The periodic function $f(\theta)$ is found in all of these cases to be governed by a differential equation of the following form:

$$[f - f_m] \frac{df}{d\theta} = -Af - Bf^2 + Cf^\tau + DF(f) \equiv H(f) \quad (29)$$

$$f_m \equiv \frac{1}{2} [f(0) + f(2)] \quad f^\tau \equiv f(\theta - \tau) \quad \int_0^2 f(\theta') d\theta' = 0 \quad (30)$$

where A , B , C , and D are positive constants and the functional $F(f)$ is an integral of f . Sirignano and Crocco (1964) had $C = D = 0$, i.e., no time lag or integral and $B \ll A$. With $B = 0$, the median value at the shock $f_m = 0$ and the solution for $f(\theta)$ is a linear function with identical discontinuities at 0 and 2 reflecting the periodicity. With a small value of B , mild exponential curvature occurs between the discontinuities but the shape is still essentially a “sawtooth” form. Sirignano (1968) had $B = C = 0$ with a history integral $F(f) = \int_{-\infty}^{\theta} v(\theta - \theta') f(\theta') d\theta'$ where v is the kernel resulting from solution of the diffusive-convective equation in the solid propellant. Mitchell et al. (1969) had $B = D = 0$ while Crocco and Mitchell (1969) had $B = 0$ with the functional $F(f)$ appearing as a (1D) volume integral of combustion sources.

The left side of Eq. (29) results only from the nonlinear gasdynamics description of the chamber flow; combustion processes and nozzle boundary conditions do not affect it. Of the four terms on the right side of the first equality in Eq. (29), the last three result only from the coupling with the combustion process. A portion of the first term can also come from the combustion process while the remainder of the first term is the effect of the nozzle boundary condition. The details behind the modeling and the determination of the particular values of the coefficients A , B , C , and D can be found in the four references cited in the previous paragraph. The Mach number at the entrance of the short nozzle remains constant; thereby, the velocity perturbation remains proportional to the sound-speed perturbation, giving a linear term in the function f . The combustion source terms also appear to linear order albeit in the second-order balancing of terms. The combustion terms appear representing velocity fluctuations at the injector end for combustion concentrated there. For the distributed combustion case, they appear representing fluctuations in the divergence of the velocity throughout the combustor volume. Note that the time-lag effect caused an infinite slope in f (albeit with a continuous variation) at one value of the argument (other than the shock at $\theta = 0$ or 2) when τ differed from one-half of the oscillation period (Mitchell et al., 1969). The history integral produces smoother profiles (Sirignano, 1968) and is more acceptable on physical grounds.

The linear stability limit is defined by neglecting the nonlinear terms on the left side of Eq. (29) and setting the left side to zero. At the stability limit, the amplitude of the oscillation goes to zero. At the stability limit, driving terms from combustion are exactly in balance with the nozzle damping. With displacement in parameter space from the stability limit, the amplitude becomes finite and is determined by the solution of the full nonlinear equation. Therefore, away from the stability limit, there is an imbalance between the combustion driving terms and the nozzle damping terms. When the former exceeds the latter, a finite-amplitude oscillation results; the left side of Eq. (29) represents that imbalance.

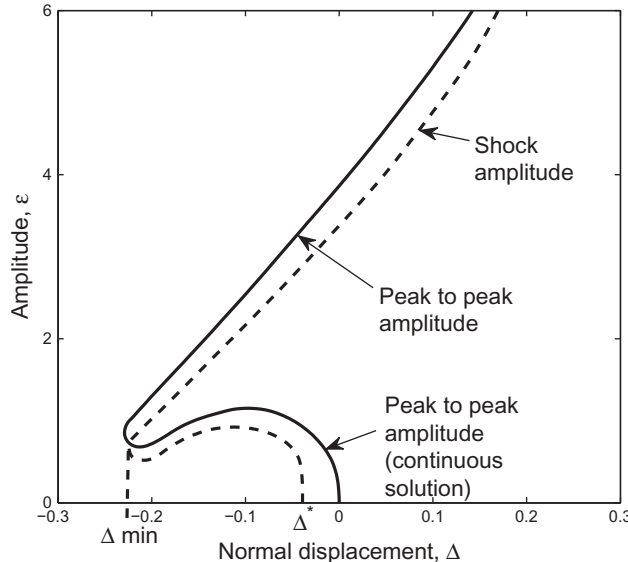


Figure 7 Amplitudes for limit cycle and triggering threshold for longitudinal-mode analysis with shock waves using the \mathbf{n}, τ theory. (Reprinted with the permission of Taylor & Francis from Mitchell et al., 1969.)

In the case where $C = D = 0$, Sirignano and Crocco (1964) obtained analytical solutions to Eq. (29). Numerical solution is required if the time lag, time history integral, or spacial integral appears. Figure 7 from Mitchell et al. (1969) shows amplitude as a function of normal displacement in \mathbf{n}, τ parameter space from the linear stability limit. The curves result from the numerical solution of Eq. (29) for $B = D = 0$. Three domains exist: unconditionally unstable (right of linear stability limit); conditionally stable or bi-stable (near left of linear stability limit); and unconditionally stable (far left). In the conditionally stable region, two solutions are found; the lower amplitude describes the unstable limit cycle, which can be regarded as the triggering threshold. Disturbances of lower amplitude decay while larger disturbances will grow to the upper value, which describes the stable limit cycle. The stable limit cycle and a portion of the unstable limit cycle are solutions with shock waves. The region near the linear stability limit gives continuous solutions that are consistent with the results of Sirignano (1964). Any disturbance with amplitude lower than the limit-cycle amplitude will grow in the unconditionally unstable region. Amplitudes larger than the limit-cycle value will decay to that value but no more. All disturbances will decay in the unconditionally stable region.

There are several conclusions that are obvious from the above-described analysis. (i) Equation (29) has the same form and can use the same general numerical procedure for solution whether or not time-lag or history integrals are included. (ii) The results of Mitchell et al. (1969) as shown in Figure 7 and Crocco and Mitchell (1969) clearly demonstrate the solution also includes a stable limit cycle whenever an unstable limit cycle is produced. A stable limit cycle occurs in unconditionally unstable domains without the appearance of an unstable limit cycle but unstable limit cycles never appeared alone in those studies. (iii) Those studies from Mitchell's dissertation also predicted, as shown in the figure, a continuous parabolic portion of the unstable limit cycle that matches the description given by Sirignano (1964) and Zinn (1968). Note that these three points are totally misrepresented

in Chapter 7 of Culick (2006), which does well describing literature of the 1970s and later but poorly describing the pioneering work of the 1960s on nonlinear combustion instability. The misunderstanding about Point (ii) was sustained by Wicker et al. (1996).

Integration of Eq. (29) over the oscillation period yields the first equality below:

$$\frac{1}{2} [(f(2) - f_m)^2 - (f(0) - f_m)^2] = \int_0^2 H(f) d\theta = 0 \quad (31)$$

The second equality results because the magnitudes of $f(2) - f_m$ and $f(0) - f_m$ are identical although their signs are opposite. Now, multiply Eq. (29) by the quantity $f(\theta) - f_m + f_m$ and integrate over the period. Using the results of Eq. (31), it follows that:

$$\frac{1}{3} [(f(2) - f_m)^3 - (f(0) - f_m)^3] = \int_0^2 f H(f) d\theta$$

or

$$\frac{2}{3} (f(0) - f_m)^3 = - \int_0^2 f H(f) d\theta = \int_0^2 [Af^2 + Bf^3 - Cff^\tau - DfF(f)] d\theta \quad (32)$$

A new result can be shown through the use of Eq. (32). In particular, the right side of that equation can be shown to be proportional to the acoustic forcing per cycle from the combination of combustion and nozzle outflow while the left side can be shown to be proportional to the energy dissipation per cycle in the shock wave. This is a remarkable result because the original second-order analysis maintained isentropic flow through the shock; i.e., entropy gain is proportional to the cube of pressure change or velocity change across the shock and thereby third order in the the perturbation series. This result is consistent with a finding by Crocco (1972) that the power required to drive at resonance a piston at one end of a closed tube (filled with an inviscid compressible gas) balances the dissipation rate due to the shock wave.

As noted by Liepmann and Roshko (1957), the entropy change Δs across a shock is of third order in terms of the pressure jump Δp and is approximated by:

$$\frac{\Delta s}{R} \approx \frac{\gamma + 1}{12\gamma^2} \left[\frac{\Delta p}{\bar{p}} \right]^3 \quad (33)$$

Note that within the accuracy of the approximation, it is allowed to substitute the mean pressure for the pressure in front of the shock. The pressure jump $\Delta p \approx \gamma \bar{p} [f(0) - f(2)] / \bar{a} = 2\gamma \bar{p} [f(0) - f_m] / \bar{a}$. Therefore, the energy dissipation through the shock occurs at the rate $\rho U_s T \Delta s \approx [2\gamma (\gamma + 1) \bar{p} / (3\bar{a}^2)] [f(0) - f_m]^3$, where within the accepted error the shock speed U_s is taken as \bar{a} . The energy dissipated by the shock over a cycle is then $[4L\gamma (\gamma + 1) \bar{p} / (3\bar{a}^3)] [f(0) - f_m]^3$. Neglecting higher-order terms in M , the period of the cycle is $2L/\bar{a}$.

The velocity at the nozzle entrance will be of the order of the mean-flow Mach number M . Thereby, the velocity and pressure fluctuations at the nozzle entrance are $u_1 = 0$; $u_2 = Ma_1 = [(\gamma - 1)/2] M [f(\theta - 1) + f(\theta + 1)]$; and $p_1 = [\gamma \bar{p} / (\bar{a})] [f(\theta - 1) + f(\theta + 1)]$. The product of p_1 and u_2 here gives the acoustic energy flux per unit area (Culick, 2006) at the nozzle. A positive amount implies that

energy is flowing out of the chamber. The integral of the product over a cycle yields $2ML\gamma(\gamma-1)[\bar{p}/\bar{a}^2]\int_0^2 f(\theta)^2 d\theta$.

For the concentrated combustion at the injector end (or end-burning solid surface), the right side of Eq. (29) is

$$H(f) \equiv -Af - Bf^2 + Cf^\tau + DF(f) = \frac{u_2|_{nozzle} - u_2|_{flame}}{\gamma + 1} = O(M) \quad (34)$$

Now, the pressure fluctuation is identical (except for phase) at the two ends. So, multiplication by the pressure fluctuation p_1 at the injector end followed by integration over the period \mathbf{T} of the cycle yields:

$$2\gamma(\gamma+1)(L\bar{p}/\bar{a}^2)\int_0^2 f(\theta)H(f(\theta))d\theta = \int_0^T [p_1u_2|_{nozzle} - p_1u_2|_{flame}]dt \quad (35)$$

Thus, multiplication of both sides of Eq. (32) by the factor $2\gamma(\gamma+1)(L\bar{p}/\bar{a}^2)$ results in a new equation with the dissipated energy by the shock over the cycle on the left side and the net acoustic flux integrated over a cycle on the right side of the equation. Consequently, when acoustic flux due to combustion adds energy to the chamber volume at a rate greater than the nozzle efflux, the difference is dissipated in the shock wave in order to establish a limit cycle. Essentially, Eq. (32) determines the amplitude of the limit cycle at an amount that maintains the necessary balance between the acoustic influx and the shock dissipation. While we have considered acoustic energy addition or subtraction only at the ends of the combustor, a double integration over the combustor volume and over the cycle time of the product of the pressure fluctuation with the combustion-driven divergence of the velocity fluctuation can also be added into this energy balance.

Realize that the coefficients A , B , C , and D in Eq. (29) are each $O(M)$ while f itself is of the order of the amplitude of the fluctuation. That amplitude can be considered to be $O(\epsilon)$. Therefore, the left side of the equation, which is quadratic, is $O(\epsilon^2)$ while the right side, which is primarily linear, is $O(\epsilon M)$. The balance implies that at the limit cycle, a distinguished limit is established and the amplitude parameter $\epsilon = M$. This result is consistent with the analysis of Sirignano and Crocco (1964) and the experiments of Bowman et al. (1965).

5.2. Nonlinear Continuous Wave Oscillations

Continuous nonlinear wave oscillations were studied by Sirignano (1964) for the longitudinal mode and Zinn (1968) for the transverse modes. Both works at Princeton used the \mathbf{n}, τ theory and concentrated combustion at the injector end. Each analysis required a perturbation series up through third order in the amplitude parameter ϵ in order to approximate the limit-cycle amplitude. Let us examine the need for a higher-order analysis than required for cases with shock waves. The character of the major results are shown in Figure 8.

The linear unstable domain is shaded in the upper sub-figures. The lowest value of \mathbf{n} on the stability limit occurs with a time lag equal to one half of the period of oscillation. There, the negative sign in front of the lagged term of Eq. (24) means that both the instantaneous term and lagged term for energy addition are in phase with the pressure. Some portions of the linear stability limit curve are adjacent to conditionally stable domains (lower left sub-figure) while other portions are immediately adjacent to

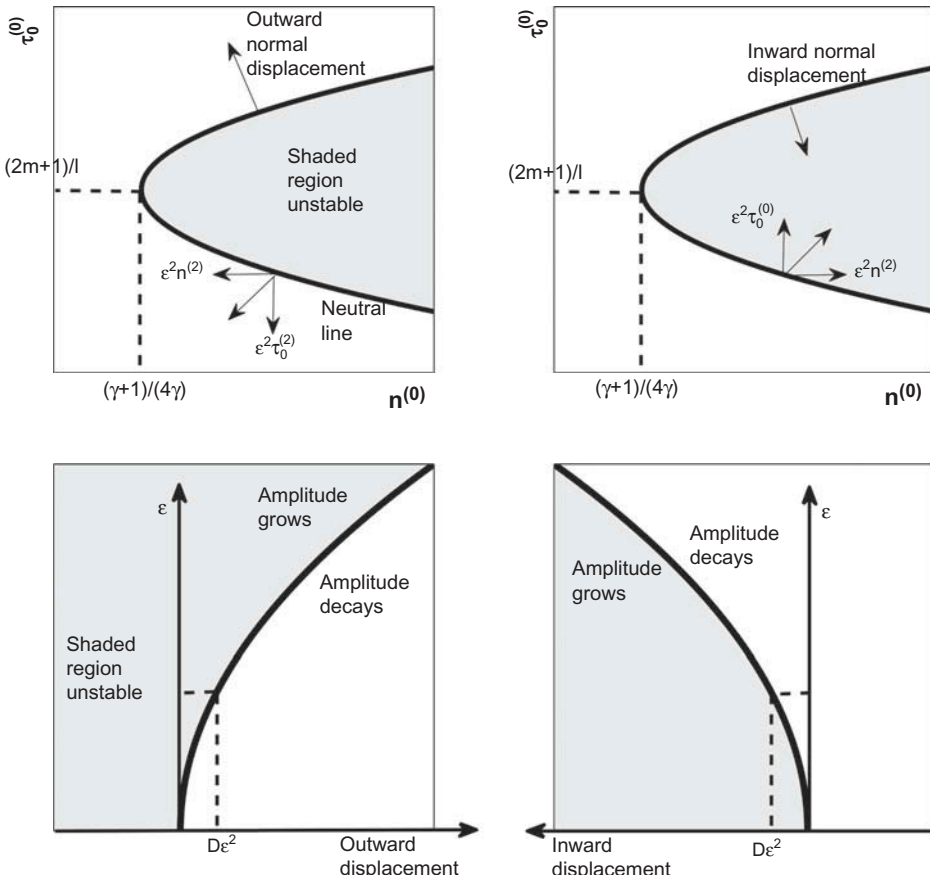


Figure 8 Schematic of perturbation results in n, τ . [© William A. Sirignano. From Sirignano and Popov (2013). Reproduced by permission of William A. Sirignano. Permission to reuse must be obtained from the rightsholder.]

unconditionally stable domains (lower right sub-figure). On the lower left, the unstable limit cycle (triggering threshold) is shown, while on the lower right a stable limit cycle is shown. Both curves are parabolas. That is, the amplitude parameter ϵ grows as the square root of the normal displacement from the linear stability limit in the n, τ plane. Essentially, the development through third order in the perturbation series was needed to obtain the parabolic curves. These two analyses predicted either a stable limit cycle or an unstable limit cycle in the neighborhood of any point on the linear stability curve in parameter space. The expected higher-amplitude, stable limit cycle that accompanies a lower-amplitude, unstable limit cycle is not predicted with a third-order analysis. Presumably, a higher-order analysis would have predicted the two amplitude solutions in the conditionally stable domain; however, the perturbation expansions of both Sirignano (1964) and Zinn (1968) terminated at third order. Note the reassuring result though about the agreement among Mitchell et al. (1969), Sirignano, and Zinn about the parabolic shape of the nonlinear curve describing a continuous limit cycle. There are certain implications of these perturbation analyses that have not yet been discussed. We will return to this point later in this subsection.

Let us first examine some recent CFD results, which will complete the understanding of triggered transverse-mode combustion instability. In particular, we will focus on

transverse instabilities in a combustion chamber with gaseous propellants following the analysis of Sirignano and Popov (2013). The chamber exit is a multi-orifice plate with many short, choked nozzles. The work has been extended by Popov et al. (2014) to quantify the uncertainty with the triggering event in practical combustors. A 2D model is developed by integrating Eqs. (18) and (5) over the primary flow direction, x_3 , after modification for an inviscid flow with gaseous propellants. A cylindrical combustion chamber is considered with the injector at $x_3 = 0$ and the nozzle entrance at $x_3 = L$. Variations of the pressure, velocity, and other variables in the x_3 direction will be smaller than variations in other directions.

Define the 2D average values: $\tilde{p} = (1/L) \int_0^L p dx_3$, $\tilde{\rho} = (1/L) \int_0^L \rho dx_3$, $\tilde{a} = (1/L) \int_0^L a dx_3$, and $\tilde{u} = (1/L) \int_0^L \vec{u} dx_3$. Now, Eq. (18) is integrated over x_3 , neglecting the difference between products of averages and averages of products. The pressure variation in the x_3 direction may be assumed to be minor for many transverse oscillations. The major variation of pressure will be in the transverse direction, as indicated by experimental findings of Harrje and Reardon (1972) and theoretical results of Reardon et al. (1964) and Zinn (1968). For a pure transverse wave behavior, there is not any acoustical oscillation in the x_3 direction; so, only advection can be expected to produce variations in that flow direction. These variations tend to be slow exponential variations according to the theory. Then, $p_{x_3=0} \approx p_{x_3=L} \approx \tilde{p}$. The average designation (i.e., superscript tilde) for pressure can be eliminated; we set $\tilde{p} = p$. The average designation is also removed for other variables. Entropy waves and other kinematic waves are neglected.

The 2D wave equation should be recast in cylindrical polar coordinates because of the combustion chamber shape. r and θ will represent radial distance from the chamber centerline and azimuthal position, respectively. The pressure and velocity are normalized by the steady-state pressure and sound speed, respectively. The velocity components are u_r and u_θ . The resulting equations may be written as:

$$\frac{\partial^2 p}{\partial t^2} - C_1 \left[\frac{\partial^2 p}{\partial r^2} + \frac{1}{r} \frac{\partial p}{\partial r} + \frac{1}{r^2} \frac{\partial^2 p}{\partial \theta^2} \right] = R(p, u_r, u_\theta) + S(p, u_r, u_\theta) \quad (36)$$

$$R(p, u_r, u_\theta) \equiv (\gamma - 1) \frac{\partial E}{\partial t} - Ap^{\frac{\gamma-1}{2\gamma}} \frac{\partial p}{\partial t} \quad (37)$$

$$S(p, u_r, u_\theta) \equiv C_1 \left[p^{\frac{\gamma-1}{\gamma}} - 1 \right] \left[\frac{\partial^2 p}{\partial r^2} + \frac{1}{r} \frac{\partial p}{\partial r} + \frac{1}{r^2} \frac{\partial^2 p}{\partial \theta^2} \right] + \frac{(\gamma-1)}{\gamma} \frac{1}{p} \left(\frac{\partial p}{\partial t} \right)^2 + \gamma p^{\frac{\gamma-1}{\gamma}} \left[\frac{\partial^2 \left(p^{\frac{1}{\gamma}} u_r^2 \right)}{\partial r^2} + \frac{2}{r} \frac{\partial \left(p^{\frac{1}{\gamma}} u_r^2 \right)}{\partial r} + \frac{2}{r} \frac{\partial^2 \left(p^{\frac{1}{\gamma}} u_r u_\theta \right)}{\partial r \partial \theta} \right. \quad (38)$$

$$\left. + \frac{2}{r^2} \frac{\partial \left(p^{\frac{1}{\gamma}} u_r u_\theta \right)}{\partial \theta} + \frac{1}{r^2} \frac{\partial^2 \left(p^{\frac{1}{\gamma}} u_\theta^2 \right)}{\partial \theta^2} - \frac{1}{r} \frac{\partial \left(p^{\frac{1}{\gamma}} u_\theta^2 \right)}{\partial r} \right]$$

$$\frac{\partial u_r}{\partial t} + C_2 \frac{\partial p}{\partial r} = -u_r \frac{\partial u_r}{\partial r} - u_\theta \frac{1}{r} \frac{\partial u_r}{\partial \theta} + \frac{u_\theta^2}{r} + C_2 \left[1 - \frac{1}{p^\frac{1}{\gamma}} \right] \frac{\partial p}{\partial r} \quad (39)$$

$$\frac{\partial u_\theta}{\partial t} + \frac{C_2}{r} \frac{\partial p}{\partial \theta} = -u_r \frac{\partial u_\theta}{\partial r} - u_\theta \frac{1}{r} \frac{\partial u_\theta}{\partial \theta} - \frac{u_r u_\theta}{r} + \frac{C_2}{r} \left[1 - \frac{1}{p^\gamma} \right] \frac{\partial p}{\partial \theta} \quad (40)$$

In the above equations, no acoustic coupling with the injection system has been considered. The model of coaxial injection, turbulent mixing, and chemical reaction discussed earlier in subsection 4.3 has been used to couple the above equations for the wave dynamics with the jet flame at the exit of each injector port. This model introduces physics and chemistry with characteristic times that will not be short compared to the period of acoustic oscillation. Therefore, time delays and a history effect are introduced. Consider a solid circular wall at radius $r = R$; that is, no acoustic lining is present. The normal velocity at the wall will be zero; thus, the following boundary conditions apply to the system of Eqs. (36), (39), and (40):

$$u_r(t, R, \theta) = 0 \quad \frac{\partial p}{\partial r}(t, R, \theta) = \frac{p^\gamma u_\theta^2}{C_3 R} \quad (41)$$

C_1 , C_2 , and C_3 are known constants.

Typical results from a calculation of Sirignano and Popov (2013) and Popov et al. (2014) are shown in Figure 9. The initial amplitude of a disturbance is shown by the hollow circles while the black circles indicate the amplitude after 12 cycles of oscillation. Below the threshold disturbance of 20 atm, the disturbance decays in time towards the steady state. Above that threshold, it grows towards a limit-cycle amplitude of 154 atm. Near the threshold, the growth or decay is slower; sample calculations up to 120 cycles show the same outcome though. Clearly, the operating conditions (mean-flow Mach number, mean chamber pressure, mixture ratio) for this case place it within a conditionally stable (bistable) domain. When operating conditions are modified sufficiently in certain directions both unconditionally unstable and unconditionally stable domains are found immediately adjacent in parameter space, a qualitatively similar situation to the portrait of Figure 7. However, in this case, no shock waves resulted. Depending on the operating conditions and the nature of the triggering disturbance, either traveling (spinning) waves or standing waves could occur. The traveling wave shapes limit cycles found could be composed of a basic resonant mode plus superimposed harmonics of that mode. In that case, the pressure wave shape did not wobble but was reasonably steady in a certain rotating frame of reference. Note that, for transverse oscillations, the resonant mode frequencies are not integer multiples of the fundamental resonant mode (unlike the longitudinal mode situation). This explains why shock waves are unlikely to form in transverse mode oscillations in a circular cylinder. (Annular chambers can cause exception here.) A second type of limit cycle found in these computations for other operating conditions could involve the superposition of several resonant modes. In fact, in one case, a subharmonic mode was added with a frequency equal to the difference between the frequencies of the first and second tangential modes, which were also present. In this second type of situation, the superimposed frequencies are not commensurate and a temporally wobbly pressure waveform is observed in any rotating frame.

The results of Sirignano and Popov (2013) and Popov et al. (2014) identify several difficulties with a Galerkin method or any reduced basis method that identifies a priori the

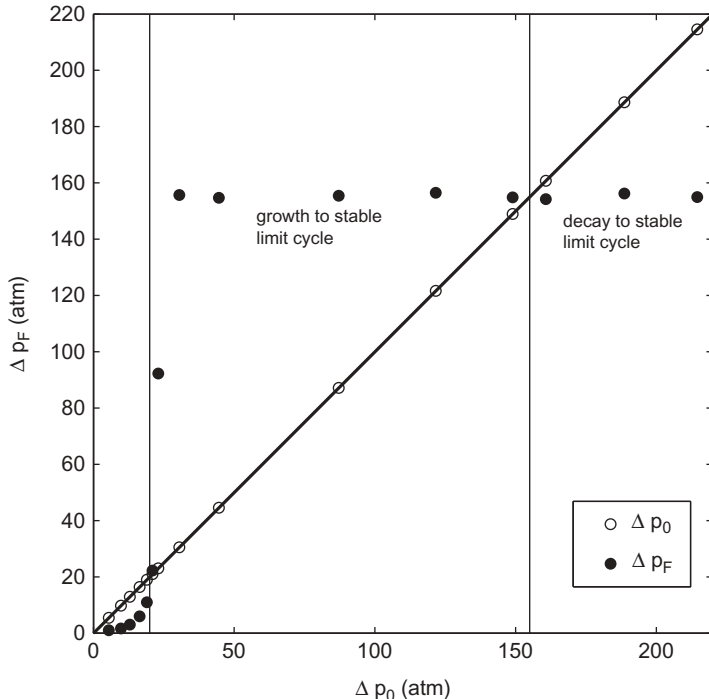


Figure 9 Oscillation pressure amplitude at 12 cycle times vs. triggering pressure amplitude. [Reprinted from P.P. Popov, A. Sideris, and W.A. Sirignano, “Stochastic modeling of transverse wave instability in a liquid propellant rocket engine,” *J. Fluid Mech.*, vol. 745, pp. 62–91, 2014.]

resonant modes that will sum to give an accurate solution. It is unclear which modes and how many modes should be represented. In addition to or instead of the resonant modes, harmonics of primary modes can appear. Also, subharmonics can be generated.

The CFD results of Figure 9 obviously present more information about the dynamic behavior than has been gained from perturbation theory. Perturbation theory can, in principle, handle transient predictions with the emergence of multiscale methods (Kevorkian and Cole, 1996) but those techniques were not used for partial differential equations in the 1960s. They can handle superposition of different resonant modes. However, like classical Galerkin methods and unlike CFD, the weakness is that the modes must be known in advance. Nevertheless, there is some more insight to be gained from perturbation theory. Equations (36), (39), and (40) have been written so that the left side has only linear terms. The nozzle boundary condition in the functional $R(p, u_r, u_\theta)$ provides a term with a first time derivative of pressure, which is a damping function for the oscillation. Some of the energy in the oscillation will be lost by nozzle outflow. The term within $R(p, u_r, u_\theta)$ having the time derivative of the energy source E can be described as the forcing function for the oscillation. A combustion model based on turbulent jet diffusion flames at the injectors relates E back to pressure, temperature, and velocity. Every term in the functional $S(p, u_r, u_\theta)$ is second order or higher in the perturbation series; those terms in S are not dissipative or forcing functions but they can have strong influence on the amplitude, and wave shape for the oscillation. Consequently, there is no major dissipative mechanism other than the nozzle outflow, unlike the cases with shock wave oscillations. Key factors are that every

term on the left side is $O(\epsilon)$ or higher; every term in R is $O(\epsilon M)$ or higher; and every term in S is $O(\epsilon^2)$ or higher.

Perturbation analysis showed that the nondimensional amplitude ϵ of limit-cycle oscillations with shock waves were of the order of the mean-flow Mach number M . We can show now that, for continuous wave oscillations, the amplitude parameter $\epsilon = O(\sqrt{M})$. This relation was implicit in the results of Sirignano (1964) and Zinn (1968) but were not identified. For simplicity, let us consider a case where the first tangential traveling mode is excited (although the argument and conclusion is not limited to a specific mode). The multi-scale perturbation method with coordinate straining will be used. Expand the variables in a perturbation series, e.g., $p = \bar{p} + \epsilon p_1(\phi, \eta, r) + \epsilon^2 p_2(\phi, \eta, r) + \epsilon^3 p_3(\phi, \eta, r) + O(\epsilon^4)$; $\phi \equiv \omega t - \theta$; $\omega = \omega_0 + \epsilon \omega_1 + \epsilon^2 \omega_2 + O(\epsilon^3)$; and $\eta = \sigma(\epsilon) t$, where ω and η are the frequency and a “slow” time. σ goes to zero as ϵ goes to zero; in fact, it will be found to go faster.

Consider that, to first order, one obtains $p_1 = [A(\eta) \cos \phi + B(\eta) \sin \phi] J_1(s_{11}r)$, where J_1 is a Bessel function of the first kind and first order while s_{11} is the lowest eigenvalue of that function. The amplitudes A and B are allowed to vary slowly with time to capture the transient behavior while ϕ carries the fast time of the oscillation. The use of two time variables produces terms of $O(\epsilon \sigma(\epsilon))$ and higher, which can be added to the right side of the governing partial differential equations; substitution into R gives terms of $O(\epsilon M)$ and higher; and substitution into S gives terms of $O(\epsilon^2)$, $O(\epsilon^3)$, and higher. The types of terms appearing on the right side of the wave equation are listed below. Each term would be multiplied by some function of radius r , which is not being detailed here. Those multiplying functions can be expanded in a Fourier–Bessel series; the $J_1(s_{11}r)$ term in the series for expansions of the coefficients of $\cos \phi$ and $\sin \phi$ will be of special interest.

$$\begin{aligned}
 O(\epsilon^2) : & A^2 ; A^2 \cos 2\phi ; AB \sin 2\phi ; B^2 ; B^2 \cos 2\phi \\
 O(\epsilon M) : & A \cos \phi ; A \sin \phi ; B \cos \phi ; B \sin \phi \\
 O(\epsilon \sigma(\epsilon)) : & \frac{dA}{d\eta} \sin \phi ; \frac{dB}{d\eta} \cos \phi \\
 O(\epsilon^3) : & A^3 \cos \phi ; A^3 \cos 3\phi ; A^2 B \sin \phi ; A^2 B \sin 3\phi \\
 & AB^2 \cos \phi ; AB^2 \cos 3\phi ; B^3 \sin \phi ; B^3 \sin 3\phi
 \end{aligned} \tag{42}$$

After substitution and eigenfunction expansion, the terms $J_1(s_{11}r) \cos \phi$ and $J_1(s_{11}r) \sin \phi$ cannot be allowed to remain on the right side of the higher-order wave equations. They are homogeneous solutions to the left side and would prevent a uniformly valid perturbation series from developing. These terms must be collected into two groups and each group must be set to zero. This is accomplished by selecting $\sigma = \epsilon^2 = M$ so that all $\cos \phi$ and $\sin \phi$ terms on the right side appear at $O(\epsilon^3)$. The appearance of nonoscillatory terms means that the average pressure is changed by the nonlinear dynamics. The types of terms appearing here were also found by Zinn (1968) for tangential-mode combustion instability and by Maslen and Moore (1956) in their classical work on nonreacting transverse waves. Maslen and Moore (1956) also examined the effects of wall friction and found that a steady acoustic streaming motion appeared to second order due to the imposed torque.

In setting those two right-side global coefficients to zero, two coupled first-order ordinary differential equations for $A(\eta)$ and $B(\eta)$ result:

$$\frac{dA}{d\eta} = f(A, B) \quad \frac{dB}{d\eta} = g(A, B) \quad (43)$$

With appropriate initial conditions, these equations describe the growth or decay of the instability with the slow time η . Of course, both slow time and fast time are converted back to a single time variable. Since the functions f and g are cubic in A and B , one or two sets of values of those amplitudes (other than the trivial $A = B = 0$) can produce zero values for the derivatives. These values would mark the unstable limit cycle (i.e., triggering threshold) and the stable limit cycle. Without shock dissipation, the acoustic energy flux at the boundaries must balance globally in the limit-cycle condition; it is expected therefore that $O(\varepsilon^2 M)$ terms and $O(\varepsilon^4)$ terms would balance each other.

Major results here are that the nondimensional limit-cycle amplitude ε is of the order of \sqrt{M} and the nondimensional (using chamber radius and mean sound speed) transient time for development of the high amplitude oscillation will be of the order of $1 / M$. Equivalently, the dimensional transient-time order of magnitude is the chamber radius divided by the mean velocity. Since there are no shock waves for dissipation here, higher amplitude waves result: i.e., $\sqrt{M} > M$ for subsonic mean flow. In fact, the amplitudes for transverse continuous waves are known to be several-fold larger than longitudinal waves, which can form shocks (Harrje and Reardon, 1972). Note that Popov et al. (2014) report a 155 atm peak-to-peak limit-cycle amplitude with a 200 atm mean pressure for a mean flow $M = 0.100$. Then, $\varepsilon = 0.387$ and $\sqrt{M} = 0.316$, which are of the same order of magnitude. Also, a rise above the original 200 atm mean pressure is calculated for the midpoint pressure between the maximum and minimum values in the limit cycle. The transient time for limit-cycle development (an e-folding time) of $1/M$ relates to roughly three cycles of oscillation in that same calculation, which agrees with the finding in the calculation. The Mach number of the mean flow is representative of the strengths of forcing by combustion and damping by nozzle in the chosen examples here. Different parameters can become representative of those critical strengths in other configurations.

5.3. General Observations

With regard to the ordering of the terms in an asymptotically correct manner, we have assumed for convenience that the same order applies to both the stable-limit-cycle amplitude and the unstable-limit-cycle amplitude. An interesting possibility worthy of future examination is that different ordering occurs. For example, different powers of M might be appropriate for the two types of limit cycles. This could explain why two distinct solutions were not found in third-order analyses (Sirignano, 1964; Zinn, 1968).

The characteristic times for combustion will affect the likelihood of instability and the amplitude of oscillations. The combustion times have this role because they affect the magnitude of the rate E , which comes in phase with pressure. However, the transient time for the oscillation to develop is determined largely by the gasdynamics and is only weakly dependent on the combustion times.

The balance of terms in determining limit-cycle amplitude to lowest order of accuracy has involved linear combustion and nozzle flow terms matched against nonlinear gasdynamic terms for both cases with shocks and without shocks and for both longitudinal and

transverse modes. These linear terms are the lowest-order approximations to the forcing and damping of the oscillation. Nonlinear forcing and damping terms should appear to higher order. Of course, in CFD computations at UCI (Popov et al., 2014; Sirignano and Popov, 2013), the full nonlinear combustion and nozzle effects have been considered. In cases where linear representation serves for a first approximation, the qualitative differences are small between the results using an ad hoc two-parameter combustion model (Crocco and Mitchell, 1969; Mitchell et al., 1969; Sirignano, 1964; Zinn, 1968) and the results using a physics-based description (Popov et al., 2014; Sirignano, 1968; Sirignano and Crocco, 1964; Sirignano and Popov, 2013); essentially two parameters can do reasonably well describing the ratio of the E perturbation to the p perturbation to lowest order.

Culick (2006) describes second-order and third-order perturbation analyses at Caltech (Awad and Culick, 1986; Yang and Culick, 1990; Yang et al., 1990), which never predicted triggering action. This is not inconsistent with the above-described results, which indicated that three types of stability zones could be predicted by any model that predicted the possibility of triggering. That is, by variation of operating parameters, the models of Sirignano (1964), Zinn (1968), Mitchell et al. (1969), and Sirignano and Popov (2013) predicted a neighboring domain of unconditional stability and a neighboring domain of unconditional instability for any bistable domain where triggering occurs. Thus, causes for not predicting triggering could be due to a wrong choice of operational parameters, a poor model, or choice of a combustor configuration not subjected to bistable operation. Culick (2006) suggests that nonlinear gasdynamics by itself is insufficient to develop triggering possibilities, i.e., bistable domains; it is further suggested that nonlinearity in the combustion description is needed to establish the needed limit cycle. Certainly, that suggestion is not consistent with the above-described Princeton asymptotic theory from the 1960s or the recent CFD findings at UCI. For a solid-rocket engine, triggering of combustion instability was predicted by Wicker et al. (1996).

Unstable and stable limit cycles have been predicted to exist together with balance of acoustic energy addition via combustion by the contribution of nonlinear gasdynamic terms. It must be understood that, for cases without shock waves, the nonlinear gasdynamics bring balance, not by direct consequence within the combustor volume, but rather by influence on the acoustic energy efflux through the nozzle. In a test (Sirignano and Popov, 2013) with an artificial example where E is a polynomial in p with no history effect or time lag, the bistable behavior is predicted. A bistable case was found using a relation $E(p)$ where both E and dE/dp were strongly monotonically increasing, positive functions of p . This implied that balance with a stable limit cycle could only occur if the gasdynamic terms grew more strongly with increasing pressure than the E combustion term.

Limited experimental results exist for comparison with computations. An interesting program at Purdue University (Shipley et al., 2013) involves a rectangular cross-section combustion chamber with transverse oscillations. For this geometry, shock waves might travel in the transverse direction. In fact, Figure 8 of that paper showing oscillatory pressure profiles indicates the classical result with shocks of steep wavefronts with different steep fronts for travel in each direction. New analyses will have to reflect this different geometry if comparisons are to be made. The experimental design also allows for study of the effect of transverse velocity on the coaxial jet flame from each injector during oscillation. A good computational analysis of this velocity coupling is needed.

The effect of entropy variation in the wave phenomenon described by Eq. (18) is generally neglected. For the inviscid, non-heat-conducting case, this leads to the existence of a velocity potential for the acoustical perturbations, i.e., no vorticity is associated with the

oscillation. However, some damping of the oscillation can be expected from the presence of that entropy term. A rough estimate based on a relation of entropy gain with temperature would yield that the expected magnitude of that entropy term in the wave equation is less than the energy addition rate due to combustion by a multiplicative factor of $(\gamma - 1)/\gamma$. Therefore, unless proven otherwise by a more exact analysis, the neglect of that term should be done with caution.

6. CONCLUDING REMARKS

Combustion instability can occur in an engine with spray flow resulting from injection of liquid propellants. The presence of the second phase modifies the wave dynamics but a wave equation can still be constructed describing the nonlinear acoustics. The wave equation contains terms reflecting the exchanges of mass, moment, and energy between the phases; however, the highest derivatives in the equation are identical to those for the single-phase wave equation.

The combustion instability phenomena present a multi-scale problem. Various length and time scales result from acoustics; kinematic waves; and the processes for injection, vaporization, mixing, and oxidation. The Sensitive-Time-Lag Theory and other heuristic approaches allow the bypass of treatment of the smaller scales associated with combustion. Mathematical and computational approaches that address all of the physically important scales are desired for the future and are beginning to appear.

Combustion instability becomes more likely when a change in operational parameters causes the fractional perturbation in the energy release rate $\Delta E/\bar{E}$ to increase for a given fractional change in pressure $\Delta p/\bar{p}$. The chemical-kinetic-controlled combustion shows this non-intuitive effect for the gas rocket engine where near-stoichiometric operation can be more stable than off-stoichiometric operation. This behavior has implications for lean-combustion systems.

Ubiquitous examples exist where the most unstable domain has a controlling characteristic time that aligns well with the resonant frequency; see the results of Figures 3 and 4. Cases of poor alignment can explain stable operation. See Figure 6 and the explanation for stable operation of H₂ – O₂ systems.

Bistable operational domains are shown to be present in some systems, making nonlinear triggering of an instability a possibility. In these domains, both a stable limit cycle and an unstable limit cycle (triggering threshold) exist. The bistable region typically lies between an unconditionally stable zone and an unconditionally unstable zone in operational parameter space.

For oscillations with shock waves, the associated dissipation keeps the nondimensional limit-cycle amplitude to the order of the mean-flow Mach number M . A perturbation analysis up to second order in amplitude is sufficient here for the lowest approximation to amplitude. Comparison with an experiment verified this asymptotic ordering. For continuous waves, larger amplitudes of the order of \sqrt{M} appear with a nondimensional transient development time of the order of $1/M$. A third-order analysis is required to estimate the amplitude. In a limited comparison with CFD results, support for this ordering was found. For the cases discussed, the Mach number of the mean flow was representative of the strengths of forcing by combustion and damping by nozzle. In other cases, different parameters can become representative of those critical strengths.

For longitudinal and transverse modes of oscillation with and without shock waves, the primary balance in determining limit cycles comes between linear terms representing

forcing by combustion and damping by nozzle and nonlinear gasdynamic terms. For higher-order refinement of the description, nonlinear forcing and damping terms can become relevant.

Some important problems remain related to driving mechanisms for combustion instability; a few examples can be briefly presented. (i) The interactions of the acoustic oscillation with the turbulent structures needs to be understood better. When is the coupling well represented as one-way? That is, when does the acoustic field influence the turbulence without the turbulence significantly affecting the acoustics? We allow here for indirect influence through the combustion process; i.e., acoustics affect turbulence, which then influences the combustion driving mechanism. (ii) More studies are needed about the driving mechanisms for continuous operation at very high pressures and also for intermittent high pressure operation during peak portions of the acoustic oscillation period. It must be determined when two phases can exist, which cannot be determined a priori by comparing the critical pressure and temperature for each propellant to the operating conditions. Studies of instantaneous and local mixture critical values are needed. (iii) The response of the combustion processes to transverse waves can be very important but is not well understood. In summary, challenging opportunities for research related to combustion instability driving mechanisms remain to be addressed further.

FUNDING

This research was supported by the Air Force Office of Scientific Research under Grant FA9550-12-1-0156, with Dr. Mitat Birkan as the Program Manager.

NOMENCLATURE

A	pre-exponential factor
A_t, A_c	cross-sectional area of nozzle throat and capture flow
A, B, C, D	constants in the generic nonlinear differential for $f(\theta)$
a	speed of sound
a_s	acceleration of liquid stream
a, b	constants in cubic equation of state
Bo	Bond number
c_p	specific heat under constant pressure
c_v	specific heat under constant volume
D	mass diffusivity
E	energy conversion rate per unit volume
E_A	activation energy
e	specific internal energy
F	functional in wave function equation
F_{Di}	aerodynamic force on droplets per unit mixture volume
f	wave function
G	response factor
H	collection of terms in Eq. (29)
h	specific enthalpy
n	droplet number density
\mathbf{n}	interaction index of Sensitive-Time-Lag Theory
p	pressure
Q	heat of combustion

R	specific gas constant
R	combustion chamber radius
R	source term in wave equation
R_u	universal gas constant
r, r_i	global rate, rate of process i
S	source term in equation
s	specific entropy
T	cycle period
T	temperature
t	time
u, v, u_i	velocity
U_s	characteristic velocity of liquid stream
v	specific volume
We	Weber number
x_i	Cartesian coordinates
Y_m	mass fraction of species m
ρ	density
ρ_l	liquid density
$\bar{\rho}$	mass of gas per unit volume in two-phase flow
σ	asymptotic order for slow time
σ_s	surface tension for liquid stream
τ	time lag
τ_M, τ_R	characteristic times for mixing and chemical reaction
τ_{ij}	viscous stress tensor
Φ	viscous dissipation
ω_m	reaction rate for species m

Superscripts

'	perturbation quantity
-	steady-state value
τ	time-lag applied to argument of term

Subscripts

c	critical thermodynamic quantity
i, j, x, y, r, θ	indices for vector direction
m	index for chemical species
1, 2, 3, . . .	order of perturbation quantity

REFERENCES

Abramzon, B., and Sirignano, W.A. 1989. Droplet vaporization model for spray combustion calculations. *Int. J. Heat Mass Transfer*, **32**(9), 1605–1618.

Awad, E., and Culick, F. 1986. On the existence and stability of limit cycles for longitudinal acoustic modes in a combustion chamber. *Combust. Sci. Technol.*, **46**, 195–222.

Bhatia, R., and Sirignano, W.A. 1991. A one-dimensional analysis of liquid-fueled combustion instability. *J. Propul. Power*, **7**, 953–961.

Bowman, C. 1967. Experimental investigation of high-frequency longitudinal combustion instability in gaseous propellant rocket motors. Report 66–2725. Air Force Office of Scientific Research.

Bowman, C., Glassman, I., and Crocco, L. 1965. Combustion instability in gas rockets. *AIAA J.*, **3**, 1981.

Continillo, G., and Sirignano, W.A. 1988. Numerical study of multicomponent fuel spray flame propagation in a spherical closed volume. *Symp. (Int.) Combust.*, **22**, 1941–1949.

Crocco, L. 1972. Coordinate perturbation and multiple scale in gasdynamics. *Philos. Trans. R. Soc.*, **272**, 275–301.

Crocco, L., and Cheng, S.-I. 1953. High frequency combustion instability in rockets with distributed combustion. *Symp. (Int.) Combust.*, **4**, 865–880.

Crocco, L., and Cheng, S.-I. 1956. *Theory of Combustion Instability in Liquid Propellant Rocket Motors*, AGARD Monograph 8, Buttersworth, London.

Crocco, L., and Mitchell, C.E. 1969. Nonlinear periodic oscillations in rocket motors with distributed combustion. *Combust. Sci. Technol.*, **1**, 147–169.

Crocco, L., and Sirignano, W.A. 1966. Effects of transverse velocity components on the nonlinear behavior of short nozzles. *AIAA J.*, **4**, 1428–1430.

Crocco, L., and Sirignano, W.A. 1967. *Behavior of Supercritical Nozzle Under Three Dimensional Oscillatory Conditions*. AGARDograph No. 117, North Atlantic Treaty Organization, Neuilly-Sur-Seine, France.

Culick, F. 1976. Nonlinear behavior of acoustic waves in combustion chambers. *Acta Astronaut.*, **3**, 715–734.

Culick, F.E.C. 1967. Calculation of the admittance function for a burning surface. *Proceedings of the Third ICRPG Combustion Conference*, CPIA Publication No. 138, Vol. **1**, p. 307.

Culick, F.E.C. 2006. *Unsteady Motions in Combustion Chambers for Propulsion Systems*. AGARDograph AG-AVT-039, North Atlantic Treaty Organization, Neuilly-Sur-Seine, France.

Delplanque, J.-P., and Sirignano, W.A. 1993. Numerical study of transient vaporization of an oxygen droplet at sub- and super-critical conditions. *Int. J. Heat Mass Transfer*, **36**, 303–314.

Delplanque, J.-P., and Sirignano, W.A. 1994. Boundary layer stripping effects on droplet transcritical convective vaporization. *Atomization Sprays*, **4**, 325–349.

Delplanque, J.-P., and Sirignano, W.A. 1995. Transcritical vaporization and combustion of lox droplet arrays in a convective environment. *Combust. Sci. Technol.*, **105**, 327–344.

Delplanque, J.-P., and Sirignano, W.A. 1996. Transcritical liquid oxygen droplet vaporization: Effect on rocket combustion instability. *J. Propul. Power*, **12**, 349–357.

Denison, R., and Baum, E. 1961. A simplified model for unstable burning in solid propellants. *ARS J.*, **31**, 112.

Godsave, G.A.E. 1953. Studies of the combustion of drops in a fuel spray: The burning of single drops of fuel. *Symp. (Int.) Combust.*, **4**, 818–830.

Harper, E.Y., Grube, G.W., and Chang, I.-D. 1972. On the breakup of accelerating liquid drops. *J. Fluid Mech.*, **52**, 565–591.

Harje, D., and Reardon, F. 1972. Liquid propellant rocket combustion instability. NASA SP194. U.S. Government Printing Office.

Heidmann, M.F., and Wieber, P. 1965. Analysis of *n*-heptane vaporization in unstable combustor with travelling transverse oscillations. NASA Technical Note 3424.

Hsiao, G.C., Meng, H., and Yang, V. 2011. Pressure-coupled vaporization response of *n*-pentane fuel droplet at subcritical and supercritical conditions. *Proc. Combust. Inst.*, **33**, 1997–2003.

Hsieh, K., Shuen, J., and Yang, V. 1991. Droplet vaporization in high pressure environments: I. near-critical conditions. *Combust. Sci. Technol.*, **76**(1–3), 111–132.

Jackson, T.L. 2012. Modeling of heterogeneous propellant combustion: A survey. *AIAA J.*, **50**(5), 993–1006.

Kevorkian, J.K., and Cole, J.D. 1996. *Multiple Scale and Singular Perturbation Methods*, Springer-Verlag, New York.

Krier, H., T'ien, J., Sirignano, W.A., and Summerfield, M. 1968. Non-steady burning phenomenon in solid propellants: Theory and experiments. *AIAA J.*, **6**, 278.

Liepmann, H., and Roshko, A. 1957. *Elements of Gasdynamics*, John Wiley and Sons, New York.

Maslen, S.H., and Moore, F.K. 1956. On strong transverse waves without shocks in a circular cylinder. *J. Aeronaut. Sci.*, **23**(6), 583–593.

Minorsky, N. 1962. *Nonlinear Oscillations*, Van Nostrand, Princeton, NJ.

Mitchell, C.E., Crocco, L., and Sirignano, W.A. 1969. Nonlinear longitudinal instability in rocket motors with concentrated combust. *Combust. Sci. Technol.*, **1**, 35–63.

Popov, P.P., Sideris, A., and Sirignano, W.A. 2014. Stochastic modeling of transverse wave instability in a liquid propellant rocket engine. *J. Fluid Mech.*, **745**, 62–91.

Priem, R.J., and Heidmann, M.F. 1960. Propellant vaporization as a design criterion for rocket-engine combustion chambers. NASA Technical Report R-67.

Ranger, A.A., and Nicholls, J.A. 1972. Atomization of liquid droplets in a convective gas stream. *Int. J. Heat Mass Transfer*, **15**, 1203–1211.

Reardon, F.H., Crocco, L., and Harrje, D.T. 1964. Velocity effects in transverse mode liquid propellant rocket combustion instability. *AIAA J.*, **12**, 1631–1641.

Roh, T.-S., Tseng, I.-S., and Yang, V. 1995. Effects of acoustic oscillations on flame dynamics of heterogeneous propellants in rocket motors. *J. Propul. Power*, **11**(4), 640–650.

Schmitt, T., Mery, Y., Boileau, M., and Candel, S. 2011. Large-eddy simulation of oxygen/methane flames under transcritical conditions. *Proc. Combust. Inst.*, **33**, 1383–1390.

Shipley, K., Morgan, C., Anderson, W.E., Harvazinski, M.E., and Sankaran, V. 2013. Computational and experimental investigation of transverse combustion instabilities. Presented at the 49th AIAA/ASME/SAE/ASEE Joint Propulsion Conference and Exhibit, San Jose, CA, July 15–17.

Sirignano, W.A. 1964. Theoretical study of nonlinear combustion instability: Longitudinal mode. PhD dissertation. Princeton University Department of Aerospace and Mechanical Sciences Report No. 677, Princeton, NJ.

Sirignano, W.A. 1968. A theory of axial-mode shock-wave oscillations in a solid-rocket combustor. *Symp. (Int.) Combust.*, **12**, 129–137.

Sirignano, W.A. 1972. Non linearita dei risonatori di Helmholtz. *L'Aerotecnica Missili e Spazio*, **51**(4), 1256–1265.

Sirignano, W.A. 2005a. Corrigendum to ‘Volume averaging for the analysis of turbulent spray flows’ [*Int. J. Multiphase Flow*, **31**, 675–705]. *Int. J. Multiphase Flow*, **31**, 867.

Sirignano, W.A. 2005b. Volume averaging for the analysis of turbulent spray flows. *Int. J. Multiphase Flow*, **31**, 675–705.

Sirignano, W.A. 2010. *Fluid Dynamics and Transport of Droplets and Sprays*, 2nd ed., Cambridge University Press, New York.

Sirignano, W.A. 2014. Advances in droplet array combustion theory and modelling. *Prog. Energy Combust. Sci.*, **42**, 54–86.

Sirignano, W.A., and Crocco, L. 1964. A shock wave model of unstable rocket combustors. *AIAA J.*, **2**, 1285–1296.

Sirignano, W.A., and Delplanque, J.P. 1999. Transcritical vaporization of liquid fuels and propellants. *J. Propul. Power*, **15**(6), 896–902.

Sirignano, W.A., and Popov, P. 2013. Two-dimensional model for liquid-rocket transverse combustion instability. *AIAA J.*, **51**(12), 2919–2934.

Spalding, D.B. 1953. The combustion of liquid fuels. *Symp. (Int.) Combust.*, **4**, 847–864.

Strahle, W.C. 1965a. Periodic solutions to a convective droplet burning problem: The stagnation point. *Symp. (Int.) Combust.*, **10**, 1315–1325.

Strahle, W.C. 1965b. Unsteady laminar jet flame at large frequencies of oscillation. *AIAA J.*, **3**, 957.

Strahle, W.C. 1965c. Unsteady reacting boundary layer on a vaporizing flat plate. *AIAA J.*, **3**, 1195.

Strahle, W.C. 1967. High frequency behavior of laminar jet flame subjected to transverse sound waves. *Symp. (Int.) Combust.*, **11**, 747–754.

Tang, P.K., Harrje, D.T., and Sirignano, W.A. 1973. Experimental verification of the energy dissipation mechanism in acoustic dampers. *J. Sound Vib.*, **26**(2), 263–267.

Tang, P.K., and Sirignano, W.A. 1973. Theory of a generalized helmholtz resonator. *J. Sound Vib.*, **26**(2), 247–262.

T'ien, J., and Sirignano, W.A. 1971. Unsteady thermal response of the condensed phase fuel to a reacting gaseous boundary layer. *Symp. (Int.) Combust.*, **13**, 529–539.

Tong, A., and Sirignano, W.A. 1989. Oscillatory vaporization of fuel droplets in unstable combustor. *J. Propul. Power*, **5**(3), 257–261.

Tsien, H.S. 1952. The transfer function of rocket nozzles. *ARS J.*, **22**, 139–143.

Westbrook, C.K., and Dryer, F.L. 1984. Chemical kinetic modeling of hydrocarbon combustion. *Prog. Energy Combust. Sci.*, **10**, 1–57.

Wicker, J.M., Greene, W.D., Kim, S.I., and Yang, V. 1996. Triggering of longitudinal combustion instabilities in rocket motors. *J. Propul. Power*, **12**(6), 1148–1158.

Williams, F.A. 1958. Spray combustion and atomization. *Phys. Fluids*, **1**(6), 541–545.

Williams, F.A. 1959. Spray combustion theory. *Combust. Flame*, **3**(2), 215–228.

Williams, F.A. 1960. On the assumptions underlying droplet vaporization and combustion theories. *J. Chem. Phys.*, **33**(1), 133–144.

Williams, F.A. 1965. Response of a burning fuel plate to sound vibrations. *AIAA J.*, **3**(11), 2112–2124.

Williams, F.A. 1985. *Combustion Theory*, 2nd ed., The Benjamin/Cummings Publishing Company, Inc., Reading, MA.

Yang, V. 2000. Modeling of supercritical vaporization, mixing, and combustion processes in liquid-fueled propulsion systems. *Proc. Combust. Inst.*, **33**, 925–942.

Yang, V., and Anderson, W.E. 1995. *Liquid Rocket Engine Combustion Instability* (Progress in Astronautics and Aeronautics 169), AIAA, Reston, VA.

Yang, V., and Culick, F. 1990. On the existence and stability of limit cycles for transverse acoustic oscillations in a cylindrical combustion chamber. 1: Standing modes. *Combust. Sci. Technol.*, **72**, 37–65.

Yang, V., Kim, S., and Culick, F. 1990. Triggering of longitudinal pressure oscillations combustion chambers. I: Nonlinear gasdynamics. *Combust. Sci. Technol.*, **75**, 183–214.

Yang, V., and Lin, N.N. 1994. Vaporization of liquid oxygen (LOX) droplets at supercritical conditions. *Combust. Sci. Technol.*, **97**, 247–270.

Zinn, B.T. 1968. A theoretical study of nonlinear combustion instability in liquid-propellant rocket engines. *AIAA J.*, **6**, 1966–1972.

Zinn, B.T., and Crocco, L. 1968. Nozzle boundary condition in nonlinear rocket instability problem. *Acta Astronaut.*, **13**, 489–496.

Zinn, B.T., and Powell, E.A. 1971. Nonlinear combustion instability in liquid-propellant rocket engines. *Symp. (Int.) Combust.*, **13**, 491–503.

Zong, N., and Yang, V. 2006. Cryogenic fluid jets and mixing layers in transcritical and supercritical environments. *Combust. Sci. Technol.*, **178**(1–3), 193–227.

Addendum 2



Transverse Combustion Instability in a Rectangular Rocket Motor

Journal:	<i>Journal of Propulsion and Power</i>
Manuscript ID:	2015-04-B35868
Manuscript Type:	Full Paper
Date Submitted by the Author:	30-Apr-2015
Complete List of Authors:	Popov, Pavel; UC-Irvine, Mechanical and Aerospace Engineering Sirignano, William; UC-Irvine, Mechanical and Aerospace Engineering
Subject Index Category:	60300 Combustion Instability < 60000 PROPULSION, 61300 Liquid Rocket Engines < 60000 PROPULSION, 20500 Computational Fluid Dynamics < 20000 FLUID DYNAMICS

SCHOLARONE™
Manuscripts

1
2
3
4
5
6
7
8
9
10
11
12
13
14
15
16
17
18
19
20
21
22
23
24
25
26
27
28
29
30
31
32
33
34
35
36
37
38
39
40
41
42
43
44
45
46
47
48
49
50
51
52
53
54
55
56
57
58
59
60

Transverse Combustion Instability in a Rectangular Rocket Motor

Pavel P. Popov*, and William A. Sirignano†

Department of Mechanical and Aerospace Engineering

University of California, Irvine, CA 92697

April 30, 2015

Abstract

A computational analysis of transverse acoustic instability is presented for an experimental combustion chamber with rectangular cross-section. The analysis is shown to be efficient and accurate. The governing equations are solved on multiple, coupled grids, which are two-dimensional in the combustion chamber and nozzle, and one-dimensional in the injector port. Thus, they allow for a fast simulation, even in a serial run. Due to the lengthscale difference, the jet flame behavior at the injectors, including effects of turbulence can be decoupled from the acoustic effects, and solved on a local grid for each jet flame emerging from an injector. Wave propagation through the injector feed ports is evaluated on additional, one-dimensional grids for each injector port. The overall algorithm is used to simulate the Purdue seven-injector rocket engine; good quantitative agreement between simulations and experiment is achieved.

*Postdoctoral Researcher.

†Professor, AIAA Fellow.

1
2
3
4
5
6
7
8 Consistently with experimental results, the simulations predict that the
9 experimental setup is unconditionally unstable, with small perturbations
10 growing to a limit cycle whose shape is a first transverse acoustic mode
11 of the chamber.
12
13

14	a	Speed of sound, m/s
15	c_p	Specific heat at constant pressure, J/ $^{\circ}\text{K}$ kg
16	D	Mass diffusivity, m^2/s
17	C_x, C_η	Rapid-distortion strain of velocity field
18	S_{ij}	Velocity field strain tensor
19	l_m	mixing length
20	E	Energy release rate, J/kg s
21	L	Chamber thickness, m
22	r	Radial position, m
23	R_c	Chamber wall radius of curvature, m
24	p	Pressure, newton m^{-2}
25	t	Time, s
26	T	Temperature, K
27	Y_i	Mass fraction of species i

41 **Greek symbols**
42

43	α, β	Schwab-Zel'dovich variables
44	γ	Ratio of specific heats
45	η	Local radial coordinate for the injector grids
46	ν_T	Turbulent kinematic viscosity, m^2/s
47	ρ	Density, kgm m^{-3}
48	ω_i	Reaction rate of species i , s^{-1}

Subscripts

10	F	Fuel
11	i	Index for chemical species
12	O	Oxidizer
13	0	Undisturbed state

Operators

20	i, j	Index for Cartesian coordinates
----	--------	---------------------------------

1 Introduction

We address the problem of liquid propellant rocket engine (LPRE) combustion instability, which is a well-known and undesirable phenomenon in rocket operation. The high energy release by combustion can, in certain conditions, reinforce acoustic oscillations, causing them to grow to destructive amplitudes. LPRE combustion instability provides a very interesting nonlinear dynamics problem as shown by both theory and experiment: [1, 2, 3].

There are two general types of acoustical combustion instability: “driven” instability and “self-excited” instability as noted by Culick [4] who describes evidence in some solid-propellant rockets of the driven type where noise or vortex shedding causes kinematic waves (i.e., waves carried with the moving gas) of vorticity or entropy to travel to some point where an acoustical reflection occurs. The reflected wave causes more noise or vortex shedding after travelling back and a cyclic character results. These driven types do not rely on acoustical chamber resonance and are much smaller in amplitude since the energy level is limited by the driving energy. The frequency of oscillation for cases where

vortex shedding is a factor depends on two velocities, the sound speed and the subsonic, kinematic speed of the vortex. Consequently, the frequency is lower than a purely acoustic resonant frequency. Oscillations of this type are found in the longitudinal mode. To the best of our knowledge, these have never been observed in LPRE operation or in any transverse-mode instability and, when occurring in solid rockets or ramjets, the amplitudes are much lower than the values of concern for LPRE. So, they will not be addressed in this research.

Interest in propellant combinations of hydrocarbon fuel and oxygen, stored as liquids, is returning in the LPRE field. The analysis and results here will address situations where the hydrocarbon and oxidizer propellants are injected co-axially as gasses. These propellants will have elevated temperatures at the injectors because they have been used prior to injection either for partial combustion for gas generation to drive a turbo pump or as a coolant before injection. In particular, the inlet temperature and the mean combustion-chamber pressure were carefully chosen to place the mixture in the supercritical (but near perfect gas) domain. Therefore, realism is maintained here when the chamber flow is treated as gaseous and the perfect gas law is used.

The dynamic coupling of the injector system with the combustion chamber of a liquid-propellant rocket engine has been a topic of interest for many decades. Two types of instabilities are known to occur. The chugging instability mode has nearly uniform but time-varying pressure in the combustion chamber. The combustion chamber acts as an accumulator or capacitor while the inflowing propellant mass flux oscillates because the oscillating chamber pressure causes a flux-controlling oscillatory pressure drop across the injector. This low frequency instability was characterized by Summerfield [5]. The second type of coupling involves a high frequency oscillation at a near-resonant chamber mode frequency. Here, the resonant frequency has been modestly adjusted because

the acoustic system involves some portion of the internal volume of the injector as well as the combustion chamber and convergent nozzle volumes. Crocco and Cheng [6] discuss both types of instability for one-dimensional (longitudinal) oscillations. Interesting discussions of coupled injector-system acoustics by Nestlerode, Fenwick, and Sack and by Harrje and Reardon can be found in Chapter 3 of the well-known NASA SP-194 [1]. More recent overviews and analyses are provided by Hutt and Rocker [7] and DeBenedictus and Ordoneau [8]. Yang et al. [9] provide several interesting articles on the design and modelling of rocket injector systems.

The disturbances that trigger combustion instability can result from fluid-mechanical disruptions in the propellant injection process, shedding in the combustion chamber of large rogue vortices that eventually flow through the choked nozzle [10], extraordinary excursions in local burning rates [11, 12], an acceleration of the entire LPRE engine [11, 13], or a synergism amongst such events.

In this paper, an analysis is presented of nonlinear, transverse-mode combustion instability in a rectangular LPRE combustion chamber with a long nozzle whose length is comparable to the length of the combustion chamber. Thus, the present study builds on previous analyses [3, 12, 11]. A particular experimental configuration, the seven-injector rocket engine studied by the Anderson group at Purdue University [14, 15, 16], is simulated. The Purdue experimental group studied transverse oscillations in a rectangular cross-section combustion chamber.

Although the rectangular cross-section combustion chamber is not practical for high-pressure operations, it has long been a useful experimental device with easier access for measurements and observations. Reference [1] contains several early works on rectangular cross-section combustion chambers. Bracco and Harrje from Princeton University, and Coultas and Nestlerode from Rock-

etdyne discuss in sub-sections 7.2.4 and 9.2.2.4, respectively, the use of square cross-sections for the study of longitudinal modes. Certain observations and measurements were made easier with this cross-section. Coulter and Nestlerode in sub-section 9.2.2.5 discuss their two-dimensional rocket motor which takes a rectangular, diametrical slice of an actual motor. Sirignano in sub-section 3.5.1 presents a generalized, three-dimensional, linear theory and applies it to several combustion chamber shapes for transverse oscillations; rectangular cross-sections are considered there. Levine [17] expounds on the Rocketdyne experience with the two-dimensional motor. With various practical propellant combinations, stable and unstable operational domains were found; transverse oscillations could be triggered.

In practice, propellant flow through the injector can be in the same liquid phase as the stored propellant, in a gaseous form mixed with combustion products because of upstream flow through a pre-burner used for a propellant turbo-pump, or in gaseous form because the liquid propellant was used as a combustion-chamber-wall coolant upstream. We consider here gaseous co-axial flow of the pure propellants, RP1, ethane and H_2O_2 , based on the last scenario.

The remainder of this paper is organized as follows: the experimental setup for the seven-injector rocket engine is presented in section 2, the governing equations of the pressure wave dynamics are given in section 3. Section 4 presents the calculation of heat release performed on local cylindrical grids for each injector. Computational results are given in section 5, and a brief discussion on the computational cost of this procedure is provided in section 6. Finally, conclusions are drawn in section 7.

2 Experimental Configuration and Results

The Purdue combustion chamber is shown in Fig. 1. Its upstream portion is rectangular, of length 13.39cm , width 26.67cm and height 3.81cm . This is followed by a straight converging nozzle of length 9.84cm whose throat has a cross-section of $15.07\text{cm} \times 1.44\text{cm}$.

The injector plate contains seven injectors spaced apart evenly in the transverse direction, with a distance of 3.81cm between adjacent injector axes. Each injector consists of an oxidizer post coaxial with a surrounding fuel inlet, with the oxidizer post diameter being 2.05cm and the fuel inlet outer diameter being 2.31cm , with an inner diameter of 2.229cm . For the central study injector, the length of the oxidizer post is 12.92cm and the length of the fuel inlet is 2.79cm ; for the driving injectors, the length of the oxidizer post is 17.04cm and the length of the fuel inlet is 2.28cm .

The oxidizer mixture for the central study element is 90% hydrogen peroxide which is partially-decomposed at the beginning of the oxidizer post, and fully-decomposed by the time it reaches the combustion chamber orifice. Thus, the inlet mixture in the combustion flame grids is, on a mass basis, 58% H_2O and 42% O_2 , for an H_2O mass flow rate of 0.106kg/s and an O_2 mass flow rate of 0.076kg/s ; the inlet temperature is $1029K$. The fuel mixture for the study element is ethane with a mass flow rate of 0.025kg/s and an inlet temperature of $319K$.

The oxidizer mixture for the driving elements element is again 58% H_2O and 42% O_2 , with an H_2O mass flow rate of 0.113kg/s , an O_2 mass flow rate of 0.083kg/s , and an inlet temperature of $1029K$. The fuel mixture for the driving elements is RP1 with a mass flow rate of 0.033kg/s and an inlet temperature of $298.15K$. Decane will be used in our model to represent the RP1. In

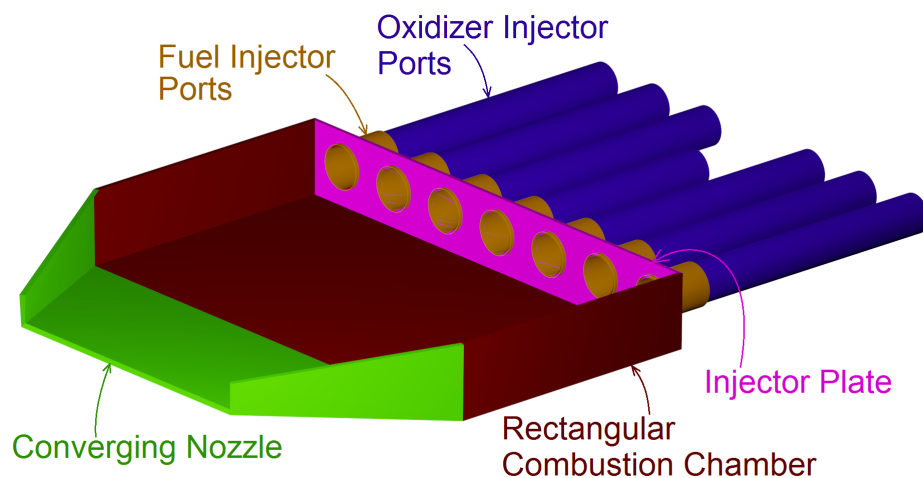


Figure 1: Rectangular combustion chamber and nozzle with injectors.

this study, we simulate several of the experimental configurations studied by the Anderson group, in particular the configurations "OOOXOXOO", "OXXOOXXO", "XOOOOOX" and "XOXOXOX", where an "X" indicates an injector port with only oxidizer inflow (i.e., the fuel ports for that injector are plugged), and "O" indicates an injector port with both fuel and oxidizer. In all of these configurations, the central study element has ethane fuel inflow, and the difference comes up to which of the driving elements have RP1 fuel inflow.

With this experimental configuration, a spontaneous instability of peak-to-peak amplitude of $620kPa$ is measured, with a mean pressure of $965kPa$. The frequency of the first transverse mode component of the instability is $2032Hz$.

3 Basic Equations for Wave Dynamics

The equations for pressure and velocity in the chamber are simplified - the scale of turbulent motions is considered to be much smaller than the acoustic wave scale, whose lengthscale is comparable to the lengthscale of the combustion chamber. Thus, it can be assumed that turbulence and molecular diffusion do not have a significant impact on the large-scale pressure and velocity wave fields, which can then be solved in inviscid form.

3.1 Three-dimensional Wave Equations

Following the developments in [3], the large-scale pressure wave equation has the form.

$$\frac{\partial^2 p}{\partial t^2} - a^2 \frac{\partial^2 p}{\partial x_j \partial x_j} = \frac{\partial \rho}{\partial t} \frac{\partial a^2}{\partial t} + (\gamma - 1) \frac{\partial E}{\partial t} + a^2 \frac{\partial^2 (\rho u_j u_i)}{\partial x_i \partial x_j} \quad (1)$$

The left-hand side of the equation represents the wave operator in three dimensions. The second term on the right represents the influence of the combustion energy release on the acoustic instability, and is thus an integral component of the study of rocket engine instability.

The large-scale velocity components evolve by

$$\frac{\partial u_i}{\partial t} + u_j \frac{\partial u_i}{\partial x_j} + \frac{C}{p^{1/\gamma}} \frac{\partial p}{\partial x_i} = 0, \quad (2)$$

where $C = \frac{p_0^{1/\gamma}}{\rho_0}$, and the assumption is made that pressure dominates over the turbulent and molecular viscosity terms.

These equations, applied previously to a cylindrical chamber [3, 12, 11], were successful in identifying three domains within the parameter space: uncondi-

tional instability, conditional instability and unconditional stability. Transients and limit cycles were produced for several different instability events.

3.2 Reduction to a Two-dimensional Wave Equation

In this study, we use the fact that the combustion chamber is narrow in the height dimension, which implies that the solution fields vary little in that dimension, and can therefore be averaged over it. The chamber height, $L(x, y)$, is constant over the initial section of the combustion chamber and varies linearly with x in the converging nozzle portion of the chamber.

Following Sirignano and Popov [3], two-dimensional averages (here, over the height dimension) of the pressure and velocity fields $\tilde{p} = (1/L(x, y)) \int_0^{L(x, y)} p dx_3$, $\tilde{\rho} = (1/L(x, y)) \int_0^{L(x, y)} \rho dx_3$, $\tilde{a} = (1/L(x, y)) \int_0^{L(x, y)} a dx_3$, and $\tilde{\vec{u}} = (1/L(x, y)) \int_0^{L(x, y)} \vec{u} dx_3$.

Integrating Equation (1) over x_3 and neglecting the difference between products of averages and averages of products, we get

$$\frac{\partial^2 \tilde{p}}{\partial t^2} - \tilde{a}^2 \left[\frac{\partial^2 \tilde{p}}{\partial x_j \partial x_j} + \frac{1}{L} \frac{\partial L}{\partial x_1} \frac{\partial \tilde{p}}{\partial x_1} \right] = \frac{\partial \tilde{\rho}}{\partial t} \frac{\partial \tilde{a}^2}{\partial t} + (\gamma - 1) \frac{\partial \tilde{E}}{\partial t} + \tilde{a}^2 \frac{\partial^2 (\tilde{\rho} \tilde{u}_j \tilde{u}_i)}{\partial x_i \partial x_j} + \tilde{a}^2 \frac{1}{L} \frac{\partial L}{\partial x_1} \frac{\partial (\tilde{\rho} \tilde{u}_1 \tilde{u}_i)}{\partial x_i} \quad (3)$$

where $i = 1, 2; j = 1, 2$. The last terms on both the left- and right-hand sides correspond to the effect which the variable combustion chamber width (in the x_3 -direction) has on the divergence operators in eq.1. The above equation contains derivatives of L only in the x_1 direction because L does not vary in the x_2 direction.

Similarly, the averaged version of equation 2 has the form:

$$\frac{\partial \tilde{u}_i}{\partial t} + \tilde{u}_j \frac{\partial \tilde{u}_i}{\partial x_j} + \frac{1}{L} \frac{\partial L}{\partial x_1} (\tilde{u}_i \tilde{u}_1) + \frac{C}{\tilde{p}^{1/\gamma}} \frac{\partial \tilde{p}}{\partial x_i} = 0 \quad (4)$$

These equations are solved on an orthogonal curvilinear coordinate system, which represents a conformal map of the present hexagonal domain onto a square. The curvilinear form of eqs. 3 and 4, with the associated nomenclature, is given in Appendix A.

At the walls of the combustion chamber, the boundary conditions on the pressure and velocity are

$$\tilde{u}_n = 0 \quad ; \quad \frac{\partial \tilde{p}}{\partial n} = \frac{\tilde{p}^{\frac{1}{\gamma}} \tilde{u}_t^2}{CR_c}, \quad (5)$$

with \tilde{u}_n, \tilde{u}_t denoting respectively the components of velocity normal and tangential to the wall boundary, and R_c denoting the wall boundary's radius of curvature. At the downstream end of the convergent nozzle, a Mach number $M = 0.9$ is enforced, and the short nozzle approximation is used to represent the additional convergence to a choked throat, as an approximation to the sonic condition in the experiment.

4 Determination of Heat Release Rate E with Co-axial Injection

We seek to model the heat release rate of change, $\frac{\partial E}{\partial t}$, which is an integral component to the acoustic instability pressure wave equation, eq.1. Following [3], we shall denote $\alpha = Y_F - \nu Y_O$, where Y_F, Y_O are the fuel and oxidizer mass fractions, and ν is their stoichiometric ratio. Then, α is a conserved scalar, which we will determine in the vicinity of each injector, on a axi-symmetric cylindrical grid with the assumption that the injector flow field is mostly in the direction co-axial to the injector. An illustration of the grids used for the jet flames emerging from the seven injectors, and their relation to the combustion

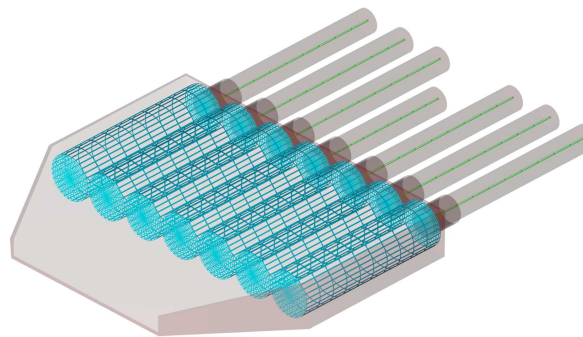


Figure 2: Cylindrical jet flame grids (blue) and 1D injector port grids (green) situated within the rocket engine.

chamber grid is given in Fig.2.

With the variable β being defined by $\beta = (Q/(c_p T_o))Y_F + T/T_o - (p/p_o)^{(\gamma-1)/\gamma}$, the evolution equations for the variables α, β, Y_F have the following form:

$$\frac{\partial \alpha}{\partial t} + u_x \frac{\partial \alpha}{\partial x} + u_\eta \frac{\partial \alpha}{\partial \eta} - D \left[\frac{\partial^2 \alpha}{\partial \eta^2} + \frac{1}{\eta} \frac{\partial \alpha}{\partial \eta} + \frac{\partial^2 \alpha}{\partial x^2} \right] = 0, \quad (6)$$

$$\frac{\partial \beta}{\partial t} + u_x \frac{\partial \beta}{\partial x} + u_\eta \frac{\partial \beta}{\partial \eta} - D \left[\frac{\partial^2 \beta}{\partial \eta^2} + \frac{1}{\eta} \frac{\partial \beta}{\partial \eta} + \frac{\partial^2 \beta}{\partial x^2} \right] = 0 \quad (7)$$

and

$$\frac{\partial Y_F}{\partial t} + u_x \frac{\partial Y_F}{\partial x} + u_\eta \frac{\partial Y_F}{\partial \eta} - D \left[\frac{\partial^2 Y_F}{\partial \eta^2} + \frac{1}{\eta} \frac{\partial Y_F}{\partial \eta} + \frac{\partial^2 Y_F}{\partial x^2} \right] = \omega_F, \quad (8)$$

where x, η are respectively the axial and radial coordinates of the cylindrical injector grids, and the source term on the right-hand side of Eq. (8) is obtained from a Westbrook-Dryer two-step oxidation mechanism [18], from the fuel (C_2H_6 for the central injector element, $C_{10}H_{22}$ for the driving injector elements) to CO , and then from CO to CO_2 . In order to obtain the concentrations of both the

injector fuel and CO from the fuel mass fraction, it is assumed that oxidation of CO occurs only after the partial oxidation of the fuel to CO has reached its completion.

Building on [3], the source term in Eq. 8 is obtained via an assumed-PDF model for α and β , so that the means of α and β evolve by Eqs. 6,7 and their subgrid distributions are assumed to be beta functions, which are standard PDFs for modeling mixing of two or more streams. The term ω_F in Eq. 8 is then obtained via integration over the sample space of α and β . The assumed PDF model has been used with great success for the simulation of turbulent non-premixed flames which are not near extinction [19]. For more details, the reader is referred to [19].

The axial and radial velocities in Eqs. (6-8) are obtained from a solution of the variable density Reynolds-Averaged Navier-Stokes axi-symmetric equations:

$$\rho \left(\frac{\partial u_x}{\partial t} + u_x \frac{\partial u_x}{\partial x} + u_\eta \frac{\partial u_x}{\partial \eta} \right) = - \frac{\partial p_l}{\partial x} + \rho \nu_T \left[\frac{\partial^2 u_x}{\partial x^2} + \frac{1}{\eta} \frac{\partial}{\partial \eta} \left(\eta \frac{\partial u_x}{\partial \eta} \right) \right] \quad (9)$$

$$\rho \left(\frac{\partial u_\eta}{\partial t} + u_x \frac{\partial u_\eta}{\partial x} + u_\eta \frac{\partial u_\eta}{\partial \eta} \right) = - \frac{\partial p_l}{\partial \eta} + \rho \nu_T \left[\frac{\partial^2 u_\eta}{\partial x^2} + \frac{1}{\eta} \frac{\partial}{\partial \eta} \left(\eta \frac{\partial u_\eta}{\partial \eta} \right) - \frac{u_\eta}{\eta^2} \right] \quad (10)$$

which are solved on each jet flame grid, where $p_l(x, \eta, t)$ is a local hydrodynamic pressure whose mean is by definition 0 and which has considerably lower magnitude than the injector pressure $p(t)$ obtained from Eq. (1). The density in Eqs. (10,11) is obtained from the species scalars and the long-wavelength pressure, $p(t)$, at the injector's location, so that the overall procedure for solving Eqs. (10,11) is elliptic.

The turbulent viscosity ν_T is evaluated based on a mixing-length model [20]:

$$\nu_T = l_m^2 \left(2\tilde{S}_{ij}\tilde{S}_{ij} \right)^{(1/2)}, \quad (11)$$

where \tilde{S}_{ij} is the strain tensor of the velocities in Eqs. (10,11) and l_m is the mixing length, defined as

$$l_m(x) = \frac{3}{1 + C_x(x) + C_\eta(x)} r_{1/2}(x). \quad (12)$$

In the above formula, $r_{1/2}(x)$ is the radius in the constant x plane at which the velocity magnitude has decreased to 1/2 if its maximum value, and $C_x(x)$, $C_\eta(x)$ are the values of strain of the approximately axi-symmetric velocity fields of Eqs. (10,11) by the chamber velocity obtained in solution to Eq.(4). Utilizing rapid distortion theory [20], the fluctuating velocity field evolves and is driven by the mean strain when the time scale of the mean strain which is much faster than that of the turbulence. Hence, C_x, C_η evolve by

$$\frac{dC_x(x)}{dt} = C_x(x) \frac{\partial \tilde{u}_1}{\partial x_1} + (1 - C_x(x)) \left(2\tilde{S}_{ij}\tilde{S}_{ij} \right)^{(1/2)}, \quad (13)$$

$$\frac{dC_\eta(x)}{dt} = C_\eta(x) \frac{\partial \tilde{u}_2}{\partial x_2} + (1 - C_\eta(x)) \left(2\tilde{S}_{ij}\tilde{S}_{ij} \right)^{(1/2)}, \quad (14)$$

where the velocity strain terms $\frac{\partial \tilde{u}_1}{\partial x_1}, \frac{\partial \tilde{u}_2}{\partial x_2}$ are evaluated at the point in the combustion chamber grid which corresponds to the point at a distance of x along the injector grid's centerline. As we shall see in section 5, the use of the rapid-distortion correction improves the agreement of the computational results with experiments: without it, the underprediction of the oscillation amplitude is much more pronounced.

Finally, following Popov, Sideris and Sirignano [11], the pressure and velocity in the injector posts are solved via the set of one-dimensional wave equations:

$$\frac{\partial^2 p}{\partial t^2} - a^2 \frac{\partial^2 p}{\partial x^2} = a^2 \frac{\partial^2 (\rho u^2)}{\partial x^2} - \frac{\partial a^2}{\partial t} \frac{\partial (\rho u)}{\partial x} \quad (15)$$

$$\frac{\partial u}{\partial t} + u \frac{\partial u}{\partial x} = -\frac{1}{\rho} \frac{\partial p}{\partial x}. \quad (16)$$

They are solved on a 1D grid upstream of each cylindrical injector grid (shown in Fig.2). In this model, velocity fluctuations affect the energy release rate through the modification of the eddy diffusivity, mixing rate and the rate of propellant inflow into the combustion chamber. Pressure fluctuations, on the other hand, affect the chemical rate and drive the injector port velocity fluctuations.

5 Results

With the simulation procedure described here, it was found that the seven-injector combustion chamber is unconditionally unstable for all experimental cases with the exception of the "XOXOXOX" case. For the rest of the cases, arbitrarily small perturbations growing to a limit cycle whose major component is the first transverse mode of the chamber in the x_2 direction.

Figure 3 shows a contour plot of the pressure field in a fully-developed limit cycle oscillation for the most unstable "OOXOXOO" case. Two different perturbation mechanisms were tested - the first consists of setting an initial condition which is a first transverse mode pressure wave of low amplitude, whereas the second consisted of the imposition on the combustion chamber of a reciprocating acceleration in the transverse, x_2 -direction. As can be seen in Fig. 3, both disturbance mechanisms produced the same instability waveform, which indicates

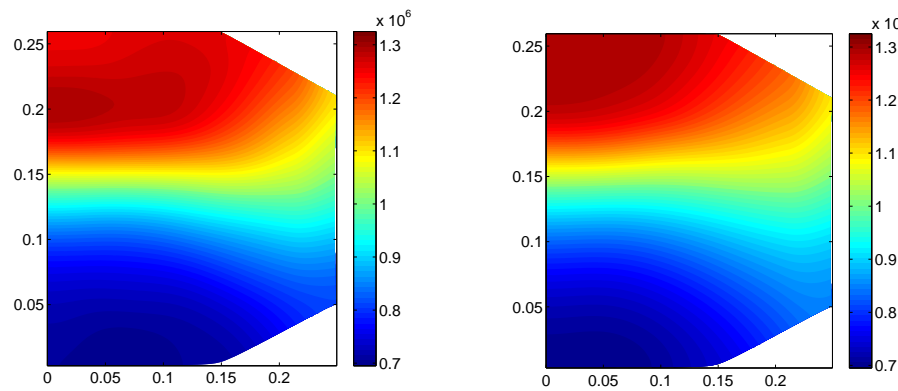


Figure 3: Pressure contours for acoustic limit cycles for the seven-injector rocket engine. Left: a limit cycle caused by an incited low-amplitude pressure wave. Right: a limit cycle caused by reciprocating acceleration.

that for this setup the shape of the limit cycle does not depend on the initial condition.

It was found that the limit cycle does not produce shocks; upon grid refinement the pressure gradients in the transverse direction do not increase. This is consistent with the experimental findings of Shipley et al. [16] which did not discover the existence of shocks in the experimentally-measured instability. For the "OOOXOXOO" case, a contour plot of the temperature field for the ethane injector is given in figure 4. As can be seen on that plot, the maximum flame temperature is $2890K$, with a coflow temperature of $2660K$, which is in good agreement with the numerical results of Shipley et al.[16], who report a maximum temperature of approximately $2800K$ and a coflow temperature of approximately $2550K$.

To illustrate the time-dependent nature of the solution, Figure 5 plots, for the "OOOXOXOO" case, the calculated pressure over 4 cycle periods at four

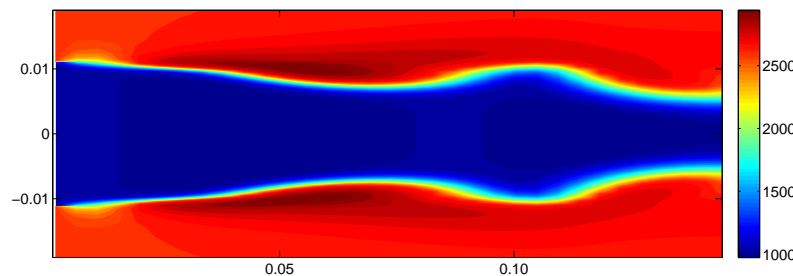


Figure 4: Temperature contour plots for the center injector ("OOXOXOO" case).

different locations: at the outlet of the central (study) injector, at the outlet of one of the outermost driving injectors, at the center of the nozzle and at the edge of the nozzle. It can be seen that the leading edge of the pressure wave has a sharper gradient than its trailing edge, but the gradient is still finite. Note that, while the central injector falls at a pressure node of the linear first transverse acoustic mode, there is still some pressure oscillation at that location, due to higher-order effects. We also note that the pressure oscillations at the central injector are out of phase with the larger amplitude oscillations near the side wall.

Figure 6 plots, for the "OOXOXOO" case, the transverse velocity at the central and outer injector, and at the center of the nozzle. We note that the transverse velocity is greatest at the central injector, which falls on a velocity anti-node of the linear first transverse mode. Time histories of the net heat releases from the central and outer driving injector are given on Figure 7. For the driving injector, we can see considerable large amplitude oscillation of the heat release over time. It is this variation that drives the transverse acoustic instability. The stronger response of the heat release rate near the outer injector

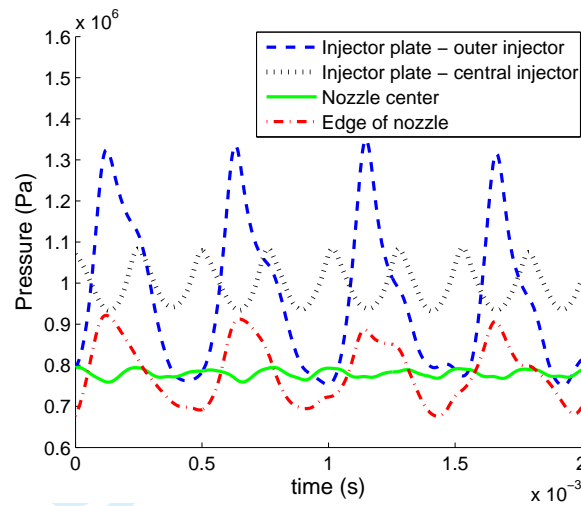


Figure 5: Pressure as a function of time at four different points in the domain ("OOXOXOO" case).

versus the inner injector implies that pressure coupling, either directly or via wave propagation in the injectors, is stronger than velocity coupling of the energy release rate.

Additional comparisons with experimental data can be made with respect to the frequency and amplitude of the limit cycle. Figure 8 plots the eventual limit cycle magnitudes, for the different experimental cases, of simulations whose initial condition is a first transverse mode wave of varying initial amplitude.

As can be seen on that figure, for the cases "OOXOXOO", "OXXOXXXO" and "XOOOOOOX" all initial perturbations, down to a magnitude of 1kPa produce a limit cycle whose amplitude is constant for the given test case. For the "XOXOXOX" case, an initial perturbation of amplitude 1kPa will decay, whereas perturbations of amplitude 2kPa will grow to an acoustic limit cycle. Thus, our simulation procedure predicts that the first three cases mentioned above are unconditionally unstable, which is in agreement with the experimen-

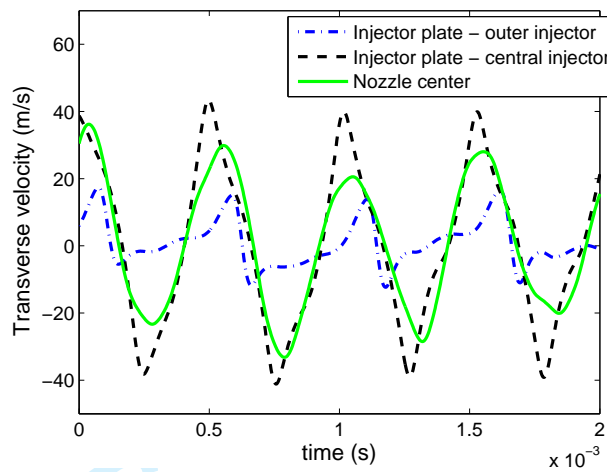


Figure 6: Transverse velocity as a function of time at three different points in the domain ("OOOXOXOO" case).

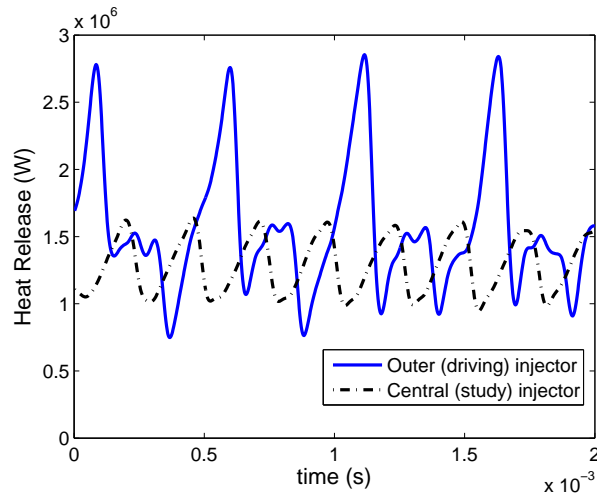


Figure 7: Net heat release, as a function of time, of the central and outermost driving injectors ("OOOXOXOO" case).

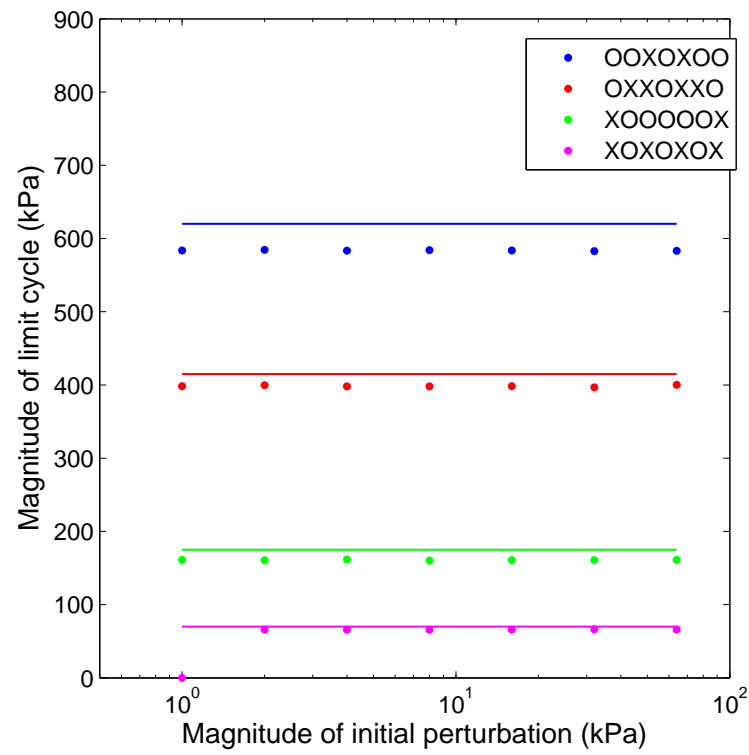


Figure 8: Limit-cycle amplitudes for simulations whose initial condition is a first transverse mode pressure wave of varying amplitude. The lines indicate the experimentally-observed limit-cycle amplitudes.

tal data (in the experiment, the instability developed spontaneously, without the need for forcing), and the "XOXOXOX" case is conditionally unstable, contrary to experimental data.

Despite this disagreement for the "XOXOXOX" case, overall the present simulation predicts the stability characteristics of the seven-injector rocket motor exceptionally well. The limit-cycle amplitudes and frequencies for the four cases (in those simulations where a limit cycle was observed) are given in Table 1.

Test Case	simulation limit- cycle ampl. (kPa)	expt. limit- cycle ampl. (kPa)	simulation freq. (Hz)	expt. freq. (Hz)	relative er- rors (ampl. / freq.)
OOXOXOO	580	620	1931	2032	6%/5%
OXXOXXO	398	415	1720	1807	4%/5%
XOOOOOX	161	175	1766	1855	8%/5%
XOXOXOX	65	70	1803	1912	7%/6%

Table 1: Comparison between computed and experimentally observed limit cycle amplitudes and frequencies.

As can be seen on this table, the present computational procedure tends to underpredict both the amplitude and frequency of the experimentally-observed limit cycles. In terms of frequency, the numerical results are consistently between 5% and 6% lower than experiment. The relative error in the limit-cycle amplitude varies more, with the maximum being 8% and the minimum being

1
2
3
4
5
6
7
8 4%. We also note that the disagreement in amplitude and frequency tends to
9 be greater in the more stable cases: "XOOOOOX" and "XOXOXOX". Overall,
10 however, the quantitative agreement is strong (6.25% mean relative error for
11 amplitude, 5.25% mean relative error for frequency) for a simulation procedure
12 such as the present, optimized for low computational cost, for design purposes.
13
14

15 We also note that the use of the rapid-distortion theory (RDT) model en-
16 capsulated by Eqs. 12 - 14 contributes to the good agreement between exper-
17 iment and simulation: without RDT, the simulated limit-cycle amplitudes are
18 543kPa, 379kPa, 157kPa and 66kPa for the "OOXOXOO", "OXXOXXO",
19 "XOOOOOX" and "XOXOXOX" cases, respectively. Thus, especially in the
20 cases with a large limit-cycle amplitude, the underprediction of experimental
21 results would be considerably more pronounced without the incorporation of
22 the RDT model.
23
24

25 Finally, we note that the stability regime of the combustion chamber can
26 be greatly affected by modifying the injector mass flow away from the reported
27 experimental values. As shown on Table 2, reducing the oxidizer mass flow of the
28 outer driving injectors of the "OOXOXOO" case, to 70% of the experimental
29 values, yields a conditionally unstable simulation: a limit cycle oscillation of
30 213kPa amplitude is predicted, but only for first transverse mode perturbations
31 whose amplitude is 98kPa or greater. Further reducing the oxidizer mass flow
32 rate, to 50% of the experimental values, leads to an unconditionally stable
33 regime.
34
35
36
37
38
39
40
41
42
43
44
45
46
47
48
49
50
51
52
53
54
55
56
57
58
59
60

Test case stability regime	H_2O mass flow rate	O_2 mass flow rate	limit cycle amplitude
Unconditionally unstable	0.113kg/s	0.083kg/s	580kPa
Conditionally unstable	0.079kg/s	0.058kg/s	213kPa
Unconditionally stable	0.0565kg/s	0.0415kg/s	0kPa

Table 2: Effects of oxidizer mass flow variation on the stability characteristics of the OOXOXOO case.

6 Computational Cost

The main advantage of the present computational procedure over existing numerical algorithms is in its very low computational cost. Due to the fact that the governing equations were simplified to a form which could be solved on coupled sets of 2D and 1D grids, each of the simulations run for this study took approximately 1000s in serial implementation. Combined with the reasonable prediction of the combustion chamber's stability characteristics, this makes the present computational procedure a useful tool in exploring the stability characteristics of a given rocket engine, and developing design strategies for stability, from both a passive and active control viewpoint.

7 Conclusions

The computational procedure, previously developed in Sirignano and Popov [3] and Popov, Sideris and Sirignano [11] for the simulation of transverse combustion instabilities in a cylindrical rocket motor, has been extended for use in rectangular, long-nozzle rocket motors. The theoretical extensions include the use of rapid-distortion theory, coupling of diffusivity with transverse velocity, an assumed-PDF flamelet model which estimates subgrid mixing, and unsteady

nozzle flow. The algorithm was applied to the Purdue seven-injector rocket engine experiment and it was discovered that three of the configurations were unconditionally unstable, with even small perturbations growing to an instability. One other configuration was conditionally unstable.

The shape of the limit cycle, which is a first transverse mode, is independent of the destabilizing event. Reasonable quantitative agreement between the computational model and experimental results was achieved, with a mean relative error (across the four test cases) of 5.25% in the frequency of the limit cycle, and a mean relative error of 6.25% in the limit cycle amplitude. Finally, it is determined that pressure oscillations have a stronger effect on the energy release rate than oscillations of the transverse velocity.

Acknowledgements

This research was supported by the Air Force Office of Scientific Research under Grant FA9550-12-1-0156 with Dr. Mitat Birkan as the Program Manager.

References

- [1] Harrje, D. and Reardon, F., "Liquid Propellant Rocket Combustion Instability," *NASA SP194*, U.S. Government Printing Office, 1972.
- [2] Oefelein, J. C. and Yang, V., "Comprehensive Review of Liquid-Propellant Combustion Instabilities in F-1 Engines," *Journal of Propulsion and Power*, Vol. 9, 1993, pp. 657-677.
- [3] Sirignano, W. A. and Popov, P. P., "Two-Dimensional Model for Liquid-Rocket Transverse Combustion Instability," *AIAA J.*, Vol. 51, No. 2919-34, 2013.

1
2
3
4
5
6
7
8 [4] Culick, F. E. C., *Unsteady Motions in Combustion Chambers for Propul-*
9 *sion Systems, AGARDograph AG-AVT-039*, North Atlantic Treaty Orga-
10 *nization, Neuilly-Sur-Seine, France, 2006.*

11
12
13 [5] Summerfield, M., "A Theory of Unstable Combustion in Liquid Propellant
14 Rocket Motors," *Journal of the American Rocket Society*, Vol. 21, 1951.

15
16
17 [6] Crocco, L. and Cheng, S.-I., *Theory of Combustion Instability in Liquid*
18 *Propellant Rocket Motors, AGARD Monograph 8*, Buttersworth, London,
19 1956.

20
21
22 [7] Hutt, J. J. and Rocker, M., "High-Frequency Injector-Coupled Combustion
23 Instability," *Liquid Rocket Engine Combustion Instability*, Vol. 169, AIAA
24 Progress in Astronautics and Aeronautics book series, (V. Yang and W.
25 Anderson, editors), 1995, pp. 345–376.

26
27
28
29
30 [8] DeBenedictus, M. and Ordoneau, G., "High Frequency Injection Cou-
31 pled Combustion Instabilities Study of Combustion Chamber / Feed Sys-
32 tem Coupling," *Joint Propulsion Conference*, Vol. AIAA Paper 2006-4721,
33 2006.

34
35
36
37 [9] Yang, V., Habiballah, M., Hulba, J., and Popp, M., *Liquid Rocket Combus-*
38 *tion Devices: Aspects of Modeling, Analysis, and Design, AIAA Progress in*
39 *Astronautics and Aeronautics Series, Volume 200*, AIAA, Washington, DC,
40 2005.

41
42
43
44 [10] Switthenbank, J. and Sotter, G., "Vortex Generation in Solid Propellant
45 Rocket," *AIAA Journal*, 1964.

46
47
48 [11] Popov, P. P., Sideris, A., and Sirignano, W. A., "Propellant Injector Influ-
49 ence on Liquid Propellant Rocket Engine Instability," *Journal of Propulsion*
50 *and Power*, Vol. 31, No. 1, 2015, pp. 320–331.

51
52
53
54
55
56
57
58
59
60

1
2
3
4
5
6
7
8 [12] Popov, P. P., Sideris, A., and Sirignano, W. A., "Stochastic Modelling of
9 Transverse Wave Instability in a Liquid Propellant Rocket Engine," *Journal*
10 *of Fluid Mechanics*, Vol. 745, 2014, pp. 62–91.
11
12
13 [13] Popov, P. P., Sideris, A., and Sirignano, W., "Uncertainty Quantification
14 of Non-Linear Oscillation Triggering in a Multi-Injector Liquid Propellant
15 Rocket Combustion Chamber," *67th APS/DFD Meeting, San Francisco,*
16 *CA*, 2014.
17
18
19
20
21 [14] Morgan, C., "Response of a gas-gas shear coaxial injector to transverse
22 instability," *M.S. Thesis, Purdue University*, 2012.
23
24
25 [15] Pomeroy, B., "Measurement and analysis of combustor response to trans-
26 verse combustion instability," *Ph.D. Thesis, Purdue University*, 2012.
27
28
29 [16] Shipley, K., Morgan, C., Anderson, W., Harvazinski, M., and Sankaran, V.,
30 "Computational and experimental investigation of transverse combustion
31 instabilities," *Joint Propulsion Conference*, pp. 1083–1099.
32
33
34
35 [17] Levine, R., "Experimental Status of High Frequency Liquid Rocket Com-
36 bustion Instability," *Proceedings of the Tenth (International) Symposium*
37 *on Combustion*, 1965.
38
39
40
41 [18] Westbrook, C. K. and Dryer, F. L., "Chemical Kinetic Modeling of Hydro-
42 carbon Combustion," *Prog. Energy Combust. Sci.*, No. 10, 1984, pp. 1–57.
43
44
45 [19] Pierce, C. and Moin, P., "Progress-Variable Approach for Large-Eddy Sim-
46 ulation of Non-Premixed Turbulent Combustion," *J. Fluid Mech.*, Vol. 504,
47 2004, pp. 73–97.
48
49
50
51 [20] Pope, S. B., *Turbulent Flows*, Cambridge University Press, 2000.
52
53
54
55
56
57
58
59
60

Appendix A: Differential Equations for Pressure and Velocity in Curvilinear Coordinates

Here, we present the form of eqs. 3 and 4 which is solved on the combustion chamber pressure and velocity orthogonal curvilinear grid. We shall use the variables q^1, q^2 to denote the coordinates of the curvilinear grid. Then, using h_i to denote the Lamé coefficients, with $J = h_1 h_2$, using g_{ij} and g^{ij} to denote respectively the covariant and contravariant metric tensors, and Γ_{ij}^k to denote the Christoffel symbols of the second kind, we have that the curvilinear form of eq. 3 is

$$\begin{aligned} \frac{\partial^2 \tilde{p}}{\partial t^2} - \tilde{a}^2 \left[\frac{1}{J} \frac{\partial}{\partial q^i} \left(\frac{J}{h_{(i)}^2} \frac{\partial \tilde{p}}{\partial q^i} \right) + \frac{1}{L} \frac{\partial L}{\partial q^i} \frac{g^{ji}}{h_{(i)}} \frac{1}{h_{(j)}} \frac{\partial \tilde{p}}{\partial q^j} \right] = \\ = \frac{\partial \tilde{\rho}}{\partial t} \frac{\partial \tilde{a}^2}{\partial t} + (\gamma - 1) \frac{\partial \tilde{E}}{\partial t} \\ + \tilde{a}^2 \frac{1}{J} \frac{\partial}{\partial q^i} \left\{ \left[\frac{\partial \tilde{\rho} \tilde{u}_m \tilde{u}_j}{\partial q^k} - \Gamma_{km}^l \tilde{\rho} \tilde{u}_l \tilde{u}_j - \Gamma_{kj}^l \tilde{\rho} \tilde{u}_m \tilde{u}_l \right] g^{mk} g^{ij} \frac{J}{h_{(i)}} \right\} + \\ + \tilde{a}^2 \frac{1}{L} \frac{\partial L}{\partial q^i} \frac{g^{ji}}{h_{(i)}} \left[\frac{\partial \tilde{\rho} \tilde{u}_m \tilde{u}_j}{\partial q^k} - \Gamma_{km}^l \tilde{\rho} \tilde{u}_l \tilde{u}_j - \Gamma_{kj}^l \tilde{\rho} \tilde{u}_m \tilde{u}_l \right] g^{mk}, \end{aligned} \quad (17)$$

where in the above equation indices with braces, such as (i) , are not summed over. Similarly, the curvilinear form of eq. 4 is

$$\begin{aligned} \frac{\partial \tilde{u}_i}{\partial t} + \left[\frac{\tilde{u}_k}{h_{(k)}} \frac{\partial \tilde{u}_i}{\partial q^k} + \frac{\tilde{u}_k}{h_{(k)} h_{(i)}} \left(\tilde{u}_i \frac{\partial h_{(i)}}{\partial q^k} - \tilde{u}_k \frac{\partial h_{(k)}}{\partial q^i} \right) \right] + \\ + \frac{1}{h_{(k)} L} \frac{\partial L}{\partial q^k} g^{kj} (\tilde{u}_i \tilde{u}_j) + \frac{C}{\tilde{p}^{1/\gamma} h_{(i)}} \frac{\partial \tilde{p}}{\partial q^i} = 0 \end{aligned} \quad (18)$$

The two-dimensional coordinates are equivalently the solutions of the Laplace equation. Thereby, they follow the streamlines and potential flow lines of a fictitious incompressible potential flow in the same chamber and convergent nozzle.



Addendum 3

**Triggering and Re-Stabilization of Combustion Instability
with Rocket Motor Acceleration**

Journal:	<i>AIAA Journal</i>
Manuscript ID:	2015-06-J054542
Manuscript Type:	Full Paper
Date Submitted by the Author:	09-Jun-2015
Complete List of Authors:	Popov, Pavel; UC-Irvine, Mechanical and Aerospace Engineering Sideris, Anthanasios; UC-Irvine, Mechanical and Aerospace Engineering Sirignano, William; UCI, MAE
Subject Index Category:	61300 Liquid Rocket Engines < 60000 PROPULSION, 60300 Combustion Instability < 60000 PROPULSION
Select ONE Subject Index for the Table of Contents. This is where your paper will show up in the Table of Contents:	60000 PROPULSION

SCHOLARONE™
Manuscripts

1
2
3
4
5
6
7
8
9
10
11
12
13
14
15
16
17
18
19
20
21
22
23
24
25
26
27
28
29
30
31
32
33
34
35
36
37
38
39
40
41
42
43
44
45
46
47
48
49
50
51
52
53
54
55
56
57
58
59
60

Triggering and Re-Stabilization of Combustion Instability with Rocket Motor Acceleration

Pavel P. Popov*, Athanasios Sideris[†] and William A. Sirignano[‡]

Department of Mechanical and Aerospace Engineering

University of California, Irvine, CA 92697

June 9, 2015

Abstract

The probability of a liquid-propulsion rocket motor to develop screeching instability is studied computationally. The combustion chamber is accelerated as a rigid body using a prescribed acceleration time history: it is found that accelerations of proper magnitude, duration and frequency induce a pressure wave inside the combustion chamber which grows to a screeching acoustic wave limit cycle. For a rectangular rocket motor, a reciprocating transverse acceleration leads to the development of a transverse pressure wave limit cycle; for a cylindrical rocket motor the limit cycle may be either a standing wave, for a transverse reciprocating acceleration, or a spinning wave, for a transverse rotating acceleration. It is found that a limit cycle may be induced by either a large acceleration pulse of short duration, or a smaller acceleration pulse of a longer duration. The Polynomial Chaos Expansion method is used to study the

*Postdoctoral Researcher, AIAA Member.

[†]Professor

[‡]Professor, AIAA Fellow.

probability of growth to a limit-cycle oscillation when the amplitude and frequency of the transverse acceleration pulse are random.

12	a	Speed of sound, m/s
13	$\mathbf{a}^C(t)$	Acceleration time history, m/s^2
14	F_i	Inertial volumetric force, N/m^3
15	c_p	Specific heat at constant pressure, $J/^{\circ}\text{K kg}$
16	D	Mass diffusivity, m^2/s
17	E	Energy release rate, J/kg s
18	L	Chamber thickness, m
19	r	Radial position, m
20	R_c	Chamber wall radius of curvature, m
21	p	Pressure, newton m^{-2}
22	t	Time, s
23	T	Temperature, K
24	Y_i	Mass fraction of species i
25	u	Fluid velocity m/s

38 Greek symbols

40	α, β	Schwab-Zel'dovich variables
41	γ	Ratio of specific heats
42	η	Local radial coordinate for the injector grids
43	ν_T	Turbulent kinematic viscosity, m^2/s
44	ρ	Density, kgm m^{-3}
45	ω_i	Reaction rate of species i , s^{-1}

52 Subscripts

54	F	Fuel
----	-----	------

1
2
3
4
5
6
7
8 i Index for chemical species
9
10 O Oxidizer
11
12 0 Undisturbed state
13
14
15 *Operators*
16
17 i, j Index for Cartesian coordinates
18
19
20
21
22
23
24
25
26
27
28
29
30
31
32
33
34
35
36
37
38
39

1 Introduction and Rocket Engine Configura- tions

40 Acoustic combustion instability of liquid-propellant rocket engines is a well-
41 known and potentially destructive phenomenon which occurs when existing
42 acoustic disturbances within a combustion chamber are amplified by the en-
43 ergy release of combustion [1, 2]. The resulting acoustic oscillations typically
44 lead to heat damage to the rocket engine, due to hot products from the com-
45 bustion chamber's interior being brought into closer proximity of the chamber
46 walls.
47

48 The typical combustion instability setting occurs for motors which are lin-
49 early stable, so that small disturbances decay, but may develop an instability
50 for a large enough perturbation, usually caused by an unforeseen event. Previ-
51 ously, it has been demonstrated that such disturbances can come in the form of
52 an acoustic wave within the combustion chamber [3], a localized pressure pulse
53 which models a bombing experiment [4] or a blockage in one of the rocket motor
54 injector ports [5]. All of these mechanisms share the characteristic that they
55 originate within the rocket engine (either in the combustion chamber or injector
56 ports) and may thus be observed either on a test stand experiment or in-flight.
57
58
59
60

1
2
3
4
5
6
7
8 For several rocket engine designs which exhibit no combustion instability in
9 test stand experiments, behavior suggesting combustion instability is observed
10 in-flight [6]. This suggests external acceleration imposed on the rocket motor,
11 due to in-flight vibration and aerodynamic forces, is an important potential
12 mechanism for instability generation in otherwise stable engine designs. This
13 study focuses on the exploration of this mechanism for combustion instability.
14
15

16 In this work, we consider the effects of externally-imposed acceleration on
17 two different types of rocket motors: a 10-injector rocket engine with a cylin-
18 drical combustion chamber, and a 7-injector rocket engine with a rectangular
19 combustion chamber. The latter of these two is based on an experimental setup
20 at Purdue University [7], with modified inflow conditions chosen so that the
21 overall system is conditionally unstable.
22
23

24 The 10-injector cylindrical rocket engine was previously studied and shown to
25 be conditionally unstable, with a limit cycle instability which could be triggered
26 by a pre-existing pressure wave [3], a pressure pulse [4], and an injector blockage
27 [8]. The combustion chamber is a cylinder whose length is $L = 0.5m$ and whose
28 radius is $R = 0.14m$, with the injectors distributed in three rings, with one
29 injector at the center of the chamber, three injectors at a radius of $r = R/2$
30 and the remaining six injectors spread evenly at a radius of $r = 3R/4$ from the
31 center (see Fig.1).
32
33

34 Each injector consists of two concentric ports, the inner of which serves as
35 the oxidizer port and has a radius of $0.898cm$, and the outer, annular port
36 has an inner radius of $0.898cm$ and an outer radius of $1.1cm$, and serves as
37 the fuel inlet. Both fuel and oxidizer injector ports have a length of $11.5cm$.
38 For this case, the fuel is CH_4 , the oxidizer is O_2 and the mean pressure inside
39 the combustion chamber at standard operating conditions is $200atm$. For more
40 details of this computational configuration, the reader is referred to [3, 8].
41
42

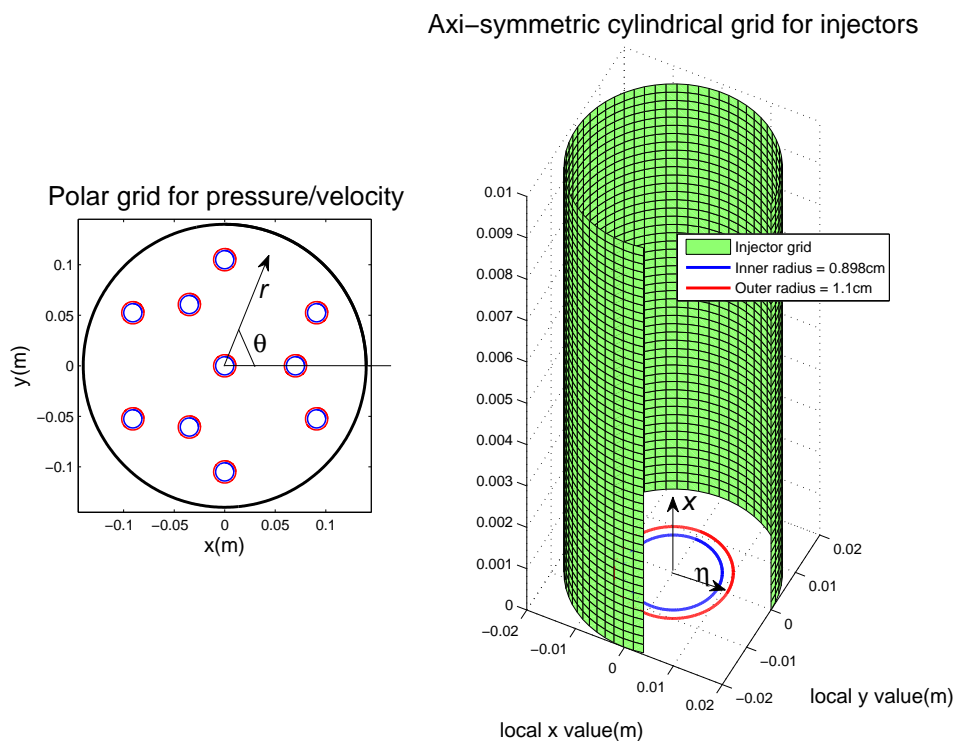


Figure 1: Left: cylindrical combustion chamber and injector distribution. Right: axi-symmetric cylindrical grid used for the solution of each of the 10 injector jet flames.

With x, y being the transverse directions as shown on the left of Fig. 1, we consider two types of combustion chamber acceleration time histories - in both of these cases, only the chamber's position changes, not its orientation. In Case 1, the acceleration is given by

$$\mathbf{a}^C = A_0 \cos(-\omega t) \hat{\mathbf{x}} + A_0 \sin(-\omega t) \hat{\mathbf{y}}, \quad (1)$$

so that the acceleration vector rotates circularly in the chamber transverse direction. As we shall later see, this type of acceleration may produce a spinning wave limit cycle. The parameters which describe a given acceleration time history are its amplitude, A_0 , angular frequency, ω , and length, T , of the acceleration period: for $t > T$, the chamber is not further perturbed.

In Case 2, the acceleration is given by

$$\mathbf{a}^C = A_0 \sin(-\omega t) \hat{\mathbf{y}}, \quad (2)$$

which describes a reciprocating vector in the y -direction which may induce a standing wave limit cycle.

The second rocket engine considered in this work has a rectangular combustion chamber with seven injectors (see Fig.2). The geometry and propellants are the same as described in [9] for the "OOOXOXOO" case: the central port of each injector runs a mixture of 58% H_2O and 42% O_2 as the oxidizer, with the fuel in the central injector being C_2H_6 , the fuel in the outer two injectors on each side is RP1 (here modelled as decane), and the injectors on both sides of the central one having no fuel inflow.

A departure is made from the experimental conditions in that the propellant mass flow rate is reduced by 30%, to 70% of the experimental values. For this mass flow rate, the numerical algorithm described in the following section predicts a conditionally unstable system, whereas for the original experimental

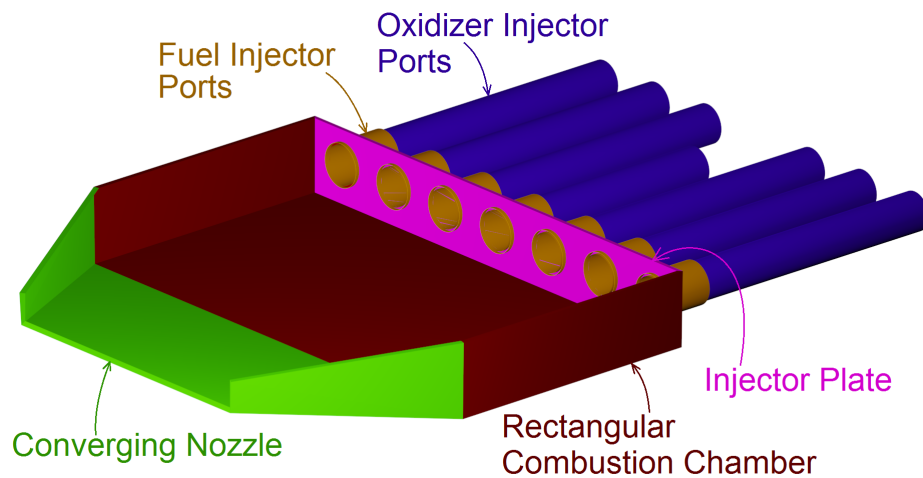


Figure 2: Geometry of the rectangular seven-injector rocket motor and propellant ports.

values, both the experimental data and numerical calculations [5] indicate an unconditionally unstable engine. As the object of this study is to determine which acceleration perturbations may destabilize an otherwise stable engine, the mass flow modification is justified.

The acceleration specification for the rectangular chamber is analogous to Case 2 for the cylindrical chamber. Namely, the acceleration time history follows Eq. 2, where \hat{y} is the transverse direction of the combustion chamber, over which the injectors are spread. With this specification, an acceleration pulse of sufficient magnitude and length, and frequency close to that of a first transverse acoustic mode, may cause the development of an acoustic wave limit cycle.

2 Wave Dynamics Equations

There are several simplifications which can be made for the equations of pressure and velocity. Because the scale of the turbulent motions is much smaller than the acoustic wave scale, we can assume that turbulence and molecular diffusion do not have a considerable influence over the large-scale pressure and velocity wave fields. Therefore, the pressure and velocity wave fields can be solved in inviscid form.

2.1 Wave Equations Without Acceleration

Following [3], the chamber pressure wave equation has the form.

$$\frac{\partial^2 p}{\partial t^2} - a^2 \frac{\partial^2 p}{\partial x_j \partial x_j} = \frac{\partial \rho}{\partial t} \frac{\partial a^2}{\partial t} + (\gamma - 1) \frac{\partial E}{\partial t} + a^2 \frac{\partial^2 (\rho u_j u_i)}{\partial x_i \partial x_j} \quad (3)$$

The left-hand side of the equation represents the wave operator in three dimensions. The second term on the right represents the influence of the combustion energy release on the acoustic instability, and is thus an integral component of the study of rocket engine instability.

The large-scale velocity components evolve by

$$\frac{\partial u_i}{\partial t} + u_j \frac{\partial u_i}{\partial x_j} + \frac{C}{p^{1/\gamma}} \frac{\partial p}{\partial x_i} = 0, \quad (4)$$

where $C = \frac{p_0^{1/\gamma}}{\rho_0}$, and the assumption is made that pressure dominates over the turbulent and molecular viscosity terms.

These equations are applied to both the cylindrical and rectangular combustion chambers by averaging over one of the spatial directions, along which there is little variation of the pressure and velocity fields. For the cylindrical chamber simulations, which focus on transverse instabilities, averaging is performed in

the axial direction [8]; for the rectangular chamber cases, the averaging is done across the short vertical distance in Figure 2 [5].

2.2 Effect of Acceleration on the Combustion Chamber Wave Equations

In this work, we solve for pressure and velocity in a reference frame fixed to the combustion chamber, which undergoes irrotational acceleration $\mathbf{a}_C(t)$. Therefore, in the accelerating frame, the fluid experiences the inertial (volumetric) force

$$F_i = -\rho \mathbf{a}^C(t). \quad (5)$$

This inertial body force acting on the fluid modifies the momentum equation, which becomes

$$\frac{\partial u_i}{\partial t} + u_j \frac{\partial u_i}{\partial x_j} + \frac{C}{p^{1/\gamma}} \frac{\partial p}{\partial x_i} + a_i^C = 0, \quad (6)$$

as well as the pressure wave equation, which, in the non-inertial frame, has the form

$$\frac{\partial^2 p}{\partial t^2} - a^2 \frac{\partial^2 p}{\partial x_j \partial x_j} = \frac{\partial \rho}{\partial t} \frac{\partial a^2}{\partial t} + (\gamma - 1) \frac{\partial E}{\partial t} + a^2 \frac{\partial^2 (\rho u_j u_i)}{\partial x_i \partial x_j} + a^2 \frac{\partial \rho}{\partial x_i} a_i^C. \quad (7)$$

Additionally, the inertial force modifies the pressure boundary condition at the chamber walls, whose form is

$$\frac{\partial p}{\partial n} = \frac{p^{1/\gamma} u_t^2}{CR_c} - \frac{p^{1/\gamma} a_n^C}{C}, \quad (8)$$

where u_t is the velocity component tangential to the boundary, R_c is the wall boundary radius of curvature, and n, a_n^C are respectively the unit outward nor-

1
2
3
4
5
6
7
8 mal vector at the boundary, and the component of the acceleration in that
9 direction.
10

11 In this study, we use the fact that the rectangular combustion chamber is
12 narrow in the height dimension, which implies that the solution fields vary little
13 in that dimension, and can therefore be averaged over it. The chamber height,
14 $L(x, y)$, is constant over the initial section of the combustion chamber and varies
15 linearly with x in the converging nozzle portion of the chamber.
16
17

18 Following Sirignano and Popov [3], two-dimensional averages (here, over the
19 height dimension) of the pressure and velocity fields $\tilde{p} = (1/L(x, y)) \int_0^{L(x,y)} pdz$,
20 $\tilde{\rho} = (1/L(x, y)) \int_0^{L(x,y)} \rho dz$, $\tilde{a} = (1/L(x, y)) \int_0^{L(x,y)} adz$, and $\tilde{\vec{u}} = (1/L(x, y)) \int_0^{L(x,y)} \vec{u} dz$.
21 Integrating Equation (3) over z and neglecting the difference between products
22 of averages and averages of products, we get
23
24

$$\begin{aligned} \frac{\partial^2 \tilde{p}}{\partial t^2} - \tilde{a}^2 \left[\frac{\partial^2 \tilde{p}}{\partial x_j \partial x_j} + \frac{1}{L} \frac{\partial L}{\partial x_1} \frac{\partial \tilde{p}}{\partial x_1} \right] &= \frac{\partial \tilde{\rho}}{\partial t} \frac{\partial \tilde{a}^2}{\partial t} + (\gamma - 1) \frac{\partial \tilde{E}}{\partial t} + \\ &+ \tilde{a}^2 \frac{\partial^2 (\tilde{\rho} \tilde{u}_j \tilde{u}_i)}{\partial x_i \partial x_j} + \tilde{a}^2 \frac{1}{L} \frac{\partial L}{\partial x_1} \frac{\partial (\tilde{\rho} \tilde{u}_1 \tilde{u}_i)}{\partial x_i} \end{aligned} \quad (9)$$

30 where $i = 1, 2; j = 1, 2$. The last terms on both the left- and right-hand sides
31 correspond to the effect which the variable combustion chamber width (in the
32 x_3 -direction) has on the divergence operators in eq.3. The above equation
33 contains derivatives of L only in the x_1 direction because L does not vary in the
34 x_2 direction.
35
36

37 Similarly, the averaged version of equation 4 has the form:
38
39

$$\frac{\partial \tilde{u}_i}{\partial t} + \tilde{u}_j \frac{\partial \tilde{u}_i}{\partial x_j} + \frac{1}{L} \frac{\partial L}{\partial x_1} (\tilde{u}_i \tilde{u}_1) + \frac{C}{\tilde{p}^{1/\gamma}} \frac{\partial \tilde{p}}{\partial x_i} = 0 \quad (10)$$

40 These equations are solved on an orthogonal curvilinear coordinate system,
41 which represents a conformal map of the present hexagonal domain onto a
42
43

square. The curvilinear form of eqs. 9 and 10, with the associated nomenclature, is given in Appendix A.

At the walls of the combustion chamber, the boundary conditions on the pressure and velocity are

$$\tilde{u}_n = 0 \quad ; \quad \frac{\partial \tilde{p}}{\partial n} = \frac{\tilde{p}^{\frac{1}{\gamma}} \tilde{u}_t^2}{CR_c}, \quad (11)$$

with \tilde{u}_n, \tilde{u}_t denoting respectively the components of velocity normal and tangential to the wall boundary, and R_c denoting the wall boundary's radius of curvature. At the downstream end of the convergent nozzle, a Mach number $M = 0.9$ is enforced, and the short nozzle approximation is used to represent the additional convergence to a choked throat, as an approximation to the sonic condition in the experiment.

3 Additional Model Equations

We seek to model the heat release rate of change, $\frac{\partial E}{\partial t}$, which is an integral component to the acoustic instability pressure wave equation, eq.3. Following [3], we shall denote $\alpha = Y_F - \nu Y_O$, where Y_F, Y_O are the fuel and oxidizer mass fractions, and ν is their stoichiometric ratio. Then, α is a conserved scalar, which we will determine in the vicinity of each injector, on an axi-symmetric cylindrical grid with the assumption that the injector flow field is mostly in the direction axial to the injector.

With the variable β being defined by $\beta = (Q/(c_p T_o))Y_F + T/T_o - (p/p_o)^{(\gamma-1)/\gamma}$, the evolution equations for the variables α, β, Y_F have the following form:

$$\frac{\partial \alpha}{\partial t} + u_x \frac{\partial \alpha}{\partial z} + u_\eta \frac{\partial \alpha}{\partial \eta} - D \left[\frac{\partial^2 \alpha}{\partial \eta^2} + \frac{1}{\eta} \frac{\partial \alpha}{\partial \eta} + \frac{\partial^2 \alpha}{\partial z^2} \right] = 0, \quad (12)$$

$$\frac{\partial \beta}{\partial t} + u_z \frac{\partial \beta}{\partial z} + u_\eta \frac{\partial \beta}{\partial \eta} - D \left[\frac{\partial^2 \beta}{\partial \eta^2} + \frac{1}{\eta} \frac{\partial \beta}{\partial \eta} + \frac{\partial^2 \beta}{\partial z^2} \right] = 0 \quad (13)$$

and

$$\frac{\partial Y_F}{\partial t} + u_z \frac{\partial Y_F}{\partial z} + u_\eta \frac{\partial Y_F}{\partial \eta} - D \left[\frac{\partial^2 Y_F}{\partial \eta^2} + \frac{1}{\eta} \frac{\partial Y_F}{\partial \eta} + \frac{\partial^2 Y_F}{\partial z^2} \right] = \omega_F, \quad (14)$$

where z, η are respectively the axial and radial coordinates of the cylindrical injector grids, and the source term on the right-hand side of Eq. (14) is obtained from a Westbrook-Dryer two-step oxidation mechanism [10], from the fuel (C_2H_6 for the central injector element, $C_{10}H_{22}$ for the driving injector elements) to CO , and then from CO to CO_2 . In order to obtain the concentrations of both the injector fuel and CO from the fuel mass fraction, it is assumed that oxidation of CO occurs only after the partial oxidation of the fuel to CO has reached its completion.

Building on [3], the source term in Eq. 14 is obtained via an assumed-PDF model for α and β , so that the means of α and β evolve by Eqs. 12,13 and their subgrid distributions are assumed to be beta functions, which are standard PDFs for modeling mixing of two or more streams. The term ω_F in Eq. 14 is then obtained via integration over the sample space of α and β . The assumed PDF model has been used with great success for the simulation of turbulent non-premixed flames which are not near extinction [11]. For more details, the reader is referred to [11].

The axial and radial velocities in Eqs. (12-14) are obtained from a solution of the variable density Reynolds-Averaged Navier-Stokes axi-symmetric equations:

$$\begin{aligned} \rho \left(\frac{\partial u_z}{\partial t} + u_z \frac{\partial u_z}{\partial z} + u_\eta \frac{\partial u_z}{\partial \eta} \right) &= - \frac{\partial p_l}{\partial z} \\ &+ \rho \nu_T \left[\frac{\partial^2 u_z}{\partial z^2} + \frac{1}{\eta} \frac{\partial}{\partial \eta} \left(\eta \frac{\partial u_z}{\partial \eta} \right) \right] \end{aligned} \quad (15)$$

$$\begin{aligned} \rho \left(\frac{\partial u_\eta}{\partial t} + u_z \frac{\partial u_\eta}{\partial z} + u_\eta \frac{\partial u_\eta}{\partial \eta} \right) &= -\frac{\partial p_l}{\partial \eta} \\ &+ \rho \nu_T \left[\frac{\partial^2 u_\eta}{\partial z^2} + \frac{1}{\eta} \frac{\partial}{\partial \eta} \left(\eta \frac{\partial u_\eta}{\partial \eta} \right) - \frac{u_\eta}{\eta^2} \right] \end{aligned} \quad (16)$$

which are solved on each jet flame grid, where $p_l(z, \eta, t)$ is a local hydrodynamic pressure whose mean is by definition 0 and which has considerably lower magnitude than the injector pressure $p(t)$ obtained from Eq. (3). The density in Eqs. (16,17) is obtained from the species scalars and the long-wavelength pressure, $p(t)$, at the injector's location, so that the overall procedure for solving Eqs. (16,17) is elliptic.

Finally, following Popov, Sideris and Sirignano [8], the pressure and velocity in the injector posts are solved via the set of one-dimensional wave equations:

$$\frac{\partial^2 p}{\partial t^2} - a^2 \frac{\partial^2 p}{\partial l^2} = a^2 \frac{\partial^2 (\rho u^2)}{\partial l^2} - \frac{\partial a^2}{\partial t} \frac{\partial (\rho u)}{\partial l} \quad (17)$$

$$\frac{\partial u}{\partial t} + u \frac{\partial u}{\partial l} = -\frac{1}{\rho} \frac{\partial p}{\partial l}. \quad (18)$$

They are solved on a 1D grid upstream of each cylindrical injector grid. In this model, velocity fluctuations affect the energy release rate through the modification of the eddy diffusivity, mixing rate and the rate of propellant inflow into the combustion chamber. Pressure fluctuations, on the other hand, affect the chemical rate and drive the injector port velocity fluctuations.

4 Deterministic and Stochastic Acceleration of a Cylindrical Rocket Motor

For both cases, rotating and reciprocating acceleration, we set the angular frequency, ω , to $2\pi/\tau_F$, where $\tau_F = 0.478ms$ is the period of the first tangential

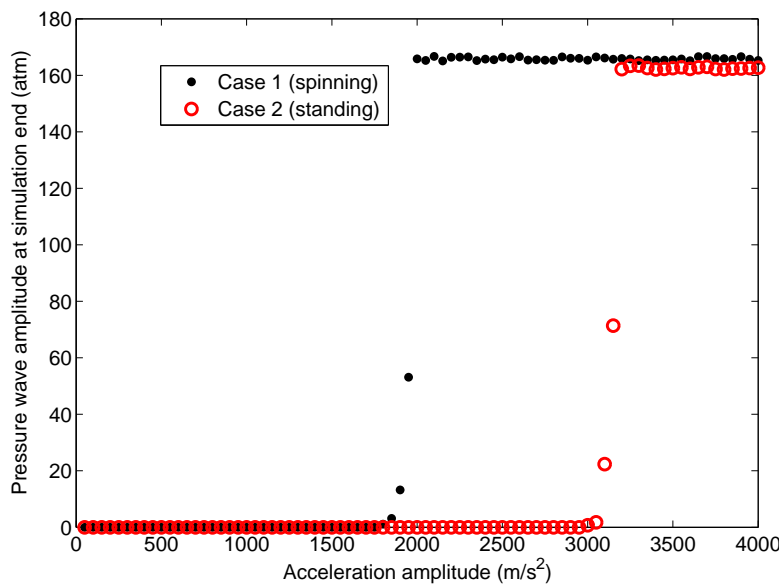


Figure 3: Final pressure wave amplitude as a function of acceleration amplitude.

acoustic mode of the combustion chamber. Setting the period to $T = 2\tau_F$ and varying the amplitude A_0 , we run several calculations for both cases 1 and 2. The resulting pressure wave amplitudes at the end of the simulation are plotted as functions of A_0 on Figure 3.

As can be seen in that figure, an amplitude above $A_0 = 1900 \text{ m/s}^2$ causes an acoustic instability for case 1, and an amplitude above $A_0 = 3100 \text{ m/s}^2$ causes the growth of an acoustic instability in case 2. Both types of instabilities have the shape of a first tangential acoustic mode, with the difference that in case 1 the wave is spinning, whereas in case 2 it is standing. It is important to note that the spinning acceleration pulse of case 1 can cause an instability at a lower amplitude, due to the larger L^2 norm of $\mathbf{a}^C(t)$ for a set A_0 in case 1.

Figure 4 shows the development of a spinning acoustic wave in case 1. It

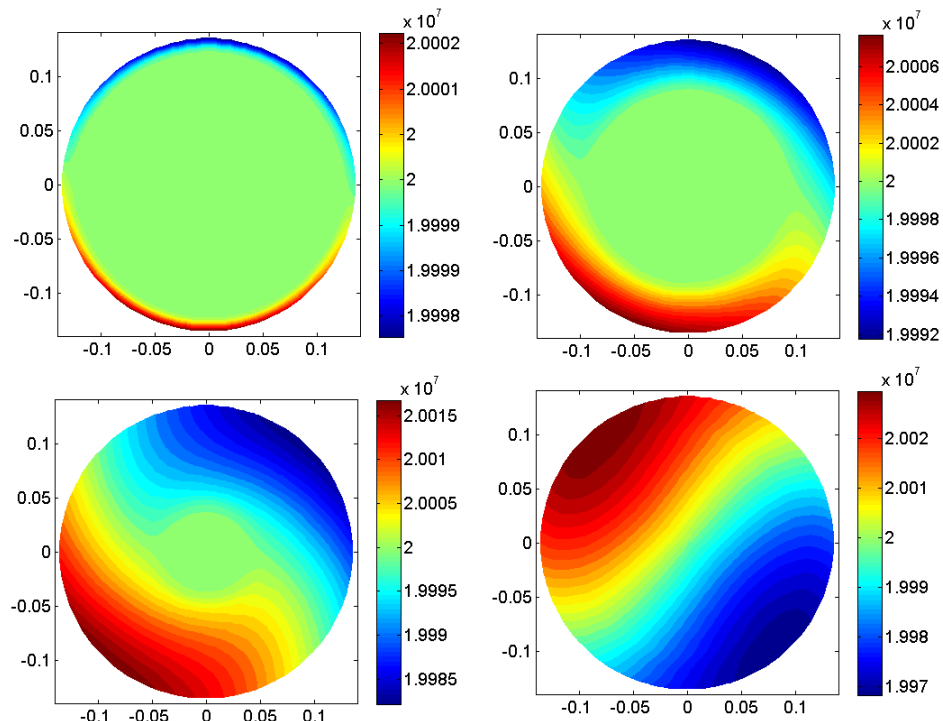


Figure 4: Initial stages of development of a spinning acoustic wave (spin direction is clockwise).

is interesting to note that at the early stages of the limit cycle's development, the pressure perturbations are localized near the chamber walls. This is due to the fact that, with the present model, the density throughout the combustion chamber is initially uniform, so that the density gradient term, $a^2 \frac{\partial \rho}{\partial x_i} a_i^C$, in Eq. 7 is equal to zero. Rather, the initial disturbance in the pressure field comes about due to the inertial force term in the boundary condition, Eq. 8, so that the pressure disturbance spreads inwards from the walls.

An acceleration pulse has the capability to not only cause the development of a limit cycle, but to also suppress it. Specifically, for all the cases from

Fig. 3, adding an additional pulse of duration $T = 2\tau_F$ and frequency $\omega = 2\pi/\tau_F$, but of amplitude $-A_0$ succeeded in arresting the growth of the acoustic instability. This finding is consistent with earlier results [4, 5] where other pulsing mechanisms could provide stabilization. In the next section, we also consider cases when the "anti-pulse" occurs after some delay.

In addition to the deterministic simulations described above, we also perform a Polynomial Chaos Expansion (PCE) [4] solution for the cylindrical rocket motor. The stochastic parameters in this case are the pulse's acceleration amplitude, $A_0 \in [500m/s^2, 4500m/s^2]$, duration, $T \in [0, 1.6 \times 10^{-3}s]$, and frequency, $f \in [1400Hz, 2800Hz]$. The values of A_0, T and f are uniformly distributed in these intervals, and independent of each other.

In order to determine the effect of each of those variables on the overall stability of the rocket motor, we calculate the marginal probability, for each of the three sample space variables, of growth of the initial disturbance to an instability.

Figure 5 shows a plot of the marginal probability as a function of A_0 of growth to an instability. As can be expected, the probability of growth increases monotonically with acceleration amplitude, with larger increments around $A_0 = 2500m/s^2$.

The probability of growth as a function of the pulse duration is shown on Fig. 6. On that figure it can be observed that the probability of growth rises monotonically with increasing duration. We note, however, that the increase of the probability is more gradual than on Fig. 5.

This can be attributed to the dissipation of acoustic waves which have not risen above the threshold for triggering: increasing the duration of an acceleration pulse increases the amount of dissipation which the resultant acoustic wave has experienced by the end of the pulse, whereas increasing the pulse's

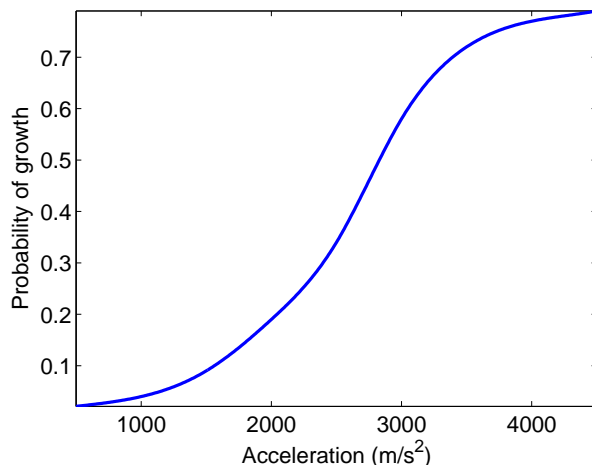


Figure 5: Marginal probability of growth to an instability as a function of the acceleration pulse's amplitude, in [m/s^2].

amplitude does not.

Finally, the probability of growth to an instability is plotted as a function of the acceleration pulse's frequency, $f [Hz]$. We see that the probability is greatest near the first tangential acoustic mode's frequency of $2090 Hz$, with frequencies above $2090 Hz$ exhibiting a larger probability of growth than those below $2090 Hz$.

Based on these results, we observe that the cylindrical rocket motor is more unstable to disturbances of larger amplitude and duration, with greater sensitivity to the former. Pulses whose frequency is near that of the first tangential acoustic mode are most likely to trigger an instability, with some preference for pulses of frequencies higher than the first tangential than those lower than it.

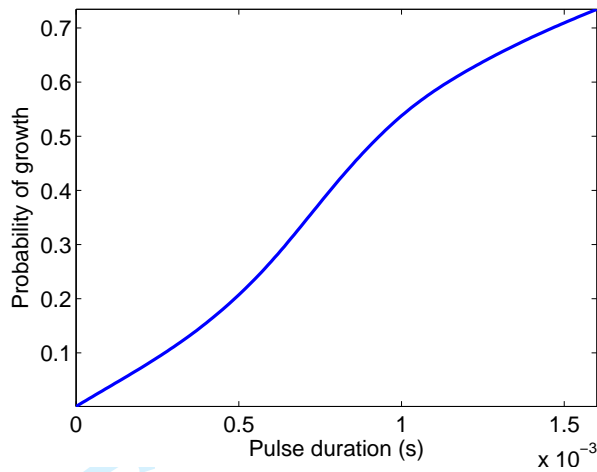


Figure 6: Marginal probability of growth to an instability as a function of the acceleration pulse's duration, in s .

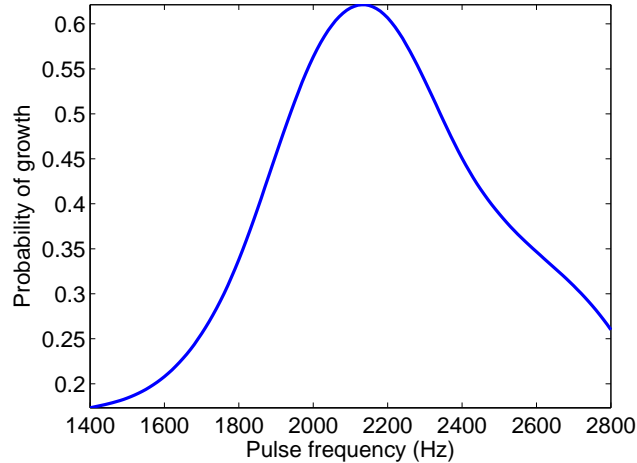


Figure 7: Marginal probability of growth to an instability as a function of the acceleration pulse's frequency, in Hz .

5 Stochastic Acceleration of a Rectangular Rocket Motor

For the rectangular rocket motor, we use the PCE scheme to test acceleration pulses of varying amplitude, frequency and for different injector total mass flow rates. Specifically, we perform a stochastic simulation over a three-dimensional sample space in which the injector mass flow rate, \dot{m} is distributed uniformly between the experimental value of $\dot{m} = 2.089\text{kg/s}$ and $\dot{m} = 1.08\text{kg/s}$, the frequency $f = \omega/2\pi$ is distributed uniformly between $f = 1400\text{Hz}$ and $f = 2600\text{Hz}$, and the acceleration pulse amplitude A_0 is distributed uniformly between $A_0 = 0$ and $A_0 = 220\text{g}$, with \dot{m} , f and A_0 being independent.

Figure 8 shows the marginal probability of growth to an acoustic instability as a function of the injector mass flow rate. As can be seen, for the experimental value of $\dot{m} = 2.089\text{kg/s}$ the motor is unconditionally unstable: the probability of growth is 1. On the other hand, for lower values, near $\dot{m} = 1.08\text{kg/s}$, the probability of growth is 0 and the rocket motor is unconditionally stable. For intermediate values of the mass flow rate we observe triggered instability, with a growth probability between 0 and 1. In all cases, the triggered instability has the shape of a first transverse acoustic wave for the rectangular pressure chamber (see Fig. 11).

The dependence of stability on the frequency of the acceleration pulse is shown in Fig. 9. As can be seen in that figure, the most destabilizing acceleration pulses are those which have a frequency around 1900Hz , close to the frequency of the first transverse mode. Note that even for frequencies much lower and higher than that, there is still some probability of growth, due to the presence of the unconditionally unstable cases, which will get destabilized by any perturbation.

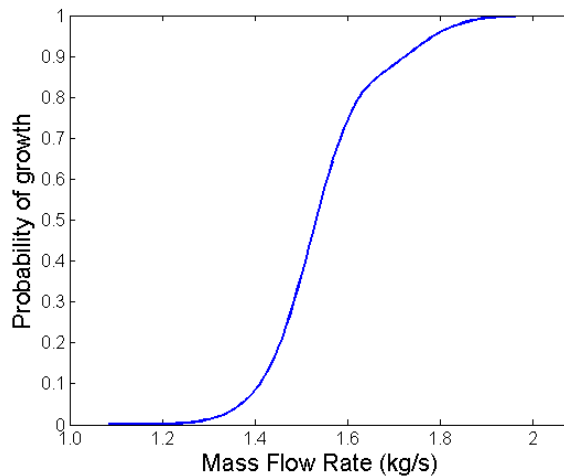


Figure 8: Marginal probability of growth to an instability as a function of the injector mass flow rate.

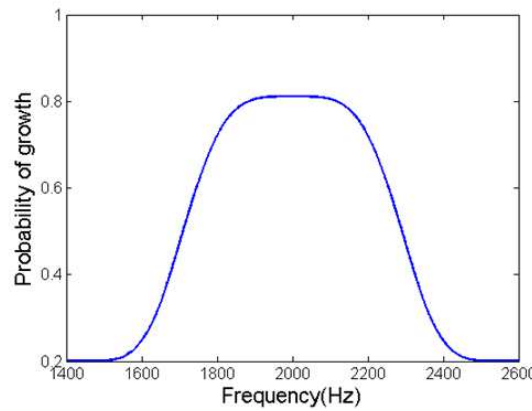


Figure 9: Marginal probability of growth to an instability as a function of the acceleration pulse frequency, $f = \omega/2\pi$.

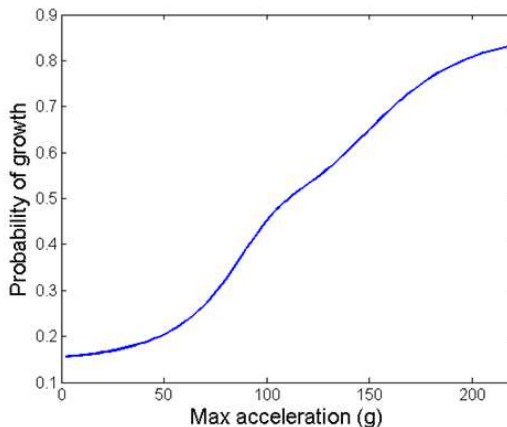


Figure 10: Marginal probability of growth to an instability as a function of the acceleration pulse magnitude

Finally, we note in Fig. 10 that, as can be intuitively expected, the probability of growth to instability increases with increasing amplitude of the acceleration pulse. Once again, we note that the probability never reaches 0, due to the unconditionally unstable cases for the mass flow rate, and neither does it rise up all the way to 1, due to the unconditionally stable cases.

In a second PCE simulation, we explore the potential for a second acceleration pulse to stabilize the rocket motor from a triggered state. Specifically, we set the frequency to $f = 1900\text{Hz}$ and the mass flow rate to $\dot{m} = 1.7\text{kg/s}$ (which is a conditionally unstable case), and we follow up the initial acceleration pulse of magnitude $A_{0,1}$ by a subsequent pulse of magnitude $-A_{0,2}$ which is initiated at a time τ after the initial pulse. The stochastic variables $A_{0,1}$, $-A_{0,2}$ and τ are independent, with $A_{0,1}$, $A_{0,2}$ being uniformly distributed between 0 and 220g , and τ uniformly distributed between $5\tau_f$ and $7.8\tau_f$, where τ_f is the period of the first transverse mode.

Figure 11 shows the initial growth of the transverse instability, and its sup-

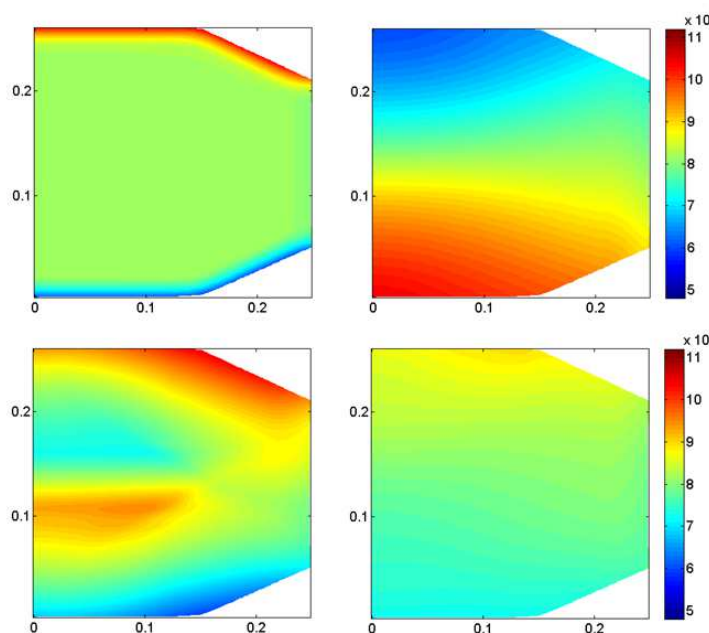


Figure 11: Development and suppression of a transverse instability in the rectangular rocket engine. Top left: initial stages of instability development, top right: grown transverse instability, bottom left: second acceleration pulse disrupting the acoustic instability, bottom right: decay to standard operating conditions.

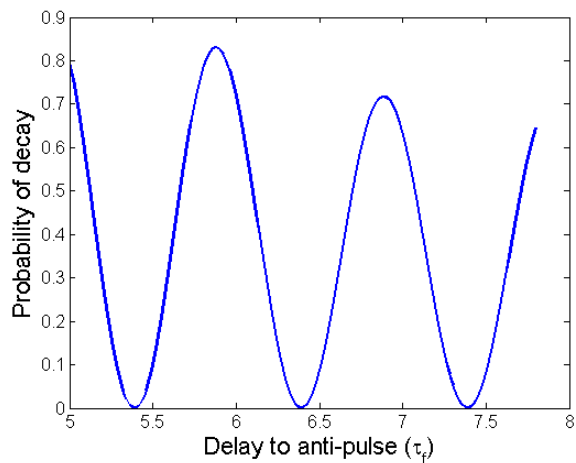


Figure 12: Probability of instability suppression as a function of the delay between the pulse and anti-pulse.

pression by the anti-pulse, for a case in which the anti-pulse is successful in arresting instability growth. As can be seen in Fig. 12, whether or not this is the case is highly dependent on the delay between the anti-pulse and the pulse - for a delay which is close to an integer number of first transverse periods, the anti-pulse has a high probability of restoring stability.

6 Conclusions

In this work, we have demonstrated the potential for whole-body acceleration pulses of a rocket engine combustion chamber to lead to the development of an acoustic instability. For both a cylindrical and a rectangular rocket engine motor, it is found that a short acceleration pulse of large amplitude, on the order of $100g$ is capable of producing an acoustic instability, if its frequency is close to the chamber's acoustic frequency. For a cylindrical rocket engine, the acoustic

1
2
3
4
5
6
7
8 limit cycle may be either a standing or a spinning wave, depending on the shape
9 of the acceleration pulse. Additionally, it is seen that a subsequent pulse can
10 also cause the decay of a growing instability, if its timing is appropriately chosen.
11
12
13
14

15 Acknowledgements 16 17

18 This research was supported by the Air Force Office of Scientific Research under
19 Grant FA9550-12-1-0156 with Dr. Mitat Birkan as the Program Manager.
20
21
22

23 References 24 25

26 [1] Harrje, D. and Reardon, F., "Liquid Propellant Rocket Combustion Insta-
27 bility," *NASA SP194*, U.S. Government Printing Office, 1972.
28
29 [2] Oefelein, J. C. and Yang, V., "Comprehensive Review of Liquid-Propellant
30 Combustion Instabilities in F-1 Engines," *Journal of Propulsion and*
31 *Power*, Vol. 9, 1993, pp. 657–677.
32
33 [3] Sirignano, W. A. and Popov, P. P., "Two-Dimensional Model for Liquid-
34 Rocket Transverse Combustion Instability," *AIAA J.*, Vol. 51, No. 2919-34,
35 2013.
36
37 [4] Popov, P. P., Sideris, A., and Sirignano, W. A., "Stochastic Modelling of
38 Transverse Wave Instability in a Liquid Propellant Rocket Engine," *Journal*
39 *of Fluid Mechanics*, Vol. 745, 2014, pp. 62–91.
40
41 [5] Popov, P. P. and Sirignano, W. A., "Transverse Combustion Instabilities
42 in a Rectangular Rocket Motor," *Journal of Propulsion and Power (in*
43 *review)*.
44
45 [6] Talley, D., *Personal Communication*, 2014.
46
47
48
49
50
51
52
53
54
55
56
57
58
59
60

1
2
3
4
5
6
7
8 [7] Shipley, K., Morgan, C., Anderson, W., Harvazinski, M., and Sankaran, V.,
9 “Computational and experimental investigation of transverse combustion
10 instabilities,” *Joint Propulsion Conference*, 2014, pp. 1083–1099.
11
12
13 [8] Popov, P. P., Sideris, A., and Sirignano, W. A., “Propellant Injector Influ-
14 ence on Liquid Propellant Rocket Engine Instability,” *Journal of Propulsion*
15 and Power, Vol. 31, No. 1, 2015, pp. 320–331.
16
17
18 [9] Pomeroy, B., “Measurement and analysis of combustor response to trans-
19 verse combustion instability,” *Ph.D. Thesis, Purdue University*, 2012.
20
21
22 [10] Westbrook, C. K. and Dryer, F. L., “Chemical Kinetic Modeling of Hydro-
23 carbon Combustion,” *Prog. Energy Combust. Sci.*, , No. 10, 1984, pp. 1–57.
24
25
26
27 [11] Pierce, C. and Moin, P., “Progress-Variable Approach for Large-Eddy Sim-
28 ulation of Non-Premixed Turbulent Combustion,” *J. Fluid Mech.*, Vol. 504,
29 2004, pp. 73–97.
30
31
32
33
34
35
36
37
38
39
40
41
42
43
44
45
46
47
48
49
50
51
52
53
54
55
56
57
58
59
60

Addendum 4

Two-time-scale Perturbation Theory for Liquid-Rocket Combustion Instability WORKING PAPER

William A. Sirignano ^{*}

Department of Mechanical and Aerospace Engineering

University of California, Irvine, CA 92697

Nonlinear, transverse-mode, liquid-propellant-rocket-motor combustion instability is examined via a two-time-variable perturbation expansion in an amplitude parameter. Both triggered and spontaneous instability domains are studied. Following an established process, a two-dimensional, unsteady chamber-wave-dynamics model is used where the three-dimensional equations are integrated over the axial direction. Nonlinear, first-tangential-mode wave oscillations in the circular combustion chamber are considered with the primary flow in the axial direction. The analysis is first generalized to match a variety of relevant injection and combustion mechanisms. Then, a specific example with co-axial injectors is used to demonstrate the matching process between wave dynamics and the injection / combustion mechanisms. Turbulent mixing of gaseous propellants with co-axial injection and a multi-orifice, short thrust nozzle are considered. The combustion has a characteristic time for mixing, producing a time lag in the energy release rate relative to pressure. The coupled combustion process and wave dynamics are calculated for a multi-injector chamber. In particular, the linear first-tangential mode is examined. Two coupled first-order ordinary differential equations are developed and solved to predict amplitude and phase angle variations in the slow time for the major component of the waveform in an eigenfunction series expansion. Limit cycles and transient behaviors are resolved. Nonlinear triggering can occur in certain operational domains; above a critical initial amplitude, the amplitude grows; otherwise, it decays with time.

Nomenclature

a	Speed of sound, m/s
-----	---------------------

^{*}Professor

A	Pressure oscillation amplitude
A_e	Cross-sectional area of nozzle entrance, m ²
A_t	Cross-sectional area of nozzle throat, m ²
c_p	Specific heat at constant pressure, J/ ^o K kg
c_v	Specific heat at constant volume, J/ ^o K kg
D	Mass diffusivity, m ² /s
E	Energy release rate per unit volume, J/m ³ s
f	Frequency, s ⁻¹
G	Green's function
h	Specific enthalpy, joules/kg
J_n	Bessel function of first kind and n^{th} order
L	Chamber length, m
L_f	Flame length, m
\dot{m}	Mass flow rate, kg/s
M	Mach number
\dot{M}	Steady-state injector mass flow rate
r	Radial position, m
$r_{1/2}$	Half-width of co-axial jet, m
R	Chamber radius, m
\mathbf{R}	Mixture specific gas constant, J/kg ^o K
\mathbf{R}_u	Universal gas constant, J/kg-mole ^o K
R_i	Innner radius of co-axial jet, m
R_o	Outer radius of co-axial jret,m
p	Pressure, newton m ⁻²
s_{nh}	h^{th} root for zero slope of Bessel function of first kind and order n
t	Time, s
T	Temperature, K
\vec{u}	Vector velocity, m/s
u_j	Cartesian velocity component, m/s
u_r	Radial velocity component, m/s
u_θ	Tangential velocity component, m/s
U	Co-axial jet velocity, m/s
Y_i	Mass fraction of species i
Y_n	Bessel function of second kind and n^{th} order
x_j	Cartesian coordinate, m

z Non-dimensional fast time

Greek symbols

α, β	Schvab-Zel'dovich variables
ε	Non-dimensional amplitude perturbation parameter
γ	Ratio of specific heats
κ	Variable defined after Equation (75)
ν	Kinematic viscosity, m^2/s
ν_T	Turbulent kinematic viscosity, m^2/s
ω	Angular frequency
ρ	Density, kgm m^{-3}
τ	Slow non-dimensional time
τ_M	Characteristic mixing time, s
θ	Azimuthal position

Subscripts

F	Fuel
i	Inflow condition
j	index for Cartesian coordinates
O	Oxidizer
ss	Steady state

I. Introduction

Liquid-propellant rocket engine (LPRE) combustion instability has been a long-standing natural phenomenon, which causes problems and creates the need for control. In LPRE, the combustion process produces a very high energy release rate per unit volume which, in many circumstances, has characteristic times that result in reinforcement of the acoustical oscillations and produces very high amplitudes. These oscillations can cause undesirable oscillations in thrust, vibrations that result in problems for people or equipment on the spacecraft, and increased heat transfer in already critical regions, e.g., the nozzle throat. Transverse spinning waves can have substantially larger amplitudes than longitudinal waves because no shock waves form and thereby dissipation is reduced. The combustion concentrates near the injector end resulting in very high heat transfer rates to the injector. The increased heat transfer at the injector and/ or nozzle throat often leads to destruction of those wall materials and disaster for the flight mission.

Theoretical, computational, and experimental research has been underway at varying levels of intensity for more than a half century. Most of the physics of the oscillations were identified in the 1950s and 1960s but the knowledge of the details of coupling with the combustion processes has trailed. An excellent compilation of major research during that early period is provided by Harrje and Reardon.¹ Also, an interesting discussion of the famous F-1 Rocket Motor instability problems is given by Oefelein and Yang.² Two types of instability occur: linear or spontaneous instability and nonlinear or triggered instability. The describing terms pertain to initiation only; all instabilities of concern have nonlinear behavior once established. Linear instabilities grow in amplitude from the normal noise associated with the high-mass flow, multi-injector rocket chamber environment; theoretically, they grow from infinitesimal disturbances. Nonlinear instabilities require a disturbance of sufficient magnitude to overcome a required threshold. Without such a disturbance, linear stability is exhibited. A disruption in propellant mass flow or a very large fluctuation caused by transient operation can provide the necessary trigger. In experiments, the use of small explosives has triggered instabilities.

A theoretical prediction of triggering was first given by Sirignano³ for the longitudinal mode followed by Zinn⁴ for the transverse mode. The approach predicts either a stable or unstable limit cycle for each point in the n, τ plane near the linear stability limit line. These early pioneering efforts on nonlinear triggering did not predict the expected higher-amplitude stable limit cycle in the n, τ domains where an unstable limit cycle and nonlinear triggering were predicted. Presumably, if the analyses were extended sufficiently beyond third-order terms in the amplitude parameter, the stable limit cycle would be determined.

The goal is to develop a model equation or small system of equations that describe the essential features of transverse nonlinear oscillations in cylindrical combustion chambers for liquid-propellant rocket engines. The combustion chamber with its many propellant injectors and associated propellant streams will be viewed as a complex system where these injectors and streams are networked but yet have some degree of local autonomy.

There is special interest in studying the nonlinear triggering phenomenon, using a first-principles description of the combustion process. It is important to keep in the model the terms which add energy or damp oscillations or produce major change to the wave shape. The injected propellants will be considered as preheated and gaseous; two-phase flows can be considered in the future. While the aim is to establish a foundation for future stochastic analysis of the LPRE combustion instability phenomenon as the behavior of a complex system, the analysis here will be deterministic and the physical phenomena are deterministic.

II. Basic Equations for Wave Dynamics

The equations for the chamber wave dynamics will be simplified by assuming inviscid, non-heat-conducting, non-mass-diffusing flow. Turbulent fluctuations will be considered small compared to acoustic amplitudes;

also, the turbulent length scales will be shorter than the acoustic wavelengths which also allows their neglect. The turbulence is generated largely by the jets of propellants entering the combustion chamber and the length scales are determined by transverse jet dimensions and spacing between adjacent jets. Acoustic wavelengths are determined by the much larger chamber dimensions. Other variations with length scales substantially shorter than the acoustic wavelength can be neglected. The propellants will be considered to be gaseous when injected into the combustion chamber. Mixing and chemical reaction will be modelled. Since the combustion chamber operates at supercritical pressure, a single-phase fluid will be considered. For the transverse mode, variations of amplitudes in the transverse direction will be much greater than variations in the axial direction of the cylindrical configuration. This will facilitate the reduction of the problem from a three-dimensional unsteady problem to a two-dimensional, unsteady formulation.

A. General Formulation of Theory

We will use a wave dynamics model previously discussed in the literature.^{5,6,7,8} Gravity and viscosity are neglected and E is the time rate of energy per unit volume which is converted from a chemical form to a thermal form. A perfect gas and constant specific heats are assumed. Of course, at the very high pressures, there should be corrections to the gas law and, at the high temperatures, the specific heats will be variable. The approximation is expected to preserve the quality of the wave dynamics and the combustion dynamics and not hide any primary physics. \mathbf{R} is the specific gas constant for the mixture of gases in the chamber; Y_n is the mass fraction for the n^{th} species in the fluid mixture; T is gas temperature; a is speed of sound; c_p is specific heat at constant pressure; c_v is specific heat at constant volume; and $\gamma = c_p/c_v$.

The above-described analysis yields

$$\frac{\partial^2 p}{\partial t^2} - a^2 \frac{\partial^2 p}{\partial x_j \partial x_j} = \frac{\partial \rho}{\partial t} \frac{\partial a^2}{\partial t} + (\gamma - 1) \frac{\partial E}{\partial t} + a^2 \frac{\partial^2 (\rho u_j u_i)}{\partial x_i \partial x_j} \quad (1)$$

The left-hand side of the equation represents the wave operator in three dimensions. A mild nonlinearity appears through the coefficient a^2 . The first and third terms on the right-hand side are strongly nonlinear terms that are conservative but will affect the wave shape. The second term on the right represents the influence of the energy conversion and can be a strong driver of the nonlinear oscillation.

B. Reduction to a Two-dimensional Wave Equation

Now, a two-dimensional model is developed by integrating Equation (1) over the primary flow direction, x_3 . Focus is made on the transverse mode instability; so, the major oscillations will be in the x_1 and x_2 directions. A cylindrical combustion chamber is considered with the injector at $x_3 = 0$ and the nozzle entrance at $x_3 = L$. Variations of the pressure, velocity, and other variables in the x_3 direction will be smaller than variations in other directions.

The mass flux per unit area flowing from the injectors will be considered to be a function of local pressure at the exit of the injector which is the injector face. So, $\rho u_3|_0 = g(p, x_1, x_2)$ where the function $g(p, x_1, x_2)$ can be determined by analysis of the flow in the orifice and upstream in the propellant feed system. For portions of the injector face where no orifice hole exists, $g = 0$.

A special nozzle configuration, which is achievable experimentally, is assumed: a multi-orifice flow exit with each orifice in a perforated plate in the exit plane being a small choked nozzle with a length much shorter than the oscillation wavelength and a residence time much shorter than the oscillation period. Then, the flow through the nozzle is quasi-steady. This nozzle boundary condition for nonlinear transverse waves was developed by Crocco and Sirignano.^{9, 10} Consider the entrance Mach number of the nozzle to be sufficiently low so that entrance stagnation values and static values can be assumed to be identical. Also, the boundary condition is abbreviated, neglecting higher order effects of the transverse velocity.

The pressure variation in the x_3 direction may be assumed to be minor for many transverse oscillations. The major variation of pressure will be in the transverse direction, as indicated by experimental findings¹ and theory.^{11, 4} For a pure transverse wave behavior, there is no acoustical oscillation in the x_3 direction; so, only advection can be expected to produce variations in that flow direction. These variations tend to be slow exponential variations according to the theory.

The nozzle boundary condition provides a first-time-derivative term which is a damping function for the oscillation. Some of the energy in the oscillation will be lost by nozzle outflow. The term with the time derivative of the energy source E can be described as the forcing function for the oscillation. A combustion model will be developed to relate that quantity E back to pressure, temperature, and velocity. The other two nonlinear terms on the right-hand side of the equation are not dissipative or forcing functions but they can have strong influence on the stability, amplitude, and wave shape for the oscillation.

Assume that the averaged pressure, temperature, density, and sound speed will be related by polytropic relations. Isentropic relations will be used to describe the thermodynamic relations during the oscillation. For transverse oscillations in a cylindrical chamber, shock waves do not form. Also, the acoustic wavelengths are sufficiently long that viscous and diffusive effects are small, except for a combustion zone near an injector. These isentropic relations can be used to eliminate density, sound speed, and temperature from Equation (1). The neglect of entropy variations in the determination of the pressure and velocity fields is not a very strong assumption.

It is useful to cast the two-dimensional construction of the wave dynamics equation in cylindrical polar coordinates because of the combustion chamber shape. r and θ will represent radial distance from the

chamber centerline and azimuthal position, respectively. The velocity components are u_r and u_θ .

$$\begin{aligned} & \frac{\partial^2 p}{\partial t^2} + B_2 p^{\frac{\gamma-1}{2\gamma}} \frac{\partial p}{\partial t} - B_1 p^{\frac{\gamma-1}{\gamma}} \left[\frac{\partial^2 p}{\partial r^2} + \frac{1}{r} \frac{\partial p}{\partial r} + \frac{1}{r^2} \frac{\partial^2 p}{\partial \theta^2} \right] \\ = & \frac{(\gamma-1)}{\gamma} \frac{1}{p} \left(\frac{\partial p}{\partial t} \right)^2 + (\gamma-1) \frac{\partial E}{\partial t} + \gamma p^{\frac{\gamma-1}{\gamma}} \left[\frac{\partial^2 (p^{\frac{1}{\gamma}} u_r^2)}{\partial r^2} + \frac{2}{r} \frac{\partial (p^{\frac{1}{\gamma}} u_r^2)}{\partial r} \right. \\ & \left. + \frac{2}{r} \frac{\partial^2 (p^{\frac{1}{\gamma}} u_r u_\theta)}{\partial r \partial \theta} + \frac{2}{r^2} \frac{\partial (p^{\frac{1}{\gamma}} u_r u_\theta)}{\partial \theta} + \frac{1}{r^2} \frac{\partial^2 (p^{\frac{1}{\gamma}} u_\theta^2)}{\partial \theta^2} - \frac{1}{r} \frac{\partial (p^{\frac{1}{\gamma}} u_\theta^2)}{\partial r} \right] \end{aligned} \quad (2)$$

where it is defined that

$$B_1 \equiv \frac{a_{ss}^2}{p_{ss}^{\frac{\gamma-1}{2\gamma}}} ; \quad B_2 \equiv \frac{a_{ss} K}{L p_{ss}^{\frac{\gamma-1}{2\gamma}}} ; \quad K \equiv \frac{A_t}{A_e} \left(\frac{\gamma+1}{2} \right)^{\frac{\gamma-3}{2(\gamma-1)}} \quad (3)$$

Note that a one-dimensional isentropic flow analysis yields for nozzle throat-to-entrance area ratio, after neglect of terms of $O(M^2)$,

$$\frac{A_t}{A_e} \approx M \left(\frac{\gamma+1}{2} \right)^{\frac{\gamma+1}{2(\gamma-1)}} \quad (4)$$

where M is the combustion chamber mean-flow Mach number with $0 < M \ll 1$. Thus, we approximate

$$K \approx M \left(\frac{\gamma+1}{2} \right) ; \quad B_2 \approx M \frac{\gamma+1}{2} \frac{a_{ss}}{L p_{ss}^{\frac{\gamma-1}{2\gamma}}} \quad (5)$$

The quantity B_2 is small and positive.

One may now cast the momentum equations in cylindrical coordinates to obtain

$$\frac{\partial u_r}{\partial t} + u_r \frac{\partial u_r}{\partial r} + u_\theta \frac{1}{r} \frac{\partial u_r}{\partial \theta} - \frac{u_\theta^2}{r} + \frac{C}{p^{\frac{1}{\gamma}}} \frac{\partial p}{\partial r} = 0 \quad (6)$$

and

$$\frac{\partial u_\theta}{\partial t} + u_r \frac{\partial u_\theta}{\partial r} + u_\theta \frac{1}{r} \frac{\partial u_\theta}{\partial \theta} + \frac{u_r u_\theta}{r} + \frac{C}{r p^{\frac{1}{\gamma}}} \frac{\partial p}{\partial \theta} = 0 \quad (7)$$

where $C \equiv p_{ss}^{1/\gamma} / \rho_{ss}$.

Consider a solid circular wall at radius $r = R$; that is, no acoustic lining is present. The normal velocity at the wall will be zero; so, the following boundary conditions apply to the system of Equations (2, 6, 7):

$$u_r(t, R, \theta) = 0 ; \quad \frac{\partial p}{\partial r}(t, R, \theta) = \frac{p^{\frac{1}{\gamma}} u_\theta^2}{CR} \quad (8)$$

The wave dynamics will be studied in Section III by imposing a postulated relation between the heat release rate E and the pressure p . However, focus will occur in Section IV on a model of co-axial injection, turbulent mixing, and chemical reaction. This model will be more realistic and will introduce physics with characteristic times that need not be short compared to the period of acoustic oscillation. Therefore, time delays will be introduced.

III. Multi-timescale Perturbation Method

Equation (2) will be simplified by neglecting injector coupling and keeping inflow mass flux constant under chamber oscillation, i.e. $f = 0$. Subscript "ss" will imply steady-state values, e.g., p_{ss} , a_{ss} and E_{ss} . These values will be used to normalize the dependent variables, creating non-dimensional forms: pressure will be normalized by the steady-state pressure p_{ss} and velocity components by the steady-state speed of sound a_{ss} , both having uniform values over the domain for the wave dynamics equation. Radial position will be normalized by the chamber radius R and time is normalized by R/a_{ss} . From this point forward, the variables t, r, p, u_r , and u_θ should be interpreted as normalized, non-dimensional quantities. Note that $a_{ss}^2 = \gamma p_{ss}/\rho_{ss}$ and the mean-flow Mach number $M = u_{ss}/a_{ss}$.

Two time scales will be introduced,¹² a fast time scale $z = \omega t$ on which the oscillations occur and a slow time scale $\tau = \sigma t$ on which amplitudes and phase slowly change. ω is the angular frequency of the oscillation and σ is a small positive quantity that goes to zero as the oscillation amplitude goes to zero. A dependent variables becomes a function of both variables: e.g., $p(z, \tau, r, \theta)$. Then, $\partial p/\partial t = \omega \partial p/\partial z + \sigma \partial p/\partial \tau$.

Equations (2,6, 7) take new forms. The non-dimensional wave dynamics equation is now

$$\begin{aligned} \omega^2 \frac{\partial^2 p}{\partial z^2} - \left[\frac{\partial^2 p}{\partial r^2} + \frac{1}{r} \frac{\partial p}{\partial r} + \frac{1}{r^2} \frac{\partial^2 p}{\partial \theta^2} \right] = & -\omega \sigma \frac{\partial^2 p}{\partial z \partial \tau} - \sigma^2 \frac{\partial^2 p}{\partial \tau^2} + (\gamma - 1) \left[\omega \frac{\partial E}{\partial z} + \sigma \frac{\partial E}{\partial \tau} \right] \\ & - B p^{\frac{\gamma-1}{2\gamma}} \left[\omega \frac{\partial p}{\partial z} + \sigma \frac{\partial p}{\partial \tau} \right] + N \end{aligned} \quad (9)$$

where B is the non-dimensional version of the dimensional B_2 ; thus,

$$B \approx M \frac{\gamma+1}{2} \frac{R}{L} \quad (10)$$

and the nonlinear acoustic terms are given as

$$\begin{aligned} N \equiv & \left(p^{\frac{\gamma-1}{\gamma}} - 1 \right) \left[\frac{\partial^2 p}{\partial r^2} + \frac{1}{r} \frac{\partial p}{\partial r} + \frac{1}{r^2} \frac{\partial^2 p}{\partial \theta^2} \right] + \frac{(\gamma-1)}{\gamma} \frac{1}{p} \left(\omega \frac{\partial p}{\partial z} + \sigma \frac{\partial p}{\partial \tau} \right)^2 \\ & + \gamma p^{\frac{\gamma-1}{\gamma}} \left[\frac{\partial^2 (p^{\frac{1}{\gamma}} u_r^2)}{\partial r^2} + \frac{2}{r} \frac{\partial (p^{\frac{1}{\gamma}} u_r^2)}{\partial r} + \frac{2}{r} \frac{\partial^2 (p^{\frac{1}{\gamma}} u_r u_\theta)}{\partial r \partial \theta} + \frac{2}{r^2} \frac{\partial (p^{\frac{1}{\gamma}} u_r u_\theta)}{\partial \theta} + \frac{1}{r^2} \frac{\partial^2 (p^{\frac{1}{\gamma}} u_\theta^2)}{\partial \theta^2} - \frac{1}{r} \frac{\partial (p^{\frac{1}{\gamma}} u_\theta^2)}{\partial r} \right] \end{aligned} \quad (11)$$

The quantity E can be expected also to go to zero as $M \rightarrow 0$. Furthermore, $\partial E/\partial t \rightarrow 0$ as $\varepsilon \rightarrow 0$ and / or as $M \rightarrow 0$.

With placement of nonlinear terms on the right sides of the equations, the non-dimensional momentum equations become

$$\omega \frac{\partial u_r}{\partial z} + \frac{1}{\gamma} \frac{\partial p}{\partial r} = -\sigma \frac{\partial u_r}{\partial \tau} - \left[u_r \frac{\partial u_r}{\partial r} + u_\theta \frac{1}{r} \frac{\partial u_r}{\partial \theta} - \frac{u_\theta^2}{r} \right] + \frac{1}{\gamma} \left[1 - \frac{1}{p^{\frac{1}{\gamma}}} \right] \frac{\partial p}{\partial r} \quad (12)$$

and

$$\omega \frac{\partial u_\theta}{\partial z} + \frac{1}{\gamma r} \frac{\partial p}{\partial \theta} = -\sigma \frac{\partial u_\theta}{\partial \tau} - \left[u_r \frac{\partial u_\theta}{\partial r} + u_\theta \frac{1}{r} \frac{\partial u_\theta}{\partial \theta} + \frac{u_r u_\theta}{r} \right] + \frac{1}{\gamma r} \left[1 - \frac{1}{p^{\frac{1}{\gamma}}} \right] \frac{\partial p}{\partial \theta} \quad (13)$$

The non-dimensional boundary conditions are given as

$$u_r(z, \tau, 1, \theta) = 0 \quad ; \quad \frac{\partial p}{\partial r}(z, \tau, 1, \theta) = p^{\frac{1}{\gamma}} u_\theta^2 \quad (14)$$

An implicit constraint is the solution must remain finite without any singularity.

A perturbation expansion is assumed. ε will be the perturbation parameter which is a measure of oscillation amplitude. We take

$$\begin{aligned}
p &= 1 + \varepsilon p_1(z, \tau, r, \theta) + \varepsilon^2 p_2(z, \tau, r, \theta) + \varepsilon^3 p_3(z, \tau, r, \theta) + O(\varepsilon^4) \\
u_r &= \varepsilon u_{r,1}(z, \tau, r, \theta) + \varepsilon^2 u_{r,2}(z, \tau, r, \theta) + \varepsilon^3 u_{r,3}(z, \tau, r, \theta) + O(\varepsilon^4) \\
u_\theta &= \varepsilon u_{\theta,1}(z, \tau, r, \theta) + \varepsilon^2 u_{\theta,2}(z, \tau, r, \theta) + \varepsilon^3 u_{\theta,3}(z, \tau, r, \theta) + O(\varepsilon^4) \\
\omega &= \omega_0 + \varepsilon \omega_1 + \varepsilon^2 \omega_2 + O(\varepsilon^3) \\
p^{\Gamma(\gamma)} &= 1 + \varepsilon \Gamma p_1 + \varepsilon^2 [\Gamma p_2 + \frac{\Gamma(\Gamma-1)}{2} p_1^2] + O(\varepsilon^3)
\end{aligned} \tag{15}$$

The zeroeth-order solutions are the steady-state solutions; thus, the non-dimensional $p_0 = 1$ and $u_{r,0} = u_{\theta,0} = 0$. It will be shown that $\omega_1 = 0$, $\sigma = M = \varepsilon^2$. For simplicity, those values will be taken now and proven later.

Now, we substitute into the equations and separate according to powers of ε .

A. First-order Equations

The resulting first-order equations become

$$\omega_0^2 \frac{\partial^2 p_1}{\partial z^2} - \left[\frac{\partial^2 p_1}{\partial r^2} + \frac{1}{r} \frac{\partial p_1}{\partial r} + \frac{1}{r^2} \frac{\partial^2 p_1}{\partial \theta^2} \right] = -(\gamma - 1) \omega_0 \frac{\partial E_{1,crit}}{\partial z} - B \omega_0 \frac{\partial p_1}{\partial z} \tag{16}$$

$$\omega_0 \frac{\partial u_{r1}}{\partial z} + \frac{1}{\gamma} \frac{\partial p_1}{\partial r} = 0 \tag{17}$$

$$\omega_0 \frac{\partial u_{\theta1}}{\partial z} + \frac{1}{\gamma r} \frac{\partial p_1}{\partial \theta} = 0 \tag{18}$$

$$u_{r1}(z, \tau, 1, \theta) = 0 \quad ; \quad \frac{\partial p_1}{\partial r}(z, \tau, 1, \theta) = 0 \tag{19}$$

The resonant modes for the chamber will be described by the homogeneous form of Equation (16). As currently stated, a homogeneous solution will appear on the right side as a forcing function. In order to maintain a finite solution, the two terms on the right side must balance and produce zero. $E_{1,crit}$ is the portion of the first-order perturbation of energy rate needed to balance the first-order nozzle damping. Thus, the right side of the equation becomes zero, yielding only the homogeneous solution. More details about E_1 and $E_{1,crit}$ follow below.

An infinite number of modes are possible, implying an infinity of solutions for the first-order equations and, consequently, an infinity of higher-order solutions. The most common mode for LPRE is the first-tangential spinning mode which we select here. If we consider the right side of Equation (16) to be zero, the

first-order solutions are the classical results:

$$\begin{aligned} p_1 &= A(\tau)J_1(s_{11}r)\cos(z - \theta + \psi(\tau)) ; \quad u_{r1} = -\frac{A}{\gamma s_{11}}\frac{dJ_1}{dr}\sin(z - \theta + \psi) ; \quad u_{\theta 1} = \frac{A}{\gamma s_{11}r}J_1\cos(z - \theta + \psi) \\ \omega_0 &= s_{11} = 1.8413 \end{aligned} \quad (20)$$

where J_1 , A , and ψ are the Bessel function of first kind and first order, slowly varying amplitude, and slowly varying phase angle, respectively.

The first five roots s_{1m} of the Bessel function $J_1(s_{1n}r)$ giving zero slope at $r = 1$ are $s_{11} = 1.8413$, $s_{12} = 5.3313$, $s_{13} = 8.5263$, $s_{14} = 11.706$, and $s_{15} = 14.864$. The lowest eigenvalue has been taken because it describes the first tangential mode. The other eigenvalues relate to modes with combined first tangential and first radial mode, combined first tangential and second radial mode, combined first tangential and third radial mode, and combined first tangential and fourth radial mode, respectively. Note that the Bessel function of the second kind has been discarded because it produces a singularity at $r = 0$.

The energy release rate $E(z, \tau, r, \theta)$ must be expanded in a perturbation series. We consider it to be the sum of a steady-state portion plus a perturbation caused by the acoustic oscillation. Thus, $E = E_{ss}(r, \theta) + E'(z, \tau, r, \theta)$ and $\partial E / \partial t = \partial E' / \partial t = \omega \partial E' / \partial z + \sigma \partial E' / \partial \tau$. Furthermore, we take $E'(z, \tau, r, \theta) = E'(\tau, r, z - \theta + \psi)$ for the travelling tangential wave. With the expectation that E' will have components in-phase and out-of-phase with pressure and its amplitude is related to the pressure amplitude, the following form is assumed:

$$\begin{aligned} E'(z, \tau, r, \theta) &= \sum_{n=0}^{\infty} \varepsilon^n [E_{c,n}(r)\cos(n[z - \theta + \psi]) + E_{s,n}(r)\sin(n[z - \theta + \psi])] \\ \frac{\partial E'}{\partial t} &= -\sum_{n=1}^{\infty} \varepsilon^n A^n s_{11} n [E_{c,n}(r)\sin(n[z - \theta + \psi]) + E_{s,n}(r)\cos(n[z - \theta + \psi])] \end{aligned} \quad (21)$$

In Appendix B, for the specific case of co-axial injection, mixing, and reaction, the assumed form will be justified. For the moment, we allow some dependencies on ε to be hidden in the coefficients $E_{c,n}$ and $E_{s,n}$. Set

$$\begin{aligned} E_{c,1}(r) &= \bar{E}_{c,1} J_1(s_{11}r) + \tilde{E}_{c,1}(r) \\ \bar{E}_{c,1} &\equiv \frac{\int_0^1 E_{c,1}(r) J_1(s_{11}r) r dr}{\int_0^1 J_1^2(s_{11}r) r dr} \\ \tilde{E}_{c,1}(r) &\equiv \sum_{m=2}^{\infty} \left[\frac{\int_0^1 E_{c,1}(r) J_1(s_{1m}r) r dr}{\int_0^1 J_1^2(s_{1m}r) r dr} \right] J_{1m}(r) \end{aligned} \quad (22)$$

Now, we define $\bar{E}_{c,1,excess} = (\bar{E}_{c,1} - \bar{E}_{c,1,crit})/\varepsilon^2$ and separate the coefficient into two parts of different order in ε :

$$\bar{E}_{c,1} \equiv \bar{E}_{c,1,crit} + \varepsilon^2 \bar{E}_{c,1,excess} \quad (23)$$

The logic for the separation will become evident as we proceed. Realize that ε appears explicitly in Equation (21) with the consequence that the above right-side terms appear to first and third order, respectively. We also consider $\tilde{E}_{c,1}(r)$ to be of higher order.

$E_{s,1}(r)$ is also expanded in an eigenfunction series and considered to be of $O(\varepsilon^2)$:

$$\begin{aligned} E_{s,1}(r) &= \varepsilon^2 \bar{E}_{s,1} J_1(s_{11}r) + \varepsilon^2 \tilde{E}_{s,1}(r) \\ \bar{E}_{s,1} &\equiv \frac{\int_0^1 E_{c,1}(r) J_1(s_{11}r) r dr}{\varepsilon^2 \int_0^1 J_1^2(s_{11}r) r dr} \\ \tilde{E}_{s,1}(r) &\equiv \Sigma_{m=2}^{\infty} \left[\frac{\int_0^1 E_{c,1}(r) J_1(s_{1m}r) r dr}{\varepsilon^2 \int_0^1 J_1^2(s_{1m}r) r dr} \right] J_{1m}(r) \end{aligned} \quad (24)$$

The result from setting the right side of Equation (16) to be zero is

$$(\gamma - 1)\omega_0 A \bar{E}_{c,1,crit} J_1(s_{11}r) \sin(z - \theta + \psi) = -B\omega_0 \frac{\partial p_1}{\partial z} = AB\omega_0 J_1(s_{11}r) \sin(z - \theta + \psi) \quad (25)$$

Thus, the definition for the critical value is obtained whereby $\bar{E}_{c,1,crit} = B/(\gamma - 1)$ and $\varepsilon^2 \bar{E}_{c,1,excess} \equiv \bar{E}_{c,1} - B/(\gamma - 1)$.

The physical interpretation from linear theory is that if $\bar{E}_{c,1} > \bar{E}_{c,1,crit}$ any small disturbance causes a growing oscillation; if $\bar{E}_{c,1} < \bar{E}_{c,1,crit}$ any small disturbance causes a decaying oscillation; and if $\bar{E}_{c,1} = \bar{E}_{c,1,crit}$, a neutral oscillation results. The difference of $E_{c,1}$ from its critical value, namely $E_{c,1,excess}$ will appear to higher order and will affect limit-cycle amplitude.

The $\varepsilon^2 E_{c,1,excess}$ term will also be of the order of the chamber-mean-flow Mach number M whereby $M \lll 1$. Essentially, we are setting $\varepsilon = \sqrt{M}$. Physically, this is realistic because, as shall be shown, the lowest frequency terms appear only to odd orders in ε . Thereby, the natural tendency in the necessary balance of certain terms is that the amplitude must adjust to the Mach number value. The amplitude of the oscillation will be defined as $\varepsilon A(\tau) = \sqrt{M} A(\tau)$.

B. Second-order Equations

The wave equation for the second-order pressure perturbation becomes

$$\omega_0^2 \frac{\partial^2 p_2}{\partial z^2} - \left[\frac{\partial^2 p_2}{\partial r^2} + \frac{1}{r} \frac{\partial p_2}{\partial r} + \frac{1}{r^2} \frac{\partial^2 p_2}{\partial \theta^2} \right] = N_2 + B s_{11} [A^2 \frac{\gamma - 1}{4\gamma} J_1^2(s_{11}r) \sin(2[z - \theta + \psi]) - \frac{\partial p_2}{\partial z}] \quad (26)$$

where

$$\begin{aligned} N_2 \equiv & \frac{\gamma - 1}{\gamma} p_1 \left[\frac{\partial^2 p_1}{\partial r^2} + \frac{1}{r} \frac{\partial p_1}{\partial r} + \frac{1}{r^2} \frac{\partial^2 p_1}{\partial \theta^2} \right] + \frac{(\gamma - 1)}{\gamma} \left(s_{11} \frac{\partial p_1}{\partial z} \right)^2 \\ & + \gamma \left[\frac{\partial^2 (u_{r1}^2)}{\partial r^2} + \frac{2}{r} \frac{\partial (u_{r1}^2)}{\partial r} + \frac{2}{r} \frac{\partial^2 (u_{r1} u_{\theta1})}{\partial r \partial \theta} + \frac{2}{r^2} \frac{\partial (u_{r1} u_{\theta1})}{\partial \theta} + \frac{1}{r^2} \frac{\partial^2 (u_{\theta1}^2)}{\partial \theta^2} - \frac{1}{r} \frac{\partial (u_{\theta1}^2)}{\partial r} \right] \end{aligned} \quad (27)$$

Note that the energy release rate does not appear to this order. The second-order momentum equations are

$$s_{11} \frac{\partial u_{r2}}{\partial z} + \frac{1}{\gamma} \frac{\partial p_2}{\partial r} = - \left[u_{r1} \frac{\partial u_{r1}}{\partial r} + u_{\theta1} \frac{1}{r} \frac{\partial u_{r1}}{\partial \theta} - \frac{u_{\theta1}^2}{r} \right] + \frac{1}{\gamma^2} p_1 \frac{\partial p_1}{\partial r} \quad (28)$$

and

$$s_{11} \frac{\partial u_{\theta2}}{\partial z} + \frac{1}{\gamma r} \frac{\partial p_2}{\partial \theta} = - \left[u_{r1} \frac{\partial u_{\theta1}}{\partial r} + u_{\theta1} \frac{1}{r} \frac{\partial u_{\theta1}}{\partial \theta} + \frac{u_{r1} u_{\theta1}}{r} \right] + \frac{1}{\gamma^2 r} p_1 \frac{\partial p_1}{\partial \theta} \quad (29)$$

$$u_{r2}(z, \tau, 1, \theta) = 0 \quad ; \quad \frac{\partial p_2}{\partial r}(z, \tau, 1, \theta) = \gamma u_{\theta 1}^2(z, \tau, r, \theta) \quad (30)$$

Now, substitution of the first-order solution into Equation (27) is possible. Standard trigonometric relations are used for simplifications. In order to remove derivatives from the result, repeated use of the following identity is made:

$$\frac{dJ_n(s_{11}r)}{dr} = \frac{n}{r} J_n(s_{11}r) - s_{11} J_{n+1}(s_{11}r) \quad (31)$$

The results are obtained that

$$N_2 = A^2 q_0(r) + A^2 q_2(r) \cos(2[z - \theta + \psi]) = -A^2 \frac{Q_0(r)}{r^2} - A^2 \frac{Q_2(r)}{r^2} \cos(2[z - \theta + \psi]) \quad (32)$$

where obviously $Q_n(r) = -r^2 q_n(r)$. The $q_n(r)$ functions are defined in Appendix A.

Consequently, we have the second-order pressure particular solution to Equation (26) created by the N_2 forcing function in the form

$$p_2* = A^2 F_0(r) + A^2 F_2(r) \cos(2[z - \theta + \psi]) \quad (33)$$

where substitution in Equation (26) yields the ordinary differential equations:

$$r^2 \frac{d^2 F_0}{dr^2} + r \frac{dF_0}{dr} = Q_0(r) \quad (34)$$

and

$$r^2 \frac{d^2 F_2}{dr^2} + r \frac{dF_2}{dr} + 4(s_{11}^2 r^2 - 1) F_2 = Q_2(r) \quad (35)$$

Equation (34) can be solved by two successive integrations of first order equations using integrating factors. However, another approach will be used related to the solution of the second-order, radial momentum equation later in this section.

Equation (35) can be solved by variation of parameters, reducing the solution to the sum of two quadratures. The homogeneous solutions to that differential equation are the Bessel function of the first kind $J_2(2s_{11}r)$ and of the second kind $Y_2(2s_{11}r)$. With $z \equiv 2s_{11}r$, the Wronskian is given as $W = 2/(\pi z) = 1/(\pi s_{11}r)$.¹³ Thus, the particular solution is given by

$$\begin{aligned} F_2(r) &= Y_2(2s_{11}r) \int_0^{2s_{11}r} \frac{J_2(z) Q_2(z/(2s_{11}))}{W(z)[z/(2s_{11})]^2} dz - J_2(2s_{11}r) \int_0^{2s_{11}r} \frac{Y_2(z) Q_2(z/(2s_{11}))}{W(z)[z/(2s_{11})]^2} dz \\ &= 2\pi s_{11}^2 \left[Y_2(2s_{11}r) \int_0^r \frac{J_2(2s_{11}r') Q_2(r')}{r'} dr' - J_2(2s_{11}r) \int_0^r \frac{Y_2(2s_{11}r') Q_2(r')}{r'} dr' \right] \end{aligned} \quad (36)$$

The first term has a singularity at $r = 0$ introduced through Y_2 . However, the multiplying integral will behave as r^2 for small radius, thereby removing the singularity through the product. In the second term, the integrand is singular and the integral will be singular. Again, the product formed with J_2 removes the singular behavior. The lower limits on the integrals are set to zero to avoid discontinuities at $r = 0$. That is, a finite value of $F_2(0)$ multiplied by the cosine function would result in discontinuous behavior for $p_2(z, 0, \theta)$.

The remaining particular solution to Equation (26) will be obtained using $p_2 \approx p_{2*}$ which is justified because $B = O(M)$ where the mean-flow Mach number M is small compared to unity. The forcing function on the right hand side of that equation now becomes $A^2 q_0(r) + A^2 q_2(r) \cos(2[z - \theta + \psi]) + A^2 q_{2s} \sin(2[z - \theta + \psi]) = -\frac{A^2}{r^2} \left[Q_0(r) + Q_2(r) \cos(2[z - \theta + \psi]) + Q_{2s} \sin(2[z - \theta + \psi]) \right]$ where $Q_{2s} \equiv -Bs_{11}r^2[2F_2(r) + \frac{\gamma-1}{4\gamma}J_1^2(s_{11}r)]$.

The differential equation for F_{2s} is

$$r^2 \frac{d^2 F_{2s}}{dr^2} + r \frac{dF_{2s}}{dr} + 4(s_{11}^2 r^2 - 1)F_{2s} = Q_{2s}(r) = -Bs_{11}r^2[2F_2(r) + \frac{\gamma-1}{4\gamma}J_1^2(s_{11}r)] \quad (37)$$

Now, we determine the particular solution $F_{2s} \sin(2[z - \theta + \psi])$.

$$F_{2s}(r) = 2\pi s_{11}^2 \left[Y_2(2s_{11}r) \int_0^r \frac{J_2(2s_{11}r')Q_{2s}(r')}{r'} dr' - J_2(2s_{11}r) \int_0^r \frac{Y_2(2s_{11}r')Q_{2s}(r')}{r'} dr' \right] \quad (38)$$

Adding that solution, we now have

$$p_2 = A^2 F_0(r) + A^2 F_2(r) \cos(2[z - \theta + \psi]) + A^2 F_{2s}(r) \sin(2[z - \theta + \psi]) \quad (39)$$

Solution of Equation (28) for u_{r2} can be obtained by first substituting solutions for $u_{r1}, u_{\theta 1}$, and p_2 to obtain

$$\begin{aligned} \frac{\partial u_{r2}}{\partial z} = & \frac{A^2}{\gamma^2 s_{11}^2} \left[\frac{J_1 J_2}{r^2} - \frac{s_{11} J_2^2}{2r} - \gamma s_{11} \frac{dF_2}{dr} \right] \cos(2[z - \theta + \psi]) - \frac{A^2}{\gamma s_{11}} \frac{dF_{2s}}{dr} \sin(2[z - \theta + \psi]) \\ & + \frac{A^2}{\gamma s_{11}} \left[-\frac{dF_0}{dr} + \frac{1}{\gamma} \left(1 - \frac{1}{s_{11}^2 r^2} \right) J_1 \frac{dJ_1}{dr} + \frac{1}{2\gamma r s_{11}^2} ((\frac{dJ_1}{dr})^2 + (\frac{J_1}{r})^2) \right] \end{aligned} \quad (40)$$

Now, to prevent u_{r2} from growing towards infinity with transformed time z , it is necessary that the last line of the above equation becomes identically zero. Thus, F_0 must satisfy the first-order differential equation

$$\frac{dF_0}{dr} = \frac{1}{\gamma} \left(1 - \frac{1}{s_{11}^2 r^2} \right) J_1 \frac{dJ_1}{dr} + \frac{1}{2\gamma r s_{11}^2} ((\frac{dJ_1}{dr})^2 + (\frac{J_1}{r})^2) \quad (41)$$

It can be shown by differentiation and substitution into Equation (34) that if F_0 satisfies Equation (41), it also satisfies (34). With expected uniqueness for the solution to the differential equation, the solution satisfies both the differential equation and the condition. So, there is no conflict and the solution for u_{r2} becomes

$$\begin{aligned} u_{r2} &= A^2 G_2(r) \sin(2[z - \theta + \psi]) + A^2 G_{2s}(r) \cos(2[z - \theta + \psi]) \\ G_2(r) &\equiv \frac{1}{2\gamma^2 s_{11}^2} \left[\frac{J_1 J_2}{r^2} - \frac{s_{11} J_2^2}{2r} - \gamma s_{11} \frac{dF_2}{dr} \right] ; \quad G_{2s}(r) \equiv \frac{1}{2\gamma s_{11}} \frac{dF_{2s}}{dr} \end{aligned} \quad (42)$$

Solution of Equation (29) for $u_{\theta 2}$ can readily be obtained by substituting solutions for $u_{r1}, u_{\theta 1}$, and p_2 , and integrating over z . The “constant” of integration (actually allowed to be a function of r) is set to zero by the condition of zero vorticity (zero circulation) to this order of the perturbation series. The result is

$$\begin{aligned} u_{\theta 2} &= A^2 H_2(r) \cos(2[z - \theta + \psi]) + A^2 H_{2s}(r) \sin(2[z - \theta + \psi]) \\ H_2(r) &\equiv \frac{1}{\gamma s_{11} r} \left[F_2 + \frac{J_1^2 - J_2^2}{4\gamma} + \frac{J_1 J_2}{2\gamma s_{11} r} \right] ; \quad H_{2s}(r) \equiv \frac{1}{\gamma s_{11} r} F_{2s} \end{aligned} \quad (43)$$

Equation (41) can be integrated to obtain F_0 with the result

$$F_0 = K + \frac{J_1^2}{2\gamma} + \frac{1}{2\gamma} \int_0^r \left[\frac{J_2^2}{r'} - \frac{2J_1 J_2}{s_{11}(r')^2} \right] dr' \quad (44)$$

The constant of integration K can be determined by the constraint that under oscillation the instantaneous value of the integral of the density over the chamber volume yields the same mass as given in steady-state operation. Thus, we have

$$\int_0^1 r F_0 dr = \frac{\gamma-1}{4\gamma} \int_0^1 r J_1^2 dr \quad (45)$$

Consequently,

$$K = \frac{\gamma-3}{2\gamma} \int_0^1 r J_1^2 dr + \frac{1}{\gamma} \int_0^1 \left[\int_0^r \left[\frac{2J_1 J_2}{s_{11}(r')^2} - \frac{J_2^2}{r'} \right] dr' \right] rdr \quad (46)$$

C. Third-order Equations

For the third-order equations, $\sigma(\varepsilon) = \varepsilon^2$ has been taken which will introduce the slow time derivatives at that order.

$$\begin{aligned} \omega_0^2 \frac{\partial^2 p_3}{\partial z^2} - \left[\frac{\partial^2 p_3}{\partial r^2} + \frac{1}{r} \frac{\partial p_3}{\partial r} + \frac{1}{r^2} \frac{\partial^2 p_3}{\partial \theta^2} \right] &= -2\omega_0 \omega_2 \frac{\partial^2 p_1}{\partial z^2} - \omega_0 \frac{\partial^2 p_1}{\partial z \partial \tau} + (\gamma-1)\omega_0 \frac{\partial E_3}{\partial z} \\ &- B\omega_0 \left[\frac{\partial p_3}{\partial z} + \frac{\gamma-1}{2\gamma} (p_2 \frac{\partial p_1}{\partial z} + p_1 \frac{\partial p_2}{\partial z}) + \frac{\gamma^2-1}{8\gamma^2} p_1^2 \frac{\partial p_1}{\partial z} \right] + N_3 \end{aligned} \quad (47)$$

$$\begin{aligned} N_3 \equiv & \frac{\gamma-1}{\gamma} p_1 \left[\frac{\partial^2 p_2}{\partial r^2} + \frac{1}{r} \frac{\partial p_2}{\partial r} + \frac{1}{r^2} \frac{\partial^2 p_2}{\partial \theta^2} \right] + \left(\frac{\gamma-1}{\gamma} p_2 - \frac{\gamma-1}{2\gamma^2} p_1^2 \right) \left[\frac{\partial^2 p_1}{\partial r^2} + \frac{1}{r} \frac{\partial p_1}{\partial r} + \frac{1}{r^2} \frac{\partial^2 p_1}{\partial \theta^2} \right] \\ & + \frac{2(\gamma-1)}{\gamma} \left(\omega_0^2 \frac{\partial p_1}{\partial z} \frac{\partial p_2}{\partial z} \right) - \frac{(\gamma-1)}{\gamma} p_1 \left(\omega_0 \frac{\partial p_1}{\partial z} \right)^2 \\ & + 2\gamma \left[\frac{\partial^2 (u_{r1} u_{r2})}{\partial r^2} + \frac{2}{r} \frac{\partial (u_{r1} u_{r2})}{\partial r} + \frac{1}{r} \frac{\partial^2 (u_{r2} u_{\theta1} + u_{r1} u_{\theta2})}{\partial r \partial \theta} + \frac{1}{r^2} \frac{\partial (u_{r2} u_{\theta1} + u_{r1} u_{\theta2})}{\partial \theta} + \frac{1}{r^2} \frac{\partial^2 (u_{\theta1} u_{\theta2})}{\partial \theta^2} - \frac{1}{r} \frac{\partial (u_{\theta1} u_{\theta2})}{\partial r} \right] \\ & + (\gamma-1)p_1 \left[\frac{\partial^2 (u_{r1}^2)}{\partial r^2} + \frac{2}{r} \frac{\partial (u_{r1}^2)}{\partial r} + \frac{2}{r} \frac{\partial^2 (u_{r1} u_{\theta1})}{\partial r \partial \theta} + \frac{1}{r^2} \frac{\partial (u_{r1} u_{\theta1})}{\partial \theta} + \frac{1}{r^2} \frac{\partial^2 (u_{\theta1}^2)}{\partial \theta^2} - \frac{1}{r} \frac{\partial (u_{\theta1}^2)}{\partial r} \right] \\ & + \left[\frac{\partial^2 (p_1 u_{r1}^2)}{\partial r^2} + \frac{2}{r} \frac{\partial (p_1 u_{r1}^2)}{\partial r} + \frac{2}{r} \frac{\partial^2 (p_1 u_{r1} u_{\theta1})}{\partial r \partial \theta} + \frac{1}{r^2} \frac{\partial (p_1 u_{r1} u_{\theta1})}{\partial \theta} + \frac{1}{r^2} \frac{\partial^2 (p_1 u_{\theta1}^2)}{\partial \theta^2} - \frac{1}{r} \frac{\partial (p_1 u_{\theta1}^2)}{\partial r} \right] \end{aligned} \quad (48)$$

$$\frac{\partial p_3}{\partial r}(z, \tau, 1, \theta) = 2u_{\theta1}u_{\theta2} + \frac{1}{\gamma}p_1u_{\theta1}^2 \quad (49)$$

The first- and second-order solutions may be substituted into N_3 to yield

$$\begin{aligned} N_3(r, z - \theta + \psi) = & A^3 q_1(r) \cos(z - \theta + \psi) + A^3 q_3(r) \cos(3[z - \theta + \psi]) \\ & + A^3 q_{1s}(r) \sin(z - \theta + \psi) + A^3 q_{3s}(r) \sin(3[z - \theta + \psi]) \end{aligned} \quad (50)$$

where the $q_n(r)$ functions are defined in Appendix A.

The derivatives of F_2 and F_{2s} can be obtained by differentiation of the relations given in Equations (36) and (38). Then, the second derivatives can be obtained in terms of F_2 and F_{2s} from the differential

equations, (35) and (37). The functions G_2, G_{2s}, H_2 and H_{2s} can be differentiated directly from their forms in Equations (42) and (43). Equation (31) would repeatedly be used. See those results in Appendix A.

The forcing function on the right side of Equation (47) is given by

$$\begin{aligned}
& -s_{11}A(\gamma-1)\bar{E}_{c,1,excess}J_1(s_{11}r)\sin(z-\theta+\psi) \\
& +s_{11}A(\gamma-1)\bar{E}_{s,1}J_1(s_{11}r)\cos(z-\theta+\psi)+2s_{11}\omega_2AJ_1(s_{11}r)\cos(z-\theta+\psi) \\
& +s_{11}\frac{dA}{d\tau}J_1(s_{11}r)\sin(z-\theta+\psi)+\frac{d\psi}{d\tau}s_{11}AJ_1(s_{11}r)\cos(z-\theta+\psi) \\
& -A^3Bs_{11}\left[\frac{\partial p_3}{\partial z}+\frac{\gamma-1}{4\gamma}(2F_0J_1+F_2J_1)\sin(z-\theta+\psi)+3\frac{\gamma-1}{4\gamma}F_2J_1\sin(3[z-\theta+\psi])\right] \\
& -A^3Bs_{11}\left[\frac{\gamma^2-1}{32\gamma^2}J_1^3\sin(z-\theta+\psi)+\frac{\gamma^2-1}{32\gamma^2}J_1^3\sin(3[z-\theta+\psi])\right] \\
& +A^3q_1(r)\cos(z-\theta+\psi)+A^3q_3(r)\cos(3[z-\theta+\psi]) \\
& +A^3q_{1s}(r)\sin(z-\theta+\psi)+A^3q_{3s}(r)\sin(3[z-\theta+\psi]) \tag{51}
\end{aligned}$$

The $J_1\sin(z-\theta+\psi)$ and $J_1\cos(z-\theta+\psi)$ terms cannot appear in the forcing function. Thus, two constraints are established:

$$\frac{dA}{d\tau}=A(\gamma-1)\bar{E}_{c,1,excess}+A^3B\left[\frac{\gamma-1}{4\gamma}\frac{\int_0^1(2F_0J_1^2+F_2J_1^2)rdr}{\int_0^1J_1^2rdr}+\frac{\gamma^2-1}{32\gamma^2}\frac{\int_0^1J_1^4rdr}{\int_0^1J_1^2rdr}\right]-A^3\frac{\int_0^1q_{1s}(r)J_1(s_{11}r)rdr}{s_{11}\int_0^1J_1^2(s_{11}r)rdr} \tag{52}$$

$$\frac{d\psi}{d\tau}=-2\omega_2-(\gamma-1)\bar{E}_{s,1}-A^2\frac{\int_0^1q_1(r)J_1(s_{11}r)rdr}{s_{11}\int_0^1J_1^2(s_{11}r)rdr} \tag{53}$$

And the modified third-order wave equation becomes

$$\begin{aligned}
\omega_0^2\frac{\partial^2p_3}{\partial z^2}-\left[\frac{\partial^2p_3}{\partial r^2}+\frac{1}{r}\frac{\partial p_3}{\partial r}+\frac{1}{r^2}\frac{\partial^2p_3}{\partial\theta^2}\right]=-A^3Bs_{11}\left[\frac{\partial p_3}{\partial z}+3\frac{\gamma-1}{4\gamma}F_2J_1\sin(3[z-\theta+\psi])\right] \\
-A^3Bs_{11}\frac{\gamma^2-1}{32\gamma^2}J_1^3\sin(3[z-\theta+\psi]) \\
+A^3Bs_{11}\frac{\gamma-1}{4\gamma}\sum_{m\neq 1}\frac{\int_0^1[2F_0J_1(s_{11}r)+F_2J_1(s_{11}r)]J_1(s_{1m}r)rdr}{\int_0^1J_1^2(s_{1m}r)rdr}J_1(s_{1m}r)\sin(z-\theta+\psi) \\
-A^3Bs_{11}\frac{\gamma^2-1}{32\gamma^2}\sum_{m\neq 1}\frac{\int_0^1J_1^3(s_{11}r)J_1(s_{1m}r)rdr}{\int_0^1J_1^2(s_{1m}r)rdr}J_1(s_{1m}r)\sin(z-\theta+\psi) \\
+A^3\sum_{m\neq 1}\frac{\int_0^1q_1(r)J_1(s_{1m}r)rdr}{s_{11}\int_0^1J_1^2(s_{1m}r)rdr}J_1(s_{1m}r)\cos(z-\theta+\psi) \\
+A^3q_3(r)\cos(3[z-\theta+\psi]) \\
+A^3\sum_{m\neq 1}\frac{\int_0^1q_{1s}(r)J_1(s_{1m}r)rdr}{s_{11}\int_0^1J_1^2(s_{1m}r)rdr}J_1(s_{1m}r)\sin(z-\theta+\psi)+A^3q_{3s}(r)\sin(3[z-\theta+\psi]) \tag{54}
\end{aligned}$$

It is not necessary to obtain the solutions for $p_3, u_{\theta 3}$, and u_{r3} in order to achieve the first approximation at growth and decay rates of the oscillation. The limit-cycle amplitude $A*$ and frequency perturbation ω_2 are given by setting the derivatives in Equations (52) and (53) equal to zero

$$A*^2=(\gamma-1)\bar{E}_{c,1,excess}\left[\frac{\int_0^1q_{1s}(r)J_1(s_{11}r)rdr}{s_{11}\int_0^1J_1^2(s_{11}r)rdr}-B\left(\frac{\gamma-1}{4\gamma}\frac{\int_0^1(2F_0J_1+F_2J_1)rdr}{\int_0^1J_1^2rdr}+\frac{\gamma^2-1}{32\gamma^2}\frac{\int_0^1J_1^4rdr}{\int_0^1J_1^2rdr}\right)\right]^{-1} \tag{55}$$

$$\omega_2=-(\gamma-1)\bar{E}_{s,1}-A*^2\frac{\int_0^1q_1(r)J_1(s_{11}r)rdr}{2s_{11}\int_0^1J_1^2(s_{11}r)rdr} \tag{56}$$

Integration of Equations (52) and (53) with prescribed initial conditions will yield transient solutions. It is clear that the sign of $dA/d\tau$ will change at the value of A giving the limit-cycle amplitude. In Appendix B, $\bar{E}_{c,1}$ and $\bar{E}_{s,1}$ are determined for the case of multiple co-axial injection of gaseous propellants.

IV. Solutions for Amplitude and Phase

Let us recast the equations. Define

$$\begin{aligned} k_1 &\equiv (\gamma - 1)\bar{E}_{c,1,excess} ; \\ k_2 &\equiv B \left[\frac{\gamma - 1}{4\gamma} \frac{\int_0^1 (2F_0 J_1 + F_2 J_1) r dr}{\int_0^1 J_1^2 r dr} + \frac{\gamma^2 - 1}{32\gamma^2} \frac{\int_0^1 J_1^4 r dr}{\int_0^1 J_1^2 r dr} \right] - \frac{\int_0^1 q_{1s}(r) J_1(s_{11}r) r dr}{s_{11} \int_0^1 J_1^2(s_{11}r) r dr} ; \\ k_3 &\equiv (\gamma - 1)\bar{E}_{s,1} ; \quad k_4 \equiv \frac{\int_0^1 q_1(r) J_1(s_{11}r) r dr}{s_{11} \int_0^1 J_1^2(s_{11}r) r dr} \end{aligned}$$

Then, Equations (52) and (53) become

$$\frac{dA}{d\tau} = k_1 A + k_2 A^3 ; \quad \frac{d\psi}{d\tau} = -2\omega_2 - k_3 - k_4 A^2 \quad (57)$$

It follows from the definition that k_2 is directly proportional to B and, from calculation, is always positive. k_1 may take either sign.

Analytical solutions can be found for these two first-order ordinary differential equations. With no loss of generality, take $A = A_0$ and $\psi = 0$ as the initial values. For the first equation, separate variables and recognize that certain differentials of logarithm are easily constructed. The integrated solution becomes after some simple algebraic manipulations

$$\frac{A(\tau)}{A_0} = \left[(1 + \frac{k_2}{k_1} A_0^2) e^{-2k_1\tau} - \frac{k_2}{k_1} A_0^2 \right]^{-1/2} \quad (58)$$

Consider first the case where k_1 and k_2 have identical signs: i.e., $k_1 > 0$ and $k_2 > 0$ (Case I). The solution for A goes to infinity in a finite time. Under this condition of unconditional instability in Case I with both k_1 and k_2 having positive values, a stable limit cycle is expected in practice. However, the perturbation series has not yet captured sufficiently high powers of ε and A to predict the stable limit cycle. So, the solution is artificially predicted to grow to infinite amplitude in a finite time; rather, if higher order analysis were applied, it is expected to grow to a finite stable amplitude in an infinite time. For example, if a A^5 term with a negative coefficient were added to the right side of the first equation in 57, a stable limit cycle could result.

If k_1 and k_2 have opposite signs, a limit cycle clearly exists at $A = A_* \equiv \sqrt{-k_1/k_2}$ where the time derivative becomes zero. For a more informative display, we may rewrite Equation (58) as

$$\frac{A(\tau)}{A_0} = \left[(1 - (\frac{A_0}{A_*})^2) e^{-2k_1\tau} + (\frac{A_0}{A_*})^2 \right]^{-1/2} \quad (59)$$

If $k_1 < 0, k_2 > 0$, and $A_0 < A^*$ (Case IIa), the solution for A decays to zero value as $\tau \rightarrow \infty$; while the solution for A grows to infinity in a finite time if $k_1 < 0, k_2 > 0$, and $A_0 > A^*$ (Case IIb). (Note that mathematically in either Case IIa or IIb, the value of A^* is approached as $\tau \rightarrow -\infty$.) In Case II here, the limit cycle at A^* is unstable. A stable limit cycle should exist at a higher value of $A > A^*$ but the truncated perturbation series does not reveal it. So, again the predicted growth to infinity in a finite time is artificial; rather, growth in an infinite time to a finite stable value is expected. The reversed signs indicate a bi-stable behavior with conditional stability; however, the expected stable limit cycle at an amplitude greater than the unstable limit-cycle amplitude A^* is not predicted unless the perturbation analysis must be carried to higher order for that prediction. Again, if a A^5 term with a negative coefficient were added to the right side of the first equation in (57), a stable limit cycle as well as the unstable limit cycle could result.

ω_2 is the frequency perturbation that applies in the limit cycle where ψ ceases to vary with time; thus, its value can be determined from Equation (57) as a function of A^* to be $\omega_2 = -(k_3 + k_4 A^{*2})/2$. Note that ω_2 can be simply ignored in those cases where a limit cycle is not found.

The second equation in (57) is readily solved by integration of a simple quadrature after substitution for A using Equation (58). The value for ω_2 can be substituted back again into that same equation. In particular, one obtains

$$\psi = -(2\omega_2 + k_3)\tau - k_4 \int_0^\tau A^2(\tau') d\tau' = k_4 A^{*2} \tau + \frac{k_4}{2k_2} \ln \left[1 + \frac{k_2}{k_1} A_0^2 (1 - e^{2k_1 \tau}) \right] \quad (60)$$

Substitution in the argument of the logarithmic function, using Equation (58), yields

$$\begin{aligned} \psi &= k_4 A^{*2} \tau + \frac{k_4}{2k_2} \ln \left[\left(\frac{A_0}{A} \right)^2 e^{2k_1 \tau} \right] = k_4 A^{*2} \tau - k_4 A^{*2} \tau + \frac{k_4}{2k_2} \ln \left[\left(\frac{A_0}{A} \right)^2 \right] = \frac{k_4}{2k_2} \ln \left[\left(\frac{A_0}{A} \right)^2 \right] \\ A \rightarrow A^* &\Rightarrow \psi \rightarrow \frac{k_4}{2k_2} \ln \left[\left(\frac{A_0}{A^*} \right)^2 \right] \end{aligned} \quad (61)$$

V. Comparison with Computational Fluid Dynamics Results

Now, reform in dimensional terms where the dimensional time $\tilde{t} = \frac{R\tau}{a_{ss}\varepsilon^2} = \frac{R\tau}{a_{ss}M}$, the dimensional mean-to-peak pressure amplitude of the major eigenfunction $\tilde{A} = \varepsilon A p_{ss} = \sqrt{M} A p_{ss}$, and the perturbed dimensional frequency of the limit-cycle $\tilde{\omega} = \frac{a_{ss}\varepsilon^2\omega_2}{R} = \frac{a_{ss}M\omega_2}{R}$. Now,

$$\frac{d\tilde{A}}{d\tilde{t}} = -\frac{Ma_{ss}k_1}{R}\tilde{A} + \frac{k_2a_{ss}}{p_{ss}^2R}\tilde{A}^3 \quad ; \quad \frac{d\psi}{d\tilde{t}} = -2\tilde{\omega} - \frac{Ma_{ss}k_3}{R} - \frac{k_4a_{ss}}{p_{ss}^2R}\tilde{A}^2 \quad (62)$$

Actually, Mk_1 and Mk_3 are independent of M . Namely,

$$\begin{aligned} Mk_1 &\equiv M(\gamma - 1)\bar{E}_{c,1,excess} = (\gamma - 1)\frac{V_3}{2} \left(\sum_{i=1}^N A_i \right) - B \\ Mk_3 &\equiv M(\gamma - 1)\bar{E}_{s,1} = \frac{V_4}{2} \left(\sum_{i=1}^N A_i \right) \end{aligned} \quad (63)$$

Unpublished data from the direct CFD solution of Equations (2, 6, 7) for given cases matches the behavior

$d\tilde{A}/d\tilde{t} = C_1\tilde{A} + C_2\tilde{A}^3$ for the domain with sufficiently small amplitudes. The coefficient C_1 could be negative or positive, depending on the operational domain. C_2 was always positive

Recognition of the pattern with the trigonometric functions leads to the expectation that higher-order perturbation analysis would yield $d\tilde{A}/d\tilde{t} = \sum_{n=1}^N C_n \tilde{A}^{2n-1}$ and $d\psi/dt = \sum_{n=1}^N K_n \tilde{A}^{2n-2}$. One could attempt to match the computational data using a differential equation with a higher-order polynomial on the right side.

In the form of Equation (62), the limit-cycle amplitude \tilde{A}^* and frequency modification $\tilde{\omega}^*$ are determined when the derivative becomes zero; thus,

$$\tilde{A}^* = p_{ss} \sqrt{-\frac{Mk_1}{k_2}} ; \quad \tilde{\omega}^* = \frac{Mk_1 k_4 a_{ss}}{2k_2 R} - \frac{Ma_{ss} k_3}{2R} \quad (64)$$

The theory predicts that the limit-cycle mean-to-peak dimensional pressure amplitude \tilde{A} scales roughly as p_{ss}/\sqrt{M} assuming a weak dependence of the combustion on the mean-flow Mach number and a small influence of Mach number dependence hidden in $\bar{E}_{c,1,excess}$ and therefore in k_1 through the B term in $\bar{E}_{c,1,crit}$. The Mach number dependence of \tilde{A}^* comes primarily from k_2 . The Mach number at the nozzle entrance scales roughly as throat area A_t for small Mach number ($M \ll 1$) while steady-state chamber pressure scales as the reciprocal of A_t . Therefore, one should be able to vary A_t at constant mass flow and show that $\tilde{A} \propto A_t^{-3/2}$. Thereby, for example, a thirty per cent change in nozzle throat area produces a nearly fifty percent change in the mean-to-peak limit-cycle amplitude. The frequency perturbation at the limit cycle, $\tilde{\omega}^*$, should vary with M (or A_t) through the first term on the right side of Equation (64).

The method here addresses a common case where the waveform consists of a basic resonant mode of oscillation with the superposition of a fundamental mode described by linear theory and the harmonics of that mode. Although we used the travelling first tangential mode, the method could be used for other tangential modes, radial modes, and mixed radial-tangential modes, including both standing and travelling modes. Situations where more than one fundamental mode appear with non-integer frequency ratios become more messy to treat but can still be approached by a generalized version of the approach here. These situations would produce "wobbly" waveforms where the solutions cannot be expressed in terms of one frequency. Energy transfer between these fundamental resonant modes would occur and sub-harmonics might be produced.

Acknowledgements

This research was supported by the Air Force Office of Scientific Research under Grant FA9550-12-1-0156 with Dr. Mitat Birkan as the Program Manager.

Appendix A

The $q_n(r)$ and $Q_n(r)$ values are given below. Unless noted otherwise, the arguments of the Bessel functions are $s_{11}r$ and non-dimensional variables are used.

$$\begin{aligned} q_0(r) &\equiv \frac{1}{\gamma r^2} \left[(J_2^2 - J_1^2)(2 - s_{11}^2 r^2) + s_{11} r J_1 J_2 \right] \\ Q_0(r) &\equiv \frac{1}{\gamma} \left[(J_1^2 - J_2^2)(2 - s_{11}^2 r^2) - s_{11} r J_1 J_2 \right] \end{aligned} \quad (65)$$

$$\begin{aligned} q_1 &\equiv \frac{\gamma - 1}{\gamma} \left[\frac{J_1 Q_0}{r^2} + \frac{J_1 Q_2}{2r^2} - s_{11}^2 J_1 F_0 - \frac{s_{11}^2 J_1 F_2}{2} + \frac{3s_{11}^2 J_1^3}{8\gamma} - \frac{s_{11}^2 J_1^3}{4} \right] \\ &- \frac{2}{s_{11}} \left[\left(\frac{J_1}{r} - s_{11} J_2 \right) \frac{d^2 G_2}{dr^2} + \left(s_{11}^2 (J_3 - J_1) - \frac{4s_{11} J_2}{r} + \frac{2J_1}{r^2} \right) \frac{dG_2}{dr} + \left(\frac{3s_{11} J_2}{r^2} - \frac{s_{11}^2}{r} (3J_1 + J_3) + s_{11}^3 J_2 \right) G_2 \right] \\ &+ \frac{1}{s_{11} r} \left[\frac{s_{11} J_2 G_2}{r} - \frac{J_1}{r} \frac{dG_2}{dr} + s_{11}^2 J_1 H_2 - (2 \frac{J_1}{r} - s_{11} J_2) \frac{dH_2}{dr} - \frac{J_1 H_2}{r^2} \right] \\ &+ \frac{\gamma - 1}{\gamma^2 s_{11} r} \left[\frac{2s_{11} J_1 (J_2^2 - J_1^2)}{r} - 2(\frac{J_1}{r})^2 J_2 + \frac{s_{11}^2}{2} J_1^2 J_2 + \frac{s_{11}^3 r}{2} J_1 (J_1^2 - J_2^2) - \frac{1}{4s_{11}} (\frac{J_1}{r})^3 + \frac{3}{2s_{11}} J_2 (\frac{J_1}{r})^2 \right] \\ &+ \frac{1}{2\gamma^2 s_{11} r} \left[2s_{11} J_2 (\frac{J_1}{r})^2 - \frac{11s_{11}^2}{2} \frac{J_1^3}{r} + 2s_{11}^2 J_2^2 \frac{J_1}{r} - \frac{7s_{11}^3}{2} J_2^3 + 6s_{11}^3 J_1^2 J_2 + s_{11}^4 r J_1^3 - \frac{7s_{11}^4 r}{2} J_1 J_2^2 \right] \end{aligned} \quad (66)$$

$$\begin{aligned} q_{1s} &\equiv \frac{\gamma - 1}{\gamma} \left[\frac{J_1 Q_{2s}}{2r^2} + \frac{3s_{11}^2 J_1 F_{2s}}{2} \right] \\ &+ \frac{1}{\gamma s_{11}^2} \left[\left(\frac{J_1}{r} - s_{11} J_2 \right) \frac{d^3 F_{2s}}{dr^3} + \left(s_{11}^2 (J_3 - J_1) - \frac{4s_{11} J_2}{r} + \frac{2J_1}{r^2} \right) \frac{d^2 F_{2s}}{dr^2} + \left(\frac{3s_{11} J_2}{r^2} - \frac{s_{11}^2}{r} (3J_1 + J_3) + s_{11}^3 J_2 \right) \frac{dF_{2s}}{dr} \right] \\ &+ \frac{1}{s_{11} r} \left[\frac{J_1}{r} \frac{dG_{2s}}{dr} - \frac{s_{11} J_2 G_{2s}}{r} + s_{11}^2 J_1 H_{2s} - \left(\frac{2J_1}{r} - s_{11} J_2 \right) \frac{dH_{2s}}{dr} - \frac{J_1 H_{2s}}{r^2} \right] \end{aligned} \quad (67)$$

$$\begin{aligned} q_2(r) &\equiv -s_{11}^2 J_1^2 + \frac{s_{11}^2}{\gamma} J_2^2 - \frac{s_{11} J_1 J_2}{\gamma r} \\ Q_2(r) &\equiv s_{11}^2 r^2 J_1^2 - \frac{s_{11}^2 r^2}{\gamma} J_2^2 + \frac{s_{11} r J_1 J_2}{\gamma} \end{aligned} \quad (68)$$

$$\begin{aligned} q_{2s}(r) &\equiv B s_{11} [2F_2(r) + \frac{\gamma - 1}{4\gamma} J_1^2(s_{11}r)] \\ Q_{2s}(r) &\equiv -B s_{11} r^2 [2F_2(r) + \frac{\gamma - 1}{4\gamma} J_1^2(s_{11}r)] \end{aligned} \quad (69)$$

$$\begin{aligned}
q_3 \equiv & \frac{\gamma-1}{\gamma} \left[\frac{J_1 Q_2}{2r^2} - \frac{9s_{11}^2 J_1 F_2}{2} + \frac{s_{11}^2 J_1^3}{8\gamma} + \frac{s_{11}^2 J_1^3}{4} \right] \\
& + \frac{2}{s_{11}} \left[\left(\frac{J_1}{r} - s_{11} J_2 \right) \frac{d^2 G_2}{dr^2} + \left(s_{11}^2 (J_3 - J_1) - \frac{4s_{11} J_2}{r} + \frac{2J_1}{r^2} \right) \frac{dG_2}{dr} + \left(\frac{3s_{11} J_2}{r^2} - \frac{s_{11}^2}{r} (3J_1 + J_3) + s_{11}^3 J_2 \right) G_2 \right] \\
& + \frac{1}{s_{11} r} \left[\frac{s_{11} J_2 (3G_2 + 4H_2)}{r} - \frac{3J_1}{r} \frac{dG_2}{dr} - 3s_{11}^2 J_1 H_2 + \left(2 \frac{J_1}{r} - 3s_{11} J_2 \right) \frac{dH_2}{dr} - \frac{J_1 H_2}{r^2} \right] \\
& + \frac{\gamma-1}{\gamma^2 s_{11} r} \left[2s_{11} \left(\frac{J_1}{r} \right)^3 - \frac{s_{11}^2}{2} J_1^2 J_2 + s_{11}^3 r J_1 (J_2^2 - J_1^2) - \frac{3}{4s_{11}} \left(\frac{J_1}{r} \right)^3 + \frac{1}{2s_{11}} J_2 \left(\frac{J_1}{r} \right)^2 \right] \\
& + \frac{1}{2\gamma^2 s_{11} r} \left[-8s_{11} J_2 \left(\frac{J_1}{r} \right)^2 + \frac{3s_{11}^2}{2} \frac{J_1^3}{r} + 6s_{11}^2 J_2^2 \frac{J_1}{r} + \frac{9s_{11}^3}{2} J_2^3 - 6s_{11}^3 J_1^2 J_2 - s_{11}^4 r J_1^3 + \frac{7s_{11}^4 r}{2} J_1 J_2^2 \right]
\end{aligned} \tag{70}$$

$$\begin{aligned}
q_{3s} \equiv & \frac{\gamma-1}{\gamma} \left[\frac{J_1 Q_{2s}}{2r^2} - \frac{13s_{11}^2 J_1 F_{2s}}{2} \right] \\
& - \frac{1}{\gamma s_{11}^2} \left[\left(\frac{J_1}{r} - s_{11} J_2 \right) \frac{d^3 F_{2s}}{dr^3} + \left(s_{11}^2 (J_3 - J_1) - \frac{4s_{11} J_2}{r} + \frac{2J_1}{r^2} \right) \frac{d^2 F_{2s}}{dr^2} + \left(\frac{3s_{11} J_2}{r^2} - \frac{s_{11}^2}{r} (3J_1 + J_3) + s_{11}^3 J_2 \right) \frac{dF_{2s}}{dr} \right] \\
& + \frac{1}{s_{11} r} \left[\frac{3J_1}{r} \frac{dG_{2s}}{dr} + \frac{s_{11} J_2 (4H_{2s} - 3G_{2s})}{r} - 3s_{11}^2 J_1 H_{2s} + \left(\frac{2J_1}{r} - 3s_{11} J_2 \right) \frac{dH_{2s}}{dr} - \frac{J_1 H_{2s}}{r^2} \right]
\end{aligned} \tag{71}$$

It is convenient to use the relations

$$\begin{aligned}
\frac{dF_2}{dr} = & 4\pi s_{11}^2 \left[\left(\frac{Y_2(2s_{11}r)}{r} - s_{11} Y_3(2s_{11}r) \right) \int_0^r \frac{J_2(2s_{11}r')Q_2(r')}{r'} dr' \right. \\
& \left. - \left(\frac{J_2(2s_{11}r)}{r} - s_{11} J_3(2s_{11}r) \right) \int_0^r \frac{Y_2(2s_{11}r')Q_2(r')}{r'} dr' \right] \\
\frac{dF_{2s}}{dr} = & 4\pi s_{11}^2 \left[\left(\frac{Y_2(2s_{11}r)}{r} - s_{11} Y_3(2s_{11}r) \right) \int_0^r \frac{J_2(2s_{11}r')Q_{2s}(r')}{r'} dr' \right. \\
& \left. - \left(\frac{J_2(2s_{11}r)}{r} - s_{11} J_3(2s_{11}r) \right) \int_0^r \frac{Y_2(2s_{11}r')Q_{2s}(r')}{r'} dr' \right] \\
\frac{d^2 F_2}{dr^2} = & \frac{Q_2}{r^2} + \frac{4F_2}{r^2} - 4s_{11}^2 F_2 - \frac{1}{r} \frac{dF_2}{dr} \quad ; \quad \frac{d^3 F_2}{dr^3} = \frac{1}{r^2} \frac{dQ_2}{dr} - \frac{3Q_2}{r^3} + (4s_{11}^2 r^2 - 12) \frac{F_2}{r^3} + \left(\frac{6}{r^2} - 4s_{11}^2 \right) \frac{dF_2}{dr} \\
\frac{d^2 F_{2s}}{dr^2} = & \frac{Q_{2s}}{r^2} + \frac{4F_{2s}}{r^2} - 4s_{11}^2 F_{2s} - \frac{1}{r} \frac{dF_{2s}}{dr} \quad ; \quad \frac{d^3 F_{2s}}{dr^3} = \frac{1}{r^2} \frac{dQ_{2s}}{dr} - \frac{3Q_{2s}}{r^3} + (4s_{11}^2 r^2 - 12) \frac{F_{2s}}{r^3} + \left(\frac{6}{r^2} - 4s_{11}^2 \right) \frac{dF_{2s}}{dr}
\end{aligned} \tag{72}$$

$$\begin{aligned}
\frac{dG_2}{dr} = & \frac{1}{2\gamma^2 s_{11}^2} \left[\frac{J_1 J_2}{r^3} - \frac{5s_{11} J_2^2}{2r^2} - \frac{s_{11} J_1 J_3}{r^2} + \frac{s_{11}^2 J_2 J_3}{r} - \gamma s_{11} \frac{d^2 F_2}{dr^2} \right] \quad ; \quad \frac{dG_{2s}}{dr} = \frac{1}{2\gamma s_{11}} \frac{d^2 F_{2s}}{dr^2} \\
\frac{d^2 G_2}{dr^2} = & \frac{1}{2\gamma^2 s_{11}^2} \left[-4 \frac{J_1 J_2}{r^4} - \frac{3s_{11} J_1 J_3}{r} - \frac{s_{11}^2 J_1 J_2}{r^2} + 9 \frac{s_{11}^2 J_2 J_3}{r^2} - \frac{s_{11}^3 J_3^2}{r} + \frac{s_{11}^2 J_1 J_4}{r^2} - \frac{s_{11}^3 J_2 J_4}{r} - \gamma s_{11} \frac{d^3 F_2}{dr^3} \right] \\
& \frac{d^2 G_{2s}}{dr^2} = \frac{1}{2\gamma s_{11}} \frac{d^3 F_{2s}}{dr^3} \tag{73}
\end{aligned}$$

$$\frac{dH_2}{dr} = \frac{1}{\gamma s_{11} r} \left[\frac{dF_2}{dr} - \frac{F_2}{r} + \frac{J_1^2 + J_2^2}{4\gamma r} - \frac{s_{11} J_1 J_2}{2\gamma} + \frac{J_1 J_2}{2\gamma s_{11} r^2} - \frac{s_{11} J_2 J_3}{2\gamma} - \frac{J_1 J_3}{2\gamma r} \right] \quad ; \quad \frac{dH_{2s}}{dr} = \frac{1}{\gamma s_{11} r} \left[\frac{dF_{2s}}{dr} - \frac{F_{2s}}{r} \right] \tag{74}$$

Appendix B: Determination of $\bar{E}_{c,1}$ and $\bar{E}_{s,1}$

A model is required to relate E to velocity and pressure. The effect is sought of the source term E on driving the acoustic oscillation. In particular, the long wavelength impact of that forcing term must be determined. That term represents the rate of conversion of chemical energy to thermal energy and will create entropy. Under oscillation, it will create kinematic entropy waves as well as directly modifying the longer wavelength acoustic oscillations. The model equation has filtered those shorter length kinematic waves. First, we will analyze an individual co-axial, mixing, and reacting gaseous propellant stream for an individual injector. Both the steady-state behavior and the unsteady perturbation will be examined.

B1 - Co-axial Flame Analysis

The axisymmetric stream will be analyzed. The flame length will be assumed to be shorter than the chamber length. Flames from neighboring injectors will not interact. Thus, each injector can be analyzed in an isolated manner, only being coupled through local oscillation in chamber pressure and velocity.

The simplification of constant c_p value for the mixture will be made and $h = c_p T$. Then, the energy equation becomes

$$\rho \frac{\partial T}{\partial t} + \rho \vec{u} \cdot \nabla T - \left(\frac{k}{c_p} \right) \nabla^2 T - \frac{1}{c_p} \frac{\partial p}{\partial t} = \rho \frac{\dot{Q}}{c_p} = \rho \frac{Q}{c_p} \omega_F \quad (75)$$

Approximating an isentropic relationship between pressure and density and defining $\kappa = T/T_{ss,\infty} - (p/p_{ss})^{(\gamma-1)/\gamma}$, we find

$$\frac{\partial \kappa}{\partial t} + \vec{u} \cdot \nabla \kappa - D \nabla^2 \kappa = \frac{Q}{c_p T_{ss}} \omega_F \quad (76)$$

where we take D to be both the thermal eddy diffusivity and the mass eddy diffusivity. For the gas ambient to the mixing, reacting stream, $\kappa = 0$. Some error is accepted when it is assumed that the isentropic relation for density applies throughout the mixing region; it is a good approximation for the ambient gas.

Consider now the mass diffusion, advection, and chemical reaction for each species. The species continuity equation for each species may be written as follows:

$$\frac{\partial Y_i}{\partial t} + \vec{u} \cdot \nabla Y_i - D \nabla^2 Y_i = \omega_i \quad (77)$$

If an infinite-rate chemical reaction is considered with the same diffusivity for fuel and oxygen, one can construct a Shvab-Zel'dovich variable $\alpha = Y_F - \nu Y_O$ where ν is the fuel-to-oxygen mass stoichiometric ratio. Similarly, one can define $\beta = (Q/(c_p T_{ss,\infty}))Y_F + \kappa$. For the gas ambient to the mixing, reacting stream, $\alpha = 0$ and $\beta = 0$.

Consider now a co-axial injector with axisymmetric behavior where the dependent variables are functions of t , x , and η . Gaseous oxygen flows from an injector at $x = 0$ for $0 \leq \eta \leq R_i$ while gaseous fuel flows through the injector at $x = 0$ for $R_i \leq \eta \leq R_o$. An Oseen approximation will be made for the velocity field with

uniform velocity $U(t)$ in the x direction. Velocities of both streams are taken to be identical although they differ in practice. Diffusion in the streamwise direction will be neglected. The diffusivity is approximated as a spatially uniform, temporal function due to turbulence modulation. The estimate is based on the turbulent viscosity approximation for a self-similar turbulent jet.¹⁴

$$\nu_T = \frac{U_{ss}(x)r_{1/2}(x)}{35}, \quad (78)$$

where in Equation (78) $U(t)$ is substituted for the centerline velocity $U_0(x)$, and R_o is the jet's half-width. Furthermore, the standard value of 0.7 is used for the turbulent Prandtl number, which yields

$$D = \frac{U(t)R_o}{24.5}, \quad (79)$$

The Oseen approximation, eddy-diffusivity approximation, and boundary- or mixing-layer approximation used here are well established in the literature. Variations in the velocity and turbulent diffusivity and diffusion in the main flow direction will cause quantitative corrections but no qualitative corrections are expected. The approximation implies that the ambient combustion-chamber gas will recirculate and parallel the injected propellants at the same velocity. The governing equations become

$$\frac{\partial \alpha}{\partial t} + U(t)\frac{\partial \alpha}{\partial x} - D\left[\frac{\partial^2 \alpha}{\partial \eta^2} + \frac{1}{\eta}\frac{\partial \alpha}{\partial \eta}\right] = 0 \quad (80)$$

and

$$\frac{\partial \beta}{\partial t} + U(t)\frac{\partial \beta}{\partial x} - D\left[\frac{\partial^2 \beta}{\partial \eta^2} + \frac{1}{\eta}\frac{\partial \beta}{\partial \eta}\right] = 0 \quad (81)$$

The ambient boundary conditions are $\alpha(t, x, \infty) = \beta(t, x, \infty) = 0$. Boundary conditions are needed at $x = 0$. Consider that, for $0 \leq \eta \leq R_i$, $T(t, 0, \eta) = T_i(t)$, $Y_O(t, 0, r) = Y_{O,i}(t)$, $Y_F(t, 0, \eta) = 0$, $\kappa(t, 0, \eta) = T_i/T_{ss,\infty} - (p/p_{ss})^{(\gamma-1)/\gamma}$, $\alpha(t, 0, \eta) = -\nu Y_{O,i}(t) \equiv f(t)$, $\beta(t, 0, \eta) = (p/p_{ss})^{(\gamma-1)/\gamma} - T_i/T_{ss,\infty} \equiv g(t)$. For $R_i \leq \eta \leq R_o$, $T(t, 0, \eta) = T_i(t)$, $Y_O(t, 0, \eta) = 0$, $Y_F(t, 0, \eta) = Y_{F,i}(t)$, $\kappa = T_i/T_{ss,\infty} - (p/p_{ss})^{(\gamma-1)/\gamma}$, $\alpha(t, 0, \eta) = Y_{F,o}$, and $\beta = (Q/(c_p T_{ss}))Y_{F,i} + (p/p_{ss})^{(\gamma-1)/\gamma} - T_i/T_{ss}$. For $\eta \geq R_o$, $Y_O(t, 0, \eta) = Y_F(t, 0, \eta) = 0$, $\kappa(t, 0, R) = 0$, $\alpha(t, 0, \eta) = 0$, and $\beta(t, 0, \eta) = 0$ where $p(t, 0, \eta)$ and $T(t, 0, \eta)$ have the ambient values.

The scaling still has the pressure wavelength much larger than the domain under study here; the acoustic wavelength is $O(100cm)$ near the wall while diffusion layers are of $O(1cm)$ and reaction zones are even smaller. So, the pressure may be considered uniform (over the domain of an individual injector but varying from one injector to another) although mass fractions and temperature will vary spatially and temporally due to the combined effects of heat and mass diffusion, convection or advection, and compression or expansion. The time for an acoustic wave to propagate through a single injector region is smaller than or comparable to the time for diffusion and reaction in that region. The wave speed order of magnitude is 10^2 to $10^3 m/s$.

over a centimeter or so in transverse dimension for a time between $O(10^{-5}s)$ and $O(10^{-4}s)$; the combustion times are about $10^{-4}s$. So, the time variation of pressure is important for the combustion dynamics.

These equations contain a characteristic time for mixing. This characteristic mixing time τ_M will result in a time lag for the response of heat release to the pressure oscillation. A rough estimate of that mixing time is given by

$$\tau_M = (R_o - R_i)^2 / D, \quad (82)$$

The τ parameter does not appear explicitly in the calculations.

Consider the separation of steady-state and linear perturbation terms: $U(t) = \bar{U} + U'(t)$, $D(t) = \bar{D} + D'(t)$, $\alpha = \bar{\alpha}(\eta, x) + \alpha'(t, \eta, x)$, $\beta(t, \eta, x) = \bar{\beta}(\eta, x) + \beta'(t, \eta, x)$. From the definition of the eddy diffusivity, it follows that

$$D' = (\bar{D}/\bar{U})U' \quad (83)$$

The equations governing the steady state become

$$\bar{U} \frac{\partial \bar{\alpha}}{\partial x} - \bar{D} \left[\frac{\partial^2 \bar{\alpha}}{\partial \eta^2} + \frac{1}{\eta} \frac{\partial \bar{\alpha}}{\partial \eta} \right] = 0 \quad (84)$$

and

$$\bar{U} \frac{\partial \bar{\beta}}{\partial x} - \bar{D} \left[\frac{\partial^2 \bar{\beta}}{\partial \eta^2} + \frac{1}{\eta} \frac{\partial \bar{\beta}}{\partial \eta} \right] = 0 \quad (85)$$

With substitution of Equations (83, 84, 85), the equations governing the linear perturbations become

$$\frac{\partial \alpha'}{\partial t} + \bar{U} \frac{\partial \alpha'}{\partial x} - \bar{D} \left[\frac{\partial^2 \alpha'}{\partial \eta^2} + \frac{1}{\eta} \frac{\partial \alpha'}{\partial \eta} \right] = -U' \frac{\partial \bar{\alpha}}{\partial x} + D' \left[\frac{\partial^2 \bar{\alpha}}{\partial \eta^2} + \frac{1}{\eta} \frac{\partial \bar{\alpha}}{\partial \eta} \right] = 0 \quad (86)$$

and

$$\frac{\partial \beta'}{\partial t} + \bar{U} \frac{\partial \beta'}{\partial x} - \bar{D} \left[\frac{\partial^2 \beta'}{\partial \eta^2} + \frac{1}{\eta} \frac{\partial \beta'}{\partial \eta} \right] = -U' \frac{\partial \bar{\beta}}{\partial x} + D' \left[\frac{\partial^2 \bar{\beta}}{\partial \eta^2} + \frac{1}{\eta} \frac{\partial \bar{\beta}}{\partial \eta} \right] = 0 \quad (87)$$

Equations (80, 81) have the same linear differential operator and are homogeneous. Physically, diffusion is occurring in individual axisymmetric planes that are advecting at velocity $U(t)$ in the x -direction. Visualize a continual set of planes perpendicular to the x -direction which advect downstream from the injector face with a temporal diffusion within each of these planes. So, one may convert the two first-derivative terms into a Lagrangian time-derivative term. That is, define $\tilde{t} = t - \tau = \int dx/U$ where τ is the time when mass in the particular plane was injected. Then, the equations become

$$\frac{\partial \alpha}{\partial \tilde{t}} - D \left[\frac{\partial^2 \alpha}{\partial \eta^2} + \frac{1}{\eta} \frac{\partial \alpha}{\partial \eta} \right] = 0 \quad (88)$$

and

$$\frac{\partial \beta}{\partial \tilde{t}} - D \left[\frac{\partial^2 \beta}{\partial \eta^2} + \frac{1}{\eta} \frac{\partial \beta}{\partial \eta} \right] = 0 \quad (89)$$

The boundary conditions at $x = 0$ can now be converted to initial conditions. That is, the boundary values at the instant when the element of mass was injected are the initial conditions for the diffusion plane to be solved for each of the plane (perpendicular to x -direction) which continually emerge from the injector face and advect downstream.

Green's function $G(r, \tilde{t}; \xi, t')$ may be used to solve this problem: The solutions to Equations (88) and (89) may be written as

$$\alpha(t, x, \eta) = 2\pi \int_0^\infty G(x, \eta; \xi) \alpha(t - \tau, 0, \xi) \xi d\xi = 2\pi \int_0^{R_o} G(x, \eta; \xi) \alpha(t - \tau, 0, \xi) \xi d\xi \quad (90)$$

and

$$\beta(t, x, \eta) = 2\pi \int_0^\infty G(x, \eta; \xi) \beta(t - \tau, 0, \xi) \xi d\xi = 2\pi \int_0^{R_o} G(x, \eta; \xi) \beta(t - \tau, 0, \xi) \xi d\xi \quad (91)$$

The conditions for α at $x = 0$ remain constant with time. For $0 \leq \eta \leq R_i$, $Y_O(t - \tau, 0, \eta) = Y_{O,i}$, $Y_F(t - \tau, 0, \eta) = 0$, $\alpha(t - \tau, 0, \xi) = -\nu Y_{O,i}$; so, $\bar{\alpha}_i = -\nu Y_{O,i}$ and $\alpha'(t - \tau, 0, \xi) = 0$. For $R_i \leq \eta \leq R_o$, $Y_O(t - \tau, 0, \xi) = 0$, $Y_F(t - \tau, 0, \xi) = Y_{F,o}$; thus, $\bar{\alpha}_o = Y_{F,o}$ and $\alpha'(t - \tau, 0, \xi) = 0$. For $\eta \geq R_o$, $Y_O(t - \tau, 0, \xi) = Y_F(t - \tau, 0, \xi) = 0$, $\alpha(t - \tau, 0, \xi) = 0$; and consequently $\bar{\alpha}(t - \tau, 0, \xi) = \alpha'(t - \tau, 0, \xi) = 0$ in that outer region. It follows that $\alpha' = 0$ throughout the domain.

B2 - Steady-state Solution

After integration of Equation (90) by parts, the steady-state solution is given. At the thin flame position $R_f(x)$, the value of $\alpha = 0$. Thus, an equation for $R_f(x)$ follows. Since the perturbation quantity $\alpha' = 0$, the value of R_f will apply through first order. The flame length L_f can be determined by setting $R_f = 0$ in the preceding equation and solving for the corresponding value of x . That is, $R_f(L_f) = 0$.

The burning rate will depend on the diffusion rate of α at the flame position. Differentiation of Equation (90) results in

$$\begin{aligned} \frac{\partial \alpha(t, x, \eta)}{\partial \eta} &= -\frac{\pi \bar{U}}{Dx} \int_0^\infty (\eta - \xi) G(x, \eta; \xi) \alpha(t - \tau, 0, \xi) \xi d\xi \\ &= \frac{\pi \bar{U}}{Dx} \int_0^\infty \xi G(x, \eta; \xi) \alpha(t - \tau, 0, \xi) \xi d\xi - \frac{\pi \eta}{Dx \bar{U}} \int_0^\infty G(x, \eta; \xi) \alpha(t - \tau, 0, \xi) \xi d\xi \\ &= \frac{\pi \bar{U}}{Dx} \int_0^\infty G(x, \eta; \xi) \alpha(t - \tau, 0, \xi) \xi^2 d\xi - \frac{\eta}{2Dx \bar{U}} \alpha(t, x, \eta) \end{aligned} \quad (92)$$

Thus, at the flame position, we find using integration by parts

$$\left. \frac{\partial \alpha}{\partial \eta} \right|_{R_f} = \frac{\pi \bar{U}}{Dx} \int_0^\infty G(x, R_f; \xi) \alpha(t - \tau, 0, \xi) \xi^2 d\xi = V_1(x) \quad (93)$$

The steady-state solution for β is found in similar fashion. At the flame position, the steady-state temperature $T_f(x)$ is found.

The diffusion-controlled steady-state burning rate per unit flame-length in the x -direction $d\bar{m}/dx$ is given by

$$\frac{d\bar{m}}{dx} = 2\pi R_f \bar{\rho}_f \bar{D} \left. \frac{\partial \alpha}{\partial \eta} \right|_{R_f} = 2\pi R_f \frac{p_{ss}}{\mathbf{R} \bar{T}_f} \bar{D} \left. \frac{\partial \alpha}{\partial \eta} \right|_{R_f} = 2\pi \bar{D} \frac{p_{ss}}{\mathbf{R}} \frac{R_f(x) V_1(x)}{\bar{T}_f(x)} \quad (94)$$

And, by integrating over the flame length L_f , the steady-state fuel-mass-burning rate associated with the injector is given as

$$\dot{M} \equiv \bar{m}(L_f) = 2\pi\bar{D}\frac{p_{ss}}{\mathbf{R}} \int_0^{L_f} \frac{R_f(x)V_1(x)}{\bar{T}_f(x)} dx \quad (95)$$

The total chamber fuel-mass-burning rate with N identical injectors is $N\dot{M}$. The total mass flow rate for injection at stoichiometric portions would be $[(\nu+1)/\nu]N\dot{M}$. However, no assumption about overall mixture ratio has been made. Rich or lean flows can be included.

B3 - Unsteady Perturbation Solution

The perturbation of mass fractions at the injector exit are zero and the temperature fluctuation at that exit is isentropic; thus, the solution for the perturbation of β is given as

$$\begin{aligned} \beta'(t, x, \eta) &= 2\pi \int_0^{R_o} G(x, \eta; \xi) \beta'(t - x/\bar{U}, 0, \xi) \xi d\xi = 2\pi \int_0^{R_o} G(x, \eta; \xi) \kappa'(t - x/\bar{U}, 0, \xi) \xi d\xi \\ &= 2\pi \int_0^{R_o} G(x, \eta; \xi) \frac{T'(t-x/\bar{U}, 0, \xi)}{T_{ss,\infty}} \xi d\xi - \frac{2\pi\gamma}{\gamma-1} \frac{p'(t-x/\bar{U})}{p_{ss}} \int_0^{R_o} G(x, \eta; \xi) \xi d\xi \\ &= \frac{2\pi\gamma}{\gamma-1} \left[\frac{T_{i0}}{T_{ss,\infty}} - 1 \right] \frac{p'(t-x/\bar{U})}{p_{ss}} \int_0^{R_o} G(x, \eta; \xi) \xi d\xi \end{aligned} \quad (96)$$

Given that the perturbations in α and flame radius R_f are zero-valued, the fluctuation in burning rate per unit length is

$$\frac{d\dot{m}'}{dx} = 2\pi\bar{D}\frac{p_{ss}}{\mathbf{R}} \frac{R_f(x)V_1(x)}{\bar{T}_f(x)} \left[\frac{p'}{p_{ss}} + \frac{D'}{\bar{D}} - \frac{T'_f}{\bar{T}_f} \right] = 2\pi\bar{D}\frac{p_{ss}}{\mathbf{R}} \frac{R_f(x)V_1(x)}{\bar{T}_f(x)} \left[\frac{p'}{p_{ss}} + \frac{U'}{\bar{U}} - \frac{T'_f}{\bar{T}_f} \right] \quad (97)$$

The constant mass flux at the injector exit with isentropic fluctuation there yields that $U'/\bar{U} = -(1/\gamma)p'/p_{ss}$.

From Equation (96), the temperature fluctuation at the flame where mass fractions become zero may be determined as

$$\beta'(t, x, R_f) = \kappa'(t, x, R_f) = \frac{T'_f(t, x)}{T_{ss,\infty}} - \frac{\gamma-1}{\gamma} \frac{p'(t)}{p_{ss}} = \frac{2\pi\gamma}{\gamma-1} \left[\frac{T_{i0}}{T_{ss,\infty}} - 1 \right] \frac{p'(t-x/\bar{U})}{p_{ss}} \int_0^{R_o} G(x, R_f; \xi) \xi d\xi \quad (98)$$

It follows that

$$\frac{T'_f(t, x)}{\bar{T}_f} = \frac{T_{ss,\infty}}{\bar{T}_f} \frac{\gamma-1}{\gamma} \frac{p'(t)}{p_{ss}} + \frac{T_{ss,\infty}}{\bar{T}_f} \frac{2\pi\gamma}{\gamma-1} \left[\frac{T_{i0}}{T_{ss,\infty}} - 1 \right] \frac{p'(t-x/\bar{U})}{p_{ss}} \int_0^{R_o} G(x, R_f; \xi) \xi d\xi \quad (99)$$

Now,

$$\frac{d\dot{m}'}{dx} = \frac{\gamma-1}{\gamma} \frac{d\bar{m}}{dx} \left(\left[1 - \frac{T_{ss,\infty}}{\bar{T}_f(x)} \right] \frac{p'(t)}{p_{ss}} - \frac{T_{ss,\infty}}{\bar{T}_f(x)} \left[\frac{T_{i0}}{T_{ss,\infty}} - 1 \right] \frac{p'(t-x/\bar{U})}{p_{ss}} V_2(x) \right) \quad (100)$$

where

$$V_2(x) \equiv 2\pi \int_0^{R_o} G(x, R_f; \xi) \xi d\xi \quad (101)$$

The integrated fuel-mass-burning-rate perturbation for the injector will depend on both the instantaneous pressure perturbation and the pressure perturbation at the time of injection for each discrete element of mass. Namely,

$$\dot{m}'(t) = \frac{\gamma-1}{\gamma} \frac{p'(t)}{p_{ss}} \int_0^{L_f} \frac{d\bar{m}}{dx} \left[1 - \frac{T_{ss,\infty}}{\bar{T}_f(x)} \right] dx - \frac{\gamma-1}{\gamma} \left[\frac{T_{i0}}{T_{ss,\infty}} - 1 \right] \int_0^{L_f} \frac{T_{ss,\infty}}{\bar{T}_f(x)} \frac{p'(t-x/\bar{U})}{p_{ss}} \frac{d\bar{m}}{dx} V_2(x) dx \quad (102)$$

B4 - Integration of N Injectors with the Chamber Dynamics

The individual injectors will experience different pressure histories, depending on their locations. We assume the same design for each injector. Thus, steady-state mass burning rate, flame temperature, and flame length do not vary from one injector stream to another stream.

Now, to be consistent with the wave dynamics perturbation analysis, the results for oscillating burning rate should be cast in non-dimensional terms. For an injector location centered at the non-dimensional position r_i, θ_i with $i = 1, 2, 3, \dots, N$, the pressure terms in Equation (102) become

$$\begin{aligned} \frac{p'(t, r_i, \theta_i)}{p_{ss}} &= \varepsilon A J_1(s_{11} r_i) \cos(z - \theta_i + \psi) \\ \frac{p'(t - x/\bar{U}, r_i, \theta_i)}{p_{ss}} &= \varepsilon A J_1(s_{11} r_i) \cos(z - s_{11}x/\bar{U} - \theta_i + \psi) \\ &= \varepsilon A J_1(s_{11} r_i) \left[\cos(s_{11}x/\bar{U}) \cos(z - \theta_i + \psi) + \sin(s_{11}x/\bar{U}) \sin(z - \theta_i + \psi) \right] \quad (103) \end{aligned}$$

where x and \bar{U} are now normalized using the chamber radius R and the steady-state sound speed a_{ss} . Multiply Equation (102) by the fuel heating value Q . Define the steady-state energy rate as $\bar{E} = Q\bar{m}$ and the energy-rate perturbation for the individual injector as $E'_i = Q\dot{m}'$. Normalize these energy rates by the quantity $p_{ss}a_{ss}R^2$. Use Equation (103) to substitute into Equation (102). At the scale of the chamber wave dynamics, the burning rate is taken as a delta function at the point r_i, θ_i , namely $\delta(r - r_i, \theta - \theta_i)$. The perturbation of the burning rate for the i^{th} injector becomes

$$\begin{aligned} E'_i(z, r_i, \theta_i) &= \frac{\gamma-1}{\gamma} \varepsilon A J_1(s_{11} r_i) \delta(r - r_i, \theta - \theta_i) \left[\cos(z - \theta_i + \psi) \left(\int_0^{L_f} \frac{d\bar{E}}{dx} \left[1 - \frac{T_{ss,\infty}}{T_f(x)} \right] dx \right. \right. \\ &\quad \left. \left. + \left[1 - \frac{T_{i0}}{T_{ss,\infty}} \right] \int_0^{L_f} \frac{T_{ss,\infty}}{T_f(x)} \cos(s_{11}x/\bar{U}) \frac{d\bar{E}}{dx} V_2(x) dx \right) \right. \\ &\quad \left. + \sin(z - \theta_i + \psi) \left[1 - \frac{T_{i0}}{T_{ss,\infty}} \right] \int_0^{L_f} \frac{T_{ss,\infty}}{T_f(x)} \sin(s_{11}x/\bar{U}) \frac{d\bar{E}}{dx} V_2(x) dx \right] \\ &= \varepsilon A J_1(s_{11} r_i) \delta(r - r_i, \theta - \theta_i) \left[V_3 \cos(z - \theta_i + \psi) + V_4 \sin(z - \theta_i + \psi) \right] \quad (104) \end{aligned}$$

where x and L_f are normalized by R and the definitions are given that

$$\begin{aligned} V_3 &\equiv \frac{\gamma-1}{\gamma} \left(\int_0^{L_f} \frac{d\bar{E}}{dx} \left[1 - \frac{T_{ss,\infty}}{T_f(x)} \right] dx + \left[1 - \frac{T_{i0}}{T_{ss,\infty}} \right] \int_0^{L_f} \frac{T_{ss,\infty}}{T_f(x)} \cos(s_{11}x/\bar{U}) \frac{d\bar{E}}{dx} V_2(x) dx \right) \\ V_4 &\equiv \frac{\gamma-1}{\gamma} \left[1 - \frac{T_{i0}}{T_{ss,\infty}} \right] \int_0^{L_f} \frac{T_{ss,\infty}}{T_f(x)} \sin(s_{11}x/\bar{U}) \frac{d\bar{E}}{dx} V_2(x) dx \quad (105) \end{aligned}$$

The two integrals with the sinusoidal oscillations of a kinematic wave with short wavelength can be expected to have lower values than the first integral. This gives support to the assumption made earlier that $|\bar{E}_{c,1}| \gg |\bar{E}_{s,1}|$.

If the pressure fluctuation at the injector and the energy release rate fluctuation of the jet flame are described respectively by $p' = \mathbf{P}e^{i\omega t}$ and $E' = \mathbf{E}e^{i\omega t}$, then the non-dimensional linear response coefficient

can be constructed for an individual injector as a complex number using the imaginary unit i .

$$\frac{E'}{p'} = \frac{\mathbf{E}}{\mathbf{P}} = V_3 - iV_4 \quad (106)$$

This complex coefficient provides information about the in-phase response of the energy release rate to a pressure fluctuation through V_3 and the out-of-phase response of the energy release rate to a pressure fluctuation through V_4 .

We must redistribute the burning rates for all N injectors in an eigenfunction series. For convenience, use the identities $\cos(z - \theta_i + \psi) = \cos(z + \psi)\cos\theta_i + \sin(z + \psi)\sin\theta_i$ and $\sin(z - \theta_i + \psi) = \sin(z + \psi)\cos\theta_i - \cos(z + \psi)\sin\theta_i$. Some convenient definitions are

$$\begin{aligned} a_i &\equiv \frac{\int_0^{2\pi} \int_0^1 \delta(r - r_i, \theta - \theta_i) J_1(s_{11}r_i) \cos\theta_i J_1(s_{11}r) \cos\theta r dr d\theta}{\pi \int_0^1 J_1^2(s_{11}r) r dr} = \frac{J_1^2(s_{11}r_i) \cos^2\theta_i}{\pi \int_0^1 J_1^2(s_{11}r) r dr} \\ b_i &\equiv \frac{\int_0^{2\pi} \int_0^1 \delta(r - r_i, \theta - \theta_i) J_1(s_{11}r_i) \sin\theta_i J_1(s_{11}r) \sin\theta r dr d\theta}{\pi \int_0^1 J_1^2(s_{11}r) r dr} = \frac{J_1^2(s_{11}r_i) \sin^2\theta_i}{\pi \int_0^1 J_1^2(s_{11}r) r dr} \\ A_i &\equiv a_i + b_i = \frac{J_1^2(s_{11}r_i)}{\pi \int_0^1 J_1^2(s_{11}r) r dr} \end{aligned} \quad (107)$$

The leading term in that eigenfunction expansion with account for contributions from all N injectors is

$$\begin{aligned} E_1(z, r, \theta) &= \varepsilon A J_1(s_{11}r) \left[V_3 (\sum_{i=1}^N a_i) \cos(z + \psi) \cos\theta + V_3 (\sum_{i=1}^N b_i) \sin(z + \psi) \sin\theta \right. \\ &\quad \left. + V_4 (\sum_{i=1}^N a_i) \sin(z + \psi) \cos\theta - V_4 (\sum_{i=1}^N b_i) \cos(z + \psi) \sin\theta \right] \\ &= \varepsilon A J_1(s_{11}r) \left[\frac{V_3}{2} \left(\sum_{i=1}^N A_i \right) \cos(z - \theta + \psi) + \frac{V_3}{2} \left(\sum_{i=1}^N A_i \cos(2\theta_i) \right) \cos(z + \theta + \psi) \right. \\ &\quad \left. + \frac{V_4}{2} \left(\sum_{i=1}^N A_i \cos(2\theta_i) \right) \sin(z + \theta + \psi) + \frac{V_4}{2} \left(\sum_{i=1}^N A_i \right) \sin(z - \theta + \psi) \right] \\ E_1(z, r, \theta) &\approx \varepsilon A J_1(s_{11}r) \left[\frac{V_3}{2} \left(\sum_{i=1}^N A_i \right) \cos(z - \theta + \psi) + \frac{V_4}{2} \left(\sum_{i=1}^N A_i \right) \sin(z - \theta + \psi) \right] \end{aligned} \quad (108)$$

After integration with the Dirac delta function, $E_1(z, r, \theta)$ is now a measure of the fluctuation in the time rate of energy per unit volume. It is seen that the burning rate has waveforms in both θ directions. However, the summations in the coefficients for the waves travelling in the negative θ direction have a mixture of positive and negative signs due to the presence of the $\cos(2\theta_i)$ factor. Therefore, the net effect is diminished. We will consider only the wave in the positive θ direction, as indicated by the final approximation above.

Comparison with Equations (22) and (24) leads to the results:

$$\bar{E}_{c,1} = \frac{V_3}{2} \left(\sum_{i=1}^N A_i \right) ; \quad \bar{E}_{c,1,excess} = \frac{1}{M} \left[\frac{V_3}{2} \left(\sum_{i=1}^N A_i \right) - \frac{B}{\gamma - 1} \right] ; \quad \bar{E}_{s,1} = \frac{1}{M} \frac{V_4}{2} \left(\sum_{i=1}^N A_i \right) \quad (109)$$

These results may now be used for substitution in Equations (52) and (53).

References

¹Harrje, D. and Reardon, F., *Liquid Propellant Rocket Combustion Instability*, NASA SP194, U.S. Government Printing Office, 1972.

²Oefelein, J. C. and Yang, V., "Comprehensive Review of Liquid-Propellant Combustion Instabilities in F-1 Engines," *Journal of Propulsion and Power*, Vol. 9, 1993, pp. 657–677.

³Sirignano, W. A., *Theoretical Study of Nonlinear Combustion Instability: Longitudinal Mode*, Ph.D. thesis, Princeton University Department of Aerospace and Mechanical Sciences Report No. 677, Princeton, New Jersey, March 1964.

⁴Zinn, B. T., "A Theoretical Study of Nonlinear Combustion Instability in Liquid-Propellant Rocket Engines," *AIAA Journal*, Vol. 6, 1968, pp. 1966–72.

⁵Sirignano, W. A. and Popov, P. P., "Two-dimensional Model for Liquid-Rocket Transverse Combustion Instability," *AIAA Journal*, Vol. 51(12), 2013, pp. 2919–34.

⁶Popov, P. P., Sideris, A., and Sirignano, W. A., "Stochastic Modeling of Transverse Wave Instability in a Liquid Propellant Rocket Engine," *J. Fluid Mech.*, Vol. 745, 2014, pp. 62–91.

⁷Popov, P. P., Sirignano, W. A., and Sideris, A., "Propellant Injector Influence on Liquid Propellant Rocket Engine Instability, in press," *J. Propulsion and Power*, 2014.

⁸Sirignano, W. A., "Driving Mechanisms for Combustion Instability, in press," *Combustion Science and Technology, Forman Williams Commemorative Issue*, 2014.

⁹Crocco, L. and Sirignano, W. A., *Behavior of Supercritical Nozzle Under Three Dimensional Oscillatory Conditions, AGARDograph No. 117*, North Atlantic Treaty Organization, Neuilly-Sur-Seine, France, 1967.

¹⁰Crocco, L. and Sirignano, W. A., "Effects of Transverse Velocity Components on the Nonlinear Behavior of Short Nozzles," *AIAA Journal*, Vol. 4, 1966, pp. 1428–30.

¹¹Reardon, F. H., Crocco, L., and Harrje, D. T., "Velocity Effects in Transverse Mode Liquid Propellant Rocket Combustion Instability," *AIAA Journal*, Vol. 12, 1964, pp. 1631–41.

¹²Kevorkian, J. K. and Cole, J. D., *Multiple Scale and Singular Perturbation Methods (Applied Mathematical Sciences)*, Springer, New York, 1996.

¹³Abramowitz, M. and Stegun, I. A., *Handbook of Mathematical Functions*, Dover, 1965.

¹⁴Pope, S. B., *Turbulent Flows*, Cambridge University Press, 2000.

Addendum 5

Numerical and Experimental Investigation for a GOX-GCH₄ Shear-Coaxial Injector Element

M. P. Celano^{**}, S. Silvestri^{*}, G. Schlieben^{*}, C. Kirchberger^{*}, and O. J. Haidn^{*}
T. Dawson^{**}, R. Ranjan^{**} and S. Menon^{**}

^{*}Institute for Flight Propulsion (LFA), Technische Universität München (TUM)
Munich, Germany

^{**}School of Aerospace Engineering, Georgia Institute of Technology (Georgia Tech)
Atlanta, GA

The present study aims to contribute to the understanding of the thermal transfer and mixing processes for GCH₄/GOX single element shear coaxial injector at operating conditions typical for rocket engines, in order to provide a benchmark for the validation of the in-house tool Thermtest and an anchoring base for the LES code of the Georgia Institute of Technology. Experimental investigations as well as LES simulations provide detailed information about the heat flux at the hot inner walls of the combustion chamber and the flame structure for pressures up to 20 bar. Heat fluxes are calculated by solving 2D unsteady heat conduction equation and by the concept of heat absorption. The flame structure and his anchoring are examined and a comparison with the experimentally measured wall pressure data is carried out.

Key Words: Methane, Green Propellants, Heat flux, Subscale Combustion Chamber, Rocket Engine

Nomenclature

a	: Inner combustion chamber width/height
A_{cc}	: Combustion chamber crossectionional area
A_{GCH_4}	: Injector annular area (GCH_4)
A_{GOX}	: Injector inner tube area (GOX)
A_{hw}	: Hot wall area (GOX)
A_{th}	: Throat crossectionional area
b	: External combustion chamber width
c	: Specific heat capacity
d_{in}	: Inner diameter (GOX)
d_{out}	: Outer diameter (GCH_4)
h	: External combustion chamber height
J	: Momentum flux ratio
m	: Mass
\dot{m}	: Mass flow rate
O/F	: Mixture ratio oxidator/fuel

P_c	: Combustion pressure
\dot{q}_{in}	: Heat flux entering the control volume
\dot{q}_{out}	: Heat flux leaving the control volume
$Re*$: Effective Reynold number
t	: Time
T	: Temperature
v_{GCH_4}	: Injection velocity gaseous methane
v_{GOX}	: Injection velocity gaseous oxygen
VR	: Velocity ratio
x	: Coordinate in the cross section plane
y	: Coordinate in the cross section plane
z	: Coordinate along the chamber axis
α_w	: Heat convection coefficient
$\alpha_{w,corr}$: Corrected heat convection coefficient
λ	: Heat convection coefficient
ρ	: Thermal conductivity
μ	: Dynamic viscosity
ΔT	: Temperature difference

1. Introduction

The demanding issues in terms of high operational and handling costs of cryogenic and storables propellants increased the attention for hydrocarbons in the pre-development of future launch vehicles [1].

*Corresponding author: research engineer, PhD student
e-mail: celano@lfa.mw.tum.de,
phone: +49 (0)89 - 289 - 16 187

LOX/hydrocarbon rocket engines have the advantage in fact of being relatively low cost, low pollution and high performance. In this context oxygen/methane is one of the most promising propellant combinations. In general methane shows, compared to other potential candidates, better overall performance from a system point of view [2], higher specific impulse [3], no risks for human health, simple extractability from natural gases, and an energy density six-times higher than hydrogen, when stored in liquid state at typical tank pressures. Although LOX/methane propellant combination is an attractive option, only a limited amount of experimental data is available for oxygen/methane combustion at relevant combustion chamber conditions and a critical gap is present in the knowledge of detailed heat transfer characteristics and injector technology. Injector design in fact plays a critical role in the design of a liquid rocket engine. Combustion performance and heat characteristic are basically determined by the injector design through its influence on the flame and flow dynamics and stability behavior. Coaxial jets in particular are utilized in a number of devices as propellant injectors. Rocket engines that use coaxial injectors include the Space Shuttle Main Engine and the Vulcain II engine of the Ariane 5. In these engines and most other booster engines, both propellants are injected in the combustion chamber in a super-critical state. Recent studies indicate that under these conditions the propellants act like dense gases and the scaling laws for gas-gas coaxial jets can be applied to super-critical jets [4]-[9]. Furthermore staged combustion cycle engines (SCC) are recently considered for use as part of the NASA Reusable Launch Vehicle (RLV) [5]. In the SCC, oxidizer rich gases drive the oxidizer turbopump and fuel-rich gases the fuel turbopump. Both propellants are then injected into the main combustion chamber as gases. Understanding the gas-gas mixing process is therefore of high interest. However experience with gas-gas injectors is limited and fundamental studies are necessary to understand the important physical/chemical mechanisms. Moreover to understand and predict the heat transfer to the chamber walls, considerable efforts need to be dedicated to model the combustion processes in a high pressure combustion device. Computational fluid dynamics, and in particular LES (Large Eddies Simulation), can become for these purposes an effective design tool for rocket combustion chamber. The validation of the fluid dynamics design tools requires, on the other hands, reliable comprehensive data in the same facility over a broad range of conditions. Given these justifications, the goal of the present work is to characterize the chamber wall heat transfer, due to its great impact on the strength,

life cycle and effectiveness of the cooling system in a LPRE (Liquid Propellant Engines), for methane and oxygen as propellants. A heavily instrumented heat sink chamber for heat flux measurements is designed and tested. Experiments are conducted for a gas-gas shear coaxial injector element over a wide range of pressure and mixture ratios. Additionally, the wall heat flux results are used as a test case for the validation of the in-house engineering tool Thermtest [6] and to determine the feasibility of LES as a tool at the Georgia Institute of Technology for the analysis of the flame structure and flow features. .

2. Hardware and Experimental Setup

In this section a description of the instrumented sub-scale rocket chamber, injector geometry, flow conditions and data analysis procedures, which are used for the wall heat flux characterization experiments, is presented. The present test campaign is performed using a modular heat-sink combustion chamber with a square cross section, designed for a testing time of up to 4 s at a chamber pressure of 20 bar and mixture ratio of 3.4. The single-element rocket combustion chamber is depicted in Fig. 1. The inner chamber dimensions are shown in Table 1. In recent years Pennsylvania State University, University of Florida, NASA MSFGC and Beijing University of Aeronautic and Astronautic made many attempts [5, 7–10]. on studying heat transfer in heat sink chambers. A heat sink chamber design is in fact preferable for research purposes because of its simplicity, low structural costs, ease to manufacture and high accessibility for thermocouples installation. The

Table 1: Combustion chamber dimensions

Chamber length	[mm]	290
Chamber width	[mm]	12
Chamber height	[mm]	12
Throat height	[mm]	4.8
Contraction ratio A_{cc}/A_{th}	[–]	2.5

material used for the chamber segments and the nozzle segment is oxygen-free copper (Cu-HCP). For the current study, a single shear coaxial injector element is integrated as shown in Fig. 2. For simplicity, the GOX post is configured flush with respect to the injection face. Table 2 shows the main injector characteristic dimensions. To ensure homogeneous injection conditions, in terms of temperature, pressure and velocity profile and to reduce the influence of the upstream feed lines, two porous plates are placed in the oxidizer and fuel manifolds respectively. In a coaxial injector

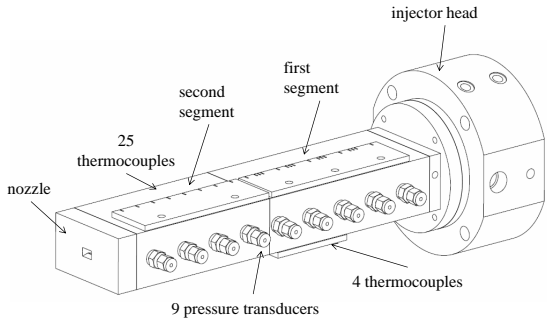


Fig. 1: Heat-sink combustion chamber

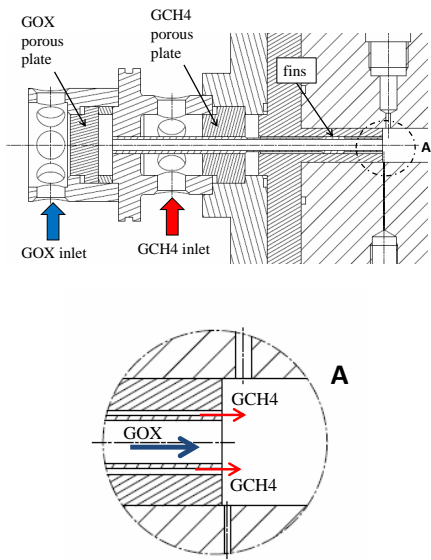


Fig. 2: Single shear coaxial injector

the shear forces between the propellants determine the mixing efficiency. Non-dimensional numbers such as the velocity ratio VR (Eq. 1), the momentum flux ratio J (Eq. 2), together with the effective Reynolds number Re^* (Eq. 3) are employed to characterize injection conditions.

$$VR = \frac{v_{GCH4}}{v_{GOX}} \quad (1)$$

$$J = \frac{(\rho v^2)_{GCH4}}{(\rho v^2)_{GOX}} \quad (2)$$

$$Re^* = \left(\frac{\rho d v}{\mu} \right)_{out} \left[1 + \frac{1 - J}{J} \left(\frac{d_{in}}{d_{out}} \right)^2 \right]^{1/2} \quad (3)$$

A schematic of the combustion chamber and the associated sensor locations are given in Fig. 1 and Fig. 3. More details about the experimental set-up can be found in [11]. Thermocouples are embedded at a series of evenly distributed axial points to determine the temperature field in the chamber walls. Type T

Table 2: Injector dimensions

GOX diameter	[mm]	4.0
GOX post wall thickness	[mm]	0.5
GCH4 diameter	[mm]	6.0
Injector area ratio A_{GCH4}/A_{GOX}	[$-$]	0.7

thermocouples of 0.5 mm diameter are located within the chamber wall with 1 mm , 2 mm and 3 mm distance to the hot wall. The thermocouples are kept in positions by a spring loaded system. The spring loading of the thermocouples provides a constant force of about 2 N , which ensures a continuous contact between the thermocouples tip and the base of the hole. This setup aims to minimize the chance of potential loss of contact as the material undergoes expansion and contraction due to changes in temperature or vibrations during the hot run [12]. The temperature variations at the mea-

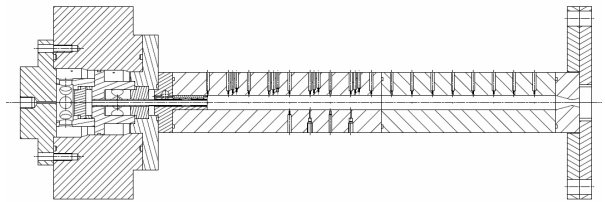


Fig. 3: Thermocouple positions along the combustion chamber axis

surement locations are direct results of the unsteady inner heat flux, which depends on the local flame and flow structure. Thus theoretically, the temperature measurements at these points can be used to calculate the temperature and the heat flux at the inner walls. The test matrix includes testing at pressure levels from nominally 20 bar down to 5 bar and at mixture ratios of 2.6 , 3.0 , 3.4 and 4 (4 only for the 5 bar case). For the O/F conditions, both the GCH4 and GOX mass flow rates are scaled accordingly with pressure. Fig. 4 shows the test envelop for the present study. Use of a

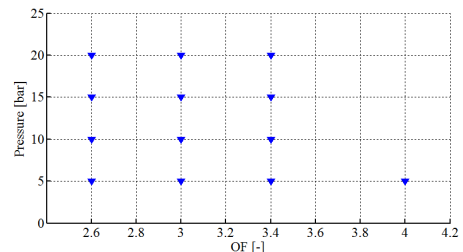


Fig. 4: Test envelop -nominal operating points

heat sink hardware limits the duration of every firing test, so the burn times are chosen to reach stable op-

eration, required for the thermal load measurements. Each of the operating point is ran at least two times to ensure the repeatability of the recorded test data. Good agreement is obtained for all load points. To minimize the influence of the igniter on the temperature measurements, the igniter runs at minimum power for only 600 ms (200 ms prior to the opening of the main valves). A typical chamber pressure and temperature output is shown in Fig. 5. Due to the transient nature of the problem, three time intervals are chosen for the evaluation of the test data. A representative time interval for the starting conditions t_0 , a characteristic hot run time step t_1 and a shutdown condition time t_2 .

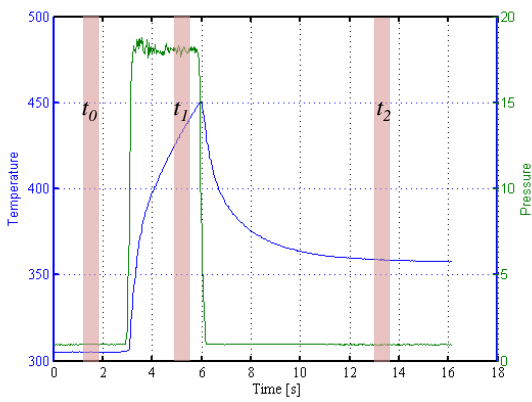


Fig. 5: Temperature and pressure build-up

3. Heat Flux Calculations

The characteristic of an injector element is mainly defined by the heat flux distribution on the hot wall along the chamber axis. The mixing mechanisms in the near injector field determine the flow conditions and influence flame and flow dynamics. In the present paragraph the distributions of the temperature and heat flux on the inner chamber wall and their transient behavior during the hot run are shown. As an example of the test results obtained in the present test campaign, in the following section the 20 bar $O/F = 2.6$ (*CaseA*) and $O/F = 3.4$ (*CaseB*) test cases are shown in more details, see Table 3. The axial and radial distribution of the thermocouples allows the determination of the heat flux variation along the axis and the reconstruction of the thermal field in the chamber wall. The temperature evolution over time shows that the steady state conditions are not reached in the chamber during the hot run. Each thermocouple provides a transient temperature measurement at a point 1 mm , 2 mm and 3 mm back

from the hot wall. Figure 6 shows the thermocouple time traces at 1 mm from the inner wall. Two main gradients could be typically recognized: a steeper increase, as the thermal wave travels through the chamber walls, and a smoother temperature increase during the remaining running time. Furthermore all temperature traces behave normally and have the same response characteristics. Since the temperature increase with time, in a heat-sink rocket chamber the transient equation needs to be solved to evaluate the wall heat flux. Measuring transient temperatures with sufficient accuracy

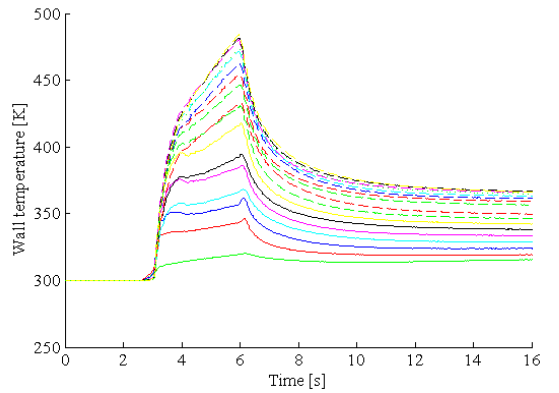


Fig. 6: Temperature signal at 1 mm distance from the hot wall, $P_c=20\text{ bar}$ and $O/F = 3.4$

accuracy for heat flux determination has been found to be challenging due to a significant sensitivity to the response time and sensitivity to positioning of the thermocouples. Previous studies [7] have already made attempt in this direction based on a 1D approximation of the heat transfer in the copper material and applying a correction for the unsteady term. The heat flux calculations based on linear approximation are however subject of error, due to the multidimensional nature of the problem. In the present work, the heat flux in each location is calculated using two different approaches: a more detailed numerical scheme and a more intuitive scheme based on experimental data observation. In the numerical method, the heat fluxes are obtained by solving the 2D unsteady heat conduction equation, while the experimental approach is based on the concept of accumulation of heat. A simple 1D approach cannot be used. Due to the rectangular cross section of the combustion chamber, the temperature gradient is not significant for only one coordinate direction and it is necessary to account for multidimensional effects. The methods are explained as follows.

Table 3: Operating conditions

Case	<i>OF</i>	<i>m</i>		<i>T</i>		<i>J</i>	<i>VR</i>
	Ratio	GOX	GCH4	GOX	GCH4		
A	2.66	44.4	16.7	280.7	275.9	0.587	1.07
B	3.48	49.1	14.1	281.7	280.5	0.347	0.83

Heat Flux Calculations by Numerical Approach

The 2D unsteady heat conduction equation needs to be solved in order to take into account the transient effect. The transverse cross section of the combustion chamber is chosen as computational domain in order to consider the cumulative effect of the copper material and the effects caused by the presence of the corners. Thermal and geometrical conditions identify two relevant symmetry planes for the proposed geometry, it is therefore possible to consider as control volume one-fourth of the complete configuration, as shown in Fig. 7. The

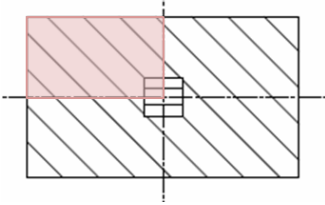


Fig. 7: Control volume for heat flux calculations

longitudinal heat flux due to conduction between the different measuring positions instead is neglected. Heat flux boundary conditions are imposed on the inner and the outer walls. The outer wall is assumed to be subject only to natural convection with a constant heat convection coefficient of $4 \text{ W}/(\text{m}^2\text{K})$. The inner surface heat transfer is evaluated differently depending on the hot run phase in order to get the right start-up and shut-down conditions. Three main phases are identified: pre-start-up, stable combustion and post-shut-down. During the pre-start-up the heat flux coming from the hot gas is set to zero, while at the post-shut-down a new value of the heat flux is calculated to take into account the forced convection between the purging gas and the hot walls. During the steady state operation the imposed heat flux is changed to different sets of computation so that the temperatures obtained from the computations matched the experimental results as closely as possible. The heat flux imposed at the inner wall for which the temperature match closely is considered to be the optimum value. The discretized

2D heat equation is:

$$\begin{aligned} & \frac{\lambda}{(\delta x)^2} (T_{i+1,j,t} - 2T_{i,j,t} + T_{i-1,j,t}) \\ & + \frac{\lambda}{(\delta y)^2} (T_{i,j+1,t} - 2T_{i,j,t} + T_{i,j-1,t}) = \\ & \quad \frac{\rho c}{(\delta t)^2} (T_{i,j,t+\delta t} - T_{i,j,t}) \end{aligned} \quad (4)$$

The discretized equations are solved simultaneously, marching forward in time and applying the transient recessed thermocouple measurements. For properties, the density, the conductivity, and the heat capacity of the copper are assumed to be constant. A similar approach can be found in [10]- [13] for GOX/GH2. The evolution of the heat flux over time is assumed to be an exponential function of the form $C_1[1 - C_2 \exp(t)]$. The heat fluxes and the time constants in the heat flux evolution are adjusted in the iteration processes, such that the experimental and the computed temperatures could be matched within $5\ldots 6\text{K}$. The selection of an exponential function is based on the observation from the experimental chamber pressure and temperature rise in time.

Heat Flux Calculations by Accumulation of Heat

The cumulative heat method is adopted by the observation of the time evolution of the temperature signal during the hot run. At the time interval t_1 , the temperature distribution is fully established and quasi-steady-state conditions can be assumed. Therefore, with the assumption of a constant heat flux, the temperature may be considered to equally change at any point of the control volume, Fig. 7. This allows defining the heat transfer problem only by the heat capacity of the control volume itself. The observation of the temperature traces over time implies a constant slope dT/dt at time t_1 . The energy balance, including the energy storage term, is defined by Eq. 5

$$\dot{E}_{in} - \dot{E}_{out} = \dot{E}_{stor} \quad (5)$$

That is then possible to write in terms of heat flux as Eq. 6

$$\dot{q}_{in} - \dot{q}_{out} = \frac{mc\Delta T}{A_{hw}\Delta t} \quad (6)$$

The temperature variation over time ($\Delta T/\Delta t$) is calculated from the measured temperature signals during t_1 . The Eq. 6 is applied at each thermocouple position, since independent from the temperature level. The properties, density, heat capacity and conductivity of the copper, are also in this case assumed constant. The heat flux dispersed outside the chamber, due to natural convection, is considered negligible. To verify the validity of this hypothesis an extreme case can be considered. If it is taken air at ambient temperature at 288 K and the outer wall temperature at 300 K , assuming forced convection with an air velocity of 15 m/s , this component of the heat flux could only account to 0.3% of the heat fluxes in the chamber wall due to combustion. These conditions are considered more dissipative than the one experienced during the experiments and the insulated wall assumption can be then assumed as valid. It is concluded that the rate of heat release to the inner walls from combustion is equal to the rate of heat absorbed by the chamber as stated in Eq. 7.

$$\dot{q}_{in} = \frac{bh - a^2}{4a} \rho c \frac{[T(t_i) - T(t_{i-1})]}{\Delta t} \quad (7)$$

Results and Discussion

A detailed analysis of the test data is performed using the described procedures. In all of the following figures the heat fluxes are calculated toward the end of the experimental time, when the steady state is reached at all axial positions and no influence can be assumed to be seen from the start-up transient. Fig. 8 and Fig. 9 show a comparison of the heat flux along the chamber axis at time interval t_1 for different chamber pressures and for different mixture ratios. In both cases the characteristic of the heat release is not significantly shifted along the chamber axis. Due to the small changes in terms of velocity ratio and impulse ratio at the injection, no significant impact can be recognized between the different operating conditions in terms of mixing processes. The dominating phenomena for the heat flux release is the combustion itself, as highlighted from the increase in steepness and absolute value of the heat flux profile with increasing pressure in the combustion chamber when the velocity ratio are varied. Test repetitions for the different load points are included in the figures and present good agreement. A slight difference is noticed with the variation in mixture ratios, between $O/F = 3.4$ and $O/F=2.6$ operating points. For the same combustion pressure, in a gas-gas injector, by changing

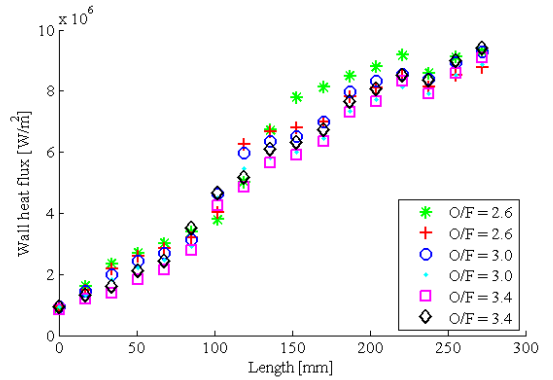


Fig. 8: Heat flux distribution along the chamber axis, $P_c = 20\text{ bar}$ at t_1

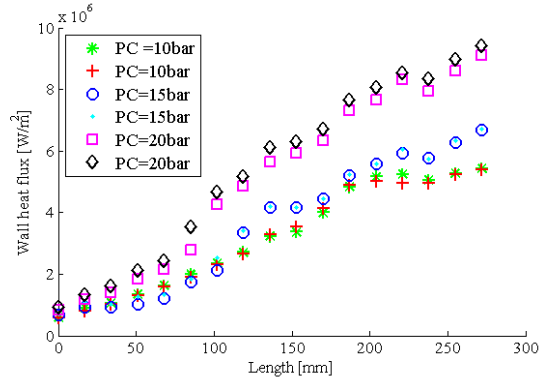


Fig. 9: Heat flux distribution along the chamber axis, $O/F = 3.4$ at t_1

the O/F the total mass flow rate stays almost constant but the injection velocity are varied. In the specific the velocity ratio changes from 0.86 to 1.2, meaning that the annular flow of methane becomes faster than the one of the central jet of oxygen. The direction of rotation of the eddies in the inner mixing layer depends on whether the velocity ratio is greater than or less than unity [14]. Furthermore, the scalar properties in the near field are defined by the effective Reynolds number, the Schmidt number (for gas-gas=1) and the stoichiometric mixing length L_s [15]. The smaller L_s is an indicator of faster mixing. For methane according to [16] this value increases linearly with the velocity ratio. This and the change in vortex direction can explain the difference in heat flux profile highlighted in Fig. 10 as a consequence of the change in the local mixing processes in the near field region of the coaxial jet. In Fig. 11 the heat flux calculated with the described numerical approach is presented. The heat flux values calculated with the numerical approach are lower than that from the cumulative heat approach ones but both calculations show the same qualitative

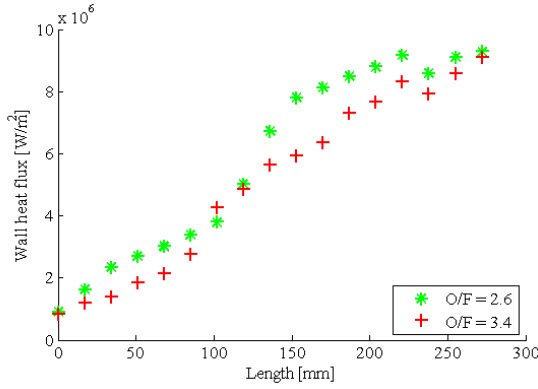


Fig. 10: Comparison of the heat flux distribution along the chamber axis, $P_c = 20\text{ bar}$ at t_1

trend. The difference in absolute value can be directly attributed to the fact that the heat flux presented are computed employing a grid size of 20×40 . Furthermore the wall heat fluxes obtained by numerically solving the two-dimensional unsteady heat conduction equation do not take into account the longitudinal heat transfer, while the accumulated heat assumes a constant linear temperature profile in the whole control volume. This last hypothesis would result in a slight overprediction of the heat flux. The heat cumulative method used

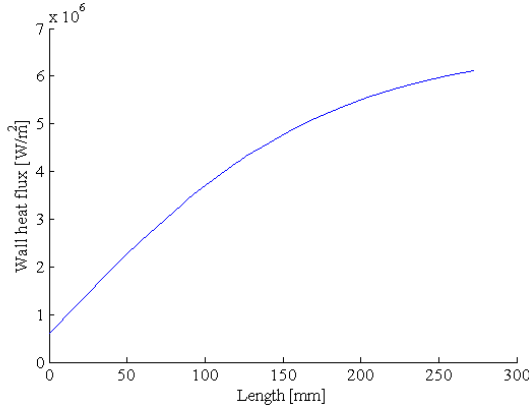


Fig. 11: Heat flux distribution along the chamber axis with numerical approach, $P_c = 20\text{ bar}$, $O/F = 3.4$ at t_1

for calculating the heat flux for these experimental conditions seems anyhow to be an efficient method to calculate the heat flux values. This method is substantially less computational demanding and gives results within a good accuracy. Inspection of empirical heat transfer correlation available in literature such as Bartz or Dittus-Böltner indicates that the heat transfer coefficient scales by the pressure to the power of 0.8. For the results discussed here, the temperature of the combustion products (3000 K) is significantly larger than the measured axial wall temperature variation (ca. 5 K , for

the 20 bar case). Therefore, for the first approximation, the wall heat flux should also scale to the $P_c^{0.8}$, since the wall heat flux is proportional to the product of heat transfer coefficient and the temperature difference between the fluid and the wall. The results of this non-dimensional analysis are shown in Fig. 12. It can be seen that all heat flux profiles collapse to a single curve and all show the same quantitative trends, which means that the heat flux in a gas-gas injector combustor correlates well with the pressure as predicted. The fact that the pressure profile remains similar across pressures, suggests that the dynamic structures with the combustion flows are pressure independent if all factors remain constant. Similar conclusions are also obtained for GOX/GH_2 in [5]- [17].

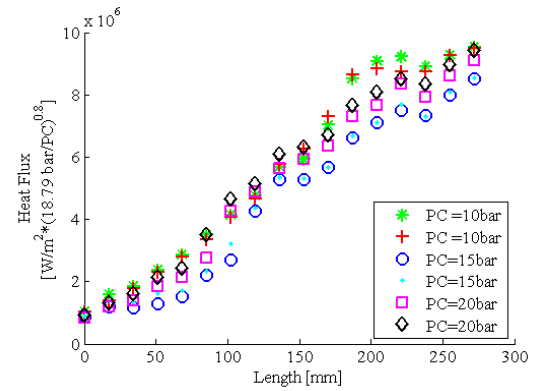


Fig. 12: Normalization of the heat flux profile, $O/F = 3.4$ at t_1

4. Thermtest Simulations

The need for a reliable prediction of the thermal behavior of the institute rocket combustion chambers has led to the development of the engineering tool Thermtest at TUM [6]. Thermtest allows the simulation of steady as well as transient thermal behavior of cooled or uncooled structures over a wide scope of chamber materials and cooling fluids. While the heat conduction inside the chamber material is solved by a 3D finite difference method, the convective heat transfer is implemented by empirical Nusselt correlations. The advantage of this approach is a satisfying accuracy maintaining a reasonably fast simulation of the conjugate heat transfer from the hot gas into the cooling fluid. Thermtest utilizes 1D hot gas properties acquired from the NASA computer program CEA2 of Sanford Gordon and Bonnie McBride [18]. The evolution of temperature caused by reaction kinetics and atomization processes is generally neglected as it is not taken into account in CEA2. The fluid properties needed for heat transfer calculations

near the hot chamber wall are obtained assuming an equilibrium composition frozen reactions temperature-pressure-problem. The hot wall heat transfer coefficient is usually calculated from a modified formulation proposed by Sinyarev [19]. Information on Thermtest as well as a comparison with experimental data and calculations from commonly available CFD code has been published [20]. The implementation of the propellant combination methane/oxygen and the adaption to the new injector characteristic and chamber design has required code adaption and validation. Results of the temperature field of a chamber cross section at $x = 300\text{ mm}$ (where $x = 0$ is at the faceplate) are shown in Fig. 13. Inspired by work of [21], a correc-

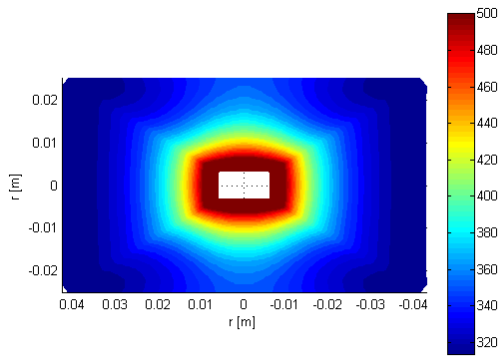


Fig. 13: Temperature distribution at $z = 300\text{ mm}$, $P_c = 20\text{ bar}$, $O/F = 3.4$ at t_1

tion function for the heat load characteristic of generic coaxial injector elements has been applied, in order to take into account the injector mixing behavior. The complete correlation is presented in Eq. 8. The hot gas film coefficient is described with three parameters: C_1 , C_2 and l_{max} . In order to account for the reduced heat transfer at the beginning of the combustion chamber, where the combustion evolves, the heat flux is shaped as a function of the axial coordinate z . The length l_{max} is the axial position where the heat transfer is at its maximum value and the combustion can be considered to be finished.

$$\alpha_{w,corr} = c_1 \alpha_{w,0} \left((1 - c_2) + c_2 \tanh \left(\frac{z}{l_{max}} \pi \right) \right) \quad (8)$$

The values of the parameters are established via an optimization problem based on the experimental data. Calculated and measured temperatures are compared and the error between these two values is minimized. The error is normalized over the number of experimental tests and sensors taken into account. Simulation results obtained with the optimization procedure are

shown in Fig. 14 where it is possible to recognize the characteristic behavior for a heat-sink rocket over time: the heat flux decreases during the hot run due to the structural temperature increase. The heat flux profile

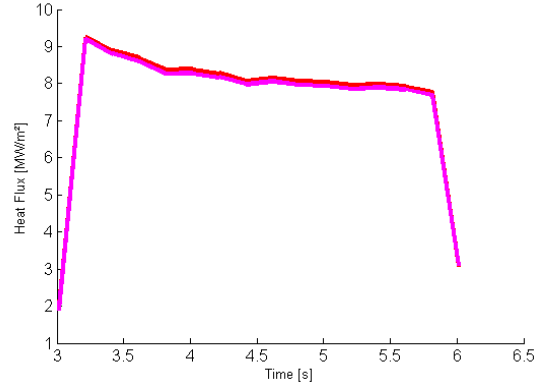


Fig. 14: Heat flux vs time at $z = 273\text{ mm}$, $P_c = 20\text{ bar}$
 $O/F = 3.4$

along the chamber axis is reported in Fig. 15. The tem-

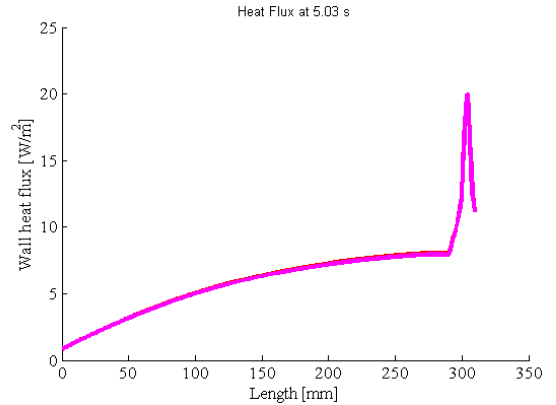


Fig. 15: Heat flux along the chamber axis, $P_c = 20\text{ bar}$
 $O/F = 3.4$

perature profile along the chamber axis is plotted in Fig. 16 at time t_1 . The results obtained from Thermtest simulation are compared with experimental ones for thermocouples at 3 different depths in the chamber wall. Results obtained show a good agreement with the experimental data both in terms of absolute values and trend.

5. Large Eddy Simulation of the Subscale Combustion Chamber

Numerical Setup and Cstrategy

A parallel numerical effort has been conducted to simulate the shear coaxial injector experimentally studied. The details of the facility and the injector and combustor assembly is as in the above experimental discussion.

Table 4: Adiabatic flame temperature adjustment

Mechanism	α_{diss}	T [K]		Flame Speed [m/s]
GRI 3.0	-	Case A	Case B	
CH4_BFER _{baseline}	0.0	3441.9	3285.9	2.55
CH4_BFER _{adjusted}	0.2319	3441.9	3261.8	1.49

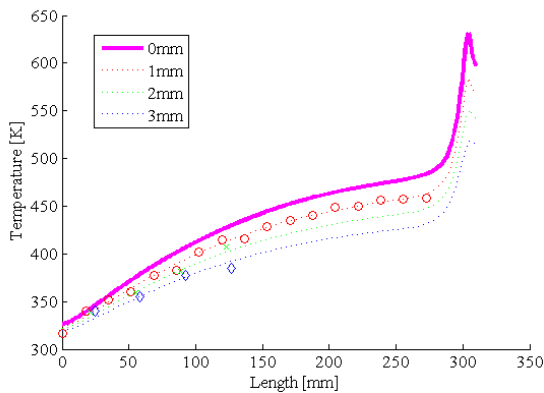
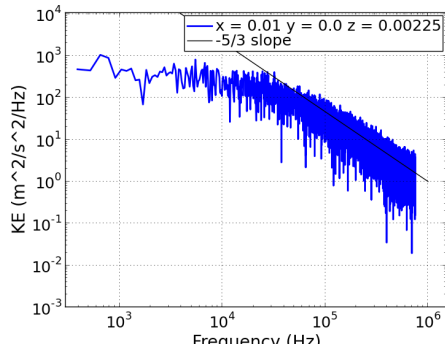


Fig. 16: Heat flux vs time at $z = 273 \text{ mm}$, $P_c = 20 \text{ bar}$, $O/F = 3.4$

The present work focuses only on a truncated injector but simulate the entire combustor including the choked nozzle. The simulation strategy employs large-eddy simulation (LES) using Georgia Tech's code LESLIE. This numerical solver is a well established finite-volume, block-structured parallel solver and has been used for similar studies in the past [22, 23]. Briefly, the Favre-filtered compressible, multi-species LES equations are closed using an eddy viscosity closure for which a transport equation for the subgrid kinetic energy is solved along with the LES equations. A hybrid upwind-central 2^{nd} order accurate (in space and time) is employed that switches automatically and dynamically between a 3^{rd} order MUSCL scheme in regions of large density gradients and a central scheme in regions of smooth flows. A two-step, five species (CH_4 , O_2 , CO_2 , CO , and H_2O) reduced mechanism developed earlier for $\text{CH}_4 - \text{O}_2$ mechanism [24] for use with oxy-methane is used here. As shown here although the original model was successful in another high-pressure oxy-methane combustion simulation [25] for the current test conditions still requires some adjustments due to the differences in operating conditions. Some attempt is reported below towards this assessment. The mechanism is employed with a thermally perfect equation of state and power-law transport models. Another issue not yet addressed is subgrid scale turbulence effect

on reaction kinetics and so the filtered reaction rates are obtained in terms of the resolved flow variables. Since the current solver is explicit in time and grid is well refined, the chemical time-scale for this reduced mechanism is much larger than the CFL time-scale employed and therefore, this strategy is considered reasonable at this time. Two cases at 20 bar with O/F mass ratios 2.66 and 3.48 have been selected for the LES study. Table 3 lists both operating conditions, including mass flow rates, temperatures, and the momentum flux ratio (J) and velocity ratio (VR) of the fuel to the oxidizer. The reactant temperatures are as measured at the inlet plane in the simulations. Analysis of the kinetics model for these operating conditions shows that the original 2-step mechanism over-predicts the flame temperature and therefore, needs to be modified. The current strategy is crude but it serves to demonstrate the sensitivity of the predictions to finite-rate kinetics. A factor, α_{diss} is introduced to rescale the total heat of formation. This factor is determined by comparison to the *GRI3.0* full mechanism predictions of the adiabatic flame temperature and procedure is as outlined in [25]. The α_{diss} is tuned to match the equilibrium temperature for *CaseA* (O/F ratio 2.66), and additionally, the Arrhenius rate coefficients of the first reaction is changed to match the laminar flame speed at stoichiometry. The resulting adiabatic flame temperature and flame speed are shown in Table 4. There is no perfect agreement and so the kinetics closure is still an unresolved issue for this study, as will be obvious from these results. The inflow boundary conditions use constant mass Navier Stokes Characteristic Boundary Conditions (NSCBC) [26] to mimic the constant mass flow conditions at the experimental inlet, while the outflow is supersonic. The walls are no-slip and adiabatic, and while the neglected heat flux is expected to cause an increase of the mean chamber pressure, it should provide a reasonable approximation of the flame structure. The shear layer is resolved with 17 grid points with spacing of around $30 \mu\text{m}$, which appears sufficient to resolve the shear-layer turbulence. The resolved turbulence kinetic energy spectra in the shear layer at a location one millimeter downstream,



(a) Kinetic energy spectrum at $x = 1$ mm in the shear layer



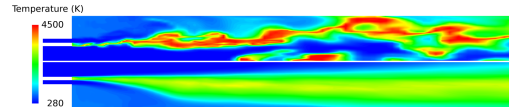
(b) Pope Criteria, $M_{res} = 20\%$ isoline in black

Fig. 17: LES Quality Assessment

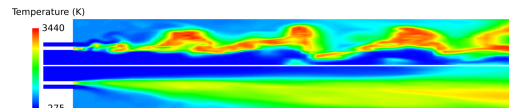
shown here in Fig. 17(a) demonstrates a reasonable $-5/3$ slope in the resolved inertial range. An additional measure of the LES quality using the so-called Pope's Criteria [27] (the ratio of the sub-grid kinetic energy to the total kinetic energy) considers 20% as an upper limit for a realistic LES. Analysis of the current results Fig. 17(b) shows that the current grid resolution in the injector and flame anchoring regions is well below this limit and so is acceptable for a LES.

Results and Discussion

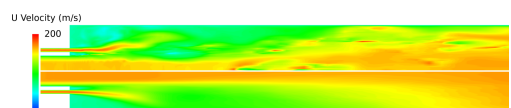
Four simulations are discussed here: two test conditions (O/F : 2.6 and 3.4) and two finite rate kinetics (the original model [24] and the modified model). All other conditions are held fixed as noted above. Time-averaged fields have been obtained by averaging over 5 flow through times of the instantaneous flow field for each case. The instantaneous (top half) and time-averaged (bottom half) views of the flow fields are compared in some of the following figures. Fig. 18 compares the instantaneous and time-averaged temperature and axial velocity features in a central plane for *Case A* using the two kinetics models. The results for *Case B* are qualitatively similar and not shown. The temperature contours show that the flame holds on the oxidizer post tip, as expected for both cases but that the unmodified chemistry predicts temperatures that are nearly 30% higher. However, flow features (especially the time-averaged) are similar. The mean axial velocity field shows very similar recirculation region at the base of the step and the extent of the shear layer is very similar. The CH_4 mass fraction field for



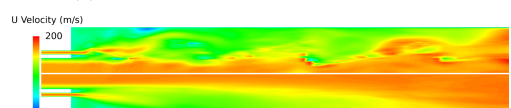
(a) Temperature, Baseline Chemistry



(b) Temperature, Modified Chemistry

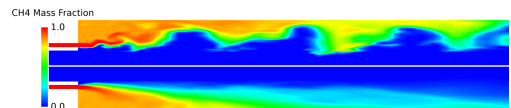


(c) Axial Velocity, Baseline Chemistry

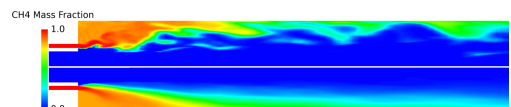


(d) Axial Velocity, Modified Chemistry

Fig. 18: Instantaneous (top half) and mean (bottom half) iso-contours of flow variables, *Case A*



(a) *Case A*

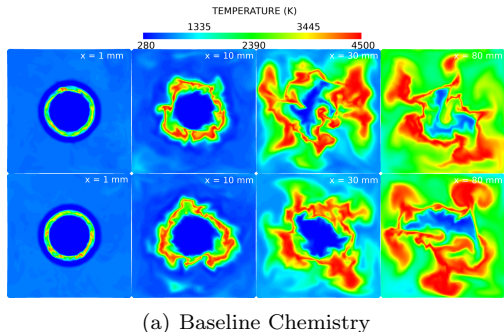


(b) *Case B*

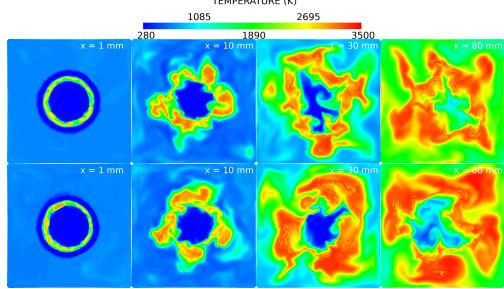
Fig. 19: Instantaneous (top half) and mean (bottom half) iso-contours of CH_4 mass fraction, with modified chemistry

the two operating cases (but using the modified kinetics) are compared in Fig. 19 and shows that some unreacted fuel remains trapped in the recirculation region. Analysis and/or data are still needed to verify this observation. Instantaneously, *Case A* shows more unreacted fuel further downstream along the wall.

In the spanwise direction, the two mechanisms predict very similar 3D structure of temperature contours, as shown Fig. 20 but the scales are very different. In addition to a higher peak temperature in the baseline chemistry the peak temperature regions are also significantly thinner whereas the adjusted mechanism appears to produce a more distributed temperature field downstream. The cool oxidizer core appears to stay intact further downstream in *Case B*, for both mechanisms. Table 5 and Fig. 21(a) show that the mean



(a) Baseline Chemistry



(b) Modified Chemistry

Fig. 20: Spanwise temperature for *Case A* (Top) vs. *Case B* (Bottom) for both chemistry mechanisms. The sequence from left to right are at $x = 0, 10, 30$, and 80 mm in the axial distance from the dump plane.

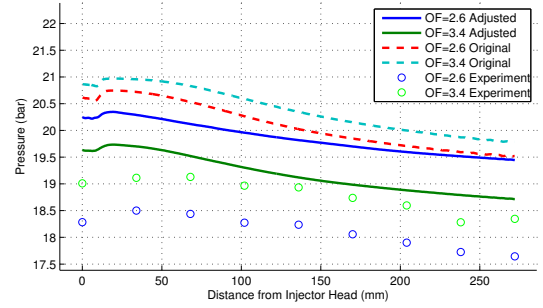
Table 5: Mean wall chamber pressures

O/F Ratio	\bar{p}_{Exp} [bar]	\bar{p}_{Sim} [bar] Modif. Chem.	\bar{p}_{Sim} [bar] Base. Chem.
3.48	18.8	19.2	20.3
2.66	18.1	19.8	20.1

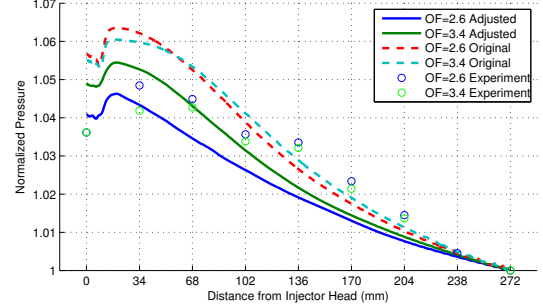
pressure along the wall is over predicted by around 10%. When normalized by the mean chamber pressure ($(p - \bar{p})/\bar{p}$) as in Fig. 21(b) the agreement in the trend appears reasonable. The modified kinetics appear to provide a better agreement for *Case B* but the discrepancy between the measured and predicted data still needs to be assessed.

6. Conclusion

Experiments are conducted over a large range of pressure (5 to 20 bar) and mixture ratio (2.6 to 4.0) in order to satisfy the need for a major understanding of the injection and combustion processes and of more reliable prediction of the thermal behavior for the propellant combination methane-oxygen. A single-element combustion chamber is designed and tested. Detailed wall temperature measurements and derived heat flux



(a) Raw values



(b) Normalized by end value

Fig. 21: Wall pressure comparison

data sets are obtained for GOX/GCH4. These data sets are valuable for both injector design and code validation. Due to the important multidimensional effects characterizing the geometry of the chamber and the transient nature of the hardware, specific methods for heat flux calculations have been considered. Temperature and heat flux traces show that the combustion process is accomplished towards the end of the chamber. The temperature and the chamber wall temperature distributions seem to have no direct pressure dependence. The lack of pressure dependence and only slight dependence on the propellant injection velocities suggests that the basic dynamic structures of the combustion process are mainly dominated by the injector and chamber geometry. The same trend was observed for all investigated load points. Simulations, conducted with Thermtest, shows good agreement with the experimental results. An optimization, according to the test data, of the heat transfer model in order to match the injector characteristics is performed and it shows to approximate the injector thermal behavior.

Acknowledgement

Part of the present work has been supported by students of the TUM, namely Felix Schily. Furthermore, the authors like to thank Christian Bauer for the sup-

port provided and Dr. Suslov (DLR Lampoldshausen) for the supervision.

References

- [1] D. Preclik, G. Hagemann, O. Knab, C. Maeding, D. Haeseler, Oskar Haidn, A. Woschnak, and M. DeRosa. LOX-Hydrocarbon Preparatory Thrust Chamber Technology Activities in Germany. *AIAA-2005-4555, 41st AIAA/ASME/SAE/ASEE Joint Propulsion Conference & Exhibit*, July 10th to 13th.
- [2] H. Burkhart, M. Sippel, A. Herbertz, and J. Klevanski. Kerosene vs Methane: A Propellant Trade-off for Reusable Liquid Booster Stages. *Journal of Spacecraft and Rockets*, 41(5):762–769, 2004.
- [3] A. Goetz, C. Maeding, L. Brummel, and D. Haeseler. Application of non-toxic propellants for future launch vehicles. *AIAA-2001-3546*, 2001.
- [4] B. Chehroudi, D. Talley, and E. Coy. Visual characteristics and initial growth rates of round cryogenic jets at subcritical and supercritical pressures. *Physics of Fluids*, 14(2):850, 2002.
- [5] W. Marshall, S. Pal, R. Woodward, and R. Santoro. Benchmark Wall Heat Flux Data for a GO₂/GH₂ Single Element Combustor. *41st AIAA/ASME/SAE/ASEE Joint Propulsion Conference & Exhibit*, (AIAA 2005-3572), 10 - 13 July 2005.
- [6] C. Kirchberger, G. Schlieben, and O.J. Haidn. Assessment of Analytical Models for Film Cooling in a Hydrocarbon/ GOX Rocket Combustion Chamber. *JPC*, 2012.
- [7] A. Conley, A. Vaidyanathan, and C. Segal. Heat Flux Measurements for a GO₂/GH₂ Single-Element, Shear Injector. *Journal of Spacecraft and Rockets*, 44(3):633–639, 2007.
- [8] G. Jones, C. Protz, B. Bullard, and J. Hulkka. Local Heat Flux Measurements with Single Element Coaxial Injectors. *42nd AIAA/ASME/SAE/ASEE Joint Propulsion Conference & Exhibit*, 9 - 12 July 2006(AIAA 2006-5194).
- [9] Aravind Vaidyanathan, Jonas Gustavsson, and Corin Segal. One- and Three-Dimensional Wall Heat Flux Calculations in a O₂/H₂ System. *Journal of Propulsion and Power*, 26(1):186–189, 2010.
- [10] A. Vaidyanathan, J. Gustavsson, and C. Segal. Heat Fluxes/OH PLIF Measurements in a GO₂-GH₂ Single-Element, Shear Injector. *43rd AIAA/ASME/SAE/ASEE Joint Propulsion Conference & Exhibit*, (AIAA 2007-5591), 8 - 11 July 2007.
- [11] M.P. Celano, S. Silvestri, G. Schlieben, C. Kirchberger, and H.J. Haidn. Injector Characterization for a GOX-GCH₄ Single Element Combustion Chamber. *5TH EUROPEAN CONFERENCE FOR AERONAUTICS AND SPACE SCIENCES (EUCASS)*, 2013.
- [12] D. Suslov, Alexander Woschnak, J. Sender, M. Oschwald, and O. Haidn. Test Specimen Design and Measurement Technique for Investigation of Heat Transfer Processes in Cooling Channels of Rocket Engines Under Real Thermal Conditions. *39th AIAA/ASME/SAE/ASEE Joint Propulsion Conference and Exhibit*, 20-23 July 2003.
- [13] J.M. Locke, S. Pal, and R.D. Woodward. Chamber Wall Heat Flux Measurements for a LOX/CH₄ Propellant Uni-Element Rocket. *43rd AIAA/ASME/SAE/ASEE Joint Propulsion Conference & Exhibit*, 8 - 11 July 2007.
- [14] Clifford E. Frieler Gré Werner J. A. Dahm and tar Tryggvason. Vortex structure and dynamics in the near field of a coaxial jet. *J. Fluid Mech.*, 241:371–402, 1992.
- [15] S.A. Schumaker and J.F. Driscoll. Coaxial turbulent jet flames: Scaling relations for measured stoichiometric mixing lengths. *Proceedings of the Combustion Institute*, 32(2):1655–1662, 2009.
- [16] S. Alexander Schumaker and James F. Driscoll. Mixing properties of coaxial jets with large velocity ratios and large inverse density ratios. *Physics of Fluids*, 24(5):055101, 2012.
- [17] Alex Conley, Aravind Vaidyanathan, and Corin Segal. Heat Flux Measurements for a GO₂/GH₂ Single-Element, Shear Injector. *Journal of Spacecraft and Rockets*, 44(3):633–639, 2007.
- [18] McBride and Gordon. *Computer Program for Calculation of Complex Chemical Equilibrium Compositions and Applications*.
- [19] G.Schmidt. Technik der Flüssigkeits-Raketentriebwerke. *DaimlerChrysler Aerospace*, Munich,, 1999.

- [20] C. Kirchberger, R. Wagner, H. P. Kau, and et al. Prediction and Analysis of Heat Transfer in Small Rocket Chambers.
- [21] A. Ponomarenko. Thermal Analysis of Thrust Chambers.
- [22] M. Masquelet and M. Suresh. Large eddy simulation of flame-turbulence interactions in a shear coaxial injector. *Journal of Propulsion and Power*, 26:942–935, 2010.
- [23] F. Genin and S. Menon. Studies of shock/turbulent shear layer interaction using large-eddy simulation. *Computers and Fluids*, 39:800–819, 2010.
- [24] B. Franzelli, E. Riber, L.Y.M. Giquel, and T. Poinsot. Large-Eddy Simulation of combustion instabilities in a lean partially premixed swirled flame. *Combustion and Flame*, 159(2):621–637, 2010.
- [25] N. Guézennec, M. Masquelet, and S. Menon. Large Eddy Simulation of Flame-Turbulence Interactions in a LOX-CH₄ Shear Coaxial Injector. *AIAA Paper*, pages 2012–1267, 2012.
- [26] T. Poinsot and S.K. Lele. Boundary conditions for direct simulations of compressible viscous flows. *Journal of Computational Physics*, 101:104–129, 1992.
- [27] S. Pope. Turbulent Flows. *Cambridge University Press*, 2000.

Addendum 6

LES of GCH₄/GOX, Shear-Coaxial, Single Element, High Pressure Rocket Combustor: Effects of Thermal Condition and Chemical Kinetics

R. Ranjan and S. Menon

School of Aerospace Engineering, Georgia Institute of Technology, Atlanta, GA 30332

1 Introduction

The design of liquid rocket engines is dictated by several requirements such as a stable combustion, low operating cost, low emission characteristics and high performance throughput under a range of operating conditions. Therefore, the elements of these engines such as type of propellant, injector design, thermal conditions of the combustion chamber wall etc., play an important role on the overall performance. Rocket engines that employ liquid oxygen (LOX)/hydrocarbon as propellant is increasingly becoming popular as they tend to satisfy most of the aforementioned requirements in comparison to the engines that employ cryogenic propellants [1]. In such engines, LOX/methane (CH₄) is considered as a more appropriate option due to its various features such as high specific energy density and specific impulse and better overall performance [2, 3]. Apart from the propellant, the injector technology also plays a crucial role in the development of a liquid rocket engine as it affects the performance by altering the flame and flow dynamics and stability of the combustor. For example, the oxidizer injector length can lead to stable/unstable combustion behavior of a shear coaxial high pressure combustor [4]. In general, propellants are injected into the combustion chamber in a coaxial manner in a supercritical state, where they act more like dense gases, thus allowing for application of gas-gas scaling laws for coaxial jets [5, 6]. Therefore, understanding the gas-gas mixing and its interaction with other transport processes becomes important. Finally, the thermal conditions on the chamber wall also affects the reactive flow dynamics due the amount of heat-loss occurring through the chamber walls, which directly affects the operating pressure. Therefore, the overall performance of the engine depends upon an interplay of the type of propellant, injector design and heat-transfer characteristics of the chamber wall. Hence, understanding the mixing process and the heat-transfer characteristics of a coaxial injector based combustion chamber under different operating conditions is very relevant for design improvement of rocket engines. However, both experimental and numerical methods face several challenges in their ability to investigate physical and chemical mechanisms occurring within the combustion chamber. For example, experimental measurements become very challenging under the operating conditions of a liquid rocket engine and therefore, the measurements are often limited to few quantities. On the other hand numerical methods suffer from uncertainties related to geometrical modeling, boundary conditions and the turbulence closure. To understand such complex processes, large-eddy simulation (LES) can serve as a promising design tool for predictive analysis. However, a comprehensive validation of LES results with the measured experimental data is crucial for reliability on such predictions.

LES investigation in the past, of a single element, shear-coaxial, high pressure combustor at two oxygen to fuel mixture ratios have shown promising results where the stable combustion was predicted in agreement with the experimental observations [7]. The study employed a reduced 5-species finite-rate chemical kinetics used in previous LES studies of combustors [8, 9] and showed good agreement with the wall pressure distribution. However, some discrepancies were also observed in comparison to experiments due to use of a simplified chemistry and adiabatic thermal conditions on the chamber wall. Recent extension of the study to

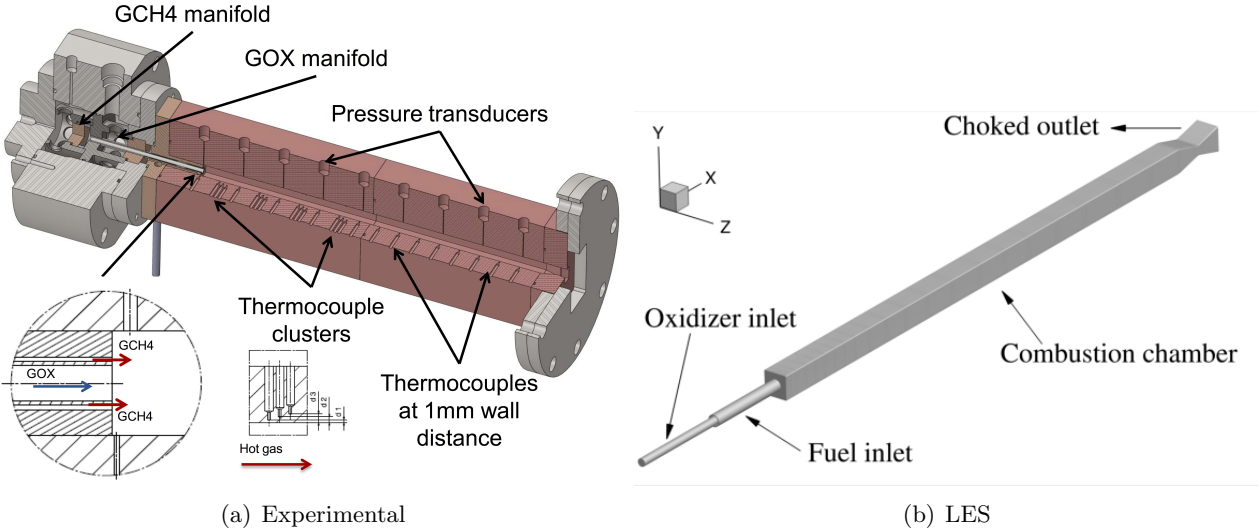


Figure 1: Experimental configuration (a) and computational domain used by LES (b) corresponding to the single element, shear-coaxial injector based combustor [7].

a reasonably complex, 8-species finite-rate chemical kinetics and use of an isothermal boundary conditions matching measured wall temperature distribution in an averaged sense, have shown improvements in quantitative predictions of the wall pressure distribution (discussed below). These results demonstrate the need of appropriate boundary conditions and chemical kinetics for reliable predictions by LES based investigation and prediction of the complex reactive flow dynamics within a high pressure combustor.

The objective of the ongoing study is to perform a comprehensive comparison of the results obtained from LES of a shear-coaxial, single element, high pressure combustor with the experimental data. In particular, the focus of the study is to characterize the role of heat-transfer occurring through the combustion chamber walls on the reactive flow physics and the flame dynamics. Another goal of the ongoing study is to analyze the role of finite-rate kinetics on the observed combustion behavior within the chamber. Such a detailed comparison will establish the predictive ability of LES to study thermal characteristics of high pressure rocket combustors.

This document is arranged as follows. Section 2 describes the reactive flow configuration and the test conditions. The details of numerical methodology and computational setup is presented in Sec. 3. Results from past investigations are briefly summarized in Sec. 4. Finally, the objectives of the currently ongoing study are detailed in Sec. 5.

2 Problem Description

Figure 1 shows the experimental configuration and the computational domain corresponding to the single element, shear-coaxial injector based combustion chamber that is considered in this study. The experiment is designed to analyze the heat transfer characteristics within a typical rocket combustion chamber so that extensive data can be provided for numerical validations. The test rig is hosted at Technische Universität München (TUM) and is a gaseous combustor, which employ a modular heat sink to investigate heat transfer mechanism and its effect on the flame dynamics. The length of chamber is $L = 303$ mm, and its cross section is square with area 12×12 mm 2 . The contraction ratio of the test rig is 2.5 and different operating pressures can be prescribed ranging from 20 bar to 100 bar. The coaxial injector have internal diameter 4 mm and 5 mm, respectively, for the oxidizer and the fuel. Note that the oxidizer post is flushed with respect to the injection face for simplicity. The computational domain comprises of the coaxial inlets of the same dimension as that by used by experiments flushed to the combustion chamber of square cross

section ending with a choked outlet. The inflow boundaries can be modeled using characteristic boundary conditions [10] with prescribed mass flow-rates, species mass fractions and temperature. The outflow is choked through the nozzle and therefore, relatively simpler supersonic conditions can be employed at the nozzle exit. No-slip with appropriate thermal conditions (adiabatic/isothermal) can be specified on the chamber walls. In the past studies [7], adiabatic thermal condition was used on the chamber walls. In addition, isothermal or temperature profile will be specified on the chamber walls.

Case	OF ratio	P_{ox} -	P_f	T_{ox}	T_f	\dot{m}_{ox}	\dot{m}_f
		(bar)	(bar)	(K)	(K)	(kg/s)	(kg/s)
TFC-R-20-26-30-10	2.62	26.4	24.4	278	269	0.045	0.017

Table 1: Details of the test condition at the oxidizer and fuel inlets.

Table 2 summarizes the test conditions at the oxidizer and the fuel inlets that include pressure at the inlet of the oxidizer (P_{ox}) and the fuel (P_f), inlet temperature of the oxidizer ($T_{\text{ref,ox}}$) and the fuel ($T_{\text{ref,f}}$), and mass flow rate of the oxidizer (\dot{m}_{ox}) and the fuel (\dot{m}_f). Note that in this study fuel is considered to be methane (CH_4) the oxidizer is pure oxygen (O_2). The reference pressure P_{ref} is set to 20 bar for the chamber.

3 Numerical Methodology, Setup Details

The numerical methodology is based on the well-established, second-order accurate (in both space and time) finite-volume solver for the unsteady Favre-filtered multi-species compressible Navier-Stokes equations [11]. A hybrid scheme, which switches between a second-order-accurate central scheme and a third-order-accurate MUSCL (Monotone Upstream-centered Schemes for Conservation Laws) scheme [12] is employed. A localized dynamic switch based on pressure and density gradients determines the spatial discretization scheme to use locally [12, 13]. Past studies have shown that the hybrid approach can capture regions of high gradients (as in shocks or thin shear layers between fuel and oxidizer) and also regions of turbulent fluctuations away from these strong gradients accurately [11–13]. The subgrid-scale (SGS) momentum and energy fluxes are closed using a subgrid eddy viscosity model, which is obtained using the local grid filter Δ and the subgrid kinetic energy k^{sgs} . An additional transport equation is solved for k^{sgs} and localized dynamic evaluation is used to obtain all the model coefficients [11, 14]. The subgrid mixing and turbulence-chemistry interaction is based on the linear eddy mixing (LEM) model [15]. Details of the LES equations, numerical method and these closures are presented in several articles cited earlier and therefore avoided here, for brevity.

In the future studies, a moderately complex finite-rate kinetics will be employed, for example, 8-species [16] or 13 species [17] methane-air mechanisms. In past studies, a 2-step 5-species (CH_4 , O_2 , H_2O , CO_2 and CO) reduced kinetics have provided reasonably accurate results [7–9]. The same mechanism has been used in a recent LES study of combustion instability phenomenon in a high-pressure, shear-coaxial injector combustor [4, 9], where reasonable agreement was observed in comparison to experimental investigations. However, in future studies the role of chemical kinetics on the flame dynamics and heat transfer characteristics will be analyzed by employing moderately complex chemical kinetics. The adiabatic flame temperatures and laminar flame speed predicted by 8-species and 13-species mechanisms compare well with the detailed GRI 3.0 mechanism.

Figure 2 (a) shows the computational grid in the shear-layer region on the symmetry plane. Overall, the multi-block structured grid comprises of 1248 blocks and approximately 3.6 million finite volume cells, where the emphasis is on resolving the regions of shear-layers and intense heat-release. The grid is suitable to perform LES investigation as demonstrated by the well known Kolmogorov’s $-5/3^{\text{rd}}$ slope in the resolved inertial range [18] for the resolved turbulent kinetic energy spectrum in the shear layer shown in Fig. 2(b).

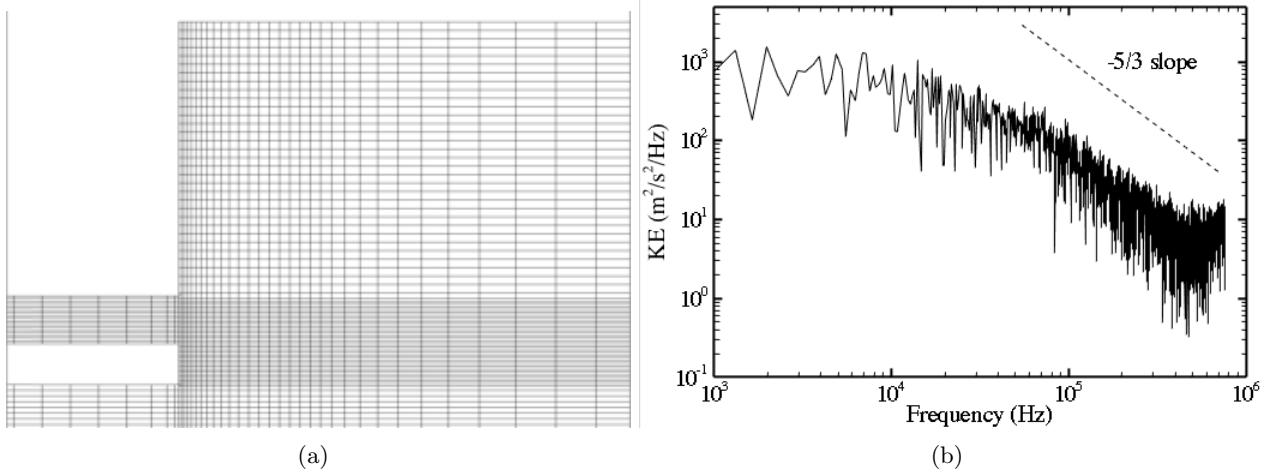


Figure 2: Computational grid on the symmetry plane in the shear-layer (a) and the resolved turbulent kinetic energy spectrum (b) in the shear layer at $(x, y, z) = (0.01, 0, 0.002)$ m [7].

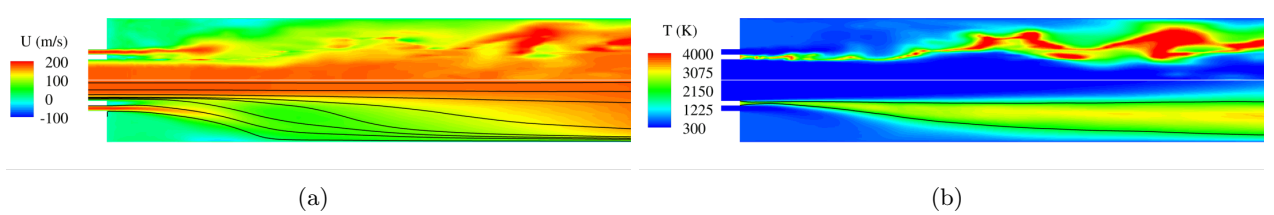


Figure 3: Contours of instantaneous and mean axial velocity and temperature fields on the symmetry plane for oxidizer fuel ratio of 2.6. Top and bottom halves correspond to instantaneous and mean quantities, respectively. Solid curves in subfigure (a) denote mean streamlines identifying the corner recirculation and the core region and in subfigure (b) denote $T = 2000$ K isoline to identify the flame region.

4 Results

In this section, we briefly describe some of the recent LES results obtained from further extension of the past study of the shear-coaxial single injector combustor for an oxidizer/fuel ratio of 2.6 [7]. These simulation show significant improvements in the results, which can be attributed to use of an isothermal boundary conditions ($T = 420$ K) on the chamber walls and use of a moderately complex (8-species) finite-rate chemical kinetics. Previously, an adiabatic condition was specified for the thermal boundary condition and a relatively simpler 5-species chemical mechanism was utilized.

Figure 3 shows contours of the reactive flow fields on the symmetry plane. The top- and bottom-halves correspond to the instantaneous and the mean fields, respectively. The contours of the axial velocity shown in Fig. 3(a) show presence of a shear-layer near the fuel injector with a jet like flow structure in the core of the chamber emanating from the oxidizer injector. In addition, a corner recirculation zone that helps in flame anchoring is also observed. The presence of the corner recirculation zone is highlighted by the mean flow streamlines overlaid on the mean axial velocity contours. The temperature field shown in Fig. 3(b) highlights the bounding region of flame, which appears to be a compact near the fuel injector, but spreads in the downstream direction towards the core and walls of the chamber. This is highlighted by $T = 2000$ K isoline, which is considered to bound the flame region. The heat transfer through the chamber walls is non-negligible as apparent from the temperature contours, which show presence of strong gradients in the temperature field at downstream locations along the axial direction. Clearly, the heat-flux through the

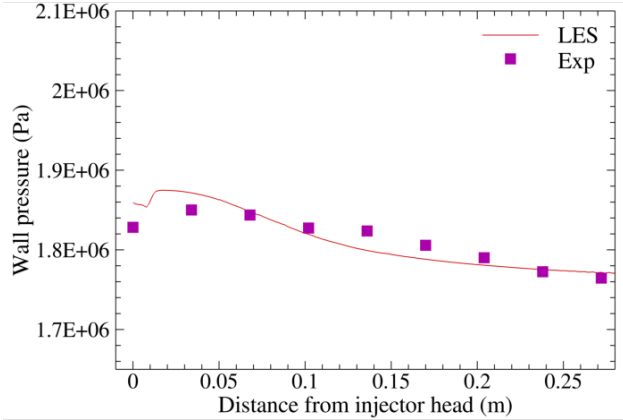


Figure 4: Wall pressure distribution obtained from LES (solid curve) and compared with experimental data (symbols).

chamber walls affects the compactness of the flame structures.

Figure 4 shows axial variation of the time-averaged pressure field obtained from LES in comparison to the measured experimental data. We observe a good agreement with the experimental data with some discrepancies near the injector head. However, compared to the profile obtained from simulations employing adiabatic conditions, the results have improved significantly, thus illustrating the role of heat-transfer characteristics on the flame dynamics within the combustion chamber. Further quantitative analysis is currently underway to characterize the role of kinetics and turbulence chemistry closure on these results.

5 Summary

This ongoing study is aimed to perform a comprehensive validation of the LES results by comparing them with the measured experimental data. The test conditions will be the same as summarized in Sec. 2 to closely match the experiments. The numerical methodology and the computational setup will be the same as discussed above in Sec. 3. However, the future simulations will be focused on quantitatively characterizing the role of heat-transfer and detailed chemical kinetics. In particular, the validation study will be performed by comparing axial profiles of the chamber wall pressure and the heat-flux across the chamber walls. As discussed above, heat-flux plays an important role in affecting the observed flame structure. The role of chemical kinetics on the flow and flame dynamics within the combustor will be analyzed by comparing contours of axial velocity, temperature and species fields on the symmetry plane for three different chemical mechanisms with increasing degree of complexity. These mechanism will include 5, 8 and 13 species, respectively. In addition, the completeness of combustion will be quantified in terms of the axial evolution of the mass fractions of the combustion products and the OH radical. To achieve these objectives, the LES framework as mentioned above will be employed. However, in the past studies the turbulence-chemistry interaction was ignored, referred to as LES with laminar chemistry. However, in some of the future simulations the turbulence-chemistry interaction will be included by employing LEM as the mixing and turbulence-chemistry interaction closure, referred as LEMLES formulation.

Table 5 lists the cases that are currently being considered. Note that the difference in these cases are only due to the employed numerical methodology, as the test conditions will remain the same across these cases. The classification is based on thermal condition (isothermal or profile), type of chemical mechanism and type of turbulence chemistry closure. The first set of simulations labeled as A1 through A3, will identify the suitable chemical mechanism, where Case A3 will serve as a reference case. Based on the selected mechanism ‘n-species’, two additional simulations labeled as cases B1 and B2 will be conducted to characterize the effect of an averaged temperature specified on the chamber wall in comparison to a profile

Case	Thermal condition	Chemical mechanism	Turbulence chemistry
A1	Isothermal	5-species	LES with laminar chemistry
A2	Isothermal	8-species	LES with laminar chemistry
A3	Isothermal	13-species	LES with laminar chemistry
B1	Isothermal	n-species	LEMLES
B2	Profile	n-species	LEMLES

Table 2: Summary of the test cases.

of the temperature field imposed on the chamber walls. Here, the profile will be based on the measured experimental data. Overall, these set of simulations will demonstrate the predictive ability of LES for reactive flow dynamics within a high pressure rocket combustor so that LES can be used as a reliable design tool.

References

- [1] D Preclik, G Hagemann, O Knab, C Mading, D Haeseler, Oskar Haidn, A Woschnak, and M DeRosa. Lox/hydrocarbon preparatory thrust chamber technology activities in germany. *AIAA-2005-4555*, 2005.
- [2] A Gotz, C Mading, L Brummer, and D Haeseler. Application of non-toxic propellants for future advanced launch vehicles. *AIAA-2001-3546*, 2001.
- [3] Holger Burkhardt, Martin Sippel, Armin Herbertz, and Josef Klevanski. Kerosene vs. methane: a propellant tradeoff for reusable liquid booster stages. *Journal of spacecraft and rockets*, 41:762–769, 2004.
- [4] S Srinivasan, R Ranjan, and S Menon. Flame dynamics during combustion instability in a high-pressure, shear-coaxial injector combustor. *Flow, Turbulence and Combustion*, 94:237–262, 2015.
- [5] Gregg Jones, Christopher Protz, Brad Bullard, and James Hulka. Local heat flux measurements with single element coaxial injectors. *AIAA-2006-5194*, 2006.
- [6] Alex Conley, Aravind Vaidyanathan, and Corin Segal. Heat flux measurements for a go2/gh2 single-element, shear injector. *Journal of Spacecraft and Rockets*, 44:633–639, 2007.
- [7] M. P. Celano, S. Silvestri, G. Schlieben, C. Kirchberger, O. J. Haidn, T. Dawson, R. Ranjan, and S. Menon. Experimental and numerical investigation of GOX-GCH₄ shear-coaxial injector element. *SP-2014-2969417*, 2014.
- [8] B. Franzelli, E. Riber, L. Y. M. Gicquel, and T. Poinsot. Large eddy simulation of combustion instabilities in a lean partially premixed swirled flame. *Combust. Flame*, 159:621–637, 2012.
- [9] N. Guézennec, T. Dawson, P. Sierra, and S. Menon. Flame holding dynamics during combustion instability in a shear coaxial injector. In *In 8th Int. Symp. On Turbulence and Shear Flow Phenomena*, Poitier, France, 2013.
- [10] T. J. Poinsot and S. K. Lele. Boundary conditions for direct simulations of compressible viscous flows. *J. Comp. Phys.*, 101:104–129, 1992.
- [11] F. Génin and S. Menon. Simulation of turbulent mixing behind a strut injector in supersonic flow. *AIAA J.*, 48:526–539, 2010.

- [12] F. Génin and S. Menon. Studies of shock/turbulent shear layer interaction using large-eddy simulation. *Computers & Fluids*, 39:800–819, 2010.
- [13] M. Masquelet and S. Menon. Large eddy simulation of flame-turbulence interactions in a shear coaxial injector. *J. Propul. Power*, 26:924–935, 2010.
- [14] W.-W. Kim and S. Menon. An unsteady incompressible Navier-Stokes solver for large eddy simulation of turbulent flows. *Int. J. Numer. Meth. Fluids*, 31:983–1017, 1999.
- [15] S. Menon and A. R. Kerstein. The linear-eddy model. *Turbulent Combustion Modeling*, 95:175–222, 2011.
- [16] T. M. Smith and S. Menon. One-dimensional simulations of freely propagating turbulent premixed flames. *Combust. Sci. Technol.*, 128:99–130, 1997.
- [17] Ramanan Sankaran, Evatt R Hawkes, Jacqueline H Chen, Tianfeng Lu, and Chung K Law. Structure of a spatially developing turbulent lean methane-air bunsen flame. *Proceedings of the combustion institute*, 31:1291–1298, 2007.
- [18] S. B. Pope. *Turbulent flows*. Cambridge university press, 2000.

On the application of the time-domain admittance boundary condition in the LES of a high-pressure, shear-coaxial injector combustor

P. Tudisco^{1,*}, R. Ranjan², S. Menon³, S. Jaensch⁴, W. Polifke⁵

Abstract

We present application of the time-domain admittance boundary condition (TDABC) formulation [1, 2] in a large-eddy simulation (LES) for investigation of thermo-acoustic longitudinal instability in a single element, shear-coaxial, high pressure combustor. The TDABC formulation, a reduced-order method, provides a robust, reliable and alternative formulation to incorporate inflow/outflow boundary conditions for LES based investigation of complex reactive flow systems. It allows to incorporate effects of a domain of interest without explicitly solving for the reactive flow field within the considered domain. For example, in a multi-element, shear-coaxial system, the formulation provides a computationally efficient approach to analyze the reactive flow physics of the combustion chamber, without explicitly requiring modeling of the geometry of multiple injectors. Therefore, the method can be used to conduct parametric design studies of such systems where the injectors play a crucial role in the thermo-acoustic stability of the combustor. Here, we first present a detailed description of the TDABC formulation in the context of an LES and then use the developed framework to simulate reactive flow within a single element combustor, also referred as Continuous Variable Resonance Combustor (CVRC); a high- pressure, shear-coaxial injector combustor studied experimentally at Purdue University. A key feature of CVRC is that depending on the length of the oxidizer injector, the thermo-acoustic stability pattern is altered in the combustor. To demonstrate the effectiveness of the TDABC formulation in an LES, we consider the combustor with a truncated injector and simulate conditions equivalent of three different oxidizer injector lengths of 9 cm, 12 cm and 14 cm, which are known to exhibit, semi-stable, unstable and highly unstable behavior. The results obtained with the TDABC formulation are compared with the LES results obtained by actual modeling of the injector and a very good agreement for the limit cycle prediction, frequency, amplitude, mode and phase shapes and flame dynamics are obtained. It is shown that this method is able to capture the highly unsteady reactive flow physics and therefore, can be extended further to study multi-injector configurations, which are challenging and computationally expensive for LES investigation.

Keywords: Large eddy simulation, admittance boundary conditions, combustion instability, linearized acoustics

1. Introduction

Numerical simulations of combustion devices represent one of the most important research topic in computational fluid dynamics. In this view, the use of Large Eddy Simulation has been well established as the most promising tool for an accurate prediction of combustors behavior. In fact, LES represents a good compromise between the solution reliability and the computational time since a direct numerical simulation (DNS) of these components would require to solve the range of scales up to the Kolmogorov scale (or even lower as in the case of passive scalars). Also, different aspects are considered in a rocket engines design, such as a stable combustion, low operating cost, and high performance throughput under a range

* Corresponding author.

Email addresses: ptudisco3@gatech.edu (P. Tudisco), reetesh.ranjan@ae.gatech.edu (R. Ranjan)

¹Ph.D Student, Computational Combustion Lab., Georgia Institute of Technology, Atlanta

²Post Doc., Computational Combustion Lab., Georgia Institute of Technology, Atlanta

³Professor, School of Aerospace Engineering, Georgia Institute of Technology, Atlanta

⁴Ph.D Student, Lehrstuhl für Thermodynamik, TU München, Germany

⁵Professor, Lehrstuhl für Thermodynamik, TU München, Germany

of operating conditions. It is commonly accepted that combustion instabilities in rocket engines represents one of the most challenging issue, still not completely solved, both from a numerical and experimental point of view. This phenomenon, usually takes place in high pressure, combustors as the result of a nonlinear coupling between the unsteady heat release with the local pressure fluctuation. This coupling produces large-amplitude pressure oscillations first described by Rayleigh [3], and then adapted to rocket engines design in the remarkable work by Harrje [4]. Coupling between local heat release and pressure fluctuations can be produced by flame dynamics or hydrodynamic flow instability as discussed in the milestone works of Poinsot [5] and Candel [6]. In general, experimental investigation of this phenomenon can be very difficult, especially for full scale rocket combustors, because of the possibility of damage and explosion. Similarly detailed measurements of such flame/acoustics coupling exhibit non-trivial challenges due to the hot and high pressure environment. Usually, low and high frequency pressure fluctuations are available at some locations, providing information about the stable or unstable nature of the combustor. One important example that has been massively studied in recent years is the continuously variable resonating chamber (CVRC) [7–9], which consists of a gaseous oxygen, gaseous methane, shear coaxial injector whose length can be continuously varied. Depending on the injector length, the combustor shows spontaneous longitudinal instabilities as a result of the acoustic modes coupling of the injector and the chamber itself with the combustion heat release. This experimental rig has been used extensively as test bench to study turbulent combustion numerical codes[10–12], providing evidence of LES and DES to be promising tool in the prediction of instabilities in rocket engines.

However, there are some cases in which the use of LES still represents a very expensive procedure due to the grid size in certain portions of the computational domain, or, due to the need of model several micro-cavities. One example is the modeling of multi-injector face plate of liquid rocket engines. In fact, if several of injector cavities need to be accounted for, difficulties in geometry, grid size and generation, and therefore computational time may arise. On the other hand, accounting the presence of the injectors in a numerical simulation is of crucial importance as demonstrated by the CVRC. In other words, injector cavities must be modeled because they play an extremely important role in driving combustion instabilities due to the fact that they have their own acoustic response that couples with all the chamber combustion dynamics. For this reason, reduced order modeling (ROM) becomes an interesting tool, that can significantly reduce the cost of simulation of multi injectors combustion chambers and at the same time, retain the level of accuracy that is needed in order to be able to capture this phenomenon.

The purpose of the approach described in this work is to illustrate an hybrid boundary conditions technique for LES (but it can also be applied to DNS) which consists in the implementation of admittance boundary conditions. This method has been first described by Polifke [1] and Kaess [2], and it is currently under further development at Georgia Institute of Technology for engineering applications investigations, mainly related to the numerical simulation of unstable rocket engines. This approach is an extension of the Navier-Stokes characteristic boundary conditions (NSCBC) described by Poinsot and Lele [13], which treats the conservation equations at the boundaries as locally inviscid and one dimensional (LODI). Once the conservation equations are written in characteristic form, acoustic wave amplitudes, indicated as \mathcal{L}_i can be directly related with their direction of propagation and speed. Each characteristic wave can be specified at the boundary by using a relaxation coefficient [14], which ensures the fulfillment of mean flow primitive variables such as the velocity for an inflow or pressure for a subsonic outflow. However, it has been demonstrated that although this approach works well for the mean flow imposition, acoustic fluctuations are not always treated as desired for non-reflecting boundaries [1, 2]. Therefore, undesired and non-physical acoustic waves are produced at the boundaries, leading to an alteration of the acoustic field inside the domain, which is undesirable, especially in simulations where acoustics plays an important role as combustion instabilities. In order to avoid such behavior, the plane wave masking approach has been introduced by Polifke et al. [1]. Basically the incoming acoustic wave at the non-reflective boundary is explicitly removed from the characteristic wave. In this way the mean flow imposition and acoustic reflection are decoupled and can be satisfied separately. This technique offers a further application based on admittance boundary condition. In fact, this modified NSCBC approach offers the possibility to address not only waves at non reflecting boundaries, but also it allows to specify the reflected wave whenever the reflection coefficient is prescribed. Then, supposing that an injector, or more in general an acoustic cavity can be described as a linearized system [15–17], a reflection coefficient can be computed analytically, allowing to simulate the presence of this cavity at the boundary, without explicitly meshing it.

The use of admittance boundary conditions is not the unique way to reduce complexity of a numerical investigation. Another well know approach is the reduced basis model (RBM), which follows a projection

based approach dependent on a modal expansion [18]. The equation complexity is reduced by expanding the vector containing the conserved variables in a series, where the orthogonal modes are recovered offline from previous LES calculations. Although this method has been recognized as a powerful approach to simulate several engineering problems [19, 20], there is no clear evidence of its applicability for complex, turbulent combustion problems. The use of admittance boundary condition does not require any a priori LES calculation, and it demonstrated to work quite well at least for a single injector combustor.

The next objective is to apply this approach to multi-injectors combustion chambers, and test the predictability of combustion instabilities in sub-scale rocket engines, even in the supercritical regime. Another immediate approach that can extend this formulation concerns the second order modeling of injector cavities, which will account for friction and thermal acoustic losses caused by the acoustic boundary layer. This article is organized as follows. The LES formulation and the numerical methodology adopted in this study is described in Sec. 2. The time domain admittance boundary condition and the determination of an injector reflection coefficient are discussed in Sec. 2.2. The problem description and assessment of the computational setup are discussed in Sec. 4. Results for flame structure, time averaged fields and mode shapes are discussed in Sec. 5. Finally, the outcomes of the present study are summarized in Sec. 6.

2. LES formulation and numerical methodology

In this section, we briefly describe the governing equations and the employed numerical methodology for LES of reactive flow systems, which is adopted in the current study. Further details of the numerical framework are provided in cited references.

2.1. Governing equations

The motion of an unsteady, compressible, reacting fluid is governed by the multi-species compressible Navier-Stokes equations, which enforce conservation of mass, momentum, energy and species mass. From these balance equations, LES equations are derived through a spatial filtering operation. The flow variables are decomposed into the resolved and unresolved (subgrid scale) components by the spatial filtering operation, such that $f = \tilde{f} + f''$, where the tilde (\sim) denotes resolved scale and double prime ($''$) denotes unresolved quantities [21]. The Favre-filtered variable is defined as $\bar{f} = \overline{\rho f}/\overline{\rho}$, where the over bar denotes the spatial-filtering operation. Application of the spatial filtering to the conservation equations leads to the Favre-filtered LES equations for conservation of mass, momentum, energy and species mass, given by

$$\frac{\partial \overline{\rho}}{\partial t} + \frac{\partial \overline{\rho} \tilde{u}_i}{\partial x_i} = 0, \quad (2.1a)$$

$$\frac{\partial \overline{\rho} \tilde{u}_i}{\partial t} + \frac{\partial}{\partial x_j} [\overline{\rho} \tilde{u}_i \tilde{u}_j + \overline{\rho} \delta_{ij} - \overline{\tau}_{ij} + \tau_{ij}^{\text{sgs}}] = 0, \quad (2.1b)$$

$$\frac{\partial \overline{\rho} \tilde{E}}{\partial t} + \frac{\partial}{\partial x_i} \left[(\overline{\rho} \tilde{E} + \overline{p}) \tilde{u}_i + \overline{q}_i - \tilde{u}_j \overline{\tau}_{ij} + H_i^{\text{sgs}} + \sigma_i^{\text{sgs}} \right] = 0, \quad (2.1c)$$

$$\frac{\partial \overline{\rho} \tilde{Y}_k}{\partial t} + \frac{\partial}{\partial x_i} \left[\overline{\rho} \tilde{Y}_k \left(\tilde{u}_i + \tilde{V}_{i,k} \right) + \mathcal{Y}_{i,k}^{\text{sgs}} + \theta_{i,k}^{\text{sgs}} \right] = \overline{\omega}_k, \quad \text{for } k = 1, 2, \dots, N, \quad (2.1d)$$

In the above equations, ρ , u_i , p , E , Y_k , denote the mixture density, i^{th} component of the velocity, pressure, total energy per unit mass and species mass fraction, respectively. Here N denotes the number of species and δ_{ij} is the Kronecker delta. In addition, $V_{i,k}$ and ω_k denote the i^{th} component of the diffusion velocity and the mass reaction rate per unit volume of the k^{th} species, respectively. The filtered viscous stress tensor $\overline{\tau}_{ij}$ and the heat flux vector \overline{q}_i are expressed as

$$\overline{\tau}_{ij} = 2\overline{\mu} \left(\tilde{S}_{ij} - \frac{1}{3} \tilde{S}_{kk} \delta_{ij} \right), \quad \overline{q}_i = -\overline{\kappa} \frac{\partial \tilde{T}}{\partial x_i} + \overline{\rho} \sum_{k=1}^N \tilde{Y}_k \tilde{h}_k \tilde{V}_{i,k} + \sum_{k=1}^N q_{i,k}^{\text{sgs}}, \quad (2.2a)$$

where $\tilde{S}_{ij} = \frac{1}{2} \left(\frac{\partial \tilde{u}_i}{\partial x_j} + \frac{\partial \tilde{u}_j}{\partial x_i} \right)$ is the resolved strain-rate tensor, \tilde{T} is the filtered temperature, \tilde{h}_k is the filtered specific enthalpy for the k^{th} species and $q_{i,k}^{\text{sgs}}$ is the subgrid diffusion of energy due to species diffusion. The filtered diffusion velocity $\tilde{V}_{i,k}$ is obtained from the Hirschfelder and Curtiss approximation [17]. In above

equations, $\bar{\mu}$ and $\bar{\kappa}$ are the filtered mixture molecular viscosity and mixture thermal conductivity, respectively. Note that these transport quantities are obtained directly in terms of the filtered quantities. The subgrid-scale (SGS) terms are denoted by the superscript ‘sgs’. These terms require further closure approximation. The system of equations given by Eq. (2.1) is complete after the filtered equation of state is specified so that the filtered pressure can be determined from

$$\bar{p} = \bar{\rho} R_u \sum_{k=1}^N \frac{\tilde{Y}_k \tilde{T}}{W_k} + \frac{T_k^{\text{sgs}}}{W_k}, \quad (2.3)$$

where R_u is the universal gas constant, W_k is the molecular weight of the k^{th} species and T_k^{sgs} is the subgrid temperature.

The closure approximations for the subgrid-scale terms corresponding to momentum, energy and species fluxes are based on a conventional eddy viscosity approach. The details of the closure models used in the present study can be found elsewhere [22, 23]. In particular, the SGS momentum and energy fluxes are closed using a subgrid eddy viscosity that employs the turbulent kinetic energy for which an additional transport equation is solved [24]. The production and dissipation coefficients are calculated in a dynamic manner through the locally dynamic kinetic energy model [22, 25]. The closure for the reaction rate follows a quasi-laminar (QL) approximation [26], i.e., subgrid turbulence-chemistry interactions are neglected, which is reasonable assumption for the present study as the objective here is to demonstrate the predictive ability of the TDABC formulation for a complex reactive flow systems. Note that the subgrid turbulence chemistry interaction is often considered to be crucial for LES of turbulent combustion. However, in some of the past studies [27, 28], it has been found that such an interaction does not play a pivotal role, although it does affect results in certain aspects.

2.2. Numerical Implementation

The Favre-filtered LES equations given by Eq. (2.1) are solved using a three-dimensional parallel, compressible, multi-species solver. The numerical approach to solve these equations is well established and has been used in the past to study both canonical and complex reactive flows [22]. The solver utilizes a finite volume based spatial discretization of the governing equations in their conservative form on structured multi-block grids. A fully explicit approach is used to perform time integration of the semi-discrete equations. Overall, the method is formally second-order-accurate in both space and time. The transport properties are evaluated using power law expressions, the species source term is computed using Cantera software and thermally perfect gas assumption is used to obtain the thermodynamic properties.

3. Time-domain admittance boundary condition

In this section we present details of the time-domain admittance boundary condition formulation. In the present study we focus on reactive flow systems where the acoustic waves are predominantly one-dimensional (1D) in nature. In addition, we ignore the non-linear acoustic effects and viscous and heat losses due to the acoustic boundary layer. As mentioned before, in several of the high pressure combustors, the thermo-acoustic instabilities are dominated by longitudinal modes [8–10, 12, 16, 29], and therefore, the method described here for specifying time-domain admittance boundary condition is appropriate for investigation of such reactive flow systems. However, the mathematical formulation discussed below can be generalized further for other problems, where some of these effects can not be neglected.

To describe the boundary conditions formulation, we first introduce the terminology related to linearized one-dimensional duct acoustics. This is followed by a description of the plane wave masking approach [1], the state-space model and formulation of the reflection coefficient for an injector. Finally, we perform computational assessment of the method by obtaining solution for a model 1D acoustics problem.

3.1. Preliminaries for one-dimensional acoustics

In a reactive turbulent flow field, the pressure, velocity and density fields can be decomposed in the following manner

$$p(\mathbf{x}, t) = \bar{p}(\mathbf{x}) + \check{p}(\mathbf{x}, t) + p'(\mathbf{x}, t), \quad (3.1a)$$

$$u(\mathbf{x}, t) = \bar{u}(\mathbf{x}) + \check{u}(\mathbf{x}, t) + u'(\mathbf{x}, t), \quad (3.1b)$$

$$\rho(\mathbf{x}, t) = \bar{\rho}(\mathbf{x}) + \check{\rho}(\mathbf{x}, t) + \rho'(\mathbf{x}, t), \quad (3.1c)$$

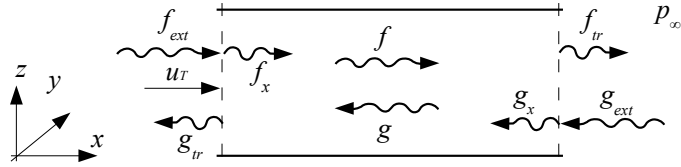


Figure 1: Identification of a generic inflow, outflow and travelling acoustic waves in a one-dimensional domain.

where $\bar{(\cdot)}$, (\cdot) and $(\cdot)'$ represent the mean flow field, turbulent fluctuations and acoustic fields, respectively. As mentioned before, we assume the acoustic fields to be 1D, i.e., $p'(\mathbf{x}, t) \equiv p'(x, t)$, where $\mathbf{x} = (x, y, z)$. For a simplified 1D linearized acoustics, an explicit solution of the acoustic fields is also available, which defines the space-time evolution of the acoustic fields with respect to the initial conditions imposed within the domain. According to D'Alembert's formula, the acoustic fields are given by

$$p'(x, t) = \bar{\rho}\bar{c}[f(x - \bar{c}t) + g(x + \bar{c}t)], \quad (3.2a)$$

$$u'(x, t) = f(x - \bar{c}t) - g(x + \bar{c}t), \quad (3.2b)$$

where \bar{c} is the mean speed of sound and f and g denote amplitude of the right- and left-travelling waves (acoustic fluctuations), respectively. The inverse relationship between the characteristic wave amplitudes f and g and the corresponding acoustic variables u' and p' , using Eq. (3.2) is given by

$$f = \frac{1}{2} \left(\frac{p'}{\bar{\rho}\bar{c}} + u' \right), \quad (3.3a)$$

$$g = \frac{1}{2} \left(\frac{p'}{\bar{\rho}\bar{c}} - u' \right). \quad (3.3b)$$

Figure 1 shows a schematic of a generic inflow boundary, outflow boundary and left- and right-travelling acoustic waves in a 1D domain. In general, for such a domain, under subsonic flow conditions, a target value of the mean velocity field u_T and the mean pressure field p_∞ is specified at the inflow and outflow boundaries, respectively. Throughout the domain, the generic wave amplitudes, f and g can be specified according to Eq. (3.3). The behavior of an acoustic wave at a boundary is determined by the mean flow conditions imposed on that boundary [1]. For this reason, in general an acoustic wave interacting with a boundary can be either reflected and transmitted. The formed waves have in general a different amplitude and phase with respect to the incident wave. Figure 1 also illustrates interaction of wave motion inside the domain with the boundaries. For instance, when the left-travelling wave g impacts the left boundary, it can be partially transmitted, g_{tr} and reflected. Once reflected, it becomes a right-travelling wave f_x which might also include an imposed external signal f_{ext} separated from the internal acoustic field. Therefore, an acoustic wave pointing into the domain contains the reflected part of the wave that just interacted with the boundary, plus a random wave imposed at the boundary itself. The linear nature of the problem allows to construct f_x as a sum of the aforementioned waves. As the external wave is imposed, therefore is known, however, the reflected part of the left-travelling wave is usually unknown since it depends on the boundary topology, and therefore, need to be either determined or modeled. Furthermore, it is important to distinguish between the right-travelling wave f_x generated at the boundary, and the corresponding f wave travelling in the domain. From a broader perspective in fact, these are different because f might contain loss effects and therefore, incur a spatial dependence. Note that due to the assumption of absence of any acoustic losses, the homentropic description of the problem can be invoked [15]. This allows to avoid the use of the energy equation for the acoustic fluctuations, and therefore, the density fluctuation can be determined in terms of the pressure fluctuation, i.e., $\rho' = p'/\bar{c}^2$. Therefore, pressure and velocity fluctuations are sufficient to describe the acoustic wave system and eliminates the need of a linearized equation of state.

Assuming the acoustic fields to be harmonic waves, they can be expressed as [15, 30, 31]

$$p'(x, t) = \Re[\hat{p}_\omega(x)e^{i\omega t}], \quad (3.4a)$$

$$u'(x, t) = \Re[\hat{u}_\omega(x)e^{i\omega t}], \quad (3.4b)$$

$$\rho'(x, t) = \Re[\hat{\rho}_\omega(x)e^{i\omega t}], \quad (3.4c)$$

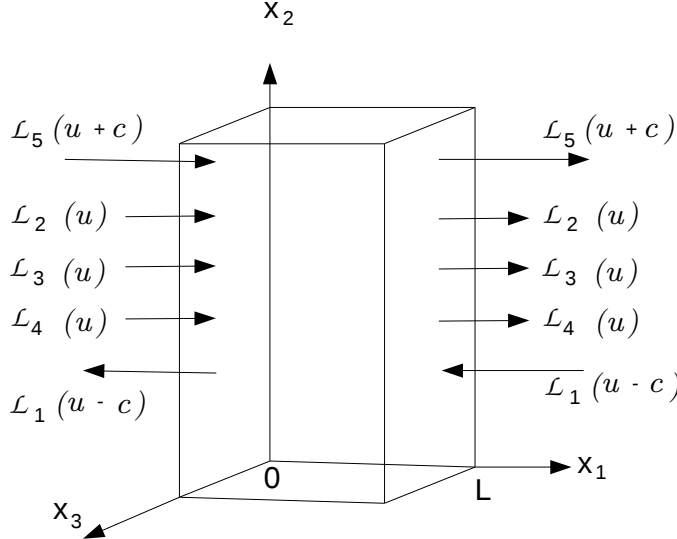


Figure 2: Schematics of a characteristic waves in a cartesian reference frame. Here $x_1 = 0$ and $x_1 = L$ represent an inlet and an outlet respectively.

where $\hat{p} \equiv \hat{p}_\omega(x)$, $\hat{u} \equiv \hat{u}_\omega(x)$ and $\hat{\rho} \equiv \hat{\rho}_\omega(x)$ are complex numbers, ω is the angular frequency and $\Re[\cdot]$ denotes the real part of a complex number. Here $\hat{\phi}_\omega(x)$ denotes the frequency domain description of a time domain field $\phi(x, t)$. Now, we introduce a well known complex-valued function, referred here onward as “admittance”, defined as

$$\mathcal{Y}_\omega(x) = \frac{\hat{u}}{\hat{p}}. \quad (3.5)$$

In the linear control theory, $\mathcal{Y}_\omega(x)$ is also known as a “transfer function” between \hat{u} and \hat{p} [32]. The notion of admittance is useful to characterize wave transmission and reflection at given section in a duct. In the frequency domain, the ratio of the reflected and the incoming wave at a particular boundary is usually referred as the “reflection coefficient”, denoted by $\mathcal{R}_\omega(x)$. For example, at the outflow boundary $\mathcal{R}_\omega(x)$ is given by,

$$\mathcal{R}_\omega(x) = \frac{\hat{g}_x}{\hat{f}}, \quad (3.6)$$

where \hat{f} and \hat{g}_x correspond to the frequency domain representation of f and g_x , respectively. From Eq. (3.3), Eq. (3.5) and Eq. (3.6), we can derive the relationship between the reflection coefficient and the admittance, which is given by

$$\mathcal{R}_\omega(x) = \frac{1 - \bar{\rho} \bar{c} \mathcal{Y}_\omega(x)}{1 + \bar{\rho} \bar{c} \mathcal{Y}_\omega(x)}. \quad (3.7)$$

Note that the value of the reflection coefficient depends upon the type of boundary condition. For example, for an infinitely long duct extending along the positive direction, $\mathcal{R}_\omega = \infty$ and $\mathcal{Y}_\omega = -1/\bar{\rho} \bar{c}$, whereas for a duct terminating on a rigid wall, $\mathcal{R}_\omega = 1$ and $\mathcal{Y}_\omega = 0$. The reflection coefficient is a key constituent to the time-domain admittance boundary condition. The method to determine the reflection coefficient at an outflow boundary is discussed next, which can also be used to obtain it at an inflow boundary.

3.2. Reflection coefficient at an outflow boundary

The admittance boundary conditions are derived based on the well known Navier-Stokes characteristic boundary conditions (NSCBC) formulation [33], where the governing equations are recast in the “characteristic form”, in which conserved variables contain the dependence of wave amplitudes \mathcal{L}_i . Figure 2 illustrates the directions of characteristic waves along the x direction of a reference Cartesian computational domain.

Following an approach similar to [34] and [33], characteristic wave amplitudes in the present study are considered as locally inviscid and are function of primitive variables. They are expressed as

$$\mathcal{L}_1 = \lambda_1 \left(\frac{\partial p}{\partial x_1} - \rho c \frac{\partial u_1}{\partial x_1} \right), \quad (3.8a)$$

$$\mathcal{L}_2 = \lambda_2 \left(c^2 \frac{\partial \rho}{\partial x_1} - \frac{\partial p}{\partial x_1} \right), \quad (3.8b)$$

$$\mathcal{L}_3 = \lambda_3 \left(\frac{\partial u_2}{\partial x_1} \right), \quad (3.8c)$$

$$\mathcal{L}_4 = \lambda_4 \left(\frac{\partial u_3}{\partial x_1} \right), \quad (3.8d)$$

$$\mathcal{L}_5 = \lambda_5 \left(\frac{\partial p}{\partial x_1} + \rho c \frac{\partial u_1}{\partial x_1} \right), \quad (3.8e)$$

where the characteristic speeds λ_i are given by

$$\lambda_1 = u_1 - c, \quad (3.9a)$$

$$\lambda_2 = \lambda_3 = \lambda_4 = u_1, \quad (3.9b)$$

$$\lambda_5 = u_1 + c. \quad (3.9c)$$

Note that \mathcal{L}_i , for $i = 1, 2, \dots, 5$, are locally defined quantities as they do not contain any assumption with respect to space and time dependence. In a similar manner, these quantities can also be defined for linearized Navier-Stokes equations, leading to a very important physical interpretation. To illustrate this, consider the characteristic wave g from Eq. (3.3). This Riemann invariant by definition is conserved along the characteristic direction identified by the equation $x + \bar{\lambda}_1 t = \text{constant}$, where $\bar{\lambda}_1 = \bar{u} - \bar{c}$ has already been defined. Therefore the following advection equation is valid for a left-running characteristic wave

$$\frac{\partial g}{\partial t} + \bar{\lambda}_1 \frac{\partial g}{\partial x_1} = 0. \quad (3.10)$$

Substituting the expression of $g(x, t)$ from Eq. (3.3) in the spatial derivative term, we get

$$\frac{\partial g}{\partial t} + \frac{\mathcal{L}'_1}{2\bar{\rho}\bar{c}} = 0, \quad (3.11)$$

where the density and the speed of sound are now assumed to be the respective mean (constant in space) values. Note that in this specific case the definition of \mathcal{L}'_1 becomes slightly different from that of (3.8a) as it contains fluctuating variables p' and u' , mean density and speed of sound, as well as constant propagation speed $\bar{\lambda}_1$. The former equation reveals that the meaning of \mathcal{L}'_1 (as well as of \mathcal{L}'_5 for a right running characteristic wave) is, for a linearized system, directly associated with the time derivative of the characteristic wave. This concept can be further expanded in order to obtain information about the behavior of characteristic boundary conditions for Large Eddy Simulations.

The characteristic wave amplitudes for linearized Navier-Stokes equations can be rewritten in the following general form

$$\mathcal{L}'_i = (\bar{u} \pm \bar{c}) \left(\frac{\partial p'}{\partial x} \pm \bar{\rho} \bar{c} \frac{\partial u'}{\partial x} \right), \quad (3.12)$$

where the subscript i corresponds to 1 for an outflow boundary and it is associated with the negative sign, whereas it corresponds to 5 for an inflow boundary and it is associated with the positive sign. If these quantities are evaluated at the boundary, \bar{u} corresponds to the velocity value at the boundary, which in turn depends on the boundary type. For example, it will correspond to $u = u_T$ for an inflow, while it matches the local value of velocity for an outflow. As mentioned before, we derive the formulation for an outflow boundary without loss of generality. The same formulation can be extended to an inflow boundary.

At an outflow boundary, using Eq. (3.3)(b) in Eq. (3.12), we get

$$\mathcal{L}'_1 = -(\bar{u} - \bar{c}) \left(\frac{\partial p'}{\partial x} - \bar{\rho} \bar{c} \frac{\partial u'}{\partial x} \right) = -\bar{\rho} \bar{c} (\bar{u} - \bar{c}) \frac{\partial g}{\partial x} = -2\bar{\rho} \bar{c} \frac{\partial g}{\partial t}. \quad (3.13)$$

where the spatial derivative is converted to a temporal derivative using (3.10). We can clearly observe that the specification of \mathcal{L}'_1 at an outlet boundary directly controls the time variation of the upstream running acoustic wave, i.e., $g(x, t)$. Assuming the acoustic waves to be harmonic in the frequency-domain, i.e., $g(x, t) = \Re[\hat{g}_\omega e^{i\omega t}]$, Eq. (3.13) can be further simplified to

$$\hat{\mathcal{L}}'_1 = -2i\bar{\rho}\bar{c}\omega\hat{g}_\omega e^{i\omega t}. \quad (3.14)$$

Past studies [1, 2] based on similar formulation for wave amplitudes have shown that a compromise is usually needed between the imposed mean flow quantities and the acoustic fluctuations at the boundaries. The mean flow quantities are imposed based on the linear relaxation coefficient introduced by [14], which generates a correction term in the \mathcal{L}_i expression, which drives the value of the primitive variable at the boundary to the imposed value. For example, for a constant pressure outflow boundary, the expression of the outgoing wave is given by

$$\mathcal{L}_1 = -K(p - p_\infty), \quad (3.15)$$

while for a subsonic inflow boundary

$$\mathcal{L}_5 = -K(u - u_T), \quad (3.16)$$

where p_∞ and u_T are the target pressure specified at the outflow boundary and the velocity specified at the inlet for a subsonic condition according to Figure 1, and K is a relaxation coefficient. We can observe that whenever a pressure drift is experienced at the boundary, this term acts to correct the drift according to the specified value of K . Since $(p - p_\infty)$ is the pressure fluctuation imposed at the outlet boundary, assuming the pressure drift fluctuation to be harmonic such that it is governed by characteristic (linearized) waves, using the definition of p' defined in Eq. (3.2) and taking its Fourier transform, we obtain

$$\hat{\mathcal{L}}_1 = \bar{\rho}\bar{c}K(\hat{f}_\omega + \hat{g}_\omega)e^{i\omega t}. \quad (3.17)$$

Since the value of \mathcal{L}_1 has been now linearized at the boundary, Eq. (3.17) and Eq. (3.15) can be equated in order to have an estimation of the reflection coefficient that the classical NSCBC approach provides, i.e. $\hat{\mathcal{L}}_1 \approx \hat{\mathcal{L}}'_1$

$$-2i\bar{\rho}\bar{c}\omega\hat{g}_\omega = \bar{\rho}\bar{c}K(\hat{f}_\omega + \hat{g}_\omega). \quad (3.18)$$

Therefore, the reflection coefficient \mathcal{R}_ω given by Eq. (3.6) at the outflow boundary with no external excitation becomes

$$\mathcal{R}_\omega = \frac{\hat{g}_\omega}{\hat{f}_\omega} = \frac{-1}{\frac{2i\omega}{K} + 1}. \quad (3.19)$$

We can observe that for $K \rightarrow \infty$, the reflection coefficient tends to -1 which indicates a complete reflection of the outgoing wave. On the other hand $\mathcal{R}_\omega \rightarrow 0$ when $K \rightarrow 0$, which implies a fully non-reflective boundary. At this point, one may think that the second choice is always correct if a non-reflective acoustic boundary is desired. However, the condition of $K = 0$ does not provide any constraint on the mean flow quantities, leading to unwanted drift from the desired mean values. It further implies that neither the mean flow imposition, nor the acoustic behavior can be simultaneously satisfied at the boundary, but in some sense a compromise is needed. Such a compromise is also a function of the frequency of the outgoing acoustic wave, as it can be observed in Eq. (3.19) that higher frequencies assume the same behavior as $K \rightarrow 0$ (fully non reflective boundary), whereas the lower frequencies can be partly reflected. The coupling of the mean flow quantities imposition with the acoustic waves at the boundary is undesirable and therefore, it requires a special treatment, which is discussed next.

3.3. Generalized plane acoustic waves masking

In order to avoid the coupling effect between the mean flow imposition and the acoustics at the boundary discussed above, a solution has been proposed by [1] and [2], which is known as the concept of “plane wave masking”. It introduces a small, but essential modification into the characteristic wave amplitude expression

by explicitly subtracting the acoustic contribution of the pressure wave amplitude at the boundary given by Eq. (3.2)(a). At a fully non-reflective outflow boundary, the acoustic pressure is simply given by the right-travelling wave (f), as the left-travelling wave (g_x) is absent, i.e., $p' = \bar{\rho}\bar{c}f$. Hence, the expression for \mathcal{L}_1 given by Eq. (3.15) gets modified to

$$\mathcal{L}_1 = -K(p - \bar{\rho}\bar{c}f - p_\infty). \quad (3.20)$$

Note that, here we are considering the characteristic formulation which contains the total pressure and velocity fields. It is clear that with such modification, the boundary condition does not depend upon acoustic fluctuations as they have been explicitly subtracted and at the same time the mean flow constraint p_∞ is ensured. There are two important observations related to the plane wave masking approach. First, it only considers plane waves approaching the boundary, i.e., the acoustic fluctuations must be parallel to the inflow/outflow boundary. Second, it requires that the acoustic fields must be known at the boundary. The knowledge of the acoustic fields requires the knowledge of time- and surface-averaged quantities due to the requirement of planar waves approaching the boundary. The surface averaging is performed on the fictitious boundary surface, while the time-averaged quantity can be either prescribed or dynamically computed as part of the solution process, knowing the surface average value in time. For example, we have

$$\bar{p}_s = \frac{1}{t_{av}} \int_{t-t_{av}}^t p(\tau) d\tau, \quad (3.21)$$

where \bar{p}_s denotes the time average of the boundary surface averaged value of the pressure field and t_{av} represents a time interval under which the time averaged quantity remains constant. After mean and fluctuating quantities are known at the boundary, the right-travelling wave (f) can be obtained through Eq. (3.3)(a).

If a partially reflective boundary condition is employed and an external acoustic excitation is imposed at the boundary, the plane wave masking approach described by Eq. (3.20) requires further generalization. In such case, the acoustic part also accounts for the left-travelling wave (g_x), which was previously eliminated. As discussed in Section 3.1, the g wave specified at the boundary is a super-imposition of the (partially) reflected f wave coming from inside of the domain (i.e. g_x), and the acoustic external excitation g_{ext} . Therefore, the pressure term that needs to be included for the masked wave into Eq. (3.15) is exactly given by Eq. (3.2)(a), and the characteristic wave \mathcal{L}_1 becomes

$$\mathcal{L}_1 = -K(p - \bar{\rho}\bar{c}(f + g_x) - p_\infty) + \mathcal{L}_1^{ext}, \quad (3.22)$$

where \mathcal{L}_1^{ext} is introduced according to Eq. (3.11) that completely relates the time derivative of the imposed signal to the characteristic wave amplitude

$$\mathcal{L}_1^{ext} = -2\bar{\rho}\bar{c}\frac{\partial g_{ext}}{\partial t}. \quad (3.23)$$

As mentioned before, the left-travelling g wave is composed of two effects, therefore it can be expressed as

$$g = [\hat{g}_x]_t + g_{ext} = \left[\mathcal{R}_\omega \hat{f}_\omega \right]_t + g_{ext}, \quad (3.24)$$

where the $[\cdot]_t$ implies a time-domain representation and it comes from Eq. (3.6). From Eq. (3.22), Eq. (3.23) and Eq. (3.24), we get the following expression for the characteristic wave amplitude at the outflow boundary

$$\mathcal{L}_1 = -K \left[p - \bar{\rho}\bar{c} \left(f + \left[\mathcal{R}_\omega \hat{f}_\omega \right]_t + g_{ext} \right) - p_\infty \right] - 2\bar{\rho}\bar{c} \frac{\partial g_{ext}}{\partial t}. \quad (3.25)$$

In this expression, p and f are computed at each time step, mean quantities $\bar{\rho}$ and \bar{c} are imposed or calculated as boundary surface averaged quantities. A similar expression for the corresponding characteristic wave amplitude at the inflow boundary is given by

$$\mathcal{L}_5 = -K\bar{\rho}\bar{c} [u - ([\mathcal{R}_\omega \hat{g}_\omega]_t + f_{ext} - g) - u_T] - 2\bar{\rho}\bar{c} \frac{\partial f_{ext}}{\partial t}. \quad (3.26)$$

Both Eq. (3.25) and Eq. (3.26) contain information about the presence of an external excitation and an admittance boundary condition. In fact, assuming that the reflection coefficient is known, the formulation

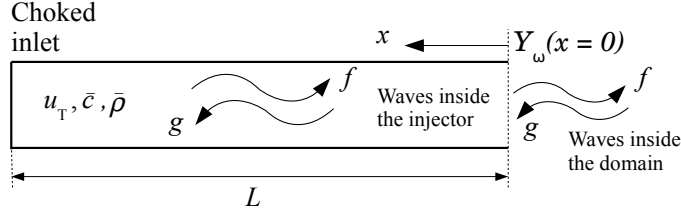


Figure 3: Schematics of a one-dimensional choked acoustic duct.

only considers the value of the f (g) wave for an outflow (inflow) at the boundary, which is known as it comes from the interior of the computational domain.

The time-domain representation of the reflected wave i.e. $[\mathcal{R}_\omega \hat{f}_\omega]_t$ is needed to completely specify the boundary condition. In general, it is always possible, for a linear system, to switch from the frequency to a time domain representation [32]. Therefore, once the reflection coefficient (transfer function) between the input \hat{f} and the output \hat{g}_x is known analytically, the acoustic system is then expressed as

$$\dot{\mathbf{x}} = \mathbf{Ax} + \mathbf{Bu}, \quad (3.27a)$$

$$g = \mathbf{Cx} + \mathbf{Du}, \quad (3.27b)$$

where, g is the desired complete left-running wave defined at the boundary in the time domain, \mathbf{x} is the space vector and \mathbf{u} is the input vector. For the generic acoustic boundary condition, the input vector is given by

$$\mathbf{u} = [f \quad g_{\text{ext}}]^T. \quad (3.28)$$

Furthermore the matrices \mathbf{A} , \mathbf{B} , \mathbf{C} and \mathbf{D} are uniquely defined by the inverse-transform of the reflection coefficient \mathcal{R}_ω . The system of equations given by Eq. (3.27) constitutes the link between the admittance formulation in the frequency domain, and the LES solver in the time domain. Particularly, Eq. (3.27)(a) is currently solved using an explicit time-integration method with the time step restricted by the CFL criterion and the applied signal g is obtained through Eq. (3.27)(b) at a particular time step. Note that this is not an unique approach [2]. Same method can be used for an inflow boundary by simply reversing the role of f and g . Next, we describe how to determine the reflection coefficient for an injector, which will complete the description of time-domain admittance boundary condition.

3.4. Reflection coefficient for an injector

Here, we describe the way to determine the reflection coefficient \mathcal{R} for a choked injector, which will be used in the application study discussed below. However, a similar approach can be followed for all the other acoustic cavities. We consider the one dimensional, linearized Euler equations, given by

$$\frac{\partial \rho'}{\partial t} + \bar{\rho} \frac{\partial u'}{\partial x} + \bar{u} \frac{\partial \rho'}{\partial x} = 0, \quad (3.29a)$$

$$\frac{\partial u'}{\partial t} + \bar{u} \frac{\partial u'}{\partial x} + \frac{1}{\bar{\rho}} \frac{\partial p'}{\partial x} = 0, \quad (3.29b)$$

$$\frac{\partial p'}{\partial t} + \bar{u} \frac{\partial p'}{\partial x} + \gamma \bar{p} \frac{\partial u'}{\partial x} = 0, \quad (3.29c)$$

where γ is the mean specific heat ratio. Assuming a space-time harmonic solution for the acoustic fields, i.e., $p'(x, t) = \hat{p} e^{i(\omega t - kx)}$, $u'(x, t) = \hat{u} e^{i(\omega t - kx)}$ and $\rho'(x, t) = \hat{\rho} e^{i(\omega t - kx)}$, where (\cdot) is the complex Fourier coefficient and k is the wavenumber. Substituting the harmonic representation into Eq. (3.29) and further simplification yields the following eigensystem

$$\underbrace{\begin{bmatrix} i\omega - i k \bar{u} & -ik\bar{\rho} & 0 \\ 0 & i\omega - i k \bar{u} & -\frac{ik}{\bar{\rho}} \\ 0 & -ik\gamma\bar{p} & i\omega - i k \bar{u} \end{bmatrix}}_{\mathbf{K}} \begin{pmatrix} \hat{\rho} \\ \hat{u} \\ \hat{p} \end{pmatrix} = 0. \quad (3.30)$$

The non trivial solution is given by calculating the eigenvalues of the \mathbf{K} matrix, which are given by

$$k_1 = \frac{\omega}{\bar{u}}, \quad k_2 = k^+ = \frac{\omega}{\bar{c}(1 + \bar{M})}, \quad k_3 = k^- = \frac{\omega}{\bar{c}(\bar{M} - 1)}, \quad (3.31)$$

where \bar{c} and \bar{M} are respectively the mean sound speed and Mach number and positive and negative superscripts correspond to the right- and left-travelling acoustic waves, respectively. The corresponding eigenvectors are given by

$$\hat{u}^+ = \frac{\hat{p}^+}{\bar{\rho}\bar{c}}, \quad \hat{u}^- = -\frac{\hat{p}^-}{\bar{\rho}\bar{c}}. \quad (3.32)$$

By separating the right- and left-travelling waves, the acoustic perturbations can be expressed as

$$p'(x, t) = \hat{p}^+ e^{i\omega t} e^{-ik^+ x} + \hat{p}^- e^{i\omega t} e^{-ik^- x}, \quad (3.33a)$$

$$u'(x, t) = \hat{u}^+ e^{i\omega t} e^{-ik^+ x} + \hat{u}^- e^{i\omega t} e^{-ik^- x}, \quad (3.33b)$$

and therefore, the admittance $\mathcal{Y}_\omega(x)$ is given by

$$\mathcal{Y}_\omega(x) = \frac{u'}{p'} = \frac{\hat{u}^+ e^{i\omega t} e^{-ik^+ x} + \hat{u}^- e^{i\omega t} e^{-ik^- x}}{\hat{p}^+ e^{i\omega t} e^{-ik^+ x} + \hat{p}^- e^{i\omega t} e^{-ik^- x}}. \quad (3.34)$$

Using Eq. (3.32) into Eq. (3.34), the expression for the admittance simplifies to

$$\mathcal{Y}(x, \omega) = \frac{1}{\bar{\rho}\bar{c}} \frac{1 + \tilde{P}e^{i\tilde{k}x}}{1 - \tilde{P}e^{i\tilde{k}x}}, \quad (3.35)$$

where

$$\tilde{P} = \frac{\hat{u}^-}{\hat{u}^+}, \quad \tilde{k} = k^+ - k^- = \frac{2\omega}{\bar{c}(1 - \bar{M}^2)}. \quad (3.36a)$$

Here, \tilde{P} is an arbitrary constant that needs to be determined by imposing the boundary condition. Let α be the value of the admittance for a choked inflow, then, by imposing the value $\mathcal{Y}_\omega(x = L) = \alpha$ and re-defining $\beta = 1/\bar{\rho}c$, the expression for the admittance at $x = 0$ (domain boundary) is given by

$$\mathcal{Y}_\omega(x = 0) = \beta \frac{\chi^2 - 1}{\chi^2 + 1 - 2\chi \cos(\tilde{k}L)} + i\beta \frac{-2\chi \sin(\tilde{k}L)}{\chi^2 + 1 - 2\chi \cos(\tilde{k}L)}, \quad (3.37)$$

where $\chi = (\alpha + \beta)/(\alpha - \beta)$. At this point the reflection coefficient can be obtained by using Eq. (3.2) and Eq. (3.6), and is given by

$$\mathcal{Y}_\omega = \frac{u'}{p'} = \frac{f - g}{\bar{\rho}\bar{c}(f + g)} = \frac{\mathcal{R}_\omega - 1}{\bar{\rho}\bar{c}(\mathcal{R}_\omega + 1)}. \quad (3.38)$$

Note that the aim of the imposition of a reflection coefficient boundary condition is to have a certain response of a certain acoustic wave coming from inside of the domain. Therefore, according to Figure 3, $\mathcal{R}_\omega = f/g$ since g is the incoming wave hitting the boundary and f is the response wave which will contain the effect of reflection coefficient. Further simplification of Eq. (3.38) by using definition of χ and Eq. (3.37), leads to the reflection coefficient given by

$$\mathcal{R}_\omega = |\chi| e^{i\tilde{k}L} = |\chi| \exp \left[\frac{2i\omega L}{\bar{c}(1 - \bar{M}^2)} \right]. \quad (3.39)$$

When a simple one dimensional duct is acoustically choked, the physical condition is the absence of mass flow rate fluctuations at the inflow. This can be used to obtain the final value of admittance [35], given by

$$\alpha = \frac{u'}{p'} = -\frac{\bar{u}}{\bar{\rho}\bar{c}^2} = -\frac{\bar{u}}{\gamma\bar{p}}, \quad (3.40)$$

where the non-linear acoustic terms such as $p'u'$ has been neglected and the isentropic relation $\rho' = p'/c^2$ has been used. From Eq. (3.40), we can obtain an explicit value of χ . In fact, substituting the value of β and α , we get

$$\chi = \frac{1 - \bar{M}}{1 + \bar{M}}. \quad (3.41)$$

We can further observe that the argument of the exponential term in Eq. (3.39), can be expressed in the form $i\omega\tau$, where τ has a dimension of time and it is given by

$$\tau = \frac{2L}{\bar{c}(1 - \bar{M}^2)}. \quad (3.42)$$

We can also obtain Eq. (3.42) by considering the time required by the g wave coming from the domain to travel upstream of the injector, hit the choked face plate and then come back at the interface of the domain. Since g is an acoustic wave, the velocity it travels in either direction is different because of the presence of the mean flow. Therefore, it can be verified that

$$\tau = \frac{L}{\bar{c} - \bar{u}} + \frac{L}{\bar{u} + \bar{c}}. \quad (3.43)$$

Finally, the expression of the reflection coefficient can be rearranged to

$$\mathcal{R}_\omega = \frac{1 - \bar{M}}{1 + \bar{M}} e^{i\omega\tau}. \quad (3.44)$$

Note that Eq. (3.44) corresponds to the so called time delay with a gain transfer function. Basically it acts to the input signal with a delay (given by the exponential term) and a gain, which instead acts on the signal amplitude. Notice that the gain, given by Eq. (3.43) is completely controlled by the mean flow Mach number and it is always less than one (for subsonic inflow). This suggests that whatever input signal g enters the acoustic domain, its amplitude is always decreased by a factor χ . This effect is controlled by the choked boundary condition which in this way acts as an acoustic damper. As a consequence the choked inlet becomes a partially reflective acoustic boundary condition which does not have any influence on the phase of the incoming signal. The signal g coming from the domain hits the choked inflow, creating a reflected and a transmitted wave. The latter leaves the domain, left-ward, while the reflected part comes back inside the domain with a reduced amplitude. Physically, this wave system is created in order to satisfy the condition that no mass flow rate fluctuations must occur.

In the above discussion we have focused on one-dimensional acoustic duct configuration to derive the boundary conditions. However, the formulation can be easily generalized to other types of acoustic cavities. For example, if the duct boundary is a simple wall rather than a choked inlet, the value of α is zero, as the acoustic wall condition does not allow to have velocity fluctuations. Therefore, under such condition, the value of χ becomes one, implying that the input signal amplitude is entirely conserved with respect to the reflected signal and the reflection coefficient becomes a simple time delay transfer function. It further implies that the reflected wave f is the same wave g with some time delay, being the amplitude the same. Furthermore, in the present formulation, all kind of viscous and heat loss effects due to the presence of an acoustic boundary layer have been neglected. Further investigations might lead to a more complete formulation that includes these losses inside the tube. The expected effect is that the presence of losses contributes to the further decrease of the wave amplitude as well as its phase. Such an extension will be presented in a future study.

3.5. Computational assessment

The implementation of the TDABC formulation discussed above is assessed now through a canonical test case. We consider a cylindrical domain of length $L = 20$ cm and radius $R = 1.8$ cm and verify the external excitation and the admittance boundary condition in terms of a reflection coefficient. Figure 4 shows a schematic of the computational setup, where the domain consists of subsonic inflow and outflow boundaries. At the inflow boundary, nitrogen is injected at a speed of 100 m/s along the axial direction, with temperature of 298.15 K and pressure of 1 atm, whereas at the outflow, a pressure condition of 1 atm is imposed.

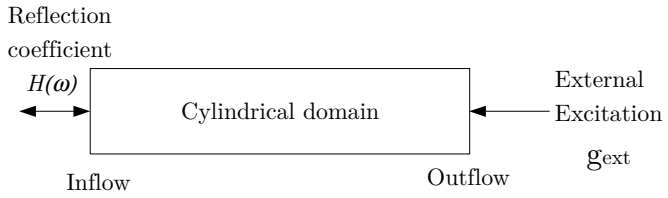


Figure 4: Assessment of the external excitation and the admittance boundary condition in a cylindrical domain.

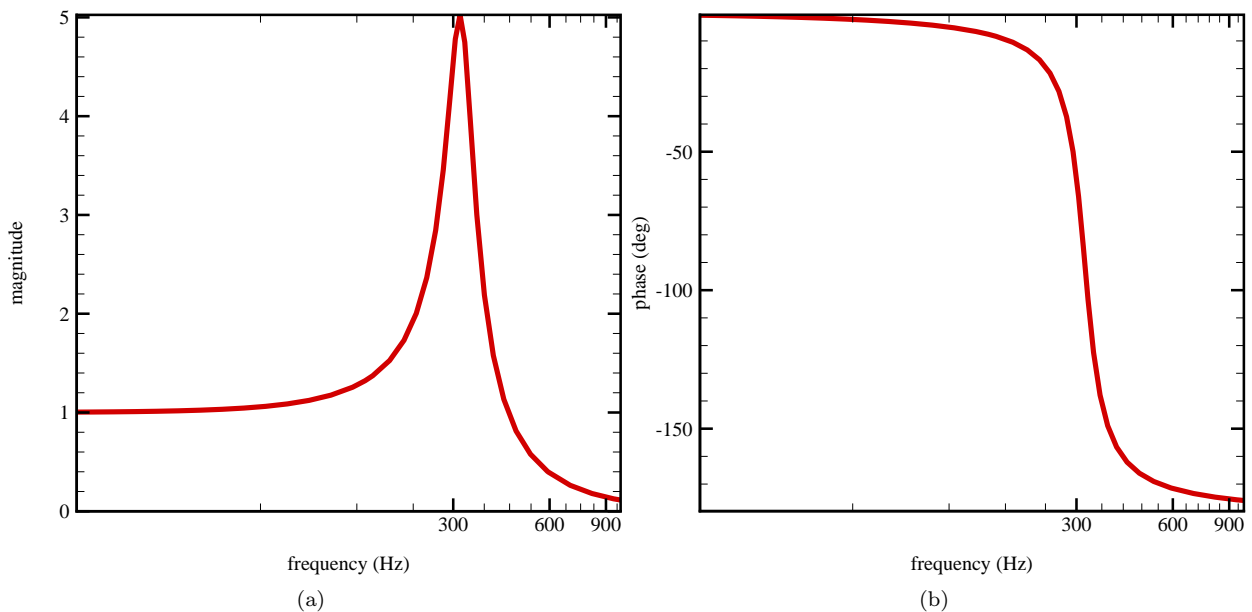


Figure 5: Amplitude (a) and phase (b) representation of the filter imposed as reflection coefficient at the inflow.

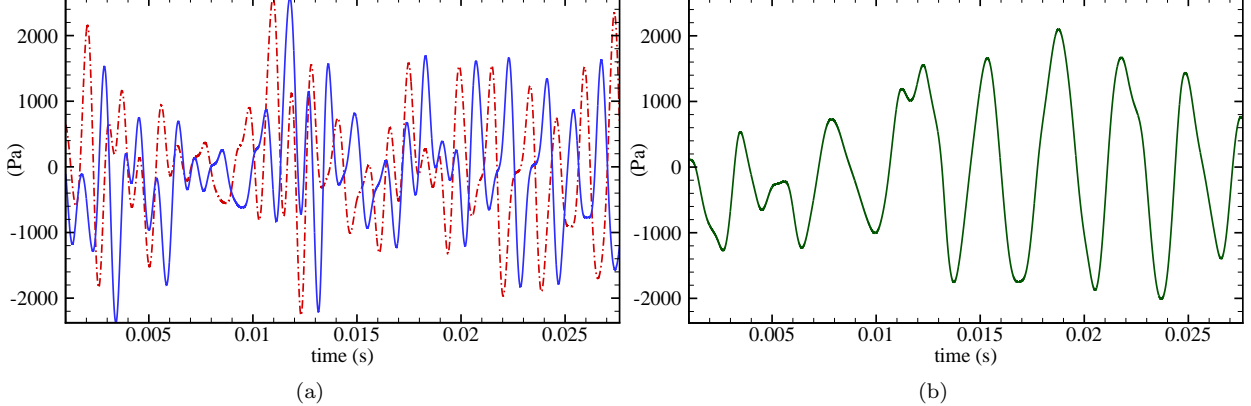


Figure 6: Normalized g wave ($\bar{\rho} \bar{c} g$) measured at both outflow and inflow (top). Reflected normalized f wave ($\bar{\rho} \bar{c} f$) at the inflow after filtering (bottom).

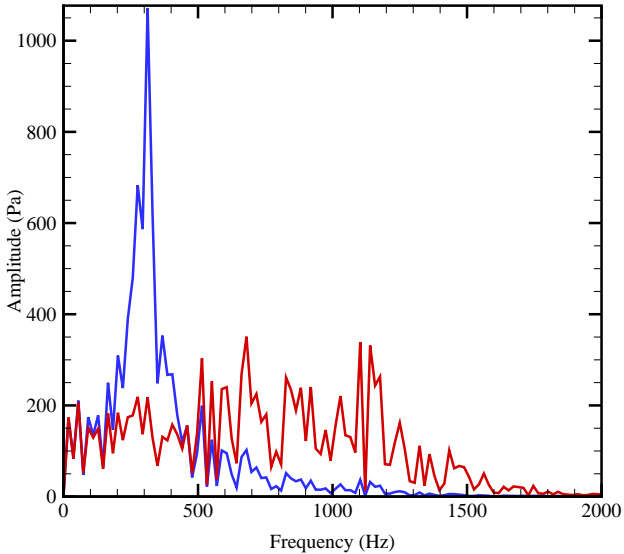


Figure 7: Amplitude spectrum of the incoming (\hat{g}) signal (red) and the reflected (\hat{f}) signal (blue).

At the outflow, an external excitation is imposed in terms of g wave, while at the inflow, a partially reflective boundary condition is imposed with a reflection coefficient $H(\omega)$. The form of the reflection coefficient does not have any physical meaning in this case, however, a band-pass filter has been chosen of the following form

$$H_\omega = \frac{\mathcal{K}}{a_1\omega^2 + a_2\omega + 1}, \quad (3.45)$$

with $\mathcal{K} = 1$, $a_1 = -2.5 \times 10^{-7}$, $a_2 = 10^4 i$. The form of the filter $H(\omega)$ is shown in Figure 5. We can observe that the frequencies below 80 Hz keep their original amplitude and frequencies above 400 Hz of the incoming signal are damped. In the region between these two cut-off values, frequencies are excited with a maximum peak (resonant point) around 320 Hz, which return an amplitude gain of about 5 times with respect to the incident signal. Again the partially reflective boundary condition must be read as $H(\omega) = \hat{f}/\hat{g}$ where \hat{f} and \hat{g} represent the frequency domain description of the reflected signal and incoming signal respectively, evaluated at the inflow boundary.

Figure 6 shows the randomly generate g wave in pressure units. Figure 6(a) compares the imposed

signal at the outflow boundary with the same signal computed at the inflow boundary, right before the filter imposition. We can observe that a slight phase drift occurs because the signals are measured at two different locations of the domain. However, it appears that structure of the signal is retained, which is sufficient for the present study. Figure 6(b) represents the f wave computed at the inflow boundary, which clearly denotes a low frequency content signal. In fact, Figure 7 compares the spectrum amplitudes of both the signals. We can see that for frequencies up to 80 Hz, spectra corresponding to both the signals are overlapped. In addition, frequencies higher than 400 Hz are removed. The peak amplitude occurs at a frequency of about 320 Hz, with a value of about ~ 1050 Pa, corresponding to about five times of the corresponding incoming signal amplitude at the same frequency (~ 210 Pa).

The canonical test case presented in this section demonstrates the reliability of the plane wave masking approach. The major advantage of the approach considered in this study is the ability to simulate properly partially reflective boundary conditions. In fact, although the applied filter $H(\omega)$ does not have a physical meaning, different situation would appear when a combustion chamber face plate has multiple injectors. With the reflection coefficient developed in 3.4, the modeling of multiple injectors can be easily achieved using the proper reflection coefficient. Before applying the formulation to a multi-element system, the objective is to verify the generality, accuracy and robustness of the formulation by simulating single element, shear coaxial system, which is discussed below.

4. Problem description

In the present study, we use the TDABC formulation to simulate thermo-acoustic combustion instability in the continuously variable resonance combustor (CVRC); an experimental rig studied at the Purdue University. Recently, [12] studied the mechanism of instability and the role of flame dynamics on it through LES employing LEM as the subgrid model for scalar mixing and kinetics. The simulations results showed good agreement with the experimental data predicting the limit cycle behavior exhibited by the acoustic pressure fluctuations, which depends upon the length of the oxidizer inlet. In the present study, we have considered the same computational setup as used by [12] to demonstrate that the TDABC formulation can predict the thermo-acoustic instability and the flame dynamics in the CVRC rig, without explicitly modeling the complete injector. As mentioned before, the present study is focused on the reliability of the use of admittance boundary conditions and therefore, QL approximation [26] is used for closure of the filtered reaction rate. Note that in the CVRC rig, as the length of the oxidizer injector is altered, the thermo-acoustic instability appears or disappears, thus illustrating a characteristic behavior of the rig at a particular length of the oxidizer inlet. It is discussed later that this characteristic feature can be captured with the QL approximation, although the amplitude and phase of the limit cycle behavior exhibited by the acoustic pressure fluctuations shows some differences with those obtained by using LEM as a subgrid closure.

The details of computational setup, choice of boundary conditions and other choices are provided in [12]. Here, we briefly summarize the relevant details of the computational setup, the way to determine the reflection coefficient for the CVRC rig and further details of the simulations.

4.1. Details of computational setup

Figure Figure 8 shows a schematic of the CVRC rig [7, 9] showing its major components. The top-half of the figure shows the entire computational domain considered in the past studies [11, 12, 36], whereas the bottom-half of the figure shows the case where the injector is modeled with a reflection coefficient through the TDABC formulation, i.e., the shaded region in Figure 8 is not modeled explicitly, but rather it is modeled in a 1D sense in a manner similar to as shown in Figure 3. The CVRC rig is a dump-combustor with a central oxidizer duct and a co-axial fuel duct. The design of the rig allows for a variation of the oxidizer injector length L_{Ox} , which leads to stable/unstable behavior of the combustor. Similar to the past studies [11, 12, 36], the inflow boundary is considered to be a constant mass flow rate and is weakly reflecting. In addition, the fuel injection system is not modeled. All the other dimensions and locations of the injector post tip and choked outflow nozzle are same as in the experiments.

The length of the oxidizer inlet is varied and we study flame stabilization and combustion instability for a fixed combustor length $L_{\text{comb}}/D = 18.61$ but for three different oxidizer injector lengths $L_{\text{Ox}}/D = 4.40, 5.86$ and 6.84 , where the diameter of the oxidizer inlet duct $D \equiv D_{\text{Ox}} = 2.047$ cm is used as a reference scale. We simulate six cases, three employing the full injector with the conventional characteristic boundary conditions and three employing TDABC formulation using the reflection coefficient model for an injector

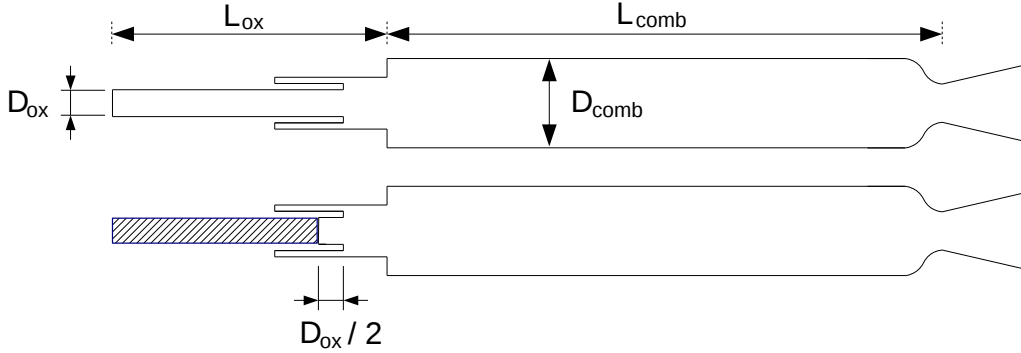
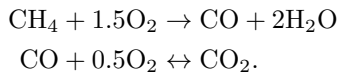


Figure 8: Schematic of the CVRC rig in two dimensions (central plane) showing the full (top-half) and truncated (bottom-half) injector geometry. The shaded region is excluded in the truncated geometry. L_{comb} , D_{comb} , D_{ox} , and L_{ox} denote length of the combustor section, diameter of the combustor section, diameter of the oxidizer injector and length of the oxidizer injector, respectively.

Table 1: Mean value used for evaluation of reflection coefficient					
Variable	U_{mean}	P_{mean}	T_{mean}	ρ_{mean}	M
Value	230.9 m/s	1.65 MPa	1030 K	4.27 kg/m ³	0.4

described in 3.4. These cases are denoted by labels Case 9F, Case 12F, Case 14F, Case 9P, Case 12P, and Case 14P, respectively, where the number corresponds to L_{Ox} and ‘F’ and ‘P’ denote full and partial (truncated) injector, respectively. Case 9 ($L_{\text{Ox}} = 9$ cm) is shown experimentally to be “stable” (i.e., low-amplitude pressure fluctuations) while Cases 12 and 14 ($L_{\text{Ox}} = 12$ cm and 14 cm, respectively) are known to be unstable with different levels of instability.

The inflow boundaries are modeled using the characteristic boundary condition formulation [13], where mass flow rates, species mass fractions and temperature fields are prescribed. The inlet Mach number for the oxidizer post is $\bar{M} = 0.4$. The outflow is choked through the nozzle and therefore, supersonic boundary conditions are employed at the nozzle exit. No-slip walls with adiabatic thermal conditions are used. The fuel is methane (CH_4) and the oxidizer is a mixture of O_2 and H_2O with mass fractions of 0.42 and 0.58, respectively. The fuel is injected through the annular injector at a constant mass-flow rate $\dot{m}_{\text{f}} = 0.027$ kg/s and constant temperature $T_{\text{f}} = 300$ K. The oxidizer is injected through the central pipe of the coaxial injector at a constant mass-flow rate $\dot{m}_{\text{Ox}} = 0.32$ kg/s and constant temperature $T_{\text{Ox}} = 1030$ K. The operating pressure of the combustion chamber is $P_{\text{ref}} = 1.34$ MPa and the global equivalence ratio is 0.8. The Reynolds number corresponding to the oxidizer and fuel passages are 481,000 and 33,000, respectively. A two-step five species (CH_4 , O_2 , H_2O , CO_2 and CO) reduced kinetics is used in this study to consider finite-rate kinetics effects. The two-steps of the mechanism are given by



The thermodynamic properties are calculated using the thermally-perfect equation of state. The simulations are conducted for about XX cycles after the limit-cycle behavior is reached.

4.2. Reflection coefficient determination

The reflection coefficient is determined through Eq. (3.42) and Eq. (3.44). Note that this boundary condition is only applied to the oxidizer post, while the fuel slot is entirely resolved. As schematically illustrated in Figure 8, we arbitrarily truncate the injector at one pipe radius upstream of the mixing region between fuel and oxidizer i.e. $L_{\text{tr}} = D_{\text{Ox}}/2 = 1.023$ cm. Since, the plane wave masking approach assumes that the acoustic wave hits the boundary in a one dimensional manner, therefore three dimensional effects are neglected. In addition, the mean values inside the modeled part of the injector are kept constant, although they can be updated during the simulation according to [2]. The sensitivity of results on choice of L_{tr} , the three-dimensional effects and time-varying mean values will be considered in future studies.

Table 2: Summary of the full oxidizer injector length (L_{Ox}), mixing length (L_{mix}), truncated injector length (L_{tr}) and the length used to determine the reflection coefficient (L)

L_{Ox} (cm)	L_{mix} (cm)	L_{tr} (cm)	L (cm)
9	1.026	1.023	6.95
12	1.026	1.023	9.96
14	1.026	1.023	11.95

Table 1 summarizes the mean value of the field variables within the modeled part of the injector, which are used to obtain the reflection coefficient. Note that the mean value of the pressure field P_{mean} is based on the past study [12], and is slightly different from the experimental data (1.34 MPa). The difference has been attributed to the use of adiabatic thermal condition on the walls of the combustor. The mean speed of sound is obtained from the mean axial velocity U_{mean} and the Mach number ($\bar{M} = 0.4$). The mean values given in Table 1 are used to compute acoustic fluctuations at the inflow boundary at each LES time step, and they are also used to compute the g -wave corresponding to the truncated location. To determine the f -wave and close the problem, the reflection coefficient needs to be determined. Since three different injector length are considered in this study, three different values of the reflection coefficient are computed. However, the truncated geometry remains the same, which is one of the major advantages of the TDABC formulation. For such complex reactive flow systems, geometry creation and grid generation are computationally intensive tasks. Clearly, with the TDABC formulation such computational costs are reduced, and are suitable for conducting parametric investigation for design and performance evaluation.

In the CVRC rig, the length of the mixing region is constant for all cases, i.e., $L_{\text{mix}} = 1.026 \text{ cm}$. Therefore, the length needed to model the injector is obtained through $L = L_{\text{Ox}} - L_{\text{mix}} - L_{\text{tr}}$. Table 2 summarizes the original injector lengths used for the full injector simulations (Case 9F, Case 12F and Case 14F) and the respective lengths used for the reflection coefficient determination, which in turn is used in the partial injector simulations (Case 9P, Case 12P and Case 14P). Following the approach described in Section 3.3 and using the values of L , \bar{M} and \bar{c} , we determine the reflection coefficient for the 9, 12 and 14 cm cases using Eq. (3.42) and Eq. (3.44).

4.3. Simulation details

A multi-block, structured grid with a baseline grid of approximately 1.4 million grid points is used in the present study. The quality of the grid is important to simulate such problems, particularly in the shear-layer region. Nearly uniform grid clustering in these regions and slow stretching (less than 5%) towards the outflow is used to keep the grid resolution reasonable for practical simulations. The minimum grid resolution, 0.045 mm, in the fuel/oxidizer shear-layer and the near uniform quality there allows the post tip region to be reasonably resolved by approximately 50 points along the axial direction up to the dump plane. In the transverse direction, there are around 16 grid points in the shear layer at the exit of the fuel injector ($0.49 \leq y/D \leq 0.54$) and 18 points at the dump plane ($0.53 \leq y/D \leq 0.59$).

All the simulations are performed initially for about 10 flow-through times to allow the initial transients to pass away and reach a statistically stationary state. Here, the flow through time is approximately 1.8 ms and is estimated based on the bulk velocity at the oxidizer inlet and the total axial length of the domain. Afterward, turbulence statistics are obtained by performing a running time average of field variables for about 14 flow-through times. The convergence of the turbulence statistics is monitored through global quantities such as the mean reattachment and flame lengths, which showed convergence after about 10 flow-through times. Note that the acoustic time based on the first dominant frequency is about 0.6 ms and therefore, simulations are long enough to ensure limit cycle behavior is captured.

5. Results

In this section, we compare the results obtained from the simulations employing the TDABC formulation (Case 9P, Case 12P and Case 14P) with those obtained from full injector simulations (Case 9F, Case 12F and Case 14F). In particular, we analyze the time-averaged reactive flow features, limit cycle behavior of acoustic pressure fluctuations and the instantaneous flame dynamics to demonstrate the predictive ability of the TDABC formulation based LES investigation of thermo-acoustic instabilities.

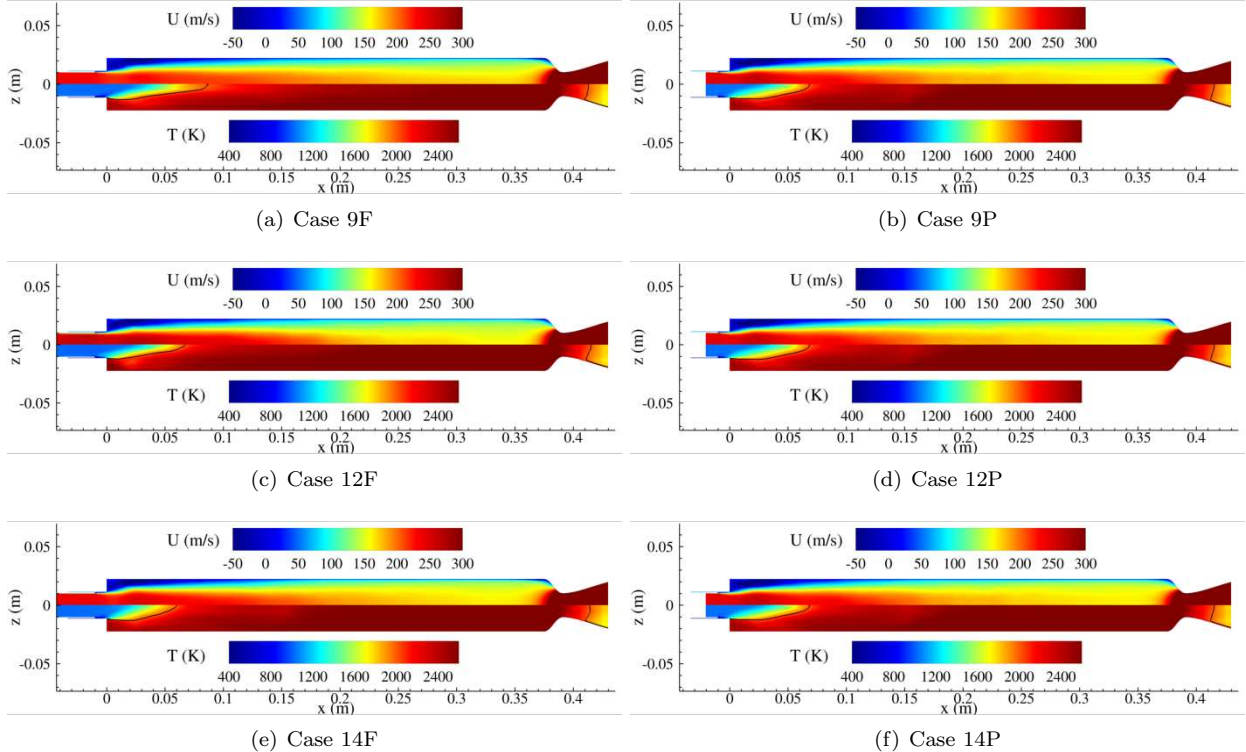


Figure 9: Contours of the time-averaged axial velocity (top-half) and temperature (bottom-half) fields in the central plane for all the six cases. Solid black curve denotes an iso-line of $T = 2000$ K characterizing the mean position of the turbulent flame brush.

5.1. Time averaged reactive flow field

Figure 9 shows the time-averaged contours of the axial velocity and temperature fields for all the six cases. We can observe a good agreement of the results obtained from the cases with the fully modeled injector (left) and the same cases where the injector is modeled with a reflection coefficient. The contours of time-averaged axial velocity shows presence of a corner recirculation zone (CRZ), which appears due fuel and oxidizer jet expansion near the dump plane, which impacts further downstream on the combustor wall leading to formation of a hot region of products. The extent of the CRZ is nearly the same for all the cases. The iso-line of $T = 2000$ K is used to identify the mean position of the turbulent flame brush and we qualitatively use the location at the centerline to identify the mean extent of the flame brush [11]. The mean flame length x_f/D is 8.2, 6.8, 5.9, 7.0, 7.1 and 6.9 for Case 9F, Case 12F, Case 14F, Case 9P, Case 12P and Case 14P, respectively. We can observe that the flame length decreases with an increase in L_{O_x} and TDABC formulation is able to predict this behavior. The reduction in the flame length suggests that the burning region becomes more compact with an increase in the inlet length suggesting a coupling between the injector and the combustor.

Figure 10 shows contours of the time-averaged reaction-rate of CH_4 and space-local Rayleigh index (R) for all the six cases. Qualitatively, the reaction rate contours look similar and they indicate the region where the methane is consumed in a time-averaged sense, thus providing details of the flame position. In particular, the reaction rate is higher in the shear layer compared to other parts of the combustor. This is consistent with the mean location of the flame brush shown in Figure 9. We can also observe that the extent of high reaction rate region increases with an increase in L_{O_x} and there is a noticeable shift upstream with an increase of L_{O_x} .

The Rayleigh index is a well known parameter typically used to characterize the coupling between the unsteady heat release and pressure oscillation. It is positive when coupling is in-phase and suggests combustion to be driving the growth of pressure fluctuations leading towards combustion instability. Based on

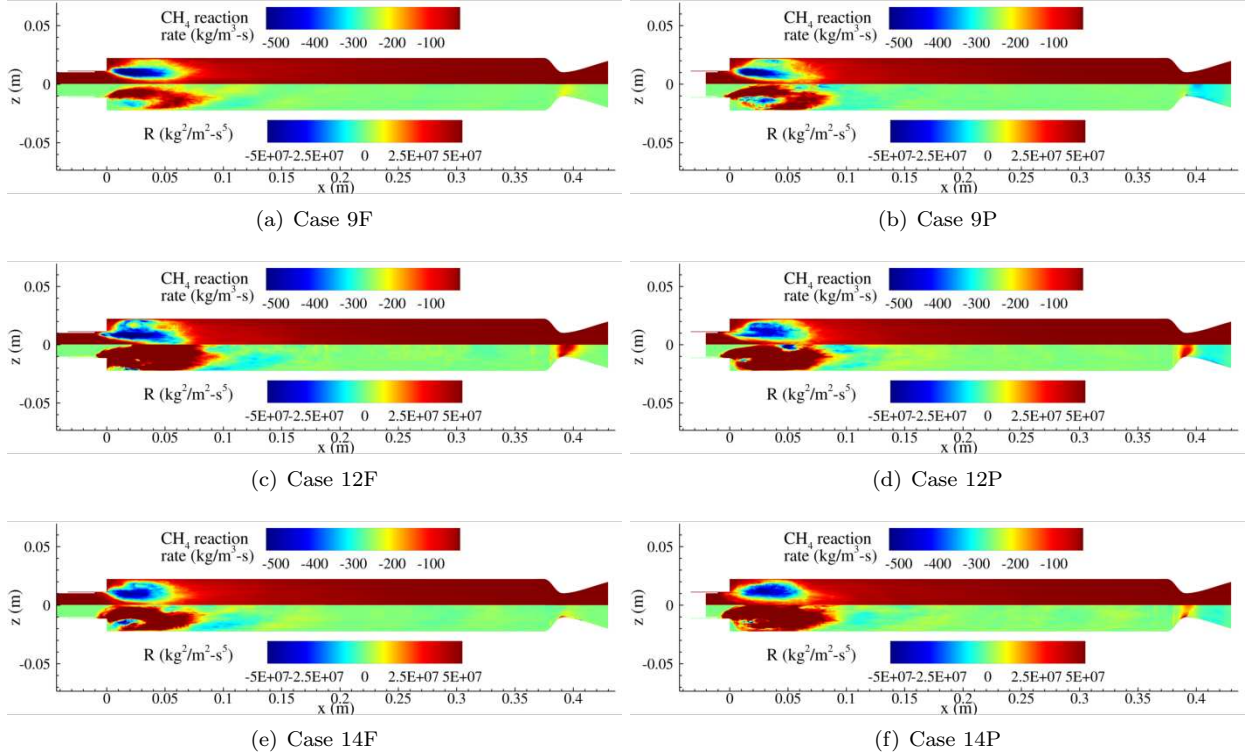


Figure 10: Contours of the time-averaged fuel reaction-rate (top-half) and space-local Rayleigh index (bottom-half) in the central plane.

the conservation equation for the acoustic energy, a space-local time-averaged Rayleigh index is defined as [5, 11]

$$R = (1/\tau) \int_t^{t+\tau} (\gamma - 1)/\gamma p' q' dt, \quad (5.1)$$

where τ is the time of averaging, $\gamma \equiv \gamma(\tilde{T})$ is the temperature dependent ratio of specific heat for thermally perfect gas, and p' and q' are the pressure and heat-release-rate fluctuations, respectively. Here, \tilde{T} denotes the filtered LES temperature field. The contours of Rayleigh index also show that coupling between p' and q'_g is very strong in the region of strong reactions. In Figure 10, the red zone indicates a region of instability while blue zone indicates damping of instability because pressure and heat release are out of phase. It can be observed that in Case 9F and Case 9P, red and blue zones coexist downstream the dump plane. This indicates that the thermo-acoustic instability appears/disappears, and therefore, 9 cm case is referred to as a “semi-stable” case. However, in 12 cm and 14 cm cases, the value of R is predominantly high in both full and partial injector simulations, which is consistent to experimental findings as these cases are fully unstable.

Overall, the time-averaged results obtained from full and partial injector simulations demonstrate a good agreement. In addition, these simulations are able to predict stable/unstable behavior exhibited by the combustor when the length of the oxidizer injector is changed in a manner consistent to the experimental observations.

5.2. Analysis of pressure oscillations

In table 3, analyses of the first three modes frequencies and amplitudes is summarized. These data is obtained by post-processing pressure data at location $x/D = 18$.

Figure 11 contains pressure signal at $x/D = 18$ for all three cases. These signals have been obtained by starting the simulations from time $t = 0 s$. This results show that the same level of instability is obtained

Table 3: Dominant frequencies and their corresponding limit cycle amplitudes at $x/D = 18$ on the combustor wall.

Case	f_1 (Hz) (Hz)	A_1 (kPa 2 /Hz)	f_2 (Hz)	A_2 (kPa 2 /Hz)	f_3 (Hz)	A_3 (kPa 2 /Hz)
9F	1663	117.3	2760	24.7	3336	2.3
9P	1579	274.4	2672	2.83	3360	0.5
Experiment	1392	17.2	2704	0.5	3772	N/A
12F	1597	593.5	3154	50.1	4751	16.1
12P	1551	882.3	3103	52.9	4654	6.6
Experiments	1385	1045.0	2777	58.4	4169	N/A
14F	1611	1054.7	3213	25.4	4832	1.4
14P	1487	941.1	2974	114.0	4462	12.7
Experiments	1331	909.5	2655	74.6	3986	N/A

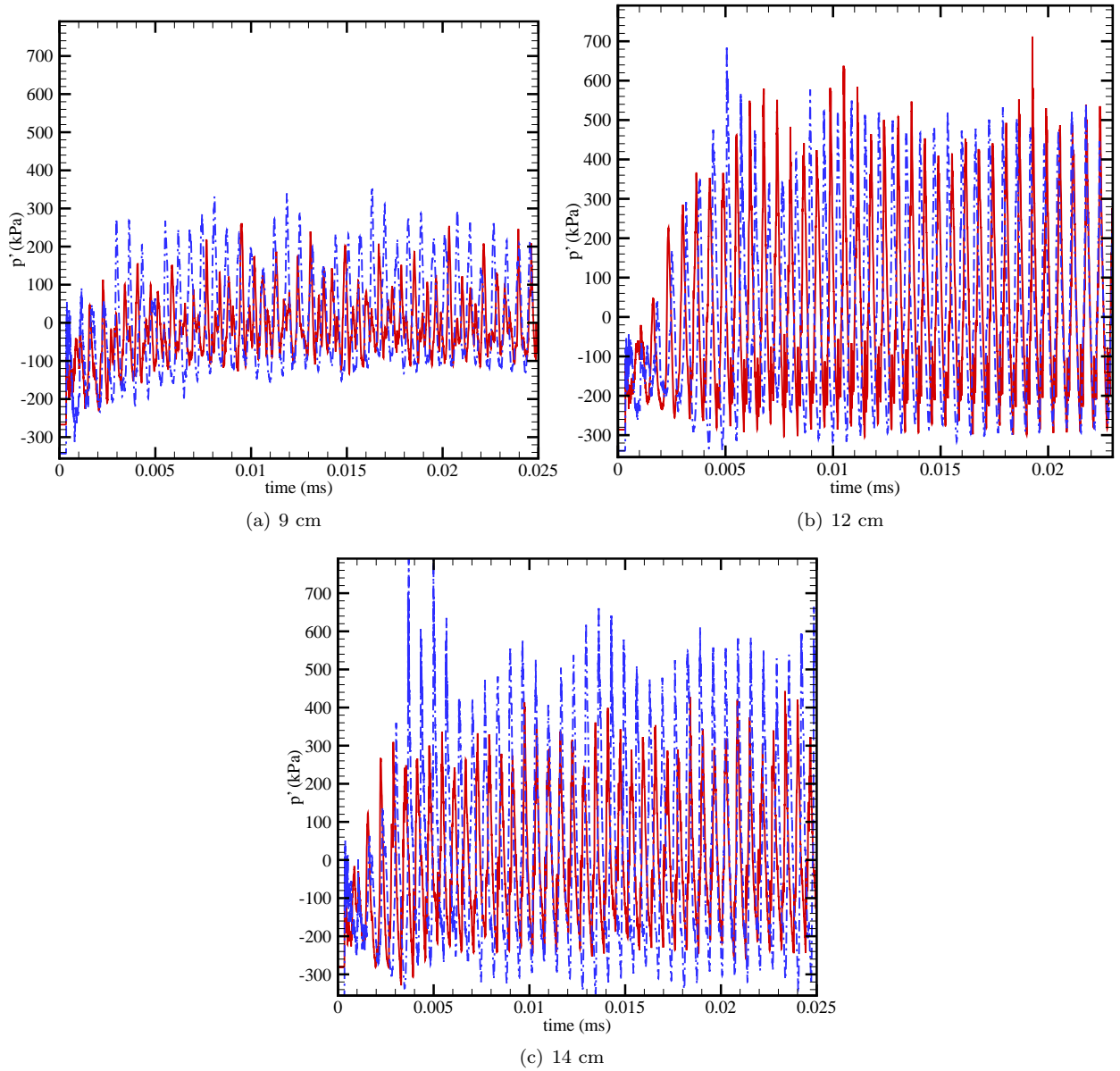


Figure 11: Time evolution of the pressure fluctuation at $x/D = 18$ on the combustor wall starting from the ignition transient. Red curves and blue curves denote the simulation with full meshed injector and with admittance boundary condition respectively.

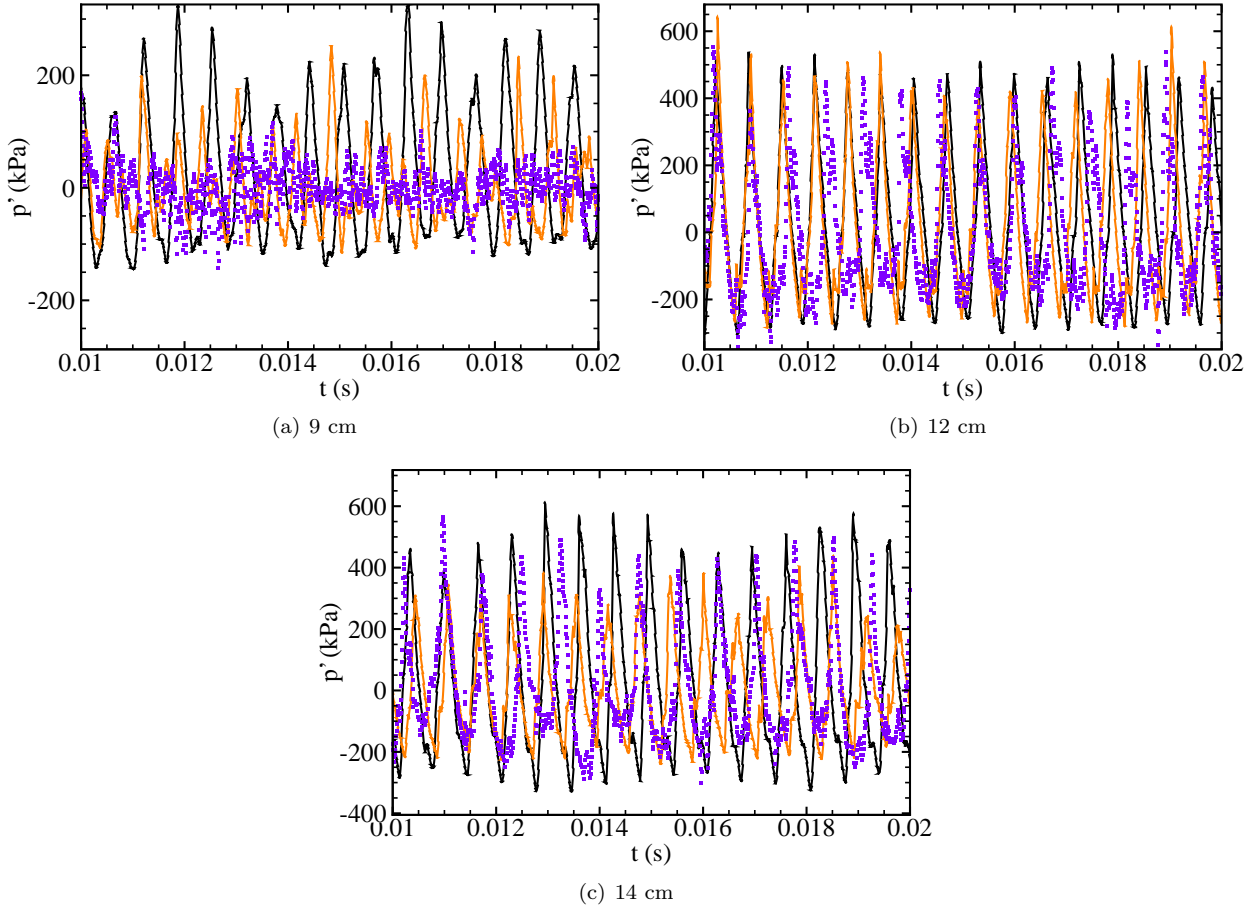


Figure 12: Time evolution of the pressure fluctuation at $x/D = 18$ on the combustor wall for approximately 10 acoustic cycles. Purple symbol denotes experimental data [38] and solid orange and black curves denote simulations with full injector (without admittance boundary condition) and partial injector (with admittance boundary condition), respectively.

in either calculations, including the transient phase. However, difference in pressure amplitude is observed, especially for cases 9 and 14. In fact, although case 12 displays good agreement in signal amplitude, the other two cases suggest that the pressure fluctuation amplitude is over predicted. This might be linked to some source of acoustic damping that is not taken into account with the current version of the reflection coefficient. In fact, acoustic damping is a function of frequency[37], therefore its magnitude can change depending of the signal and therefore depending of the injector size. Future work will include an extended model for the reflection coefficient, including frictional and thermal losses due to the acoustic boundary layer, so that a separate analysis for acoustic losses can be performed. Overall, the pressure fluctuations signals display good agreement with either full injector analyses and experimental data obtained from Purdue measurements data set[38] as shown in Figure 12, revealing that this approach is actually working at least for the current case.

Figure 5.2 shows spatial structure of the first two modes and their phase along the centerline of the combustor for all cases. All cases show a pressure node for the first longitudinal mode at about $x/D = 10$ downstream of the dump plane. This mode correspond to a half-wave standing mode in the combustor. The second mode shows two nodes in the combustor at around $x/D = 4$ and 14 for all cases. The third mode (not shown here) is not very distinct in amplitude in all cases, although Case 14 shows the presence of three possible nodes at around $x/D = 4, 10$ and 16. The phase change occurring across the nodes by 180° shows that the modes within the combustor correspond to standing waves. The amplitude of all the modes at the dump plane, i.e., $x/D = 0$ is significantly higher in Cases 12 and 14 compared to the semi-stable Case 9. These observations are consistent with the variation of the peak-to-peak oscillations of pressure fluctuations

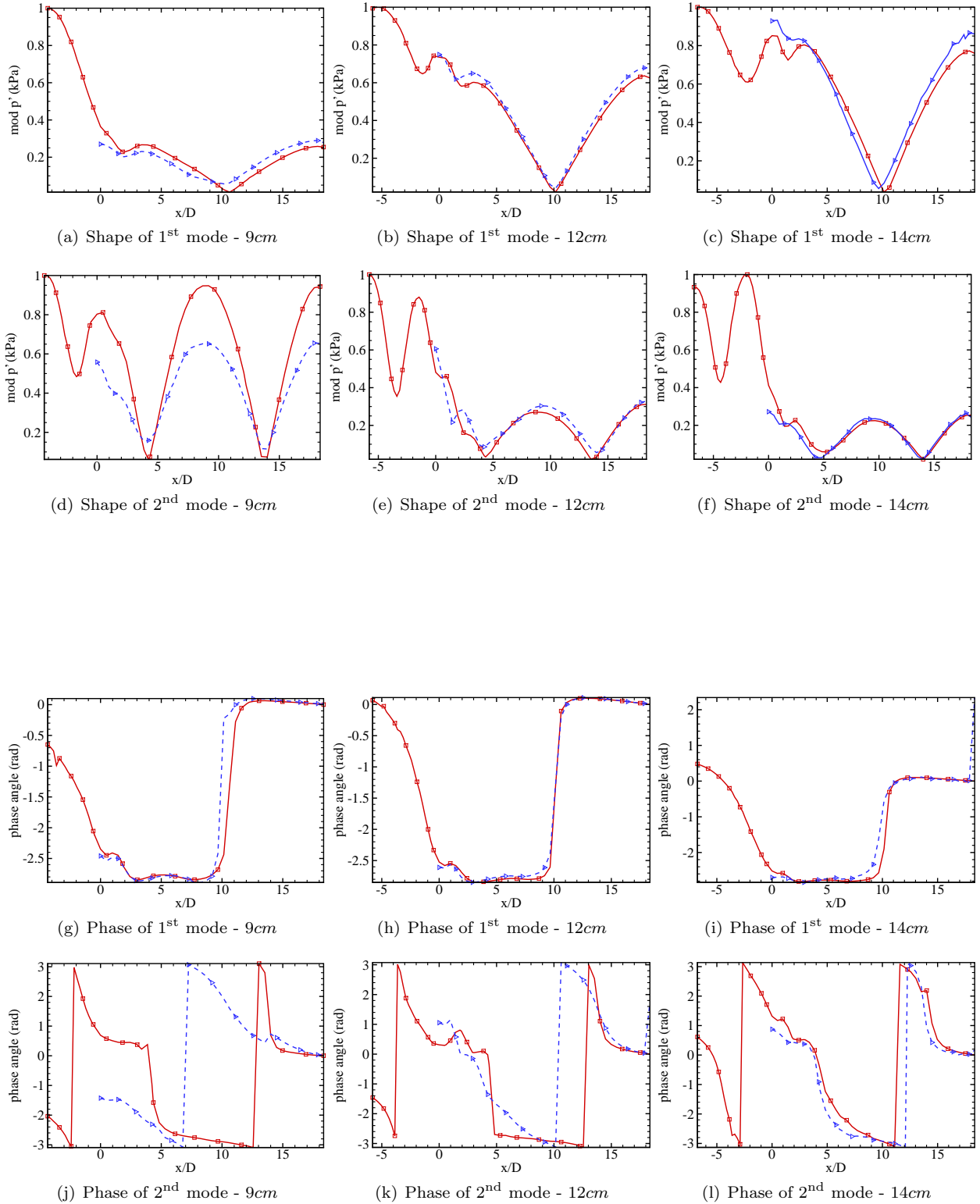


Figure 13: Mode shape and phase for the first two longitudinal modes.

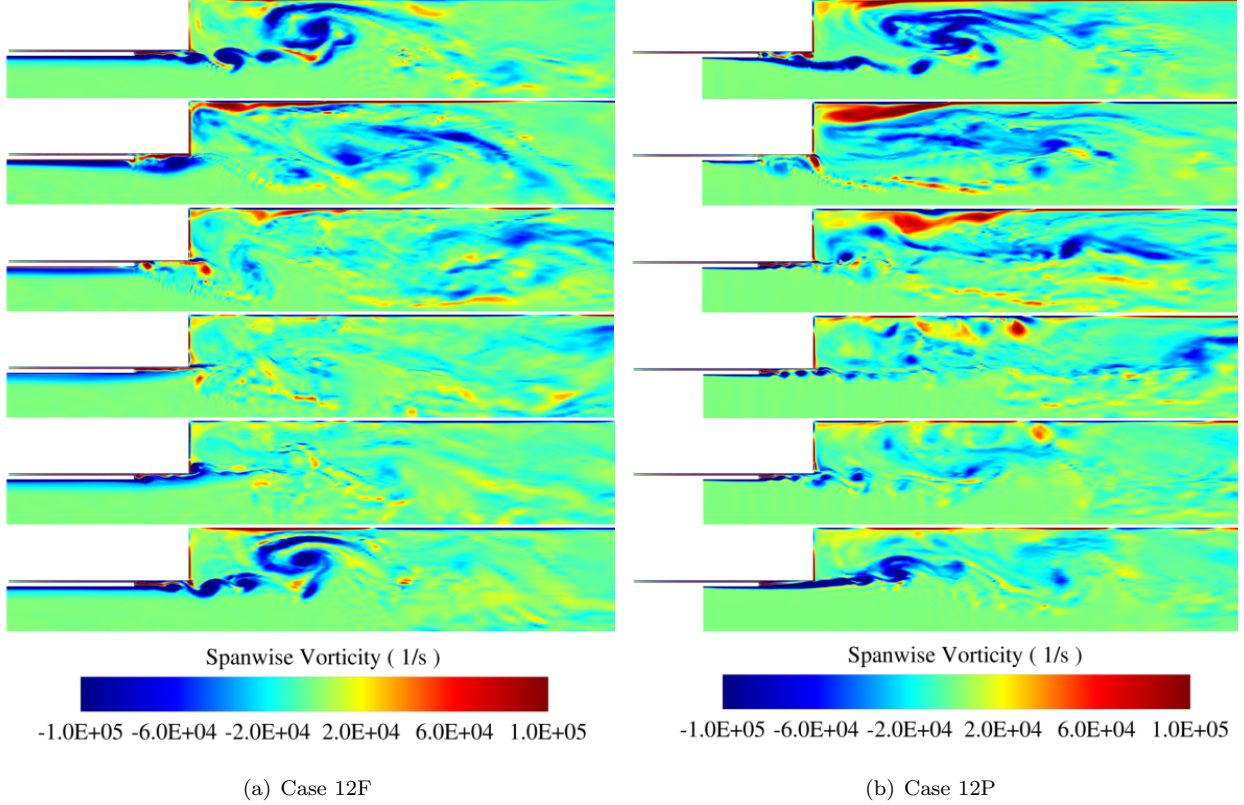


Figure 14: Contours of the spanwise vorticity ω_3 for Cases 12F and 12P in the positive half of the symmetry plane. The six frames are separated in phase by roughly 60° .

across different cases shown in Fig. 12. The amplitude of the first propagating mode at the oxidizer inlet decreases with an increase in the oxidizer length while the second mode has a higher magnitude in the unstable cases compared to the semi-stable Case 9. The higher magnitude of first mode at the inlet for Case 9 may be responsible for movement of the flame further downstream compared to the other two cases. Even for the mode shapes, the plane wave masking approach reveals a good level of agreement, except for some phase lag observed for the second modes.

5.3. Flame dynamics

Figure 14 shows the instantaneous contours of the span wise vorticity ω_3 for Cases 12F and 12P at six different time instants, approximately separated by a phase of 60° and taken within a cycle starting at 15 ms. We can clearly observe that the magnitude of ω_3 in the combustor dump plane region does not remain constant, which is associated with the fluctuations of the oxidizer and fuel mass flow rates occurring due to the traveling acoustic waves [12]. This in turn affects the vortex shedding phenomenon at the separated shear layer. These features are similar to those reported in past studies [12, 39]. For all cycles, the vortex shedding frequency closely corresponded to that of f_1 ; 1597 Hz and 1551 Hz, respectively for Cases 12F and 12P. The beginning of each cycle is characterized by strong vorticity packets released from the dump plane towards the chamber walls. After the impact, the vortex breaks generating counter-rotating structures in correspondence of the chamber corner. These structures are more emphasized in the admittance case. Afterwards no clear vorticity evidence is present in the chamber because the wave is far from the dump plane, except some vorticity pockets shed from the mixing layer zone. When the acoustic wave approaches back to the dump plane the big vortex is again formed, possibly due to the coupling between the acoustic mode with the vorticity mode determined by the fact that the pressure wave amplitude needs to be adjusted because of the change in the cross sectional area. Overall the mechanism of vorticity release is well reproduced by

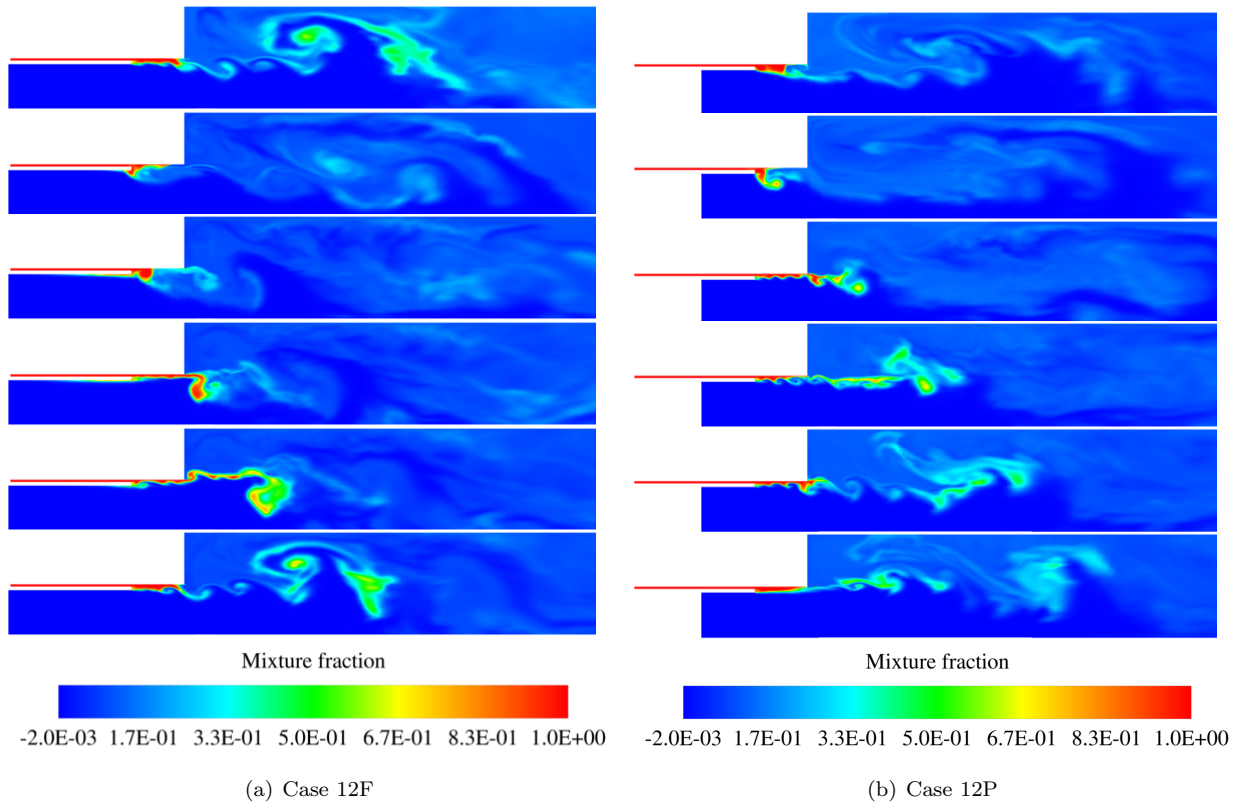


Figure 15: Contours of the mixture fraction field z near the dump-plane for Cases 12F and 12P in the positive half of the symmetry plane. The six frames are separated in phase by roughly 60° and correspond to same time-instants as Figure 14.

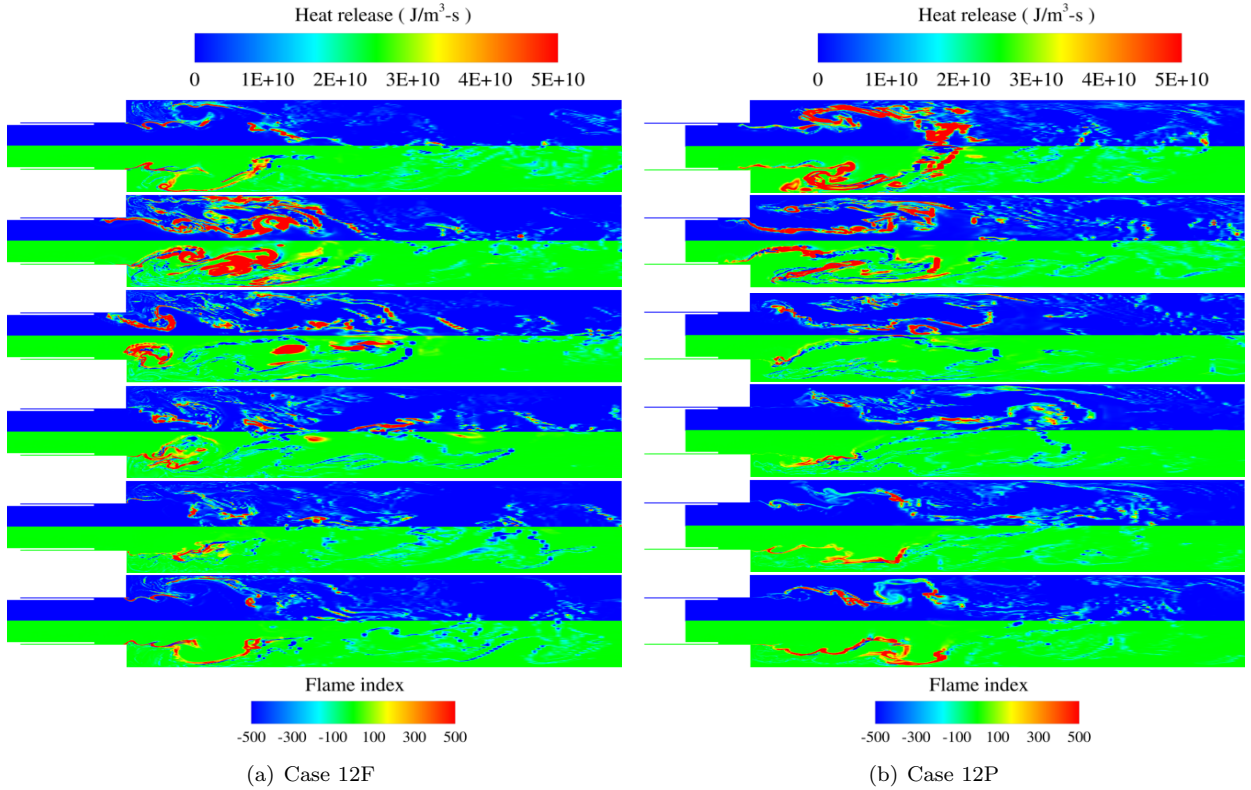


Figure 16: Contours of the flame index FI and the heat-release rate HRR for Cases 12F and 12P in the symmetry plane at the same six time instants within one cycle.

the admittance case. Figure 15 shows instantaneous contours of the mixture-fraction field z obtained from Cases 12F and 12P at the corresponding time instants of Figure 14. The mixture fraction is defined using elemental carbon mass fraction as [29]:

$$z = \frac{Z_c - Z_{c,\text{Ox}}}{Z_{c,f} - Z_{c,\text{Ox}}}, \quad (5.2)$$

where, the carbon based passive scalar, Z_c is given by,

$$Z_c = \sum_k \frac{W_c}{W_k} Y_k. \quad (5.3)$$

In the above equation, W_k represents the molecular weight of the k^{th} species and W_c is the atomic weight of elemental carbon. The summation spans the carbon containing species, CH_4 , CO and CO_2 . The subscripts “Ox” and “f” correspond to the passive scalar’s value at the oxidizer and fuel inlets respectively. The stoichiometric mixture fraction, $z_{\text{st}} = 0.095$ based on this definition. From the contours of z thus defined, the intermittent nature of fuel flow is apparent - the fuel mass flow rate, \dot{m}_f is affected by the local magnitude of pressure oscillation such that a period of quasi-steady fuel injection is followed by sudden drops in flow rates (when locally, the pressure is higher than the mean). We observe qualitatively similar behavior in both these cases and the features are similar to those reported in a recent LES investigation [12]. The flame structure can also be characterized by using the flame index [40], which is defined as

$$FI = \frac{\nabla Y_f \cdot \nabla Y_{\text{Ox}}}{|\nabla Y_f| |\nabla Y_{\text{Ox}}|} |\dot{\omega}_f|. \quad (5.4)$$

It is representative of the nature of burning, whether premixed (positive) or diffusion (negative). Figure 16 compare the flame index FI as well as the heat release for the 12F and 12P cases. It can be observed

the presence of both positive and negative values of the flame index, recognizing the double nature of the combustion zone as a partially premixed flame. Previously, researchers [11, 36, 39] have noted them to be triple-flames or tri-branchial flames. Here too we note that similar flame structures occur when fresh fuel mixture makes contact with the hot-products in the recirculation region. Due to a highly unsteady nature of the flow, these locations are not quasi-stationary but move in time and space, and even in the azimuthal direction. Additionally at some locations, the intersection of rich-premixed flame and a weak diffusion flame is seen as a double-flame structure. Presence of independent premixed flames closer to the dump plane and diffusion flames further away in the combustor are also seen. Thus, all possible types of burning modes can be seen depending upon the instant of observation. The flame structure and its burning modes are very similar in both calculations, meaning that the admittance implementation does not affect the flame behavior and dynamics. In fact, it seems that this is completely governed by the mixing zone, i.e. the zone between the fuel slot ending and the dump plane, where propellants start to mix and interact with the left traveling waves, which is explicitly solved.

6. Conclusions

Study of combustion instabilities in a typical shear coaxial, multi-element systems by LES is challenging from computational point of view due to the complex geometry and a need to resolve multiple scales present in such systems. In this study, we present application of the time domain admittance boundary conditions, that have been already tested with LES in recent works [1, 2] to study thermo-acoustic longitudinal instabilities in a model shear coaxial, high-pressure, single element combustor. Within the assumption of one dimensional, acoustic wave approaching the boundary, the admittance boundary condition, translated as a reflection coefficient can easily provide the response of a forced acoustic cavity in the linearized, inviscid conditions. This approach fits very well in the modeling of multi-injectors face plate, as each injector cavity can be associated with an explicit, analytic reflection coefficient that modulates either the amplitude and the phase of the initial signal coming from the combustion chamber. The first attempt of this long-term goal is discussed in this work, where a single injector, self-unstable, combustion chamber is considered. This rig, known as CVRC [7, 8] expresses spontaneous longitudinal instability for specific length of the injector. The injector itself is characterized by a shear-coaxial element: the upstream part flows oxidizer, while the circular annular slot flows fuel. The admittance model obtained for a single injector is completely determined by knowing the injector length and the mean flow properties, which have been determined by previous calculations and from the experiments. Therefore three injector lengths have been compared by using the full explicit cavity representation and the admittance boundary condition. Pressure trace results obtained from the TDABC calculations showed good agreement with the full injector case and the experiment as well, revealing a capturing of the unstable frequencies in a reasonable manner. Some differences arise from the signal amplitude point of view, but it is retained to be not only a side effect of the TDABC, as the same shifts have been observed in previous calculations for the full injector case [12], and have been attributed to the use of adiabatic wall boundary condition. Comparison between the full pressure signals in all the cases, starting from the same initial conditions provides an evidence that the different levels of instability dictated by the injector lengths, and also the mode shapes have been quite well captured. The vorticity analysis showed the presence of a similar cycle of the vorticity modes that couples with the acoustic mode in correspondence of the dump plane, determining the release of large vortical structures impinging the chamber walls and causing localized heat release. Finally, the study of flame index reveals the presence of a partially premixed flame as shown by the explicit injector modeling. Overall, this work illustrated the application of TDABC can be a promising tool that can be used to reduce the overall size of the computational grid, i.e., the computational cost and at the same time retaining the overall injector response, which plays an essential role in the combustion instability sustainment. In future, the method will be extended to study multi-element combustion chambers, transverse instability, and non perfect gaseous propellant.

Acknowledgment

This work is supported by AFOSR. The computational resources provided by DoD HPC Centers at the Engineer Research and Development Center is greatly appreciated.

References

- [1] W. Polikfe, C. Wall, and P. Moin. Partially reflecting and non-reflecting boundary conditions for simulation of compressible viscous flow. *J. Comp. Phys.*, 213:437–449, 2006.
- [2] R. Kaess, A. Huber, and W. Polikfe. High a time-domain impedance boundary condition for compressible turbulent flow. *14th AIAA/CEAS Aeroacoustics Conference*, 2008.
- [3] John William Strutt Baron Rayleigh. *The theory of sound*, volume 2. Macmillan, 1896.
- [4] David T Harrje. Liquid propellant rocket combustion instability. 1972.
- [5] T. J. Poinsot, A. C. Trouv , D. P. Veynante, S. M. Candel, and E. J. Esposito. Vortex-driven acoustically coupled combustion instabilities. *J. Fluid Mech.*, 177:265–292, 1987.
- [6] S bastien M Candel. Combustion instabilities coupled by pressure waves and their active control. In *Symposium (International) on Combustion*, volume 24, pages 1277–1296. Elsevier, 1992.
- [7] Y. C. Yu, S. M. Koeglmeier, J. C. Sisco, and W. E. Anderson. Combustion instability of gaseous fuels in a continuously variable resonance chamber (CVRC). *AIAA 2008-4657*, pages 1–12, 2008.
- [8] J. C. Sisco. *Measurement and Analysis of an Unstable Model Rocket Combustor*. PhD thesis, Purdue University, 2007.
- [9] Y. C. Yu. *Experimental and Analytical Investigations of Longitudinal Combustion Instability in a Continuously Variable Resonance Combustor*. PhD thesis, Purdue University, 2009.
- [10] M. E. Harvazinski. *Modeling Self-Excited Combustion Instabilities Using a Combination of Two- and Three-Dimensional Simulations*. PhD thesis, Purdue University, 2012.
- [11] R. Garby, L. Selle, and T. Poinsot. Large-eddy simulation of combustion instabilities in a variable-length combustor. *Comptes Rendus Mecanique*, 341:220–229, 2013.
- [12] S Srinivasan, R Ranjan, and S Menon. Flame dynamics during combustion instability in a high-pressure, shear-coaxial injector combustor. *Flow, Turbulence and Combustion*, 94(1):237–262, 2015.
- [13] T J& Poinsot and SK Lelef. Boundary conditions for direct simulations of compressible viscous flows. *Journal of computational physics*, 101:104–129, 1992.
- [14] D.H. Rudy and J.C. Strikwerda. A nonreflecting outflow boundary condition for subsonic navier-stokes calculation. *J. Comp. Phys.*, 36:55–70, 1980.
- [15] S. W. Rienstra and A. Hirschberg. *An Introduction to Acoustics*. Eindhoven University of Technology, 2013.
- [16] T. C. Lieuwen. *Unsteady Combustor Physics*. Cambridge University Press, 1st edition, 2012.
- [17] T.J. Poinsot and D. Veynante. *Theoretical and Numerical Combustion*. Edwards, Inc., second edition, 2005.
- [18] Ramakanth Munipalli, Zhining Liu, Xueyu Zhu, Suresh Menon, and Jan S Hesthaven. Model reduction opportunities in detailed simulations of combustion dynamics. In *52nd Aerospace Sciences Meeting, 13-17 January 2014, National Harbor, Maryland*, 2014.
- [19] Dinh Bao Phuong Huynh, David J Knezevic, and Anthony T Patera. A static condensation reduced basis element method: approximation and a posteriori error estimation. *ESAIM: Mathematical Modelling and Numerical Analysis*, 47(01):213–251, 2013.
- [20] Alfio Quarteroni, Gianluigi Rozza, and Andrea Manzoni. Certified reduced basis approximation for parametrized partial differential equations and applications. *Journal of Mathematics in Industry*, 1(1):1–49, 2011.
- [21] G. Erlebacher, M. Y. Hussaini, C. G. Speziale, and T. A. Zang. Toward the large-eddy simulation of compressible turbulent flows. *J. Fluid Mech.*, 238:155–185, 1992.

- [22] F. Génin and S. Menon. Studies of shock/turbulent shear layer interaction using large-eddy simulation. *Computers & Fluids*, 39:800–819, 2010.
- [23] M. Masquelet and S. Menon. Large eddy simulation of flame-turbulence interactions in a shear coaxial injector. *J. Prop. Power*, 26:924–935, 2010.
- [24] S. Menon and N. Patel. Subgrid modeling for simulation of spray combustion in large-scale combustors. *AIAA J.*, 44:709–723, 2006.
- [25] W. W. Kim and S. Menon. An unsteady incompressible Navier-Stokes solver for large eddy simulation of turbulent flows. *I. J. for Numer. Meth. Fluids.*, 31:983–1017, 1999.
- [26] F. F. Grinstein and K. Kailasanath. Three-dimensional numerical simulations of unsteady reactive square jets. *Combustion and flame*, 101(1):192, 1995.
- [27] K-J Nogenmyr, C Fureby, Xue-Song Bai, P Petersson, Robert Collin, and Mark Linne. Large eddy simulation and laser diagnostic studies on a low swirl stratified premixed flame. *Combustion and Flame*, 156:25–36, 2009.
- [28] M Berglund, E Fedina, C Fureby, J Tegner, and V Sabel’Nikov. Finite rate chemistry large-eddy simulation of self-ignition in supersonic combustion ramjet. *AIAA journal*, 48:540–550, 2010.
- [29] T. Poinsot and D. Veynante. *Theoretical and Numerical Combustion*. <http://elearning.cerfacs.fr/>, 3rd edition, 2012.
- [30] Schlichting H. and Gersten K. *Boundary Layer Theory*. Springer, 2000.
- [31] White F. *Viscous Fluid Flow*. Tata McGraw Hill, 2011.
- [32] Ogata K. *Modern control engineering*. Prentice Hall Inc., 5th edition, 2002.
- [33] T. J. Poinsot and S. K. Lele. Boundary conditions for direct simulations of compressible viscous flows. *J. Comp. Phys.*, 101:104 – 129, 1991.
- [34] Kevin W Thompson. Time dependent boundary conditions for hyperbolic systems. *Journal of computational physics*, 68(1):1–24, 1987.
- [35] J Enrique Portillo, James C Sisco, Martin J Corless, Venkateswaran Sankaran, and William E Anderson. Generalized combustion instability model. *AIAA Paper*, 4889:9–12, 2006.
- [36] N. Guézennec, T. Dawson, P. Sierra, and S. Menon. Flame holding dynamics during combustion instability in a shear coaxial injector. In *In 8th Int. Symp. On Turbulence and Shear Flow Phenomena*, Poitier, France, 2013.
- [37] F. E. C. Culick. *Unsteady Motions in Combustion Chambers for Propulsion Systems*. North Atlantic Treaty Organization, 2006.
- [38] T. W. Feldman and W. E. Anderson. Experimental dataset for CVRC setup, private communication, 2013.
- [39] M. E. Harvazinski, C. Huang, V. Sankaran, T. W. Feldman, W. E. Anderson, C. L. Merkle, and D. G. Talley. Combustion instability mechanisms in a pressure-coupled gas-gas coaxial rocket injector. *AIAA Paper 1013–3990*, pages 1–21, 2013.
- [40] N. Patel and S. Menon. Simulation of spray-turbulence-flame interactions in a lean direct injection combustor. *Combust. Flame*, 153:228–257, 2008.

Flame Dynamics During Combustion Instability in a High-Pressure, Shear-Coaxial Injector Combustor

S. Srinivasan · R. Ranjan · S. Menon

Received: 30 December 2013 / Accepted: 3 September 2014 / Published online: 26 September 2014
© Springer Science+Business Media Dordrecht 2014

Abstract We present a large-eddy simulation based investigation of combustion instability in the Continuous Variable Resonance Combustor (CVRC); a high-pressure, shear-coaxial injector combustor studied experimentally at Purdue University. An important characteristic of the CVRC setup is the role that the oxidizer injector length plays in the stable/unstable combustion dynamics occurring within the combustor. We perform three simulations corresponding to different stability regions; one is a semi-stable case whereas the other two cases are unstable. The acoustic pressure fluctuation exhibits a limit cycle behavior in all cases. An abrupt change in the predicted amplitude between stable and unstable cases is also observed, consistent with the experimental trends. Further investigations to characterize the mechanism driving such abrupt change in the stability pattern when the oxidizer injector length is varied, show that acoustic interactions with the flow field lead to subtle changes in the vorticity (and mixing) dynamics, which significantly alters the distribution of species and heat release. In addition, aspects related to flame stabilization such as the mean flame anchoring location and the mode of burning, premixed or non-premixed, are also affected. The analysis of flame structures shows the presence of multi-mode burning regions where premixed and non-premixed flames appear to coexist. However, the dominant burning mode switches from premixed to non-premixed within an acoustic cycle, potentially playing an important role in flame stabilization.

Keywords Large eddy simulation · Linear eddy mixing · Combustion instability · Non-premixed combustion

S. Srinivasan (✉) · R. Ranjan · S. Menon
School of Aerospace Engineering, Georgia Institute of Technology,
270 Ferst Drive, Atlanta, GA, 30332-0150, USA
e-mail: ssrinivasa7@mail.gatech.edu

S. Menon
e-mail: suresh.menon@ae.gatech.edu

1 Introduction

Combustion instability is a phenomenon observed in several systems such as liquid/solid rocket engines, premixed gas turbines, ramjets, and afterburners under certain operating conditions. It is understood to be the result of nonlinear coupling of unsteady heat release with local pressure (acoustic) fluctuations resulting in large-amplitude pressure oscillations [1–7]. Such oscillations manifest very quickly in time, resulting in large thermo-mechanical stresses and ultimately causing catastrophic damage. Eliminating or controlling combustion instability has been a focus of many past studies. However, both experimental and numerical methods face several challenges in their ability to capture and investigate this phenomenon. Sustaining combustion instability in a test facility can be nearly impossible due to the possibility of damage. Furthermore, due to high pressure and hot operating conditions, detailed measurements are nearly impossible. Typically, only the pressure fluctuation data is available from wall sensors and combustion instability is inferred from such a signature. A facility called the continuously variable resonance combustor (CVRC) in Purdue University [8–10] has been shown to exhibit spontaneous combustion instability and is the focus of this study. In this rig, the injector length can be changed during or in-between the tests. It has been shown that the acoustic wave-modes in the injector can either constructively or destructively interact with the acoustic modes of the combustor resulting in stable or unstable combustion behavior [10]. Thus, this facility offers a unique opportunity to investigate different operating conditions that bracket the conditions for combustion instability.

The choice of appropriate numerical models and realistic boundary conditions are vital to the successful simulation of real world systems that exhibit combustion instability. Due to the unsteady nature of these problems, large eddy simulation (LES) and detached eddy simulation (DES) are two of the appropriate numerical approaches. In the past, LES has been actively used for many combustion instability studies in ramjets or dump combustors [2, 11, 12] and gas turbine combustors [13–15]. The CVRC configuration has also been studied using both LES and DES. Both axisymmetric and three-dimensional (3D) DES [16–18] and LES [19, 20] have been conducted to investigate the sensitivity of predictions to various operating parameters. It was found using axisymmetric DES [21] that when the choked slotted inlet of the experiment (discussed further below) was replaced by a subsonic inflow boundary condition, the amplitude of oscillations was underpredicted, although the key modes were excited as in the experiments. The flow through the slotted injector was also modeled and it was shown that in the axisymmetric configuration, vortical structures shed from the slot, persisted well into the regions of combustion. On the other hand in a 3D simulation, these structures were much less organized and more dissipated. These results suggest that 3D effects cannot be ignored. These studies also confirmed the presence of multiple acoustic modes in the combustor and showed that some of the key modes in the combustor are predicted in reasonable agreement with the experimental data. However, both the amplitude and the frequency showed differences [18].

LES has also been used to study the limit cycle behavior of the acoustic pressure fluctuation for different cases using a constant mass flow rate based characteristic inflow boundary condition in lieu of the slotted inlet [19, 20]. Although different codes and subgrid closures were employed in these studies, the prediction of acoustic modes was consistent. However, some differences related to the flame length and other mean quantities were noted; the fundamental frequency was over-predicted, attributed to the adiabatic wall conditions that do not account for heat loss from the system. Guézennec et al. [20] studied flame holding dynamics for two different injector lengths using the adiabatic-wall approximation, but

were still able to reproduce the semi-stable behavior in the short injector case and the more unstable behavior for the long injector case, consistent with the experimental results.

All previous 3D LES and DES studies showed that the mixing of fuel and oxidizer occurs downstream of the injector post tip, as typically observed in many shear coaxial systems. However, in the CVRC, due to a high strain-rate in the mixing layer, the diffusion flame cannot be sustained and instead, the flame is typically anchored at the dump plane corner as a partially premixed flame. Downstream of the dump plane, the flame burning mode becomes more complex due to mixing of the reactant-product mixture with the remaining oxidizer. In addition to the premixed mode, the non-premixed burning mode is also observed. In some cases, features reminiscent of the triple flame structure seen in canonical studies [22] were also qualitatively observed in the CVRC simulations [19, 23]. However, the 3D, unsteady and cyclic nature of burning in this rig makes a complete interpretation difficult and other possibilities can coexist, as shown in this paper. The flame anchoring process is also complicated due to partial premixing. For example, due to premixing downstream of the oxidizer post-tip, the leading flame can propagate upstream (lift off from the dump corner) if the boundary conditions are correctly specified. As will be shown in this paper, flame propagation in the CVRC is linked to the pressure oscillation signature and is a feature of combustion instability in this rig.

The objective of the present study is to investigate flame dynamics for different injector lengths. Three cases are chosen - one semi-stable and two unstable operating cases occurring due to three different injector lengths under otherwise identical operating conditions. The previous study [20] is extended to study flame dynamics and pressure-heat release coupling for these operating conditions. Comparisons with experimental data are made where available.

The article is arranged as follows. Section 2 describes the formulation, the modeling conditions, the numerical setup and grid assessment. This is followed by Section 3 where details of the three cases and the observations of pressure signature, flame dynamics and combustion instability are analyzed and compared with past predictions and data. Finally, conclusions and future directions are summarized in Section 4.

2 Formulation and Methodology

The numerical methodology is based on the well-established, second-order accurate (in both space and time) finite-volume solver for the unsteady Favre-filtered multi-species compressible LES equations [24]. A hybrid scheme, which switches between a second-order-accurate central scheme and a third-order-accurate MUSCL (Monotone Upstream-centered Schemes for Conservation Laws) scheme is employed [25]. A localized dynamic switch based on pressure and density gradients determines the spatial discretization scheme to use locally [24, 26]. Past studies have shown that the hybrid approach can capture regions of high gradients (as in shocks or thin shear layers between fuel and oxidizer) and also regions of turbulent fluctuations away from these strong gradients accurately [24–27].

The subgrid-scale (SGS) momentum and energy fluxes are closed using a subgrid eddy viscosity model, which is obtained using the local grid filter Δ and the subgrid kinetic energy k^{sgs} . An additional transport equation is solved for k^{sgs} and localized dynamic evaluation is used to obtain all the model coefficients [25, 28]. Details of the LES equations, numerical method and these closures are presented in several articles cited earlier and therefore avoided here, for brevity.

The closure of reaction-diffusion in the current approach is a two-scale scalar transport model called the linear eddy mixing (LEM) model, which too has been described elsewhere [29–33] and therefore, is not repeated here. The LEM approach when used in a LES (called LEMLES hereafter) is a two-scale method whereby, the reaction-diffusion small-scale process and turbulent stirring by sub-grid eddies (i.e., eddies smaller than Δ) are solved on a 1D grid embedded inside each LES cell at their respective time-scales. Concurrently, the large-scale turbulent transport (by eddies larger than Δ) of the scalar fields in the 3D domain is achieved using a Lagrangian transport algorithm that convects the subgrid scalar fields ensuring mass conservation. The fully coupled LEMLES has been used for many combustion applications [31, 32, 34–38]. Further details of the LEMLES formulation are available in the cited literature and only specific information relevant for this study are reported below.

2.1 The CVRC test conditions and modeling approach

Figure 1a shows a sketch of the CVRC rig [8] where the shaded region indicates the modeled domain. The view of the computational domain is shown in Fig. 1c along with the dimensions of the oxidizer injector tube and the combustor. The relative locations of the LES oxidizer and fuel inflow planes, and the recessed position of the injector post tip with respect to the dump plane are shown in Fig. 1d. The rig is essentially a dump-combustor with a central oxidizer duct and a coaxial fuel duct. The design of the rig allows for a variation of the oxidizer injector length L_{Ox} , which leads to stable/unstable behavior of the combustor. Some approximations are necessary to simplify the computational domain for LES. In the experiments, oxidizer flow occurs through the slotted inlet section (see Fig. 1b) and is assumed to be choked. In this study and as in previous studies [19, 20], we do not resolve the slotted inlet but assume that the inflow occurs with a fixed mass flow rate. Further details regarding the inflow boundary condition are provided below.

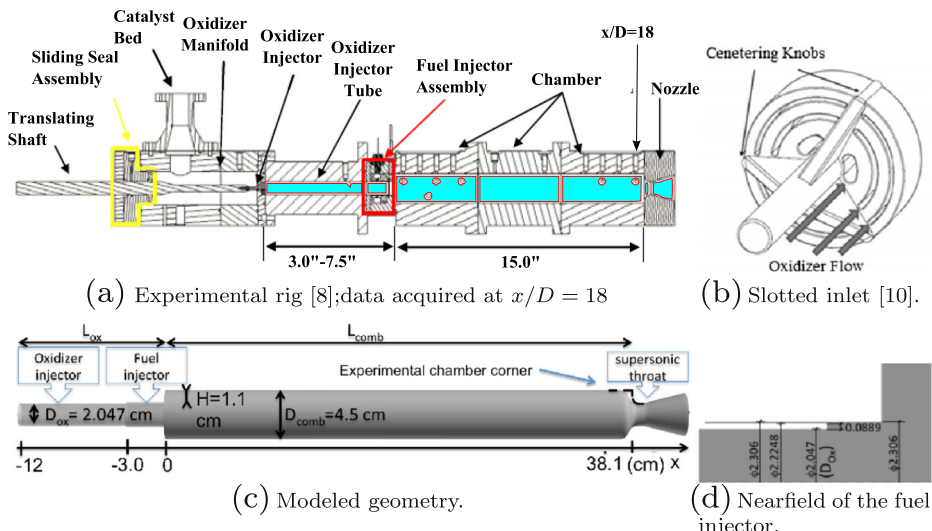


Fig. 1 The experimental and modeled geometry details. Dimensions are in cm except in (a)

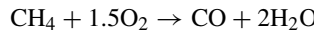
The fuel injection system is also not modeled but is assumed to come through a narrow annular slot as in the experiments and consistent with past studies [16–20]. All the other dimensions and locations of the injector post tip and choked outflow nozzle are as in the experiments. The length of the oxidizer inlet is varied and we study flame stabilization and combustion instability for a fixed combustor length $L_{\text{comb}}/D = 18.61$ but for three different oxidizer injector lengths $L_{\text{Ox}}/D = 4.40, 5.86$ and 6.84 , where the diameter of the oxidizer inlet duct $D \equiv D_{\text{Ox}} = 2.047$ cm is used as a reference scale. The three configurations are referred to as Case 9, Case 12 and Case 14, respectively, where the number corresponds to L_{Ox} in centimeters. Case 9 ($L_{\text{Ox}} = 9$ cm) is shown experimentally to be “semi-stable” (i.e., low-amplitude pressure fluctuations) while Cases 12 and 14 ($L_{\text{Ox}} = 12$ cm and 14 cm, respectively) are known to be unstable with different levels of instability.

The inflow boundaries are modeled using characteristic boundary conditions [39] where the mass flowrates, the species mass fractions and the temperature are prescribed. In the experiments, both the fuel and the oxidizer inlets are choked to provide well defined acoustic boundary conditions. Under isentropic assumptions, the constant mass flowrate based boundary condition is associated with an impedance, Z , which depends on the Mach number, Ma as $Z = -1/Ma$ (here, $Ma=0.4$ for the oxidizer) and hence, has a finite value. The experimental oxidizer injector is possibly associated with an impedance, which differs from the conventionally choked throat due to the slotted design. Its impedance, however, is unknown and the recent DES [18] suggests that its impact is mostly restricted to the vorticity distribution in its immediate downstream region but does not have a major effect on the dominant acoustic modes. Nevertheless, this issue will be revisited in the future.

Outflow is choked through the nozzle and supersonic conditions are employed at the nozzle exit. No-slip walls with adiabatic thermal conditions are used. Although heat loss from the walls is likely to play some role as noted earlier [19, 40], there is no experimental data pertaining to the thermal conditions at the wall. Therefore, we focus here mainly on flame stabilization during combustion instability and its sensitivity to the variation in the injector length without accounting for any heat loss through the walls. However, to investigate the sensitivity of the thermal boundary condition to the stability behavior of the combustor, we simulate two additional cases corresponding to the baseline Case 12, labeled as Case 12T1 and Case 12T2, where isothermal boundary conditions are employed on the combustor wall with temperatures of 1800 K and 1200 K, respectively. Harvazinski et al. [41] examined the effect of isothermal boundary condition by simulating cases with four different combustor wall temperatures, namely, 300, 600, 900 and 1200 K. At 300 and 600 K, no combustion was observed to occur, whereas limit cycle behavior was observed at 900 and 1200 K. In particular, a reduction in the amplitude of the instability was observed relative to the setup with adiabatic boundary conditions. These results indicate that the flame holding dynamics and stability of the combustor due to a coupling of the heat-release with the acoustic pressure oscillations can be studied by employing adiabatic boundary condition on the combustor wall.

The fuel is methane (CH_4) and the oxidizer is a mixture of O_2 and H_2O with mass fractions of 0.42 and 0.58, respectively. The fuel is injected through the annular injector at a constant mass-flow rate $\dot{m}_f = 0.027$ kg/s and constant temperature $T_f = 300$ K. The oxidizer is injected through the central pipe of the coaxial injector at a constant mass-flow rate $\dot{m}_{\text{Ox}} = 0.32$ kg/s and constant temperature $T_{\text{Ox}} = 1030$ K. The operating pressure of the combustion chamber is $P_{\text{ref}} = 1.34$ MPa and the global equivalence ratio is 0.8. The Reynolds number corresponding to the oxidizer and fuel passages are 481,000 and 33,000, respectively.

Finite-rate kinetics is employed in this study. Again, some approximation is required to make the problem tractable. A two-step, five species (CH_4 , O_2 , H_2O , CO_2 and CO) reduced kinetics is used in this study based on earlier studies [42] and is same as the one employed earlier for this rig [20]. The two-steps of the mechanism are given by



The mechanism involves correction functions that depend on the local equivalence ratio, ϕ to modify the pre-exponential factors appearing in the two rate expressions. The parameters used earlier [42] are retained in their unmodified form and tested for the flow conditions of the current investigation. Although a two-step model is a major approximation, for combustion instability, proper heat release is more critical than radical predictions and therefore, is considered acceptable [18].

Since the LEM subgrid model is used, the laminar rates are used in the subgrid LEM, which do not require explicit closure. The thermodynamic properties are calculated using the thermally-perfect equation of state.

2.2 Assessment of the numerical setup

Generally, the grid quality in the region of heat release is important due to the presence of large scalar gradients. The resolution in the shear layer in the base of the injector post tip is also important for the shear injector system [20, 26, 43]. Nearly uniform grid clustering in these regions and slow stretching (less than 5 %) towards the outflow is used to keep the grid resolution reasonable for practical simulations. A multi-block structured grid with a baseline grid of approximately 1.4 million grid points is employed for most of the reported simulations. Figure 2 shows the computational grid in the positive half of the symmetry $x - y$ plane with a close-up view of the grid in the shear-layer region near the dump plane and the fuel injector. The minimum grid resolution is 0.045 mm and occurs in the fuel/oxidizer shear-layer. Additionally, the near uniform quality there allows the post tip region to be reasonably resolved by approximately 50 points along the axial direction up to the dump plane. In the transverse direction, there are around 16 grid points in the shear layer at the

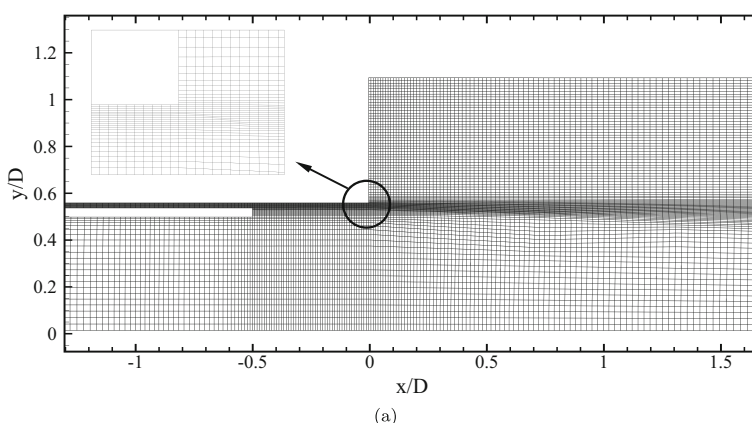


Fig. 2 The computational grid in the positive half of the symmetry $x - y$ plane with a close-up view of the shear layer near the oxidizer injector and the dump plane of the combustor

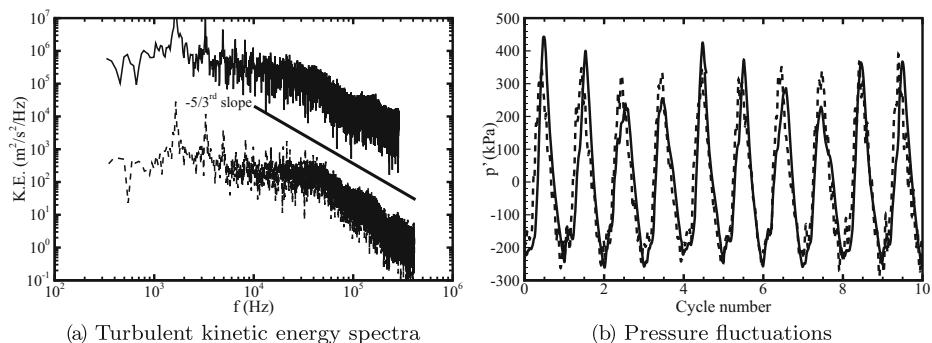


Fig. 3 Turbulent kinetic energy spectra (a) at $x/D = 0.6$ on the centerline of the combustor and time evolution of the pressure fluctuations (b) at $x/D = 18$ on the combustor wall, for Case 12 (solid curve) and Case 12F (dashed curve). The spectra for Case 12 is scaled by a factor of 10^3 for sake of clarity in (a)

exit of the fuel injector ($0.49 \leq y/D \leq 0.54$) and 18 points at the dump plane ($0.53 \leq y/D \leq 0.59$). Past studies [20, 26, 37] have shown that these resolutions are reasonable for an engineering level LES of such complex configurations. The subgrid LEM field is resolved with 12 LEM cells per LES cell based on the estimate of the Kolmogorov length scale computed from the subgrid kinetic energy, the local grid-size and the laminar viscosity.

All simulations are performed initially for about 7 flow-through times to allow the initial transients to wash out and reach a statistically stationary state. Here, the flow through time is approximately 1.8 ms and is estimated from the bulk velocity at the oxidizer inlet and the total axial length of the domain. Later, turbulence statistics are obtained by performing a running time average of field variables for about 14 flow-through times. The convergence of the turbulence statistics is monitored through global quantities such as the mean reattachment (x_r) and flame (x_f) lengths (discussed later). Convergence was achieved after approximately 10 flow-through times. Note that the acoustic time based on the first dominant frequency is about 0.6 ms and therefore, simulations are long enough to ensure limit cycle behavior is captured. All simulations are performed using 1488 cores with Intel Xeon Sandy Bridge architecture, with a core speed of 2.6 GHz. The computational cost of one flow-through time is approximately 6,000 CPU hours.

The LES grid quality is partly determined by analyzing flow features such as the turbulence spectrum in the shear layer and the acoustic signature for the reacting flow once limit cycle behavior is achieved. Figure 3a shows the kinetic energy spectrum obtained for $L_{\text{Ox}} = 12$ cm (Case 12) and another case with a finer grid of around 3.2 million points (called Case 12F) at a location in the shear layer ($x/D, y/D = (0.6, 0)$) in the symmetry plane. In Case 12F, the azimuthal grid resolution is improved. In both cases the turbulent kinetic energy spectra capture the inertial range and the dominant peaks in a reasonable manner. Figure 3b shows the pressure fluctuation signature $p' = p - \bar{p}$ at $x/D = 18$ at the wall (a location where pressure data is available for comparison and discussed later). Here \bar{p} denotes the mean (LES resolved) pressure at the corresponding location. Note that p' is the pressure fluctuation that includes both the acoustic and the turbulent fluctuations. Since the magnitude of fluctuations associated with an acoustic instability observed in typical combustors is usually much higher than the hydrodynamic turbulent fluctuations, we will refer p' to be the acoustic pressure hereafter. The dominance of the acoustic content is apparent from the contours of the instantaneous pressure fluctuation shown in Fig. 4. Here we can observe

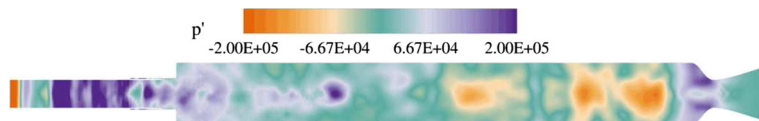


Fig. 4 Contours of instantaneous fluctuating pressure field p' in the symmetry $x - y$ plane obtained from Case 12

that the spatial variation of the fluctuating pressure is mainly due to acoustics with small-scale perturbations imposed by the turbulent fluctuations. The time is non-dimensionalized by defining a cycle number as: Cycle number $\equiv (t - t_0)f_1$, where t_0 is an arbitrary starting time and f_1 is the dominant frequency corresponding to the first unstable mode. We can observe that both cases show the limit cycle behavior. The peak-to-peak instantaneous pressure oscillations range from about -18 % to 30 % of the mean value in both cases, with slightly higher values predicted by Case 12F. We observe a very good agreement in cycle-to-cycle variations of the acoustic pressure oscillations and the overall signature.

Analyses of the acoustic mode and phase of the excited frequencies show very good agreement between the two grids. The spectral content of the acoustic pressure oscillations is obtained by first smoothing p' through convolution with the Hanning window function, followed by an application of the fast Fourier transform (FFT) to obtain the power spectral density (PSD). The three lowest excited frequencies are for Case 12 (Case 12F): 1613 Hz (1643 Hz), 3268 Hz (3285) and 4881 Hz (4928 Hz). Analysis of their mode shapes shows that the first mode has a node (around $x/D \sim 11$), whereas two nodes (around $x/D \sim 5$ and $x/D \sim 14$) are observed in the second mode. Both cases predict nodes at the same location although the amplitude of the first mode is 36 % higher for Case 12F. The nodes are identified as locations where $\text{mod}(p') \approx 0$ and a phase shift of 180° occurs across them. Here, $\text{mod}(p')$ denotes amplitude corresponding to a particular mode, obtained from the PSD of the acoustic pressure oscillations. The close agreement between both grids in predicting the key modes of interest suggests that the baseline grid is adequate for such studies. Further discussion and comparison with data are given below.

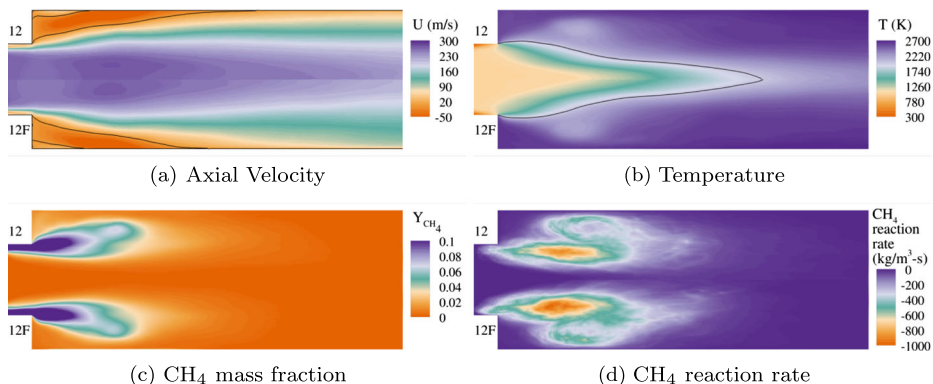


Fig. 5 Contours of the time-averaged flow properties in the symmetry $x - y$ plane. Iso-lines for $U = 0$ m/s and $T = 2000$ K are shown in (a) and (b), respectively. Top and bottom halves correspond to Cases 12 and 12F, respectively

Both instantaneous and time-averaged data are analyzed for grid sensitivity. Obviously, some instantaneous fine-scale features are expected when the grid is refined, but the time-averaged data shows minimal effect. This is demonstrated in Fig. 5 where contours of the time-averaged fields on a symmetry plane for the two cases are shown. We observe a good agreement between the two cases for prediction of the overall features of the corner recirculation zone (CRZ), the high temperature core downstream of the dump-plane, and the distribution of fuel and its burning rate. In the next section, we will revisit these time-averaged data for the three cases with different L_{Ox} to highlight the similarities and differences when the stability of the system is changed.

The predicted frequencies and amplitudes for Case 12 and the corresponding experimental data are shown in Table 1. Since Case 12 involves adiabatic conditions at the wall, heat-loss effects are not taken into account. Heat loss can affect flame holding and consequently, the stability behavior of the combustor. For example, in the adiabatic wall approximation, the mean pressure of the combustor is likely to be over-predicted. This in turn affects the sound speed, resulting in the modification of the acoustic response of the system [19]. To assess the sensitivity to the adiabatic wall approximation, the previously mentioned isothermal cases, Case 12T1 and Case 12T2, are considered for the $L_{\text{Ox}} = 12\text{cm}$ baseline configuration. In the setups for these cases, temperatures of 1800 K and 1200 K, respectively, are specified at the combustor walls.

Similar to Case 12, we observe a limit cycle behavior in both Case 12T1 and Case 12T2. Table 1 compares the first three dominant frequencies and corresponding amplitudes of the acoustic pressure fluctuations obtained from Cases 12, 12T1 and 12T2 with the experimental data. We can observe that as the temperature is lowered, the dominant frequencies show a minor reduction by approximately 1 – 3 % compared to Case 12. However, the amplitudes of the acoustic oscillations show significant variation. In particular, Case 12T1 predicts higher amplitudes for all three modes. But with a decrease in the combustor wall temperature, as expected, the calculated amplitudes decrease. Clearly, the unstable behavior of the combustor is not affected in the three cases considered here, although the amplitudes appear to be sensitive to the conditions on the combustor wall. This implies that the flame holding dynamics and instability behavior of the combustor can be studied with adiabatic conditions. Therefore, we only analyze results for the adiabatic Cases 9, 12 and 14 hereafter.

3 Results and Discussion

Experimental investigations of the CVRC setup have shown that the variation of L_{Ox} leads to spontaneous combustion instabilities. In particular, the system remains stable when $L_{\text{Ox}} < 9.5\text{ cm}$ and $L_{\text{Ox}} > 18\text{ cm}$, and is unstable for $9.5\text{ cm} < L_{\text{Ox}} < 16\text{ cm}$ [10].

Table 1 Dominant frequencies and their corresponding limit cycle amplitudes at $x/D = 18$ on the combustor wall for the baseline case with different thermal boundary conditions on the combustor wall

Case	f_1 (Hz) (Hz)	A_1 (kPa^2/Hz)	f_2 (Hz)	A_2 (kPa^2/Hz)	f_3 (Hz)	A_3 (kPa^2/Hz)
Experiments	1385	1045.0	2777	58.4	4169	26.1
12	1613	351.8	3268	25.0	4881	2.9
12T1	1602	789.3	3204	29.8	4771	6.1
12T2	1600	404.5	3150	18.9	4750	7.1

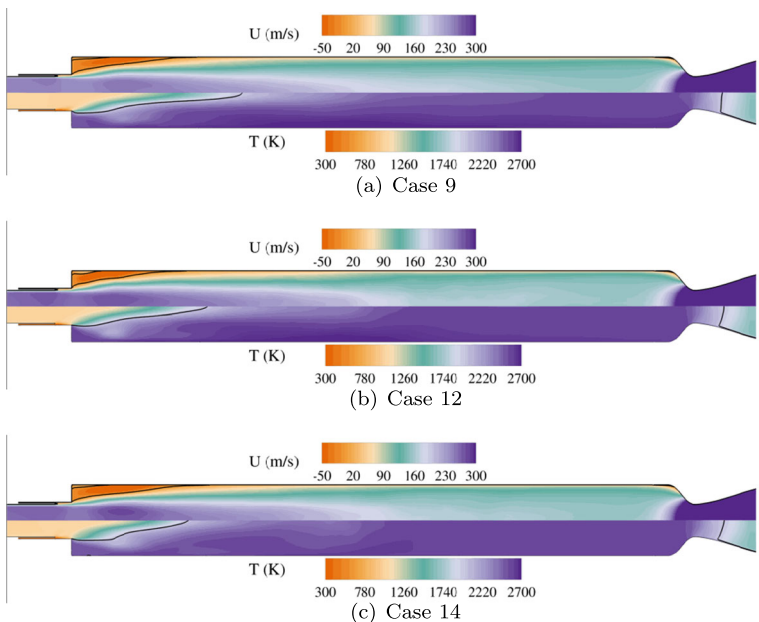


Fig. 6 Contours of the time-averaged axial velocity (top half) and temperature (bottom half) fields in the $x - y$ symmetry plane. Solid lines denote iso-lines of $U = 0$ m/s in the top-half and $T = 2000$ K in the bottom-half of each subfigure

Although no time-averaged data is available from the experiments, some key features predicted by the simulations facilitate discussions that follow based on instantaneous pressure fluctuation data. We compare the three cases with different L_{Ox} in the following discussions.

3.1 Time averaged fields

Figure 6 shows the time-averaged axial velocity and the temperature fields for the three cases in the entire combustor. A large corner recirculation zone primarily containing hot burned products is observed in all cases downstream of the dump plane. The iso-line of $U = 0$ m/s shown in Fig. 6 identifies the extent of the CRZ, and is nearly the same for all the cases with $x_r/D = 3.9, 3.7$ and 4.2 for cases 9, 12 and 14, respectively. The iso-line

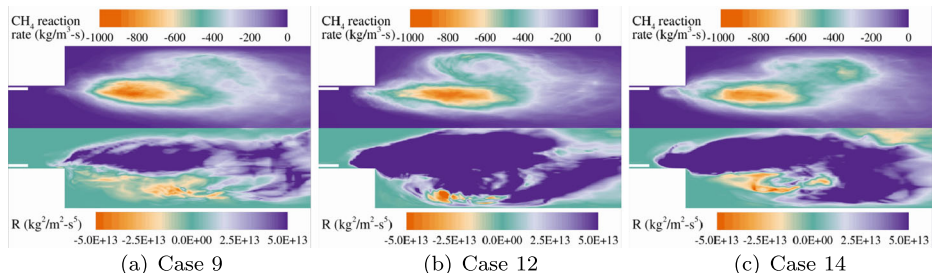


Fig. 7 Contours of the time-averaged methane reaction rate (top half) and space-local Rayleigh index R (bottom half) in the $x - y$ symmetry plane

of $T = 2000$ K is used to identify the mean position of the turbulent flame brush and we qualitatively use the location at the centerline to identify the mean extent of the flame brush [19]. The mean flame length x_f/D is 5.2, 4.1 and 3.6 for the three cases respectively and suggests that the flame length decreases with an increase in L_{Ox} . The reduction in the flame length is indicative of the burning region becoming more compact with an increase in the inlet length. The structure of the flame and its anchoring mechanism as well as its coupling with the pressure oscillations will be discussed later.

The Rayleigh index is a well known parameter typically used to characterize the coupling between unsteady heat release and pressure fluctuation. It is positive when coupling is in-phase and suggests combustion to be driving the growth of pressure fluctuations leading towards combustion instability. Based on the conservation equation for the acoustic energy, a space-local time-averaged Rayleigh index is defined as $R = (1/\tau) \int_t^{t+\tau} (\gamma - 1)/\gamma p' q'_g dt$ [1, 19] where τ is the time of averaging, $\gamma \equiv \gamma(\tilde{T})$ is the temperature dependent ratio of specific heat for thermally perfect gas, and p' and q'_g are the pressure and heat-release-rate fluctuations, respectively. Here, \tilde{T} denotes the filtered LES temperature field. The integrated Rayleigh index \bar{R} is obtained by performing integral of R on a finite-width slice normal to the axial direction through $\bar{R} = \left(\int_A R dA \right) \Delta x_{\text{bin}}$ where A is the cross-sectional area of the slice with Δx_{bin} as its finite width. The integrated Rayleigh index provides an overall measure of the coupling between heat release and pressure fluctuations, whereas the space-local Rayleigh index represents a local coupling effect that can be used to interpret flame holding dynamics as discussed below.

In Fig. 7 the time-averaged reaction rate contours of CH_4 show that the reaction rate is higher in the shear layer compared to other parts of the combustor. This is consistent with the mean location of the flame brush shown in Fig. 6. The extent of high reaction rate region increases with an increase in L_{Ox} and there is a noticeable shift upstream with an increase of L_{Ox} . This observation will be revisited later in the context of flame holding. The contours of Rayleigh index also show that the coupling between p' and q'_g is very strong in the region of large reaction rates. This is confirmed in Fig. 8, where axial variation of the Rayleigh index is shown. The value of \bar{R} is predominantly positive, particularly in-between the location of the dump plane and the reattachment in all three cases, and two

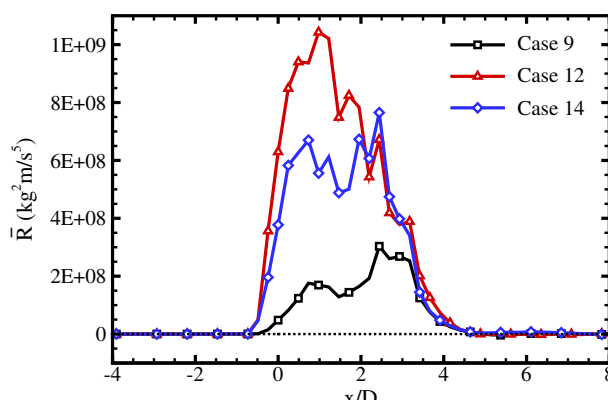


Fig. 8 Profile of the time-averaged integrated Rayleigh index along the axial direction

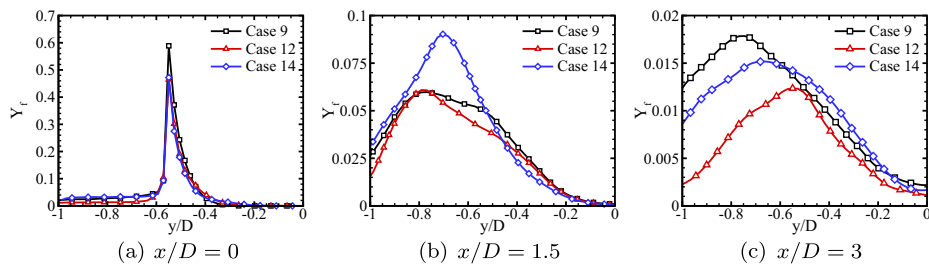


Fig. 9 Transverse profiles of the time-averaged methane mass fraction at different axial locations in the bottom half of the combustor

separated peaks are observed. The first peak occurs downstream of the dump plane, whereas second peak occurs close to reattachment location. The first peak location corresponds to the region where intense heat release is observed in the shear layer, whereas the second peak corresponds to mixing and burning regions occurring due to vortex impingement on the wall-surface. These two locations also exhibit different types of flame structure as discussed below.

It is clear that Cases 12 and 14 are more unstable compared to Case 9, and this observation is consistent with the experimental data. Further downstream of the reattachment location, \bar{R} decreases rapidly beyond $x/D > 4$ suggesting all the amplification is confined to a small axial region downstream of the dump plane. Upstream of the dump plane and just downstream of the injector there is also some amplification for Cases 12 and 14 indicating that some burning occurs there as well, although much weaker than in the combustor.

Figure 9 shows the time-averaged profile of the fuel mass fraction $Y_f \equiv Y_{CH_4}$ along the transverse direction at three different axial locations $x/D = 0, 1.5$ and 3 , which are within the axial extent of the CRZ. At the dump plane, i.e., $x/D = 0$, the profile of Y_f shows a peak due to the fuel injection, which occurs just upstream. Further downstream, the peak location moves closer to the wall and the profile becomes broader in the transverse direction. This occurs due to spreading of the shear layer, which enhances mixing of the fuel with the oxidizer as well as some mixing in the recirculation zone. Note that the magnitude has dropped significantly indicating consumption of the fuel species as well. In all cases at $x/D = 3$, the maximum value of fuel mass fraction reduces to about 3 % of the value at the fuel inlet location and the fuel is consumed well before $x/D = 12$.

3.2 Analysis of pressure oscillations

We now assess the predictions against available pressure fluctuation data from the experiments [44]. Figure 10 shows the pressure fluctuation signature, p' at $x/D = 18$ on the combustor wall for all cases separately for 20 and 10 acoustic cycles. The results for 10 cycles are presented for the sake of clarity. We observe the limit cycle behavior of pressure fluctuations in all cases, consistent with previous experimental and numerical studies [8, 19]. As L_{Ox} is increased from Case 9 to Case 12, the magnitude of peak-to-peak oscillations increases whereas it remains nearly the same in Cases 12 and 14. The sudden increase in the magnitude of pressure oscillations from Case 9 to Case 12 can be attributed to the combustion instability as described in Section 3.1. It is also observed that the positive peaks in the fluctuation are much higher than the negative ones and this is also a feature seen in the data. This behavior impacts flame motion and overall dynamics as discussed below. Note

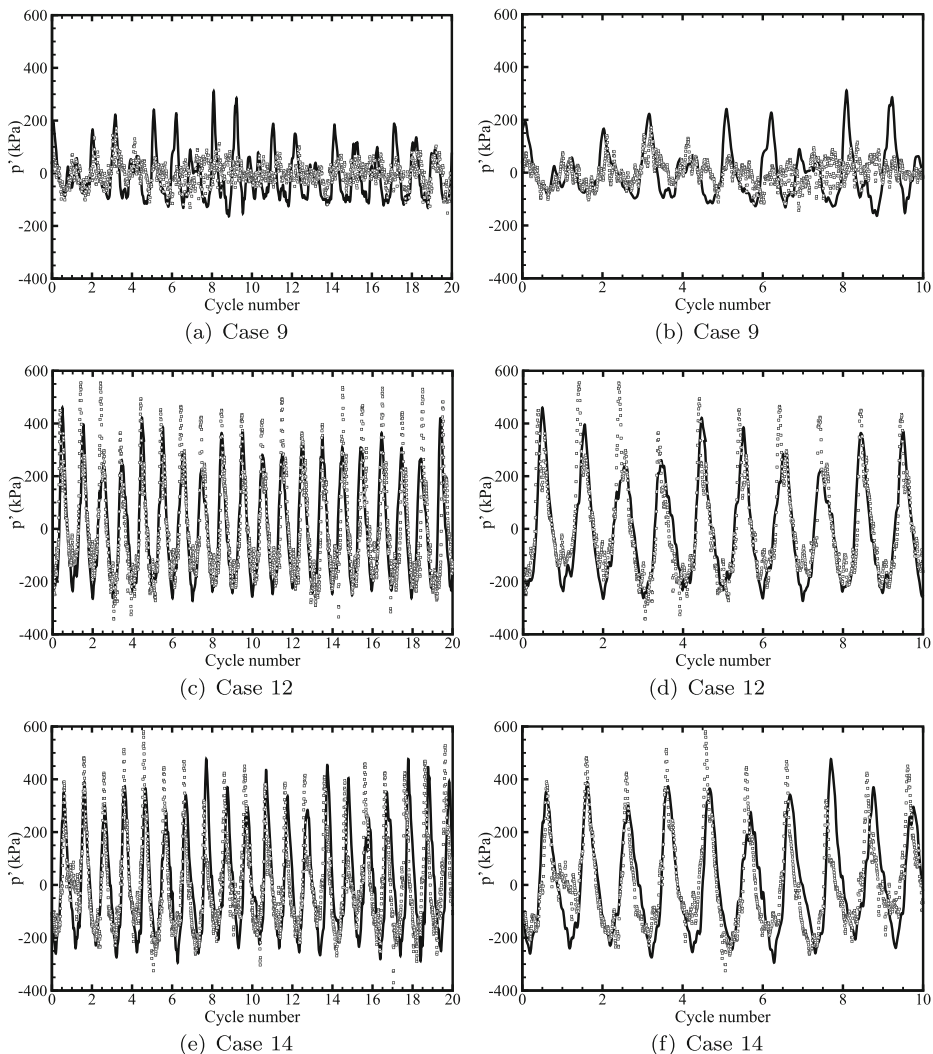


Fig. 10 Time evolution of the pressure fluctuation at $x/D = 18$ on the combustor wall for 20 (**a, c, e**) and 10 (**b, d, f**) acoustic cycles. Symbol (\square) denotes experimental data [44]

that Case 9 is a semi-stable case and does show a limit cycle behavior. However, the cycle to cycle variation of the pressure fluctuation is much smaller compared to the other two unstable cases.

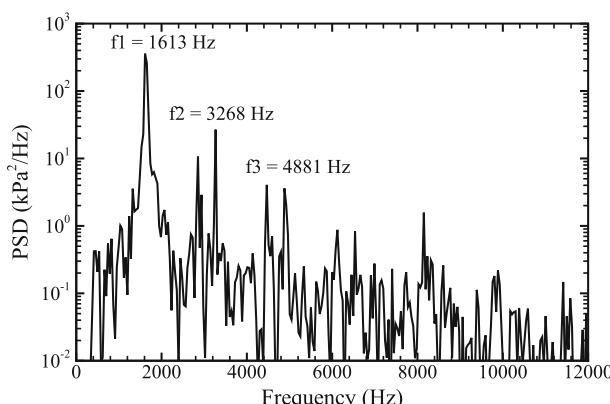
Table 2 shows the first three dominant frequencies and corresponding amplitudes of the acoustic pressure fluctuations shown in Fig. 10. Also included are the measured data. As mentioned before, the spectral content of the acoustic pressure oscillations is obtained by first smoothing the signal, followed by application of the FFT. Figure 11 shows the PSD plot of the acoustic pressure oscillations obtained for Case 12, where the three dominant frequencies are also highlighted. The numerical simulation over-predicts the frequency of the first two modes by approximately 18 % in all cases. In Case 9, the amplitude of the

Table 2 Dominant frequencies and their corresponding limit cycle amplitudes at $x/D = 18$ on the combustor wall

Case	f_1 (Hz) (Hz)	A_1 (kPa 2 /Hz)	f_2 (Hz)	A_2 (kPa 2 /Hz)	f_3 (Hz)	A_3 (kPa 2 /Hz)
9	1686	74.7	2791	20.3	3373	1.6
Experiment	1392	17.2	2704	0.5	3772	0.3
12	1613	351.8	3268	25.0	4881	2.9
Experiments	1385	1045.0	2777	58.4	4169	26.1
14	1592	423.2	3130	29.5	4722	8.3
Experiments	1331	909.5	2655	74.6	3986	24.0

dominant modes is over-predicted compared to experiments, whereas in the unstable cases, i.e., Cases 12 and 14, the amplitudes are under-predicted. The significant difference in the amplitude of the first two modes between stable (Case 9) and unstable (Cases 12 and 14) cases is consistent with the experimental data. The pressure achieved in the simulations is higher than the experiments by about 19 % and this can cause an increase in the speed of sound, thus shifting the acoustic frequency. It can also impact the amplitude of the fluctuations. The higher operating pressure is possibly due to the lack of heat-loss modeling in our simulations [19, 20]. As mentioned in Section 2.2, the amplitudes of observed instability are sensitive to the type of boundary conditions, even though the stability pattern remains the same.

Figure 12 shows spatial structure of the first two modes and their phase along the centerline of the combustor for all cases. All cases show a pressure node for the first longitudinal mode at about $x/D = 11$ downstream of the dump plane. This mode corresponds to a half-wave standing mode in the combustor. The second mode shows two nodes in the combustor at around $x/D = 5$ and 14 for all cases. The third mode (not shown here) is not very distinct in amplitude in all cases, although Case 14 shows the presence of three possible nodes at around $x/D = 4, 10$ and 16. The phase change occurring across the nodes by 180° shows that the modes within the combustor correspond to standing waves. The amplitude of all the

**Fig. 11** Power spectral density (PSD) of acoustic pressure oscillations for Case 12

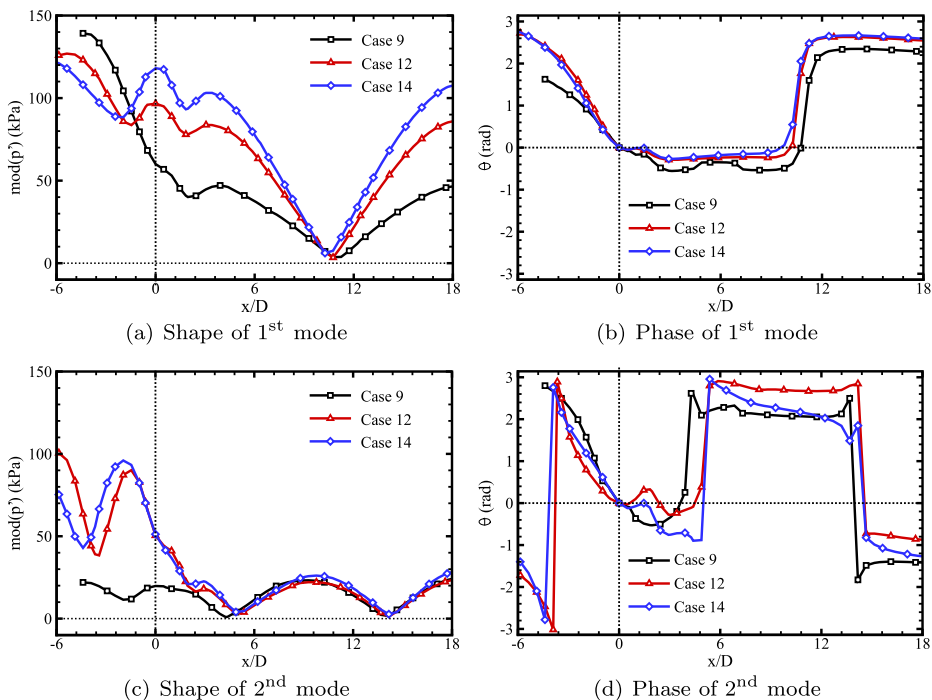


Fig. 12 Mode shape and phase for the first two longitudinal modes

modes at the dump plane, i.e., $x/D = 0$ is significantly higher in Cases 12 and 14 compared to the semi-stable Case 9. These observations are consistent with the variation of the peak-to-peak oscillations of pressure fluctuations across different cases shown in Fig. 10. The amplitude of the first propagating mode at the oxidizer inlet decreases with an increase in the oxidizer length while the second mode has a higher magnitude in the unstable cases compared to the semi-stable Case 9. The higher magnitude of first mode at the inlet for Case 9 may be responsible for movement of the flame further downstream compared to the other two cases as observed in Fig. 7.

3.3 Flame dynamics and stabilization mechanism

Instantaneous snapshots of the flowfield at the positive half ($y/D > 0$) of the symmetry plane ($z/D = 0$) are shown for an arbitrary cycle corresponding to time-instants that are approximately separated in phase by an angle of 60° . Notwithstanding the inevitable cycle-to-cycle variations, global commonalities are observed that lends the combustion process, a cyclic character. The similarities and differences between the three cases are discussed below.

Figure 13 shows the contours of spanwise vorticity for Cases 9 and 12. Case 14 is not shown since it exhibits a behavior qualitatively similar to Case 12. It is evident from these snapshots that the level of vorticity in the CRZ is not constant. This is related to the fluctuations in mass flowrates (oxidizer and fuel), occurring due to the traveling acoustic waves. Consequently, vortex shedding at the separated shear layer is affected, as also has been observed elsewhere [23]. Globally (i.e., for all cycles), the vortex shedding frequency

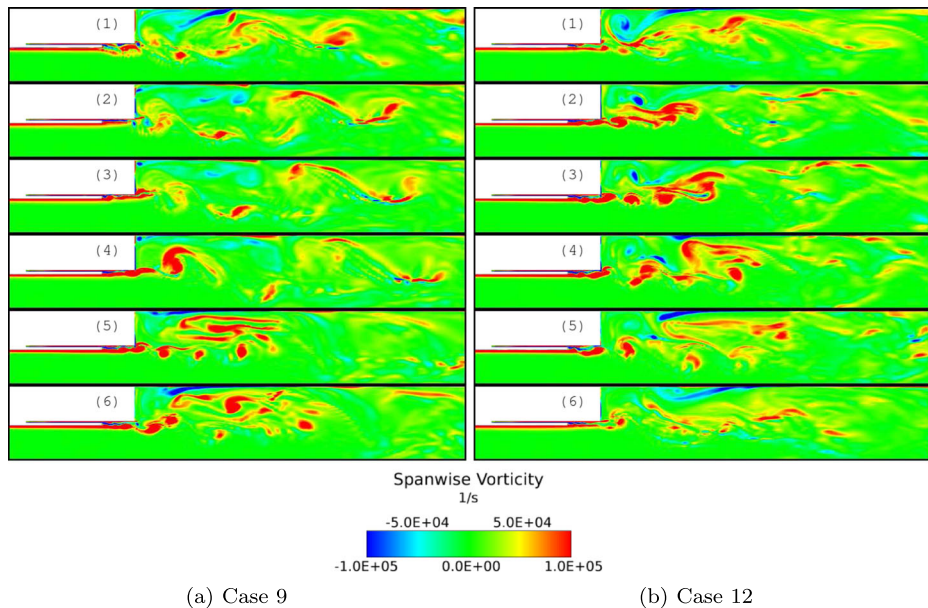


Fig. 13 Spanwise vorticity from Cases 9 and 12 at the positive half of the symmetry plane. The six frames are separated in phase by approximately 60°

closely corresponded to that of f_1 ; 1600 Hz, 1644 Hz and 1635 Hz, respectively for Cases 9, 12 and 14. Based on the oxidizer diameter, the bulk inflow velocity and the shedding frequency, the Strouhal number, $St \sim 0.12$ for these cases, which is within the jet preferred mode shedding frequency range $St \sim 0.1 - 0.3$ [45]. A noticeable difference between Case 9 and Cases 12/14 is a more rapid merging of the shed vortices for the latter two cases. This is probably related to the larger magnitudes of p' relative to Case 9 [see Fig. 10] which can affect the convective motion of the shed vortices.

The corresponding sequence of mixture-fraction evolution is shown in Fig. 14. The mixture fraction is defined using elemental carbon mass fraction as [46]:

$$z = \frac{Z_c - Z_{c,Ox}}{Z_{c,f} - Z_{c,Ox}} \quad (3.1)$$

Here, the carbon based passive scalar, Z_c is defined as:

$$Z_c = \sum_k \frac{W_C}{W_k} Y_k \quad (3.2)$$

In the above equation, W_k represents the molecular weight of the k^{th} species and W_C is the atomic weight of elemental carbon. The summation spans the carbon containing species, CH₄, CO and CO₂. The subscripts “Ox” and “f” correspond to the passive scalar’s value at the oxidizer and fuel inlets respectively. The stoichiometric mixture fraction, $z_{st} = 0.095$ based on this definition. From the contours of z thus defined, the intermittent nature of fuel flow is apparent - the fuel mass flowrate, \dot{m}_f is affected by the local magnitude of pressure oscillation such that a period of quasi-steady fuel injection is followed by sudden drops in flowrates (when locally, the pressure is higher than the mean).

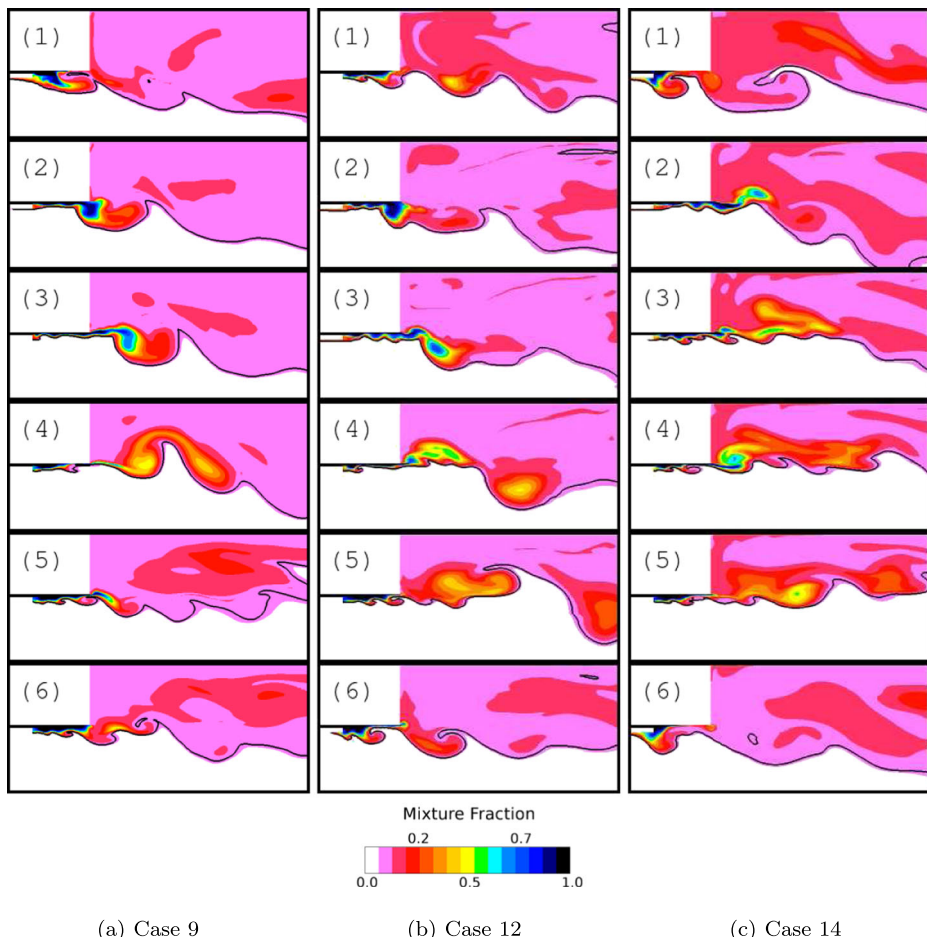


Fig. 14 Mixture fraction field near the dump-plane in the positive half of the symmetry plane for Cases 9, 12 and 14. These frames correspond to the same time-instants as Fig. 13. The stoichiometric mixture fraction iso-contour is shown using a *black line*

The fuel flowrate computed at the exit of the fuel injector and normalized by the inlet value, \dot{m}_0 is shown in Fig. 15. In the instantaneous plots, Fig. 15a–d, the sudden drops in \dot{m}_f are particularly correlated with the peak of p' at $x/D = 0$ (dump plane) suggesting progressively increasing coupling between p' (at $x = 0$) and \dot{m}_f (at the fuel injector exit) from Case 9 to Case 12. Case 14 is not shown here, but has a behavior similar to Case 12. In the same figure, p' at the $x/D = 18$ location has also been plotted to demonstrate the phase-shifted nature of acoustic pressure at different axial locations. This is consistent with the mode and phase shape plots of Fig. 12. In all further discussions, the $x/D = 0$ point is used as the reference location. The phase averaged fuel mass flow rate and p' at $x/D = 0$, computed from 50 acoustic cycles is shown in Fig. 15e for Case 12. The time-period over which a decrease in mass-flow rate occurs is smaller than the time-duration when the flow rate fluctuates about \dot{m}_0 , consistent with the instantaneous response shown in Fig. 15c. Furthermore, the part of the cycle where \dot{m}_f decreases, corresponds to that when

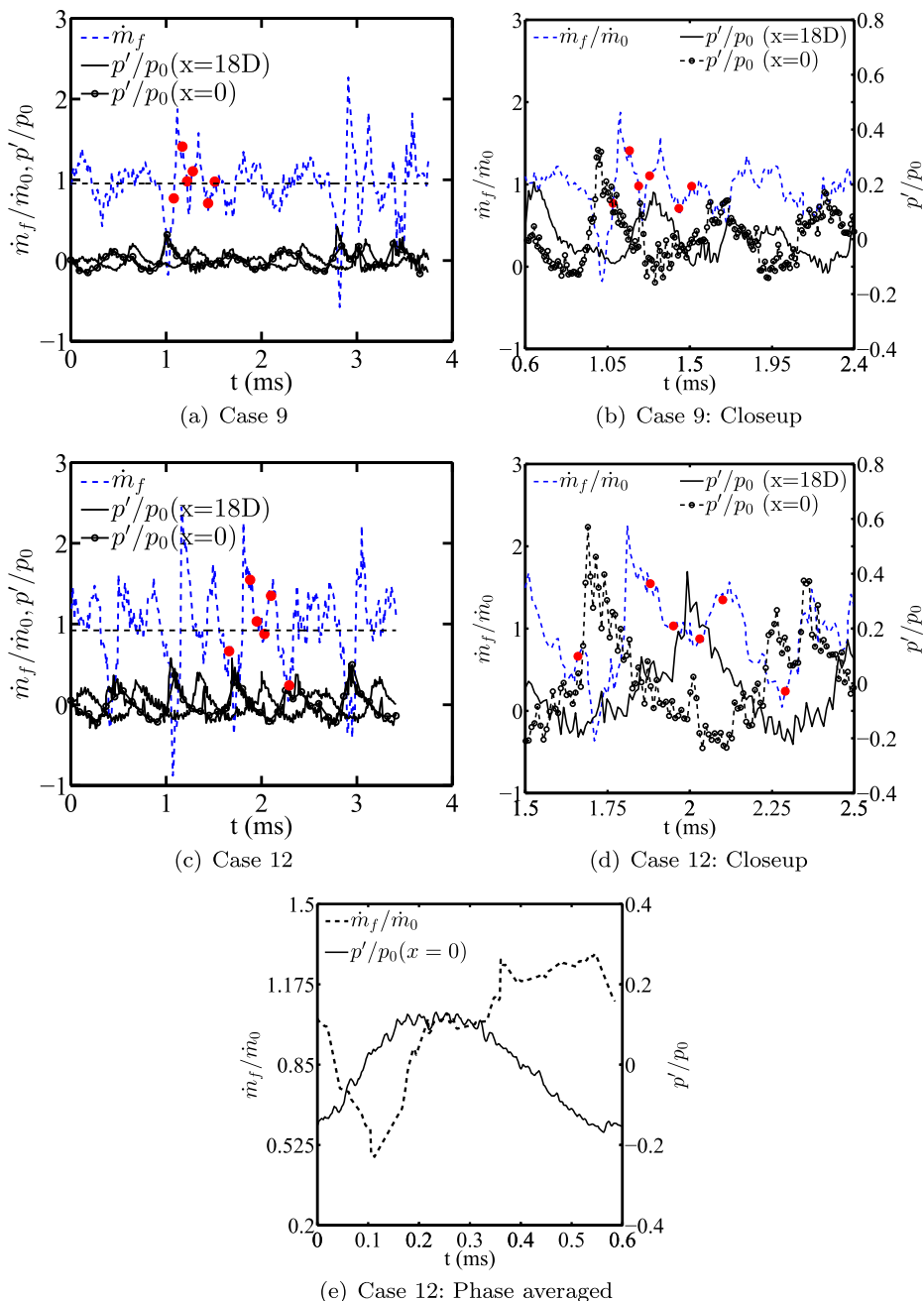
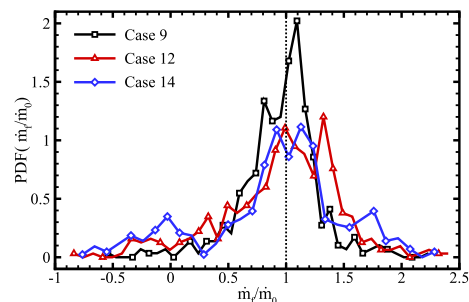


Fig. 15 Cyclic variation of the normalized fuel mass flowrate \dot{m}_f/\dot{m}_0 and pressure fluctuation p'/p_0 at two different locations. The six time-instants corresponding to Fig. 14 are also shown as symbols. Here, $p_0 = 1.34$ MPa

Fig. 16 PDF of normalized mass flow-rate of the fuel \dot{m}_f/\dot{m}_0 . The dotted reference line correspond to $\dot{m}_f/\dot{m}_0 = 1$



p' increases. Similarly, the part of the cycle where \dot{m}_f is nominally steady, corresponds to a cycle-window of decreasing p' . Due to the similarity in qualitative trends between the phase-averaged and the instantaneous responses, the instantaneous fields are mainly used for discussing flame dynamics in the following discussions. The phase-averaged plots for Case 12 are included wherever necessary to augment the discussions.

The oscillations observed in the mass flowrate at the exit of the injector about the prescribed flowrate is further highlighted in the probability density function (PDF) of the normalized mass flowrate shown in Fig. 16. We can observe that the PDF assumes a negatively skewed shape with longer tails along both positive and negative direction about the mean, which further underscores the presence of highly unsteady and intense fluctuations in the mass flowrate. The comparison of the mixture fraction sequences (in Fig. 14) with those of vorticity in (Fig. 13) indicates the importance of vorticity in transport of fuel to the CRZ. Additionally, as mentioned in the discussion of Fig. 13, the distinct merging patterns of Case 12/14 relative to Case 9 result in differences in the fuel concentration in the CRZ closer to the dump-plane. This is also evident in the mean profile of the fuel mass fraction in Fig. 9b.

The sequence of the heat release rate (HRR) distribution is shown in Fig. 17 for all cases. The heat-release region is localized around the peripheries of the combustor/CRZ vortices and decreases near the dump-corner at the moments when fuel supply becomes quasi-steady. However, sustained combustion occurs when the injected fuel eventually premixes, preheats and reacts in the combustor shear-layer. Some HRR can be seen upstream of the dump-plane especially for Case 14 at certain instances. Typically, coaxial configurations are usually associated with diffusion flames that are lifted or attached to the injector lip [26]. In the CVRC as well, there are moments when the flame is convected closer to the fuel injector [see Fig. 17c] but such combustion cannot be sustained since the strain rate dynamically changes with the phase of the cycle to allow stabilization of a diffusion flame along the stoichiometric mixture fraction isoline.

It is seen that the oxidizer mass flowrate also fluctuates due to pressure fluctuations in the inlet. However, since the oxidizer flow rate is much larger than the fuel mass flowrate, combustion is limited by the latter. On the other hand, due to its larger magnitude, oxidizer mass flowrate affects combustion dynamics via vorticity to a larger extent relative to the fuel mass flowrate. To investigate the effect on HRR, the correlation of instantaneous fluctuations in \dot{m}_f and the integrated heat release, \dot{q}_g is shown in Fig. 18a. Both quantities have been normalized by reference values equal to the prescribed fuel mass flowrate and the maximum value (over time) of the global heat-release, respectively. The correlation is mostly negative in all cases such as the one shown here, for Case 12. This suggests a scenario where the fuel injection and the flame associated events in the combustor are, in an average sense,

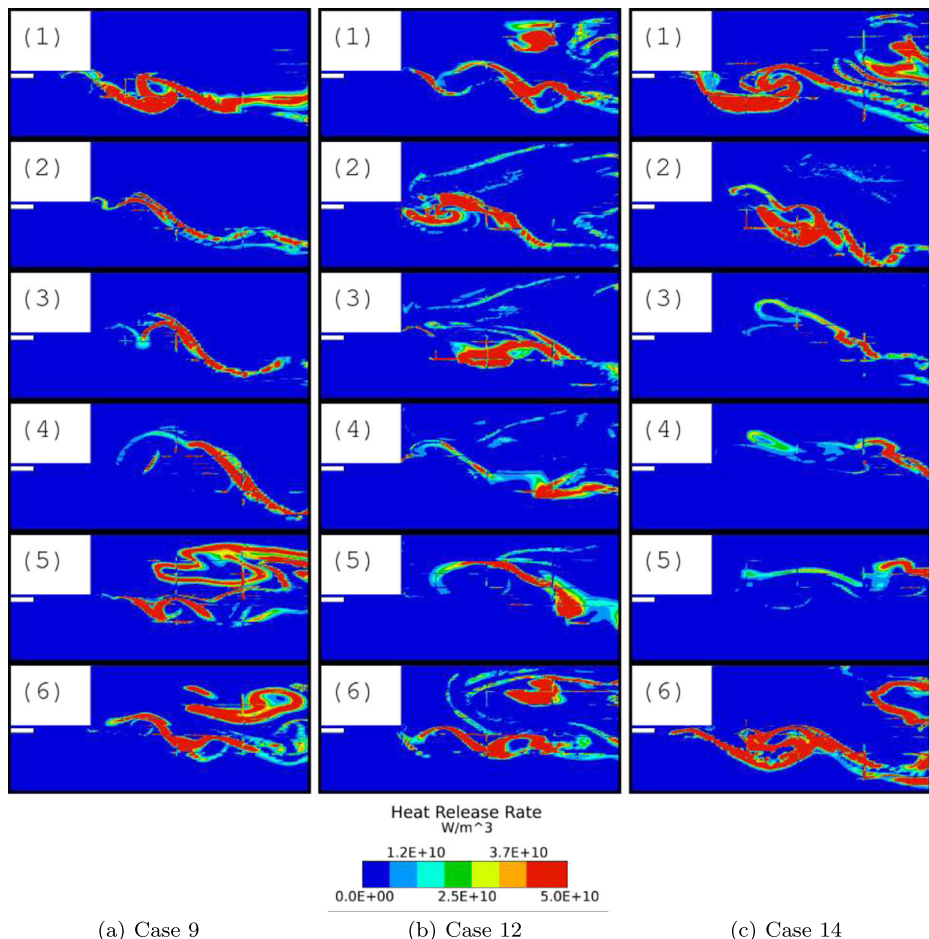


Fig. 17 Heat release distribution in the symmetry plane at the same locations and time-instants as in Fig. 13

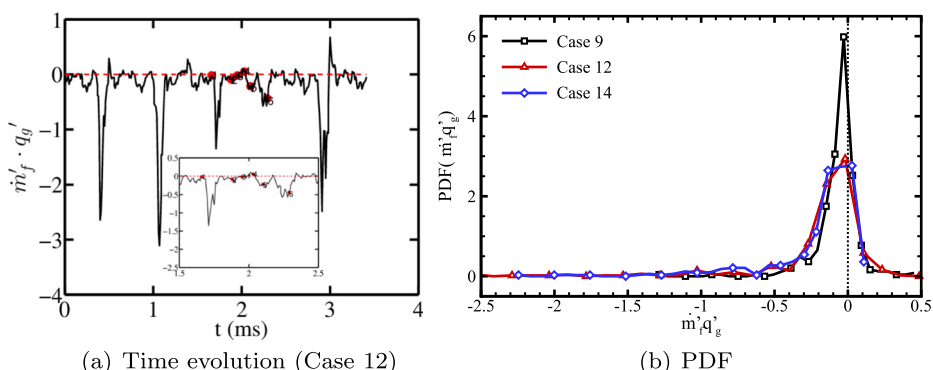


Fig. 18 Time evolution and PDF of the correlation between heat release and fuel mass fraction $\dot{m}'_f q'_g$. The six time-instants corresponding to Fig. 14 are denoted by (●) in subfigure (a). The time evolution is only shown for Case 12

mutually exclusive. Stronger negative correlation is observed between q'_g and \dot{m}'_f in Cases 12 and 14 (not shown) compared to Case 9 (not shown), which further demonstrates that Cases 12 and 14 are more unstable compared to Case 9. As can be qualitatively observed for Case 12, the instant of large HRR in the combustor corresponds to a period of reduced fuel injection [see Figs. 15c and d]. The predominantly negative correlation is also evident from the shape of its PDF shown in Fig. 18b, which is negatively skewed. Additionally, we observe a long tail in the PDF, particularly for Cases 12 and 14, implying less-frequent but very strong fluctuations in the mass flowrate and the unsteady heat-release.

The high temperature/HRR regions are occasionally convected upstream of the dump plane. To quantify these flame-excursions, the temporal evolution of the most upstream axial location of the flame in the symmetry plane is shown in Fig. 19. This is just a qualitative measure to compare the bounds of flame-excursions relative to its mean anchoring location. The flame-location is defined on the basis of combination of $T > 2000$ K and the local heat-release rate, $q_{HRR} > 1 \times 10^{10}$ J/m³-s. The temperature condition was chosen based on the observation that the heat-release contours predominantly coincided with the $T = 2000$ K iso-line. This choice for an iso-line has also been used earlier [19]. The heat-release threshold is chosen by considering the time-averaged contours at the symmetry plane and

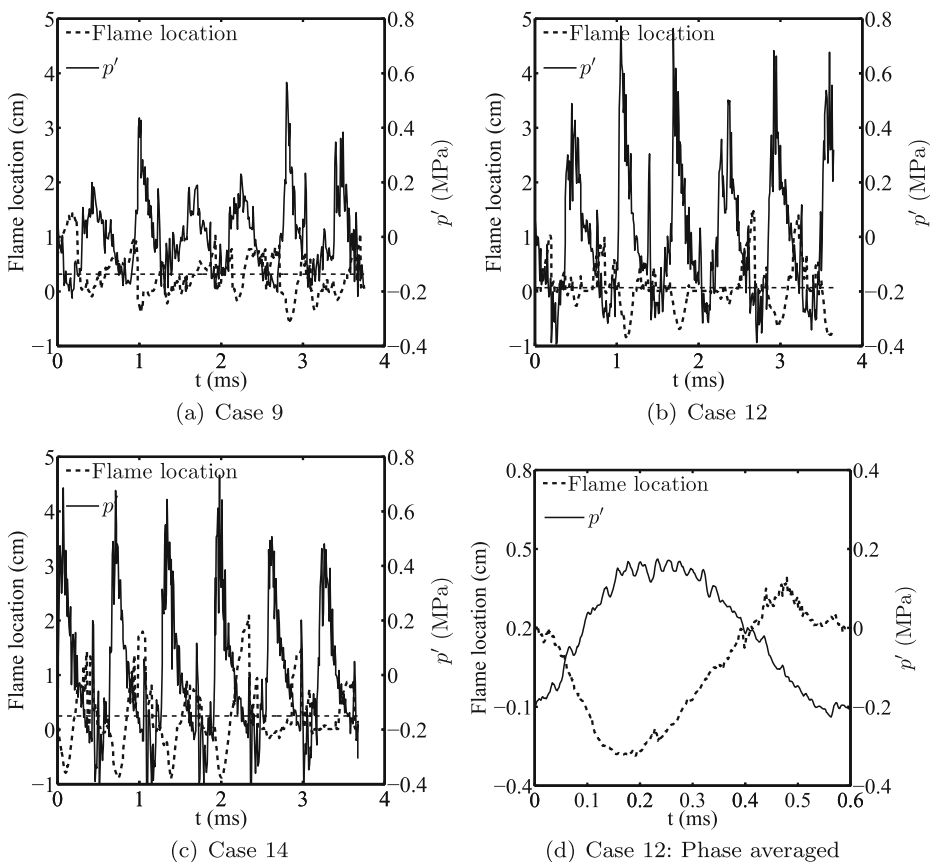


Fig. 19 The instantaneous axial location of the flame. Black dotted line in each figure indicates the temporal mean location of the flame for the duration shown here. The p' curve is plotted at $x/D = 0$

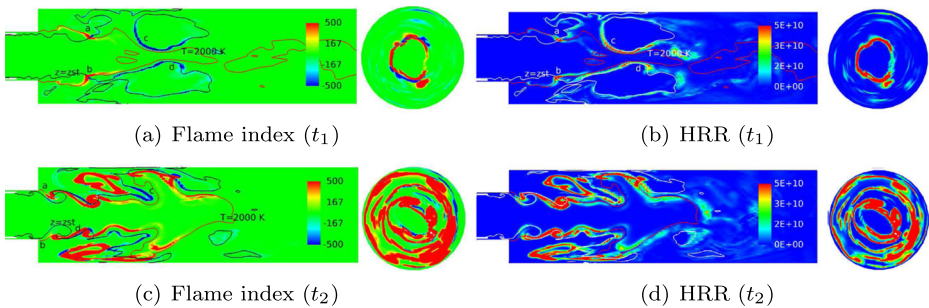


Fig. 20 Flame index and HRR for two different instants of time in a Case 12 cycle. The cross-sectional view of these quantities at $x/D = 1.17$ is also shown in the right

computing a spatial average over the reacting regions, i.e., regions where the methane reaction rate is non-zero. Naturally, the downstream bounds ($x > 0$) of the flame-excursions are sensitive to these choices, but the upstream limit is found to be relatively insensitive as long as a temperature higher than the oxidizer temperature was chosen. As seen in Fig. 19, all cases show flame-movement upstream of the dump plane to different extents with Cases 9 and 14, respectively, bracketing the lower and the upper displacement values. It is notable that in Cases 12 and 14, the peaks and troughs in the p' curve (at $x/D = 0$) nominally correspond, respectively, to troughs and peaks in the displacement curve. This is even more apparent in the phase averaged plot, Fig. 19d for Case 12. This suggests a strong and direct influence of acoustics on the flame movement. On the other hand for Case 9, the correlation between the two curves appears to be relatively not as emphatic.

The flame structure can also be characterized by using the flame index. The flame index is defined here as [32]:

$$FI = \frac{\nabla Y_f \cdot \nabla Y_{Ox}}{|\nabla Y_f| |\nabla Y_{Ox}|} |\dot{\omega}_f| \quad (3.3)$$

and is representative of the nature of burning, whether premixed (positive) or diffusion (negative). Since it is the product of the classical Takeno index and reaction rate, non-zero values correspond to the actual reacting layers. Only sample images are shown here. Figures 20a and b correspond to instants when heat-release has decreased in the combustor due to fuel injection intermittency and Figs. 20c and d correspond to an instant when HRR is significant. At the time when the mass flowrate becomes quasi-steady, occasionally highly localized high HRR “spots” such as those in Fig. 20b (see points marked “a” and “b”) are observed. Previously, researchers [19, 20, 23] have noted them to be triple-flames or tri-brachial flames. These are marked by their location at the intersection of the $T = 2000$ K iso-line and the $z = z_{st}$ lines. Here too we note that similar flame structures occur when fresh fuel mixture makes contact with the hot-products in the recirculation region. Due to a highly unsteady nature of the flow, these locations are not quasi-stationary but move in time and space, and even in the azimuthal direction. Additionally at some locations, the intersection of rich-premixed flame and a weak diffusion flame is seen as a double-flame structure. Presence of independent premixed flames closer to the dump plane and diffusion flames further away in the CRZ are also seen. Thus, all possible types of burning modes can be seen depending upon the instant of observation.

The time-evolution of the dominant burning mode is shown in Fig. 21. This is computed by performing volume integration of the HRR conditioned on the sign of the flame index. The ratio of the premixed HRR contribution to the total HRR is plotted here. A value

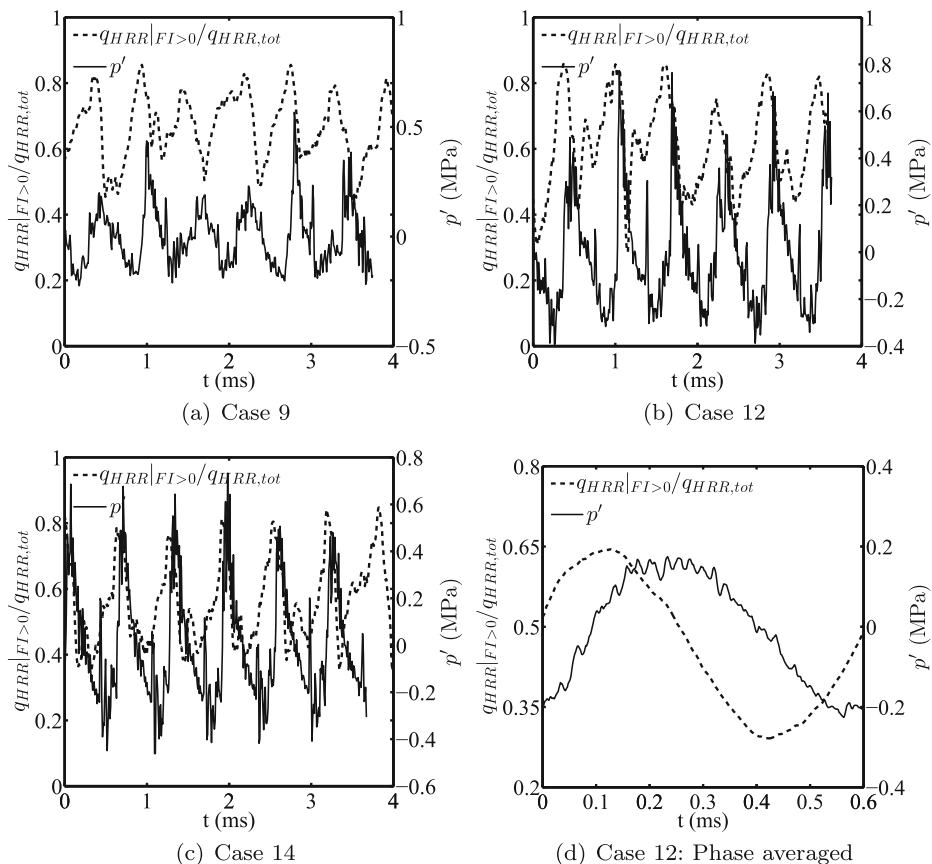


Fig. 21 The time evolution of the ratio of HRR conditioned on $FI > 0$ to total HRR is plotted along with p' at $x/D = 0$

larger than half, therefore, indicates the dominance of premixed mode burning at a given time instant. The time-averaged HRR due to premixed burning ($HRR|FI>0$) contributed to approximately 60 % of the total HRR in all three cases. The LES predicted pressure p' at the measurement point $x/D = 0$ is overlaid in order to correlate the flame structure with what is typically measured. In the instantaneous plots, Fig. 21a–c, the peaks of the conditional heat-release ($FI > 0$) are almost aligned with the peaks of p' , at $x/D = 0$. Conversely, troughs ($FI < 0$) are closer to the troughs of p' . The phase averaged plot for Case 12 in Fig. 21d also confirms this relationship between p' and the premixed HRR.

Previously in Fig. 19, it was shown that the troughs of p' (at $x/D = 0$) coincided with the downstream movements of the leading heat-release location. Correlating these two trends, it therefore follows that during these moments, the burning mode is predominantly non-premixed. This is found to be consistent with the sequences of the flame index (not shown here), where instances corresponding to weak HRR near the dump-corner also corresponds to instances where premixed burning and total HRR in general is small (but dominated by non-premixed burning). Therefore, these instances correspond to moments in the cycle where fuel-flow into the combustor has just resumed (compare frames 3-5 in Figs. 14

and 17). Conversely, the instances of strong upstream motion of the flame correspond to instances where HRR is primarily due to premixed flame burning and the flame is either anchored at the step or moves upstream. Key to the understanding of this apparent mode switching is the localization of non-premixed burning in the CRZ as discussed earlier. Since the residence time of the unburned fuel entrained during the quasi-steady injection phase is large in this region, the HRR due to the non-premixed burning does not show as much variations as the premixed-burning mode. Indeed, on computation of the mean-normalized variance of HRR conditioned on the flame index, Cases 9, 12 and 14 were associated with values of 0.37, 0.43 and 0.37, respectively, for the non-premixed component of the total heat release. For the premixed-mode, these ratios were 0.69, 0.90 and 0.91. The relative invariance associated with the former burning mode, especially for the unstable Cases 12 and 14, therefore, represents a crucial aspect of flame-stabilization in the CVRC.

4 Conclusions

LES of the CVRC setup is performed for three different injector configurations, which correspond to one semi-stable and two unstable cases. The simulations were able to reproduce both qualitatively and quantitatively, the limit cycle behavior and the typical signature of combustion instability. The dominant frequencies corresponding to the first three longitudinal modes are observed to be similar to those in the experiments. Although their values were over-predicted possibly due to a higher operating pressure and burnt products temperature, qualitatively, however, the trends of the experiments are captured. Cases 12 and 14 are found to be more unstable compared to Case 9. The pressure oscillations also impact flame characteristics and its stabilization. With a change in the injector length, vorticity dynamics is impacted resulting in changes to the time averaged distribution of scalar fields and heat release. Instantaneously, the pressure fluctuation is negatively correlated with mass flowrate and the latter, in turn, is negatively correlated with the heat release. The mass flowrate fluctuations impact instantaneous flame anchoring locations, showing correlations with acoustics too. The leading edge flame location is found to oscillate about a mean location. It is found that flame movements upstream of the dump plane are least in Case 9, consistent with the time-averaged picture. The time-averaged reaction rate contours prominently show heat-release occurring close to the fuel injector for Cases 12 and 14, although the maximum heat release region is still located inside the combustor for all three cases.

The analysis of the flame structure reveals presence of multiple burning modes, which include both premixed and non-premixed flame structures that coexist locally as well as in exclusion. However, the dominance of a certain mode of burning (premixed or non-premixed) is shown to depend on the phase of the cycle. Therefore, the pressure oscillation level and its phase dictate the switching between the dominant modes of heat release. The non-premixed mode based heat release magnitude is relatively more invariant than that due to the premixed mode, possibly representing an important feature of flame stabilization in the CVRC setup.

Many issues still remain to be addressed. Sensitivity of the predicted frequencies and amplitudes to some of the obvious modeling simplifications needs to be assessed. In this study, the sensitivity to heat loss at the walls was investigated using isothermal boundary conditions. While the frequency response showed little sensitivity when compared with the adiabatic baseline configuration case, the predicted amplitudes showed significant sensitivity. Nevertheless, the predictions still showed considerable deviation from data. Future studies will focus on the analysis of heat-loss effects in more detail to explain these

discrepancies. In addition to the assumptions regarding thermal boundary conditions, over-prediction of mean temperature and pressure in the CVRC is also related to the use of simple two-step kinetics. Although the laminar flame-speed is tuned for CVRC conditions, the adiabatic temperatures are over-predicted due to absence of many endothermic reactions present in a more detailed mechanism. Finally, the acoustic response is affected by the assumption of characteristics based treatment of the inflow boundary conditions. In the real-system, the injector is slotted and choked. The sensitivity to inflow boundary conditions will be assessed by including the slotted injector in the computations.

Acknowledgments This work was supported in part by NASA Glenn Research Center (Dr. N.-S. Liu, PM) and AFOSR (Dr. M. Birkan, PM). The computing resources provided by DoD HPC Centers at the Engineer Research and Development Center, MS is greatly appreciated. We would like to thank Prof. W. E. Anderson and Dr. T. Feldman for providing the experimental data for a direct comparison with the LES.

References

1. Poinsot, T.J., Trouvé, A.C., Veynante, D.P., Candel, S.M., Esposito, E.J.: Vortex-driven acoustically coupled combustion instabilities. *J. Fluid Mech.* **177**, 265–292 (1987)
2. Menon, S., Jou, W.-H.: Large-eddy simulations of combustion instability in an axisymmetric ramjet combustor. *Combust. Sci. Technol.* **75**, 53–72 (1991)
3. Candel, S.M.: Combustion instabilities coupled by pressure waves and their active control. *Symp. (International) Combust.* **24**, 1277–1296 (1992)
4. Oefelein, J.C., Yang, V.: Comprehensive review of liquid-propellant combustion instabilities in F-1 engines. *J. Propul. Power* **9**, 657–677 (1993)
5. McManus, K.R., Poinsot, T., Candel, S.M.: A review of active control of combustion instabilities. *Prog. Energy Comb. Sci.* **19**, 1–29 (1993)
6. Lieuwen, T., Zinn, B.T.: The role of equivalence ratio oscillations in driving combustion instabilities in low NO_x gas turbines. *Proc. Combust. Inst.* **27**, 1809–1816 (1998)
7. Huang, Y., Yang, V.: Dynamics and stability of lean-premixed swirl-stabilized combustion. *Prog. Energy Comb. Sci.* **35**, 293–364 (2009)
8. Yu, Y.C., Koeglmeier, S.M., Sisco, J.C., Anderson, W.E.: Combustion instability of gaseous fuels in a continuously variable resonance chamber (CVRC). *AIAA 2008-4657*, pp. 1–12 (2008)
9. Yu, Y.C., O’Hara, L., Sisco, J.C., Anderson, W.E.: Experimental study of high-frequency combustion instability in a continuously variable resonance combustor (CVRC). *AIAA 2009-234*, pp. 1–12 (2009)
10. Yu, Y.C., Sisco, J.C., Rosen, S., Madhav, A., Anderson, W.E.: Spontaneous longitudinal combustion instability in a continuously-variable resonance combustor. *J. Propul. Power* **28**, 876–887 (2012)
11. Poinsot, T., Angelberger, C., Egolfopoulos, F., Veynante, D.: Large eddy simulation of combustion instabilities. In: 1st International Symposium on Turbulence and Shear Flow Phenomena. Santa Barbara (1999)
12. Roux, A., Gicquel, L.Y.M., Sommerer, Y., Poinsot, T.J.: Large eddy simulation of mean and oscillating flow in a side-dump ramjet combustor. *Combust. Flame* **152**, 154–176 (2008)
13. Staffelbach, G., Gicquel, L.Y.M., Boudier, G., Poinsot, T.: Large eddy simulation of self-excited azimuthal modes in annular combustors. *Proc. Combust. Inst.* **32**, 2909–2916 (2009)
14. Boudier, G., Lamarque, N., Staffelbach, G., Gicquel, L.Y.M., Poinsot, T.: Thermo-acoustic stability of a helicopter gas turbine combustor using large eddy simulation. *Int. J. Aeroacoust.* **8**, 69–94 (2009)
15. Fureby, C.: LES of a multi-burner annular gas turbine combustor. *Flow Turbul. Combust.* **84**, 543–564 (2010)
16. Smith, R., Xia, G., Anderson, W., Merkle, C.L.: Computational simulations of the effect of backstep height on nonpremixed combustion instability. *AIAA J.* **48**, 1857–1868 (2010)
17. Smith, R., Xia, G., Anderson, W., Merkle, C.L.: Computational studies of the effects of oxidiser injector length on combustion instability. *Combust. Theory Model.* **16**, 341–368 (2012)
18. Harvazinski, M.E., Anderson, W.E., Merkle, C.L.: Analysis of self-excited combustion instabilities using two- and three-dimensional simulations. *J. Propul. Power* **29**, 396–409 (2013)
19. Garby, R., Selle, L., Poinsot, T.: Large-eddy simulation of combustion instabilities in a variable-length combustor. *C.R. Mecanique* **341**, 220–229 (2013)

20. Guézennec, N., Dawson, T., Sierra, P., Menon, S.: Flame holding dynamics during combustion instability in a shear coaxial injector. In: 8th International Symposium on Turbulence and Shear Flow Phenomena. Poitier (2013)
21. Harvazinski, M.E., Talley, D.G., Sankaran, V.: Influence of boundary condition treatment on longitudinal mode combustion instability predictions. AIAA 2013-3994, pp. 1–14 (2013)
22. Jiménez, C., Cuenot, B.: DNS study of stabilization of turbulent triple flames by hot gases. Proc. Combust. Inst. **31**, 1649–1656 (2007)
23. Harvazinski, M.E., Huang, C., Sankaran, V., Feldman, T.W., Anderson, W.E., Merkle, C.L., Talley, D.G.: Combustion instability mechanisms in a pressure-coupled gas-gas coaxial rocket injector. AIAA Paper 1013-3990, pp. 1–21 (2013)
24. Génin, F., Menon, S.: Simulation of turbulent mixing behind a strut injector in supersonic flow. AIAA J. **48**, 526–539 (2010)
25. Génin, F., Menon, S.: Studies of shock/turbulent shear layer interaction using large-eddy simulation. Comput. Fluids **39**, 800–819 (2010)
26. Masquelet, M., Menon, S.: Large eddy simulation of flame-turbulence interactions in a shear coaxial injector. J. Propul. Power **26**, 924–935 (2010)
27. Génin, F., Menon, S.: Dynamics of sonic jet injection into supersonic crossflow. J. Turbulence **11**, 1–30 (2010)
28. Kim, W.-W., Menon, S.: An unsteady incompressible Navier-Stokes solver for large eddy simulation of turbulent flows. Int. J. Numer. Meth. Fluids **31**, 983–1017 (1999)
29. Kerstein, A.R.: Linear-eddy modeling of turbulent transport. II: Application to shear layer mixing. Combust. Flame **75**, 397–413 (1989)
30. Menon, S., McMurtry, P.A., Kerstein, A.R.: A linear eddy mixing model for large eddy simulation of turbulent combustion. In: Galperin, B., Orszag, S.A. (eds.) Large Eddy Simulation of Complex Engineering and Geological Flows, pp. 87–314. Cambridge University Press, Cambridge (1993)
31. Chakravarthy, V., Menon, S.: Large eddy simulation of turbulent premixed flames in the flamelet regime. Combust. Sci. Technol. **162**, 175–222 (2001)
32. Patel, N., Menon, S.: Simulation of spray-turbulence-flame interactions in a lean direct injection combustor. Combust. Flame **153**, 228–257 (2008)
33. Menon, S., Kerstein, A.R.: The linear-eddy model. In: Echekki, T., Mastorakos, E. (eds.) Turbulent Combustion Modeling of Fluid Mechanics and its Applications, vol. 95, pp. 221–247. Springer Netherlands (2011)
34. Sankaran, V., Menon, S.: Structure of premixed turbulent flames in the thin reaction zones regime. Proc. Combust. Inst. **28**, 203–209 (2000)
35. Menon, S., Patel, N.: Subgrid modeling for simulation of spray combustion in large-scale combustors. AIAA J. **44**, 709–723 (2006)
36. El-Asrag, H., Menon, S.: Large eddy simulation of soot formation in a turbulent non-premixed jet flame. Combust. Flame **156**, 385–395 (2009)
37. Undapalli, S., Srinivasan, S., Menon, S.: LES of premixed and non-premixed combustion in a stagnation point reverse flow combustor. Proc. Combust. Inst. **32**, 1537–1544 (2009)
38. Sen, B.A., Menon, S.: Linear eddy mixing based tabulation and artificial neural networks for large eddy simulations of turbulent flames. Combust. Flame **157**, 62–74 (2010)
39. Poinsot, T.J., Lele, S.K.: Boundary conditions for direct simulations of compressible viscous flows. J. Comp. Phys. **101**, 104–129 (1992)
40. Garby, R.: Simulations of flame Stabilization and Stability in High-Pressure Propulsion Systems. Ph.D. thesis, Université de Toulouse (2013)
41. Harvazinski, M.E., Sankaran, V., Talley, D.G.: Parametric trends in the combustion stability characteristics of a single-element gas-gas rocket engine. AIAA Paper 2014-0577 (2014)
42. Franzelli, B., Riber, E., Gicquel, L.Y.M., Poinsot, T.: Large eddy simulation of combustion instabilities in a lean partially premixed swirled flame. Combust. Flame **159**, 621–637 (2012)
43. Zong, N., Yang, V.: Near-field flow and flame dynamics of LOX/methane shear-coaxial injector under supercritical conditions. Proc. Combust. Inst. **31**, 2309–2317 (2007)
44. Feldman, T.W., Anderson, W.E.: Experimental dataset for CVRC setup, private communication (2013)
45. Schadow, K.C., Gutmark, E.: Combustion instability related to vortex shedding in dump combustors and their passive control. Prog. Energy Comb. Sci. **18**, 117–132 (1992)
46. Poinsot, T., Veynante, D.: Theoretical and Numerical Combustion, 3rd edn. (2012). <http://elearning.cerfacs.fr/>

Numerical Investigation of Transverse Combustion Instability in a Multi-Element, Shear-Coaxial, High Pressure Combustor

P. Tudisco, R. Ranjan, S. Menon

*School of Aerospace Engineering,
Georgia Institute of Technology,
270 First Drive, Atlanta, GA, 30332.*

Abstract

We present a large-eddy simulation (LES) based investigation of transverse thermo-acoustic combustion instability in a rectangular combustion chamber. The configuration, referred to as transverse instability combustor (TIC) rig, is a high pressure, shear coaxial, seven element combustor, representative of a typical liquid rocket engine. The seven injector elements are designed to supply both fuel and oxidizer with different possible combinations so that stable/unstable combustion can be studied. Experimental investigation of the TIC rig at Purdue University has shown presence of transverse thermo-acoustic instabilities resulting from a non-linear coupling of the unsteady heat release due to combustion with the vortical structures impinging on the combustion chamber walls [1, 2]. These vortical structures originally contain both fuel and oxidizer and their impact on the combustion chamber wall leads to formation of a concentrated region of unsteady heat release. The non-linear coupling of the unsteady heat release with the transverse acoustic waves leads to appearance of a self-sustained limit-cycle behavior of the acoustic pressure fluctuations. Appearance of thermo-acoustic instabilities in practical engines can possibly damage the combustor due to stress and heat flux. In the present study, we first simulate the model combustor with only three active injector elements and modeling rest of the injectors as a constant mass inlet section. Such a modification of the geometry alters physics of the injection process, especially near the combustion chamber walls leading to a stable combustion within the rig. LES is able to predict the stable combustion exhibited by the three-element configuration, thus demonstrating ability of LES to capture complex reactive flow physics. The numerical investigation is currently being extended to simulate the entire TIC rig comprising of seven injector elements to analyze the self-sustained transverse instabilities and the flame holding dynamics under such conditions.

Keywords: Transverse combustion instability, large eddy simulation, multi-element, shear-coaxial

1. Introduction

Thermo-acoustic combustion instability is a phenomenon that is observed in several reactive flow systems such as liquid/solid rocket engines, premixed gas turbines, ramjets, and afterburners under certain operating conditions. It is understood to be the result of a non-linear coupling of the unsteady heat release with the local pressure (acoustic) fluctuations leading to a large-amplitude pressure oscillations [3–9]. Such instability can occur in two forms, usually referred to as longitudinal or transverse instability. They can quickly manifest themselves in time leading to large stresses and heat fluxes, and can possibly damage the combustion system. Therefore, eliminating or controlling combustion instability has been a focus of many past studies. However, both experimental and numerical methods face several challenges in their ability to capture and predict this phenomenon. For example, experimental investigation of a sustained combustion instability is nearly impossible due to the possibility of damage. Furthermore, due to high pressure and hot operating conditions, detailed measurements are difficult to obtain. Numerical investigation of such phenomenon is also difficult as it requires accurate and robust methods and models to simulate realistic test conditions. In this study we demonstrate the ability of LES to predict transverse combustion instability by simulating a model high pressure, shear-coaxial, multi-element combustion system.

An experimental test rig called the transverse instability combustor (TIC) in Purdue University [1, 2, 10] has been shown to exhibit spontaneous and self-sustained transverse combustion instability and is the focus of this study. The test rig comprise of a seven injector elements, which can inject fuel and oxidizer with different combinations within a rectangular combustion chamber. It is shown in the experimental investigation that the concentrated heat release on the side walls of the chamber resulting from the impingement of the vortical structures on the side walls can interact with the transverse acoustic waves causing appearance of self-sustained limit-cycle behavior, i.e., transverse combustion instability. Numerically modeling this rig is challenging due to several factors such as, complex geometry, finite-rate kinetics, unsteady flow physics, test conditions, turbulence chemistry interaction etc. Here, we use LES to investigate the self-sustained transverse instability and the flame dynamics within the TIC rig.

Due to the unsteady nature of the combustion instability, LES or detached eddy simulation (DES) are usually considered to be appropriate to study such dynamical systems. In the past, LES has been actively used for many combustion instability studies in ramjets or dump combustors and gas turbine combustors [4, 11–21]. These studies have shown the need to accurately model the three-dimensional (3D) and unsteady effects in addition to an accurate modeling of the injector element geometry. The injector geometry alters the characteristic impedance of the system, which in turn affects the frequency and amplitude of the acoustic fluctuations. Typically, combustion instabilities comprises of multiple acoustic modes, and therefore, requires an accurate modeling of geometry, boundary conditions and operating conditions to ensure that all the relevant modes are captured. For example, in past studies of longitudinal combustion instability in the continuously variable resonance combustor (CVRC) rig [19–21], the fundamental frequency was overpredicted and this was attributed to the adiabatic wall conditions employed by the numerical investigations, which do not account for heat loss from the system. The modeling of combustor walls with an isothermal condition lead to improvement in the prediction of characteristics of the acoustic fluctuations.

The objective of the present study is to investigate stable/unstable combustion within the TIC rig for different configurations of the seven injector system. The first case considers a configuration where only three injectors are active and rest injectors are modeled as constant mass inflow sections. This case is known to have a stable combustion behavior [2], and therefore, is chosen to demonstrate that the computational approach employed in the present study can capture the reactive flow physics and the flame dynamics. The second case is the original TIC configuration, which has all the seven injector elements active, and is considered to demonstrate that the numerical method employed in the present study can capture the unsteady dynamics of the self-sustained transverse instabilities. We analyze the mechanism of stable/unstable combustion in these two cases by studying the interaction of flow and flame dynamics with the change in the configuration.

The article is arranged as follows. Section 2 describes the details of the TIC rig. This is followed by Sec. 4 where the numerical methodology and the computational setup are discussed. The results are presented in Sec. 4 for instantaneous and time averaged reactive flow field. Finally, conclusions and future directions are summarized in Sec. 5.

2. Details of Experimental Setup

The transverse instability combustor (TIC) combustion system is an experimental test rig, which comprises of seven shear coaxial injector elements in a row ending into a rectangular combustion chamber [10]. Each injector element can supply gaseous fuel or oxidizer, thus leading to different possible configurations. The oxidizer used in this test rig is decomposed hydrogen peroxide, while two different types of fuels have been used at the same time, namely RP1 and ethane [10]. RP1 fuel is used mainly because of its ability to shows spontaneous ignition in the presence of hot decomposed hydrogen peroxide, and therefore, it avoids the need to have a spark within the combustion chamber. On the other hand ethane is used as the main fuel and is considered to investigate different possible configurations of typical rocket engine propellants. Figure 1 shows a schematic of the TIC rig comprising of the seven injectors and the rectangular chamber. We can observe the presence of a quartz window, which is used for the high speed video data processing in experimental investigations. The study is primarily focused on the central injector, referred here onwards as as the “study injector”, whereas the other six injector elements are referred as the “driving injectors”, because these injectors presumably provide majority of the thermal energy needed to sustain the transverse instability. The inflow conditions for all the seven elements are choked. A major difference between the driving and the study elements is the presence of a choke plate, apparent in Figure 1, which is due to a need to have a different resonant frequency of the central injector compared to the side injectors. The choked

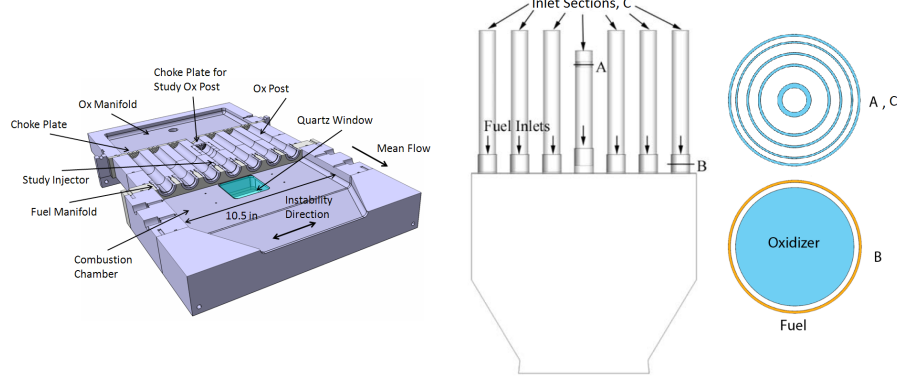


Figure 1: Schematic of the transverse combustion instability (TIC) rig showing the injector elements and the rectangular chamber [22].

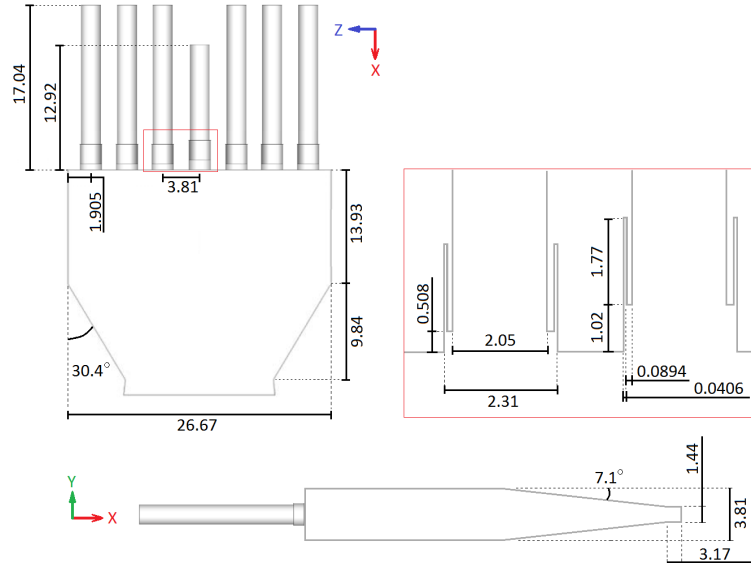


Figure 2: Geometrical details of the seven injectors of the TIC rig.

plate is constituted by coaxial inlets as illustrated in Figure 1, where the blue area indicates the oxidizer inlet configuration, while the orange part indicates the fuel inlet. This detail is ignored in the computational setup and each oxidizer inlet section is treated as a uniform inlet, where the original mass flow rate is spread on the whole circular cross section. The geometrical details of the TIC rig employed in the present investigation is summarized in Figure 2, where all the dimensions are expressed in centimeters. A zoomed-in view shows the configuration of the coaxial fuel slot, which is slightly longer in the case of the central study injector.

In the experiments changing the inflow configuration of the seven injector elements lead to different levels of combustion instability within the combustor [1, 2, 10]. Figure 3 shows the possible three configurations pertaining to the injectors, namely, the oxidizer alone setup, oxidizer and ethane setup and oxidizer and RP1 setup. We denote the configuration with both fuel and oxidizer flow by O and the oxidizer only flow by X .

Table 1 summarizes the different conditions considered in the experimental investigation. Experimental studies have shows that the most unstable configuration is the first case, which reveals a peak-to-peak pressure fluctuation of about 65% of the mean chamber pressure. Therefore, this configuration appears to

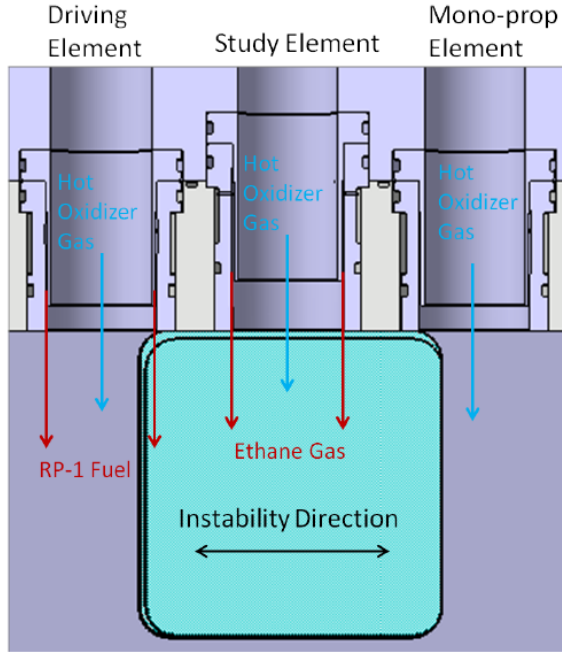


Figure 3: Possible configuration of each injector in the TIC rig.

Table 1: Experimental test conditions for the TIC rig

Case number	Configuration	P_c [kPa]	p' [kPa]	p' [% P_c]	$1W$ [Hz]
1	OOXOXOO	965	620	65	2032
2	OXXOXO	830	415	50	1807
3	XOXOXOX	815	70	8	1855
4	XOOOOOX	895	175	20	1920

Table 2: Operating conditions of the driving elements

Parameter	Value
O/F , ($H_2O_2/RP1$)	5.94
O/F , ($O_2/RP1$)	2.51
H_2O_2 Flow rate per element [kg/s]	0.196
O_2 Flow rate per element [kg/s]	0.083
$RP1$ Flow rate per element [kg/s]	0.033
$RP1$ inlet temperature [K]	298.15
Oxidizer inlet temperature [K]	1029
Inlet pressure [kPa]	965

Table 3: Operating conditions of the study element

Parameter	Value
Inlet pressure [kPa]	965
F/O density ratio	4.5
Injector O/F ratio	3.08
Equivalence ratio	1.21
H_2O_2 Flow rate [kg/s]	0.182
O_2 Flow rate [kg/s]	0.076
C_2H_6 Flow rate [kg/s]	0.025
C_2H_6 Inlet temperature [K]	319
Oxidizer inlet temperature [K]	1029

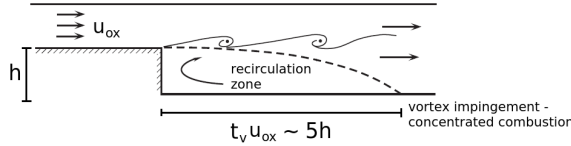


Figure 4: Sketch of vortex shedding on chamber walls.

be the most interesting setup for numerical investigation and is considered in the present study.

Table 2 and 3 summarizes all the details of the operating conditions of the driving and study elements, respectively, which include oxidizer to fuel ratio, inlet mass flow rate of fuel and oxidizer, inlet temperature and inlet pressure.

As mentioned before, in the TIC rig, the self-sustained acoustic oscillations occur due to a non-linear coupling of the unsteady heat release with the transverse acoustic waves. According to the Rayleigh criterion, if the acoustic pressure fluctuation p' is positively coupled with the fluctuating heat release q' (i.e. the phase between them is within zero and 180 degrees), then energy is supplied in phase to the acoustics of the chamber, and as a result, an amplification of the acoustic pressure amplitude occurs. The space-local Rayleigh index, RI is defined as

$$RI = \frac{1}{\Delta t} \int_o^t \frac{p' q'}{\bar{p} \bar{q}}, \quad (1)$$

where $\overline{(\cdot)}$ denote a time averaged quantity over the time interval Δt . RI by definition varies from -1 to 1. A positive values of RI indicates self sustained oscillations, while a negative values suggest that the acoustic fluctuations and the unsteady heat release are out of phase, leading to a decay of the acoustic fluctuations.

One of the possible reason for thermo-acoustic instability observed in the past studies [23–26] is the *vortex shedding* phenomenon, which leads to a continuous release of vortical structures from the injectors. The impingement of these structures on the chamber walls leads to a concentrated heat release, which shows a highly unsteady dynamics. If the local pressure maximum is present in the instance of intense heat release due to combustion, then a positive Rayleigh index occurs, thus leading to a self-sustained oscillation. Past studies have predicted that the vortex impingement on the chamber walls occurs at approximately $5h$, where h is the step height between the injector and the wall. For this reason, in the experimental investigation of the TIC rig, the step height was chosen to ensure that the vortex impingement occurs close to the location of a local pressure maxima.

Figure 4 shows a sketch of the vortex shedding phenomenon on the chamber walls. The time between the vortex shedding and vortex impingement is expressed as

$$t_v = \frac{5h}{u_{ox}}, \quad (2)$$

where h is the unknown step height and u_{ox} is the mean oxidizer speed. The time difference between the vortex shedding and the vortex impingement to the wall of the chamber can be estimated as one fourth of

the first transverse acoustic mode and is given by

$$t_i = \frac{T}{4} = \frac{1}{4f}. \quad (3)$$

From Eq. (2) and Eq. (3), we can estimate the step height, which is given by

$$h = \frac{u_{ox}}{20f}. \quad (4)$$

The first transverse mode can be estimated by knowing the mean speed of sound and the chamber width. In a similar manner, the oxidizer posts of the driving injectors were designed to be half-wave resonators of the first transverse mode and their length is given by

$$\frac{L_{ox}}{\lambda} = \frac{1}{2}, \quad (5)$$

where

$$\lambda = \frac{a_{ox}}{f_w}, \quad (6)$$

with a_{ox} , and f_w being the oxidizer speed of sound and the transverse frequency of the chamber, respectively. The central study element was designed following the same approach, with a slight different length, which was set to be three quarters of the second transverse mode.

The major objective of the present numerical investigation is to reproduce the most unstable case reported by the experimental studies. However, before that, we follow the approach of Shipley [2], where a reduced geometry case with three active injectors was considered to reduce the computational cost. This aspect is specifically related to the computational setup, which is discussed below.

3. Details of computational setup

In this section, we first briefly describe the numerical methodology. Afterward, we provide details of the three and seven injector configurations. The seven injector configuration is studied experimentally, however, the three-injector configuration is investigated first to demonstrate predictive ability of the numerical methodology employed in this study. In particular, this configuration is used to establish the computational framework employed in this study and some of the choices such as use of a finite-rate reduced chemical kinetics, computational grid, turbulence closures etc.

3.1. Numerical methodology

The numerical methodology is based on the well-established, second-order accurate (in both space and time) finite-volume solver for the unsteady Favre-filtered multi-species compressible LES equations [27]. A hybrid scheme, which switches between a second-order-accurate central scheme and a third-order-accurate MUSCL (Monotone Upstream-centered Schemes for Conservation Laws) scheme is employed [28]. A localized dynamic switch based on pressure and density gradients determines the spatial discretization scheme to use locally [27, 29]. Past studies have shown that the hybrid approach can capture regions of high gradients (as in shocks or thin shear layers between fuel and oxidizer) and also regions of turbulent fluctuations away from these strong gradients accurately [27–30]. The subgrid-scale (SGS) momentum and energy fluxes are closed using a subgrid eddy viscosity model, which is obtained using the local grid filter Δ and the subgrid kinetic energy k^{sgs} . An additional transport equation is solved for k^{sgs} and localized dynamic evaluation is used to obtain all the model coefficients [28, 31]. The turbulence-chemistry interaction is modeled through the quasi-laminar approximation [32], i.e., subgrid turbulence-chemistry interactions are neglected, which is reasonable assumption for the present study. Note that the subgrid turbulence chemistry interaction is often considered to be crucial for LES of turbulent combustion. However, in some of the past studies [33, 34], it has been found that such an interaction does not play a pivotal role, although it does affect results in certain aspects. Details of the LES equations, numerical method and these closures are presented in several articles cited earlier and therefore avoided here, for brevity.

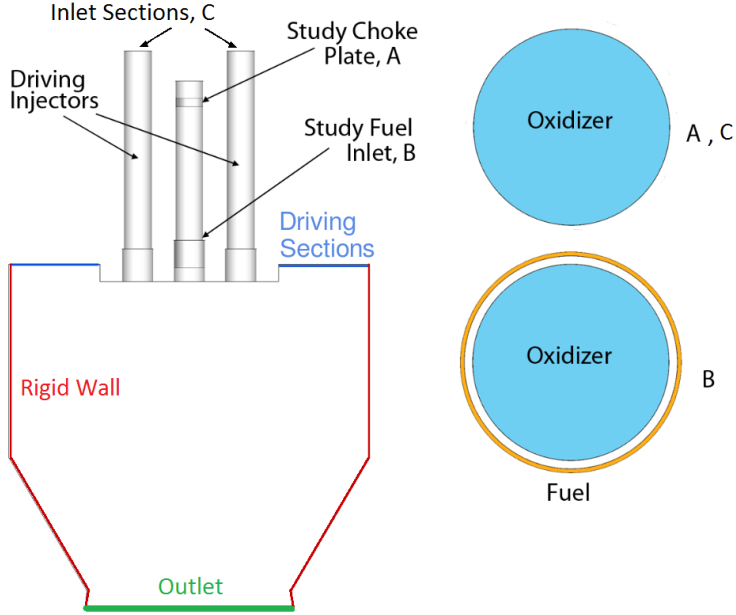


Figure 5: Schematic of the reduced geometry in the three injector configuration.

3.2. Three injector configuration

The three-injector configuration is a reduced geometry case with three active injectors and four implicitly modeled injectors. Note that this configuration is known to exhibit stable combustion within the TIC rig. Therefore, the ability of the numerical framework can be assessed in terms of prediction of stable/unstable combustion. Figure 5 shows the reduced geometry used in the present study. This particular configuration correspond to case 1 in Table 1. The geometry simplification is achieved by removing the four injector elements on both sides of the combustion chamber. In Case 1, only oxidizer flows in the last two driving injectors, and therefore, these injectors are replaced with a constant mass flow rate inlet section. The details of the dimensions of the reduced geometry in the three injector configuration is shown in Figure 6. We can observe that the oxidizer inlets are modeled as a constant mass flow rate and there is no explicit representation of the choked plate. Additionally, only the study element fuel slot is explicitly modeled in this study. In fact, as the other fuel slots does not have fuel flowing through them, there is no specific need to model the fuel cavity (as represented in the zoomed-in view in Figure 6).

Figure 7 shows the details of the computational grid of the three-injector configuration. The computational domain is spatially discretized using a multi-block structured grid. The grid parameters are chosen to ensure adequate resolution in the vicinity of the flame zone and the shear layer, where both turbulent transport and combustion processes interact with each other. Note that it is essential to have enough resolution in this region to capture unsteady mixing, transport and heat-release processes as they directly affect the flow and flame dynamics, particularly the flame anchoring mechanism. In addition, the grid in the vicinity of the dump plane should be carefully designed as the dump plane links the coaxial injector elements with the rest of the combustion chamber. Taking into all these considerations, a multi-block structured grid comprising of 564 blocks is generated with approximately 8.5 million computational cells.

The operating pressure of the combustion chamber is $P_{ref} = 0.96$ MPa. The study injector comprises of oxidizer and fuel injectors. The oxidizer is a mixture of O_2 and H_2O with mass fractions of 0.42 and 0.58, respectively [22]. The experimental investigation of the TIC rig was originally performed using ethane as the fuel. However, in the present study we consider methane (CH_4) as the fuel. A reduced version of the chemical kinetics for ethane is currently under development and will be considered in a future study. Note that a similar approach has been used at Purdue University [2] for investigation of the the seven injectors configuration, where the self-sustained instability has been demonstrated. Therefore, the choice of methane as the fuel instead of ethane seems reasonable for current investigation of transverse instability.

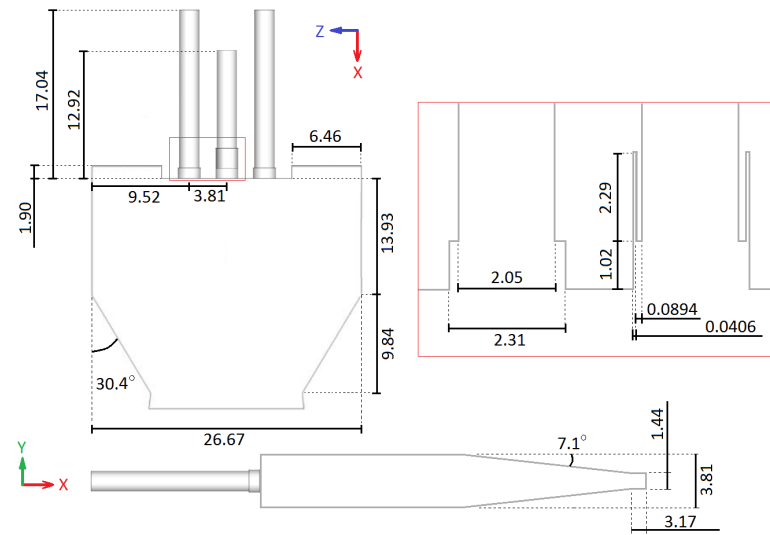


Figure 6: Dimension of the three injectors case (measurements in centimeters).

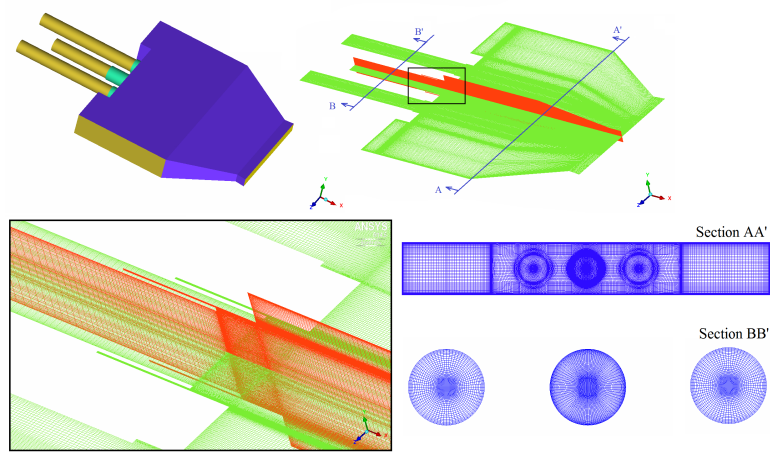
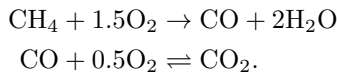


Figure 7: Geometry and computational grid employed by the three injector configuration.

The boundary conditions play an important role on the dynamics of reactive flow within the combustor. Particularly, they affect the vorticity dynamics immediately downstream of the dump plane, which can affect the overall stability pattern of the combustor. The mass flow rates of O_2 and H_2O through the study injector are, 0.076 kg/s and 0.182 kg/s, respectively and the oxidizer is injected at $T_1 = 1029$ K. The fuel is injected through the coaxial inlet surrounding the study element. The inlet temperature of the fuel is $T_2 = 319$ K and the mass flow rate is 0.023 kg/s. The two driving injectors located at both sides of the study element have only oxidizer flowing through them according to the most unstable configuration. As shown in Figure 6, the driving sections represent the last two driving injectors in the original seven injector configuration on each side of the combustion chamber. Both of these sections are rectangular and a constant mass flow rate inflow boundary condition is used for these section. According to the past experimental [22] and numerical [2] investigations of the TIC rig, the driving sections contain either oxidizer or RP1 as a fuel. However, the reduced methane chemistry adopted here does not consist of RP1 and therefore, we consider the equilibrium products between H_2O_2 and RP1, with mass flow rate of 0.196 kg/s and 0.033 kg/s for H_2O_2 and RP1, respectively and temperature of $T_{H_2O_2} = 1029$ K and $T_{RP1} = 298$, respectively. Since each driving section is supposed to model two of these injectors, therefore the mass flow rate for one driving section is obtained as 0.458 kg/s. The equilibrium composition (mass-fraction) is given by $Y_{H_2O} = 0.67752$, $Y_{CO_2} = 0.09257$, $Y_{H_2O} = 0.22986$, $Y_{H_2O} = 0.00005$, with an adiabatic flame temperature of $T_3 = 2621.61$ K.

All of the inflow boundaries are modeled using the characteristic boundary conditions [35] where the mass flowrates, the species mass fractions and the temperature are prescribed. Outflow is choked through the nozzle and therefore, supersonic conditions are employed at the nozzle exit. No-slip walls with adiabatic thermal conditions are used for the chamber walls. Although heat loss from the walls is likely to play some role as noted earlier [19, 36], there is no experimental data pertaining to the thermal conditions at the wall. Therefore, we focus here mainly on the flame dynamics and transverse instability mechanism without accounting for any heat loss through the walls.

The finite-rate chemical kinetics is employed through a reduced kinetics to make the problem computationally tractable. A two-step, five species (CH_4 , O_2 , H_2O , CO_2 and CO) reduced kinetics is used in this study based on earlier studies [37] and is same as the one employed in past studies for study of longitudinal instabilities [20, 21]. The two-steps of the mechanism are given by



The mechanism involves correction functions that depend on the local equivalence ratio, ϕ to modify the pre-exponential factors appearing in the two rate expressions. The parameters used earlier [37] are retained in their unmodified form and tested for the flow conditions of the current investigation. Although a two-step model is a major approximation, for combustion instability, proper heat release is more critical than radical predictions and therefore, is considered acceptable [18].

The simulation has been performed for approximately 13 milliseconds, i.e., about 18 flow through times. After the initial transients are passed and the flame is established within the central region of the rectangular chamber anchored in the vicinity of the dump plane, time averaging is performed to obtain turbulence statistics.

3.3. Seven injector configuration

Figure 8 shows the seven injector combustor geometry along with the details of the computational grid. In particular, the most challenging part of the grid generation step is to have adequate resolution with a better quality grid in the vicinity of the dump plane where the coaxial injectors end at the start of the rectangular combustion chamber. Similar to the three injector configuration discussed in Sec. 3.2, grid is designed to have enough resolution in the region where interaction of shear layer with the unsteady flame dynamics occur. In other parts of the combustion chamber, a coarser grid resolution is used by stretching the grid appropriately. For example, the convergent part of the nozzle and the outlet zone do not require fine grid resolution, and therefore, the grid is generated by exploiting the double O-grid structure created in the injector zone, and expanding the grid till the original circular shape gets modified to an octagonal shape. Such an approach eliminates the need to have the O-grid topology of the injector part up to the outflow section and still leads to better quality grid. The resulting multi-block structured grid comprises of 936 blocks with approximately about 16 million computational cells.

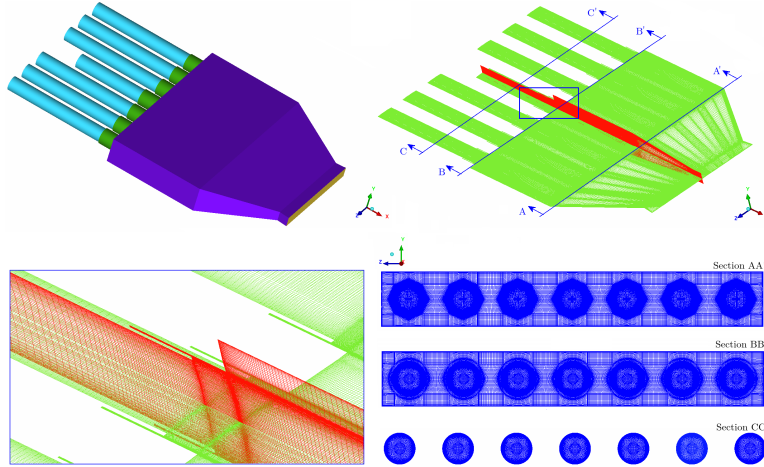


Figure 8: Geometry and computational grid employed by the seven injector configuration.

Contrary to the three-injector configuration, the full injector configuration does not employ any simplification compared to the past experimental studies except the reduced chemical kinetics. Similar to the three injector case, we consider the fuel to be methane instead of ethane and RP1. The mass flow rate of methane is chosen with respect to the values given in Table 2 and 3 by matching the equivalence ratio used in the experiments. In this case, we also include the driving injectors on the two sides of the combustion chamber and therefore, appropriate mass flow rate need to be specified. We use the corresponding equivalence ratio used for these injectors given in Table 2, and by representing RP1 as $nC_{12}H_{26}$, we obtain the required mass flow rate. The boundary conditions and all other computational details employed in the study of this configuration are similar to the three injector configuration described in Sec. 3.2.

4. Results

In this section, we first describe the instantaneous results for the three injector configuration with emphasis on flow and flame dynamics. Afterward, we describe the acoustic pressure fluctuation in the three injector configuration. Finally, we describe some preliminary results obtained from the ongoing study of the seven injector configuration.

4.1. Three injector configuration

4.1.1. Instantaneous reactive flow features

The quality of the computational grid and the predictive ability of the employed turbulence closures are assessed first to ensure that the follow-up discussion does not show a grid sensitive behavior. Figure 9 shows the spectrum of the resolved turbulent kinetic energy. It is obtained at a location in the middle of the chamber where the flame development occurs. We can clearly observe an agreement with the $-5/3$ slope, which is expected to be observed in the inertial range of turbulent fluid flow. This demonstrates that the computational grid and the turbulence closure approximations employed in the present study are adequate and accurate.

Figure 10 shows contours of the instantaneous pressure field at two different times in the central $x-z$ and $x-y$ planes. We can observe that initially there are acoustic waves throughout the combustion chamber. These waves enter the injectors and experience a phase shift with respect to the dump plane because of the different length of the injectors. After the initial transient phase, the pressure field becomes nearly uniform within the chamber, although some low intensity acoustic activity still remains in the injectors. These low amplitude perturbations result from the unstable mixing layer and the area change occurring at the dump plane. We can also observe the sonic line in proximity of the nozzle that eventually leads to supersonic conditions. Note that we do not observe any transverse instability in this configuration, which is consistent with the past studies [2] and demonstrate predictive ability of the employed computational framework in this

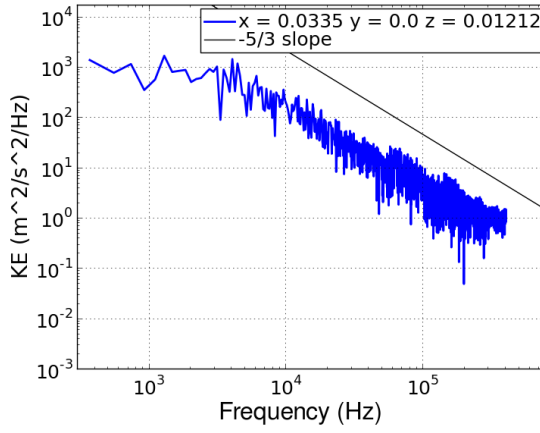


Figure 9: Pressure trace at the central injector.

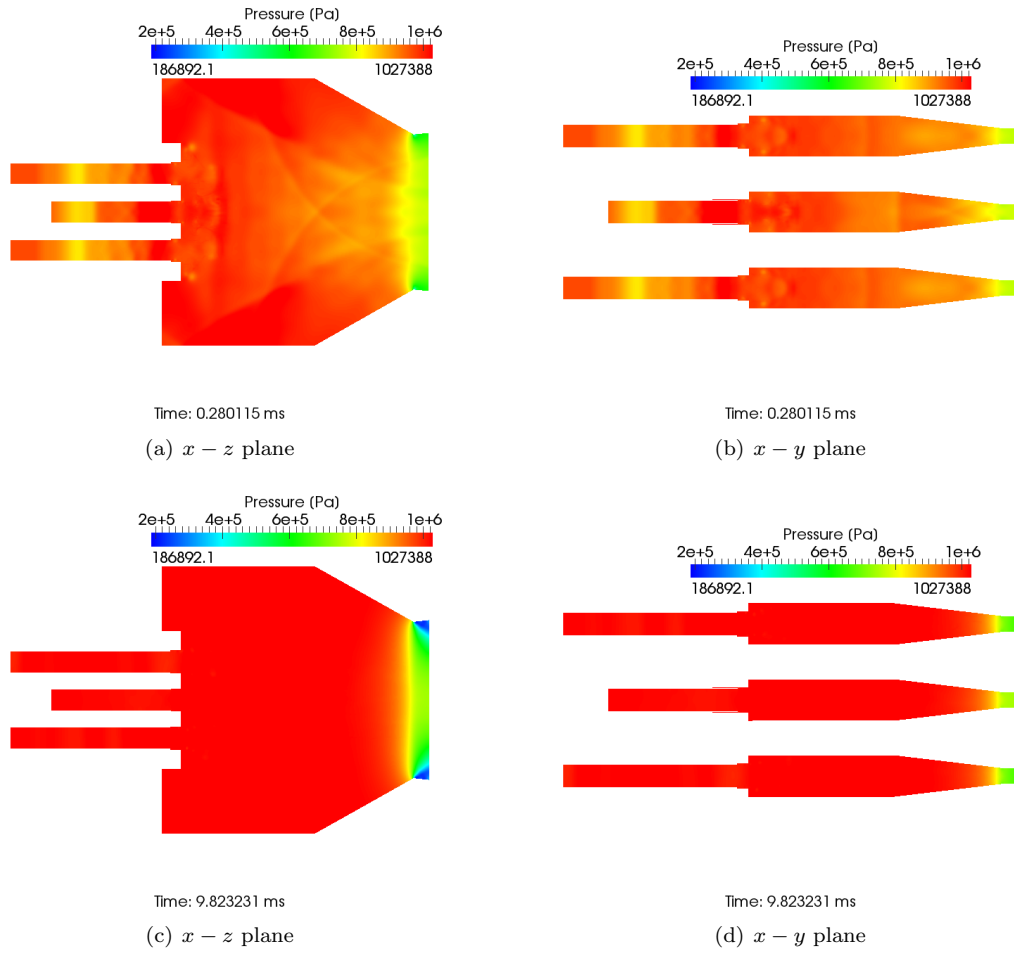


Figure 10: Contours of the instantaneous pressure field in the central $x - z$ (a, c) and $x - y$ (b, d) planes at initial ($t \approx 0.28$ ms) and later ($t \approx 9.8$ ms) times.

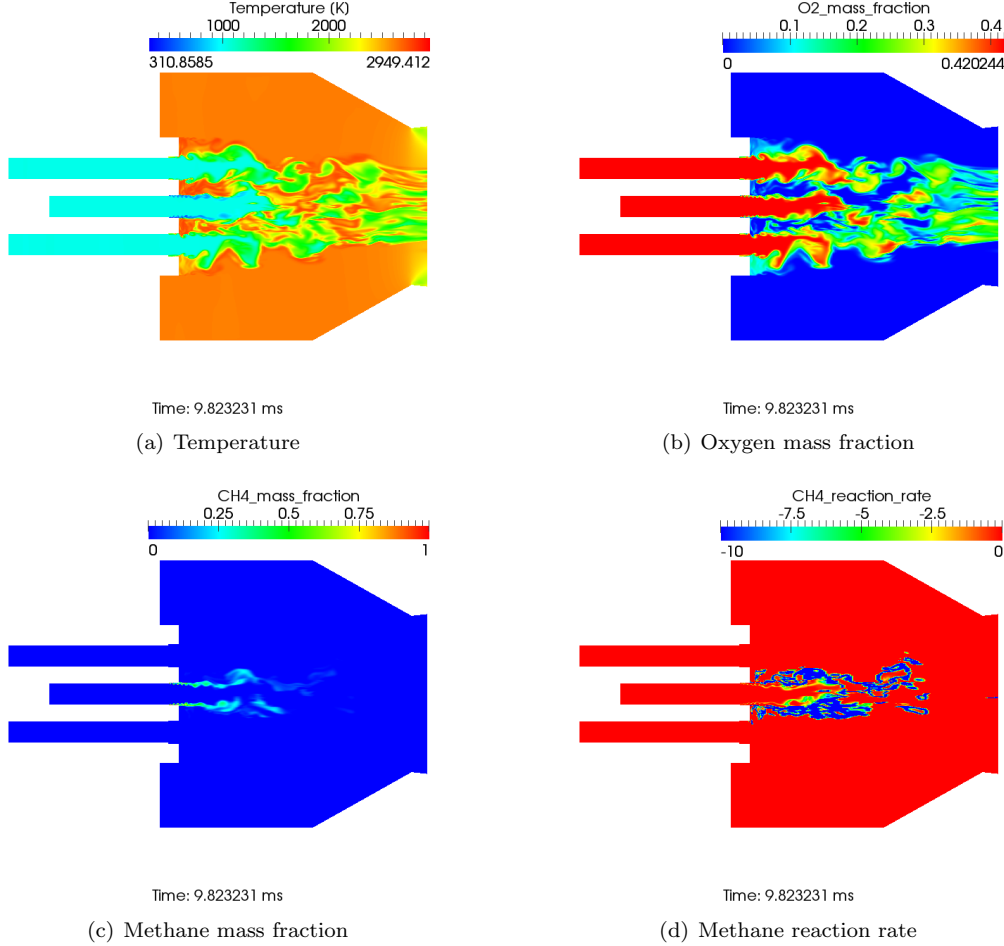


Figure 11: Instantaneous contours of temperature and species mass fraction in the central $x - z$ plane.

study. As mentioned before, this is related to the modeling of the side injectors though a simple constant mass flow inlets rather than explicitly representing them in the computational setup. This approximation of the computational geometry leads to a substantial change in the vortex shedding phenomenon, which in turn is responsible for the transverse instability observed in the full TIC rig.

Figure 11 shows the instantaneous contours of temperature and fuel and oxidizer mass fractions in the central $x - z$ plane. We can observe the region of hot products and flame development close to the central injector in Figure 11(a). In the same region, we can also observe presence of complex flow structures, which evolve forming vortices and developing the mixing layer between the fuel and the oxidizer. These flow structures are clearly not visible in the other two driving injectors because of the lack of the supplied fuel and therefore, the lack of shear forces at the interface between the oxidizer post and the fuel slot. However, some vortical structures are formed near the dump plane because of the sudden cross-sectional area change. These structures then form recirculation regions in between the study element and the driving element, where higher temperature can be observed. The contours of the oxidizer shown in Figure 11(b) shows the convection of the oxidizer downstream, which reacts with the fuel forming carbon monoxide and carbon dioxide (not shown here). Note that that the mass fraction drops by almost by 50% in the central part of the combustion chamber and the remaining oxidizer is convected downstream because of the lean conditions at which the combustion takes place. Similarly, methane mass fraction shown in Figure 11(c) also drops by half length of the chamber, thus demonstrating a complete combustion. Finally, the methane reaction rate shown in Figure 11(d), highlights the flame structure established near the central injector. We can observe that the flame is anchored at the dump plane, where the vortex formation and the recirculation zone create a region of small velocity magnitude.

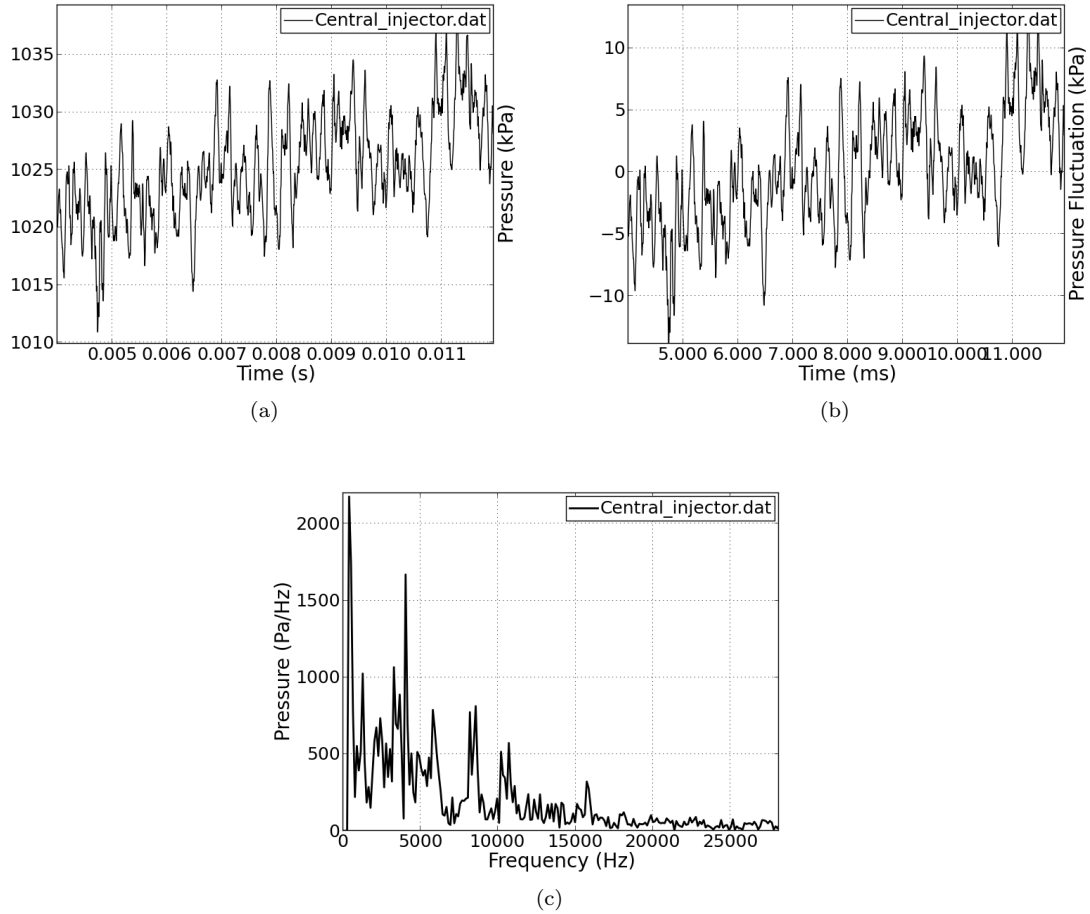


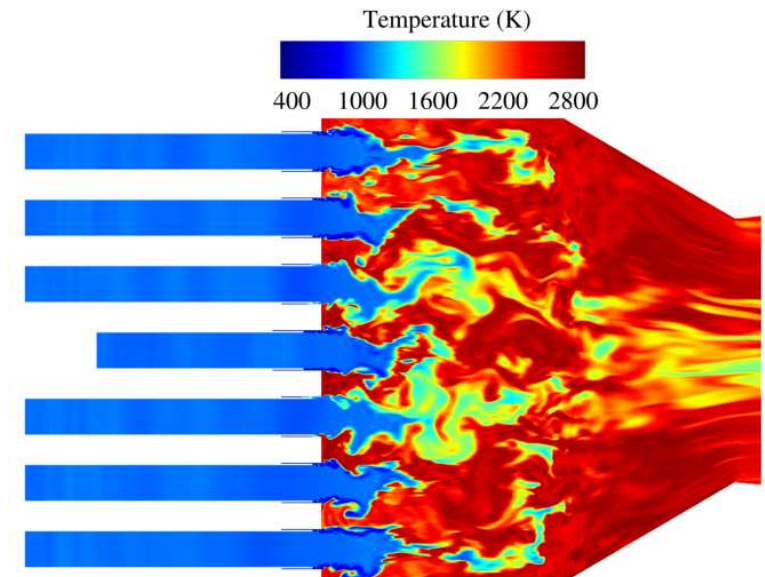
Figure 12: Time evolution of the pressure signal (a), acoustic fluctuation (b) at the central injector and the power spectrum density (c) of the pressure signal.

4.2. Acoustic pressure fluctuations

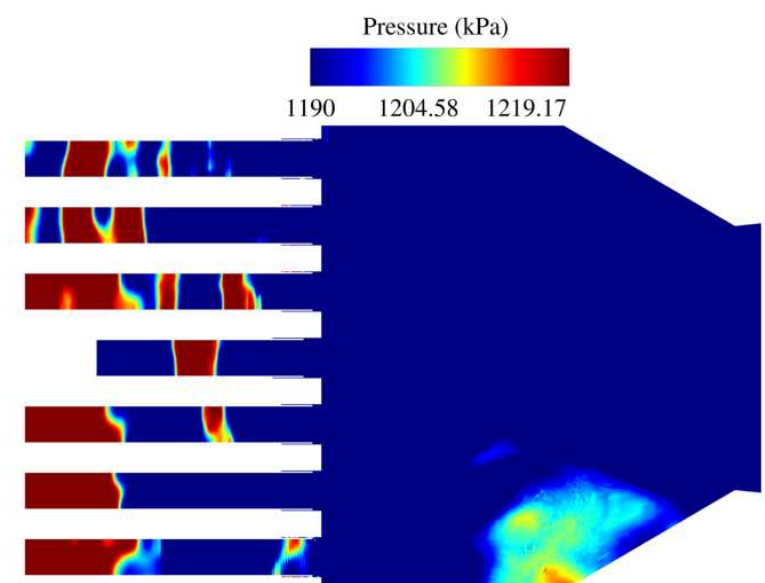
Figure 12 shows the time evolution of the pressure signal at the interface between the oxidizer post and the fuel slot for the study injector. In particular, the pressure signal is recorded only in the oxidizer region because this is the region where further studies will be conducted for the development of a reduced-order model referred as time-domain admittance boundary condition formulation. In fact, each of the injectors essentially behave in a one-dimensional (1D) manner from an acoustic point of view. Therefore, the interface between the oxidizer injector and the fuel slot is of particular interest because it represents the threshold between a 1D (oxidizer post) and a fully 3D (mixing region and combustion chamber) region. The time varying pressure field is obtained after the initial transient phase, and we can observe in Figure 12 that the time varying pressure field comprises of different high frequency components. The first two of these dominant frequencies are the most important and are examined further through the spectral analysis of the same signal. These dominant modes correspond to the first and the second longitudinal acoustic mode of the study injectors. However, the other part of the signal is still not completely negligible and it may result from the interaction between the injector acoustics and the mixing layer formed a little downstream.

4.3. Seven injector configuration

In this section we present some preliminary results for the seven injector configuration. Note that the simulations are currently underway and detailed results will be reported in future.



(a) Temperature



(b) Pressure

Figure 13: Instantaneous contours of the temperature (a) and pressure (b) fields at 2.5 ms.

Figure 13 shows instantaneous contours of the temperature and pressure fields at about 2.5 ms. We can observe that the reacting mixture is already ignited as the chamber is filled with the hot products. The flame development occurs throughout the chamber and is characterized by large scale vortical structures that break the original mixing layer formed by the fuel and the oxidizer in vicinity of the dump plane. Part of these large structures created by the most external driving injectors seems to impact at the chamber walls, however, this will require further evaluations. We can notice two interesting features of the pressure field. First, we can observe appearance of a pressure pulse in the bottom-right part of the chamber, which may represent the starting point of the transverse wave propagation. The second feature, is the presence of high pressure longitudinal waves inside the injectors. These waves are mostly one dimensional and carry the pressure information. When these waves interact with the mixing zone, i.e., the zone right before the dump plane, where fuel and oxidizer start to mix, the reacting mixture is locally altered, causing a different response to the combustion processes. Such a behavior, known as injector dynamics or response, is crucial for combustion instabilities, as it is responsible for the coupling of the chamber acoustics with the unsteady heat release due to combustion.

5. Conclusions and future work

LES based investigation of the TIC rig is performed to analyze transverse thermo-acoustic combustion instabilities in a model configuration representative of a typical rocket engine. Two different geometrical configurations for the TIC rig are considered in the present study. The first setup is a reduced three injector element configuration where the combustion behavior is reported to be stable. The second configuration is the complete rig, which exhibit presence of transverse combustion instabilities due to a non-linear coupling of the transverse acoustic fluctuations with the unsteady heat release due to combustion. The reduced geometry configuration is considered to establish the predictive ability of the employed computational framework in this study. In particular it is used to asses the quality of the computational grid, accurate predictions by the employed turbulence closures, finite-rate kinetics modeled through a reduced mechanism and modeling of the driving injectors by a constant mass inflow section. Due to removal of the driving injectors near the side walls of the combustion chamber in the first setup, the vortex shedding pattern is altered leading to a stable combustion with the flame region restricted to the central part of the chamber. These results are consistent with past investigation of a similar configuration of the TIC rig [2]. The second configuration, which is a seven injector setup is currently being investigated. Preliminary results show appearance of transverse acoustic disturbances, which may interact with the combustion processes leading to a transverse combustion instability.

In future detailed investigation of both the three- and seven-injector configurations will be performed to analyze the flame holding dynamics and the mechanism behind appearance of the transverse combustion instability. In addition, the time varying pressure data will be used to develop a time-domain admittance boundary condition formulation, which will allow for computationally efficient investigation of the multi-element configuration.

Acknowledgment

This work is supported by AFOSR (Dr. M. Birkan, PM). The computational resources provided by DoD HPC Centers at the Engineer Research and Development Center are greatly appreciated.

- [1] C.J. Morgan, B.R. Pomeroy, and W.E. Anderson. Implementation of a 2d chamber to study the response of a gas-gas injector to transverse instability. Technical report, Purdue University, IN, April 2013.
- [2] K.J. Shipley. Multi-injector modeling of transverse combustion instability experiments. Master's thesis, Purdue University, West Lafayette, IN, May 2014.
- [3] T. J. Poinsot, A. C. Trouv , D. P. Veynante, S. M. Candel, and E. J. Esposito. Vortex-driven acoustically coupled combustion instabilities. *J. Fluid Mech.*, 177:265–292, 1987.
- [4] S. Menon and W.-H. Jou. Large-eddy simulations of combustion instability in an axisymmetric ramjet combustor. *Combust. Sci. Technol.*, 75:53–72, 1991.

- [5] S. M. Candel. Combustion instabilities coupled by pressure waves and their active control. *Symposium (International) on Combustion*, 24:1277–1296, 1992.
- [6] J. C. Oefelein and V. Yang. Comprehensive review of liquid-propellant combustion instabilities in F-1 engines. *J. Propul. Power*, 9:657–677, 1993.
- [7] K. R. McManus, T. Poinsot, and S. M. Candel. A review of active control of combustion instabilities. *Prog. Energy. Comb. Sci.*, 19:1–29, 1993.
- [8] T. Lieuwen and B. T. Zinn. The role of equivalence ratio oscillations in driving combustion instabilities in low NO_x gas turbines. *Proc. Combust. Inst.*, 27:1809–1816, 1998.
- [9] Y. Huang and V. Yang. Dynamics and stability of lean-premixed swirl-stabilized combustion. *Prog. Energy. Comb. Sci.*, 35:293–364, 2009.
- [10] K. Shipley, C.J. Morgan, W.E. Anderson, M.E. Harvazinski, and V. Sankaran. Computational and experimental investigation of transverse combustion instabilities. Technical report, Joint Propulsion Conference, 2014.
- [11] T. Poinsot, C. Angelberger, F. Egolfopoulos, and D. Veynante. Large eddy simulation of combustion instabilities. In *In 1st Int. Symp. On Turbulence and Shear Flow Phenomena*, Santa Barbara, USA, 1999.
- [12] A. Roux, L. Y. M. Gicquel, Y. Sommerer, and T. J. Poinsot. Large eddy simulation of mean and oscillating flow in a side-dump ramjet combustor. *Combust. Flame*, 152:154–176, 2008.
- [13] G. Staffelbach, L. Y. M. Gicquel, G. Boudier, and T. Poinsot. Large eddy simulation of self-excited azimuthal modes in annular combustors. *Proc. Combust. Inst.*, 32:2909–2916, 2009.
- [14] G. Boudier, N. Lamarque, G. Staffelbach, L. Y. M. Gicquel, and T. Poinsot. Thermo-acoustic stability of a helicopter gas turbine combustor using large eddy simulation. *Int. J. Aeroacoust.*, 8:69–94, 2009.
- [15] C. Fureby. LES of a multi-burner annular gas turbine combustor. *Flow Turbulence Combust.*, 84:543–564, 2010.
- [16] R. Smith, G. Xia, W. Anderson, and C. L. Merkle. Computational simulations of the effect of backstep height on nonpremixed combustion instability. *AIAA J.*, 48:1857–1868, 2010.
- [17] R. Smith, G. Xia, W. Anderson, and C. L. Merkle. Computational studies of the effects of oxidiser injector length on combustion instability. *Combust. Theory Modelling*, 16:341–368, 2012.
- [18] M. E. Harvazinski, W. E. Anderson, and C. L. Merkel. Analysis of self-excited combustion instabilities using two- and three-dimensional simulations. *J. Propul. Power*, 29:396–409, 2013.
- [19] R. Garby, L. Selle, and T. Poinsot. Large-eddy simulation of combustion instabilities in a variable-length combustor. *Comptes Rendus Mecanique*, 341:220–229, 2013.
- [20] N. Guézennec, T. Dawson, P. Sierra, and S. Menon. Flame holding dynamics during combustion instability in a shear coaxial injector. In *In 8th Int. Symp. On Turbulence and Shear Flow Phenomena*, Poitier, France, 2013.
- [21] S Srinivasan, R Ranjan, and S Menon. Flame dynamics during combustion instability in a high-pressure, shear-coaxial injector combustor. *Flow, Turbulence and Combustion*, 94(1):237–262, 2015.
- [22] C.J. Morgan. Response of a gas-gas shear coaxial injector to transverse instability. Master’s thesis, Purdue University, West Lafayette, IN, December 2012.
- [23] J.C. Sisco. *Measurement and analysis of an unstable mode rocket combustor*. PhD thesis, Purdue University, West Lafayette, IN, August 2007.
- [24] K. Miller, J. Sisco, N. Nugen, and W. Anderson. Combustion instability with a single-element swirl injector. *Journal of Propulsion and Power*, 23, September 2007.

- [25] D.A. Smith and E.E. Zukoski. Combustion instability sustained by unsteady vortex combustion. *American Institute of Aeronautics and Astronautics*, July 1985. in AIAA/SAE/ASME/ASEE 21st Joint Propulsion Conference.
- [26] R.W. Pitz and J.W. Daily. Combustion in a turbulent mixing layer formed at a rearward-facing step. *AIAA Journal*, 21, November 1983.
- [27] F. Génin and S. Menon. Simulation of turbulent mixing behind a strut injector in supersonic flow. *AIAA J.*, 48:526–539, 2010.
- [28] F. Génin and S. Menon. Studies of shock/turbulent shear layer interaction using large-eddy simulation. *Computers & Fluids*, 39:800–819, 2010.
- [29] M. Masquelet and S. Menon. Large eddy simulation of flame-turbulence interactions in a shear coaxial injector. *J. Propul. Power*, 26:924–935, 2010.
- [30] F. Génin and S. Menon. Dynamics of sonic jet injection into supersonic crossflow. *J. Turbulence*, 11:1–30, 2010.
- [31] W.-W. Kim and S. Menon. An unsteady incompressible Navier-Stokes solver for large eddy simulation of turbulent flows. *Int. J. Numer. Meth. Fluids*, 31:983–1017, 1999.
- [32] FF Grinstein and K Kailasanath. Three-dimensional numerical simulations of unsteady reactive square jets. *Combustion and flame*, 101:192, 1995.
- [33] K-J Nogenmyr, C Fureby, Xue-Song Bai, P Petersson, Robert Collin, and Mark Linne. Large eddy simulation and laser diagnostic studies on a low swirl stratified premixed flame. *Combustion and Flame*, 156:25–36, 2009.
- [34] M Berglund, E Fedina, C Fureby, J Tegner, and V Sabel'Nikov. Finite rate chemistry large-eddy simulation of self-ignition in supersonic combustion ramjet. *AIAA journal*, 48:540–550, 2010.
- [35] T. J. Poinsot and S. K. Lele. Boundary conditions for direct simulations of compressible viscous flows. *J. Comp. Phys.*, 101:104–129, 1992.
- [36] R. Garby. *Simulations of flame stabilization and stability in high-pressure propulsion systems*. PhD thesis, Université de Toulouse, 2013.
- [37] B. Franzelli, E. Riber, L. Y. M. Gicquel, and T. Poinsot. Large eddy simulation of combustion instabilities in a lean partially premixed swirled flame. *Combust. Flame*, 159:621–637, 2012.

The Zeldovich spontaneous reaction wave propagation concept in the fast/modest heating limits

D. R. KASSOY [†]

Department of Mechanical Engineering
University of Colorado, Boulder, CO 80309-0424, USA

(Received 5 March 2015)

Quantitative mathematical models describe planar, spontaneous, reaction wave propagation (Zeldovich, Comb. Flame (1980), *39*, 211–214) in a finite hot spot volume of reactive gas. The results describe the complete thermomechanical response of the gas to a one-step, high activation energy exothermic reaction initiated by a tiny initial temperature non-uniformity in a gas at rest with uniform pressure. Initially, the complete conservation equations, including all transport terms, are non-dimensionalized to identify parameters that quantify the impact of viscosity, conduction and diffusion. The results demonstrate unequivocally that transport terms are tiny relative to all other terms in the equations, given the relevant time and length scales. The asymptotic analyses, based on the reactive Euler equations, describe both induction and post-induction period models for a fast heat release rate (induction time-scale short compared to the acoustic time of the spot), as well as a modest heat release rate (induction time-scale equivalent to the acoustic time). Analytical results are obtained for the fast heating rate problem and emphasize the physics of near constant-volume heating during the induction period. Weak hot spot expansion is the source of fluid expelled from the original finite volume and is a “piston-effect” source of acoustic mechanical disturbances beyond the spot. The post-induction period is characterized by the explosive appearance of an ephemeral, spatially uniform high-temperature and pressure spot embedded in a cold, low-pressure environment. In analogy with a shock tube the subsequent expansion process occurs on the acoustic time scale of the spot and will be the source of shocks propagating beyond the spot. The modest heating rate induction period is characterized by weakly compressible phenomena that can be described by a novel system of linear wave equations for the temperature, pressure and induced velocity perturbations driven by nonlinear chemical heating, which provides physical insights difficult to obtain from the more familiar “Clarke equation”. When the heating rate is modest, reaction terms in the post-induction period Euler equations exhibit a form of singular behavior in the high activation energy limit, implying the need to use a nonlinear exponential scaling for time and space, developed originally to describe spatially uniform thermal explosions (Kassoy, Quart. Jl. Mech. Appl. Math., 1977, *30*, 71–89). Here again the result will be the explosive appearance of an ephemeral spatially uniform high temperature and pressure hot spot. These results demonstrate that an initially weak temperature non-uniformity in a finite hot spot can be the source of acoustic and shock wave mechanical disturbances in the gas beyond the spot that may be related to rocket engine instability and engine knock.

[†] email address for correspondence: david.kassoy@colorado.edu. Written as a tribute to J.F. Clarke, my late paradigm, mentor and co-author

1. Introduction

Zeldovich *et al.* (1970) are concerned with preferential autoignition sites occurring in reactive gases characterized by a momentary nonuniform temperature distribution varying around a relatively low mean temperature. A transient, cartesian, one dimensional model, based on the reactive Euler equations, is developed to describe the evolution of the combustion process from an initially imposed local, negative linear temperature gradient in a hot spot surrounded by a much larger semi-infinite domain at relatively low temperature. After correcting a typo in Eq. 3.2 of the 1970 manuscript, it is clear that the model is developed for a characteristic chemical heat release time-scale similar to the local acoustic time scale, based on the distance a wave can propagate during the heat release process. The objective is to identify the dependence of combustion wave evolution on the amplitude of the linear temperature gradient. They seek to identify critical gradients that facilitate relatively strong shocks that can couple to an adjacent reaction zone leading to detonation formation. Following up on these ideas, Zeldovich (1980) describes an intuitive, qualitative theory for the propagation of a “spontaneous reaction wave” through a reactive gas, initiated by an imposed temperature inhomogeneity (hot spot gradient) in an initially constant pressure gas at rest. He argues that the inhomogeneity will initiate a sequence of adiabatic thermal explosions that propagate down an imposed negative temperature gradient due to the sensitivity of the local induction time to the temperature at each point, with the result that a reaction front can be identified and tracked. He considers “... the extreme case of large space lengths and small gradients so that one may neglect interaction between adjacent volumes of reacting substance (so that)... in each particle of the substance thermal explosion occurs independently.” In other words, he postulates a continuous sequence of perfectly constant volume thermal explosions. Zeldovich contrasts this type of propagating chemical reaction wave to traditional transport dominated flames, high-speed deflagration and detonation waves. It is implicit in such a process that the localized energy addition cannot induce gas motion or any form of gas dynamic disturbance, limitations recognized subsequently by many researchers (Short 1995, 1997; Kapila *et al.* 2002; Seitenzahl *et al.* 2009; Kassoy 2010, 2014a, 2014b). The qualitative theory lacks a quantitative mathematical model for the evolution of the reaction wave, including relevant time and length scales, the characteristic gradient magnitude, as well as the characteristic chemical power and the energy deposition.

Subsequently, Zeldovich *et al.* (1988) used numerical solutions based on the Euler equations to study the effect of initial concentration and temperature gradients on the generation of pressure waves with the objective of explaining detonation initiation. The model and interpretation of the numerical data recognizes the importance of the thermo-mechanical response of the gas to thermal energy deposition. The authors state “...that spontaneous generation of shock and detonation waves may occur in conditions close to self-ignition of the reactive mixture.”, results that “...may provide insight into the onset of nonlinear combustion instability in various technical systems.” (e.g. rocket engines and knock in internal combustion engines are mentioned). The authors cite numerous related technical papers by themselves, their colleagues and others addressing the detonation initiation and evolution problem.

Makhviladze and Rogatykh (1991) formulate a mathematical model for reaction initiation and evolution in a localized hot spot, with an imposed negative linear temperature gradient, initially at constant pressure with zero speed. The model is based on the planar, reactive, nonstationary Euler equations with one-step Arrhenius kinetics used to produce transient, spatially distributed heat release. The nondimensional space and time

variables are chosen to facilitate a characteristic time-scale for heat release (the induction time of a thermal explosion) comparable with the acoustic time-scale (wave passage time) in the spot. Significant nondimensional parameters are identified in the conservation equations, boundary and initial conditions and then used in a succession of numerical solutions to determine solution dependence on the parameter values. The authors identify a criterium for "...dangerously explosive regimes...", in terms of the nondimensional temperature gradient parameter λ , Eq. 16 in their text. An *ad hoc* assumption of zero speed is used to define a reduced equation set describing constant density, adiabatic heat addition to the gas. The analytical solution is used to describe the spatially dependent time for maximum heat release rate. This model for the Zeldovich spontaneous reaction wave is characterized by a thermal explosion propagating down the negative gradient at a specific speed. The temperature reaches the adiabatic explosion value just behind the propagating front, with a concomitant high-pressure value (pressure rises with temperature in a constant density heat addition process. Kassoy (2010, 2014a,b) has explained the physical consequences of relatively rapid heat addition with near inertial confinement.) Numerical solution of the full equations are used to discuss the relationship between a propagating spontaneous "chemical" reaction wave and familiar propagating gasdynamic waves (shocks and detonations). The authors note that an induction period with relatively small changes in dependent variables is followed by a full scale explosion on a substantially shorter "excitation" time-scale (Gu *et al.* 2003) during which most the heat release and fuel consumption occurs. It is this relatively rapid heat addition process that occurs in a nearly inertially confined gas volume as described in the cited Kassoy references above.

During the 1980's and extending to the present, there has been extraordinary interest in using asymptotic and/or computational methods to resolve reaction initiation phenomena, and/or gasdynamic consequences arising from either inhomogeneous initial conditions or thermal energy deposition into a gas volume. A non-exhaustive selection of these studies is cited in brevity below, primarily to inform the interested reader of the modeling diversity. More detailed information can be obtained from the publication introduction sections and their bibliographies.

Sileem, Kassoy & Hayashi (1991) use numerical methods to study planar detonation initiation following **thermal energy deposition** into a reactive gas volume adjacent to a planar boundary. Clarke, Kassoy & Riley (CKR) (1984) describe a related modeling effort where a **hot planar boundary** is an energy source that heats the adjacent inert gas by conduction causing localized gas expansion. The induced motion (... "piston effect") is the source of a shock wave propagating into the adjacent cold environment.

Jackson *et al.* (1989) study the evolution of a high activation energy ($\varepsilon \rightarrow 0$) chemical reaction within a finite slot when the chemical time-scale for the induction period is identical to the acoustic time-scale. A traditional thermal explosion formulation facilitates a quantitative description of the thermomechanical response of the gas to transient, spatially resolved, chemical heat addition, initiated by an $O(\varepsilon)$ negative temperature gradient in the slot. The describing equations are essentially those for linear acoustics driven by a nonlinear reaction term and are equivalent to "Clarke's equation" (Clarke 1978). Numerical solutions of the system show that the induction period temperature and pressure perturbations become unbounded in the vicinity of the $O(\varepsilon)$ temperature maximum in the initial condition and at a finite thermal explosion time, t_e . The failure of the numerical method as $t \rightarrow t_e$ is interpreted to mean that a familiar thermal explosion logarithmic singularity characterizes the runaway process. The authors then use coordinate expansion asymptotics to describe the spatially multiscale evolution of the hot spot. The solution development is confined to the vicinity of the $O(\varepsilon)$ initial tempera-

ture maximum. A post-induction period analysis employs nonlinear rescaling of the time and space, the former developed originally by Kassoy (1977), to describe the full scale explosion in the vicinity of the original $O(\varepsilon)$ temperature maximum. The results show that the reactant is totally consumed on exponentially short time and space scales while the spatially uniform temperature rises to the adiabatic explosion value in an essentially constant volume process, with a concomitant increase in pressure and nearly no induced fluid speed. The post induction theory is also confined to a very thin region adjacent to the original temperature maximum.

The consequences of spatial inhomogeneities in pressure, temperature, concentration and speed, on the evolution of a reaction process at relatively modest activation energy are predicted by Short (1995, 1997). He provides a thorough review of the literature available in that period. A high activation energy theory (based on the familiar small parameter $\epsilon = R'T'_0/E' \ll O(1)$) is formulated to describe the initiation of a chemical process by $O(\epsilon)$ spatial inhomogeneities in the initial values of the dependent variables leading ultimately to the appearance of a detonation. His models describe chemical heat deposition into a volume of reactive gas, characterized by dimension l'_R , when the induction time scale of the thermal explosion, denoted by t'_R , is compared to the acoustic time scale $t'_a = l'_R/c'_0$ where c'_0 is the characteristic speed of sound. He considers models for the time-scale ratio $\mu = t'_R/t'_a = 1$ and also $\mu \ll O(1)$ ("long-wave length analysis"). The former describes a weakly compressible response of the gas to minor heat addition during the induction period of a thermal explosion. In contrast, the latter corresponds to **nearly** constant volume heat addition. Short recognizes the limitations of the Zeldovich concept cited above and develops an asymptotic analysis for variable density corrections to the lowest order constant volume solution valid for $\mu = 0$.

In contrast to the self-initiation phenomena in the references above (small amplitude initial disturbances), direct initiation of gaseous detonations is the subject of a paper by Eckett *et al.* (2000). A spherical blast wave, generated by the rapid deposition of a large amount of thermal energy into a small volume of reactive gas[†], ignites a chemical reaction in a reactive gas through which it propagates. The study seeks to determine blast wave properties (critical energy) that lead to a sustained spherical detonation, associated with the "competition between heat release, wave front curvature and unsteadiness."

Vasquez-Espi' and Liñan (2001) model the initiation of a high activation energy chemical reaction in a reactive gas following "instantaneous" spatially resolved thermal energy deposition to create a well-defined hot, high pressure spot (it is assumed that the energy addition occurs at constant volume and that "...there is no time for the generation of motion...", thus neglecting the thermomechanical response of the gas to energy addition.) The problem formulation is developed for reaction time scales of the order of the local acoustic time, $\mu = O(1)$. The acoustically linearized reactive Euler equations with a nonlinear chemical energy term found by Clarke (1978) are derived. Highly resolved numerical methods are used to ascertain a critical value of the "Dahmkohler number," $(1/\mu)$. Beyond the critical value, a well-defined ignition process occurs because the local chemical power addition is large enough to overcome the cooling effect of local gas expansion.

Kapila *et al.* (2002) develop a model for detonation formation arising from an existing tiny linear temperature gradient in a semi-infinite domain. The compressible non-dimensional equations are valid when the characteristic thermal energy deposition time (really the thermal explosion induction time) is similar in magnitude to the local acoustic

[†] Traditional blast wave theory is based on an unphysical idealization; **instantaneous** deposition of energy into a **point**.

time. Familiar high activation energy thermal explosion theory is employed to study the impact of asymptotically small gradients on induction period history. The analysis leads to a recognition that the post induction period time-scale will be exponentially short compared to the local acoustic time. The asymptotic methodology enables a cause-effect understanding of the physics of shock formation that is difficult to obtain from numerical experiments alone. “Accurate and well-resolved numerical computations are (used) to determine the mode of detonation formation as a function of the size of the initial gradient.” Solutions are obtained for a wide range of temperature gradients to demonstrate the diversity of evolutions to detonation. The authors recognize that “...Zeldovich ideas, while extremely instructive, are limited in accuracy...” due to the lack of gasdynamic response of the gas to spatially distributed transient heat deposition.

Gu *et al.* (2003) use computational solutions to the reactive compressible flow equations, including all transport terms to study the sensitivity of reaction front propagation to small linear temperature gradients imposed on a spherical hot spot. Detailed kinetic schemes for stoichiometric H₂-CO-air and H₂-air mixtures are used to describe the autoignition process. Initially, the temperature rises significantly throughout the spot in a nearly spatially homogenous process with a slight temperature maximum evolving at the origin, far larger than the maximum associated with the initial tiny gradient. A rapid reaction process follows in the vicinity of the maximum, leading to a localized hot spot. A reaction wave then spreads quickly across the spot creating a region of very high temperature. Subsequently the entire spot explodes and all fuel is consumed on the relatively short “excitation time-scale,” t'_e . A nondimensional parameter, ξ , related to the magnitude of the initial linear temperature gradient† is used to discriminate between five different modes of reaction front propagation. The authors note the importance of a second parameter, the ratio (t'_a/t'_e) where t'_a is the acoustic time-scale of the spot. The transient reaction process is distinct from that in a traditional thermal explosion (Kassoy 1977). The latter is described in terms of a relatively long induction time, where little fuel is consumed and only small temperature changes occur, followed by an extremely rapid full explosion where the temperature rises to the adiabatic explosion value as all the fuel is consumed.

Kurdyumov *et al.* (2003) extend the aforementioned CKR model for a planar compact heat source to cylindrical and spherical geometries. Conduction heat transfer from the source to the adjacent gas raises the temperature of a volume with characteristic length scale r'_h on an energy deposition time-scale t'_d , where the latter is compared to the characteristic acoustic and conduction time-scales of the volume, $t'_a = r'_h/a'_0$ (a'_0 is the characteristic speed of sound at the initial temperature T'_0) and $t'_c = r'^2_h/\kappa'_0$ (κ'_0 is the characteristic thermal diffusivity), respectively. A continuum gas theory requires that the **ratio** of the acoustic time to the conduction time, equivalent to the Knudsen number: $\mathbf{Kn} = (\alpha'_0/a'_0 r'_h) \ll O(1)$. The compact heat source, a spark, hot wire or laser shot delivers a specified amount of energy E'_j during the deposition time scale, which heats the volume such that $\rho'_0 C'_p T'_0 r'^{j+1}_n \sim E'_j$ ($j = 0, 1, 2$ for planar, cylindrical and spherical geometries, respectively) defines the dimension r'_h . C'_p is the characteristic specific heat at constant pressure. When $t'_d = t'_a$, energy from the source to the gas volume raises the local temperature $O(T'_0)$ in a nearly isobaric process, with the density decrease inversely proportional to the temperature increase. Gas expelled from the heated volume acts as a piston to drive mechanical disturbances into the unheated gas. The thermomechanical analysis is carried out for a wide range of deposition time scales: $(t'_d/t'_a \ll O(1))$, rapid

† The parameter ξ is in fact the inverse of the reaction wave propagation Mach number.

heating), ($t'_d/t'_a = O(1)$, modest heating), ($t'_d/t'_a \gg O(1)$), slow heating). The mechanical consequences of each ratio are articulated in the Conclusion section of the cited reference.

High fidelity computational simulations based on the compressible reactive Navier-Stokes equations including transport terms, with hydrogen chemistry for the kinetics are carried out to simulate phenomena that may occur in an HCCI engine (Sankaran *et al.* 2005). A turbulent flow field in a high-pressure gas with an uncorrelated turbulent temperature field is imposed as an initial condition. The field consists of individual hot spots with relatively small temperature inhomogeneities being strained and dissipated by the turbulence. The results identify a first ignition site and subsequent combustion elsewhere in the field. The authors note the impact of localized gas compression on the heat budget of auto-igniting hot spots. Ignition development is found to be sensitive to "...temperature distribution statistics." Two regimes of ignition are identified; "...spontaneous propagation and deflagration...". "...a criterion based on the propagation speeds (of the waves) is proposed to distinguish between the two...regimes." However, cause-effect relations cannot be determined from the computational data set.

Spontaneous initiation of detonation in astrophysical objects (white dwarfs) is the subject of a computational modeling effort by Seitenzahl *et al.* (2009). The dimensional reactive Euler equations are solved for appropriate astrophysical thermodynamic conditions and thermonuclear reaction kinetics to determine whether a hot spot of fixed size with an initial temperature inhomogeneity can be the source of a detonation. In particular the authors seek to determine "...the smallest size for a heated region that still leads to detonation..." Several different initial spatial temperature distributions are incorporated in the modeling. The differing gradients in induction times (Zeldovich model) play a major role in outcome although the authors recognize that "...Zeldovich's spontaneous wave concept...ignores nonlinear gasdynamic evolution...". The use of dimensional equations prevents the reader from identifying nondimensional parameters that characterize the reactive gasdynamics. Many of the results can be understood in terms of the thermo-mechanical response of a compressible gas to transient, spatially resolved thermal energy addition (CKR 1984; Kassoy 2010).

Poludnenko *et al.* (2011) focuses on turbulent flames interacting with a turbulent flow field as a source of detonation initiation, with application to unconfined systems (e.g. gas cloud explosions, supernovae). Results are obtained from a DNS based on the compressible flow equations with one-step Arrhenius kinetics, including transport effects. A planar turbulent flame interacts with a previously created a turbulent flow field. The flame is observed to accelerate during a runaway process to supersonic propagation speeds under specifically defined physical conditions. "...burning is controlled by flame propagation and not by autoignition....(precluding) the formation of global spontaneous reaction waves." Unlike most of the previously cited studies, specific hot spot properties are not required. A semi-quantitative (order-of magnitude) steady state analysis for spontaneous runaway is presented, based on thermal power deposition on the local acoustic time scale with the result that a CJ deflagration propagation speed is predicted. "...the spontaneous DDT mechanism....does not place any ...constraints on equation of state, reaction model or ...flame properties."

LES methods are used by Kulkarni *et al.* (2013) to determine the impact of turbulence on autoignition in a non-premixed hydrogen-air system. The objective is to determine physical processes (mixing) that enable autoignition to occur in isolated volumes (hot spots) of fuel-air mixture. Results are presented for autoignition lengths with respect to turbulent flow properties.

The relationship between super-knock and autoignition of pre-ignition kernels in supercharged spark-ignition engines is the topic of research described in Peters *et al.* (2013). A

new theory of turbulence, developed by the first author, is used to describe the stochastic properties of likely small-scale temperature inhomogeneities as they might appear during phases of cylinder compression. 3D DNS simulations of homogeneous isotropic turbulence are used to obtain the necessary statistical information. The basic premise is that some of the hot spots are sites for the Zeldovich gradient-determined spontaneous reaction wave propagation to be initiated. A “resonance” between the acoustic waves generated by the thermomechanical response of the gas to localized transient, spatially resolved thermal energy deposition, and the spreading reaction wave is the source of a detonation (the super-knock).

Kassoy's (2010) thermomechanical model employs systematic asymptotic methods to predict the consequences of spatially resolved, transient thermal energy deposition into a volume of inert gas. In contrast to the compact initial source approach, a generalized thermal source term with explicitly defined properties is used in the energy equation to represent a spark, laser shot, heated electric wire or chemical heat addition. The model quantifies both the thermodynamics and fluid mechanical responses of the gas to volumetric energy deposition on a time-scale short compared to the acoustic time of the volume. The analysis leads to a non-intuitive result: **nearly** constant volume heat addition prevails when the energy deposited is less than a specific critical value. The internal expansion Mach number is subsonic. Gas expelled from the volume acts as a piston to drive mechanical disturbances into the unheated environment. Beyond the critical value of energy deposition, the heat addition process is fully compressible, characterized by an $O(1)$ internal gas expansion Mach number and a large expelled gas Mach number responsible for a blast wave propagating into the adjacent environment. This finite source, heated on a finite time-scale, replaces the classical blast wave model of **instantaneous** energy addition into a **point** (e.g. Taylor 1946). The thermomechanical modeling has been extended to a reactive gas with a high activation energy reaction by Kassoy (2014a) and to a wide range of heat deposition time scales (Kassoy 2014b). The latter model quantifies the nearly isobaric response of an inert gas to energy deposition on a time scale long compared to the acoustic time of the volume. Each of these asymptotic models quantifies the role of viscous, conductive and mass diffusion in the thermomechanical response.

Radulescu *et al.* (2013) provide an extensive review of a parameter, used to “...characterize the detonability and explosion hazard of reactive media.” Theory and experiment suggest that hot spot ignition and the subsequent appearance of strong shock waves is uniquely related to the parameter magnitude. The thermomechanical response to localized, spatially distributed heat addition transients can be predicted if the parameter is known.

The current paper presents a systematic and rational asymptotic formulation for autoignition within a finite volume of reactive gas with an instantaneous spatially nonuniform temperature distribution, T' , varying around a mean temperature T'_0 . This configuration may occur in a nonuniform mixture of reactive gas where some volumes of the gas are warmer than the mean and others are colder leading to a preferred ignition site. The reaction initiation process is driven by an imposed dimensional temperature gradient, measured by $\Delta T'/\ell' \ll O(T'_0)/\ell'$ characterizes the local gradient and where ℓ' is the length-scale of the temperature inhomogeneity. A primary objective is integrate the thermomechanical response of the gas into the Zeldovich model (1980) for both fast and modest rates of chemical energy addition (both quantified in sections 2.1 and 3) in a rational manner in order to identify physical conditions compatible with constant volume heat addition physics implicit in his model. The analysis, related to Short's work (1995, 1997) that of Jackson *et al.* (1989) and Kapila *et al.* (2002) should enable the reader to gain a fundamental and quantitative physical understanding of how autoignition driven

initially by a small temperature gradient generates a propagating, spatially distributed, high activation energy thermal explosion, aka as a spontaneous reaction wave, including induced fluid motion and the generation of mechanical waves (acoustics, shocks and blast waves).

2. Mathematical model.

The mathematical model is formulated by using asymptotic techniques described by Clarke and Kassoy (1984) as well as Kassoy (2010, 2014a, 2014b). It quantifies the multi-faceted heat transfer phenomena evolving from an imposed inhomogeneous temperature distribution like that in figure 1. The primary objectives are to establish the physical conditions that must exist for a spontaneous reaction wave to propagate down the negative gradient and for the Euler equations to be an appropriate model.

2.1. Generalized thermomechanical analysis

The analysis begins with the complete planar dimensional (primes') conservation equations for a perfect gas including all transport terms and a generalized thermal source term in the energy equation that may represent external energy addition from a spark or laser shot, or from an exothermic chemical reaction. These equations are chosen to emphasize the thermomechanical physics of gaseous systems with imposed energy addition. An important objective is to identify nondimensional parameters modulating the transport terms in order to justify the use of the reactive Euler equations in a subsequent study of reactive gas autoignition and thermomechanics.

$$\rho'_{t'} + (\rho' u')_{x'} = 0 \quad (2.1)$$

$$\rho'(u'_{t'} + u' u'_{x'}) = -p'_{x'} + V' \quad (2.2)$$

$$\rho' C'_v (T'_{t'} + u' T'_{x'}) = -p' u'_{x'} + C' + \rho' \dot{Q}'_s + D' \quad (2.3)$$

$$p' = \rho' R' T' \quad (2.4)$$

$$Y_{t'} + u' Y_{x'} = \frac{\dot{Q}'_s}{q'_R} + \mathcal{D}' \quad (2.5)$$

where V' , C' , D' and \mathcal{D}' represent familiar planar viscous, conduction, dissipation and mass diffusion operators, respectively. The thermal power heat source is defined by

$$\dot{Q}'_s = \frac{q'_R}{t'_s} \dot{Q}_s \quad (2.6)$$

where q'_R is the heat of reaction per unit mass, t'_s is the source heat addition time scale and \dot{Q}_s is the nondimensional heat source.

The initial conditions, defined by

$$t' = 0, \quad 0 \leq x' \leq \ell' : \quad (T', p', \rho') = (T'_i(x'), p'_0, p'_0/R'T'_i(x')) \quad , \quad (2.7a)$$

$$u' = 0, \quad Y = 1 \quad , \quad (2.7b)$$

describe a gas at constant pressure (p'_0), at rest ($u' = 0$), with imposed temperature and density inhomogeneities. The thermal boundary conditions are defined by

$$x' = 0; \quad T' = T'_1 > T'_0 \quad (2.8a)$$

$$x' = \ell' \quad T' = T'_0 \quad (2.8b)$$

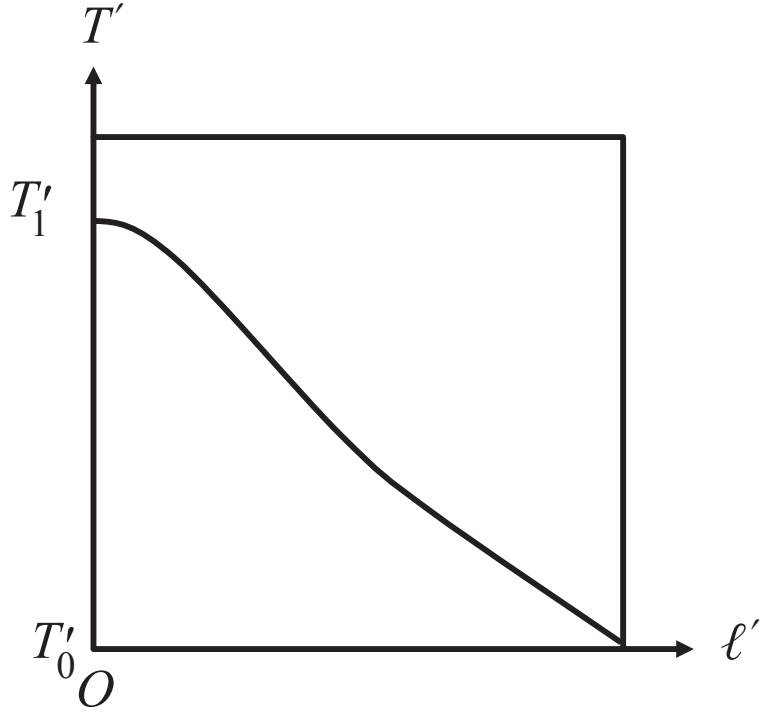


FIGURE 1. A spatially non-uniform temperature distribution $T'(x')$ varying around a mean value, T'_0 where the former is larger than the latter for $0 \leq x' \leq l'$ and less beyond l' on a similar length scale.

The boundary at ℓ' is open, allowing fluid to be expelled into a cold fluid beyond.

The details of the initial gradient $dT'_i/dx'(t' = 0, x')$ are left undefined so long as the gradient is negative for $0 < x' < \ell'$ and $T'_i < T'_0$ in some domain beyond $x' = \ell'$. Nondimensional variables are defined by:

$$(T, p, \rho) = (T'/T'_0, p'/p'_0, \rho'/\rho'_0) \quad (2.9a)$$

$$u = u'/a'_0 \quad (2.9b)$$

$$x = x'/\ell' \quad (2.9c)$$

$$t = t'/t'_s \quad (2.9d)$$

where a'_0 is the characteristic speed of sound at T'_0 . When used in (2.1)-(2.9), the nondimensional equations take the form

$$\rho_t + (t'_s/t'_A)(\rho u)_x = 0 \quad (2.10)$$

$$\rho \left[u_t + (t'_s/t'_A)uu_x \right] = -(t'_s/t'_A)\frac{p_x}{\gamma} + (t'_s/t'_v)V \quad (2.11)$$

$$\rho \left[T_t + (t'_s/t'_A)uT_x \right] = -(\gamma - 1)(t'_s/t'_A)p_{ux} + (t'_s/t'_{CD})C + (q'_R/e'_0)\rho\dot{Q}_s + (\gamma)(\gamma - 1)(t_s/t'_v)D \quad (2.12)$$

$$p = \rho T \quad (2.13)$$

$$\left[Y_t + (t'_s/t'_A)uY_x \right] = -\dot{Q}_s + (t'_s/t'_{DIFF})\mathcal{D} \quad (2.14)$$

where the characteristic acoustic, viscous, conduction and mass diffusion time scales are defined by

$$t'_A = \ell'/a'_0, \quad t'_v = \ell'^2/\nu'_0, \quad t'_{CD} = \ell'^2/\alpha'_0, \quad t'_{DIFF} = \ell'^2/D'_m \quad , \quad (2.15a, b, c, d)$$

respectively, where ν'_0 , α'_0 , D'_m are the characteristic kinematic viscosity, thermal diffusivity and the mass diffusivity, respectively.

The nondimensional initial conditions are

$$t = 0; \quad (T, p, \rho) = (T_i(x), 1, 1/T_i(x)) \quad (2.16a)$$

$$u = 0, \quad Y = 1 \quad (2.16b, c)$$

where $T_i(x) = T'_i(x')/T'_0$.

The boundary condition in (2.8) can be written in nondimensional terms as

$$x = 0, \quad T = 1 + \tau, \quad \tau = \frac{T'_1 - T'_0}{T'_0} \quad (2.17)$$

where the parameter τ quantifies the temperature difference across the gradient.

The viscous, conductive and diffusive transport terms in (2.11), (2.12) and (2.14) are modulated by the time scale ratios t'_s/t'_v , t'_s/t'_{CD} and t'_s/t'_{DIFF} , respectively. These ratios can be rewritten as $(t'_s/t'_A)(t'_A/t'_v)$, $(t'_s/t'_A)(t'_A/t'_{CD})$ and $t'_s/t'_A(t'_A/t'_{DIFF})$. Given the definitions in (2.15), the ratios of the acoustic time to each of the viscous, conductive and diffusion time scales are proportional to the Knudsen number $Kn = \nu'_0/a'_0\ell'$, which must be very small in a continuum gas. Except for exceptionally large ratios t'_s/t'_A , all transport terms are suppressed in (2.11), (2.12) and (2.14) in the limit $Kn \rightarrow 0$. In particular, when $t'_s = t'_A$, the full nonlinear compressible Euler equations for a source-driven (\dot{Q}_s) system are recovered in the limit $Kn \rightarrow 0$. The thermomechanically induced Mach number, $M = u'/a' = a'_0 u / a'_0 a = O(1)$. However, it must be stated that for sufficiently large values of τ , the combination $(t'_s/t'_{CD})C$ could be $O(1)$, thus accounting for a very large heat flux due to an asymptotically large τ . This is not a likely physical scenario. In the absence of transport physics, traditional flame propagation cannot occur leaving only the possibility of spontaneous reaction waves or what Kassoy and Clarke (1985) called “fast flames”, and reactive gasdynamic waves.

The limit $t'_s/t'_A \rightarrow 0$ is studied initially with the objective of developing a transparent understanding of the physics of the evolving system when the heat addition process is relatively fast. This corresponds to what many authors refer to as “instantaneous” heat addition. A second advantage is that a fully analytical solution can be obtained. In order to include a pressure gradient driven flow field in the limit, (2.11) implies that the speed must be rescaled

$$u = (t'_s/t'_A)U \quad , \quad (2.18)$$

so that the associated induced Mach number

$$M = \frac{u'}{a'} = \frac{u'/a'_0}{a'/a'_0} \equiv \frac{u}{a} = O(t'_s/t'_A) \ll 1, \quad a = O(1) \quad (2.19)$$

is subsonic. It follows from (2.11) and (2.16) that the momentum equation takes the form,

$$\rho \left[U_t + (t'_s/t'_A)UU_x \right] = -\frac{p_x}{\gamma} + (t'_s/t'_A)Kn \tilde{V} \quad (2.20)$$

where $Kn \rightarrow 0$ in the limit and \tilde{V} is the rescaled nondimensional viscous term.

If (2.18) is used in (2.10), it follows that the density must be rescaled by

$$\rho = 1/T_i(x) + (t'_s/t'_A)^2 R \quad (2.21)$$

with the results that in the limit

$$R_t + (\rho U)_x = 0 \quad (2.22)$$

Then the energy equation (2.12) is transformed to

$$\begin{aligned} \rho \left[T_t + (t'_s/t'_A)^2 U T_x \right] &= -(\gamma - 1)(t'_s/t'_A)^2 p U_x + (t'_s/t'_{CD}) C + \\ &\quad + \gamma(\gamma - 1)(t'_s/t'_v)(t'_s/t'_A)^2 D + q_R \rho \dot{Q}_s \quad , \end{aligned} \quad (2.22a)$$

$$q_R = q'_R/e'_0 \quad , \quad (2.22b)$$

the species equation is

$$Y_t + (t'_s/t'_A)^2 U Y_x = -\dot{Q}_s + (t'_s/t'_{DIFF}) \mathcal{D} \quad , \quad (2.23)$$

and the state equation becomes

$$p = \left[\frac{1}{T_i(x)} + (t'_s/t'_A)^2 R \right] T \quad (2.24)$$

The asymptotically reduced describing equations, initial and boundary conditions are

$$R_t + (U/T_i(x))_x = 0 \quad (2.25)$$

$$U_t = -\frac{p_x}{\gamma} T_i(x) \quad (2.26)$$

$$p = T/T_i(x) \quad (2.27)$$

$$T_t = q_R \dot{Q}_s \quad (2.28)$$

$$Y_t = -\dot{Q}_s \quad (2.29)$$

$$t = 0; \quad (T, p, \rho) = \left(T_i(x), 1, \frac{1}{T_i(x)} \right), \quad u = 0, \quad Y = 1 \quad (2.30)$$

where $T_i(0) = 1 + \tau$ and $T_i(1) = 1$. It is implicit in the analysis that the nondimensional parameters q_R and τ , defined in (2.22b) and (2.16), respectively, are $O(1)$ quantities. Asymptotically large heat of reaction or temperature differences would imply the need for rescaling of T , p and U . Kassoy (2010) has considered heat addition large compared to the initial internal energy, which has a nonintuitive consequence on the thermomechanics.

The physical interpretation of the reduced equation system (2.25)-(2.30) enables a fundamental understanding of the thermomechanical consequences of “fast” heating, $t'_s/t'_A = o(1)$. Equation (2.28) describes constant volume heating from the source. The rising temperature is accompanied by rising pressure, defined in (2.27). The induced speed, described by (2.26), demonstrates that regardless of how fast energy deposition occurs, ($t'_s/t'_A \rightarrow 0$), there will be a mechanical response as long as a temperature-pressure gradient exists. The weak density change is given by (2.25) in the context of (2.21). Similar equations appear in Kassoy (2010, 2014a, 2014b). Fully analytical solutions for (2.25)-(2.29) subject to the initial conditions in (2.30) follow,

$$T = T_i(x) + q_R \int_0^t \dot{Q}_s(x, \hat{t}) d\hat{T} \quad (2.31)$$

$$p = 1 + q_R \int_0^t \frac{\dot{Q}_s(x, \tilde{t})}{T_i(x)} d\tilde{t} \quad (2.32)$$

$$U = -\frac{T_i(x)}{\gamma} q_R \int_0^t d\tilde{t} \int_0^{\tilde{t}} \left(\frac{\dot{Q}_s(x, \tilde{t})}{T_i(x)} \right)_x d\tilde{t} \quad (2.33)$$

$$R = - \int_0^t \left(\frac{U}{T_i(x)} \right)_x d\tilde{t} \quad (2.34)$$

$$y = 1 - \int_0^t \dot{Q}_s d\tilde{t} \quad (2.35)$$

The reader should recognize that the results are valid for any source \dot{Q}_s . The formal analytical solutions in (2.31)-(2.35) provide insights into the dependence of variables on the nondimensional heat of reaction, q_R , and the nondimensional heat source distribution in space and time, $\dot{Q}_s(x, t)$, as well as on the initial temperature distribution $T_i(x)$. In addition, (2.33) can be used to identify the speed of the fluid expelled from the hot spot at $x = 1$, where $T_i = 1$. Given the small Mach number in (2.18), the thermomechanical disturbances, in the unheated gas, $x > 1$, will be weak acoustic waves.

The solutions in (2.31-2.35) can be simplified considerably for an asymptotically small linear negative temperature gradient represented by

$$T_i(x) = 1 - \alpha x \dots, \alpha = o(1) \quad , \quad (2.36)$$

so that the variables depend only on the heat source distribution $Q_s(x, t)$ in a first approximation. This perspective will be useful in the subsequent study of an Arrhenius, high activation energy reaction as the source of thermal energy addition.

When the energy addition time-scale is longer, $t'_s/t_A = O(1)$, (2.10)-(2.14) are essentially the compressible Euler equations with a heat source, $q'_R/e'_0 = O(1)$. The transport terms remain suppressed. These equations describe a fully compressible thermo-mechanical process evolving from the transient, spatially resolved energy addition on the time-scale t'_s . In this case wave propagation within the hot spot occurs on the same time-scale as the energy addition, thus facilitating the compressible (variable density) response. The equation structure implies unequivocally that all thermodynamic variables undergo $O(1)$ changes, in contradistinction to the fast heating limit process, and that the induced Mach number,

$$M = u'/a' = u/a = u/(T)^{1/2} = O(1) \quad . \quad (2.37)$$

The Mach number of the fluid expelled from the heat spot is of the same order and is the source of the “piston effect” driving strong mechanical disturbances (e.g. shocks) into the unheated cold environment. During the heat addition time scale, t'_s , the order of magnitude of fluid motion in the hot spot and beyond is quantified by

$$D' = O(u't'_s) = O(a'_o \ell' / a'_0) = O(\ell') \quad (2.38)$$

while the generated shock wave will move the same order of magnitude distance,

$$d'_s = O(a'_0 t'_s) = O(\ell') \quad , \quad t'_s/t'_A = O(1) \quad (2.39)$$

This result implies that the expelled fluid will be able to support the shock during the entire heat addition process, $\dot{Q}_s(x, t) > 0$.

3. Thermomechanical analysis for a reactive gas in the fast heating limit: $\mu \ll 1$.

In the following paragraphs an Euler-based analysis is presented for a single-step, high activation energy, exothermic reaction in order to include a specific chemical heat source, similar to that in Kassoy (2014a). The objective is to address the Zeldovich concept with a rational systematic mathematical model.

The dimensional (primed (')) Euler equations can be written as:

$$\rho'_{t'} + (\rho' u')_{x'} = 0 \quad (3.1a)$$

$$\rho'(u'_{t'} + u' u'_{x'}) = -p'_{x'} \quad (3.1b)$$

$$\rho'(e'_{t'} + u' e'_{x'}) = -p' u'_{x'} + \rho' A' q'_R Y e^{-E'/R'T'} \quad (3.1c)$$

$$Y_{t'} + u' Y_{x'} = -A' Y e^{E'/R'T'} \quad (3.1d)$$

where ρ' , p' , T' are the usual thermodynamic variables, u' represents the gas speed induced by energy addition, e' is the internal energy ($C'_v T'$), where the specific heat is treated as a constant, A' is the preexponential (frequency) factor in the Arrhenius rate term, E' is the activation energy, R' is the universal gas constant, q'_R is the heat of reaction and Y is the nondimensional reactant concentration.

Nondimensional thermodynamic variables are defined relative to an equilibrium gas state denoted by ρ'_0 , p'_0 , T'_0 : $(\rho, p, T = (\rho'/\rho'_0, p'/p'_0, T'/T'_0))$. It follows that $e = e'/e'_0$, where $e'_0 = C'_v T'_0$. The gas speed is nondimensionalized by the equilibrium speed of sound, $(a'_0 = \sqrt{\gamma R' T'_0})$, $u = u'/a'_0$. The space and time variables are defined by $x = x'/\ell'$ and $t = t'/t'_s$ where ℓ' defines the characteristic length scale of prescribed initial spatial inhomogeneities in the variables, ρ' , p' , T' , Y and $t'_s = \varepsilon \exp(1/\varepsilon)/A'$. (a traditional thermal explosion induction time), where $\varepsilon = R' T'_0/E$ is the small activation energy parameter and $q_R = q'_R/e'_0$. Many of these variable definitions differ from those used by Short (1997).

The nondimensionalized conservation equations take the form:

$$\rho_t + \mu(\rho u)_x = 0 \quad (3.2a)$$

$$\rho(u_t + \mu u u_x) = -\mu p_x/\gamma \quad (3.2b)$$

$$\rho(T_t + \mu u T_x) = -\mu(\gamma - 1)p u_x + A' t'_s q_R \rho Y e^{-1/\varepsilon T} \quad (3.2c)$$

$$Y_t + \mu u Y_x = -A' t'_s Y e^{-1/\varepsilon T} \quad (3.2d)$$

where $\mu = t'_s/t'_A$ is the ratio of the characteristic thermal explosion induction time to the local acoustic time $t'_A = \ell'/a'_0$. The nondimensional state equation for a perfect gas:

$$p = \rho T \quad (3.3)$$

completes the mathematical model. The variables in (3.2) and (3.3) are subject to the following initial conditions:

$$t = 0 : \rho = \rho_i(x), p = 1, T = T_i(x), u = 0, Y = 1, 0 \leq x \leq 1, \quad (3.4)$$

corresponding to an initial nonhomogeneity in density and temperature on the dimensional length scale ℓ' . This finite model of an initial disturbance is chosen with the explicit objective of identifying the thermomechanical response of the disturbed gas and consequences of the response to the gas external to the disturbed volume.

3.1. Induction time theory for a spatially dependent thermal explosion

Following Short (1997), an asymptotic analysis is formulated for a high activation energy reaction ($\varepsilon \ll O(1)$) where the induction time is short compared to the acoustic time of the heated volume ($\mu \ll O(1)$), again to obtain a complete analytical solution. The former requires that the thermodynamic variables be defined by the traditional thermal explosion asymptotic expansions, valid in the limit $\varepsilon \rightarrow 0$.

$$(\rho, p, T) = \left(1 + \varepsilon(R, P, \varphi) + O(\varepsilon^2) \right) \quad (3.5)$$

where R, P, φ are spatially variable, time-dependent descriptions of chemically driven perturbations from the initial thermodynamic state: e.g. $t = 0$. $(R, P, \varphi) = (R_i(x), 1, \varphi_i(x))$, where each is nonzero only in $0 \leq x \leq 1$. The asymptotic expansions in (3.5) imply that the appropriate initial conditions for temperature, pressure and density take the form: $T(0, x) = T_i = 1 + \varepsilon\phi_i(x)$. $p(0, x) = 1$, $\rho(0, x) = 1 - \varepsilon\phi_i(x)$.

As a result, the temperature difference parameter in (2.17), $(\tau) = O(\varepsilon)$, so that an asymptotically small imposed temperature gradient is the driver for the entire evolutionary process to follow.

Similarly,

$$Y : 1 - \varepsilon W + O(\varepsilon^2) \quad (3.6)$$

where W is the perturbation in the reactant concentration: at $t = 0$, $W = W_i(x) = 0$ in $0 \leq x \leq 1$.

Initially (3.2a)-(3.2d) take the form:

$$R_t + (\mu/\varepsilon)(\rho u)_x = 0 \quad (3.7a)$$

$$\rho(u_t + \mu uu_x) = -\mu\varepsilon P_x/\gamma \quad (3.7b)$$

$$\rho(\varphi_t + \mu u\varphi_x) = -(\mu/\varepsilon)(\gamma - 1)p u_x = \rho q_R e^\varphi \quad (3.7c)$$

$$W_t + \mu u W_x = e^\varphi \quad (3.7d)$$

This mathematical system contains two independent nondimensional parameters (μ and ε). The speed and density variables are to be rescaled to obtain a lowest order reduced mathematical model that couples an explicit mechanical response of the gas to localized spatially distributed transient heating. Gas motion induced by an evolving spatial pressure gradient in (2.46b) can be assured in the limit $\varepsilon \rightarrow 0$, and $\mu \ll O(1)$ if

$$u = \varepsilon\mu U \quad (3.8)$$

It follows that (3.7a-d) takes the form

$$R_t + \mu^2(\rho U)_x = 0 \quad (3.9a)$$

$$\rho(U_t + \varepsilon\mu^2 U U_x) = -P_x/\gamma \quad (3.9b)$$

$$\rho(\varphi_t + \varepsilon\mu^2 U \varphi_x) = -\mu^2(\gamma - 1)p U_x + \rho q_R e^\varphi \quad (3.9c)$$

$$W_t + \varepsilon\mu^2 U W_x = e^\varphi \quad (3.9d)$$

Equation (3.9a) and the initial conditions imply that to account for density variation associated with the gas motion, the density perturbation must be rescaled by

$$R = -\varphi_i(x) + \mu^2 \tilde{R} \quad (3.10)$$

where $\varphi_i(x)$ represents the initial density distribution compatible with (3.5). Equation

(3.9a) takes the form

$$\tilde{R}_t + (\rho U)_x = 0 \quad (3.11)$$

The equation set composed of (3.9b-d) and (3.11) describe a weakly variable density response of a gas to relatively rapid energy deposition, ($\mu \ll O(1)$). The local expansion Mach number is characterized by

$$M = \frac{\mu'}{a'} = \frac{u}{a} = \frac{u}{\sqrt{T}} = \frac{\varepsilon \mu U}{\sqrt{T}} = O(\varepsilon \mu) = o(1) \quad (3.12)$$

In the limit $\varepsilon \rightarrow 0$, and $\mu \ll O(1)$, (3.11), (3.9b-d), (2.3) and (2.4) yield the reduced system of initial value equations and conditions:

$$\tilde{R}_t + U_x = 0, \quad t = 0 : \quad \tilde{R} = \tilde{R}_i(x) = 0, \quad U = U_i(x) \quad (3.13a)$$

$$U_t = -P_x/\gamma, \quad t = 0 : \quad P = 0 \quad (3.13b)$$

$$\varphi_t = q_R e^\varphi, \quad t = 0 : \quad \varphi = \varphi_i(x) \quad (3.13c)$$

$$P = \varphi + O(\mu^2) \quad (3.13d)$$

$$W_t = -e^\varphi, \quad t = 0 : \quad W = W_i(x) = 0 \quad (3.13e)$$

Equation (3.13c) describes a constant volume heat addition process as envisaged by Zeldovich (1980), for the temperature perturbation φ , response to energy addition. The rate of temperature perturbation increase is proportional to the size of q_R , the heat of reaction defined in (2.22b). The solution is given by

$$\varphi = \ln \frac{1}{(e^{-\varphi_i(x)} - q_R t)} = \varphi_i(x) + \ln \frac{1}{(1 - t/t_e(x))} \quad (3.14)$$

where $\varphi_i(x)$ is an imposed initial (small) temperature disturbance of the type considered by Zeldovich (1980) in his spontaneous wave theory. The temperature perturbation solution in (3.14) appears in Short (1997). It has a classical thermal explosion singularity at a spatially dependent time t_e where

$$t_e(x) = \frac{e^{-\varphi_i(x)}}{q_R} \quad (3.15)$$

A simple calculation demonstrates that $\frac{d\varphi}{dq_R} > O$, as expected from physical perspectives. As noted by numerous authors (Jackson, Kapila and Stewart 1989; Kapila and Dold 1989; Short 1997), (3.15) implies that the thermal explosion spreads down an imposed negative initial temperature gradient ($\varphi'_i(x) < 0$), where the bold prime denotes a spatial derivative. The inverse of the thermal explosion propagation speed is found from (2.15) to be

$$\frac{dt_e}{dx} = \frac{-\varphi'_i(x)e^{-\varphi_i(x)}}{q_R} \quad (3.16)$$

while a comparison of the dimensional propagation speed relative to the characteristic dimensional speed of sound, a'_0 can be obtained from (3.16) as

$$\frac{dx'/dt'_e}{a'_0} = -\frac{q_R}{\mu} \frac{e^{\varphi_i(x)}}{\varphi'_i(x)} \quad (3.17)$$

showing quantitatively that the thermal explosion moves through the volume of heated gas at a locally supersonic speed, proportional to q_R , when $\mu \ll O(1)$ as noted by Friedman and Herrera (1990), Kapila and Dold (1989), and referred to in Short (1997). Equation (3.17) demonstrates that when the gradient of the initial temperature distribution

x	$\phi_i(x) = 1 - x$	$t_e(x)$
0	1	0.37
0.25	0.75	0.47
0.5	0.5	0.61
0.75	0.25	0.78
1.0	0	1.0

TABLE 1. The explosion time $t_e(x)$ as a function of location for a linear temperature gradient $\varphi_i(x) = 1 - x$, with $q_R = 1$.

is zero, the propagation speed is infinite, a non-physical result noted by Short (1997), interpreted to mean that a spatially homogeneous thermal explosion occurs. Jackson, Kapila and Stewart (1989) have noted that the reaction evolution process differs if at a symmetry point $x = 0$, the gradient is zero or less than zero. Equation (3.17) can be used to show that the reaction wave moves a distance $O(\ell')$ in the heat release time t'_e .

Equation (3.14) demonstrates that an initial temperature inhomogeneity is essential for φ to be spatially dependent. This is crucial to supporting the induced gas motion described by (3.13b). The pressure disturbance is equal to the temperature disturbance. It must be emphasized that in the **absence** of an initial small temperature disturbance, the solution in (3.14) shows that the thermal explosion induction period is characterized by a spatially homogeneous thermal temperature, that the spatial pressure gradient is absent and that no local gas motion can occur. Kassoy (2010) has discussed the role of localized gas expansion as an immediate source of mechanical disturbances.

A Schwab-Zeldovich formulation can be used with (3.13c) and (3.13e) to show that

$$W = \frac{1}{q_R} \ln \frac{1}{(1 - t/t_e(x))} \quad (3.18)$$

when $W(0, x) = 0$.

The thermally induced gas speed can be found from the integral of (3.13b) ((3.13d) and (3.14) are employed):

$$U = -\frac{\varphi'_i(x)}{q_R \gamma} e^{-\varphi_i(x)} \ln \frac{1}{(1 - t/t_e(x))} \quad (3.19)$$

where it is assumed that there is no initial speed disturbance, $U_i(x) = 0$. Equation (3.19) demonstrates that $U > 0$ when $\varphi'_i(x) < 0$, meaning that gas expansion occurs and that the speed is singular when the explosion time t_e is reached at a given location. Equation (3.19) also shows that there is thermally induced low Mach number gas motion throughout the heated volume as the reaction wave propagates.

The analytical solution in (3.14) and (3.19) and the results in tables 1 and 2 enable a complete description of the thermomechanical response of the heated gas. Table 1 lists the value of the explosion time by location x when an initially linear temperature distribution exists, $\varphi_i(x) = 1 - x$ and $q_r = 1$. The results show that a thermal explosion occurs at $x = 0$ when $t = 0.37$ for $q_r = 1$ and then propagates through the inhomogeneity arriving at $x = 1$ when $t = 1$.

Finally (3.13) and (3.20) can be used to find the solution for the weak density change represented by \tilde{R} . The logarithmic dependence in (3.18) and (3.19) is found once again.

t	$U(0, t)$	$U(0.5, t)$	$U(1, t)$
0	0	0	0
0.1	.08	.08	.08
0.1	.21	.18	.16
0.3	.44	.30	.33
.37	∞	.41	.33

TABLE 2. The induced fluid speed at locations $x = 0, 0.5$ and 1.0 for times values $t \leq t_e(0) = 0.37$ calculated with $\gamma = 1.4$ and $\varphi_i(x) = 1 - x$, with $q_R = 1$.

3.2. Thermal explosion singularity analysis

The theory predicts a continuous sequence of thermal explosions propagating down the specified gradient. The initial singularity occurs at $x = 0$ when $t_e = 0.37$ for $q_r = 1$. In particular, the expansions in (3.5) and (3.6) fail when $\varepsilon\varphi(0, t) = O(1)$. Similarly, from (3.6), (3.10), and (3.19), $\varepsilon\tilde{R}(0, t) = O(1)$ and $\varepsilon W(0, t) = O(1)$ in the limit $t \rightarrow t_e(0)$. It follows from (2.53) that

$$\varepsilon \ln \left[1 / \left(1 - t/t_e(0) \right) \right] = O(1) \quad (3.20)$$

or

$$\left[t_e(0) - t \right] = \exp(O(-1/\varepsilon)) \quad (3.21)$$

implying that when t is exponentially close to $t_e(0)$, a full scale explosion will occur in the vicinity of $x = 0$, characterized by $O(1)$ changes in T and Y , as well as $\rho = 1 + O(\mu^2)$, as all the fuel is consumed and the complete heat of reaction is released. Equation (3.21) demonstrates that the time scale of the full scale explosion is exponentially short compared to the induction time scale $t_e(0)$. This concept has been used by Kassoy (1977) to describe the full scale explosion in a spatially homogeneous system by defining a nonlinear time scale transformation:

$$t_e - t = \exp(-s/\varepsilon) + O(1) , \quad (3.22)$$

where $s > 0$ is the $O(1)$ explosion time variable. The application of this unusual scaling to the current spatially distributed system is the subject of section 4. This scaling transformation differs fundamentally from that used by Short (1997) to describe the post-induction period phenomena. In particular, the ε -parameter is absent from the transformation used. As a result, the subsequent analysis cannot describe post-induction physics on the exponentially short time scale defined in (3.22).

Table 2 lists the induced speed at $x = 0$, $x = 0.5$ and the edge of the heated region, $x = 1$, demonstrating that gas is expelled at the nonhomogeneity edge ($x = 1$) for all times up to and including $t_e = 0.37$, for the case $\varphi'_i(x) = -1$. Furthermore, (3.19) can be used to show that the gas speed at $x = 1$ will continue to increase for time values up to $t = 1$ when the thermal explosion singularity leads to an unbounded value of the scaled speed U . It should be noted here that the thermal energy released during the induction period is asymptotically small, $O(\varepsilon)$ because so little reactant is consumed and that the induced nondimensional kinetic energy,

$$u'^2 / e'_o = O(\varepsilon^2 \mu^2) \quad (3.23)$$

It should be clear that the initial disturbance in the temperature perturbation $\varphi_i(x)$

considered by Zeldovich (1980) is absolutely essential to describing a meaningful thermo-mechanical response to localized, spatially resolved, transient energy deposition. Short (1997) has examined the consequences of nonzero initial conditions in the remaining variables.

In summary, during the induction period, a weak reaction process occurs throughout the hot spot until a thermal explosion occurs initially at $x = 0$ and $t_e(0) = 0.37$ and then propagates into the entire hot spot reaching the edge at $t = 1$. The results in table 2 show that the localized heat addition induces a gas expansion speed $U(x, t)$ throughout the spot. The fluid expelled at the edge, $x = 1$, with speed $U(1, t)$ acts as a piston driving weak $O(\varepsilon\mu)$, acoustic disturbances into the unheated environmental gas $x > 1$.

4. The post-induction time analysis: $\mu \ll 1$.

A full scale explosion characterized by an $O(1)$ increase in temperature and pressure will be initiated at $x = 0$, $t = 0.37$, on a time scale exponentially short compared to the induction time scale, in a tiny region around the origin. Thermomechanical analyses for relatively rapid addition (Kassoy 2010, 2014a) of a large amount of energy suggest that the energy addition will be characterized by a nearly constant volume process with pressure rising with temperature. The latter will maximize at the adiabatic explosion value $1 + q_R$. The result will be an isolated high temperature and pressure spot in a cold, low temperature environment. Subsequent to the reaction completion, the ephemeral high temperature and pressure spot will expand on the acoustic time scale, far larger than the induction time and the exponentially short post-induction reaction time scale defined by (3.22), leading to a substantial mechanical disturbance in the unheated gas.

The post-induction period mathematical formulation is based on the nonlinearly rescaled time in (3.22) and the related rescaling of the planar space variable, x ,

$$x = x_F(t) - X \exp(-s/\varepsilon) \quad (4.1)$$

The spatial rescaling defines the distance traveled by the propagating thermal explosion (reaction front) during the exponentially short time scale defined by (3.22). Both the length and time scales germane to the physics of the post-induction period are exponentially short with respect to the spot dimension ℓ' and the induction time-scale, t'_e , defined in the paragraph above (3.2a). When (3.22) and (4.1) are employed in (3.2), and the limit $\varepsilon \rightarrow 0$ is taken the lowest order result is related closely to that in the analysis of a post-induction period process in a spatially homogeneous system (Kassoy 1977):

$$T = 1/(1-s) , \quad p = 1/(1-s) , \quad Y = 1 - \frac{sq_R}{(1-s)} \quad (4.2a, b, c)$$

$$\rho = 1 + O(\mu^2) , \quad u = \mu V \quad (4.2d, e)$$

$$T_{MAX} = T_{ADIABATIC} = 1 + q_R , \quad 0 \leq s \leq s_{MAX} = \frac{q_R}{(1+q_R)} < 1 \quad (4.3a, b)$$

These results describe the consequences of complete reactant consumption and concomitant heat release in an essentially inertially confined, constant volume heat addition process on a time scale exponentially short compared to characteristic induction period time-scale t'_e . To lowest order the temperature and pressure are spatially homogeneous in the exponentially thin reaction zone just behind the propagating thermal explosion singularity. The scaled variables can be used to demonstrate that in the reaction zone the characteristic reaction time scale is $t'_R = O(t'_s e^{-s/\varepsilon})$ compared to the local acoustic time scale, $t'_{RA} = O(t'_A e^{-s/\varepsilon})$ based on the thickness of the reaction zone and characteristic

acoustic speed, a result compatible with the inertial confinement mentioned earlier. It is also important to note that the local conduction time scale, based on the width of the reaction zone and a characteristic value of the thermal diffusivity is small compared to the local reaction time if $\exp(-1/\varepsilon) \gg (\mu)(Kn)$ where the latter parameter represents the Knudsen number. As a result the reaction zone is not affected by transport effects relative to the cooler, unburned gas in front of the propagating thermal explosion. The post-induction period solutions above, evolving on a phenomenally short time scale show that the propagating thermal explosion leaves behind a spatially homogeneous hot, high pressure spot, that can expand on the relatively long acoustic time scale, ℓ'/a_0 in analogy with a shock tube process. The $O(1)$ pressure differential, defined by $p_{MAX} = 1 + q_R$ is the source of a strong shock wave.

5. Modest heating rate theory: $\mu = 1$.

The modest heating rate models considered by Short (1997), Vasquez-Espi' and Liñan (2001), Jackson *et al.* (1989), among many others, describe the thermal response to chemical heat addition on a time scale identical to the acoustic time of the hot spot. The conservation equations derived and employed for solution development are equivalent to the Clarke equation (1985) describing only the temperature response. It is useful to revisit the models in the context of the Zeldovich problem (1980) to describe a novel set of equations that describe pressure and velocity responses of the gas to the transient, spatially resolved temperature distribution described by the Clarke equation, as well as to display an alternative to the Clarke equation. The foundational equations are those in (3.2) and (3.3) with $\mu = 1$:

$$\rho_t + (\rho u)_x = 0 \quad (5.1a)$$

$$\rho(u_t + uu_x) = -p_x/\gamma \quad (5.1b)$$

$$T_t + uT_x = -(\gamma - 1)Tu_x + A't'_s q_R Y e^{-1/\varepsilon T} \quad (5.1c)$$

$$Y_t + uY_x = -A't'_s Y e^{-1/\varepsilon T} \quad (5.1d)$$

$$p = \rho T \quad (5.1e)$$

$$t = 0 : \quad p = 1 \quad , \quad T = 1 + \varepsilon\varphi_i(x) \quad , \quad Y = 1 \quad , \quad \rho = 1 - \varepsilon\varphi_i(x) \quad , \quad u = 0 \quad (5.1f)$$

subject to the initial conditions in (2.30) where,

$$A't'_s = \varepsilon e^{1/\varepsilon} \quad (5.2)$$

given the definition of the traditional thermal explosion induction period time-scale, t'_s , in the paragraph just above (3.2). The variable definitions differ from those used in Short (1997). The current choices, beginning with (2.6) and (2.9), are used to derive non-dimensional equations that can be interpreted physically in terms of parameters significant to the physical phenomena.

If a high activation energy analysis is used to describe the thermal induction period when $\mu = 1$, the dependent variables are:

$$(p, \rho, T) = \left(1 + \varepsilon(P, R, \varphi) + O(\varepsilon^2) \right) \quad , \quad Y = 1 - \varepsilon W \quad (5.3a, b)$$

$$u = \varepsilon U \quad (5.3c)$$

where (5.3e) is needed to derive a momentum equation capable of describing the thermomechanically induced velocity. In particular, the model is constructed for a hot spot of specific dimension ℓ' and a nondimensional heat of reaction, q_R , defined relative to the

characteristic initial internal energy rather than the enthalpy. Equation (5.2) enables the model equation (5.1c) to display explicitly the role of the heat of reaction in the energy dynamics of the problem.

If (5.2) and (5.3) are used in (5.1) and the limit $\varepsilon \rightarrow 0$ is taken, the reduced conservation and state equations for the thermodynamic perturbation quantities, the fuel concentration and induced velocity U are given by

$$R_t + U_x = 0 \quad (5.4a)$$

$$U_t = -P_x/\gamma \quad (5.4b)$$

$$\varphi_t = -(\gamma - 1)U_x + q_R e^\varphi \quad (5.4c)$$

$$W_t = e^\varphi \quad (5.4d)$$

$$P = R + \varphi \quad (5.4e)$$

These equations are subject to the following initial conditions:

$$t = 0; \quad P = 0, \quad \varphi = \varphi_i(x), \quad W = 0, \quad R = -\varphi_i(x), \quad U = 0 \quad (5.5)$$

These Eulerian coordinate equations describe perturbation variable changes due to chemical heat release, modeled by e^φ , and the initial temperature disturbance. In the absence of the heat source term, e^φ , they describe classical linear acoustical disturbances (Liewen 2012) driven by an initial disturbance. Equation (5.4c) shows that local gas expansion, $U_x > 0$, retards growth in the temperature disturbance, noted earlier by Vasquez-Espi and Liñan (2001), among others. The scaling on u in (5.3c) enables a fully integrated thermoacoustic model with the induced speed generated by a pressure gradient in (5.4b).

Familiar manipulations with (5.4) enable a pressure-temperature relationship to be derived:

$$P - \left(\frac{\gamma}{\gamma - 1} \right) \varphi = \left(\frac{\gamma}{\gamma - 1} \right) \varphi_i(x) - \frac{q_R}{(\gamma - 1)} \int_0^t e^\varphi d\hat{t} \quad (5.6)$$

a result that replaces the standard isentropic relation for an adiabatic system. The integral represents the accumulated effect of chemical heat addition during an interval of time, t . Equation (5.6) can then be used to derive the following set of describing equations:

$$U_{tt} = U_{xx} - \frac{q_R}{\gamma} e^\varphi \varphi_x \quad (5.7a)$$

$$P_{tt} = P_{xx} + q_R e^\varphi \varphi_t \quad (5.7b)$$

$$\varphi_{tt} = \varphi_{xx} + \frac{q_R}{\gamma} \left(e^\varphi \varphi_t - \int_0^t (e^\varphi \varphi_x)_x d\hat{t} - \varphi''_i(x) \right) \quad (5.7c)$$

Equations (5.7a,b) describe a thermoacoustic wave propagation process within the hot spot driven by transient, spatially resolved chemical heat release. The integro-differential equation, (5.7c) provides a related description for the thermoacoustic response of the hot spot gas to auto-ignition and is an alternative to the Clarke equation,

$$\left(\varphi_t - q_R e^\varphi \right)_{tt} = \left(\varphi_t - \frac{q_R}{\gamma} e^\varphi \right)_{xx} \quad (5.8)$$

The former can be differentiated with respect to t to derive the latter. It is often stated that (5.8) describes the competition between simultaneous constant volume and constant pressure heat addition. Equation (5.7) appears to provide a clearer, physically oriented

interpretation of the impact of localized heating on the generation of small amplitude disturbances associated with the common wave equation operator in each equation.

6. Conclusions

A comprehensive, systematic, asymptotic analysis is employed to quantify the evolution of a “spontaneous reaction wave” propagating within a finite hot spot, defined by an imposed weak temperature non-uniformity embedded in a larger volume of relatively cold reactive gas. One-step, high activation energy ($\varepsilon \rightarrow 0$) kinetics define the reaction process. Ignition occurs at the local temperature maximum, only $O(\varepsilon)$ larger than the colder value external to the spot. The reaction spreads down the $O(\varepsilon)$ negative temperature gradient. Classical thermal explosion induction period analysis for both fast ($\mu \rightarrow 0$) and modest ($\mu = 1$) heat release time scales describes a period of $O(\varepsilon)$ reactant consumption, limited energy addition leading to $O(\varepsilon)$ increases in temperature and pressure and a concomitant weak gas expansion with the hot spot, the source of expelled gas at the surface of the hot spot.

When the induction time-scale (characteristic of chemical heat release) is short compared to the acoustic time-scale of the hot spot (the limit $\mu \rightarrow 0$) a nearly constant-volume process characterizes the thermomechanical response of the gas. An $O(\varepsilon)$ spatial pressure distribution corresponding to the temperature disturbance of the same size is the source of an $O(\varepsilon\mu)$ induced gas seed. Gas expelled through the hot spot surface is the source of weak acoustic compression waves (The “piston” effect) in the gas external to the spot. A complete analytical solution of the asymptotically reduced equations is possible in the limit ($\varepsilon \rightarrow 0, \mu \rightarrow 0$). Results define the end of the induction period at each x -location when a local thermal explosion singularity occurs at $t_e(x)$. The propagation of the singularity down the asymptotically small negative temperature gradient defines the Zeldovich “spontaneous reaction wave” properties. The value of $t_e(x)$ increases from the hottest to the coldest locations in the spot and can be inverted to define the supersonic propagation Mach number for the translating singularity.

When the induction time-scale is equal to the local acoustic time ($\mu = 1$), the asymptotically reduced equations describe compressible heat addition. The $O(\varepsilon)$ temperature perturbation is described by a physically transparent alternative to the “Clarke” equation. The $O(\varepsilon)$ pressure and induced speed responses to transient, spatially resolved heat release are described by non-homogeneous linear wave equations. These equations have no obvious analytical solutions, but define clearly the character and properties of the induction period physics. Numerical results from Clarke’s equation are reported by many authors cited in the introduction. They can be interpreted to mean that a classical logarithmic thermal explosion singularity will occur at finite values of time, $t^*(x)$, to be distinguished from the analytically obtained value $t_e(x)$ for the fast heating limit. New results from numerical solutions of (5.7) will be the subject of future work.

The post-induction period analyses offer new opportunities to understand the physics of extremely fast (explosive) reaction processes. In the limit $\mu \rightarrow 0$ the nonlinear transformations define exponentially short time and length scales. During and within these two scales, respectively, the reactant is totally consumed as the spatially homogeneous temperature rises to the adiabatic explosion value in a nearly constant-volume process, with a concomitant increase in the spatially homogeneous pressure. In the absence of a pressure gradient, there is no additional change in the fluid speed induced during the induction period. The analytical results are interpreted to mean that the reaction front, located at the thermal explosion singularity, propagates through the hot spot on the induction time-scale leaving behind a spatially uniform ephemeral high pressure and

temperature hot spot located in a larger volume of colder, low pressure gas. In analogy with a shock tube, the spot will expand on the much, much longer acoustic time scale with the result that a strong compression wave moves into the spot itself. In this regard the thermomechanical response of the spot, initiated by a tiny temperature gradient, is the primary source of major mechanical disturbances in the gas external to the original spot.

When $\mu = 1$, the high activation energy limit $\varepsilon \rightarrow 0$ for the post induction period produces the result that the temperature dependent part of the reaction term in the energy equation, $\exp((1/\varepsilon)[1 - (1/T)])$, is unbounded in the limit when $T > 1$. This type of singular behavior implies that the time derivative term in the energy equation must be equally large to obtain physically viable $O(1)$ -increases in temperature. These mathematical properties of the describing equations motivate the use of a nonlinear time rescaling, similar to that described earlier, but entirely independent of the logarithmic thermal explosion singularity found in the fast heating limit. It is hypothesized that an “explosion time” $t^*(x)$ can be defined and used to describe the exponentially short time scale. Here again one can expect essentially constant volume heating with pressure and temperature rising together as the adiabatic value is approached. The ephemeral high temperature and pressure spot will relax, with a process similar to that in a shock tube, on the longer acoustic time scale of the spot. It is important to recall that the reaction wave will cross the spot on the acoustic time scale so that the spot expansion process will be initiated during the induction period of the modest heating rate problem. The explicit analysis of the physical process is the subject of current research and will be reported in the future.

The present study describes physical phenomena occurring when transient, spatially distributed chemical heat addition takes place in a compressible gas. In particular, the quantitative analysis provides a cause-effect source for mechanical disturbances arising from localized energy addition. Applications to combustion chamber instability and engine knock are of interest. These phenomena can occur in a turbulent reactive flow environment characterized by localized temperature and/or mixture concentration inhomogeneities, which can act as preferential sites for ignition.

Acknowledgments

This research has been supported by Subcontract 2012-2756 between the Regents of the University of California, Irvine, and Kassoy Innovative Science Solutions LLC. The Air Force Office of Scientific Research provides the funding for the research effort “Reduced Basis and Stochastic Modeling of a Liquid Propellant Rocket Engine as a Complex System.” The principal investigator is Professor William Sirignano at the University of California, Irvine. His encouragement is appreciated as is the encouragement of the program manager, Dr. Mitat Birkan. Inspiring discussions about thermomechanics with my late colleague and co-author, J. F. Clarke, were influential in the development of this study and are gratefully acknowledged. Expert word-processing by Ellen Romig is much appreciated.

REFERENCES

CLARKE, J. F. 1978 A progress report on the theoretical analysis of the interaction between a shock wave and an explosive gas mixture. *College of Aeronautics Report 7801*, Cranfield Institute of Technology, Cranfield, U.K.

CLARKE, J. F. Finite amplitude waves in compressible gases, in *The Mathematics of Combustion*, J. D. Buckmaster, ed. SIAM Publications, Philadelphia, 1985, 183–245.

CLARKE, J. F. & KASSOY, D. R. 1984 High Speed Deflagration and Compressibility Effects in Dynamics of Shock Waves, Explosions and Detonations. eds. Bowen, J. R., Manson, N., Oppenheim, A. K. & Soloukhin, R. I. *Prog. in Astronautics and Aeronautics* **94**, 1975-185.

CLARKE, J. F., KASSOY, D. R. & RILEY, N. 1984 Shocks generated in a confined gas due to rapid heat addition at the boundary I. Weak shock waves. *Proc. Roy. Soc. Lond.* **A393**, 309-329.

CLARKE, J. F., KASSOY, D. R. & RILEY, N. 1984 Shocks generated in a confined gas due to rapid heat addition at the boundary II. Strong shock waves. 1984 *Proc. Roy. Soc. Lond.* **A393**, 331-351.

ECKETT, C. A., QUIRK, J. J. & SHEPHERD, J. 2000 The role of unsteadiness in direct initiation of gaseous detonations. *J. Fluid Mech.* **421**, 147-183.

FRIEDMAN, A. & HERRERO, M. A. 1990 A nonlinear, nonlocal wave-equation arising in combustion theory. *Nonlinear Anal.* **14**, 93-106.

GU, X. J., EMERSON, D. R. & BRADLEY, D. 2003 Modes of reaction front propagation from hot spots. *Comb. Flame* **133**, 63-74

JACKSON, T. L., KAPILA, A. K. & STEWART, D. S. 1989 Evolution of a reaction center in an explosive material. *SIAM J. Appl. Math.* **49**, 432-458.

KAPILA, A. K. & DOLD, J. W. 1989 A theoretical picture of shock-to-detonation transition in a homogeneous explosive. *Proceedings of the 9th Int'l Symposium on Detonation*, OCNR 113291-7, Office of Naval Research, Washington, D.C., 219-227.

KAPILA, A. K., SCHWENDEMAN, D. W., QUIRK, J. J. & HAWA, T. 2002 Mechanisms of detonation formation due to a temperature gradient. *CTM* **6**, 553-594.

KASSOY, D. R. 1977 The supercritical spatially homogeneous thermal explosion: initiation to completion. *Q. Jl. Mech. Appl. Math.* **30**, 71-89.

KASSOY, D. R. 2010 The response of a compressible gas to extremely rapid transient, spatially resolved energy addition: an asymptotic formulation. *J. Eng. Math.* **68**, 249-262.

KASSOY, D. R. 2014a Non-diffusive ignition of a gaseous reactive mixture following time-resolved, spatially distributed energy addition. *CTM* **18**, 101-116.

KASSOY, D. R. 2014b Mechanical disturbances arising from thermal power deposition in a gas. *AIAA J.* doi:10.2514/1 J052807

KASSOY, D. R. & CLARKE, J. F. 1985 The structure of a high speed deflagration with a finite origin. *J. Fluid Mech.* **150**, 253-280.

KULKARNI, R., ZELLHUBER, M. & POLIFKE, W. 2013 LES based investigation of autoignition in turbulent co-flow configurations. *Comb. Theory and Modeling* **17**, 224-259.

KURDYUMOV, V., SANZHEZ, A. L. & LIÑAN, A. L. 2003 A heat propagation from a concentrated external energy source in a gas. *J. Fluid Mech.* **491**, 379-410.

MAKVILADZE, G. M., & ROGATYKH, D. I. 1991 Non-uniformities in initial temperature and concentration as a cause of explosive chemical reaction in combustible gases. *Combust. Flame* **87**, 347-356.

MEYER, J. W. & OPPENHEIM, A. K. 1972 Dynamic response of a plane-symmetrical exothermic reaction center. *AIAA J.* **10**, 1509-1513.

PETERS, N., KERSCHGENS, B. & PACZKO, G. 2013 Super-knock predictions using a refined theory of turbulence. *SAE International Journal of Engines* **6**, 953-967.

POLUDNENKO, A. Y., GARDINER, T. A. & ORAN, E. S. 2011 Spontaneous transition of turbulent flames to detonation in unconfined media. *Phys. Rev. Letters* **107**, 054501-(1-4).

RADULESCU, M. I., SHARPE, G. J. & BRADLEY, D. 2013 A universal parameter quantifying explosion hazards, detonability and hot spot formation: The λ number. *Proc. of the Seventh International Seminar on Fire and Explosion Hazards*, edited by D. Bradley, G. Makhliladze, V. Molikov, P. Sunderland, & F. Tamini, University of Maryland/ publisher, Research Publishing, ISBN 978-981-08-7724-8, doi: 10.3850/978-08-7724-8.

SANKARAN, R., HONG, G. I., HAWKES, E. R. & CHEN, J. H. 2005 The effects of non-uniform temperature distribution on the ignition of a lean homogeneous hydrogen-air mixture. *Proc. Comb. Inst.* **30**, 875-882.

SEITENZAHL, I. R., MEAKIN, C. A., TOWNLEY, D. M. LAMB, D. Q. & TRURAN, J. W. 2009 Spontaneous initiation of detonations in white dwarf environments: determination of critical sizes. *Astrophysics. J.* **696**, 515-527.

SHORT, M. 1995 The initiation of detonation from general non-uniformly distributed initial conditions. *Phil. Trans. R. Soc. London A* **353**, 173-203.

SHORT, M. 1997 On the critical conditions for the initiation of a detonation in a nonuniformly perturbed reactive fluid. *SIAM J. Appl. Math* **57**, 1242-1280.

SILEEM, A., KASSOY, D. R. & HAYASHI, A. K. 1991 Thermally initiated detonation through deflagration to detonation transition. *Proc. Roy. Soc. Lond. A* **435**, 459-482.

VASQUEX-ESPI', C. & LIÑAN, A. 2001 Fast-non-diffusive ignition of a gaseous reacting mixture subject to a point energy addition. *CTM* **5**, 495-498.

ZELDOVICH, YA. B., LIBROVICH, V. B., MAKVILADZE, G. M. & SIVASHINSKY, G. J. 1970 On the development of detonation in a non-uniformly preheated gas. *Astronautica Acta* **15**, 313-321.

ZELDOVICH, YA. B. 1980 Regime classification of an exothermic reaction with nonuniform initial conditions. *Combust. Flame* **39**, 211-214.

ZELDOVICH, YA. B., GELFAND, B. E., TSYGANOV, S.A., FROLOV, S. M. & POLENOV, A. N. 1988 Concentration and temperature nonuniformities of combustible mixtures as reason for pressure wave generation. *Progr. Astronaut. Aeronaut.* **114**, 99-123.

1.

1. Report Type

Final Report

Primary Contact E-mail

Contact email if there is a problem with the report.

sirignan@uci.edu

Primary Contact Phone Number

Contact phone number if there is a problem with the report

949-824-3700

Organization / Institution name

University of California, Irvine

Grant/Contract Title

The full title of the funded effort.

Reduced Basis and Stochastic Modeling of a
Liquid Propellant Rocket Engine as a Complex System

Grant/Contract Number

AFOSR assigned control number. It must begin with "FA9550" or "F49620" or "FA2386".

FA9550-12-1-0156

Principal Investigator Name

The full name of the principal investigator on the grant or contract.

William A. Sirignano

Program Manager

The AFOSR Program Manager currently assigned to the award

Dr. Mitat Birkan

Reporting Period Start Date

06/01/2012

Reporting Period End Date

05/31/2015

Abstract

The four-institution research team has developed a framework for stochastic analysis of nonlinear combustion instability with triggering and in the use of reduced-basis models (RBM), large-eddy simulations, and multi-scale asymptotic models for the analysis. Results published during these three years and ongoing researches are briefly discussed and addenda with more detail are provided.

Distribution Statement

This is block 12 on the SF298 form.

Distribution A - Approved for Public Release

Explanation for Distribution Statement

If this is not approved for public release, please provide a short explanation. E.g., contains proprietary information.

SF298 Form

Please attach your SF298 form. A blank SF298 can be found [here](#). Please do not password protect or secure the PDF

The maximum file size for an SF298 is 50MB.

[Report documentation Page-Prof. Sirignano.pdf](#)

Upload the Report Document. File must be a PDF. Please do not password protect or secure the PDF . The maximum file size for the Report Document is 50MB.

[Reduced Basis and Stochastic Modeling --Final Performance Report- June, 2015.pdf](#)

Upload a Report Document, if any. The maximum file size for the Report Document is 50MB.

Archival Publications (published) during reporting period:

Publications are attached as Addenda to this Final Report or were attached in two prior Annual Reports.

Changes in research objectives (if any):

None.

Change in AFOSR Program Manager, if any:

None.

Extensions granted or milestones slipped, if any:

None.

AFOSR LRIR Number

LRIR Title

Reporting Period

Laboratory Task Manager

Program Officer

Research Objectives

Technical Summary

Funding Summary by Cost Category (by FY, \$K)

	Starting FY	FY+1	FY+2
Salary			
Equipment/Facilities			
Supplies			
Total			

Report Document

Report Document - Text Analysis

Report Document - Text Analysis

Appendix Documents

2. Thank You

E-mail user

Jun 15, 2015 19:04:27 Success: Email Sent to: sirignan@uci.edu